

German Microwave Conference - GeMiC 2005 -

University of Ulm

April 5 - 7, 2005

www.gemic2005.de

Conference Proceedings

Editor: Wolfgang Menzel, University of Ulm

VDE

ITG INFORMATIONSTECHNISCHE
GESELLSCHAFT IM VDE

Expert Groups:

Antennas
Microwave Techniques

 **IEEE**

 **MTT-S**

German IEEE
MTT/AP Chapter

IMA

Institut für Mikrowellen-
und Antennentechnik e. V.

Exhibition:

 **GEROTRON**

www.gerotron.de

ISBN 3-00-015423-X



EINSTEIN

Session 1

Plenary Session I

Large-Signal IMPATT-Mode Operation of AlGaIn/GaN HFET's

R.J. Trew and G.L. Bilbro
ECE Department, Box 7243
North Carolina State University
Raleigh, NC 27695-7243

Abstract — AlGaIn/GaN HFET's have produced RF output power density greater than 30 W/mm at microwave frequencies. These devices demonstrate excellent potential for use in microwave power applications such as transmitters for radars and communications systems. However, before these devices find practical application a variety of physical effects that currently limit RF performance must be investigated and controlled. In this work it is shown that an IMPATT mode of operation can be generated in these devices when avalanche breakdown occurs in the conducting channel during the high voltage portion of the RF cycle. A pulse of charge is generated. The electrons drift through the channel depletion region in the gate-drain region inducing a RF current in the external circuit. The effect can be modeled with a negative drain resistance, and produces an increase in RF output power.

Index Terms — AlGaIn/GaN HFET's, High voltage effects, IMPATT mode HFET's, Channel Breakdown in FET's.

I. INTRODUCTION

The generation of high RF output power, on the order of 100's to 1000's of watts necessary for transmitters for radars and wireless communications systems, remains a difficult challenge for semiconductor devices. RF power devices fabricated from standard semiconductors such as Si and GaAs are limited in the RF output capability by the inherent breakdown voltage of the semiconductor material. Recently, the development of wide bandgap semiconductors, such as SiC and the AlGaIn/GaN heterojunction, offers the potential to fabricate transistors with significantly improved RF output power compared to traditional devices. In particular, the development of microwave field-effect transistors fabricated from the AlGaIn/GaN heterostructure offers the potential to fabricate FET's with significantly improved output power performance. The improved RF output power is possible due to high critical field for breakdown in the nitride-based semiconductors. AlGaIn and GaN have breakdown fields greater than $E_c > 10^6$ V/cm, which is significantly higher than comparable fields of slightly over $E_c > 10^5$ V/cm in standard semiconductors such as Si and GaAs. The increase in critical field results in the ability to sustain a much increased bias voltage.

The AlGaIn/GaN heterojunction yields a two-dimensional electron gas with a sheet charge density greater than $n_{ss} = 10^{13}$ cm⁻². This is a factor of five larger

than is obtained with the traditional AlGaAs/GaAs heterojunction, and over twice the sheet charge density obtained from the GaInAs/InP heterojunction. The high sheet charge density results in high dc and RF currents, and the product of high device current and high bias voltage results in the development of high RF output power. Field-Effect Transistors fabricated from the AlGaIn/GaN heterostructure demonstrate the ability to produce RF output power on the order of 100's of watts, and these devices can be easily combined to fabricate kW level and higher transmitters.

The generation of high RF output power by microwave field-effect transistors requires that high bias voltage be applied. However, the drain bias that can be applied is limited in magnitude for FET's by electronic breakdown of the gate electrode. Standard power GaAs FET's are generally limited to drain bias voltages in the range of 8-12 v, which limits the RF voltage and RF output power that can be developed [1]. It has been shown that the use of field-plate technology suppresses gate breakdown and permits significantly higher drain bias voltages to be applied [2]. Field-plate power GaAs FET's biased with drain voltage of 35 v have produced RF power density of 1.7 W/mm of gate periphery, and a 230 W amplifier when the FET was biased at $V_{ds} = 24$ v [3]. Wide bandgap semiconductors such as those based upon the III-N materials system have much improved critical electric fields for breakdown compared to GaAs and HFET's fabricated from these materials can sustain significantly improved bias voltages, with $V_{ds} > 40$ v before breakdown is observed. Field-plate technology is also being widely used with nitride-based HFET's [4] to permit even greater drain voltage to be applied, and a field-plate HFET when biased at a $V_{ds} = 120$ v has produced over 30 W/mm RF power density at S-band [5], and over 5 W/mm at 30 GHz with a drain bias of $V_{ds} = 30$ v [6].

Although the use of field-plates permit high drain voltage to be applied operation of the device at high bias can produce physical effects that influence the performance of the device. In particular, the electric field in the conducting channel can obtain magnitude greater than the critical field for avalanche. Channel breakdown under RF operation can occur, and this can result in a

previously unrecognized IMPATT-mode of operation in these devices.

II. CHANNEL ELECTRIC FIELD

It is well known that charge dipole domains form in the conducting channel of field-effect transistors. This domain supports the majority of the potential drop from the drain to source and produces a high electric field region under the gate edge in the conducting channel. In particular, it is known that the magnitude of the electric field at the edge of the gate electrode on the drain side can be very high, depending upon the magnitude of both the drain potential and the RF voltage. For high RF drive the peak of the RF voltage will add to the drain potential and a terminal voltage on the order of twice the dc bias can result. When the magnitude of the electric field at the gate edge exceeds the tunnel limit electrons tunnel from the gate electrode to the semiconductor creating a leakage current that is the primary breakdown mechanism in field-effect transistors [7]. The electric field for a GaAs MESFET with a $0.6 \mu\text{m}$ gate length is shown in Fig. 1. The electric field is shown at the GaAs surface, at mid-channel, and at the channel/substrate interface.

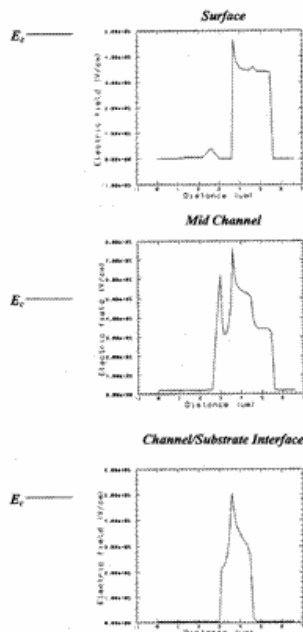


Fig. 1. Electric Field in the Conducting Channel of a GaAs MESFET for $V_{ds}=9\text{v}$. Breakdown Field is Shown for Reference.

The magnitude of the electric field within the conducting channel can also obtain high magnitude, as shown in Fig. 1. The electric field in the conducting

channel can exceed the breakdown field for the semiconductor, which for GaAs is on the order of $E_c \sim 500 \text{ kV/cm}$. As the bias voltage is increased, either by an increase in the drain bias or by the application of a large-signal RF voltage, the magnitude of the electric field will increase and the device will experience breakdown, either at the gate edge, or in the conducting channel. Impact ionization in the conducting channel of short-gate FET's has previously been reported [8]. The use of field plates has been demonstrated to reduce the magnitude of the electric field at the gate edge, thereby suppressing the gate leakage and permitting high drain voltages and large RF voltage to be applied. However, the field-plate introduces a high electric field region within the conducting channel and located under the edge of the field plate, as shown in Fig. 2. The field plate does not increase the threshold for breakdown in the conducting channel. The field-plate moves the high electric field region away from the gate edge, but moves it into the conducting channel region between the gate and drain where it can facilitate channel breakdown, as shown in Fig. 2 for an AlGaIn/GaN HFET.

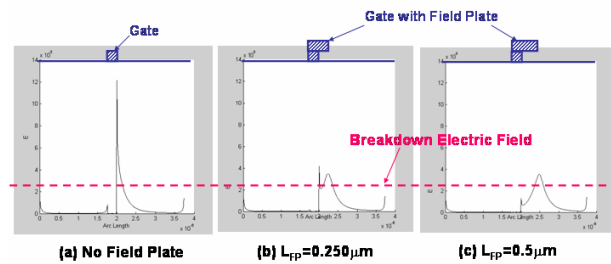


Fig. 2 Electric Field in the Channel Between the Gate and Drain of an AlGaIn/GaN HFET with $V_{ds}=100\text{v}$ for Various Field-Plate Lengths

III. IMPATT OPERATING MODE

When driven with large-signal RF voltages the magnitude of the electric field in the high field domain will oscillate in magnitude as shown in Fig. 3.

During the high voltage portion of the RF cycle the total dc and RF fields can increase until the critical field for avalanche ionization is exceeded. When this occurs a pulse of charge, consisting of electrons and holes, is generated in the conducting channel as illustrated in Fig. 4. The holes have very low mobility and move slowly towards the source where they recombine with free electrons, thereby reducing the electron density in the source region of the channel. The reduction in electron density in the gate-source region contributes to an increase

in source resistance, which increases as a function of RF drive [9]. This phenomenon contributes to the ‘RF knee walkout’ effect often observed in practical devices.

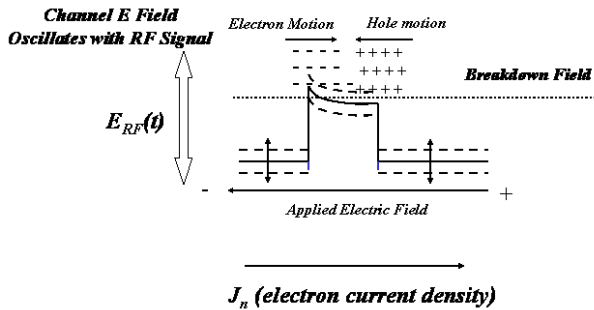


Fig. 3. Electric Field in the Conducting Channel Oscillating with RF Drive

The application of the high drain bias creates a depletion region that extends from under the gate into the region between the gate and drain. Simulations reveal that under high drain voltage the depletion region exists in AlGaIn/GaN HFET’s, even under forward gate bias open channel conditions [9]. The combination of the electron-hole charge pulse generation during the high voltage portion of the RF cycle, and the existence of the channel depletion region create the necessary conditions for IMPATT operation.

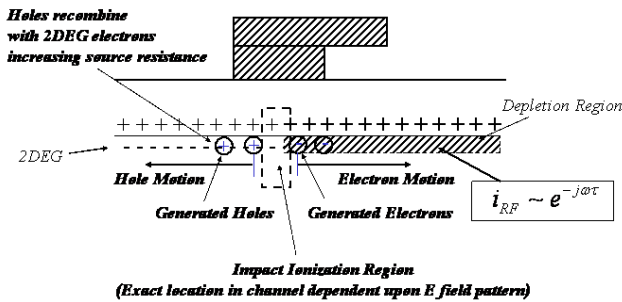


Fig. 4. Electron-Hole Generation in the Conducting Channel Under RF Drive in an AlGaIn/GaN HFET

The electrons generated during the breakdown pulse are injected into the depletion region, where they drift at saturated velocity towards the drain. The drifting electrons induce an RF current in the external circuit that is more than 90° out of phase with the RF voltage, thereby creating an IMPATT mode of operation. A current controlled instability (i.e., the i-v characteristic is multi-valued in current which is generally termed ‘S-type’) that can be represented as a negative resistance with an inductive phase delay in the drain circuit is generated. The

breakdown charge generation is synchronized with the RF signal and is, therefore, phase-locked. Once initiated, the dc current increases and the RF signal is amplified by the negative resistance. An electron transit-time delay that affects frequency response is introduced. This effect is sometimes referred to an ‘gate lag’, or ‘dispersion’.

The negative resistance can be observed in the S22 for the device, which can exceed unity when the IMPATT mode conditions are satisfied. Parameter extraction for a series of GaAs FET’s with varying gate width yield the parameter values shown in Fig. 5a and 5b. Note that the magnitude of the drain resistance is negative.

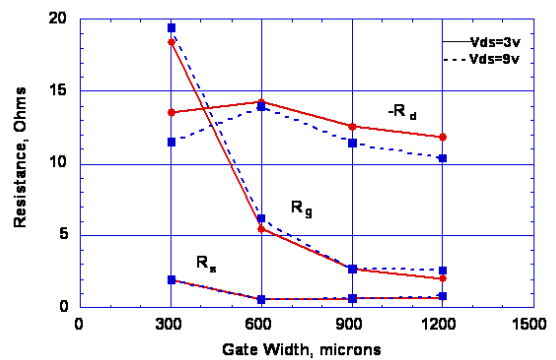


Fig. 5a. R_d , R_s , and R_g Determined by Parameter Extraction

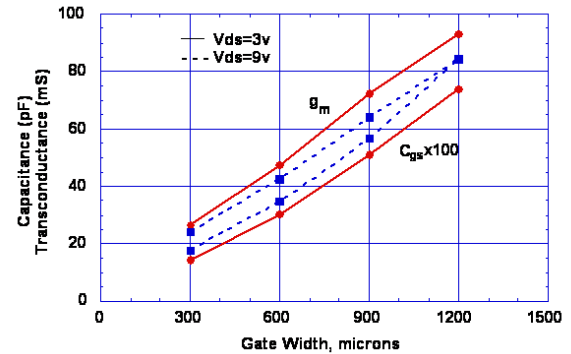


Fig. 5b. g_m and C_{gs} Determined by Parameter Extraction

An equivalent circuit with negative drain resistance models the experimental data with very high accuracy, as is shown in Fig. 6, which shows the measured and modeled RF performance for a GaAs MESFET with gate length $L_g=0.6\mu m$ and gate width $W=600\mu m$. The measured and modeled 2-18 GHz S-parameters are in agreement to high accuracy, as indicated in the H21, G_{max} , and K factor shown in Fig. 6.

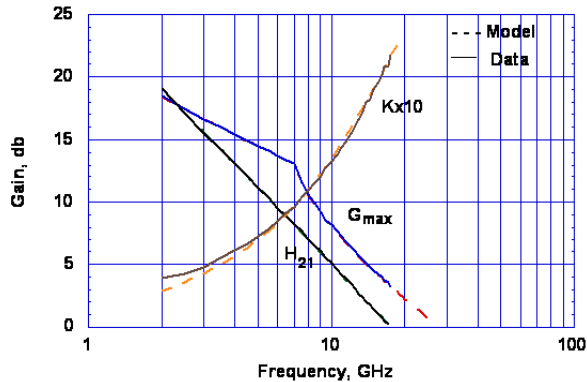


Fig. 6. Measured and Modeled RF Performance

IV. CONCLUSION

AlGaIn/GaN HFET's demonstrate potential for fabrication of improved RF output power devices. These devices should find application as microwave amplifiers for radars and communications systems. However, current devices are affected by physical effects that limit RF performance. One effect is an IMPATT mode of operation that can be excited under high RF voltage conditions. The electric field that exists in the conducting channel can approach or exceed the conditions for avalanche breakdown with increasing drain bias and/or large-signal RF voltage. Under large-signal RF voltage during the high voltage portion of the RF cycle a pulse of electron-hole pairs is generated. The electrons are injected into the depletion region in the gate-drain region of the conducting channel, where they drift at saturated velocity towards the drain contact. This induces a current in the external circuit that is more than 90° of phase with the RF voltage. An IMPATT mode of operation is generated that increases the bias current and increases the RF output power of the device. The mode is observed as an S22 with magnitude greater than unity and can be modeled as a negative drain resistance. The IMPATT mode increases the dc current and amplifies the RF signal, thereby increasing the RF output power of the device.

ACKNOWLEDGEMENT

This work was partially supported by the Office of Naval Research on grant N00014-03-1-0803 and the Army Research Office on grant DAAD19-03-1-0148.

REFERENCES

- [1] T.A. Winslow and R.J. Trew, "Principles of Large-Signal MESFET Operation," *IEEE Trans. Microwave Theory Tech.*, vol. 42, pp. 935-942, June 1994.
- [2] A. Asano, Y. Miyoshi, K. Ishikura, Y. Nashimoto, M. Kuzuhara, and M. Mizuta, "Novel High Power AlGaAs/GaAs HFET with a Field-Modulating Plate Operated at 35v Drain Voltage," *1998 IEDM Digest*, pp. 59-62
- [3] A. Wakejima, K. Ota, K. Matsunaga, and M. Kuzuhara, "A GaAs-Based Field-Modulating Plate HFET with Improved WCDMA Peak-Output-Power Characteristics," *IEEE Trans. Electron Dev.*, vol. 50, pp. 1983-1987, Sep. 2003.
- [4] S. Karmalkar, and U.K. Mishra, "Enhancement of Breakdown Voltage in AlGaIn/GaN High Electron Mobility Transistors Using a Field Plate," *IEEE Trans. Electron Dev.*, vol. 48, pp. 1515-1521, Aug. 2001.
- [5] Y-F Wu, A. Saxler, M. Moore, R.P. Smith, S. Sheppard, P.M. Chavarkar, T. Wisleder, U.K. Mishra, and P. Parikh, "30-W/mm GaN HEMTs by Field Plate Optimization," *IEEE Electron Dev. Lett.*, vol. 25, pp. 117-119, Nov. 2004.
- [6] C. Lee, P. Saunier, J. Yang, and M.A. Khan, "AlGaIn-GaN HFEMT's or SiC with CW Power Performance >4 W/mm and 23% PAE at 35 GHz," *IEEE Electron Dev. Lett.*, vol. 24, pp. 616-618, Oct. 2003.
- [7] R.J. Trew and U.K. Mishra, "Gate Breakdown in MESFETs and HEMTs," *IEEE Electron Dev. Lett.*, vol. 12, pp. 524-526, Oct. 1991.
- [8] M.S. Gupta, "Detection of Avalanching in Submicrometer FET's," *IEEE Electron Dev. Lett.*, pp. 469-471, Oct. 1987.
- [9] R.J. Trew, "Microwave AlGaIn/GaN HFET's," *IEEE Microwave Magazine*, March 2005.

High-Speed Analog and Digital IC's: Research Results and Applications

W. Simbürger¹, K. Aufinger¹, J. Böck¹, S. Boguth¹, D. Kehrer¹
C. Kienmayer¹, H. Knapp¹, T.F. Meister¹, W. Perndl², M. Rest¹
C. Sandner³, H. Schäfer¹, R. Schreiter¹, R. Stengl¹, R. Thüringer^{1,4}
M. Tiebout¹, H.D. Wohlmuth¹, M. Wurzer¹ and A.L. Scholtz⁴

¹Infinion Technologies AG, Otto-Hahn-Ring 6, D-81739 Munich, Germany

²now with BMW Motoren GmbH, Hinterbergerstraße 2, A-4400 Steyr, Austria

³Infinion Technologies AG, Siemensstrasse 2, A-9500 Villach, Austria

⁴Vienna University of Technology, Gusshausstr. 25/389, A-1040 Vienna, Austria

E-Mail: Werner.Simbuerger@infineon.com

Abstract — This paper presents recent circuit results which demonstrate the high-speed and low-power potential of state-of-the-art CMOS and SiGe bipolar technologies. In 0.13 μm CMOS a 17 GHz ISM/WLAN RF front-end with only 130 mW power consumption is described. An injection locked frequency divider with a power consumption as low as 3 mW at 40 GHz is presented in 0.13 μm CMOS. A fully integrated 2:1 multiplexer IC which operates up to 60 Gbit/s data rate with only 10 mW power consumption at 0.7 V supply voltage has been realized in 90 nm CMOS.

A 100 Gbit/s amplifier in SiGe bipolar technology with 16 dB gain has been realized. A 65 GHz - 95 GHz double-balanced SiGe mixer for 77 GHz automotive radar applications achieves >20 dB gain with <14 dB SSB noise figure. A 100 Gbit/s 2^7-1 and a 54 Gbit/s $2^{11}-1$ PRBS generator with high integration scale shows an excellent eye diagram at high data rates. Finally, a 102 GHz static 1:32 frequency divider has been realized to demonstrate the performance of a 225 GHz/300 GHz f_T/f_{max} SiGe bipolar technology.

I. INTRODUCTION

The demand for access to information, anywhere, anytime, and anytime, will require whole new kinds of information systems. This demand for novel communication systems will translate into innovation in emerging technologies, circuit design methodologies and fabrication techniques. The call for miniaturization, low power consumption, low cost and the move towards higher frequencies for wireless and wireline applications are critical trends influencing the direction of communications system development.

At the core of these approaches, heavy emphasis is placed on finding the right match between circuit techniques and fabrication-process technology. The current cycle sees radio frequency (RF) and microwave integrated circuit engineering having grown rapidly in importance in recent years, stimulated in particular by booming digital mobile communications.

Current indium phosphide (InP) bipolar integrated-circuits support high-performance mixed-signal applications at frequencies up to 200 GHz and beyond [1], [2], [3], [4]. The high cut-off frequencies and high breakdown voltages present a unique combination which addresses some major issues. In the meantime, silicon bipolar and CMOS technologies are not standing still. Silicon germanium (SiGe) technologies have brought substantial improvements in bipolar circuit performance [5], [6], [7], [8], [9], [10], [11]. Recently, CMOS is capturing a

significant portion of wireless RF and wireline applications with the promise of lower costs and increased integration scale at highest frequencies [12], [13], [14], [15], [16], [17], [18].

This paper summarizes recent circuit results to demonstrate the performance of state-of-the-art CMOS and SiGe technologies. The presented circuits use a standard 0.13 μm and 90 nm bulk-CMOS technology and a production-near SiGe bipolar technology with up to 225 GHz/300 GHz f_T/f_{max} at Infineon.

II. A 17 GHz ISM/WLAN RF FRONT-END WITH ONLY 130 mW POWER CONSUMPTION IN 0.13 μm CMOS

With growing interest in broadband wireless communication systems and faster and high-performance transceivers at data rates of 100 Mbit/s to 1 Gbit/s and beyond, sub-micron CMOS is particularly attractive for RF and digital baseband processing because of its low power consumption and high integration scale. Emerging short-range applications, such as a high-speed wireless USB 2.0 interface for example, will rely on a low power consumption for mobile systems.

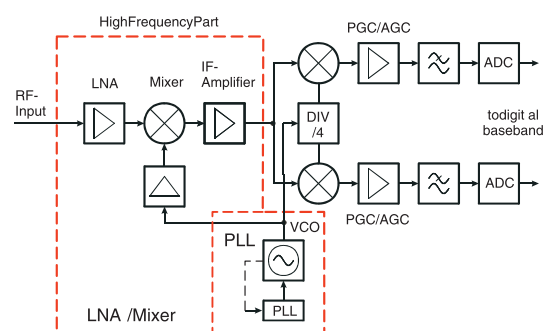


Fig. 1. 17 GHz ISM/WLAN RF frontend block diagram [19], [20].

Fig. 1 shows the block diagram of an integrated RF front-end for 17.1-17.3 GHz ISM band application. The high frequency part of the RF transceiver consists of a LNA and mixer [19] and a high-performance PLL [20]. The concept of the dual conversion (Fig. 1) results in a large frequency separation between the RF and LO frequencies and avoids the generation of I/Q signals at the first LO frequency.

LNA and mixer design is one of the main challenges, since this circuit determines the total gain, noise figure and linearity

performance of a receiver. Fig. 2 shows a simplified schematic diagram of the 17 GHz LNA and mixer in 0.13 μm CMOS.

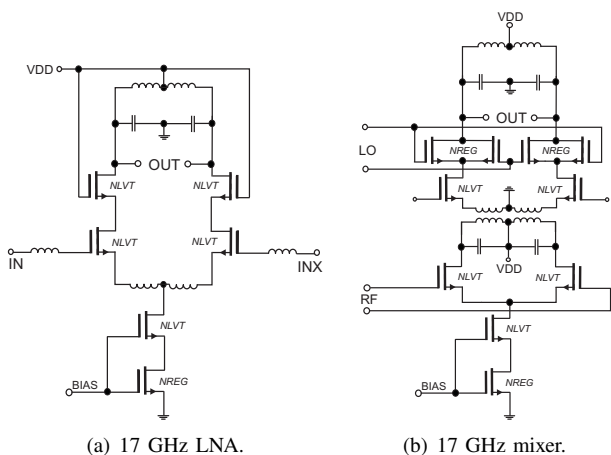


Fig. 2. 17 GHz LNA / mixer schematic diagram [19].

The LNA core in Fig. 2(a) consists of a cascoded, inductively degenerated common source input stage. Inductive degeneration is employed at the common source node of the LNA to achieve a real valued input impedance and low noise figure. The LNA-output is loaded by an integrated LC-tank to increase the gain. Due to the high frequency of 17 GHz all inductors can nicely be integrated without significant area penalty (see chip photograph Fig. 3(a)). A simplified schematic diagram of the mixer is shown in Fig. 2(b). The classical Gilbert-type mixer was preferred to achieve acceptable gain, low noise figure and high linearity. To overcome problems caused by the low supply voltage of 1.5 V in 0.13 μm CMOS, a fully differential integrated transformer was connected between the input transconductance stage and the mixer switching pairs. This topology effectively doubles the voltage headroom available for the circuit design and enables the insertion of cascode transistors to improve the linearity and to control the current in the mixer switching stage. Fig. 3(a) shows the chip photograph of the LNA / mixer. The block diagram of the LNA / mixer is shown in Fig. 1.

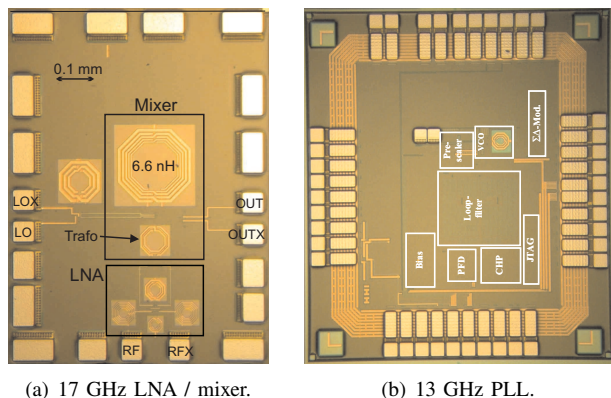


Fig. 3. 17 GHz LNA mixer and 13 GHz PLL chip photograph [19], [20].

In Tab. I the measured performance of the 17 GHz LNA / mixer is summarized.

The block diagram of the PLL is shown in Fig. 4. The PLL is completely integrated including VCO, prescaler, phase frequency detector, charge pump, loop filter, biasing, delta-sigma modulator and a JTAG controller [20]. The PLL uses a

TABLE I
17 GHz LNA / MIXER MEASUREMENT RESULTS [19].

Power supply	1.5 V
Total power consumption	70 mW
LNA power consumption	5.2 mW
Mixer power consumption	27 mW
LO-Driver power consumption	12 mW
IF-Amplifier power consumption	25.8 mW
IF frequency	3.4 GHz
LO frequency	13.95 GHz
RF frequency	17.35 GHz
Power gain	34.7 dB
Noise figure SSB	6.6 dB
CP _{1dB} (input)	-39 dBm
IIP3	-34.4 dBm
3 dB bandwidth	200 MHz
Testchip die area	0.88 mm ²
Technology	0.13 μm CMOS

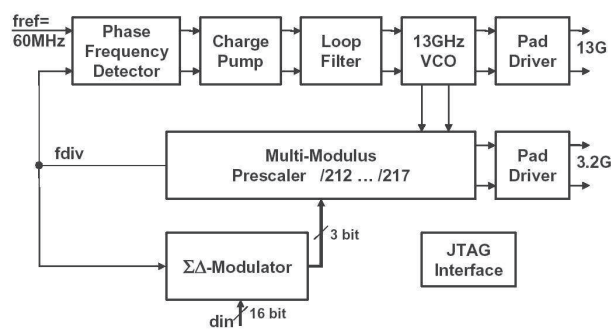


Fig. 4. 13 GHz PLL block diagram [20].

multi-modulus prescaler with a division rate of 212...217 to allow effective fractional-N synthesis and delta-sigma modulation. Aiming at a fully integrated high performance 17 GHz transceiver including LNA and output driver, special care was invested to avoid substrate crosstalk, so a differentially tuned LC-VCO was implemented.

TABLE II
13 GHz PLL MEASUREMENT RESULTS [20].

Center frequency	13 GHz
VCO tuning range	8 %
Reference frequency	60 MHz (64 MHz for N=200)
Inband phase noise (@ f _{vco} /4)	-100 dBc/Hz
RMS Phase error (@ f _{vco} /4) (10kHz to 100MHz)	1.6 deg (N=214.5044) 3.0 deg (N=214.992)
Power supply	1.5 V
Total Power consumption	60 mW
VCO	5 mW
Div/4	40 mW
Prescaler	1 mW
Loop Filter	5 mW
Charge pump	3 mW
Others, incl. digital	6 mW
Testchip die area	1.8 mm by 1.6 mm
Technology	0.13 μm CMOS

In Tab. II the performance of the PLL is summarized [20]. The total power consumption of LNA / mixer and PLL is only 130 mW in 0.13 μm CMOS at 17 GHz.

III. 40 GHz, 3 mW LOW-POWER INJECTION LOCKED FREQUENCY DIVIDER IN 0.13 μm CMOS

RF Phase locked loops are widely used in wireless and wire-line applications as frequency synthesizers or clock sources. Crucial high frequency PLL-components are the voltage controlled oscillator (VCO) and the high frequency dividers. Main concern for VCO-design is low phase noise and low power consumption. Main concern for the frequency divider is lowest power consumption and high frequency capability. High frequency dividers can be realized using CML-logic, using dynamic logic, using a Miller divider or through the injection locking of oscillators. Miller-dividers and CML dividers have been realized up to very high frequencies, unfortunately with high or very high power consumption. Dynamic logic frequency dividers feature a very small power consumption, but the maximum frequency of operation is limited to a few GHz. Injection locked oscillators consume generally less power than CML- or Miller-dividers due to the tuned nature of the circuit. One disadvantage of injection locked oscillators is the limited input bandwidth (or input locking range), which fortunately is not very relevant in LC-VCO based PLL's, as LC-VCO's anyway feature a limited tuning range. The main disadvantage of today's widely used CMOS differential injection locked oscillator topology is found in the large input capacitance and in its small input locking range. A CMOS low power direct injection locking scheme [21] for LC-oscillators is presented in Fig. 5 to divide highest frequency signals with lowest input capacitance.

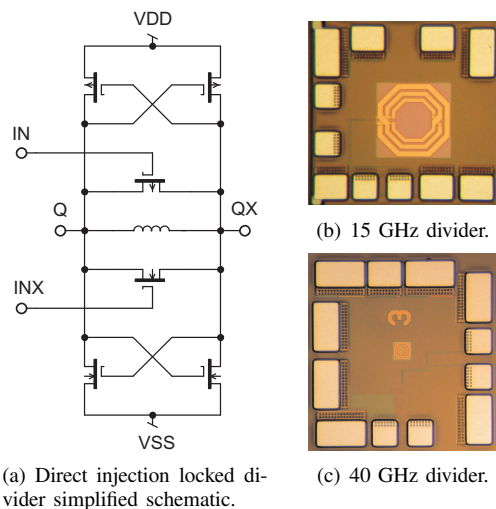


Fig. 5. Direct injection locked divider simplified schematic diagram. 15 GHz and 40 GHz injection locked divider chip photograph [21].

The proposed topology consists of MOS-switches directly coupled to the tank. The concept is verified with two fully integrated injection locked oscillators aiming at different frequencies. The measured frequency locking characteristics and phase noise clearly verifies the circuit implementation. A CMOS low power injection locked oscillator performs highest frequency division by two consuming only 3 mW from 1.5 V supply voltage. The measured circuit divides 41 GHz by two with a locking range of 1.5 GHz. A second oscillator aiming at 15 GHz features a total locking range of 14.2-17 GHz at a power consumption of 23 mW. The increased locking-range of this divider results in increased power consumption [21]. The measurement results are summarized in Tab. III.

TABLE III
INJECTION LOCKED DIVIDER PERFORMANCE [21].

Technology	0.13 μm CMOS	
Supply voltage	1.5 V	
Power Consumption	3 mW	23 mW
Locking Range	40.5 - 42 GHz	14.2 - 17 GHz

IV. A 60-GBIT/S 0.7-V 10-mW MONOLITHIC TRANSFORMER-COUPLED 2:1 MULTIPLEXER IN 90 NM CMOS

Data multiplexers (MUX) are key blocks in high-speed data communication systems. Current 2:1 MUX already achieve operating speeds of 50 Gbit/s in CMOS [22], [17]. However, these MUX circuit concepts suffer from low-supply voltages of future CMOS technologies. In this work a monolithic transformer is used in a high-speed MUX circuit to achieve 60 Gbit/s operation at a ultra-low supply voltage of 0.7 V [23].

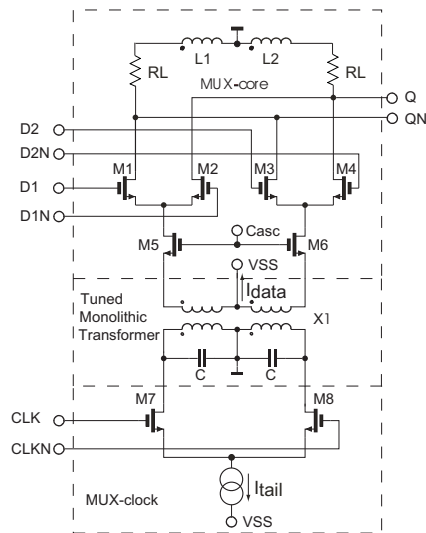


Fig. 6. 60-Gbit/s 0.7-V monolithic transformer-coupled 2:1 multiplexer schematic diagram [23].

Fig. 6 shows the schematic diagram of the monolithic transformer-coupled MUX circuit. The transformer splits the conventional CML-MUX design into the MUX-Core and the MUX-Clock section and couples the clock signal from the MUX-Clock to the MUX-Core (Fig. 6). There are outstanding advantages due to the on-chip transformer. Because of the missing DC-path between primary and secondary side of the transformer the MUX-core and the MUX-clock section can use the full supply voltage. The effective supply voltage for the MUX 2:1 circuit is doubled. The supply voltage of MUX-core and MUX-clock is connected to the center taps of the monolithic transformer. In this circuit only two transistors are in series using the full supply voltage. The higher drain-source voltage per transistor offer a higher f_t and therefore a higher circuit speed.

Fig. 7 illustrates a 3-dimensional view of the monolithic transformer X1 (Outer diameter: 35 μm) The transformer X1 is connected as a parallel resonant device. The MOS capacitors C are connected in parallel to the primary windings of the transformer. The resonant tuning increases the current transfer ratio of the transformer. The cascode transistors M5 and

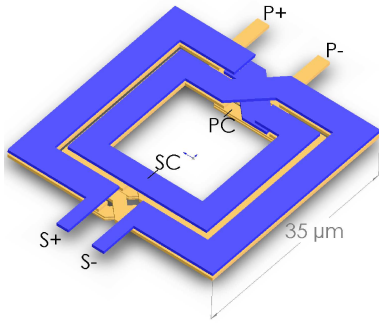
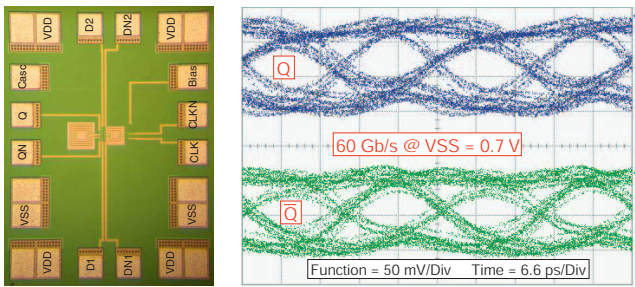


Fig. 7. 3D-view of monolithic transformer X1 (Outer diameter: 35 μm) [23].

$M6$ provide isolation between the data-path transistors $M1$ - $M4$ and the transformer's parasitic capacitances. The cascode also sets the bias current for the MUX-core. The data-path transistors $M1$ - $M4$ switch the current to the load resistor. Shunt peaking is used to enhance the bandwidth of the MUX [24]. The shunt peaking inductor is realized as a differential inductor. The inductance value of $L1$ and $L2$ is 0.36 nH. The tail current I_{tail} is set to 8 mA. A resistive divider sets the DC level of the sinusoidal clock signal to $VSS/2$ and works as input matching network for the clock signal.



(a) Chip photograph. (b) 60 Gbit/s measured eye diagram.

Fig. 8. 60-Gbit/s 0.7-V 2:1 MUX in 90 nm CMOS: chip photograph and measured eye diagram [23].

For measurement the 2:1 MUX IC is bonded on a ceramic microwave substrate. The multiplexer is tested with two pseudo-random bit sequences (PRBS of $2^{11}-1$). The input voltage swing is 2×350 mV_{pp}. The sinusoidal clock signal has a voltage swing of 2×400 mV_{pp}. Fig. 8(b) shows the measured eye diagram of the single-ended outputs at a data rate of 60 Gbit/s. Tab. IV shows the performance summary of the MUX.

TABLE IV

60 GBIT/S 2:1 MUX 90 NM CMOS MEASUREMENT RESULTS [22].

Power supply	0.7 V
Total power consumption	10 mW
Maximum data rate	60 Gbit/s
Output voltage swing (50 Ω)	2×50 mV _{pp}
Testchip die area	0.63 mm by 0.47 mm
Technology	90 nm CMOS

V. A 100 GBIT/S AMPLIFIER IN SiGe BIPOLAR TECHNOLOGY

A broadband amplifier with 16 dB gain and a 3-dB bandwidth of 62 GHz has been realized in a 200 GHz f_T , 275 GHz

f_{max} SiGe bipolar technology [25], [26]. Broadband amplifiers are very important building blocks for a large variety of applications, including wireless transceivers, mm-wave applications and optical communication systems. In general, they are based on a lumped [27], [28], [29] or on a distributed concept [30], [31], [27].

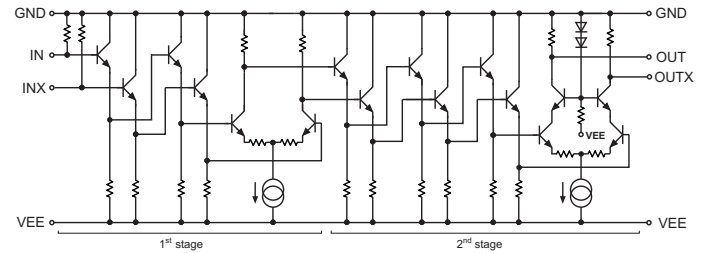
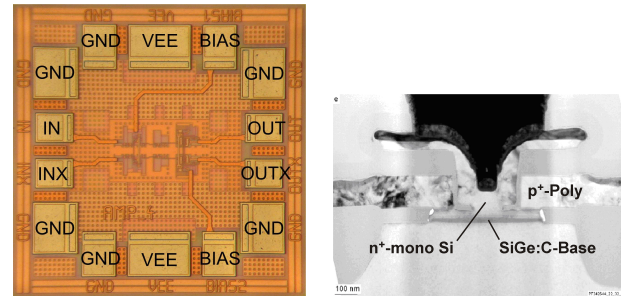


Fig. 9. 62 GHz, 16 dB gain broadband amplifier schematic diagram [25].

The circuit diagram of the broadband amplifier based on lumped elements realized in this work is shown in Fig. 9. The amplifier is based on a fully differential design and consists of two stages.



(a) Amplifier chip photograph. (b) SiGe BJT TEM cross section.

Fig. 10. Chip photograph of the 62 GHz, 16 dB gain broadband amplifier in SiGe (chip size: 550 $\mu\text{m} \times 550 \mu\text{m}$) [25] and TEM cross section of the emitter-base complex of a SiGe transistor with effective emitter width of 0.14 μm [26].

The chip photograph of the amplifier is shown in Fig. 10(a). The amplifier is fabricated in a preproduction SiGe bipolar technology [26]. The transistors have a double-polysilicon self-aligned emitter-base configuration with a minimum effective emitter width of 0.14 μm . A TEM cross section of the emitter-base complex is given in Fig. 10(b). The SiGe:C base of the transistors has been integrated by selective epitaxial growth. The emitter contact exhibits a monocrystalline structure. The transistors manufactured in this technology offer a transit frequency f_T of 200 GHz, a maximum oscillation frequency f_{max} of 275 GHz and a ring oscillator gate delay of 3.5 ps. Current density for maximum f_T and f_{max} is at about 8 mA/ μm^2 . The collector-emitter breakdown voltage BV_{CE0} is 1.7 V. The technology provides four copper metallization layers, two different types of polysilicon resistors, a TaN thin film resistor and a MIM capacitor.

The single-ended low-frequency gain is 10 dB and the 3-dB bandwidth is 62 GHz. The differential gain is 16 dB. The current consumption is 155 mA at a supply voltage of -5 V. Degradation of S_{22} at about 50 GHz can be observed. In the case of a single-ended excitation together with an inductance in the supply path this behavior can be verified by simulations. In differential operation such an inductance will have no effect.

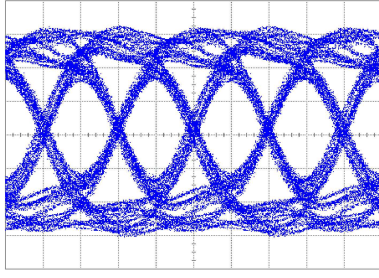


Fig. 11. 100 Gbit/s measurement result (250 mV/div, 5 ps/div) [25].

TABLE V

BROADBAND AMPLIFIER MEASUREMENT RESULTS [25].

SiGe bipolar technology,	200/275 GHz f_T/f_{max}
min. eff. emitter width,	0.14 μm
ring osc. gate delay	3.5 ps
Bandwidth (3 dB)	62 GHz
Differential gain	16 dB
CP_{1dB} (input)	-9.5 dBm
IIP3	+2.1 dBm
Supply voltage	-5.0 V
Supply current	155 mA
Chip size	550 $\mu\text{m} \times 550 \mu\text{m}$

In Fig. 11 the measured output eye diagram for a 100Gbit/s excitation signal is shown. A high-performance PRBS-generator chip [10] and the broadband amplifier chip have been mounted closely on a substrate. Short bond wires connect the outputs of the PRBS-generator and the amplifier inputs. The clear output eye diagram at a data rate of 100Gbit/s demonstrates the feasibility for high-speed communications. Tab. V shows the performance summary.

VI. A 65 GHz - 95 GHz DOUBLE-BALANCED MIXER FOR AUTOMOTIVE RADAR FRONT-ENDS IN SiGe BIPOLAR TECHNOLOGY

An active mixer for down-conversion with a conversion gain of more than 24 dB and single-sideband (SSB) noise figure of less than 14 dB in the frequency range from 76 GHz to 81 GHz has been realized [32]. The gain is >22 dB from 65 GHz up to 95 GHz with slightly decreased noise performance.

A simplified circuit diagram of the mixer is shown in Fig. 12. The mixer consists of a mixer core, an LO buffer, a balun at the RF input and an IF buffer. The mixer core is based on the Gilbert-mixer. The mixer has a double-balanced structure and utilizes differential LO and RF signals. Transistor sizes and bias currents are optimized in order to obtain a good compromise between gain, linearity and low noise figure. The size of the switching transistors is designed at the current density for maximum f_T , whereas the RF transistors are designed for minimum noise contribution. The differential signals required for LO and RF inputs of the mixer core are generated by the LO buffer and a LC balun, respectively. The LO buffer consists of a differential amplifier which provides a differential output signal from the single-ended input.

Fig. 13(a) shows the chip photograph of the mixer. Building blocks and important pads are indicated in the photograph. The LC balun (Fig. 13(b)) is placed directly at the RF input, followed by the mixer core. The LC balun consisting of the transmission lines TRL_1 and TRL_2 and the MIM-capacitors

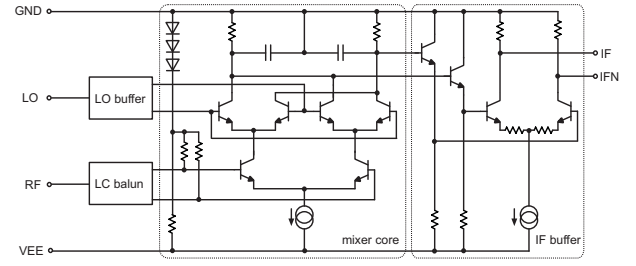
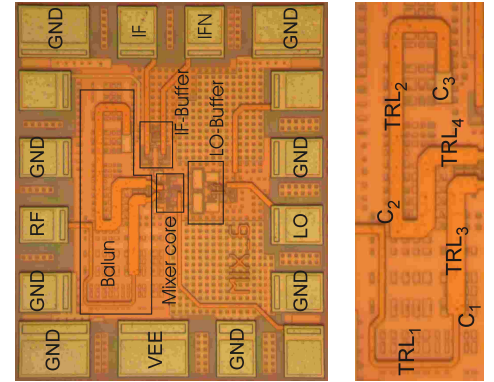
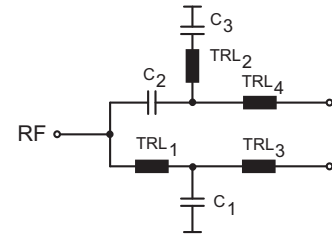


Fig. 12. Simplified circuit diagram of the mixer (GND = 0 V, VEE = -5 V) [32].



(a) Mixer chip photograph.

(b) Detailed view of the LC balun.



(c) Schematic diagram of the LC balun.

Fig. 13. Chip photograph of the mixer (chip size: 550 $\mu\text{m} \times 450 \mu\text{m}$), detailed view of the LC balun and schematic diagram of the LC balun [32].

C_1 and C_2 (Fig. 13(c)). This balun converts the unbalanced RF signal to a balanced signal and provides an impedance transformation for 50 Ω matching at the RF input. Capacitor C_3 is required to achieve an RF ground at TRL_2 . The LC balun was designed based on the calculation of a lumped element balun [33]. Then the inductances were substituted with transmission line TRL_1 and TRL_2 [34]. Further optimization was done using an EM-field simulator.

The mixer is fabricated in a SiGe bipolar technology which is based on the process technology presented in [35]. The transistors have a double-polysilicon self-aligned emitter-base configuration with an effective emitter width of 0.18 μm . The SiGe:C base of the transistors has been integrated by selective epitaxial growth and the transistors exhibit a monocrystalline emitter contact. The transistors manufactured in this technology offer a transit frequency f_T and a maximum oscillation frequency f_{max} of more than 200 GHz and a ring-oscillator gate delay of 3.7 ps. The technology provides four copper metallization layers, two different types of polysilicon resistors and a TaN thin film resistor.

In Fig. 14 the measured conversion gain and SSB noise

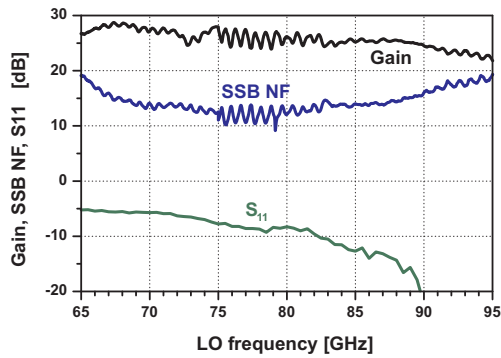


Fig. 14. Measured conversion gain, SSB noise figure and RF input return loss versus LO frequency. IF frequency is 500 MHz, LO power is 2 dBm. [32].

TABLE VI
MIXER PERFORMANCE SUMMARY [32].

SiGe bipolar technology, min. eff. emitter width, ring osc. gate delay	200 GHz f_T , 200 GHz f_{max} 0.18 μm 3.7 ps
Conversion gain	>24 dB (65.0 - 90.8 GHz) >22 dB (65.0 - 94.9 GHz)
SSB noise figure	<14 dB (72.3 - 82.5 GHz) <16 dB (66.5 - 90.0 GHz)
CP _{1dB} (input)	-30 dBm
Supply voltage	-5 V
Supply current	60 mA
Chip size	550 μm \times 450 μm

figure versus LO frequency of the mixer at a constant IF frequency of 500 MHz are shown. The LO input power is set to 2 dBm at the center frequency. The measured conversion gain is higher than 24 dB and the SSB noise figure is lower than 14 dB at the frequency range from 72.3 GHz to 82.5 GHz. The mismatch of the mixer RF input and the noise source output result in a ripple seen in the measurement plot. The V-band noise source (frequencies below 75 GHz) exhibits a better match than the W-band noise source (frequencies above 75 GHz). Tab. VI shows the performance summary of the mixer.

VII. 100 GBIT/S 2^7-1 AND 54 GBIT/S $2^{11}-1$ PRBS GENERATORS IN SiGe BIPOLAR TECHNOLOGY

Pseudo-random bit sequence (PRBS) generators are widely used to provide test signals for circuits such as multiplexers, de-multiplexers and amplifiers. The maximum data rate provided by commercial PRBS generators is in many cases insufficient to test high-speed circuits manufactured in advanced CMOS and SiGe bipolar technologies. Therefore we have designed two PRBS generator ICs to simplify testing of these high-speed CMOS and SiGe ICs.

PRBS generators are based on linear feedback shift registers. The number of shift register stages N determines the length of the resulting pseudo-random sequence, which is $2^N - 1$ bits. Typical values for N range from 7 to 31. The large number of flip-flops in the shift register, which have to be clocked synchronously, poses the main challenge in the design of high-speed PRBS generators. By making use of special properties of the pseudo-random sequences it is possible to clock the shift register at a fraction (e.g. one half [36], [37] or one quarter [38]) of the output data rate. The output signal is

then generated by using additional XOR gates and multiplexers (Fig. 15).

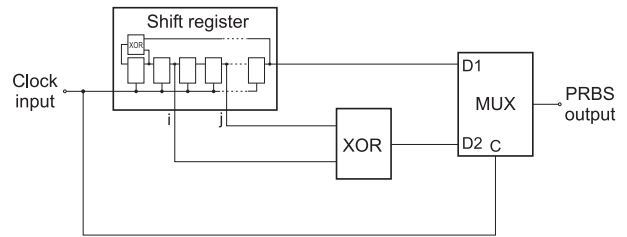


Fig. 15. PRBS generator using a half-rate shift register clock.

We have developed two PRBS generator ICs. One circuit is designed for high output data rates in the 100 Gbit/s range and consists of a seven-stage shift register operating at one half of the output data rate. The second circuit evaluates the possibility of a full-rate design for 40 Gbit/s applications, combined with a longer pseudo-random sequence. It contains an eleven-stage shift register operating at the full clock rate. It does not require a multiplexer at its output and is therefore not susceptible to duty-cycle distortion.

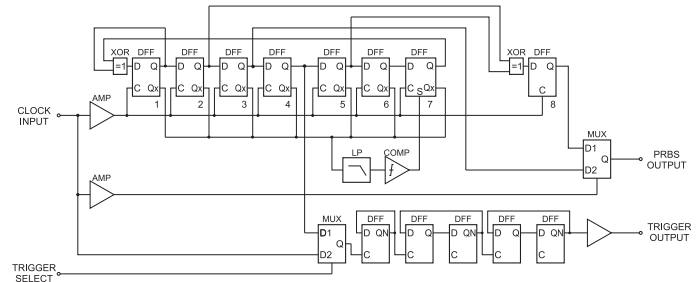


Fig. 16. Block diagram of the 2^7-1 PRBS generator.

The PRBS generator ICs contain additional circuitry to provide a trigger output. Depending on the level at the trigger select input this output provides either a trigger signal for the display of eye diagrams or a trigger synchronous to the output data sequence to display the bit pattern. This pattern trigger is generated by applying the output data to a frequency divider with a divide ratio of 2^{N-2} [36].

Fig. 16 shows the block diagram of the 2^7-1 PRBS generator. The shift register contains seven master-slave flip-flops. An eighth flip-flop is used for re-timing between the XOR gate and the multiplexer. The multiplexer provides the output signal without any additional buffer or amplifier.

A five-stage frequency divider generates the trigger output signal. Depending on the level at the trigger select input the divider input is either connected to the clock input to provide a trigger output for eye diagrams, or to one of the shift register stages to provide a pattern trigger.

The $2^{11}-1$ PRBS generator contains eleven shift register stages which operate at the full clock rate. Therefore no multiplexer is required at the output and a two-stage buffer is used to provide the output signal. The trigger circuit (consisting of nine divider stages) and the auto-start circuit are implemented similar to the 2^7-1 PRBS generator. The chip size is only 0.9 x 0.7 mm² (Fig. 17).

First measurements of the PRBS generator ICs were done on wafer using 40 GHz GSSG probes. Both circuits operate with

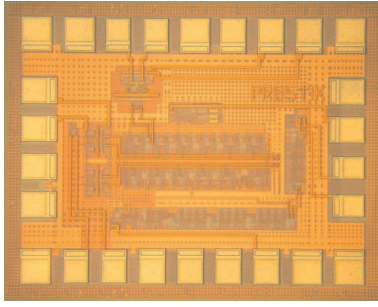
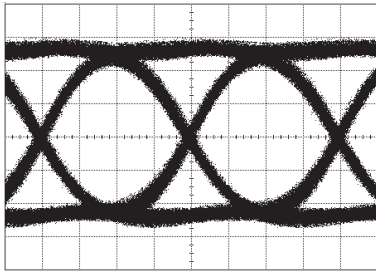
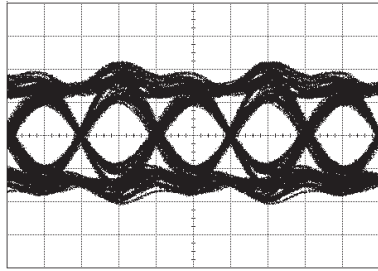


Fig. 17. Chip photograph of the $2^{11}-1$ PRBS generator [39].

a supply voltage of 5 V. The $2^{11}-1$ PRBS generator consumes 380 mA and operates up to 54 Gbit/s with a differential output voltage swing larger than 600 mVpp (Fig. 18(a)).



(a) $2^{11}-1$ PRBS: 54 Gbit/s output signal (4.6 ps/div, 150 mV/div)



(b) 2^7-1 PRBS: 100 Gbit/s output signal (5 ps/div, 100 mV/div)

Fig. 18. Measured eye diagrams of 54 Gbit/s $2^{11}-1$ and 100 Gbit/s 2^7-1 PRBS generators [39].

The 2^7-1 PRBS generator consumes 300 mA and operates up to 100 Gbit/s (Fig. 18(b)). The eye opening at this data rate is degraded by the limited bandwidth of the measurement setup.

VIII. A 102 GHz STATIC 1:32 FREQUENCY DIVIDER IN SiGe BIPOLAR TECHNOLOGY

The static frequency divider has a divide ratio of 32 and consists of five master-slave flip-flops [11], [40]. Fig. 19 shows the block diagram of the frequency divider.

The input signal is applied to the first divider stage via a pair of emitter followers. The first master-slave stage determines the maximum operating frequency of the frequency divider.

The mixer is fabricated in a SiGe bipolar technology which is based on the process technology presented in [40]. The minimum effective emitter width of $0.14 \mu\text{m}$. The transistors manufactured in this technology offer a transit frequency f_T of 225 GHz and a maximum oscillation frequency f_{max} of 300 GHz and a ring-oscillator gate delay of 3.3 ps.

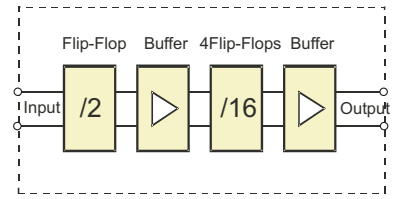


Fig. 19. 102 GHz static divider block diagram [40].

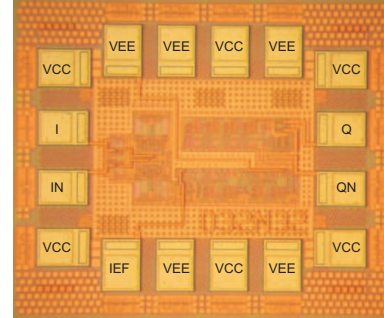


Fig. 20. 102 GHz static divider chip photograph (size $550 \times 450 \mu\text{m}^2$) [40].

TABLE VII

102 GHz STATIC FREQUENCY DIVIDER PERFORMANCE SUMMARY [40].

SiGe bipolar technology, min. eff. emitter width, ring osc. gate delay	225/300 GHz f_T/f_{max} 0.14 μm 3.3 ps
Max. input frequency	102 GHz
Divide ratio	32
Supply voltage	-5 V
Supply current	127 mA
Chip size	$550 \mu\text{m} \times 450 \mu\text{m}$

The IC has been measured on wafer using a single-ended input signal. Fig. 21 shows the output signal at an input frequency of 102 GHz. The total current consumption is 127 mA at a supply voltage of 5 V. To our knowledge, up to now this is the highest reported input frequency for static divider operation for any silicon technology. Tab. VII shows the performance summary of the frequency divider.

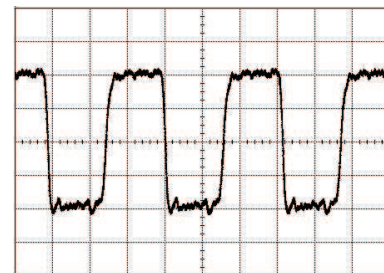


Fig. 21. Measured single-ended output signal of the 1:32 static frequency divider at 102 GHz input frequency (x-axis: 100 ps/div, y-axis: 50 mV/div) [40].

IX. CONCLUSION

Silicon-based analog and digital high-speed ICs have been realized to demonstrate wireline, wireless and sensor applications up to 100 Gbit/s and 100 GHz. Finding the right match between circuit techniques and process technology is a major issue to push the circuit performance to the limits. Further

advances in process technologies and circuit design will result in continuing the upward shift of the integration scale and the frequency limits in silicon.

ACKNOWLEDGEMENT

The authors would like to thank all Infineon CMOS and SiGe teams which are responsible for the process technology development and fabrication.

REFERENCES

- [1] V. Paidi, Z. Griffith, Y. Wei, M. Dahlstrom, M. Urteaga, N. Parthasarathy, M. Seo, L. Samoska, A. Fung, and M. Rodwell, "G-Band (140-220) GHz and W-Band (75-110) GHz InP DHB T Medium Power Amplifiers," *IEEE Transactions on Microwave Theory and Techniques*, vol. 53, no. 2, pp. 598–605, February 2005.
- [2] L. Samoska, A. Peralta, M. Hu, M. Micovic, and A. Schmitz, "A 20 mW, 150 GHz InP HEMT MMIC power amplifier module," *IEEE Microwave and Wireless Components Letters*, vol. 14, no. 2, pp. 56–58, February 2004.
- [3] M. Urteaga, D. Scott, S. Krishnan, W. Yun, M. Dahlstrom, Z. Griffith, N. Parthasarathy, and M. Rodwell, "G-band (140-220-GHz) InP-based HBT amplifiers," *Journal of Solid State Circuits*, vol. 38, no. 9, pp. 1451–1456, Sept 2003.
- [4] M. Mokhtari, C. Fields, and R. D. Rajavel, "100+ GHz Static Divide-By-2 Circuit in InP-DHBT Technology," in *GaAs IC Symposium Digest*, Oct 2002, pp. 291–294.
- [5] B. Floyd, S. Reynolds, U. Pfeiffer, T. Zwick, T. Beukema, and B. Gaucher, "SiGe bipolar transceiver circuits operating at 60 GHz," *IEEE Journal of Solid-State Circuits*, vol. 40, no. 1, pp. 156–167, January 2005.
- [6] M. Meghelli, "132-Gb/s 4:1 multiplexer in 0.13 μm SiGe-bipolar technology," *IEEE Journal of Solid-State Circuits*, vol. 39, no. 12, pp. 469–471, December 2004.
- [7] H. Li, H. Rein, and T. Suttrop, "Design of W-Band VCOs with High Output Power for Potential Application in 77 GHz Automotive Radar Systems," in *25th GaAs IC Symposium*. IEEE, November 2003, pp. 263–266.
- [8] A. Ryllyakov and T. Zwick, "96 GHz static frequency divider in SiGe bipolar technology," in *Gallium Arsenide Integrated Circuit (GaAs IC) Symposium*, Nov 2003, pp. 280–290.
- [9] M. Meghelli, "A 108 Gb/s 4:1 Multiplexer in 0.13 μm SiGe-Bipolar Technology," in *International Solid-State Circuits Conference ISSCC*. IEEE, February 2004.
- [10] H. Knapp, M. Wurzer, W. Perndl, K. Aufinger, T. F. Meister, and J. Böck, "100-Gb/s 2^7-1 and 54-Gb/s $2^{11}-1$ PRBS Generators in SiGe Bipolar Technology," in *Compound Semiconductor IC Symposium*. IEEE, Oct. 2004.
- [11] H. Knapp, M. Wurzer, T. Meister, K. Aufinger, J. Böck, S. Boguth, and H. Schäfer, "86 GHz Static and 110 GHz Dynamic Frequency Dividers in SiGe Bipolar Technology," in *International Microwave Symposium*. IEEE, June 2003, pp. 1067–70.
- [12] F. Ellinger, "60-GHz SOI CMOS traveling-wave amplifier with NF below 3.8 dB from 0.1 to 40 GHz," *IEEE Journal of Solid-State Circuits*, vol. 40, no. 2, pp. 553–558, February 2005.
- [13] C. Doan, S. Emami, D. Sobel, A. Niknejad, and R. Brodersen, "Design considerations for 60 GHz CMOS radios," *IEEE Communications Magazine*, vol. 42, no. 12, pp. 132–140, December 2004.
- [14] F. Ellinger, T. Morf, G. Buren, C. Kromer, G. Sialm, L. Rodoni, M. Schmatz, and H. Jackel, "60 GHz VCO with wideband tuning range fabricated on VLSI SOI CMOS technology," in *Microwave Symposium Digest*. MTT-S, June 6-11 2004, pp. 1329–1332.
- [15] L. Franca-Neto, R. Bishop, and B. Bloechel, "64 GHz and 100 GHz VCOs in 90 nm CMOS Using Optimum Pumping," in *International Solid-State Circuits Conference ISSCC*. IEEE, February 2004.
- [16] R. Liu, H. Chang, C. Wang, and H. Wang, "A 63 GHz VCO Using a Standard 0.25 μm CMOS Process," in *International Solid-State Circuits Conference ISSCC*. IEEE, February 2004.
- [17] D. Yamazaki, T. Yamamoto, M. Horinka, H. Nomura, K. Hashimoto, and H. Onodera, "A 25 GHz Clock Buffer and a 50 Gb/s 2:1 Selector IC in 90 nm CMOS," in *International Solid-State Circuits Conference ISSCC*. IEEE, February 2004, pp. 240–241.
- [18] Guan, X. and Hajimiri, A., "A 24 GHz CMOS Front-end," in *European Solid-State Circuit Conference*, Florence, Italy, September 2002.
- [19] C. Kienmayer, R. Thüringer, M. Tiebout, W. Simbürger, and A. L. Scholtz, "An Integrated 17 GHz Front-End for ISM/WLAN Applications in 0.13 μm CMOS," in *IEEE Symposium on VLSI Circuits*, Juni 2004.
- [20] M. Tiebout, C. Sandner, H. Wohlmuth, N. Da Dalt, and E. Thaller, "A Fully Integrated 13 GHz Delta-Sigma Fractional-N PLL in 0.13 μm CMOS," in *International Solid-State Circuits Conference ISSCC*. IEEE, February 2004.
- [21] M. Tiebout, "A CMOS Direct Injection Locked Oscillator Topology as High frequency Low Power Frequency Divider," *IEEE Journal of Solid-State Circuits*, vol. 39, no. 7, pp. 1170–74, July 2004.
- [22] D. Kehrer, H.D. Wohlmuth, M. Wurzer, and H. Knapp, "50 Gb/s 2:1 Multiplexer in 0.13 μm CMOS Technology," *Electronics Letters*, vol. 40, no. 02, pp. 100–101, Jan. 2004.
- [23] D. Kehrer and H. Wohlmuth, "A 60-Gb/s 0.7-V 10-mW Monolithic Transformer-Coupled 2:1 Multiplexer in 90 nm CMOS," in *Compound Semiconductor IC Symposium (CSICS)*, Monterey, CA, USA, Oct 24-27 2004, late news paper.
- [24] D. Kehrer, H.D. Wohlmuth, H. Knapp, M. Wurzer, and A.L. Scholtz, "40-Gb/s 2:1 Multiplexer and 1:2 Demultiplexer in 120 nm Standard CMOS," *Journal of Solid-State Circuits*, vol. 38, no. 11, pp. 1830–1837, Nov. 2003.
- [25] W. Perndl, W. Wilhelm, H. Knapp, M. Wurzer, K. Aufinger, T. F. Meister, J. Böck, W. Simbürger, and A. L. Scholtz, "A 60 GHz Broadband Amplifier in SiGe Bipolar Technology," in *Bipolar/BiCMOS Circuits and Technology Meeting BCTM*, Sept 2004.
- [26] J. Böck, K. Aufinger, R. Stengl, S. Boguth, R. Schreiter, M. Rest, H. Knapp, M. Wurzer, W. Perndl, T. Böttner, and T. F. Meister, "SiGe Bipolar Technology for Automotive Radar Applications," in *Bipolar/BiCMOS Circuits and Technology Meeting BCTM*, Sept 2004.
- [27] O. Wohlgenuth, P. Paschke, and Y. Baeyens, "SiGe broadband amplifiers with up to 80 GHz bandwidth for optical applications at 43 Gbit/s and beyond," in *European Microwave Conference*, 2003, pp. 1087–1090.
- [28] Y. Baeyens, G. Georgiou, J. S. Weiner, A. Leven, V. Houtsmä, P. Paschke, Q. Lee, R. F. Kopf, Y. Yang, L. Chua, C. Chen, C. T. Liu, and Y. K. Chen, "InP D-HBT ICs for 40-Gb/s and Higher Bitrate Lightwave Transceivers," *IEEE Journal of Solid-State Circuits*, vol. 37, no. 9, pp. 1152–1159, Sept. 2002.
- [29] D. Choudhury, M. Mokhtari, M. Sokolich, and J. F. Jensen, "DC to 50 GHz Wideband Amplifier with Bessel Transfer Function," in *Radio Frequency Integrated Circuits Symposium*. IEEE, June 2004, pp. 329–332.
- [30] S. Masuda, T. Hirose, T. Takahashi, M. Nishi, S. Yokokawa, S. Iijima, K. Ono, N. Hara, and K. Joshin, "An Over 110-GHz InP HEMT Flip-chip Distributed Baseband Amplifier with Inverted Microstrip Line Structure for Optical Transmission Systems," in *GaAs IC Symposium*. IEEE, 2002, pp. 99–102.
- [31] C. Meliani, G. Rondeau, G. Post, J. Decobert, W. Mouzannar, E. Dutisseuil, and R. Lefèvre, "A high gain-bandwidth product InP HEMT distributed amplifier with 92 GHz cut-off frequency for 40 Gbit/s applications and beyond," in *GaAs IC Symposium*. IEEE, 2002, pp. 103–106.
- [32] W. Perndl, H. Knapp, M. Wurzer, K. Aufinger, T. F. Meister, J. Böck, W. Simbürger, and A. L. Scholtz, "A low-noise and high-gain double-balanced mixer for 77 GHz automotive radar front-ends in SiGe bipolar technology," in *Radio Frequency Integrated Circuits Symposium RFIC*. Texas USA: IEEE, 6-8 June 2004, pp. 47–50.
- [33] P. Viztmüller, *RF Design Guide - Systems, Circuits, and Equations*, 1st ed. Norwood, MA 02062: Artech House, 1995.
- [34] Mongia, R., Bahl, I., and Bhartia, P., *RF and Microwave Coupled-Line Circuits*, 1st ed. Norwood, MA 02062: Artech House, 1999.
- [35] T. F. Meister, H. Schäfer, K. Aufinger, R. Stengl, S. Boguth, R. Schreiter, M. Rest, H. Knapp, M. Wurzer, A. Mitchell, T. Böttner, and J. Böck, "SiGe Bipolar Technology with 3.9 ps Gate Delay," in *Bipolar/BiCMOS Circuits and Technology Meeting*, September 2003, pp. 103–106.
- [36] M. G. Chen and J. K. Notthoff, "A 3.3-V 21-Gb/s PRBS Generator in AlGaAs/GaAs HBT Technology," *IEEE Journal of Solid-State Circuits*, vol. 35, no. 9, pp. 1266–1270, Sep 2000.
- [37] H. Knapp, M. Wurzer, J. Böck, T. F. Meister, G. Ritzberger, and K. Aufinger, "40 Gbit/s 2^7-1 PRBS Generator IC in SiGe Bipolar Technology," in *Proc. of Bipolar/BiCMOS Circuits and Technology Meeting*. Monterey, CA, USA: IEEE, September 2002, pp. 124–127.
- [38] S. Kim, M. Kapur, M. Meghelli, A. Ryllyakov, Y. Kwark, and D. Friedman, "A 45-Gb/s SiGe BiCMOS PRBS Generator and PRBS Checker," in *Custom Integrated Circuits Conference*, 2003, pp. 313–316.
- [39] H. Knapp, M. Wurzer, W. Perndl, K. Aufinger, T. Meister, and J. Böck, "100-Gb/s 2^7-1 and 54-Gb/s $2^{11}-1$ PRBS Generators in SiGe Bipolar Technology," in *Compound Semiconductor IC Symposium (CSICS)*, Monterey, CA, USA, Oct 24-27 2004.
- [40] J. Böck, H. Schäfer, H. Knapp, K. Aufinger, M. Wurzer, S. Boguth, T. Böttner, R. Stengl, W. Perndl, and T. F. Meister, "3.3 ps SiGe Bipolar Technology," in *IEDM International Electron Devices Meeting*, San Francisco, CA, USA, December 13-15 2004.

Session 2a

Passive Circuits

Low-complexity RF-MEMS technology for microwave phase shifting applications

C. Siegel¹, V. Ziegler¹, U. Prechtel¹, H. Schumacher²

¹ EADS Deutschland GmbH, Corporate Research Centre, LG-ME, 81663 München, Germany, +49 89 60724203

² Dep. of Electron Devices and Circuits, University of Ulm, Albert Einstein Allee 45, 89081 Ulm, Germany

Abstract — This paper presents a very low complexity RF-MEMS process with only one metallisation layer and some phase shifting applications produced in this technology. The MEMS are fabricated on silicon, with a bimorph metallisation. Affected by a mechanic stress gradient in the bimorph layer, free standing parts of the structure roll up. These bended beams can be switched onto the substrate by electrostatic actuation.

Using these bended structures in a transmission line or a loaded line, the effective dielectricity of the line and thus the phase shift of the line is changed. The concepts of switchable loaded lines and switchable transmission lines are compared in terms of phase shift and insertion loss. A 20° phase shifter with IL < 0.5dB @ 30GHz is shown, produced in a MEMS process with only 2 lithographic steps.

I. INTRODUCTION

Phase shifting devices are a key component for electronically steerable antennas. State of the art for phase shifters in the GHz range are pin diode or FET based circuits. An emerging technology that could supplement the existing phase shifting technologies due to its higher performance figure of merits (IL, IS) and their negligible power consumption are RF-MEMS. [1]

Despite their impressive performance, reliability problems due to their technology are hindering these devices from applications. To circumvent most of these problems we are proposing a new low complexity RF-MEMS technology.

II. LOW-COMPLEXITY TECHNOLOGY

The process starts with the thermal oxidation of a 300µm thick high resistive silicon wafer (I). The oxide on the backside is removed and a thin sacrificial layer or anti sticking coating is deposited and patterned (II). Next a bimorph aluminium silicon layer is deposited (III) and patterned with standard photo lithography (IV) and wet etching (V). Then, the backside metallisation is deposited and the sacrificial layer is removed by wet chemistry.

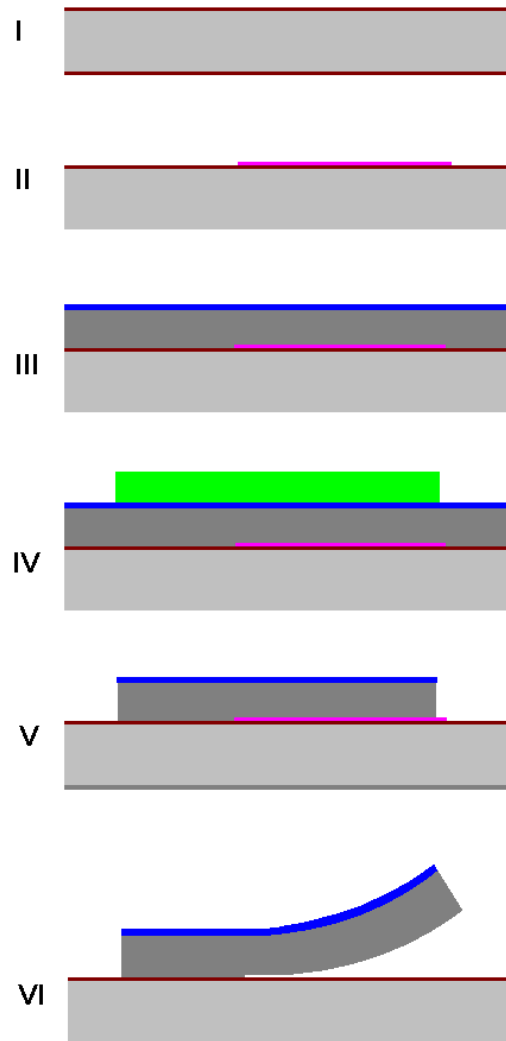


Fig. 1. Process flow for low complexity technology

While there is no residual stress in the aluminium after the deposition, the top layer of the bimorph structure has an intrinsic tensile stress of about 350MPa. By removing of the sacrificial layer by wet chemistry the device structures bend up uniformly (VI) and (Fig. 2).

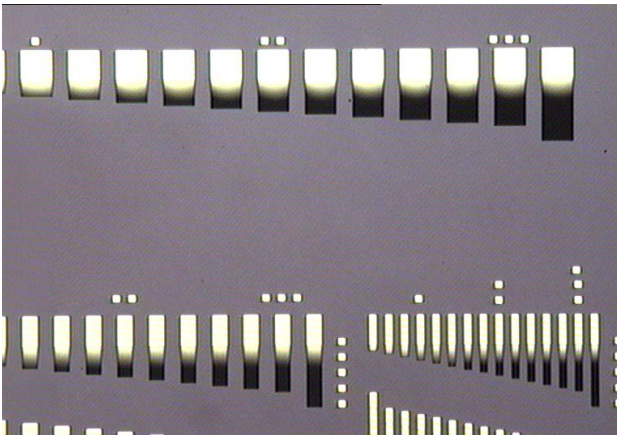


Fig. 2. bent beams of different lengths, black parts are bended up

To avoid in-process sticking, the wafers are immersed in hot propanol before drying with nitrogen. No critical point drying is needed.

Due to the small conductivity of the silicon bulk material no actuation path metallisation is needed. Voltage is applied between the RF-line and the backside metallisation. So the published devices are produced with only two lithographic steps, which is, compared with other MEMS, an extremely low complexity and low cost approach.

III. CREEP BEHAVIOR OF ALUMINIUM

Since aluminium is used as bulk material of the beams, its thermal behaviour was analysed. One result is that pure and stress free deposited aluminium starts with creep at 80°C. Heating a non-etched Al-layer above 80°C results in a tensile stress after returning to room temperature of 1MPa/°C up to 150°C. Cooling in liquid nitrogen leads to compressive stress of (-60MPa) after reaching room temperature again. Higher stress values than 40MPa are not stable, because aluminium creeps back at room temperature with an exponential decrease over time to about 40 MPa.

After etching the structures, the beams deflect in a way that in the up-state the aluminium is nearly stress free. In down-state the Al layer is stressed and will, if held in the down state long enough, also creep until a maximum stress of 40 MPa is reached. For reproducible results, temperature and time steps during processing have to be controlled carefully.

To improve the thermal behaviour of Al one might use alloys, [2] which on the other hand reduce the electric conductivity. With 5% Copper inside creep starts with 5°C higher

temperatures and the maximum resulting tensile stress after temperature cycling is 30MPa higher. There is no more observable creep effected by cooling the alloy in liquid nitrogen. The conductivity on the other hand decreases about 20%.

There is no observable creep in the investigated temperature range of -190°C to +200°C in the top silicon layer.

IV. MECHANICAL CHARACTERISATION

Since intrinsic stress of the silicon is isotropic, a beam deflects three-dimensional. Using narrow beams can reduce this effect. The length of the investigated beams is between 100µm and 400µm. This results in a deflection of 20µm to 40µm for the 400µm beams, and 5 to 10µm for a 200µm beam, depending on the thickness of the top layer. As the deflection has the shape of a part of a circle, the height of the actuation path grows with the second order of the length of the beams.

The actuation voltage is independent of the length of the beam, but is related to the bending radius and the stiffness. Realised actuation voltages are between 30V and 80V. A thinner sandwich results in lower voltages, but reduces also the pull back force and ultimately can lead to in-process sticking problems and reduced RF- power handling capability.

For switching, alternating voltages are used, otherwise the switch does not stay in the down position due to charging effects of the dielectric [3]. If the switched cantilevers are in the down-state the actuation voltage can be reduced by about 10% with the switch staying down. By decreasing the actuation voltage by 20% the cantilevers switch up.

V. DESIGN OF PHASE SHIFTING ELEMENTS

By switching transmission lines either down on the substrate or up in the air, the effective dielectricity of the RF-signal line changes, which results in a phase shift. Two principle designs are presented in this publication.

The first consist of switchable stub loaded lines in coplanar (Fig. 3 right) and microstrip (Fig. 4 right) topology.

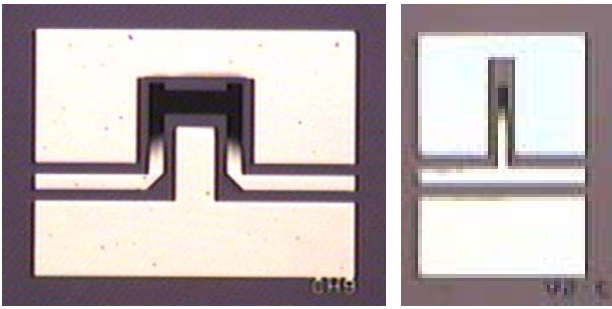


Fig. 3. Photos of coplanar U-shaped switchable transmission line (right) and stub-loaded line phase shifter (left).

The second of elevated transmission lines realize as the coplanar switchable U-shaped transmission line (Fig. 3 left), and in the switchable microstrip line (Fig. 4 left).

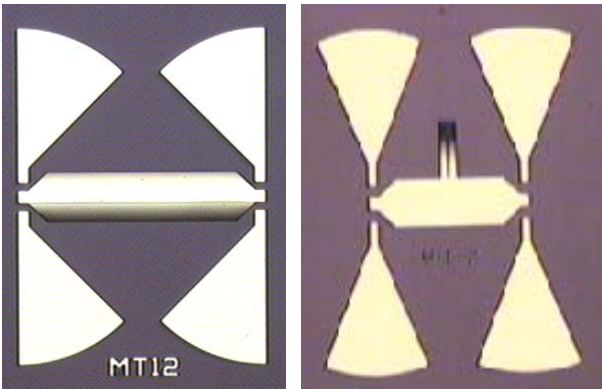


Fig. 4. Photos of switchable transmission line (right) and stub-loaded line in microstrip configuration (left).

VI. RF-MEASUREMENT RESULTS

First the transmission line losses were analyzed. Without any actuation voltage applied a 1mm long transmission line has an insertion loss of 0,15dB at 25GHz. With $-35V$ on the line, it increases to 0,17dB, applying $+35V$ leads to 0,25dB. The influence of light is with 0,03dB/mm almost negligible. The additional loss is caused by surface loadings of the oxide. The following measurements are with light and deembedded with a line without applied voltage (worst case for IL extraction).

A. Stub Loaded Lines

In the first design (Fig. 3 right) a short coplanar transmission line is loaded with an open stub with $300\mu\text{m}$ length and a width of $40\mu\text{m}$. The phase shift is $4,8^\circ$ at 30GHz, maximum insertion loss is 0,36dB in down-state.

In microstrip design the $300\mu\text{m}$ long and $100\mu\text{m}$ wide stub (Fig. 4 right) switches the phase only $2,8^\circ$. Maximum insertion loss at 30GHz is 0,28dB in the down-state.

B. Switchable Microstrip Transmission Line

The microstrip 50Ω transmission line is $260\mu\text{m}$ wide. In order to change the effective dielectricity, $100\mu\text{m}$ of the lines width were switchable up and down on each side. The loss in the down state is like the value of a line with applied voltage, 0,28dB/mm at 35GHz (Fig. 5) in the up-state S_{21} is just 0,14dB/mm.

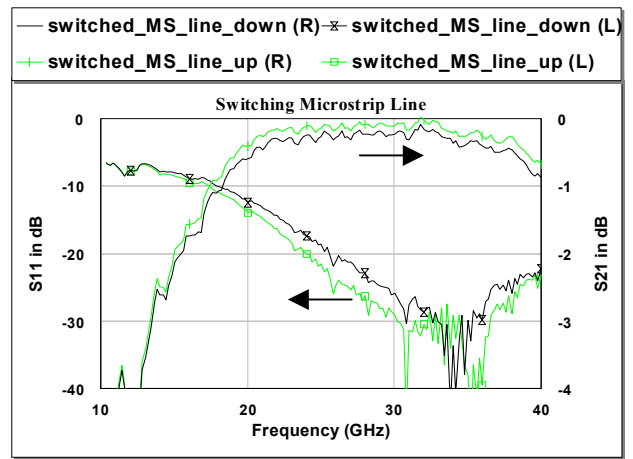


Fig. 5. Switchable microstrip transmission line S-parameters (line length 1mm).

For a length of 1mm a switched phase shift of $4,3^\circ$ at 25GHz and $6,5^\circ$ at 35GHz was achieved (Fig. 6). With an asymmetric design where $200\mu\text{m}$ of the lines width were switchable at one side, a bigger height above the substrate can be reached, which increases the phase shift to $11^\circ/\text{mm}$ at 35GHz according to simulations.

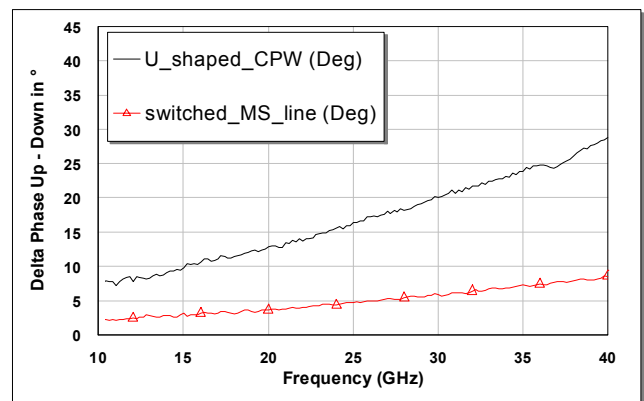


Fig. 6. Change in phase for CPW U-shaped line and microstrip line by switching

C. U-Shaped Coplanar Transmission Line

In this design (Fig. 3 left), a long part of the line is about $20\mu\text{m}$ above the substrate. Therefore, a larger switched phase shift of 16° at 25GHz and 24° at 35GHz is obtained (Fig. 6). The loss in the down-state is 0,32dB at 35GHz. Due to applied voltage this loss value is expected. In the up-state the IL is 0,6 dB (Fig. 7), but the device is mismatched. S11 is $-8,6\text{dB}$. If the upper state in a redesign is matched to about -15dB , an insertion loss of 0,3dB at 35GHz instead of 0,6dB is expected.

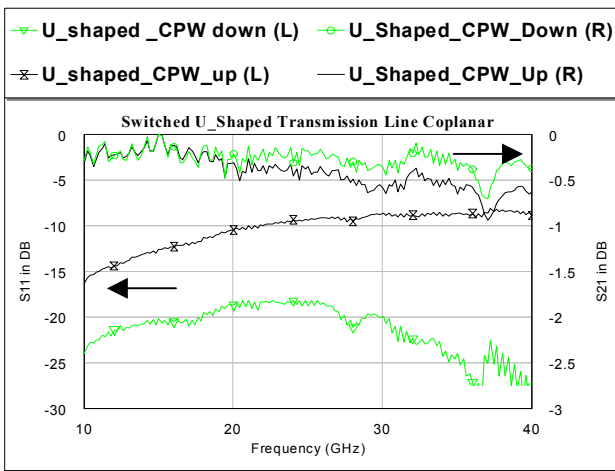


Fig. 7. U-shaped transmission line S- parameter up and down.

For the U-shaped lines (Fig. 3 left), a model has been extracted by keeping the physical length of the lines and changing only the ϵ_r of the substrates. For lines, which are fixed on the substrate, ϵ_r is 11,7. Switched in the down-state an ϵ_r value of 9,6 has to be adjusted to the simulator, because of a remaining air gap between the aluminium and the oxide. In the up state an ϵ_r value of 4,1 represents the phase and reflectivity behaviour correctly.

VII. CONCLUSIONS

In this paper, we presented a low-complexity RF-MEMS process for phase shifting applications at microwave frequencies. Several switchable transmission line topologies were proposed, fabricated and characterised with promising results for realizing the small phase shifting bits in a digital phase shifter.

The technology can also be used for switchable filters, by switching up parts of a resonant structure.

With the implementation of a second metallisation layer switching circuits for the larger bits are possible.

REFERENCES

- [1] J.B. Muldavin, G. M. Rebeiz, "High Isolation CPW MEMS Shunt Switches, 1. Modeling" *IEEE Transactions on Microwave Theory and Techniques*, pp.1045-1052, June 2000.
- [2] W. M. Van Spengen, "MEMS Reliability Stiction, Charging and RF MEMS", *PhD thesis*, IMEC, Leuven, Belgium, May 2004.
- [3] T.Lisec, C. Huth, B.Wagner "Dielectric Material Impact on Capacitive RF MEMS Reliability", *EuMW - 12. GAAS Symposium*, Amsterdam, p.471 - 474, 2004.

Microwave Breakdown Prediction in Rectangular Waveguide Based Components

C. Vicente¹, M. Mattes², D. Wolk³, B. Mottet¹, H. L. Hartnagel¹, J. R. Mosig², D. Raboso⁴

¹Technical University of Darmstadt, Institut für Hochfrequenztechnik, Germany,
Email: quiles@hf.tu-darmstadt.de

²Laboratoire d'Electromagnétisme et Acoustique (LEMA), Ecole Polytechnique Fédérale de Lausanne (EPFL), Switzerland,
Email: michael.mattes@epfl.ch

³TESAT-Spacecom GmbH & Co. KG, Gerberstr. 49, 71522 Backnang, Germany,
Email: Dieter.Wolk@tesat.de

⁴ESA-ESTEC, Keplerlaan 1, Postbus 299, 2200 AG Noordwijk, The Netherlands,
Email: David.Raboso@esa.int

Abstract — This paper describes a new software tool capable to predict the corona discharge threshold in microwave devices. The two necessary calculations when investigating such a phenomenon have been performed: computation of the electromagnetic fields inside the structure and determination of the corona breakdown onset itself. The corona discharge routine is fully integrated into the electromagnetic tool providing accuracy when using the electromagnetic fields as well as efficiency. The software has been tested for a particular component for which experimental measurements have been also performed. The agreement between the predicted breakdown values and the experimental results fully shows the validity of the approach followed.

I. INTRODUCTION

The phenomenal growth in the telecommunication industry in recent years has brought significant advances in filter technology as new communication systems emerged, demanding more stringent filter characteristics. In particular, the growth of the wireless communication industry has spurred tremendous activity in the area of microwave filter miniaturisation. Today, telecommunication systems demand for a higher component integration and an increase of services implying larger bandwidths, thus higher frequency ranges. To achieve these objectives the size of microwave devices on the one hand incessantly decreases whereas at the same time the power levels increase. Both trends lead to a higher electric field density inside the components. This development in turn leads to serious problems with respect to RF breakdown due to corona discharges.

The term “gas discharge” originates with the process of discharge of a capacitor into a circuit incorporating a gap between electrodes. If the voltage is sufficiently high, an electric breakdown occurs in the gas and an ionised state is formed. The circuit is closed and the capacitor discharges. Later the term “discharge” was applied to any flow of electric current through ionised gas, and to any process of ionisation of the gas by the applied electric field [1]. One of the pioneers to investigate microwave breakdown in gases was MacDonald [2].

Due to the increasing problem of corona discharge in microwave devices a big effort has been dedicated in the past to understand, model, and predict the occurrence of discharges. For example, the authors of [3] showed that the thresholds

in microwave systems can be much lower than the theoretically predicted ones due to the presence of absorbing inhomogeneities in an air-filled microwave waveguide. In [4] the case of output multiplexer filters is studied. A theoretical and experimental investigation of microwave breakdown in air-filled resonators is presented in [5]. The effects on the breakdown threshold of air pressure, pulse length in a multi-carrier operation, and the strong inhomogeneity of the electromagnetic field of resonators are analysed. In a recent publication [6] several aspects of microwave breakdown in resonators are discussed and approximate analytical criteria are formulated for some illustrative model geometries like circular symmetric resonators.

To predict the breakdown threshold inside microwave devices two problems need to be solved: First of all, the spatial electric field distribution has to be computed. Afterwards, a diffusion type problem for the evolution of the electron density must be solved using the afore computed electric field distribution.

Most of the publications in recent years studying the problem of corona discharge in microwave devices deal with special cases or simplified geometries to obtain the electromagnetic field distribution. Complex geometries or complete waveguide devices, e. g. filters, are not considered or a parallel plate configuration is assumed.

In this paper we describe some preliminary results of the ESA/ESTEC activity “AO-4026 ITT ESA - Multipactor and Corona Discharge: Simulation and Design in Microwave Components” (Contract No. 16827/02/NL/EC) that is intended to create a software tool capable to predict the microwave breakdown onset inside complex geometries, such as filters, based on rectangular waveguide technology. For this, first of all, the software tool computes the electric field density inside the microwave device. Afterwards, this field distribution is used to determine the breakdown threshold. The organisation of the paper is as follows: We first briefly describe the software tool to compute the electromagnetic field distribution inside waveguide filters. Then, the approach chosen to predict the breakdown threshold for corona discharge is outlined. The predicted results are compared to measurements showing a good agreement between simulation and measured data.

II. COMPUTATION OF ELECTROMAGNETIC FIELD DISTRIBUTION

For an accurate corona discharge analysis, it is indispensable to know the electromagnetic field distribution inside the microwave device, e. g. a filter. For this, the software tool FEST (Full-wave Electromagnetic Simulation Tool) is used that has been recently developed by ESA/ESTEC [8]. This software uses a full-wave approach, which assures a high accuracy and efficiency, also for complex geometries like microwave filters, and is based on the integral equation technique [9], [10] and microwave network theory. An analysis example is shown in Fig. 1. It compares measurements and simulation of return and insertion loss of a diplexer, taken from [11], demonstrating a good agreement between theory and measurements.

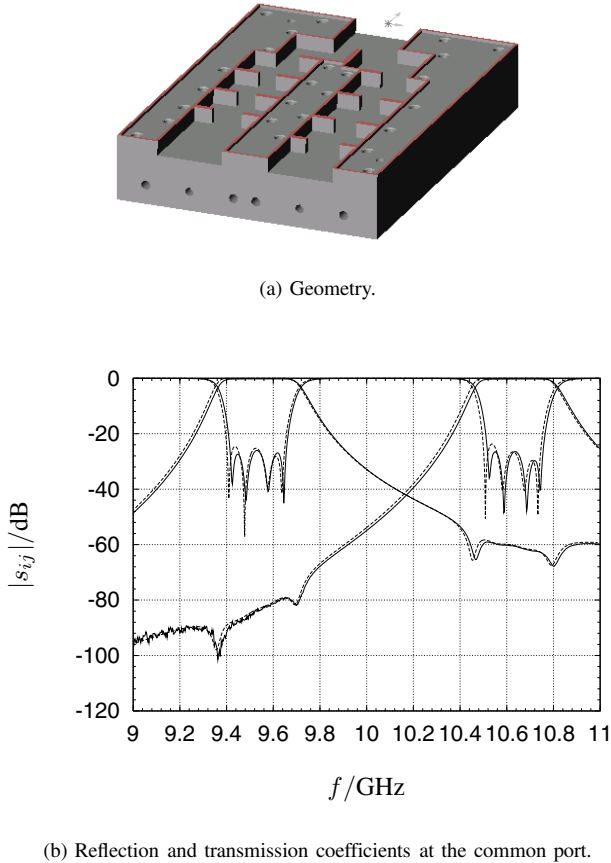
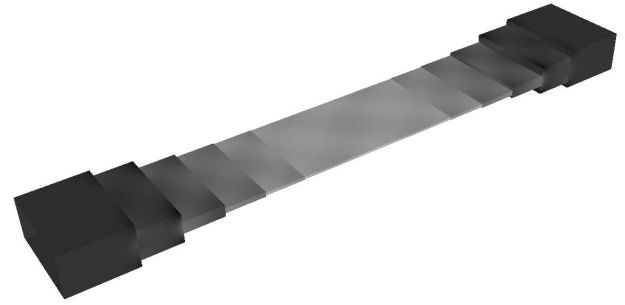


Fig. 1. Geometry and frequency response of a diplexer. Fig. (a) shows the reflection and transmission coefficients at the common port. Measurements are drawn in solid lines, simulation results in dashed lines. Measurements have been obtained applying an averaging over 4096 samples per frequency point for noise reduction.

Fig. 2 presents the results of the electromagnetic field computation inside a transformer based on rectangular waveguides, that has been used to test the theoretical model to predict the threshold of corona discharge. High field values are represented by light, low values by dark grey tones. The vertical electric field along the centre line has been compared to Microwave Studio[®] showing a good agreement between both simulation tools, fully validating the field computation of FEST. Whereas the analysis of such a structure can take up to several hours with Microwave Studio[®], it is only a matter of seconds, at the worst of minutes, with FEST due to

its full-wave approach, making it therefore easy for a design engineer to quickly verify the field distribution, which then can be further used to compute the breakdown threshold.



(a) Surface current.

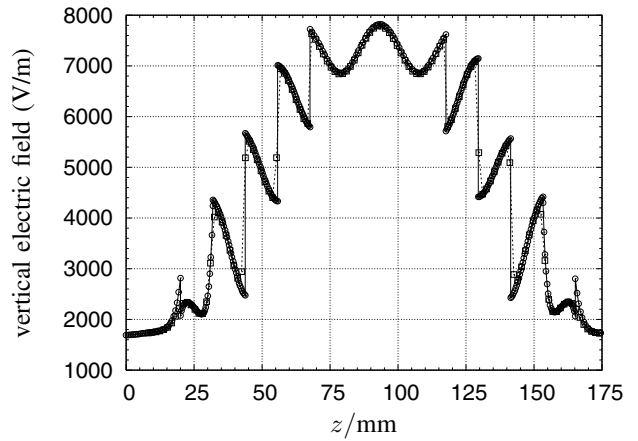


Fig. 2. Structure used for testing the theoretical approach to predict corona discharge. Frequency: 7.4 GHz. Input power: 1 W rms. Figure (a) represents the surface current and (b) the vertical electric field along the centre axis of the structure. The circles represent the field values actually computed with FEST. Their straight line interpolation is represented by the solid line. The results of FEST have been compared to Microwave Studio[®], represented by rectangles respectively the dashed line, showing a very good agreement fully validating the results of FEST.

III. CORONA BREAKDOWN: CALCULATION AND COMPARISON WITH MEASURED DATA.

In order to calculate the corona discharge threshold, one has to compute the free electron density originated by ionisation of the gas molecules inside the waveguide structure. To do this, the continuity equation for the evolution of the electron density must be solved:

$$\nabla^2(D \cdot n) + (\nu_i - \nu_a)n = \frac{\partial n}{\partial t}, \quad (1)$$

where:

n is the electron current density,

D is the Diffusion coefficient,

ν_i is the ionisation rate,

ν_a is the attachment rate.

This equation shows the basic physics of the corona discharge phenomenon. On the one hand ionisation tends to increase the electron density, whereas diffusion and attachment inhibit the process. Diffusion is due to the motion of electrons from high field regions to low field ones. On the other hand, attachment is the process by which electrons are "absorbed" by neutral molecules forming ions which are too massive for taking part in the discharge. Other mechanisms like recombination can be neglected for the calculation of the threshold [2].

In the continuous wave regime, the corona threshold condition is just $\frac{\partial n}{\partial t} = 0$, i.e., it is only defined by the moment in which the electron density starts to grow with time. This results in

$$\nabla^2(D \cdot n) + (\nu_i - \nu_a)n = 0. \quad (2)$$

This equation defines the problem: once ionisation is capable to overcome the losses due to diffusion and attachment, the plasma develops.

The relevant parameters ν_i , ν_a and D depend on the microwave electric field (E_{rms}), the gas pressure (p) and the frequency ($f = \omega/2\pi$). In [12], expressions for these coefficients for dry air are given:

$$D \approx \frac{10^6}{p} \text{ cm}^2 \text{ s}^{-1}, \quad (3)$$

$$\nu_i/p \approx 5.14 \times 10^{11} \exp(-73\alpha^{-0.44}) \text{ s}^{-1}, \quad (4)$$

$$\nu_a/p \approx 7.6 \times 10^{-4} \alpha^2 (\alpha + 218)^2 \text{ s}^{-1}, \quad (5)$$

where:

$$E_{eff} = \frac{E_{rms}}{(1+(\omega/\nu_c)^2)^{1/2}},$$

$$\alpha = \frac{E_{eff}}{p},$$

$$\nu_c \approx 5 \cdot 10^9 \text{ p.}$$

The effective field E_{eff} is a measure of the capability of the microwave field of transferring energy to the surrounding gas. The higher the pressure of a gas the most efficient the RF field transfers energy. At very high pressures, the RF effective field indeed behaves like a DC field.

The solution to (2) has to be found using numerical methods if the particular device is complex and therefore, the electric field highly inhomogeneous. However, if there are zones with a high and homogeneous electric field, an analytical approach to (2) can be used [2]:

$$-\left(\frac{\pi}{b}\right)^2 + \frac{\nu_i - \nu_a}{D} = 0 \quad (6)$$

where b is the distance between the plates, in our case, the waveguide height.

When the gap is small compared to the rest of the waveguide dimensions (parallel plate approximation case), (6) gives accurate results. In the cases where this approach can not be applied, resort must be taken to numerical analysis. In order to solve (2), a finite difference scheme has been used. The solution is searched iteratively assuming an initial solution for the electron density n . If, for a given applied power, the electron density is sufficiently higher than the initial value, breakdown occurs. On the contrary, if the electron density falls below the initial solution, the threshold has not been reached. The input power is varied regarding this and finally, when the

required precision is achieved, the input power is taken as the breakdown power of the device. Fig. 3 shows the corona onset obtained for the structure of Fig. 2.

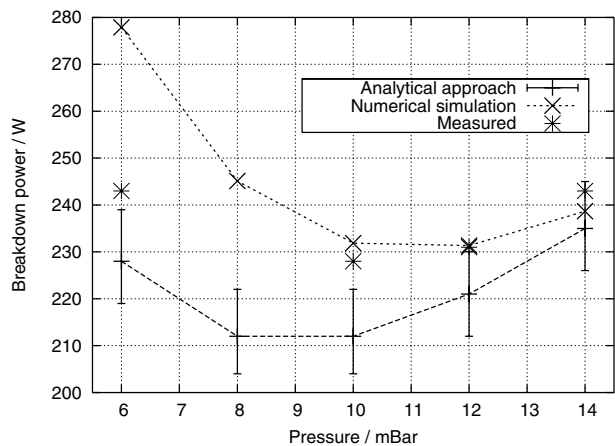


Fig. 3. Corona discharge threshold for the structure of Fig. 2 at 7.4 GHz. All data are for ambient temperature.

Two main results are presented: on the one hand, both the analytic (solution to 6) and the numeric calculation (solution to 2). On the other hand, the experimental breakdown values. For the analytic result, the maximum field inside the structure for each waveguide element has been used in the determination of ν_i and ν_a in (6). The breakdown power is therefore determined for each element and the lowest of all of them is taken as the breakdown threshold of the device. Employing the maximum field, one ensures that this is the worst possible case (i.e. lowest threshold).

For the experimental detection of corona, the pressure was fixed and the input power was slowly increased. Two detection methods have been used to ensure that corona occurs: third harmonic generation and I/P reflection nulling measurements. The results show a very good agreement between measurements and simulation (the largest error is only around 0.2 dB). It is remarkable the fact that the analytical solution approaches to the measurements and to the numerical result as the pressure increases. This behaviour occurs because the diffusion losses become less important and therefore the field inhomogeneities is less critical in the corona onset determination (see (2)) since diffusion is highly field dependent. The result of the decrease in the diffusion losses is that the discharge becomes more and more local and thus the maximum field represents better the final result. This also explains why the analytical approach improves with the pressure.

Apart from the breakdown onset value it is also interesting from the microwave component designer to locate the place where the discharge occurs. Fig. 4 shows a plot of the electron density for a power just above the breakdown threshold. It is seen how the discharge (peak) occurs in the transformer at the right of the inner gap. The point where the electron density is maximum is in fact $z = 128.3$ mm. It is worthwhile to underline that despite the fact that the field is maximum in the centre of the structure, the breakdown does not occur there. The explanation to this has to do with the diffusion losses which are more important for smaller gaps. Thus, the ionisation is maximum in the centre but the diffusion losses are also maximum there. However, in the transformer located

at the right of the inner gap the field is also quite high and the losses due to diffusion are less important due to its higher size.

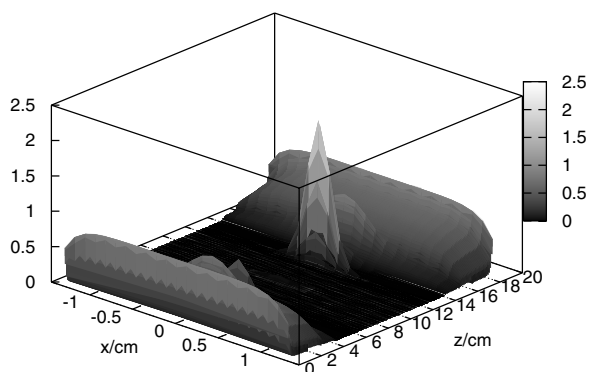


Fig. 4. Electron density inside the structure for a pressure of 10 mBar and a power of 234 W. The location of the discharge (peak) is clearly shown.

IV. CONCLUSIONS

In this paper we have presented some preliminary results of an ESA/ESTEC activity towards a simulation tool for the prediction of corona discharge inside arbitrary geometries, such as filters, based on rectangular waveguide technology. Theoretical results and measurements have been provided for a test structure showing good agreement between predicted and measured data.

V. ACKNOWLEDGEMENT

The authors would like to thank TESAT-Spacecom GmbH & Co. KG, Gerberstr. 49, 71522 Backnang, Germany, for providing the test structure Envisat as well as the measurements for corona discharge breakdown that have been used to verify the simulation tool.

REFERENCES

- [1] Y. P. Raizer, *Gas Discharge Physics*. Berlin, Heidelberg, New York, London, Paris: Springer-Verlag, 1991.
- [2] A. D. M. Donald, *Microwave breakdown in gases*. John Wiley & Sons, 1966.
- [3] D. G. Anderson, M. Lisak, and P. T. Lewin, "Thermal lowering of the threshold for microwave breakdown in air-filled waveguides," *IEEE Transactions on Microwave Theory and Techniques*, vol. 35, no. 7, pp. 653–656, July 1987.
- [4] C. Boussavie, D. Baillargeat, M. Aubourg, S. Verdeyme, P. G. A. Catherinot, S. Vigneron, and B. Theron, "Microwave breakdown in output multiplexer filters," *IEEE MTT-S International Microwave Symposium Digest*, vol. 2, pp. 1185–1188, June 2000.
- [5] T. Olsson, D. Andersson, J. Jordan, M. Lisak, V. Semenov, and M. Ahlander, "Microwave breakdown in air-filled resonators," *IEEE MTT-S International Microwave Symposium Digest*, vol. 3, pp. 915–918, June 1999.
- [6] D. Anderson, U. Jordan, M. Lisak, T. Olsson, and M. Ahlander, "Microwave breakdown in resonators and filters," *IEEE Transactions on Microwave Theory and Techniques*, vol. 47, no. 12, pp. 2547–2556, Dec. 1999.
- [7] D. Anderson, , D. S. Dorozhkina, U. Jordan, M. Lisak, T. Olsson, J. Puech, and V. E. Semenov, "Microwave breakdown around a metal wedge," in *Proceedings of the 4th International Workshop of Multipactor, Corona and Passive Intermodulation in Space RF Hardware (MULCOPIM)*, ESTEC, 2200 Noordwijk, The Netherlands, Sept. 2003.
- [8] M. Mattes and J. R. Mosig, "Integrated CAD tool for waveguide components, Final Report," Dec. 2001, contract ESA/ESTEC No. 12465/97/NL/NB.

- [9] G. Gerini, M. Guglielmi, and G. Lastoria, "Efficient Integral Equation Formulations for Admittance or Impedance Representation of Planar Waveguide Junctions," *IEEE MTT-S International Microwave Symposium Digest*, vol. 3, pp. 1747–1750, 1998.
- [10] M. Mattes, "Contribution to the Electromagnetic Modelling and Simulation of Waveguide Networks Using Integral Equations and Adaptive Sampling," Ph.D. dissertation, Ecole Polytechnique Fédérale de Lausanne, CH-1015 Lausanne, Switzerland, 2003, thesis No. 2693.
- [11] A. Alvarez-Melcón, M. Mattes, and J. R. Mosig, "A Simple Waveguide Diplexer for Satellite Communications," in *PIERS 2002 Conference Proceedings*, Cambridge, MA, USA, 2002, p. 613.
- [12] W. Woo and J. DeGroot, "Microwave absorption and plasma heating due to microwave breakdown in the atmosphere," *IEEE Physical Fluids*, vol. 27, no. 2, pp. 475–487, 1984.

Advanced Broadband 2nd-Level-Interconnects for LTCC Multi-Chip-Modules

Torben Baras and Arne F. Jacob

Arbeitsbereich Hochfrequenztechnik - Tech. Univ. Hamburg-Harburg, 21073 Hamburg, Germany

Tel: +49 40 42878 3370, Fax: +49 40 42878 2755, email: t.baras@tuhh.de

Abstract — In this paper highly integrated 2nd-Level interconnects for use in LTCC-Packages up to 50 GHz are presented. They are based on an advanced implementation of a surface mount interconnect referred to as Land-Grid-Array (LGA) and on Ball-Grid-Array (BGA) technology. The optimization process was supported by a quasi 2D inverse scattering technique in order to localize and reduce discontinuities in the signal propagation path. The optimized transitions were subject to various numerical studies to identify impacts of package mount displacements and tolerances in manufacturing. Finally, numerical results of a package-to-package path is shown.

I. INTRODUCTION

Miniaturization and high integration levels of multi-chip-modules while simultaneously maintaining low production costs appear to be one challenging aspect of tomorrow's communication equipment. Low Temperature Co-fired Ceramics (LTCC) in this context is a promising technology not only to allow for innovative packaging solutions, but also for advanced passive integration of RF-functionality due to high layer counts and low losses up to millimeter wave frequencies. Especially recent developments in LTCC processing technology with smaller feature sizes allow highly integrated and versatile components [1]. Successful implementations of LTCC multi-chip-modules have already been demonstrated for applications in e.g. Ka-band satellite communications [2] and general microwave applications up to 50 GHz [3].

In this paper, a package style as shown in Fig. 1 serves as the basic concept of hosting integrated passives and active devices such as bare dies. While the bare electronic package is one aspect, the package mounting costs, yield and reliability is another important figure. The electrical and mechanical contact between the motherboard and the module (known as 2nd-Level interconnect) is a vitally dependent interface for proper system and long term performance. Since analog RF-chips usually only require a low I/O count compared to e.g. digital processors, the RF-contacts are solely located at the edge of the package. Some microwave applications such as power amplifiers may also require thermal paths within the module, which makes electrical contacts impractical in this area. In the following, advanced LGA- and BGA-contacts for this type of package are investigated.

II. INTERCONNECT OPTIMIZATION USING INVERSE SCATTERING TECHNIQUES

Time domain reflectometry in conjunction with inverse scattering have been employed in this investigation to efficiently optimize the interconnects. The device under test (DUT) is excited with an arbitrary waveform (commonly a step) and the reflected response contains all necessary information about the composition of the DUT. Efforts have been made to de-convolve the response with knowledge of the excitation signal

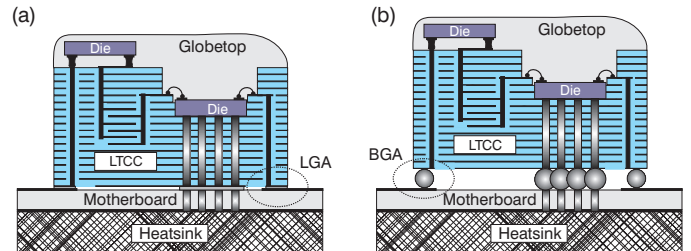


Fig. 1. LTCC electronic packages with high performance 2nd-Level Interconnects: (a) Land-Grid-Array (LGA) and (b) Ball-Grid-Array (BGA).

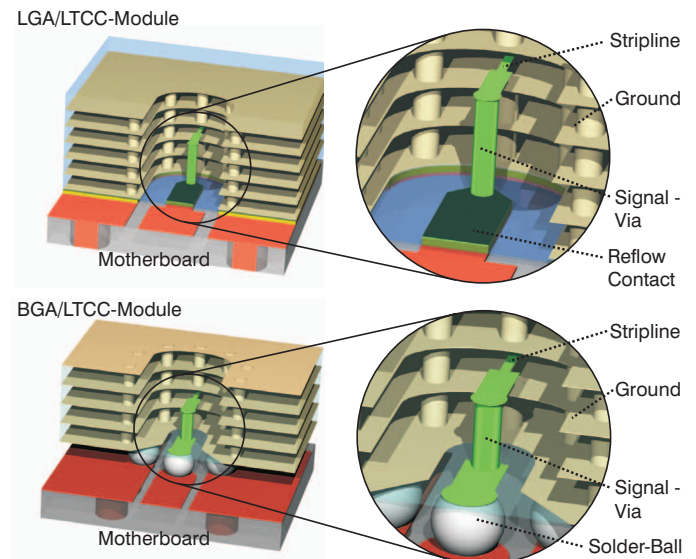


Fig. 2. Designed high performance 2nd-Level Interconnects: Land-Grid-Array (LGA) and Ball-Grid-Array (BGA). Close-ups show details of the vertical transitions and solder interfaces.

to obtain the internal impedance layers of the DUT [4], known as inverse scattering, which found application in e.g. design of planar, arbitrary shaped filters [5] or investigation of bond wire interconnects [6]. This original approach for two-dimensional objects can be extended to many 3D-problems in multi-layer circuit boards like LTCC, bearing in mind the following restrictions: The propagation through the interconnect must follow along one defined path of signal conduction without any junctions. In addition, higher order modes (e.g. parasitic parallel plate modes) must be avoided, since they represent a partial parallel path to the desired one and give rise to false results. Here, higher order modes in the motherboard substrate could be sufficiently suppressed by introducing a perfect conducting boundary at the substrate end in the calculation domain. This optimization approach allows to localize discontinuities in the path and simultaneously reduces the simulation time, since the

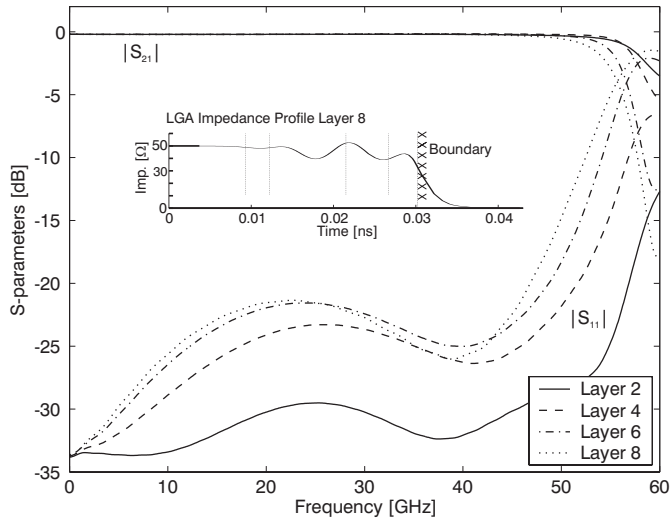


Fig. 3. LGA: Scattering parameters of launches from different stripline layers. Inset: Impedance profile of launch from layer 8.

first response from the final layer stage is sufficient.

A. Land-Grid-Array (LGA) Interconnect

The designed LGA transition from module to motherboard was implemented for a LTCC stack consisting of DP943 Tape with a nominal thickness of $110\ \mu\text{m}$ (see Fig. 2). The signal is launched from a stripline waveguide inside the module. The line is connected to a via stack leading to a reflow contact at the bottom of the module. The stack and the surrounding recessed ground layers can be interpreted as a semi-open quasi-coaxial transmission line. At the edges of the recess, vias with a pitch of $400\ \mu\text{m}$ connect all ground layers. At the module's bottom side, both ground area and patch connect to the motherboard using a solder reflow process. The signal-to-ground pitch in the area of the contact is $600\ \mu\text{m}$. On the motherboard the signal is guided by a grounded coplanar waveguide. Prior to optimization, a local inductance originating from the connection of the stripline to the via stack was revealed by the impedance profile. This discontinuity could be largely eliminated by broadening the line in this section. In the proximity of the landpad, a parasitic capacitance could be reduced by introducing chamfered edges. The inset in Fig. 3 shows the obtained impedance profile of the LGA interconnect versus propagation time after optimization. The dashed lines are boundaries between different geometries (e.g. stripline, via, landpad), which have been estimated from effective propagation velocities and geometrical dimensions. Because of the said conductive boundary the impedance in the profile declines to zero.

Launches from stripline layers of different heights (Layer 2 is the closest to the motherboard) have been simulated. Ideally, the scattering parameters should be unchanged. However, due to manufacturing limits and unavoidable discontinuities in the signal path a small influence remains, as Fig. 3 depicts.

B. Ball-Grid-Array (BGA) Interconnect

A Ball-Grid-Array is another approach to contact the module. The solder balls are self-formed by surface tension and simultaneously align the module. Earlier investigations could demonstrate this technology for frequencies up to 30 GHz [7]

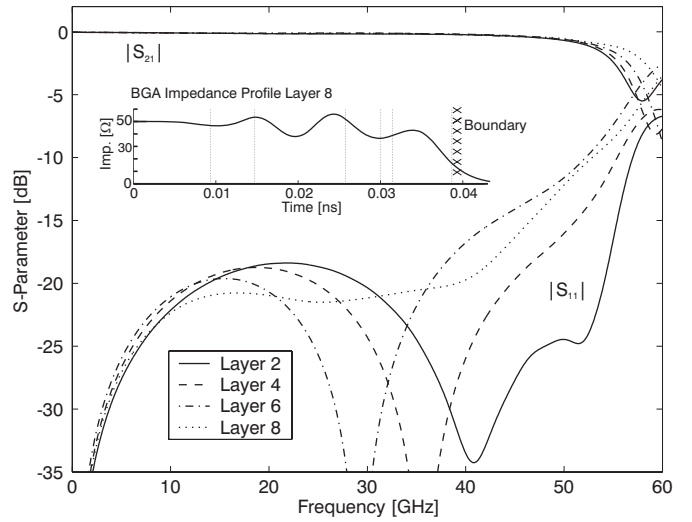


Fig. 4. BGA: Scattering parameters of launches from different stripline layers. Inset: Impedance profile of launch from layer 8.

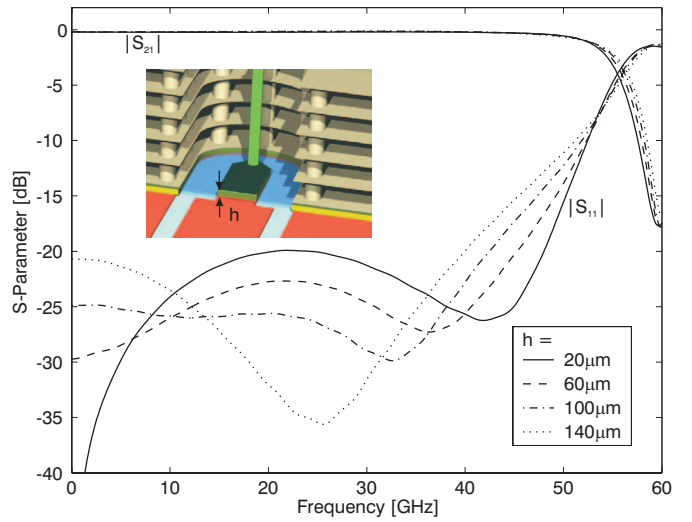


Fig. 5. Impacts of reflow layer height variations on the LGA transition performance.

in LTCC packages and even up to 60 GHz in hybrid packages [8]. In this study, the edge-located BGA contact was derived from the optimized LGA contact, wherein the reflow area was redesigned (see Fig. 2). The bottom ground was narrowed to form a CPW transmission line. This measure could significantly improve the broadband performance. In addition, the solder balls were staggered to increase the impedance of the ball contacts. The entire impedance profile is shown in Fig. 4 (see inset). Compared to the impedance profile of the LGA contact, the BGA transition reveals greater variations in the proximity of the reflow contact. This is attributed to the discontinuities due to the changes of dielectric layers from LTCC ($\epsilon_r = 7.4$) to air ($\epsilon_r = 1.0$) to the motherboard ($\epsilon_r = 3.27$). As with the LGA, a study on the layer dependency of the launch has been performed. Here, significant changes in the return loss are solely visible at frequencies beyond 30 GHz.

III. PACKAGE MOUNT DISPLACEMENT ANALYSIS

While the BGA uses self-aligning techniques to help mounting the package, the LGA-contact does not provide this feature. In order to estimate the sensitivity of the transition

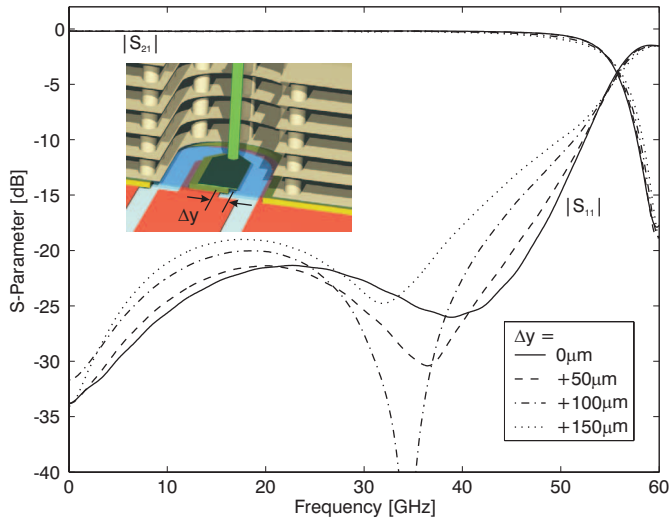


Fig. 6. Impacts of module displacements in y-direction on the LGA transition performance (Reflow layer is $40 \mu\text{m}$).

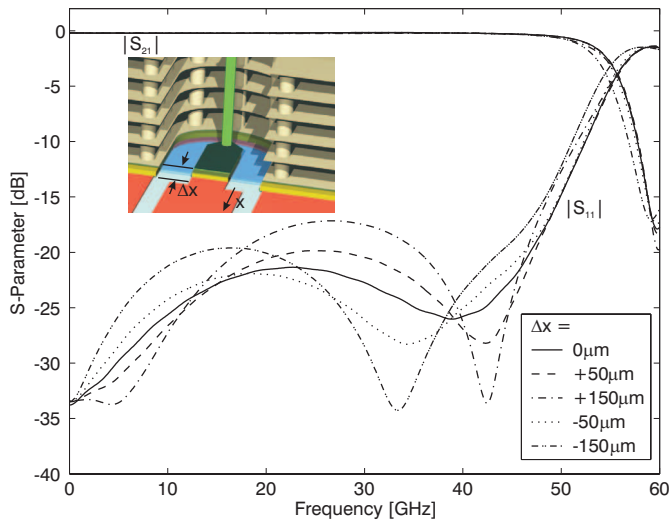


Fig. 7. Impacts of module displacements in x-direction on the LGA transition performance (Reflow layer is $40 \mu\text{m}$).

to manufacturing tolerances and placement errors, results of a numerical study are shown in the following. The solder paste to attach the module can be dispensed in a large variety of techniques as e.g. stencil print or screen print, which can give rise to varying thicknesses of the final solder layer. As shown in Fig. 5, variations from $20 \mu\text{m}$ to $140 \mu\text{m}$ only have a minor impact on the transition performance. A broadband transfer function with low insertion loss and low return loss for frequencies beyond 50 GHz is revealed. Additionally, misalignments between package and footprint on the motherboard were simulated. As shown in Fig. 6, a shift of the package into y-direction causes a slight increase in return loss, originating from a change in the optimized impedance of the center reflow contact. A misalignment in x-direction shows two tendencies: A shift in positive x-direction causes more increase in return loss than in negative x-direction, which is attributed to the capacitive overlap from the motherboard footprint occurring solely in positive sense. Overall, the performance is very insensitive to misalignments between package and board.

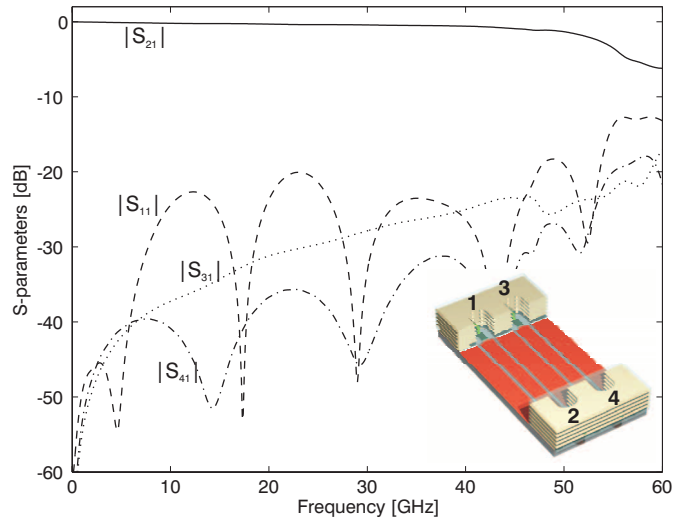


Fig. 8. Scattering parameters of a package-to-package interconnect using LGAs.

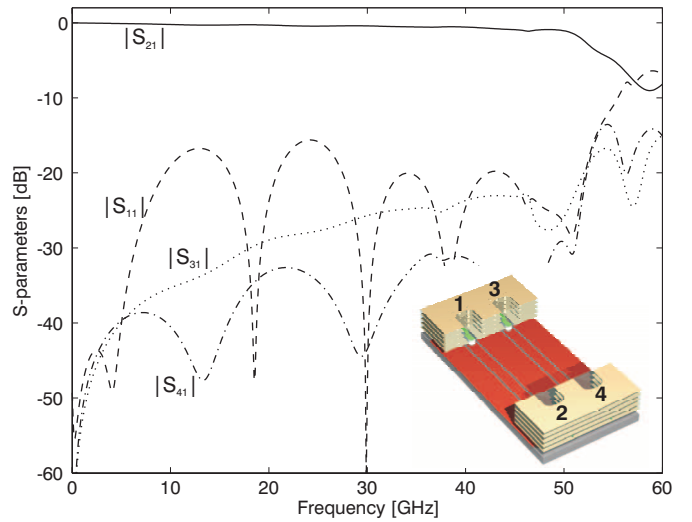


Fig. 9. Scattering parameters of a package-to-package interconnect using BGAs.

IV. PACKAGE-TO-PACKAGE SIMULATION

A 10 mm link between two multi-chip modules across the motherboard is a final point in this investigation. This setup is more likely to occur than just a single transition, since the communication system may comprise a set of microwave modules serving as building blocks for the entire system. The link consists of a pair of identical channels in order to determine the crosstalk due to mutual coupling between transitions and lines. The simulation results and setups for both LGA and BGA interconnects are displayed in Figs. 8 and 9. The distance between the transitions on a module and CPWG lines on the motherboard measures 2 mm , respectively. Both CPWG transmission lines share one ground strip, which provides electrical through-holes to the bottom metallization. This measure reduces crosstalk on the motherboard level and inhibits modal degeneration. For the 2^{nd} -Level interconnect, a launch from Layer 2 in all modules was chosen. Furthermore, perfect alignment with a reflow layer thickness of $40 \mu\text{m}$ was assumed. As shown in the results, both electronic packages perform very similar in terms of insertion loss, return loss and

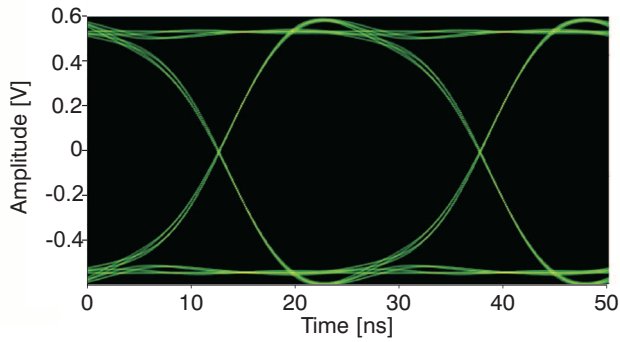


Fig. 10. Simulated eye-diagram of the broadband package-to-package path using LGAs at 40 Gbps. RMS-Jitter=0.16 ps.

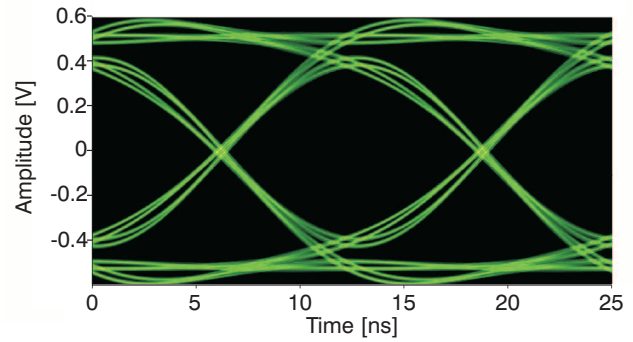


Fig. 12. Simulated eye-diagram of the broadband package-to-package path using LGAs at 80 Gbps. RMS-Jitter=0.21 ps.

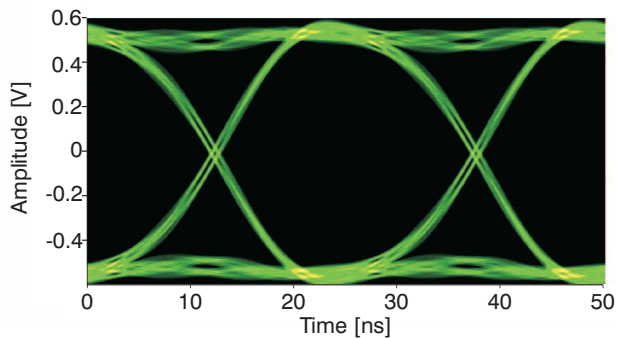


Fig. 11. Simulated eye-diagram of the broadband package-to-package path using BGAs at 40 Gbps. RMS-Jitter=0.36 ps.

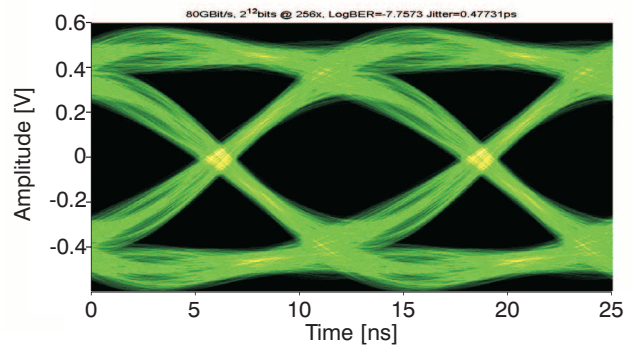


Fig. 13. Simulated eye-diagram of the broadband package-to-package path using BGAs at 80 Gbps. RMS-Jitter=0.48 ps.

crosstalk. The LGA version provides a slightly lower return loss as a result of a better impedance control. Both types of transitions provide a flat transfer function past the 50 GHz mark with low crosstalk. Good performance for broadband data applications is revealed in Figs. 10-13. Here, simulations have been carried out for data rates of 40 Gbps and 80 Gbps in NRZ format. A random sequence of 2^{12} bits transmitted in single ended mode from one module to another was simulated. The LGA-transitions show improved jitter and a larger eye-opening as a measure for the quality of the data channel. This becomes even more obvious at the higher data rate of 80 Gbps.

V. CONCLUSIONS

Two broadband 2^{nd} -Level interconnects for LTCC based multi-chip modules were presented. Possible applications are general microwave packaging and broadband communication systems up to 50 GHz. Proper impedance control allows launches from virtually any layer of the LTCC package. The LGA interconnect was analyzed for placement and manufacturing tolerances and showed only little sensitivity. Package-to-Package simulations showed a very broadband transfer function with very little crosstalk. Here, the LGA performed slightly better compared to the BGA. Validation by measurements will be performed in the near future.

ACKNOWLEDGMENT

The authors would like to acknowledge financial support from *BMBF* (Bundesministerium für Bildung und Forschung) and *DLR* (Deutsches Zentrum für Luft- und Raumfahrt) under research contract 50YB0314 (*KERAMIS*).

REFERENCES

- [1] D. Anderson, "Trends in LTCC processing," *2003 IMAPS Conference and Exhibition on Ceramic Interconnect Technology: The Next Generation*, 2003.
- [2] R. Kulke, J. Kassner, G. Möllenbeck, M. Rittweger, and P. Waldow, "Ka-band power-distribution networks on multilayer LTCC for broadband satellite multimedia application," *EuMC, Workshop WS-8: "Ceramic based Microwave Circuits", Proceedings*, pp. 17–20, 2003.
- [3] K. Yoshida, T. Shirasaki, S. Matsuzono, and C. Makihara, "50 GHz broadband SMT package for microwave applications," *2001 IEEE Electronics Components and Technology Conference*, pp. 744–749, 2001.
- [4] A. Bruckstein and T. Kailath, "An inverse scattering framework for several problems in signal processing," *IEEE ASSP Magazine*, pp. 6–20, 1987.
- [5] P. P. Roberts and G. E. Town, "Design of microwave filters by inverse scattering," *IEEE Transactions on Microwave Theory and Techniques*, vol. 43, no. 4, pp. 739 – 743, 1995.
- [6] C. Schuster and W. Fichtner, "Signal integrity analysis of interconnects using FDTD method and a layer peeling technique," *IEEE Transactions on Electromagnetic Compatibility*, vol. 42, no. 2, pp. 229–233, 2000.
- [7] J. Heyen, T. v. Kerksenbrock, A. Chernyakov, P. Heide, and A. F. Jacob, "Novel LTCC-/BGA-modules for highly integrated millimeter-wave transceivers," *IEEE Transactions on Microwave Theory and Techniques*, vol. 51, no. 12, pp. 2589 – 2596, 2003.
- [8] J. Galière, J. Valard, and E. Estèbe, "Millimetre-wave MMIC packaging compatible with surface-mount technology," *34th European Microwave Conference, Amsterdam*, pp. 353 – 355, 2004.

2D Periodic Defected Ground Structure for Coplanar Waveguide

Ehab K. I. Hamad¹, Amr M. E. Safwat², and Abbas S. Omar¹

¹ Chair of Microwave and Comm. Eng., Otto-von-Guericke-University Magdeburg, Magdeburg 39016, Germany

² Electronics and Comm. Eng. Dept., Faculty of Eng., Ain Shams University, Cairo 11517, Egypt

ehamad@iesk.et.uni-magdeburg.de, asafwat@ieee.org, and a.omar@ieee.org

Abstract — A two-dimensional (2D) periodic defected ground structure for coplanar waveguide (PDGSCPW) is proposed. It is based on the repetition of a unit-cell in a simplified and systematic way. The equivalent circuit model of the defected ground is a simple parallel resonance circuit, which is connected to the main line. The 3D EM simulation and the equivalent circuit model suggest that the capacitance is almost constant while the inductance varies linearly relative to the number of cells, which implies the simplicity of the design process. The center frequency varies from 7 GHz down to 4 GHz with more than 20 dB rejection in the stopband when the number of cells increase from 2 to 9-cells. Measurements are in excellent agreement with theoretical predictions.

Index Terms — Defected ground structure (DGS), Coplanar waveguide, 2D Periodic defected ground structure.

I. INTRODUCTION

Defected ground structures (DGS) have shown increasing potential for implementation in different applications: MIC, MMIC, and RFIC [1-5]. They provide sharp, distinct electromagnetic band-gap and high slow wave factor, which lead to smaller size circuits. They have been used numerously in the recent years, however most of the applications are in microstrip structures [6-8]. In these structures, well-defined shapes are etched at the back metal. This requires a precise double-sided processing and adequate packaging to keep an air-gap between the ground and the package. Coplanar waveguides (CPW) on the other hand have both signal and ground on the same surface. Though they occupy larger area than microstrip lines, they can be considered as a good compromise for DGS. Moreover, CPWs are used for circuit design since they can be easily integrated into existing RF ICs without the need for incorporating via-holes. They are less sensitive to the substrate thickness and substrate dielectric constant than the microstrip structures [9].

To our knowledge, few applications for DGS on CPW have been reported, among them are: The dumbbell shaped DGS is presented in [1], a vertically periodic DGS is proposed in [3] for microstrip and CPW line in which the periodicity takes place in the vertical direction only, a one-dimensional DGS structure where the periodicity is in the horizontal direction is presented in [4], and a spiral shaped DGS is proposed in [10].

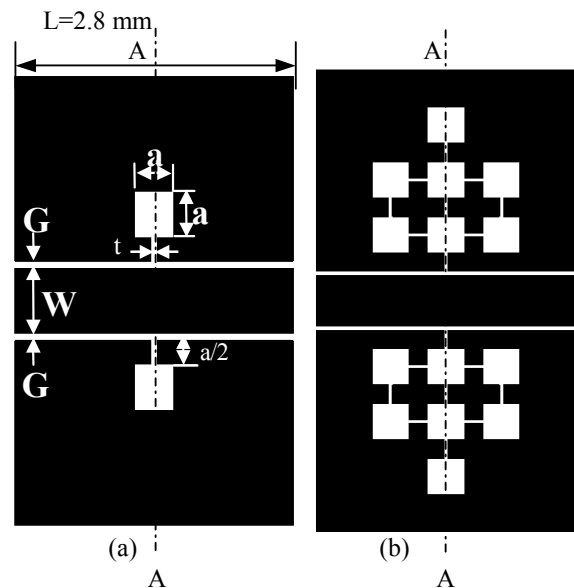


Fig. 1. Schematic diagram of (a) Standard dumbbell structure, (b) PDGSCPW structure, A-A is symmetrical axis of the structure

In this contribution, a 2D periodic dumbbell structure is proposed, the dumbbell structure is added as a unit-cell in a systematic way in both horizontal and vertical directions to construct the 2D periodic DGS. This technique best utilizes the area to get very low stop band frequencies. Design methodology, electromagnetic simulation and equivalent circuit model are presented in the next section. These are followed by the experimental verification in section III.

II. STRUCTURE DESIGN METHODOLOGY

The periodic DGSCPW structure is based on the standard dumbbell structure, shown in Fig. 1.a. The cells are added such that the symmetry along the axes (A-A) of the dumbbell is kept unchanged. Thus, for the two-cells structure, the cell is added above cell one. For three-cells, two-cells are placed to the left and to the right of the original cell. The same process is applied for larger number of cells. The schematic diagram of 7-cells is shown in Fig. 1.b. The schematic diagrams of 2, 3, 4, 5-cells are shown in

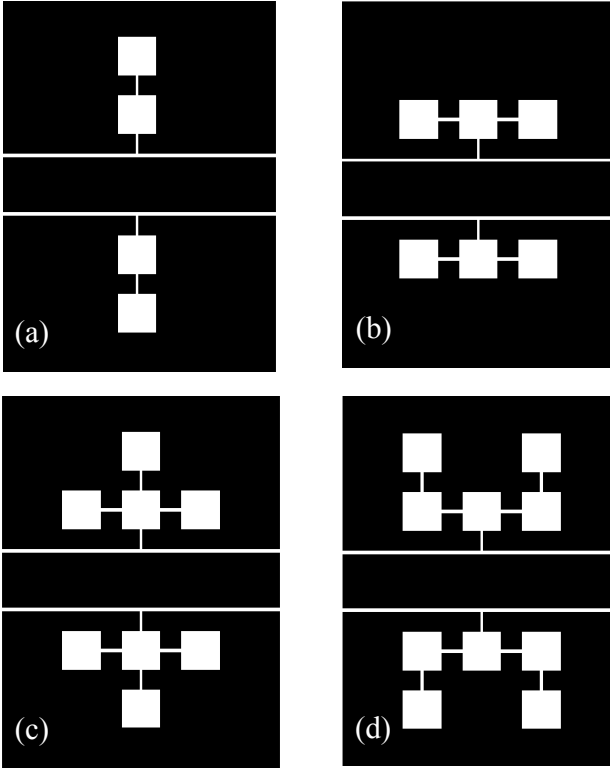


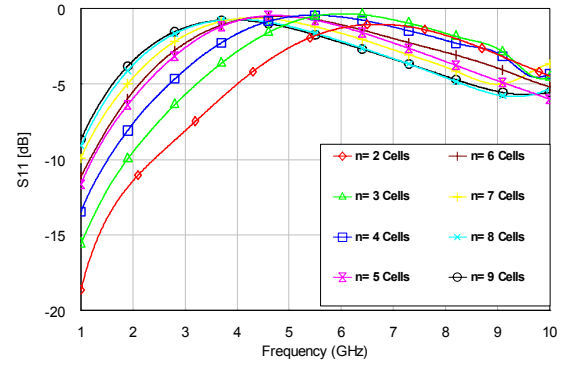
Fig. 2. The Proposed periodic DGSCPW (a) 2-Cells, (b) 3-Cells, (c) 4-Cells, and (d) 5-Cells

Fig. 2 respectively. For the case of 7 and 8-cells, we preferred to put them in the third row instead of the first row.

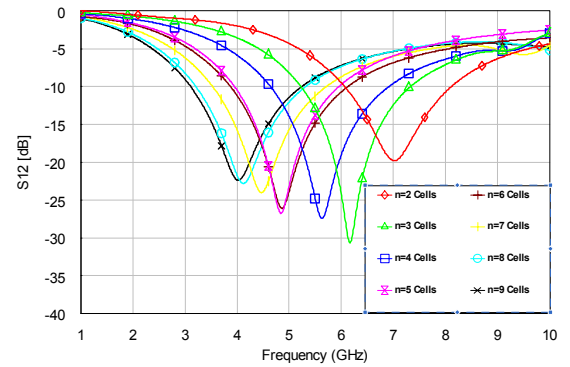
A. 3D EM Simulation

The unit dumbbell structure was designed for coplanar waveguide line with $50\text{-}\Omega$ characteristic impedance for good RF impedance matching. $G/W/G$ is $0.2/2.8/0.2$ mm, where W is the width of the center conductor and G is the slot width as shown in Fig. 1. The dielectric constant of the substrate is 3.38, its height is 0.813 mm, and the metal thickness is $35\text{ }\mu\text{m}$. The first step in the design is to optimize the parameters of the unit-cell to get a stop band response centered at a certain frequency, e.g. 12 GHz, with the constraint that the unit-cell has dimensions of $a \times a$ and it has been etched in both ground planes symmetrically a distance $a/2$ far from the slot of the CPW line. This was achieved using the 3D EM simulator, Microwave Studio v. 5. The optimized dimensions for the unit-cell are: $a \times a = 2 \times 2$ mm, and gap width $t = 0.2$ mm.

Two, three and up to nine-cells are arranged as explained in the previous section. Their performances are investigated using Microwave Studio. The S-parameters of the 8 structures are shown in Fig. 3. S_{12} depicts a minimum at a frequency determined by the structure geometry. Its value



(a)



(b)

Fig. 3. Frequency response for the PDGSCPW with different number of cells (a) S_{11} , and (b) S_{12}

decreases as the number of cells increase. For $n=2$ (n is the number of cells) this frequency is 7 GHz, while for $n=9$, the frequency is 4 GHz. In all structures, the magnitude of S_{12} at the resonance frequency is more than 20 dB.

B. Circuit Modeling

The performance of the periodic defected ground structures is modeled using circuit lumped elements. Fig. 4. illustrates the equivalent circuit model. It consists of a shunt capacitance, inductance, and resistance to model the defected region [11] and two sections of transmission lines connected in series at both sides. The length of the transmission line is equal to the distance from the center of the basic unit-cell to the reference plane, $L/2 = 14$ mm, the characteristic impedance is $50.6\text{-}\Omega$ and the effective dielectric constant is 1.885 as determined by the EM simulator. This equivalent circuit model is the same for any number of repeated cells. Fig. 5. shows the variation of the equivalent capacitance, the equivalent inductance and the equivalent resistance as a function of the number of cells. The equivalent capacitance is approximately constant independent of the number of cells, the equivalent inductance increases linearly as the number of cells

increases and there are minor changes in the resistance. These results can be interpreted to the structure geometry as follows: As the number of cells increases, the path of the current increases, which increases the value of the inductance linearly since all cells have constant perimeter. The capacitance is mainly determined by the capacitance of the gap of the first cell, which is kept constant in all iterations. The resistance corresponds to the radiation, conductor, and dielectric losses in the defect.

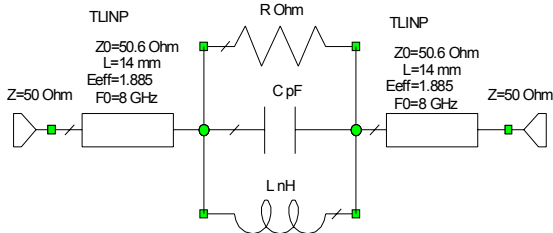


Fig. 4. Equivalent circuit model of the PDGSCPW structure, L, C, and R correspond to the defected region.

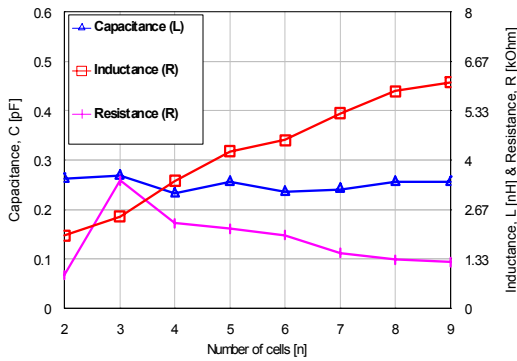


Fig. 5. Equivalent capacitance, inductance, and resistance versus the number of cells for the PDGSCPW

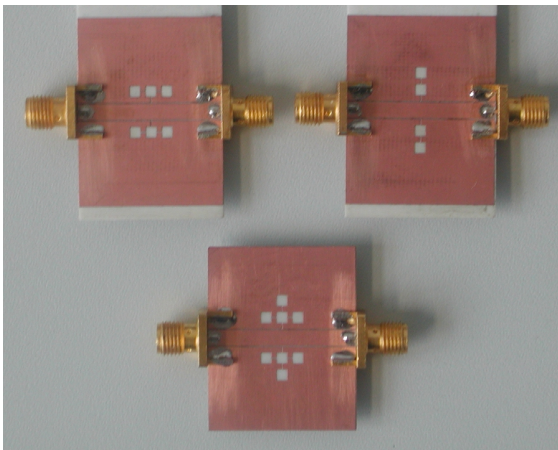


Fig. 6. Picture of the fabricated PDGSCPW 2, 3 and 4 cells

III. EXPERIMENTAL VERIFICATIONS

Two, three and four-cells periodic DGS for CPW line are fabricated on Ro4003c substrate with all design parameters similar to that described in the simulation. The picture of the fabricated structures is shown in Fig. 6. The structures are measured using 8722D vector network analyzer from 1-10 GHz. Fig. 7. shows the measured S-parameters for the three structures. Results of the EM simulator and circuit simulator are also shown on the same graph. Excellent agreement has been achieved.

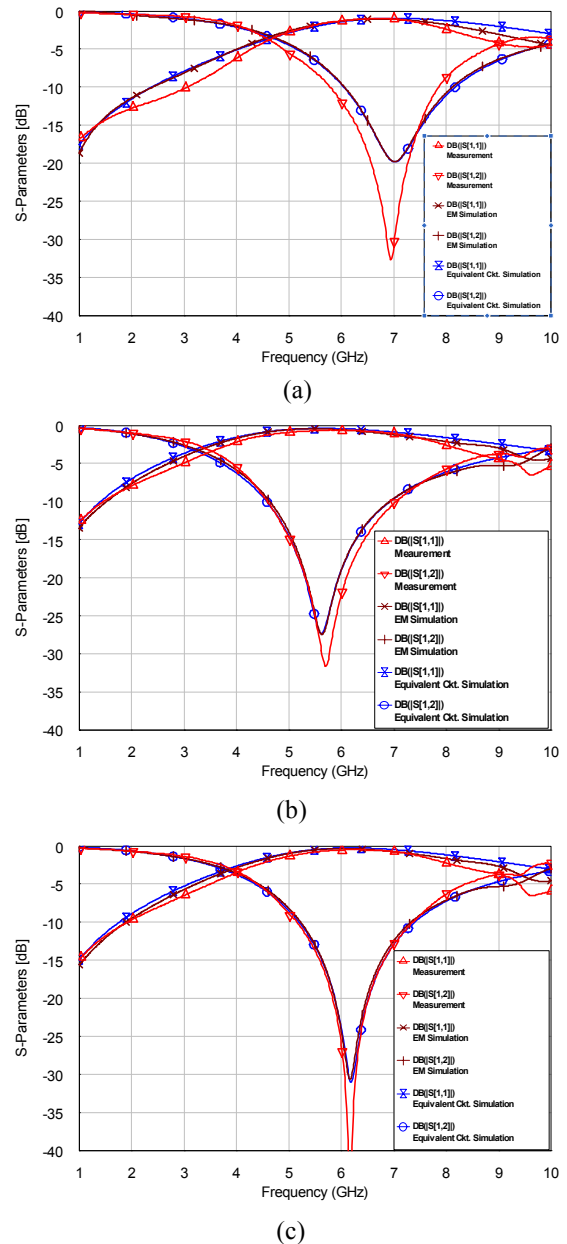


Fig. 7. Measurement, EM simulation, and circuit simulation for the PDGSCPW (a) 2-Cells, (b) 3-Cells, and (c) 4-Cells

IV. CASCADED PDGSCPW

The PDGS is cascaded to get a wide stop band with very sharp edges filter. The number of cells in the cascaded PDGS sections controls the center frequency of the stop band. The number of the cascaded sections and the separation between them control the sharpness and the width of the band. Two, and four sections separated by 3 mm using four-cells PDGSCPW are fabricated and measured with 2.5, 3.8 GHz bandwidth and more than 27, 33 dB rejection respectively. Pictures for the fabricated structures are shown in Fig. 8.a. The measured and simulated RF performances are shown in Fig. 8-b and c. Good agreement has been achieved.

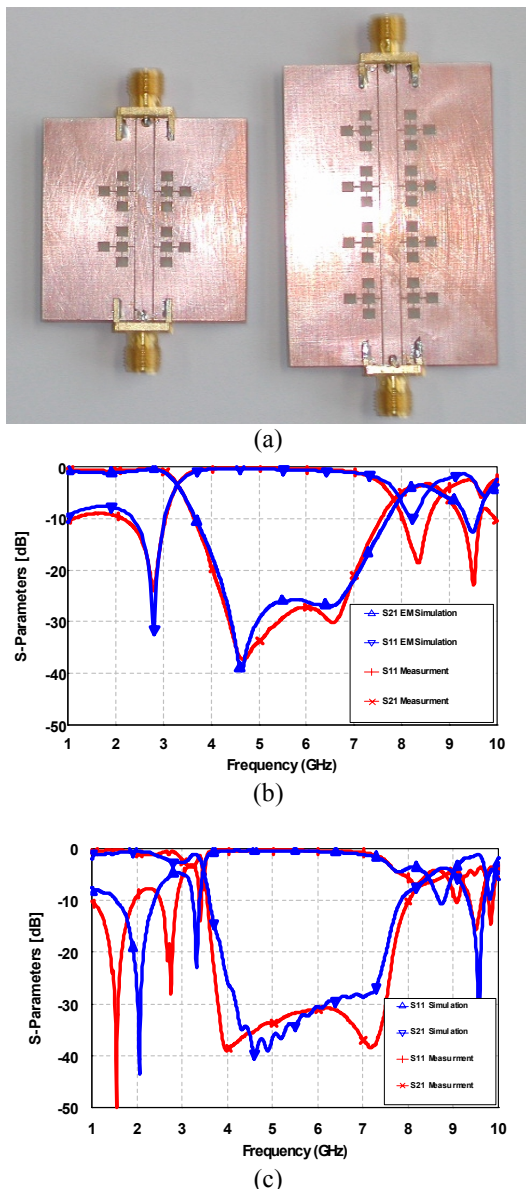


Fig. 8. (a) Picture of 2 and 3-sections of 4-cells PDGSCPW, (b) RF performance for the fabricated 2-sections, and (c) 3-sections of the 4-cells PDGSCPW

V. CONCLUSION

A 2D periodic defected ground structure for coplanar waveguide has been proposed. The proposed structure is based on the standard dumbbell structure, which is repeated periodically to control the central frequency. The proposed structure has the advantage of having an almost constant capacitance while the inductance varies linearly as the number of cell increases, which simplifies the design process. Two and four sections of PDGS are cascaded to form wide-bandstop filters with high rejection. Excellent agreement has been achieved between the EM simulation, the circuit simulation and the experimental results.

REFERENCES

- [1] D. Ahn, J. S. Park, C. S. Kim, Y. Qian, and T. Itoh "A Design of the Lowpass Filter Using the Novel Microstrip Defected Ground Structure," *IEEE Transactions on Microwave Theory and Techniques*, Vol. 49, No. 1, pp. 86-93, January 2001.
- [2] J.-S. Lim, Ch.-S. Kim, Y.-T. Lee, et al, "A new type of low pass filter with defected ground structure", *European Microwave Week 2002* in Milan, Italy, 24-26 September 2002.
- [3] Jong-Sik Lim, Young-Taek Lee, Chul-Soo Kim, Dal Ahn, and Sangwook Nam, "A Vertically Periodic Defected Ground Structure and Its Application in Reducing the Size of Microwave Circuits", *IEEE Microwave And Wireless Components Lett.*, Vol. 12, No. 12, pp. 479-481, Dec. 2002.
- [4] Tae-Yeoul Yun and Kai Chang, "Uniplanar one-dimensional Photonic-Bandgap Structures and Resonators", *IEEE Transactions on Microwave Theory and Techniques*, Vol. 49, No. 3, pp. 86-93, March 2001.
- [5] Man-Long Her, Chin-Min Chang, Yu-Zhen Wang, Fan-His Kung, and Yi-Chyun Chiou, "Improved Coplanar Waveguide (CPW) Bandstop Filter with Photonic Bandgap (PBG) Structure", *Microwave and Optical Technology Letters*, Vol. 38, No. 4, pp. 274-277, August 2003.
- [6] Q. Xue, K. M. Shum, and C. H. Chan, "Novel 1-D microstrip PBG cells," *IEEE Microwave Guided Wave Letters*, Vol. 10, pp. 403-405, October 2000.
- [7] Jong-Sik Yoon, Jun-Goo Kim, Jun-Seok Park, Choe-Seok Park, Jea-Bong Lim, Hong-Gu Cho, and Kwang-Yong Kang, "A New DGS Resonator and Its Application to Bandpass Filter Design", *IEEE MTT-S Int. Symp. Dig.*, Texas, USA, pp1605-1608, 2004.
- [8] V. Radisic, Y. Qian, R. Coccioli, and T. Itoh, "Novel 2-D photonic bandgap structure for microstrip lines," *IEEE Microwave Guided Wave Letter*, vol. 8, pp. 69-71, Feb. 1998.
- [9] K. T. Chan, Albert Chin, Ming-Fu Li, Dim-Lee Kwong, Sean P. McAlister, D. S. Duh, W. J. Lin, and C. Y. Chang, "High-Performance Microwave Coplanar Bandpass and Bandstop Filters on Si Substrates", *IEEE Trans. on Microwave Theory and Techniques*, vol. 51, no. 9, pp. 2036-2040, Sept. 2003.
- [10] Young-Taek Lee, Jong-Sik Lim, Sungwon Kim, Jaechun Lee, Sangwook Nam, Kwang-Seok Seo, and Dal Ahn, "Application of CPW Based Spiral-Shaped Defected Ground Structure to The Reduction of Phase Noise in V-Band MMIC Oscillator", *IEEE MTT-S International Symposium Digest*, Pennsylvania, USA, pp. 2253-2256, 2003.
- [11] Insik Chang and Bomson Lee, "Design of Defected Ground Structures for Harmonic Control of Active Microstrip Antenna", *IEEE APSIS*, Vol. 2, pp. 16-21, June 2002.

A Compact Differential Inductor with Improved Self-Resonance Frequency

Vito Minerva

Polytechnic of Milan, Dept. of Electronics and Information, P.za Leonardo da Vinci, 20133 Milan, Italy,
phone: +39-02-2399 9610, email: minerva@elet.polimi.it

Abstract — An original multi-layer structure is proposed for the realization of monolithic differential inductors. Compared with standard differential topologies of equal inductance, it can reduce the area occupation by more than 50% and increase the self-resonance frequency f_{SR} up to 30%. However, because of the high resistivity of the lower metal layers, the quality factor Q decreases by 25–40% and makes this inductor mainly interesting for applications like chokes.

The higher f_{SR} is obtained through an optimized sequencing of wires. In fact, a second stacked differential inductor without wiring optimization gives no benefits in f_{SR} , but only in area reduction, and shows the importance of a proper layout. The novel structure was fabricated in a silicon-germanium technology; measurements report $f_{SR} = 5.66$ GHz for a 14-nH inductance. An analytical model for single- and multi-layer differential inductors is also introduced. The model is in good agreement with experimental results, with a 5% error in f_{SR} and a 6% error in inductance.

I. INTRODUCTION

Monolithic inductors are extensively used in RF integrated circuits like amplifiers, oscillators and mixers [1]. Because of their low quality factor Q , several topologies and/or mechanisms for increasing it have been reported in the literature – see for instance the bibliography in [2] – while only little efforts have been concentrated on the area reduction and on the increase in self-resonance frequency f_{SR} . These issues are especially important when a high inductance is required, since inductance L is in direct proportion to area, which in turn is in inverse relation to f_{SR} [1]. Furthermore, as integrated inductors are used at higher and higher frequencies, it becomes more and more important to extend their operational bandwidth.

One of the most promising topologies to emerge in the last couple of years is the differentially-driven, symmetric inductor. Compared to a single-ended inductor, it has better Q , higher f_{SR} and occupies less chip area [2].

To shrink the size and increase f_{SR} , it makes sense, then, to start from differential inductors. First, an analytical model is introduced to predict f_{SR} of differential structures on a single metal layer (Section II). This model can be easily extended to multiple-layer inductors; two of them are presented in Section III. Both reduce the area occupation and one also increases the self-resonance frequency, while the other has about the same f_{SR} as the single-layer topology. The new high- f_{SR} structure and the standard differential inductor are investigated in relation with their dimensions in Section IV. Experimental results and comparisons with the analytical model are provided in Section V. Finally, conclusions are drawn in Section VI.

II. ANALYTICAL MODEL

In order to evaluate the frequency behaviour of a novel single-ended inductor, a distributed capacitance model (DCM)

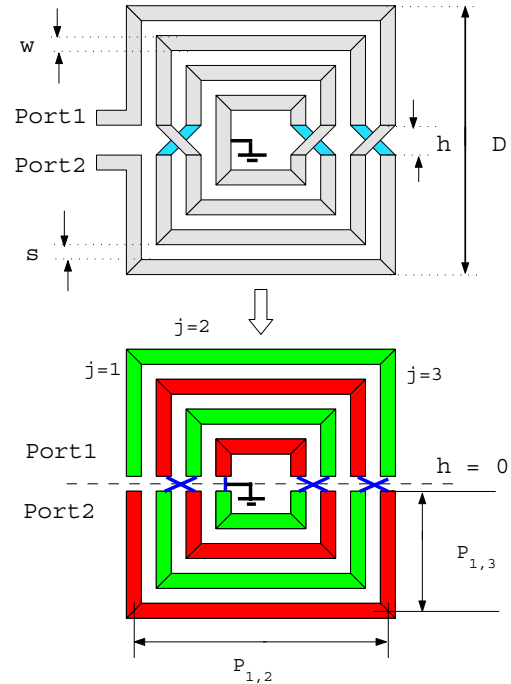


Fig. 1. Differential inductor with $N = 4$ turns (top) and corresponding approximation used in the model (bottom). $P_{n,i}$, with $n = 1, \dots, N$, $i = 1, \dots, 3$, are the lengths of the wires; $n = 1$ is the outermost turn.

was presented in [3]. This model has been extended in [4] to take into account the spacing between the metal lines; another add-on is that voltage is not constant in each turn, but in each segment. Moreover, capacitances are computed with analytical formulas instead of using values provided by the technology manuals. This way, the model is more general and can also be applied to differential structures.

In fact, in differentially-driven inductors, the two halves of each turn have opposite voltages, so that the hypothesis of constant voltage per turn does not apply. Furthermore, the effect of parasitic capacitances between adjacent turns, and therefore the spacing, can not be neglected, because adjacent tracks are 180° out of phase to each other.

To simplify the model, a standard differential inductor (SDI for short), like the one reported on top of Fig. 1, is approximated by a set of concentric squares (bottom of Fig. 1). The crossings, which have a physical dimension h , are replaced by ideal cross-connections with $h = 0$. The other dimensions, namely D , w and s and the number of turns N (see Fig. 1), are equal for the real and for the approximated structure.

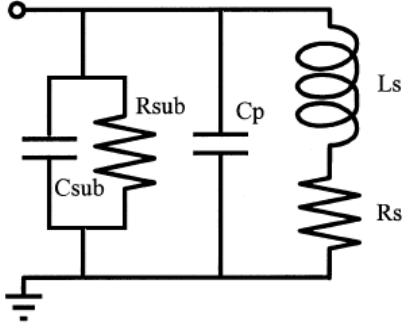


Fig. 2. Equivalent circuit of an integrated inductor.

Actually, a differential structure is composed of two inductors, as the different colours used in the approximated structure in Fig. 1 highlight. Considering either of them, the length $P_{n,i}$ of i -th metal strip in the n -th turn is (see Fig. 1)

$$P_{n,i} = \begin{cases} \frac{D-w}{2} - (n-1) \cdot (w+s) & \text{for } i = 1, 3, \\ D-w-2 \cdot (n-1) \cdot (w+s) & \text{for } i = 2, \end{cases} \quad (1)$$

The total length of the two inductors is then

$$P = 2 \cdot \sum_{n=1}^N \sum_{i=1}^3 P_{n,i} = 4 \cdot N [D-w - (N-1) \cdot (w+s)], \quad (2)$$

If the voltage applied at Port 1 is V and if the voltage drops linearly from input to ground [3], then the voltage in the middle of the i -th metal strip in the n -th turn is

$$V_{n,i} = \frac{2V}{P} \cdot \left(i \cdot P_{n,i} + \sum_{k=n+1}^N \sum_{j=1}^3 P_{k,j} \right), \quad (3)$$

for the inductor starting at Port 1 and $\tilde{V}_{n,i} = -V_{n,i}$ for the one starting at Port 2.

Then, the total electric energy stored by the differential inductor can be expressed as

$$U_{E,tot} = \frac{1}{2} \cdot \left\{ C_g w \sum_{n=1}^N \sum_{i=1}^3 P_{n,i} (V_{n,i}^2 + \tilde{V}_{n,i}^2) + C_m t \sum_{n=1}^{N-1} \sum_{i=1}^3 \frac{P_{n+1,i} + P_{n,i}}{2} \cdot \left[(V_{n+1,i} - \tilde{V}_{n,i})^2 + (\tilde{V}_{n+1,i} - V_{n,i})^2 \right] \right\}, \quad (4)$$

where C_g is the metal to substrate capacitance per unit area (p.u.a.) and C_m is the mutual capacitance between adjacent turns p.u.a. They are calculated with expressions in [5], but other formulas could also be as effective.

The differential inductor can be represented as a whole by the equivalent circuit in Fig. 2, where L_s and R_s are the total series inductance and the total series resistance, respectively, C_p is the inter-turn capacitance, R_{sub} the substrate resistance

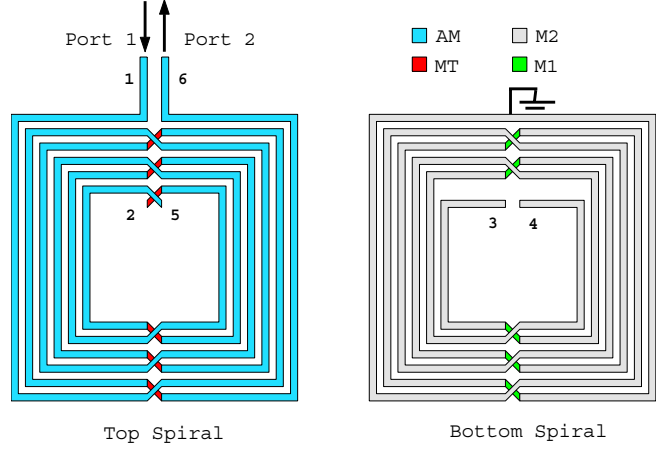


Fig. 3. A Vetically Stacked Differential Inductor, or VSDI. Current flows as indicated by numbers.

and C_{sub} the substrate capacitance. From Fig. 2 it follows that $U_{E,tot}$ can also be expressed as

$$U_{E,tot} = \frac{1}{2} C_p (2V)^2 + \frac{1}{2} C_{sub} (2V)^2, \quad (5)$$

where $2V$ is the voltage difference at the input ports. The equivalent capacitances C_p and C_{sub} are found by equating (4) with (5).

Finally, the self-resonance frequency is

$$f_{SR} = \frac{1}{2\pi\sqrt{L_s C_{tot}}}, \quad (6)$$

where $C_{tot} = C_p + C_{sub}$. L_s is computed with the quasi-static formulas in [6], while R_{sub} is obtained from [7].

III. STACKED DIFFERENTIAL INDUCTORS

Compared with single-ended structures, differential inductors reduce by 35% the area occupation [2]. But, to further decrease their overall dimensions, they can be fabricated on multiple metal layers (see Figs. 3, 4). The extension of the analytical model of Section II to stacked inductors is straightforward, with the only addition of an equivalent capacitance C_{ol} between the top and the bottom spiral and the further hypothesis of a total voltage equally divided among the metal layers¹.

The structure in Fig. 3 is called *Vetically-Stacked Differential Inductor*, or VSDI [4], [8], and is composed of two series-connected spirals. The model shows that the electric energy in VSDI inductors is mainly stored between the overlapped spirals, so that C_{ol} is the main contribution to C_{tot} and negatively affects f_{SR} .

The contribution of C_{ol} to C_{tot} can be reduced by the sequencing of turns in Fig. 4. Roughly speaking, this structure (called *Radially Stacked Differential Inductor*, or RSDI [4], [8]) consists of one turn on the top layer, two turns on the bottom layer, another two on the top layer and so on, until the ground node is reached. Thanks to this continuous shifting from the top to the bottom spiral, and vice versa, the voltage difference between overlapped wires is reduced and so is $U_{E,tot}$. The net result is an increase in f_{SR} .

¹However, see [4] for more details.

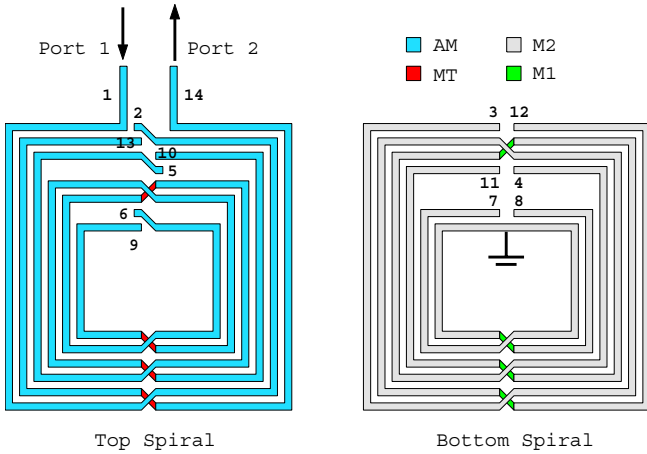


Fig. 4. A Radially Stacked Differential Inductor, or RSDI. Current flows as indicated by numbers.

TABLE I

SiGe5AM TECHNOLOGY PARAMETERS. T IS THE METAL THICKNESS, H IS THE DISTANCE FROM THE SUBSTRATE AND R IS THE METAL RESISTIVITY IN “OHM PER SQUARE”.

Metal	$T(\mu\text{m})$	$H(\mu\text{m})$	$R(\Omega/\square)$
AM	4.00	9.61	0.00725
MT	0.83	5.78	0.045
M2	0.85	3.73	0.045
M1	0.63	1.90	0.076

Notice that RSDI’s turns are not equally spaced and hence the top and bottom spiral’s overlapping is not maximum (see Fig. 4). This is necessary to accommodate the numerous crossings. By contrast, in VSDI inductors the two spirals overlap almost perfectly (Fig. 3).

A larger overlapping results in a larger inter-wire capacitance and thus lower f_{SR} [9]. However, this is a second-order effect in the RSDI’s frequency enhancement, since 87.5 to 100% (depending on N) of the spiral is overlapped.

In [8] comparisons between RSDI, VSDI and SDI are reported for equal values of inductance. All structures are evaluated in IBM SiGe5AM technology [10], whose parameters of interest are reported in Tab. I.

Both stacked structures can reduce the area occupation by more than 50% for a given inductance of 15 nH [8]. But while VSDI does not give any improvement in f_{SR} compared with SDI, RSDI can increase f_{SR} by as much as 25%. In that case, though, the area reduction is just 27%, so that a trade-off exists between area-saving and increment in f_{SR} .

Unfortunately, the high resistivity of the bottom metals and the proximity of the stacked inductors to the substrate, which induces stronger parasitic currents, decrease the quality factor by $\approx 50\%$ for RSDI and $\approx 60\%$ for VSDI [8]. This reduction can be partially compensated, though.

In fact, differential spirals do not lie on adjacent metal layers because of the crossings; they lie on AM and M2 metals, while the in-between MT metal is reserved only for the underpasses (see Figs. 3, 4 and Tab. I). Therefore, the spiral on M2 can be replicated on MT, where there are no underpasses, and the wires on M2 and the resulting wires on MT can be shunted together through vias. This way, Q almost doubles, so that the

overall RSDI’s reduction in Q compared with SDI inductors is 30 – 40% (and 40 – 50% for VSDI).

IV. MODEL-BASED ANALYSIS

Comparisons between RSDI and SDI inductors can be carried out in a systematic way through the analytical model. (From now on, VSDI inductors will be left out because they perform significantly worse than RSDI, as seen in the previous section).

Results from the model are compared with experimental data of various inductors in [11]. Errors in inductance are usually less than 5%, while errors in f_{SR} are within 8%. So, the model can be confidently applied to study electrical parameters in relation with dimensions. An equivalent analysis based on electromagnetic simulations will be much more time-consuming. Electromagnetic simulations are left for validation once the model-based analysis has found the optimum inductor.

In Tab. II are six sets of RSDI and SDI inductors, denoted by letters A,B,...F. For each group of N , w and s is reported the outer dimension D that gives a 10-nH inductance, together with f_{SR} and the quality factor at 1 GHz.

When an equal number of turns is used (sets A and B), RSDI’s outer dimension is 46% smaller than SDI’s. In this case, though, SDI inductors are extremely hollow; they have $N = 6$ from set C to set F for a fairer comparison. Even then the reduction in D goes from 25 to 31% for an area reduction between 43 and 51%. Notice that the area-saving grows as wider metals are used.

The improvement in f_{SR} goes from 17.3 to 27.1% and is bigger for $s = 10 \mu\text{m}$ (sets E and F).

The RSDI’s quality factor is always significantly smaller than SDI’s (from -41.4 to -28.2%). Nonetheless this reduction can be contained by using larger metal widths (sets B,D,F vs. sets A,C,E).

The best compromise between f_{SR} , Q and D can be easily obtained from Tab. II, depending on requirements. For instance, on the one hand a large spacing should be used to augment f_{SR} and a wide metal width is necessary to improve the RSDI’s quality factor, but on the other hand, w and s should be as small as possible to get the minimum area occupation.

V. EXPERIMENTAL RESULTS

An RSDI inductor with $D = 200 \mu\text{m}$, $w = 5 \mu\text{m}$, $s = 10 \mu\text{m}$ and $N = 6$ turns was fabricated in IBM SiGe5AM process (Fig. 5). It is clear from Tab. II that this choice of w and s gives the maximum increase in f_{SR} and a very good area reduction, but it imposes the most severe penalty on Q .

Measurements were performed in the 1 – 10 GHz frequency range, after a full SOLT calibration, using a GS (ground-signal) probe. An open dummy structure was also fabricated to de-embed shunt parasitic.

The measured effective inductance and quality factor are reported in Fig. 6, together with results from the analytical model. The fabricated inductor has $L_{eff}^2 = 14$ nH, $Q_{max} \approx 6.5$ at around 3 GHz and resonates at 5.66 GHz. For comparison, a 8.8-nH stacked inductor in a BiCMOS process has $f_{SR} = 3.3$ GHz [9]. Even in the context of different silicon processes, the RSDI’s frequency enhancement is really remarkable.

² L_{eff} is the *effective inductance* seen at the input ports.

TABLE II

SETS OF 10-nH INDUCTORS WITH DIFFERENT N , w AND s . DIMENSIONS ARE IN μm , FREQUENCIES IN GHz AND Q IS CALCULATED AT 1 GHz.

Set		N	w	s	D	f_{SR}	Q
A	SDI	4	5	5	330	5.67	6.12
	RSDI	4	5	5	177	6.71	3.91
					-46%	+18.3%	-36.1%
B	SDI	4	10	5	382	4.74	9.92
	RSDI	4	10	5	206	5.69	7.12
					-46%	+20.0%	-28.2%
C	SDI	6	5	5	235	5.72	6.67
	RSDI	4	5	5	177	6.71	3.91
					-25%	+17.3%	-41.4%
D	SDI	6	15	5	336	4.20	14.26
	RSDI	4	15	5	233	5.10	10.09
					-31%	+21.4%	-29.2%
E	SDI	6	5	10	280	6.35	6.20
	RSDI	4	5	10	202	8.07	3.65
					-28%	+27.1%	-41.1%
F	SDI	6	10	10	329	5.20	10.29
	RSDI	4	10	10	231	6.54	6.68
					-30%	+25.8%	-35.1%

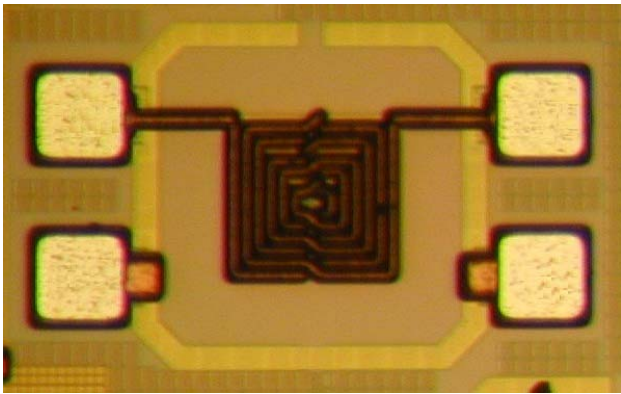


Fig. 5. Die photo of the fabricated inductor.

Moreover, the model is also in good agreement with measurements; in fact, in spite of its approximations, it gives $L_{eff} = 13.2$ nH (-5.7 %), $Q_{max} = 6.4$ at 2.75 GHz and $f_{SR} = 5.94$ GHz (+4.9 %).

VI. CONCLUSION

In this paper a novel stacked differential inductor has been presented. Compared with a standard single-layer differential inductor of equal inductance, it not only shrinks the size, but also increases the self-resonance frequency. The improvement is the result of an optimum metal-wire sequencing that reduces the stored electric energy and thus enhances f_{SR} . A fabricated 14-nH inductor with $f_{SR} = 5.66$ GHz and a $200 \times 200 \mu\text{m}^2$ area proves the effectiveness of this topology. An analytical model has also been introduced, validated by measurements and used to analyze the inductors' characteristics in relation with their dimensions.

ACKNOWLEDGEMENTS

The author thanks Prof. M. Politi for useful discussions and guidance and people at Ericsson Lab Italy for carrying out measurements and for fabrication support.

REFERENCES

[1] J. Craninckx and M.J. Steyaert, "A 1.8 GHz Low-Phase-Noise CMOS VCO Using Optimized Hollow Spiral Inductors," *IEEE J. Solid-State Circuits*, vol. 32, no. 5, pp. 736–744, May 1997.

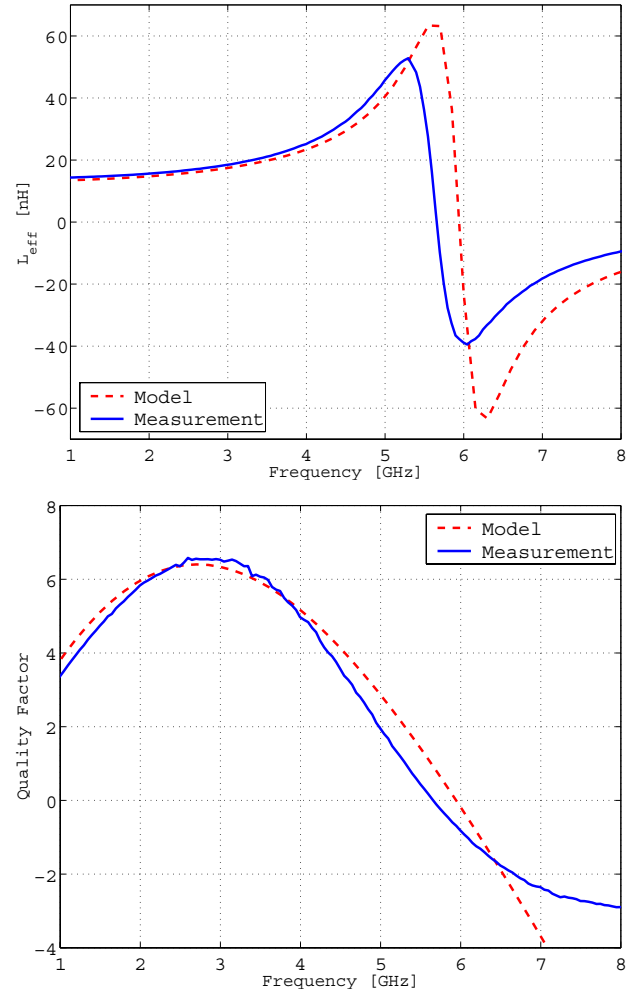


Fig. 6. Effective inductance (top) and quality factor (bottom); both measured (solid line) and modelled (dashed line) values are reported.

- [2] M. Danesh and J.R. Long, "Differentially Driven Symmetric Microstrip Inductors," *IEEE Trans. Microwave Theory Tech.*, vol. 50, no. 1, pp. 332–341, Jan. 2002.
- [3] C.-C. Tang, C.-H. Wu and S.-I. Liu, "Miniature 3D Inductors in Standard CMOS Process," *IEEE J. Solid-State Circuits*, vol. 37, no. 4, pp. 471–480, Apr. 2002.
- [4] V. Minerva, "Analysis and design of integrated inductors for RF application," Ph.D. dissertation, Politecnico di Milano, Milan, Italy, May 2004.
- [5] S.-C. Wong, T.G.-Y. Lee, D.-J. Ma and C.-J. Chao, "An Empirical Three-Dimensional Crossover Capacitance Model for Multilevel Interconnect VLSI Circuits," *IEEE Trans. Semiconduct. Manufact.*, vol. 13, no. 2, pp. 219–227, May 2000.
- [6] F.W. Grover, *Inductance Calculations: Working Formulas and Tables*, D. Van Nostrand, New York, 2nd Printing, 1947.
- [7] Y. Eo and W.R. Eisenstadt, "High-Speed VLSI Interconnect Modeling Based on S-Parameter Measurements," *IEEE Trans. Comp., Hybrids, Manufact. Technol.*, vol. 16, no. 5, pp. 555–562, Aug. 1993.
- [8] M. Politi, V. Minerva and S. Cavalieri d'Oro, "Multi-layer Realization of Symmetrical Differential Inductors for RF Silicon IC's," in *Proc. 33rd European Microwave Conf.*, vol. 1, Munich, Germany, Oct. 2003, pp. 159–162.
- [9] J.N. Burghartz, K.A. Jenkins and M. Soyuer, "Multilevel-Spiral Inductors Using VLSI Interconnect Technology," *IEEE Electron Device Lett.*, vol. 17, no. 9, pp. 428–430, Sept. 1996.
- [10] D. Harnam & al., "Current Status and Future Trends of SiGe BiCMOS Technology," *IEEE Trans. Electron Devices*, vol. 48, no. 11, pp. 2575–2594, Nov. 2001.
- [11] V. Minerva, M. Politi, G.G. Gentili and S. Cavalieri d'Oro, "Modellizzazione di Induttori Integrati per Applicazioni a Radio-Frequenza," in *Proc. XVth RiNEM*, Cagliari, Italy, Sept. 2004, pp. 561–564 (in Italian).

Session 2b

Measurement Techniques

Neural Networks for Microwave Characterization of Arbitrary Shaped Material Samples in Leaky Cavities

Andreas Penirschke¹, Martin Schüßler¹, Martin Vossiek²,
Peter Gulden³, and Rolf Jakoby¹

¹ Technische Universität Darmstadt, Institut für Hochfrequenztechnik, Merckstr. 25, 64283 Darmstadt, Germany, +49-6151-16-3162, penirschke@hf.tu-darmstadt.de

² Technische Universität Clausthal, 38678 Clausthal-Zellerfeld, Germany, +49-5323-72-2544, vossiek@iei.tu-clausthal.de

³ Siemens Coporate Technology, Otto-Hahn-Ring 6, 81730 München, Germany

Abstract — In this paper, we present simulations of a microwave sensor in a cylindrical leaky metallic cavity partially filled with arbitrary shaped material samples. E_{01n} resonant modes where excited by a funnel shaped monopole inside the front door of the cavity.

A preprocessing stage was used to generate a proper database of characteristic values from the magnitude of the scattering parameter $|S_{11}|$ of the received signal only, since the phase information is not available for low cost applications. Subsequently, by using a multilayer perceptron (MLP) network, the dielectric constant, the dielectric losses and the amount of the unknown material can be accurately extracted from these characteristic values.

Detailed investigations to the input values where done to understand the complexity of the problem. MLP-networks with different numbers of inner neurons where trained using only less than half of the generated database for test and validation. Accurate results for the detection of the dielectric constant and the losses of the material where obtained whereas the detection of the material size is relatively poor.

I. INTRODUCTION

In microwave technology, a cavity completely loaded with unknown dielectric lossy material is widely used to characterize it, e.g. to extract its dielectric constant and its losses. However, it is difficult to characterize a material sample, if it is not possible to fill the whole cavity with unknown material or at least, to use a sample with well defined dimensions. The problem becomes even worse, if only the magnitude of the scattering parameter $|S_{11}|$ is known, since the phase of S_{11} is often not available from microwave measurements in low cost applications. Nevertheless, to extract the dielectric constant, its losses and the amount of the material samples, we already introduced a novel neural network model, which only requires the magnitude of $|S_{11}|$ in a previously defined frequency range. So far, this method works very well for material samples with low losses as already shown in [1]. The reverse case, to extract the resonance frequency in dependence of the dimensions and the properties of a load using neural networks can be found in [2]. In this paper simulations where done in order to characterize material samples with unknown *dielectric constant* ϵ_r , *losses* $\tan\delta$ and *amount of material* in a model of a real leaky cavity. The model was replicated as true as possible to the original cavity, so that several fixtures in the

real cavity and also hollows in the door where added to a simple model of the cavity. Simulations to this problem where done using the commercial FITD based simulation tool CST-Microwave Studio. The model was implemented into the simulation tool and two databases consisting of altogether 150 datasets where generated.

Multilayer perception networks with different numbers of neurons where trained only by using the characteristic parameters from $|S_{11}|$ to extract these unknown parameters.

To compare two trained neural networks a figure of merit was defined for each neural network, which is given by the percentage of misclassified datasets. A dataset is misclassified if either the material parameters ($\epsilon_r, \tan\delta$) or the amount of material differ more than one parameter step.

II. NEURAL NETWORKS

Today, neural networks represent a good alternative to classical approaches solving problems without any analytical solution. Several types of architectures of neural networks for different applications can be found in [3].

The connection between material properties as well as the amount of material and the corresponding resonance spectrum can be approximated by linear continuous functions, when the dielectric and magnetic properties of the materials in the cavity differ only slightly. When there is a big difference between the material properties as it is in this case, the functions are no longer linear. Nevertheless, the assumption of a continuous behavior of the parameters is still a good approximation.

Multilayer feed forward networks are an appropriate choice to approximate these functions. This is stated by the universal approximation theorem which proves that any continuous function can be approximated by a suitable three layer feed forward network (input-, hidden-, and the output-layer) [4].

The architecture of the neural network model is shown in Fig. 1. The input parameter vector R is weighted by the input weights $IW^{1,1}$ and added to the bias vector b^1 . A set of sigmoid activation functions is required to determine the activation states of each neuron in the first layer. The

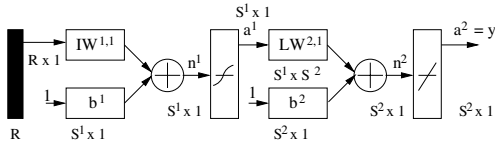


Fig. 1. Multilayer feed forward network model.

second layer is identical to the first layer except the activation functions. To get output parameters with large linear ranges the activation functions in the last layer have to be linear. The investigated neural networks are trained by the Bayesian method, which is extreme efficient for such problems [5]. Because of the size and the redundancy of the frequency samples measuring $|S_{11}|$, it is not possible to use all samples as input parameters for the neural network, in fact a preprocessing stage is necessary to extract characteristics of the spectrum (resonance modes, radiated power etc.). For these analyses a mode tracking process was chosen to extract resonance modes from the spectrum.

III. EXPERIMENTAL APPROACH OF A LEAKY CYLINDRICAL CAVITY

For the applications in mind, a leaky cylindrical cavity is given to detect the dielectric properties of materials in the microwave region. For further processes within the cavity often it is necessary to know the complex dielectric properties (ϵ_r and $\tan\delta$) as well as the amount of material. If the cavity is completely filled with the unknown material, the parameters can be obtained by the use of analytic equations extracting complex resonant frequencies of different modes of the cavity. If the cavity is only partly filled with material an analytical solution is no longer possible.

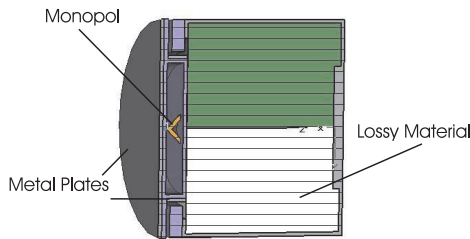


Fig. 2. Model of a leaky cavity, partly filled with material in the cavity.

In Fig. 2 a model of a leaky cylindrical cavity is shown. The cavity is partly opened on the left side and there are several fixtures in the cavity. A funnel shaped monopole is used to insert the microwave signal into and out of the cavity. The cavity itself is partly filled with material and air. The neural network model is used to extract the complex dielectric properties as well as the amount of material in the cavity. The position of the monopole is chosen so that TM_{01n} modes can exist.

If the cavity is empty, the field distribution is symmetrical (shown in Fig. 3, on the upper left picture). If dielectric material with low conductivity is inserted into the cavity, the field distribution changes. At the transition from air to material, the direction of the field vectors are changed according to the

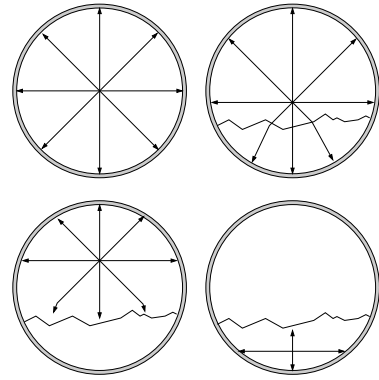


Fig. 3. Field distribution of the TM_{01n} mode dependent on the amount and losses of the material in the cavity.

law of refractions for dielectric materials at microwaves. The field distribution is shown in the upper right part of Fig. 3. If the conductivity is increased, the fields within the material vanishes. The corresponding field is shown in the lower left part of Fig. 3. If the losses within the material are low then also resonances within the material can exist according to the lower right part of Fig. 3.

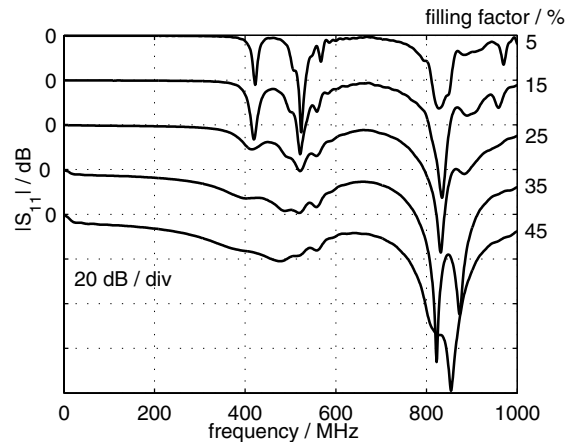


Fig. 4. Shift of the investigated resonant modes depending on the losses of the material.

The corresponding reflection parameter $|S_{11}|$ of the partially filled cavity in dependency of the losses and the filling factor is shown in Fig. 4. If the losses of the material increase, the resonances vanish and the extraction with the neural network system is no longer possible.

To find neural networks that are able to extract the complex permittivity of the material in the cavity as well as its amount, frequencies below 1 GHz were investigated. Four resonant modes (TM_{011} , TM_{012} , TM_{013} and the TM_{014} mode) can exist in this frequency range. Only the TM_{011} and TM_{012} modes are used to generate the training and test databases, because these modes are still available for a high fillings and moderate losses.

A preprocessing stage extracts the resonant frequency, the corresponding value of $|S_{11}|$ and a value K which is inversely proportional to the quality factor of the cavity for both modes in the database. The low quality factor of the cavity itself and moderate losses due to the material in the cavity can lead to ambiguous values of the Q-factor. Therefore the maximum

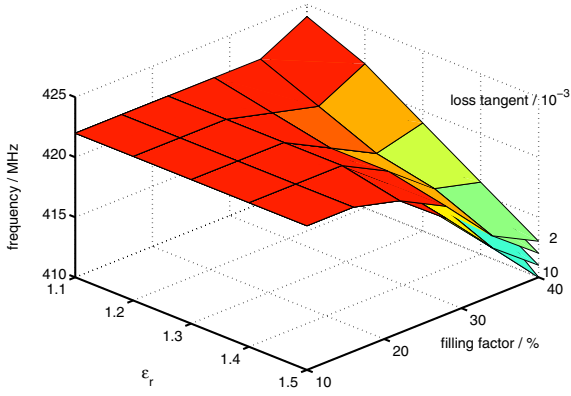


Fig. 5. resonance frequency as a function of permittivity and the filling factor for the E_{011} mode.

value of the autocorrelation function of the band pass filtered signal is chosen as a characteristic value due to the inverse of the Q-factor. The database is divided into two parts, one to train and one to test the neural networks.

The extraction of the complex scattering parameter S_{11} would increase the accuracy of such a system, but is accompanied with significantly higher costs. However, the practical constraints to design a sensor system for low cost and to accept a moderate accuracy leads to skip the phase information.

Fig. 5 to 7 show the behavior of the parameters extracted from the TM_{011} mode. In Fig. 5, the resonance frequency of the TM_{011} mode versus the relative permittivity and the filling factor of the cavity is shown. As one can see, the resonance frequency is proportional to the permittivity and to the filling factor of the cavity. A change in the losses of material in the cavity causes a decrease of the resonance frequency as shown by the different parameter planes in the figure.

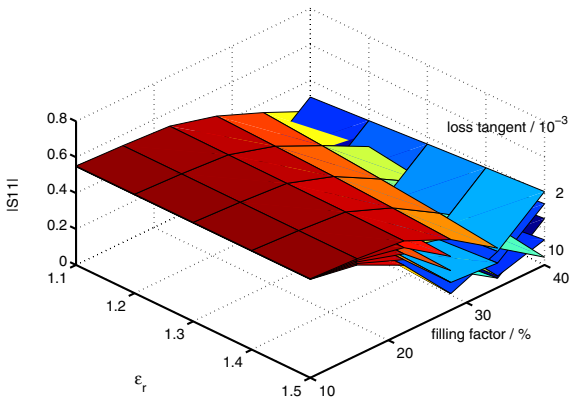


Fig. 6. $|S_{11}|$ as a function of permittivity and the filling factor for the E_{011} mode.

Fig. 6 shows the behavior of the absolute value of S_{11} versus permittivity and filling factor. The filling factor is the volumetric percentage of the cavity volume. If the filling factor or the permittivity rises the absolute value of S_{11} first decreases and then rises up again and therefore causes to ambiguous values when the losses rise.

The K-factor of the TM_{011} mode behaves in the same way then the resonance frequency. In Fig. 7 this behavior is

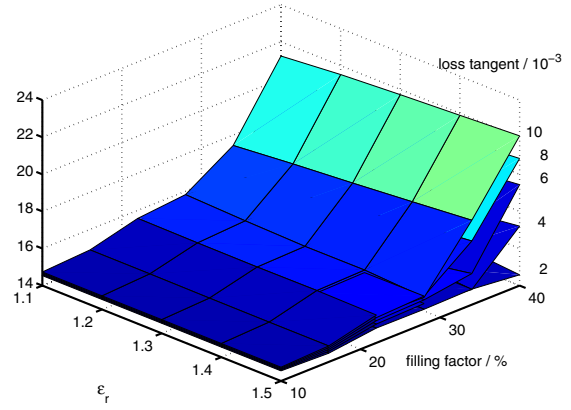


Fig. 7. K as a function of permittivity and losses for the E_{011} mode.

shown. Rising up the losses of the material in the cavity causes to lower changes of the K-factor.

The second resonance frequency investigated is the TM_{012} mode. In principle, figures 8 to 10 show the same behavior than for the TM_{011} mode except for higher filling factors and higher dielectric constants.

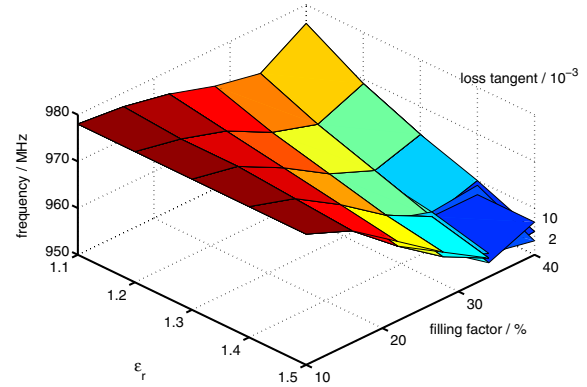


Fig. 8. Resonance frequency as a function of permittivity and losses for the E_{012} mode

Fig. 8 exhibits the resonance frequency of the TM_{012} mode dependent on the permittivity and the losses. This figure shows that the behavior due to the losses is no longer unambiguous. The behavior of the absolute value of S_{11} , shown in Fig. 9, is similar to the one of the TM_{011} mode.

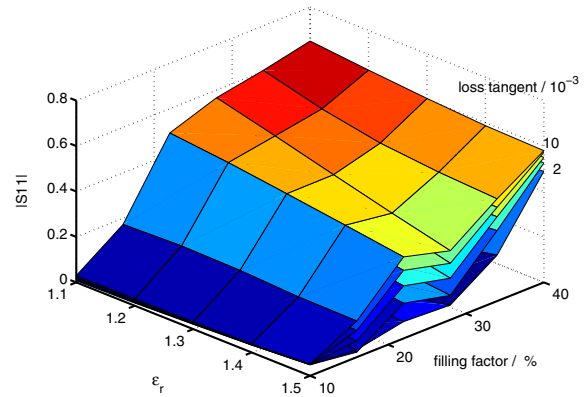


Fig. 9. $|S_{11}|$ as a function of permittivity and losses for the E_{012} mode

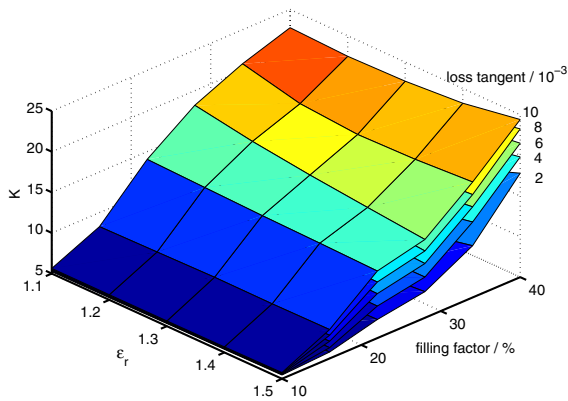


Fig. 10. K- factor as a function of permittivity and losses for the E_{012} mode

Two databases were created to train and test the neural networks.

Database 1 consists of

- filling factors from 5% up to 30% in 5% steps,
- losses from $\tan \delta = 0.002$ up to $\tan \delta = 0.01$ in steps of 0.004 and
- relative permittivities from $\varepsilon_R = 1.1$ to $\varepsilon_R = 1.5$ in steps of 0.2.

Database 2 consists of

- filling factors from 5% up to 30% in 5% steps,
- losses from $\tan \delta = 0.004$ up to $\tan \delta = 0.008$ in steps of 0.004 and
- relative permittivity from $\varepsilon_R = 1.2$ to $\varepsilon_R = 1.4$ in steps of 0.2.

IV. RESULTS

In the upper part of Fig. 11 the classification errors for different trained neural networks are shown. Here a misclassification occurs, when one or more of the detected material samples are misdetected. That means, if the detected filling factor differs more than 2.5% of the cavity height or the detected losses differ more than 0.002 or the relative permittivity differs more than 0.1 from the real simulated parameters. The upper part of Fig. 11 shows that a well trained neural network is able to detect more than 75% parameter sets of the test database. A neural network with only 21 neurons (11 neurons in the first layer and 10 neurons in the second layer) is sufficient. The upper part of Fig. 11 shows the classification errors due to the different neural networks whereas the lower part shows the absolute errors detected by the neural Network 11 10. If the threshold of the classifier is doubled for all three values, which means that the network is not able to differentiate between two adjacent parameter sets, but between two the parameter sets next to the adjacent ones, the neural network is able to detect more than 90% of the test database correct.

V. CONCLUSION AND OUTLOOK

A novel model has been developed only from the simulated magnitude of the scattering parameter $|S_{11}|$ with the aid of a neural network to extract the material parameters and the filling factor of partially filled loads in a cavity at microwaves. The simulations show that it is possible to extract properties of lossy dielectric materials using well trained neural networks.

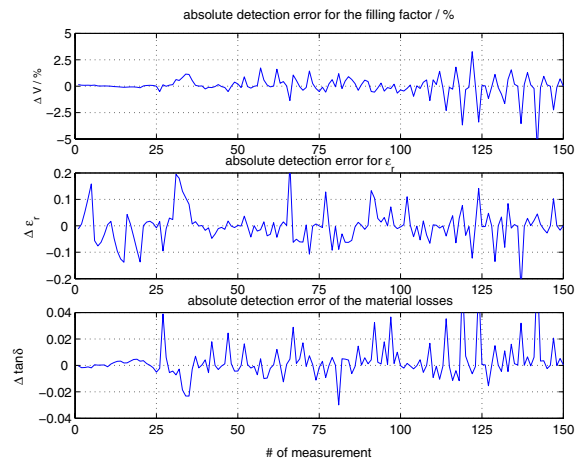
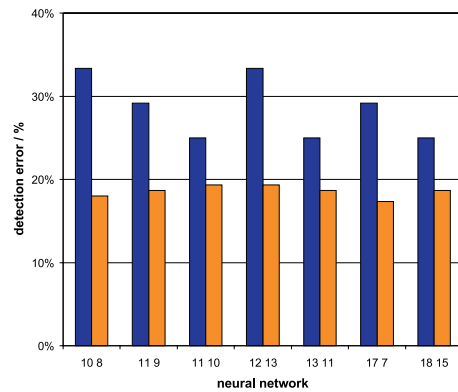


Fig. 11. Classification error for different Network sizes and the absolute error using the neural network 11_10.

The results showed that a well trained neural network is able to detect more than 75% parameter sets with high accuracy and more than 90% of the test database for a moderate accuracy. The experimental verification of the material parameter extraction from cylindrical leaky cavities are of interest for a certain industrial application and will be considered in near future.

VI. ACKNOWLEDGEMENT

The authors want to thank the CST-GmbH for provision of the CST Microwave Studio software package.

REFERENCES

- [1] Penirschke A., Freese J., Schüssler M., Jakoby R., "Neural Networks for Material Characterization of Material Samples in Rectangular Cavities.", in *IEEE 3rd International Symposium on Signal Processing and Information Technology (ISSPIT)*, 2003.
- [2] Milovanovic B., Stankovic Z., Ivkovic S., "Modeling of the Cylindrical Metallic Cavity Loaded by Lossy Dielectric Slab Using Neural Networks.", in *IEEE 5th. Seminar on Neural Network Applications in Electrical Engineering NEUREL 2000*, 2000, pp. 141- 145
- [3] Haykin S., "Neural Networks A comprehensive Foundation", in *IEEE Press Hamilton*, Ontario, Canada 1994",
- [4] Burrascano P., Dionigi M., Fancelli C., Mongiardo M., "A Neural Network Model for CAD and Optimization of Microwave Filters.", in *IEEE MTT-S International*, Vol. 1, 7-12 Jun 1998, pp. 13- 16
- [5] MacKay D.J.C., "Bayesian Interpolation.", in *Neural Computation*, Vol. 5, pp. 415-447, 1992

A Multi-Layered Waveguide Technique for Determining Permittivity and Conductivity of Composite Materials

M. J. Akhtar¹, L. Feher¹, M. Thumm^{1,2}

¹ Forschungszentrum Karlsruhe, Institut für Hochleistungsimpuls- und Mikrowellentechnik, Postfach 3640, D-76021 Karlsruhe, Germany, Tel: +49 7247 82 8025, E-Mail: Jaleel.Akhtar@ihm.fzk.de

² Universität Karlsruhe, Institut für Höchstfrequenztechnik und Elektronik, Germany

Abstract — A waveguide based multi-layered technique is presented to determine the relative permittivity and conductivity of Carbon Fiber Reinforced Plastic (CFRP) materials. The technique requires the placement of material under test (CFRP in this case) sandwiched between two other types of materials, whose dielectric properties are known in advance, in a WR-340 waveguide section. The reflection and transmission coefficient data of this multi-layered waveguide structure are measured in the specified frequency band using a vector network analyzer (VNA). To determine the relative permittivity and conductivity of the material under test (MUT), the square sums of error between the measured and computed scattering data are minimized using a proposed nonlinear optimization algorithm. The computation of the reflection and transmission coefficient data for this multi-layered waveguide structure is carried out using a transmission matrix (TM) approach. The proposed technique is validated by measuring some known dielectric materials, and a good agreement between the measured and published values is observed.

I. INTRODUCTION

The role of advanced composites, such as CFRP materials, in the airframe and transport industry has been continuously increasing in recent years because of their high strength-to-weight ratios as compared to conventional metals like Aluminum [1]. The main advantage of being light weight is less fuel consumption, which is obviously much of the concern in today's scenario. However, one of the main reasons for the composite materials not being extensively used till now are their higher costs, which are mainly due to the extensive processing involved in the autoclave curing. It has recently been demonstrated that the use of microwaves in combination with an automated setup for the curing of composite materials can result in lower processing costs thereby reducing the overall price of CFRP materials [2]. The microwave processing provides the uniform, rapid and selective heating of reinforced materials, which can generally not be achieved with the conventional autoclave curing. However, till now the complex nature of interaction of electromagnetic waves with composite materials has not been fully understood. It is also not fully clear, how the dielectric properties of these reinforced materials may change with different parameters such as the cure cycle, the composite

thickness, and the proportion of different fibers and resins. The present paper describes a novel technique for measuring the permittivity and conductivity of reinforced composites, which can be applied to find the absorption and reflection characteristics of these materials at different stages of curing.

There are various kinds of resonant and non-resonant methods presently available to measure the dielectric properties of materials in the RF and microwave frequency range [3], [4]. In this paper, a rectangular waveguide technique is employed, which is reasonably accurate and where the machining of the MUT is not very critical. As the CFRP materials are generally difficult to machine, hence to position it accurately inside the waveguide, it is sandwiched between two other known dielectric samples. The overall reflection and transmission coefficient of this multi-layer waveguide structure is computed using the proposed TM approach. Finally, the relative permittivity and equivalent conductivity of the MUT are determined by minimizing the squared difference between the computed and the measured scattering data using a nonlinear least-square optimization algorithm.

II. BASIC FORMULATION

The MUT of thickness $d_{(2)}$ sandwiched between two known dielectric materials of thicknesses $d_{(1)}$ and $d_{(3)}$, and placed into a waveguide section of length L can be realized by a multi-layered media as shown in Fig. 1. The whole structure is positioned at the reference plane 2, and it is assumed that only the dominant TE_{10} mode propagates over the whole length of the waveguide, which is generally valid for these types of measurements. Now, to compute the overall reflection and transmission coefficients at reference planes 1 and 2 of the multi-layered media shown in Fig. 1, a transmission matrix (TM) approach is used [5]. The advantage of using the TM representation is that the transmission [T] matrix of a number of cascaded sections can simply be determined by multiplying the matrices of the individual sections altogether.

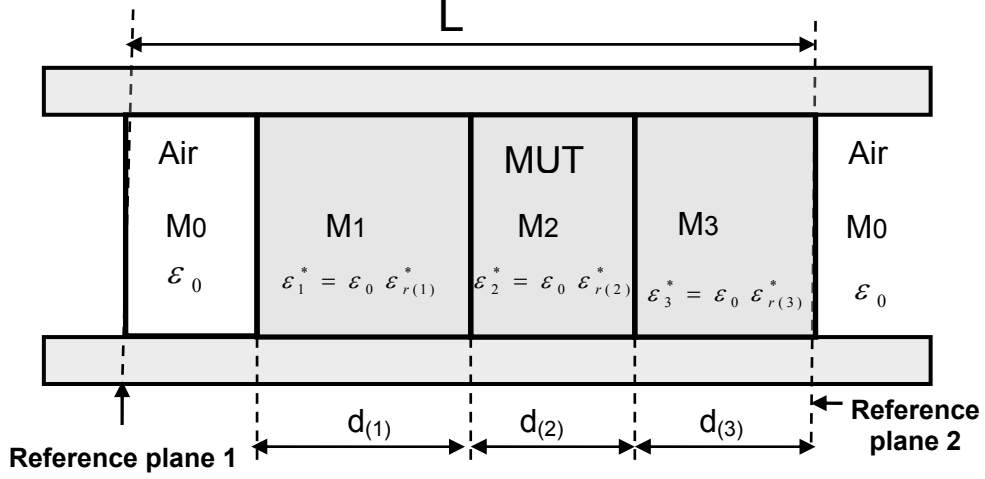


Fig. 1. The MUT sandwiched between two known dielectric materials into a waveguide section. Reference planes 1 and 2 represent the two ports of a vector network analyzer.

In Fig. 1, the overall two-port $[T]$ matrix defined at reference planes 1 and 2 can be written as:

$$[T_{\text{overall}}] = \begin{bmatrix} T_{11} & T_{12} \\ T_{21} & T_{22} \end{bmatrix} \quad (1)$$

$$= [T_0][T_{0,1}][T_1][T_{1,2}][T_2][T_{2,3}][T_3][T_{3,0}]$$

where the subscript 0 corresponds to the air medium, $[T_{i-1,i}]$ is the $[T]$ -matrix of the junction between $(i-1)^{\text{th}}$ and i^{th} layers, and $[T_i]$ represents the $[T]$ -matrix of i^{th} layer shown in Fig. 1. To compute the 2-port $[T]$ -matrix of all the junctions/sections defined in (1), we define the impedance and the propagation constant for each layer in Fig. 1, assuming the dominant TE_{10} mode propagation and the $\exp(j\omega t)$ time dependence. The propagation constant for any i^{th} layer may be written as [5]:

$$\beta_{(i)} = \sqrt{k_0^2 \varepsilon_{r(i)}^* - k_c^2} = k_0 \sqrt{\varepsilon_{r(i)}^* - (c/2af)^2} \quad (2)$$

$$\equiv k_0 \sqrt{\tilde{\varepsilon}_{r(i)}^*(f)} ; \quad i = 0,1,2,3$$

where,

$$\tilde{\varepsilon}_{r(i)}^* = \varepsilon_{r(i)}^* - (c/2af)^2 \quad (3)$$

is defined as the effective value of complex relative permittivity for the i^{th} layer inside the waveguide medium,

$$\varepsilon_{r(i)}^* = \varepsilon'_{r(i)} - j\varepsilon''_{r(i)} \equiv \varepsilon'_{r(i)} - j(\sigma_{(i)}/\omega\varepsilon_0) \quad (4)$$

is the complex relative permittivity of the i^{th} layer with $\sigma_{(i)}$ being the effective conductivity of that layer, k_0 is the free-space wave number, and $k_c = \pi/a$ is the cut-off wave number of the dominant mode with a being the broader dimension of the waveguide. The impedance for the i^{th} layer inside the waveguide considering the dominant TE_{10} mode can be derived as:

$$Z_{(i)} = \frac{\omega\mu_0}{\beta_{(i)}} = \frac{\omega\mu_0}{k_0 \sqrt{\tilde{\varepsilon}_{r(i)}^*(f)}} = \frac{\eta_0}{\sqrt{\tilde{\varepsilon}_{r(i)}^*(f)}} \quad (5)$$

where, η_0 is the intrinsic impedance of the free-space.

After defining the propagation constant and the impedance in (2)-(5), the individual transmission matrices of (1) can be computed making use of the equivalent circuit theory approach, and they are given by:

$$[T_{i-1,i}] = \begin{bmatrix} \frac{\sqrt{\tilde{\varepsilon}_{r(i-1)}^*} + \sqrt{\tilde{\varepsilon}_{r(i)}^*}}{2\sqrt{\tilde{\varepsilon}_{r(i-1)}^*}\tilde{\varepsilon}_{r(i)}^*} & \frac{\sqrt{\tilde{\varepsilon}_{r(i-1)}^*} - \sqrt{\tilde{\varepsilon}_{r(i)}^*}}{2\sqrt{\tilde{\varepsilon}_{r(i-1)}^*}\tilde{\varepsilon}_{r(i)}^*} \\ \frac{\sqrt{\tilde{\varepsilon}_{r(i-1)}^*} - \sqrt{\tilde{\varepsilon}_{r(i)}^*}}{2\sqrt{\tilde{\varepsilon}_{r(i-1)}^*}\tilde{\varepsilon}_{r(i)}^*} & \frac{\sqrt{\tilde{\varepsilon}_{r(i-1)}^*} + \sqrt{\tilde{\varepsilon}_{r(i)}^*}}{2\sqrt{\tilde{\varepsilon}_{r(i-1)}^*}\tilde{\varepsilon}_{r(i)}^*} \end{bmatrix} \quad (6a)$$

$$[T_i] = \begin{bmatrix} \exp(-j\beta_{(i)}d_{(i)}) & 0 \\ 0 & \exp(j\beta_{(i)}d_{(i)}) \end{bmatrix} \quad (6b)$$

where $d_{(i)}$ is the thickness of the i^{th} layer as shown in Fig.1, and we have made use of (2)-(5). The individual $[T]$ matrices of (6) are substituted in (1) to obtain the overall transmission matrix $[T_{\text{overall}}]$, which is then transformed into the overall $[S]$ -matrix using the following relationship:

$$[S_{\text{overall}}^{\text{computed}}] = \begin{bmatrix} S_{11} & S_{12} \\ S_{21} & S_{22} \end{bmatrix} \quad (7)$$

$$\equiv \frac{1}{T_{22}} \begin{bmatrix} T_{12} & (T_{11}T_{22} - T_{12}T_{21}) \\ 1 & -T_{21} \end{bmatrix}$$

where S_{11} and S_{22} are the overall reflection coefficients computed at port 1 and 2 respectively in Fig. 1, and

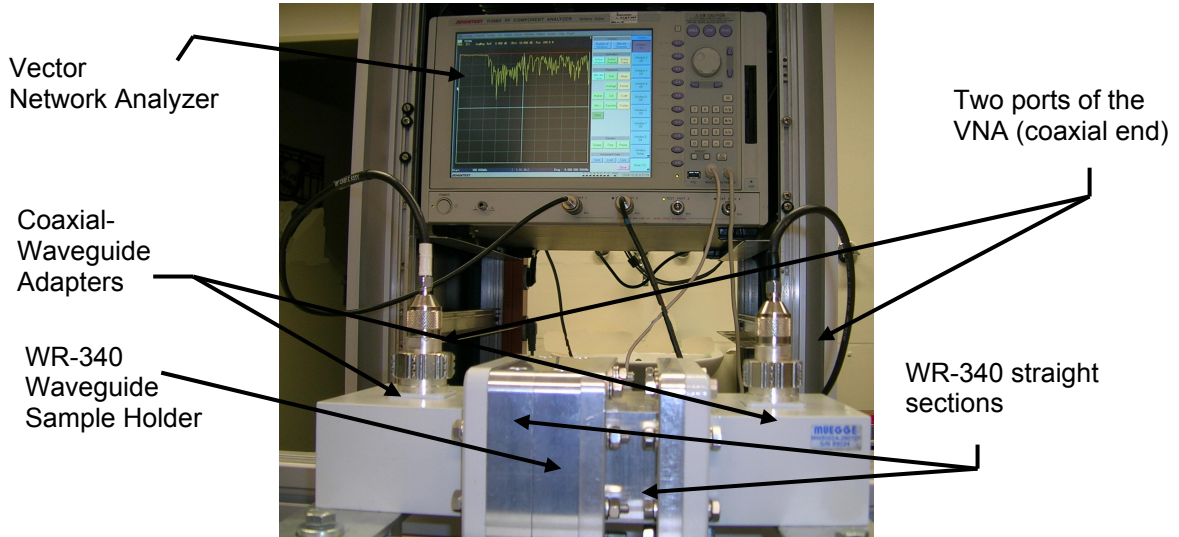


Fig. 2. The waveguide measurement setup for the material characterization

S_{21} (S_{12}) is the overall computed transmission coefficient from port 1(2) to port 2(1). After the computation of reflection and transmission coefficients, we define error functions representing the difference between the computed and measured scattering data as follows:

$$S_{nm}(\text{computed}) - S_{nm}(\text{measured}) ; n = 1, 2; m = 1, 2 \quad (8)$$

As the overall measurement setup is reciprocal, hence there would be two sets of reflection coefficients data defined at each port, and one set of transmission coefficient data. These all three sets of scattering data are measured using the procedure described in the next section. After the measurement of scattering data, the error functions defined by (8) are computed. The square sums of these error functions are then minimized in the specified frequency range using MATLAB based nonlinear least-square optimization algorithms in order to obtain the relative permittivity and effective conductivity of the MUT (2nd layer) in Fig. 1. It may be noted here that the overall reflection and transmission coefficient defined at ports 1 and 2 in Fig. 1 depends upon the dielectric properties of the MUT as well as on the material properties of other two layers. However, as the dielectric properties of other two layers are determined in advanced, hence (8) can be optimized for the material properties (relative permittivity and effective conductivity) corresponding to MUT. It may be pointed out that the optimization algorithms sometimes might produce the false solution due to the presence of local minima of error functions unless special care is taken. To avoid this situation, and to achieve *global* minima of the error functions, the optimization algorithms are executed with different initial conditions and the material parameters corresponding to the *minimum* residual error are taken as the real solution.

III. EXPERIMENTAL MEASUREMENT SETUP

The reflection and transmission coefficient data of the MUT are measured in the frequency range of 2.4-2.5 GHz by placing it in between two PVC samples into a WR-340 waveguide section as shown in Fig. 2. The VNA is first calibrated at the coaxial reference plane using the Auto-Cal kit supplied by the manufacturer. After calibrating at the coaxial reference plane, the coaxial-waveguide adapters are connected at each port. Additional pieces of WR-340 waveguide straight sections are connected to each port to minimize the effect of higher order modes. The calibration of the VNA at the *waveguide reference plane* is carried out using a *TRL (Thru-Reflect-Line)* algorithm developed in-house [6]. To check the accuracy of the calibration, the test data of the actual calibration standards (*line, short*) are computed, and the *corrected* data are found to be close to ideal standards. The waveguide section used in the TRL calibration as the *line* standard is also being utilized as the actual sample holder for the measurement of the MUT. As the dielectric values of even standard materials might some times vary from sample to sample, hence the scattering data of actual PVC samples used in our setup on both sides of MUT are first measured in order to determine the exact dielectric properties of these samples. The MUT is then sandwiched between these two PVC samples to measure the scattering data of the multi-layered structure. The measured data are corrected using the TRL calibration algorithm. The *corrected* reflection and transmission data are used in the proposed optimization algorithm to determine the value of relative permittivity and effective conductivity of the MUT as described in the previous section.

IV. RESULTS AND DISCUSSIONS

The material parameters of a number of samples including plastics, wood, and CFRP have been determined using the proposed technique as shown in Table I. It may be noted that the CFRP sample used here does not have orientation of carbon fibers in any particular direction. The material properties of samples of glass-fiber, alumina, and CFRP shown in this table are measured using multi-layered structures by sandwiching the MUT between two PVC pieces. The dielectric parameters of PVC are measured beforehand as given in the first row of this table. The dielectric properties of some of the known samples (PVC, Alumina etc.) are found to be in good agreement with values available in the literature. It can be clearly seen from this table that the CFRP has a very high value of relative permittivity and conductivity as compared to conventional lossy dielectrics.

S. No. / Sample	Relative Permittivity	Effective Conductivity (Sm ⁻¹)
1. PVC	2.9	0.0033
2. Wood	3.4	0.0995
3. Glass- Fiber	3.8	0.0051
4. Alumina	9.1	0.0082
5. CFRP	2530.0	28.30

TABLE I

THE MEASURED MATERIAL PROPERTIES OF DIFFERENT SAMPLES

As the actual parameters for CFRP materials are not available in the literature, hence the results are compared by computing the reflection and transmission coefficients for the determined permittivity and conductivity with the measured data in the specified frequency range. A very good agreement between the measured and predicted data for both reflection and transmission coefficients as shown in Figs. 3-4 shows the validity of the proposed approach.

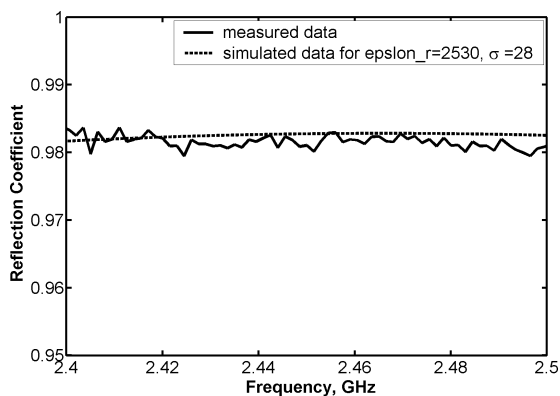


Fig. 3. Measured and simulated reflection coefficient data for the CFRP material.

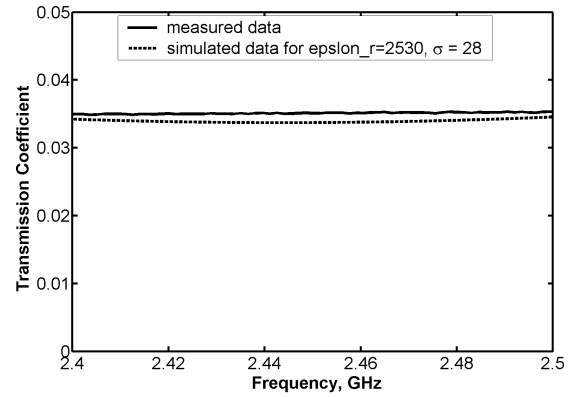


Fig. 4. Measured and simulated transmission coefficient data for the CFRP material.

It may be mentioned here that for the determination of dielectric properties given in Table I, we have only used the magnitude of the reflection and transmission coefficient data. The material properties are assumed to be frequency independent in the used frequency range of 2.4-2.5 GHz.

V. CONCLUSION

A novel method has been presented to determine the relative permittivity and effective conductivity of carbon fiber composite materials. The proposed method uses a global optimization procedure to determine the material properties from the measurement of reflection and transmission coefficient data in the specified frequency band. The measurement of some known plastics and ceramics shows the applicability of the proposed scheme.

REFERENCES

- [1] C. Y. Niu, *Composite Airframe Structures*, Hong Kong Conmlit Press Ltd., 1992.
- [2] L.Feher and M.Thumm, "Microwave innovation for industrial composite fabrication-the HEPHAISTOS technology," *IEEE Transactions on Plasma Science*, vol. 32, no. 1, pp.73-79, February 2004.
- [3] M. Afsar *et al.*, "The measurement of the properties of materials", *Proceedings IEEE*, vol. 74, pp.183-199, 1986.
- [4] J. B. Jarvis *et al.*, "Improved technique for determining complex permittivity with the transmission/reflection method," *IEEE Trans. Microwave Theory Tech.*, vol. MTT-38, pp. 1096-1103, Aug. 1990.
- [5] Robert E. Collin, *Foundations for Microwave Engineering*, McGraw-Hill International Edition 1992.
- [6] G. F. Engen and C. A. Hoer, "TRL: an improved technique for calibrating the dual six-port automatic network analyzer", *IEEE Trans. Microwave Theory Tech.*, vol. MTT-27, pp. 987-993, Dec. 1979

Development of a broadband real-time frequency measurement system for high power mm-wave gyrotrons

H. O. Prinz¹, A. Arnold^{1,2}, K. Koppenburg¹, M. Thumm^{1,2}

¹ Forschungszentrum Karlsruhe, Association EURATOM-FZK, Institut für Hochleistungsimpuls- und Mikrowellentechnik (IHM),

Address: Postfach 3640, D-76021 Karlsruhe, Germany; e-mail: Oliver.Prinz@ihm.fzk.de

² Universität Karlsruhe (TH), Institut für Höchsthfrequenztechnik und Elektronik (IHE),

Address: Kaiserstr. 12, D-76128 Karlsruhe, Germany

Abstract — A broadband real-time frequency measurement system for frequency diagnostics on megawatt gyrotrons has been developed. It is based on a broadband superheterodyne receiver operating between 100 GHz and 175 GHz. The aim is to determine the oscillating mode in the gyrotron's cavity. The concept is introduced and first measurements are presented.

I. INTRODUCTION

The name "Gyrotron" is composed of the Greek words "Gyros" (English: circle) and "Elektron". The operation mechanism is based on the interaction of the gyrating electrons with the magnetic field inside a cavity (Electron Cyclotron Maser, ECM). The advantage of gyrotrons is the use of a cavity with a large diameter compared to the wave length. Because of the large diameter a high order mode has to be used. The selected mode minimizes the wall currents which leads to a minimum of losses. The principle can be used for oscillators and amplifiers. In this paper high power oscillator tubes are discussed. They produce output powers up to megawatts at wavelengths in the range of millimeters [1], [2]. The main application is plasma heating in large fusion devices, a minor field is materials processing.

Output power and frequency are the key parameters to be monitored. The power measurement is done with a calorimeter which is integrated into the water cooled load. The frequency measurement [3] shows the operating cavity mode and observes if any other competing modes are resonating at the same time. In addition thermal effects can be detected. This is for example the increase of the cavity's diameter during long pulses which results in a frequency decrease. This demands a frequency resolution in the order of Kilohertz with a small bandwidth in contrast to the detection of competing modes. This requires a large bandwidth but a far less frequency resolution. As those demands can not be satisfied by a single real-time device, one for each task was realized.

The frequency measurement system combines the advantages of a filterbank spectrometer which is used for a broadband measurement with a rough frequency resolution and a frequency and time interval analyzer which is used for a narrowband measurement with a fine frequency resolution. As both measurement systems are working at lower frequencies the input signal has to be down converted. A superheterodyne receiver architecture is employed.

The real-time measurements which are performed at an intermediate frequency (IF) up to 18 GHz pay special attention to three major aspects:

- broadband frequency measurement with a rough frequency resolution,
- narrowband frequency measurement with a fine frequency resolution, and
- measurement of the pulse length.

II. CONCEPT OF THE FREQUENCY MEASUREMENT SYSTEM

As discussed above two different systems carry out the measurement to fulfill the needs: filterbank spectrometer and frequency time analysis. First the input signal has to be downconverted. Figure 1 shows the block diagram.

A. Superheterodyne Receiver

A very small amount of the gyrotron's output power is coupled into a waveguide and propagates to the frequency measurement system as shown on the left side of figure 1. To extend the dynamic range of the frequency measurement system a variable waveguide attenuator is located in front of the isolator. As stray radiation is mostly used for the frequency measurement the power level may differ. The attenuator is set to protect the downconverter. The next stage, an isolator, provides a better match and suppresses reflected waves. As shown in figure 1 the isolator is followed by the downconverter. It converts the input frequency range of 100 GHz to

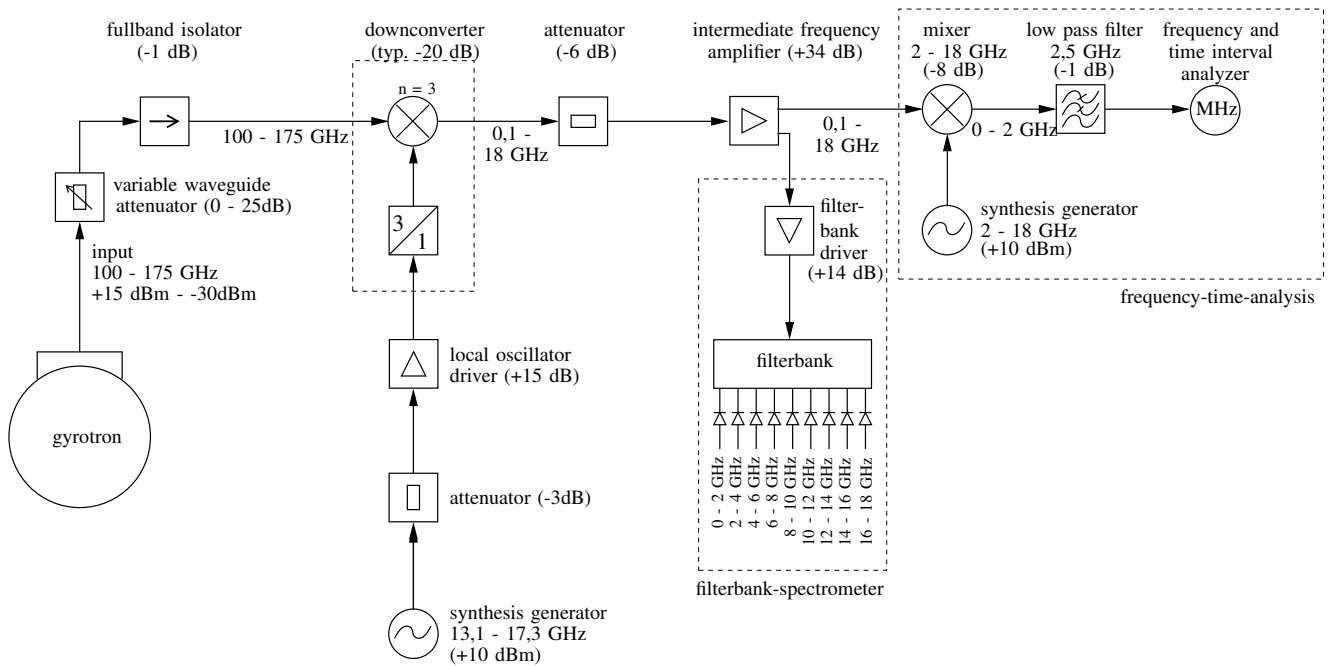


Fig. 1. Block diagram of the frequency measurement system with filterbank spectrometer and frequency time analysis.

175 GHz down to the IF. As the IF bandwidth is limited to 18 GHz the downconverter converts an input band of 36 GHz (upper and lower sideband of 18 GHz each) dependent of the local oscillator (LO) frequency to the IF band of 100 MHz to 18 GHz. To achieve such a broadband system the LO signal has to be variable in a wide range. In order to use a source with a rather low frequency the mixer itself works on the third harmonic and at the LO port a frequency tripler is flange mounted. All together the LO signal is multiplied by nine and a Ku-band source generated by a commercial available synthesizer is used. As the maximum level of the generator is not sufficient to drive the passive tripler an amplifier is inserted between synthesizer and LO port. A coaxial attenuator at the input of the amplifier has the advantage of minimizing the frequency dependencies. This is an issue because the tripler's operating specifications are very close to the maximum power rating. The concept of the harmonic mixer with the tripler at the LO port makes it possible to build up such a broadband receiver. From the downconverter's output the signal with a frequency range of 100 MHz to 18 GHz as labeled in figure 1 propagates into a coaxial attenuator to optimize the match between the mixer's output and the following amplifier. This amplifier divides the signal into two paths: one for the filterbank spectrometer and one for the frequency time analysis. The combination of amplifier and splitter has the advantage that the feedback of the two paths to each other is minimized to 30 dB or more.

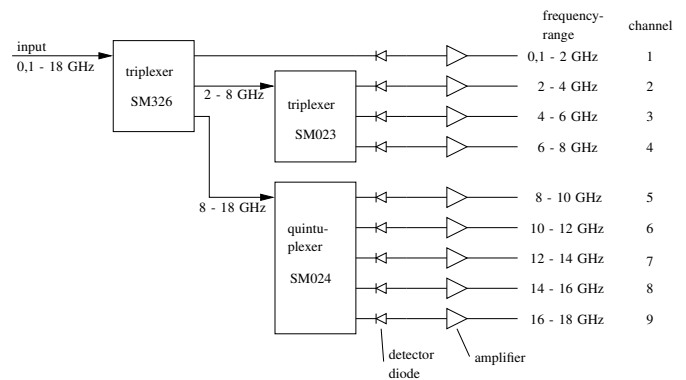


Fig. 2. Filterbank spectrometer with multiplexers.

B. Filterbank Spectrometer

As figure 1 depicts another amplifier is used to match the signal levels of the downconverter and the detectors. The amplifier is followed by the filterbank consisting of three multiplexers as shown in figure 2. They divide the input frequency range into nine bands. The first multiplexer is a triplexer (SM326). It splits the input frequency range of 100 MHz to 18 GHz into three bands:

- 1) 100 MHz to 2 GHz
- 2) 2 GHz to 8 GHz
- 3) 8 GHz to 18 GHz

To have nine channels with a bandwidth of 2 GHz each the second band is connected to another triplexer (SM023) and the third band is connected to a quintuplexer (SM024).

At each output of the multiplexers a broadband detector diode is connected. As the detectors output voltage is dependent on the impedance at its output a driver ampli-

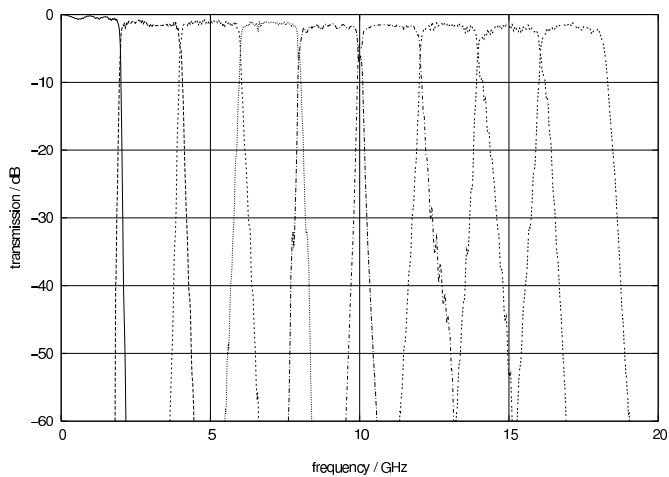


Fig. 3. Measured throughput of the filters.

fier is inserted. This provides a measurement independent of the cable length and its amplification enhances the sensitivity. The analogue output signal is visualized on a storage oscilloscope. The DC signal of each channel shows the presence of an RF signal in real-time.

A real-time measurement in a 36 GHz band with a resolution of 2 GHz is performed.

C. Frequency Time Analysis

The path of frequency time analysis is shown on the right side of figure 1. Here a second mixer is followed by the IF amplifier. The mixer converts a segment out of the IF range to the band between 1 MHz to 2.5 GHz. The segment is chosen by the LO signal which is provided by a second synthesizer. As no filter is in front of the mixer it has to be taken care of high or low side injection. At the mixer's output port there is a 2.5 GHz lowpass filter to suppress higher frequencies. They may result from the mixing process and may cause problems at the analyzer's input. The frequency and time interval analyzer is an Agilent 53310A and has a frequency range up to 2.5 GHz. With this analyzer, a frequency measurement with a resolution better than 100 Hz in quasi real-time is possible.

The measuring procedure is to carry out a rough measurement with the filterbank spectrometer. Knowing the frequency span the LO of the frequency time analysis is adjusted and the fine frequency measurement is carried out.

D. Downconverter

The downconverter is the core of the real-time frequency measurement system. The most important fact of this specific development is its outstanding broadbandness with low conversion losses. It converts the whole input frequency range from 100 GHz to 175 GHz in sections to an IF from 100 MHz to 18 GHz. This is only possible through a wide tunable LO signal in the

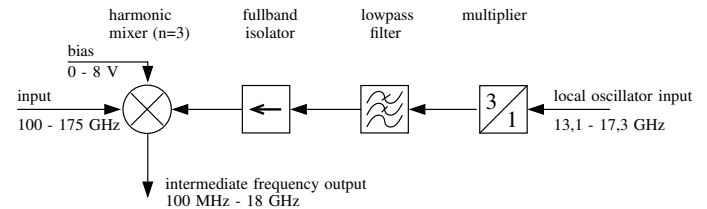


Fig. 4. Block diagram of the downconverter.

Ku-band. The block diagram of the downconverter in figure 4 shows the principle.

The LO signal, which is in the Ku-band, is multiplied by nine and mixed with the input signal. As the mixer itself works on the third harmonic, the LO signal has to be multiplied by three to be in the right frequency range. This is done by a frequency tripler which is the very right block of figure 4. As a tripler has a nonlinear characteristic, not only the third harmonic of the input signal is generated but also the second, fourth and so on. To suppress the unwanted higher harmonics a lowpass filter follows the tripler. This results in a problem with a very broadband system because adjacent harmonics only have a small frequency separation. The input frequency into the tripler of 13.1 GHz results in an output of 39.3 GHz. At the same time the fourth harmonic is generated, which is at 52.4 GHz. The highest input frequency into the tripler is 17.3 GHz. This frequency multiplied by three results in 52.4 GHz. So the fourth harmonic of 13.1 GHz and the third harmonic of 17.3 GHz add up to the same frequency. The lowpass filter can not suppress the unwanted fourth harmonic of the lowest input signal. The consequence at low LO frequencies is that there might be spurious responses at the mixer's IF output. Another fact is the steepness of the lowpass filter which can not be arbitrary. A solution is an optimization of the tripler for the third harmonic. Offsets in the level of 20 dB are reachable. So the undesired mixing products at the mixer's output can be attenuated in the same magnitude.

The next block after the lowpass filter is an isolator used to suppress reflections inside the waveguide and enhance the match of the mixer's LO port. Without this isolator there could be multiple reflections between the mixer's LO input and the lowpass filter. This would result in a degraded frequency response of the whole system.

The harmonic mixer represented by the very left block in figure 4 is optimized to the third harmonic. This is done through internal arrangements as filters for higher harmonics and external biasing. The conversion loss of the downconverter is typically 20 dB and increases a little at the band edges. It is dependent on the input frequency, the LO frequency, and the bias voltage. A minimum of conversion loss leads to the maximum of sensitivity. Thus, a PC based software knowing the mixer's parameters controls the LO frequency to adjust

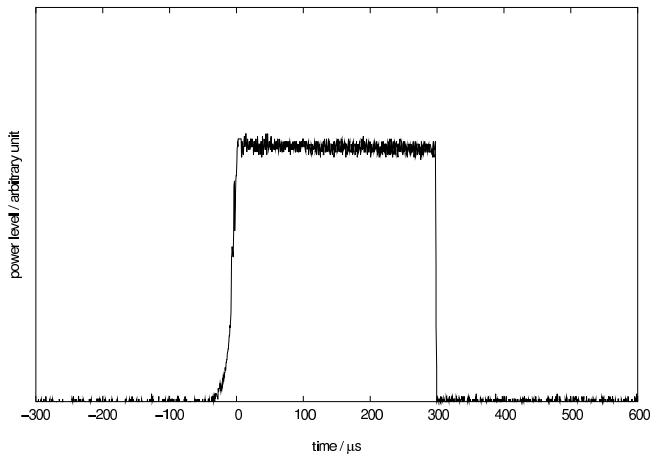


Fig. 5. Output of the filterbank spectrometer.

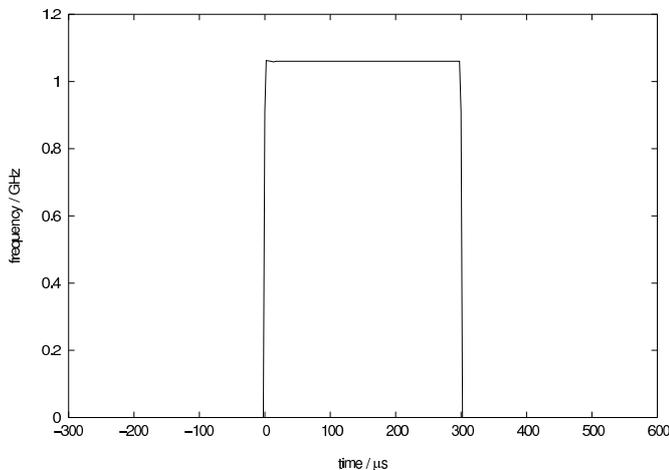


Fig. 6. Measurement of the frequency and time interval analyzer.

for minimum conversion loss.

III. MEASUREMENTS

The first frequency measurements at the gyrotron experiment were done at 140 GHz. A small part of the output power was coupled into a waveguide which feeds the real-time frequency measurement system. At the input there is a taper to adapt circular to rectangular waveguides. A 300 μs pulse can be visualized on the filterbank spectrometer with a storage oscilloscope and also on the frequency and time interval analyzer, as shown in figures 5 and 6. The frequency and time interval analyzer shows a frequency of 1060 MHz with a pulse length of 300 μs . Figure 5 shows the output of the filterbank spectrometer as a pulse with nearly no noise. For this measurement the LO frequency for the first mixer was 14.55 GHz with low side injection and the local oscillator frequency of the second LO is 10 GHz with high side injection. Consequently the measured frequency is 139.940 GHz.

IV. CONCLUSION

A very cost efficient frequency measurement system for frequency diagnostics of high power gyrotrons in the frequency range of 100 GHz to 175 GHz has been developed. The concept has been presented, and the key features have been pointed out. The principle of operation has been illustrated by means of the system's block diagram.

The described measurements validate the design and show the utilizability to observe frequency drifts and oscillating modes of gyrotrons. A special advantage is the very broadband frontend which has a good sensitivity. The compact system will be used for future diagnostics on gyrotrons at Forschungszentrum Karlsruhe (FZK).

REFERENCES

- [1] M. Thumm, *Progress in gyrotron development*; Fusion Engineering and Design, **66-68**, pp. 69-90, 2003
- [2] C.J. Edgcombe, *Gyrotron Oscillators*; Taylor&Francis, 1993
- [3] K. Koppenburg, A. Arnold, G. Dammertz, H. Kunkel and M. Thumm, *Design of a broadband frequency measurement system (100-175 GHz) for gyrotrons*, 2001, 26th International Conference on Infrared and Millimeter Waves, Toulouse, France, Conf. Digest, pp. 5-177-5-179

A Modular Vector Field Measurement System at 150 GHz, 300 GHz and 450 GHz

A. Hofmann, G. Seibert, M. Manglberger, A. Kalb, A. Göbel, S. Yao,
J. Weinzierl, L.-P. Schmidt, H. Brand

University of Erlangen-Nuremberg, Institute for Microwave Engineering (Lehrstuhl für Hochfrequenztechnik, LHFT),
Cauerstr. 9, D-91058 Erlangen, Federal Republic of Germany
Tel. : ++49/(0)9131/85-27221
arnd@lhft.eei.uni-erlangen.de

Abstract — The paper describes the design and the implementation of a modular high precision heterodyne vector field measurement system at 150 GHz, 300 GHz and 450 GHz. The system uses two channels for the measurement of the magnitude as well as the phase characteristics of an electromagnetic field. The fundamental mixers at 150 GHz respectively the harmonic mixers at 300 GHz and 450 GHz are pumped by a phase locked two-channel local oscillator unit at 150 GHz consisting of a one-channel frequency synthesizer at 9.375 GHz and a frequency multiplier cascade with a 0° power splitter at 75 GHz and two subsequent frequency doublers separately for each channel. The IF receiver unit enables a minimum detection level of -80 dBm with 80 MHz bandwidth at 160 MHz center frequency and a phase uncertainty better than 2 degrees. The RF signal is received by dielectric field probes in both channels and is fed via a flexible dielectric waveguides system to the mixer ports. The dielectric antennas, the flexible waveguides as well as the mixers are modularly mounted on a high precision 3D-scanning platform. A considerable reduction of the measurement time is achieved by moving the measurement probe continuously with exact position triggering by an electronic linear encoder and simultaneous sampling of the measurement values. The measurement accuracy is significantly enhanced by fast software correction algorithms.

I. INTRODUCTION

In the millimeter and sub-millimeter wavelength region above 100 GHz, the availability of tunable and compact signal generators with sufficient output power is a well-known problem which has not been satisfyingly solved so far. One promising strategy to overcome this is to combine the fields of an array of diode oscillators quasi-optically in free space as well as to multiply the resulting fields effectively by quasi-optical frequency multiplier setups.

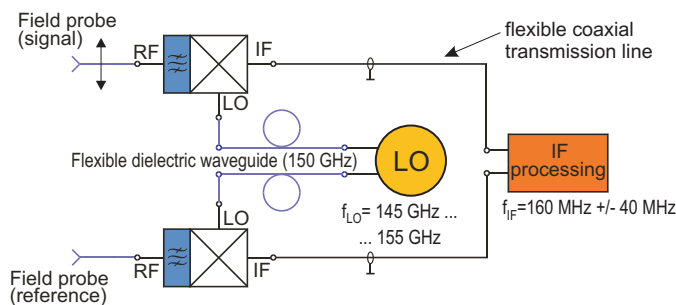


Fig. 1. Principle of the heterodyne measurement system

This has been successfully demonstrated at a fundamental frequency of 150 GHz by the MEMSTIC (an acronym for Multi Element Multi Substrate THz Integrated Circuits)

project, a joint research project of several German university institutes [1]. For optimizing the efficiency of the spaciouly extended quasi-optical holographic power combining setup [2], a vector field measurement system at 150 GHz has been developed [3]. The key components of this system are low-loss flexible rectangular dielectric waveguides (DWGs) made from HD-PE ([4],[5]), to guide the field from the dielectric field probe [6], which is mounted on the moving mechanical scanning system, or from the adjustable reference antenna to the mixers which are directly mounted to the local oscillator system (LO).

Following the basic structure of the system described above, an advanced vector measurement system has been designed recently to fulfill the following extended requirements:

- Vector field measurements at 150 GHz, 300 GHz and 450 GHz by use of one single LO at 150 GHz
- IF receiver bandwidth increase from 40 MHz to 80 MHz, minimum detection power at -80 dBm and a dynamic range of 70 dB
- Reduction of measurement time by continuous instead of stepped field scanning
- Separation of unwanted harmonics by dielectric directional coupler filters

The different components of the measuring system are presented in this paper.

II. THE LOCAL OSCILLATOR SYSTEM AND THE MIXERS

In figure 1, the general setup of the vector field measurement system at 150 GHz, 300 GHz and 450 GHz is shown.

In order to enable phase measurements, the heterodyne receiver consists of a signal channel and a spatially fixed reference channel. As both of the fundamental mixers at 150 GHz respectively the harmonic mixers at 300 GHz and 450 GHz have to be pumped by this single local oscillator, 150 GHz was again chosen as LO frequency. To reduce transmission losses caused by the DWGs at 300 GHz and 450 GHz, which are considerably higher than at 150 GHz (150 GHz: 4 dB/m, 300 GHz: 9 dB/m, 450 GHz: <15 dB/m), the lengths of the DWGs at the RF frequency should be kept as short as possible. Therefore, the mixers are mounted on the 3D scanning platform together with the dielectric field probes and the coupler filters.

The LO signals are transmitted via flexible DWGs at 150 GHz. As seen in figure 2, the LO system consists of a one-channel frequency synthesizer at 9.375 GHz and a frequency multiplier cascade with a 0° power splitter at

75 GHz and two subsequent frequency doublers separately for each channel. It is electronically tunable via a serial interface over the entire LO bandwidth between 145 GHz and 155 GHz. The impedance has to be matched by tunable backshorts at the input and the output of the multiplier heads of the LO as well as the mixers. The LO as well as the mixers have been designed and built by Radiometer Physics RPG in Meckenheim, Germany.

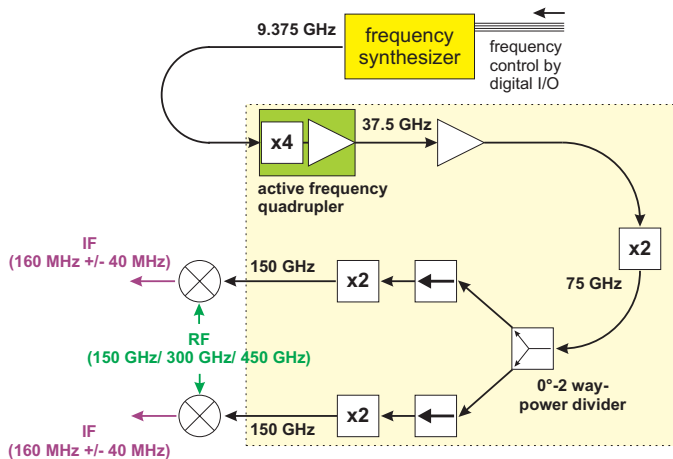


Fig. 2. Principle of the local oscillator system at 150 GHz consisting of a frequency synthesizer at 9.375 GHz \pm 312.5 MHz and an active multiplier cascade

The conversion loss of the fundamental mixers is 8.5 dB at 150 GHz, 11 dB for the harmonic mixers at 300 GHz and 24 dB at 450 GHz. All mixers convert the received RF signal directly down to the IF center frequency at 160 MHz.

III. THE INTERMEDIATE FREQUENCY RECEIVER

The intermediate frequency (IF) receiver which performs the vector analysis of the measured signals at 160 MHz \pm 40 MHz is a key component of the system with respect to measurement precision. Figure 3 shows a block diagram of the IF processing unit.

The input signal in both channels is amplified by a low noise amplifier (LNA, $F < 2$ dB) and bandpass filtered to lower the minimum input level down to -80 dBm. To achieve the required high IF bandwidth, further signal processing is done by a commercially available logarithmic amplifier / limiter amplifier chip (Analog Devices AD 8306). The RSSI (received signal strength indicator) output signal, a DC signal, is directly sampled by a 16-bit digital analog converter (DAC).

To avoid phase errors caused by amplitude variation, the limiter output of the AD 8306 is used to achieve constant signal levels. As the reference input of the IQ demodulator acts as "LO channel" for the IQ mixers, the limited reference signal is amplified to 9 dBm. The hereto used amplifier has a very flat gain ($\Delta P < 0.15$ dB) over the entire 80 MHz bandwidth.

A small part (-10 dB) of the limited reference signal power is used to feed a frequency counter. Correspondingly, the power coupled out of the signal path can be used to monitor the measurements by a spectrum analyzer.

The phase between signal and reference channel is measured by an IQ demodulator. The phase information is represented by the in-phase ($\sim \cos(\varphi)$) and the quadrature ($\sim \sin(\varphi)$)

output. All components have been integrated in a 19" rack. Special attention has been paid to avoid EMC problems. Both the RSSI signals of the two signal amplitudes as well as both IQ outputs are sampled simultaneously to allow a continuous field scan.

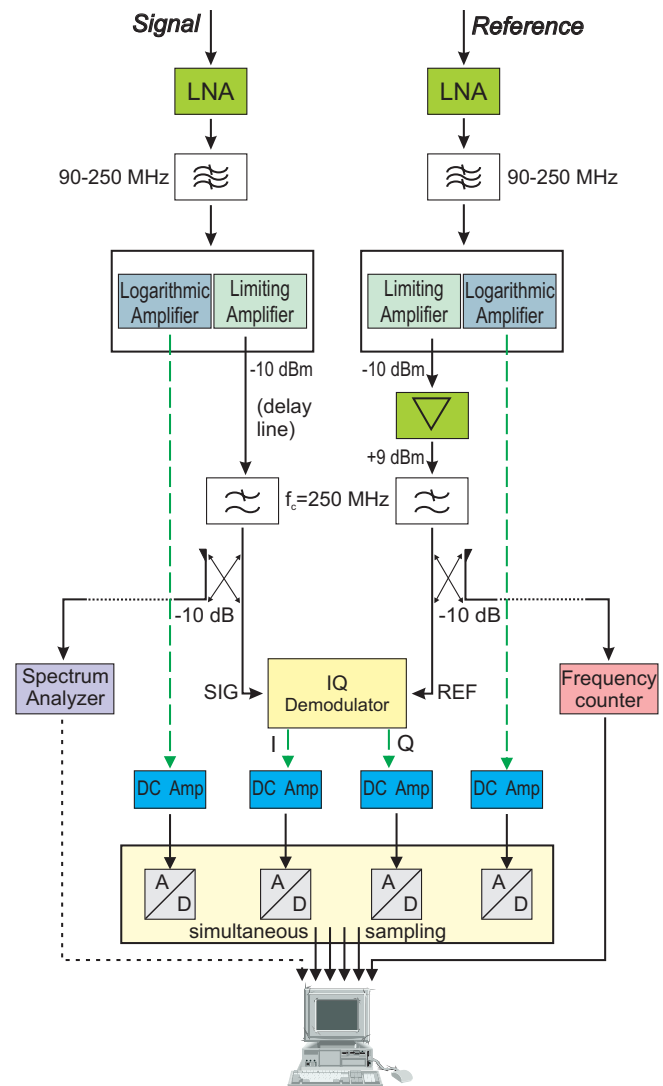


Fig. 3. Block diagram of the IF processing unit

To enhance the measurement accuracy of the IF receiver system, software algorithms for real-time reconstruction of the signal power by linear interpolation as well as a correction algorithm for the phase measurement have been developed in C++. Both algorithms can be loaded as DLL into Visual Basic as well as in graphical programming languages like LabView to allow highest programming flexibility.

The information of the RSSI outputs is stored in a single look-up table for both channels versus power and frequency to reduce the time of loading the data into the RAM of the PC. The amplitude reconstruction algorithm has been examined by random experiments, whereby frequency and power are uniformly distributed. Figure 4 shows the result of such a random experiment. To achieve this extremely high accuracy, the tests have been undertaken with the same signal generator and the same coaxial cables used to calibrate the system. To improve the phase accuracy, the in-phase and the quadrature voltage from the IQ demodulator are normalized

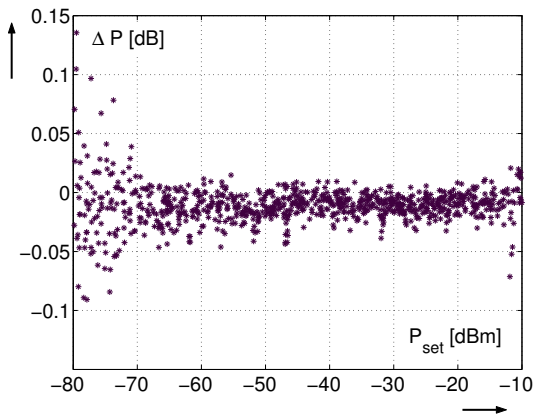


Fig. 4. Difference between reference random signals (frequency and power uniformly distributed) from a signal generator (Rohde & Schwarz SML 03) and the reconstructed values

(between ± 1), and the offset is corrected. The phase is then calculated with these processed values. As the resulting phase error shows periodic behavior over 360° , we further increase the accuracy by subtracting $K \cdot \cos(2\varphi)$ from the angle φ calculated before. K is a frequency-dependent correction factor and stored in a look-up table. The remaining error is $< \pm 1.5^\circ$ over full IF bandwidth (compare figure 5).

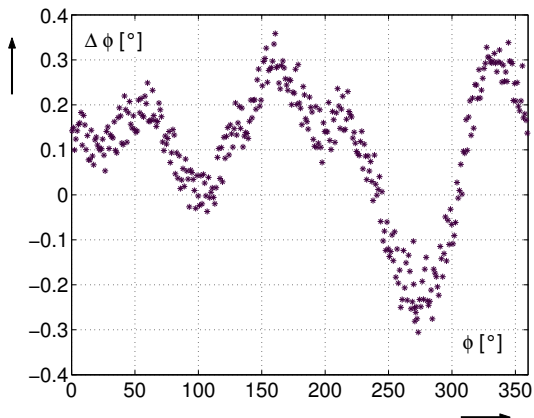


Fig. 5. Measured phase error at an IF of 160 MHz

IV. THE FIELD SCANNING SYSTEM

The mechanical base for the field measuring system is a 3-axis field scanning unit driven by high resolution stepper motors ($0,9^\circ/\text{step}$) and ball screws with a thread lead of 2.5 mm, resulting in a spatial resolution of $6.25 \mu\text{m}$.

For reducing the measuring time significantly, the field probe, a long asymmetric tapered dielectric antenna [6] is moved continuously parallel to the y-axis. The drive is designed as compact as possible to reduce reflections. The probe is triggered by an electronic linear encoder with a maximum resolution of $1 \mu\text{m}$. This high resolution permits a minimum spatial step size of $\lambda/10$ (300 GHz: $100 \mu\text{m}$). The encoder position is read out simultaneously with the 4 ADCs sampling the amplitude and phase information to avoid errors due to the movement of the probe.

V. CONCLUSION

A modular high precision heterodyne field measurement system with two channels for vector measurements at

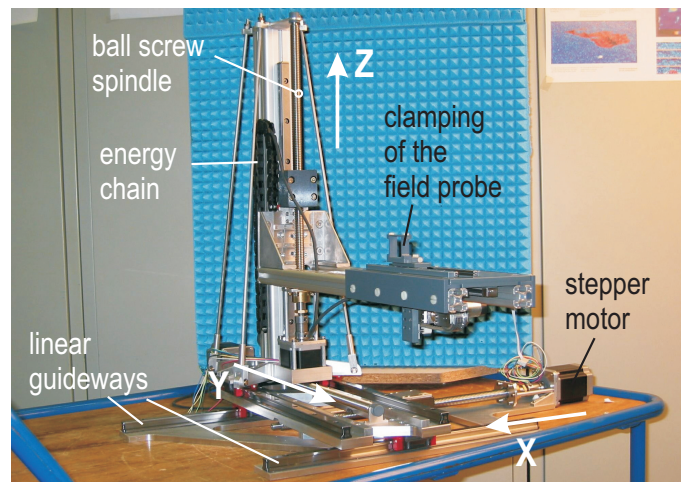


Fig. 6. 3D field scanning unit with continuously moving probe, field probe and electrical control wires not mounted



Fig. 7. Detailed view of the continuously moving probe (MoP)

150 GHz, 300 GHz and 450 GHz is presented. One phase locked two-channel local oscillator unit at 150 GHz pumps the mixers at all 3 frequencies. The latter are modularly attached to the field measurement system which allows fast changes between the measurement frequencies. The IF receiver unit offers a minimum detection level of -80 dBm with 80 MHz bandwidth at 160 MHz center frequency and a phase uncertainty better than 1.5 degrees. The measurement accuracy is significantly enhanced by fast software correction algorithms. The RF signal is received by dielectric field probes and is fed via a flexible dielectric waveguides system to the mixer ports. The dielectric antennas, the flexible waveguide as well as the mixers are modularly mounted on a high precision 3D-scanning platform. A considerable reduction of measurement time is achieved by moving the measurement probe continuously with exact position triggering by a linear encoder and simultaneous sampling.

ACKNOWLEDGEMENT

The authors want to express their thanks to G. Bauer, L. Höpfel and J. Popp of the mechanical workshop of the LHFT for their fast, precise and dedicated fabrication of the mechanical components, as well as to O. Wick from the electronic workshop of the LHFT for his support at assembling the IF receiver unit and the many fruitful discussions. The authors also indebted their thanks to H. Trägler from the electronic workshop of the Lehrstuhl für Fertigungstechnik, University of Erlangen, for his invaluable advices.

This work is sponsored by the DFG (German Research Society, Bonn, F.R.G.) which is gratefully acknowledged.

REFERENCES

- [1] H. Brand, J. Weinzierl, "MEMSTIC - eine neue Schaltungstechnologie für den Submillimeter-Wellenlängenbereich", *Frequenz*, 54(3-4), pp. 106–111, 2000
- [2] M. Höft, J. Weinzierl, R. Judaschke, "Broadband Analysis of Holographic Power Combining Circuit", *IEEE Trans. MTT*, vol. 49, no. 12, pp. 101–110, 2001
- [3] J. Weinzierl, R. Schulz, H. Brand, L.-P. Schmidt, "A Vector Field Measurement System for 150 GHz", in *Proc. 25th Intl. Conf. on Infrared and Millimeter Waves*, Beijing, P.R.C., pp. 353–354, 2000
- [4] J. Weinzierl, Ch. Fluhrer, H. Brand, "Dielectric Waveguides at Submillimeter Wavelengths", in *Proc. 6th Intl. Conf. on THz Electronics THz98*, Leeds, U.K., pp. 166–169, 1998
- [5] A. Hofmann, E. Hörster, J. Weinzierl, L.-P. Schmidt, H. Brand, "Flexible Low-Loss Dielectric Waveguides for THz Frequencies with Transitions to Metal Waveguides", in *Proc. 33rd EuMC*, Munich, Germany, pp. 955–958, 2003
- [6] J. Weinzierl, J. Richter, G. Rehm, H. Brand, "Simulation and Measurement of Dielectric Antennas at 150 GHz", in *Proc. 29th EuMC*, Munich, Germany, pp. 185–188, 1999

Application of Double Reflector Compact Ranges for Time Domain RCS Measurements

Dietmar Fasold¹, Jürgen Hartmann², Philipp Rittsteiger¹

¹Munich University of Applied Sciences, Electrical Engineering and Information Techn. Department ,
Lothstraße 65, 80335 Munich, Germany, Phone: +49 89 / 1265 – 4406, Fax: +49 89 / 1265 – 3403,
E-mail: fasold@ee.fhm.edu, philipprittsteiger@web.de

²EADS Astrium GmbH, Measurement Technology, 81663 Munich, Germany, Phone: +49 89 / 607 – 22420,
Fax: +49 89 / 607 – 25538, E-mail: Juergen.Hartmann@Astrium.EADS.net

Abstract — RF test setups of antenna test facilities are designed and optimized for antenna pattern and gain measurements. However, the operation of test facilities, especially the here considered 'Double Reflector Compact Ranges', can be extended, so that they can also be used for RCS testing.

A simple and very practical expansion of the RF antenna test setup - while maintaining the real-time measurement capability - can be achieved with the aid of a hardware gating system. With this type of setup, RCS measurements have successfully been performed in Compensated Compact Ranges. The applied gating system was the high resolution Hardgating System HG2000 of EADS Astrium, developed together with the Munich Univ. of App. Sciences.

Within this paper, the applied facility and gating system will be described. Further, the modified test setup and the test results of calibration measurements will be shown. They will give an indication of the achievable resolution for the extended test system w.r.t. object size detection and resulting amplitude dynamic range.

I. INTRODUCTION

Nowadays, compact range test facilities represent a standard in fast real time and high precision antenna and RCS measurements within a frequency range from 1 to 500 GHz and beyond. With the development of the Compensated Compact Ranges (CCR), a fundamental improvement by suppressing the system inherent cross-polarization was achieved.

For Radar Cross Section (RCS) measurements, a high resolution in time domain as well as in Signal-to-Interference-Ratio (SIR) is necessary. RF pulses with an amplitude dynamic range between 70 to 100 dB are required to achieve such a good amplitude resolution.

The Hardgating System, which originally was developed to suppress undesired distorting fields in antenna test facilities [1]-[2] can also be applied for RCS measurements. The system isolation between the on-to-off switching status of the PIN-switches can be extended up to 120 ... 140 dB. The spatial resolution of 1.2 m corresponds to the minimum system pulse width, which can be adjusted down to 4 ns. This flexible and adjustable switching capability is preferably applicable for antenna as well as RCS testing.

In the following, investigation results, concerning the application of the proposed Hardgating System for RCS measurements in CCR's designed by EADS Astrium will

be presented. The System was already installed and implemented in the CCR 20/17 at the Munich Univ. of App. Sciences, in the CCR 75/60 at EADS Astrium as well as the Compact Payload Test Range (CPTR) of ESA/ESTEC. The achieved RCS results rely on measurements with calibration standards like spheres with different diameters or plane, circular and rectangular discs.

II. TEST FACILITY

Compensated Compact Ranges provide the highest standard of compact antenna RF testing mainly for satellite antennas requiring different sizes of test zones. The CCR's main advantage in antenna - and especially in satellite antenna - testing is the high cross-polar purity up to at least - 40 dB. The remaining cross-polar component of the facility below this value is produced from secondary effects as reflector distortions, rim design and feed performance, only. The CCR 20/17 applied for the measurements described within this paper is shown in Fig. 1.



Fig. 1. CCR 20/17 at Munich University of Applied Sciences for Research and Development Activities.

For mono-static RCS testing, the required single feed is nominally positioned with its phase centre in the focal point of the reflector system. In case of bi-static RCS testing, a boresight deviation w.r.t. the nominal situation occurs, depending on the relationship of the lateral feed position to the resulting boresight angle. Up to now, RCS

measurements with the aid of hardware gating have already been performed in the CCR 75/60 and in the CCR 20/17. A top view of the CCR 20/17 visualizing the distorting fields (DF) is shown in Fig. 2.

distorting fields in the test facility. The principle test setup for e.g. bi-static measurements with a Hardgating System implemented is shown in Fig. 3.

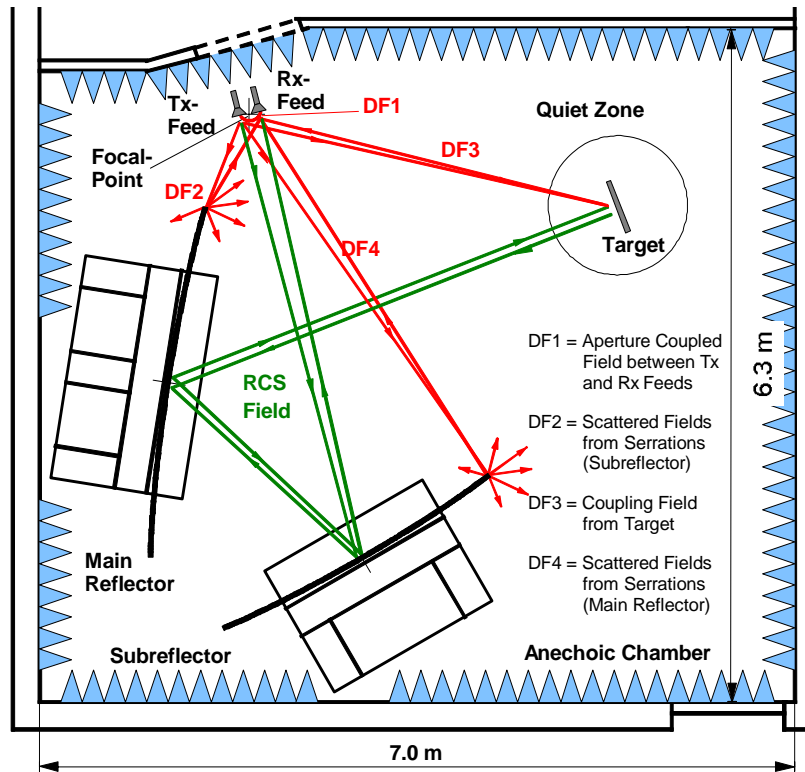


Fig. 2. Ground Plane of CCR 20/17 with Significant Ray Paths

III. HARDGATING SYSTEM

The applied gating hardware is the Hardgating System HG2000 of EADS Astrium GmbH. Hardgating was selected in comparison to software gating as it is a real-time measurement method, which does not require a high number of time consuming measurements. By that, a time saving factor of 10 to 100 can be achieved [3].

Selective measurements of the plane wave field and the different interfering fields or their suppression, respectively, can be performed by insertion of a second fast RF switch at the receiver side between the test antenna and receiver. This switch generates a 'window' in the time domain in which the detected field of the test antenna is forwarded to the receiver. With the system, pulses with a minimum width down to a value of 4 ns - corresponding to a spatial resolution of 1.2 m - can be generated.

IV. RCS TEST SETUP

The principle RF test setup for antenna and RCS measurements is typically based on the distributed mixer concept. In order to achieve higher measurement accuracies, the above described gating technique can additionally be applied for antenna pattern and RCS measurements to suppress unwanted reflecting or

In the setups, one switch unit is inserted in the Tx signal path and one in the Rx signal path. Both switch units are synchronized, controlled and powered by the centrally placed control unit of the system and connected via the coaxial synchronization cables. The mechanical test setup is shown in Fig. 4.

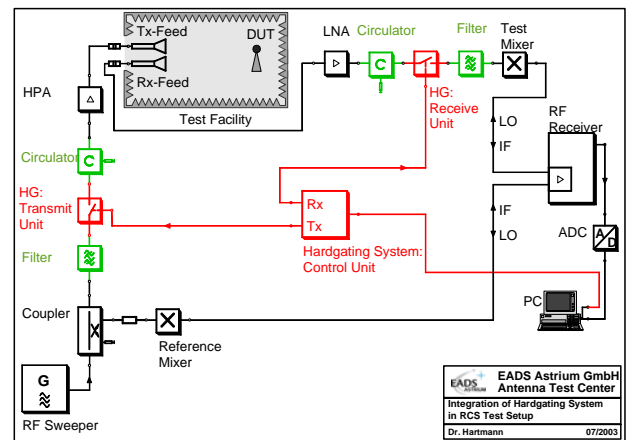


Fig. 3. Principle RF Test Setup for Bi-Static RCS Testing with a Hardgating System



Fig. 4. Mechanical Test Setup with Sphere and Pylon in the Quiet Zone of the CCR

Fig. 5 shows the arrangement of the receive and transmit units for bi-static measurements.

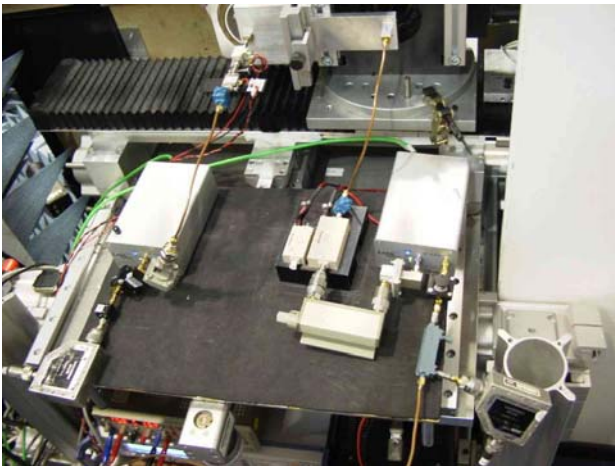


Fig. 5. Transmit and Receive Units for a Bi-Static Test Setup (Receive, Left; Transmit, Right)

V. FACILITY ANALYSIS

Before starting the RCS measurements, detailed analyses of the test facility have to be performed in order to determine the incidence of target and disturbing signals at the Rx feed in the time domain. The timing diagram valid for the CCR 20/17 is shown in Fig. 6. The diagram is related only to the time delay of the pulses in the facility (see Fig. 2) without regarding delays caused by RF cables and RF components. This constant delay values are already subtracted and do not influence the relative positions of the field contributions to each other.

For the CCR 20/17 detailed error analyses were performed for the antenna pattern and gain measurement accuracy. Main disturbers as the diffracted fields from the sub- and main reflector serrations as well as the direct leakage from the feed could clearly be identified. For RCS testing, additional disturbers are the feed coupled field - in case of bi-static setup - and the disturbing fields from the surrounding of the target and from the backwall. With an optimum setting of the Hardgating System the feed coupled field, the field from the backwall and partly

the diffracted fields from the serrations can significantly be suppressed.

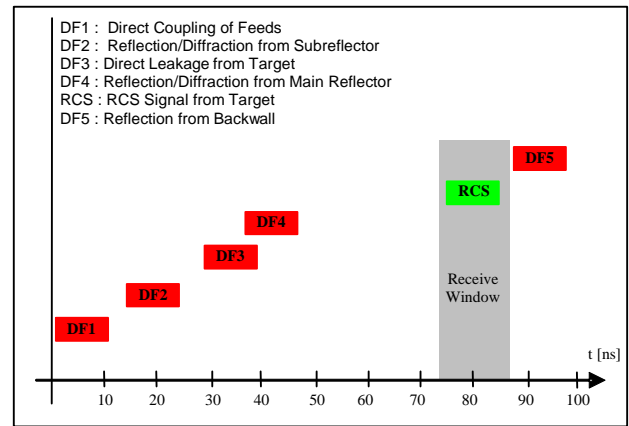


Fig. 6. Timing Diagram with Different Distorting Fields (DF1...5) and RCS Target Signal (RCS)

VI. MEASUREMENT RESULTS

Prior to performing RCS measurements on unknown targets, calibration data have to be generated in order to verify the test setup and to perform the necessary amplitude normalization of the test data itself. In the RCS test campaigns, described within this paper, the calibration was performed with a sphere (Diameter 0.08 m), a rectangular plate (Dimension: 0.1 m x 0.1 m) and a corner reflector (Dimension: 0.1 m x 0.1 m, H = 0.1 m).

$$\begin{aligned} \sigma_{\text{Sphere}} &= -22.99 \text{ dBsm} \\ \sigma_{\text{Plate}} &= 3.39 \text{ dBsm @ 12.5 GHz} \\ \sigma_{\text{CornerRefl.}} &= 6.40 \text{ dBsm @ 12.5 GHz} \end{aligned}$$

The comparative RCS bi-static measurement results of the sphere, the plate and the corner reflector are shown in Fig. 7 for a test frequency of 12.5 GHz and for co-polarization.

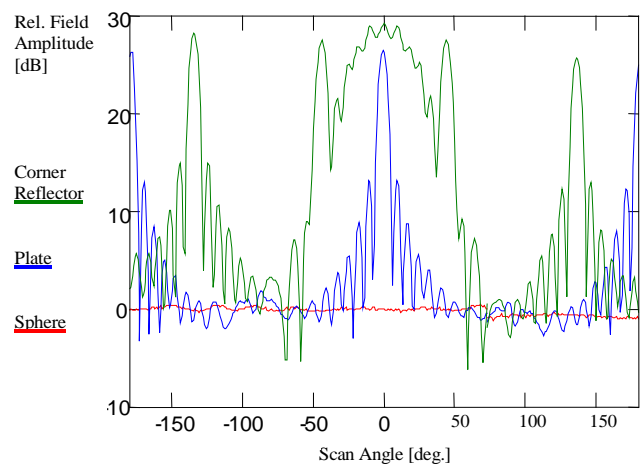


Fig. 7. RCS Test Results of Sphere, Plate and Corner Reflector for Bi-Static Measurement, VV-Polarization Adjusted

Fig. 8. shows a comparison between mono- and bi-static measurement results at a test frequency of 12.5 GHz for co-polarization.

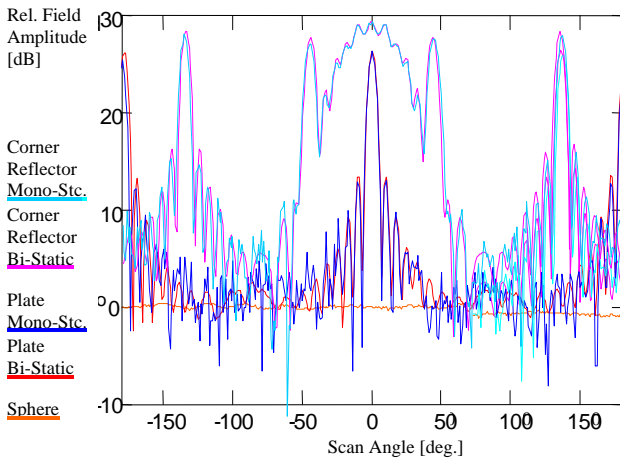


Fig. 8. Comparison Between Mono- and Bi-Static RCS Test Results of Sphere, Plate and Corner, VV-Polarization Adjusted

Fig. 9. shows test and analysis results for co-polar bi-static measurements in the frequency range of 12 to 15 GHz. The diameter of the applied sphere is 8 cm

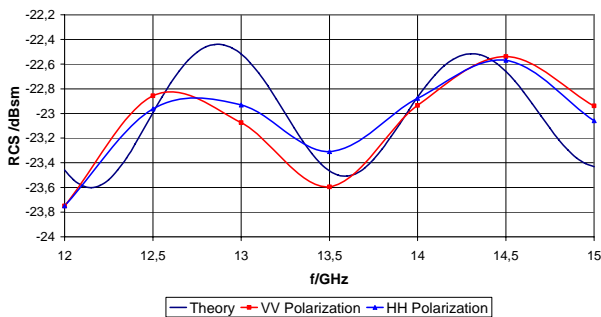


Fig. 9. Theoretical and Measured RCS Figures as Basis for a Frequency Model of a Sphere, Bi-Static Measurements

A comparison between predicted and measured RCS figures of a circular disc with a diameter of 15.912 cm is shown in Fig. 10.

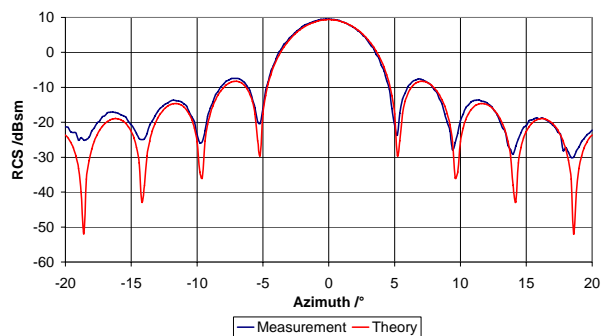


Fig. 10. Comparison Between RCS Measurement Results and Theory for a Circular Disc of 15.912 cm Diameter. Bi-static Measurements, VV-Polarization Adjusted.

The measurement results of the calibration targets exhibit a good agreement of the amplitude differences between the applied sphere to the rectangular plate and also to the corner reflector as well as between the rectangular plate to the corner reflector. Also a close agreement between measurement results and theoretically established models of the calibration standards could be achieved.

VII. CONCLUSIONS

The standard RF test setup of antenna test facilities can be extended to a RCS setup by applying hardware gating. For two different high performance compact test ranges as the CCR 20/17 at the Munich Univ. of Appl. Sci. and the CCR 75/60 of EADS Astrium in Ottobrunn, Germany, related RCS tests with a Hardgating System were performed. The Hardgating System HG 2000, which originally was designed for improvement of the antenna measurement accuracy, was now adapted to the requirements of RCS testing [4].

Validation measurement results, shown within this paper, exhibit a close agreement of relative measurement values compared to absolute theoretical values of the applied calibration standards like a sphere, a rectangular plate and a corner reflector. A measurement accuracy of better than ± 0.5 dB could be achieved with the verification measurements. The value was predicted from the measurement accuracy of the calibration standards. The dynamic range or signal-to-interference (SIR) value was determined to a figure up to 70 dB.

REFERENCES

- [1] J. Hartmann, D. Fasold, "A Flexible Hardgating System as a Diagnostic Tool in Single and Double Reflector Compact Ranges", AMTA 1998, Montreal, Canada, 1998
- [2] J. Hartmann, D. Fasold, "Identification and Suppression of Measurement Errors in Compact Ranges by Application of an Improved Hardgating System", 22nd ESTEC Antenna Workshop on Antenna Measurements, ESA/ESTEC, Noordwijk, The Netherlands, 1999
- [3] J. Lemanczyk, J. Hartmann, D. Fasold, "Evaluation of Hard Gating in the ESA/ESTEC CPTR", AMTA 2004, Stone Mountain Park, Georgia, USA, 2004
- [4] J. Hartmann, D. Fasold, "RCS Measurements with a High Resolution Hardgating System", AMTA2004, Stone Mountain Park, Georgia, USA, 2004

Session 3a

Passive Filters

Q-factor improvement of combline resonators

Michael Höft and Stefan Burger

Communications Laboratory of European Technology Center, (www.panasonic-eutc.com),
Panasonic Electronic Devices (Europe) GmbH, Zeppelinstr. 19, D-21337 Lueneburg, Germany,
phone: +49 (0) 4131 899-228, fax: +49 (0) 4131 899-262, e-mail: Michael.Hoefl@eu.panasonic.com

Abstract — In this paper, possibilities for increasing the quality factor of combline resonators are presented. Emphasis is placed on low fabrication costs. Circular and square shaped resonators are compared. The analysis is performed with a finite element simulator. To overcome numerical uncertainties of the Q-factor calculation, parametric sweeps and polynomial curve fitting are applied. As a result, the Q-factor can be increased by 5 % by introduction of a base rounding.

I. INTRODUCTION

Comblines microwave filters are widely applied in mobile and satellite communication systems because of their wide and easy tunability, relatively wide spurious free stop band, and low cost. Due to the inner conductor only medium Q-factors can be achieved. In [1] the Q-factor is increased by 14 % via a periodic 6-disk inner conductor. Due to the slow wave property of periodic structures the height of the resonator is virtually enlarged, i.e. the inductance of the equivalent circuit is increased. The drawback of the structure is its higher manufacturing cost. The same holds for the introduction of dielectric materials [2], [3].

Another possibility to increase the Q-factor is the minimization of ohmic losses. In this work, the focus is set on modifications of the geometrical shape which are simple to realize. The analysis is performed at 2 GHz, since our objective is the application in base-stations for third generation mobile communication systems [4].

II. BASIC ANALYSIS

The basic setup of a cylindrical combline resonator with a circular base area is sketched in Fig. 1. The influence of the tuning rod and inter-resonator coupling is neglected in our analysis. The Q-factor can be estimated via the well known first order TEM-line model by calculation of power losses due to the corresponding surface currents [5]. The current distribution on the outer surface has already been depicted in Fig. 1.

As a result the maximum Q-factor will be obtained, if the ratio of the outer and inner diameter ratio is $D/d = 3.59$. In that case the damping of the equivalent coaxial waveguide is minimal [5]. As will be shown in the next section the ratio D/d should be slightly smaller. Note, that in our application a capacitor defined by the gap h is sufficient. In principle, it could be increased by enlarging the tuning rod into a hole in inner conductor or a larger termination dish [5], [6]. The latter has to be preferred in case of high power applications.

For comparison of different resonator setups, calculations have been performed which are based on the results of Ansoft HFSS simulations. With the aid of the eigenmode solver the resonant frequency f_r and Q-factor can easily be determined. In those calculations the resulting frequency f_r of the adaptive

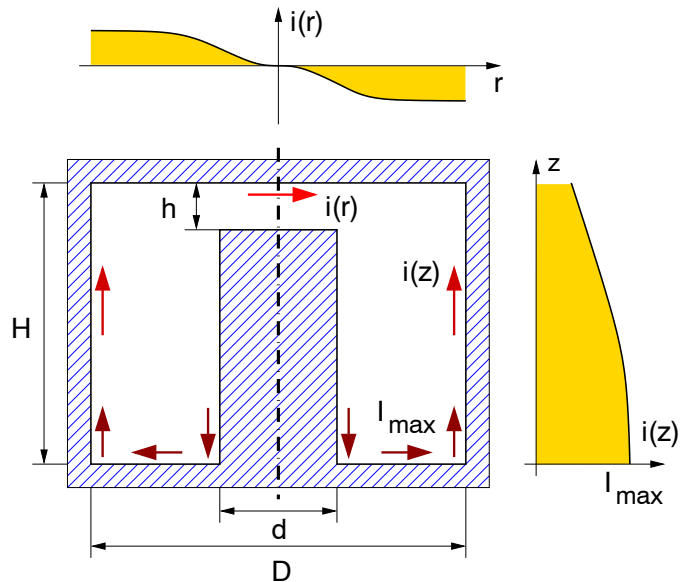


Fig. 1. Basic setup of a circular combline resonator and current flow on the outer surface.

finite element mesh refinement shows a good convergence behavior while the Q-factor bears numerical uncertainties. To avoid excessive mesh refinement we applied the following method. It is based upon the fact that we want to study the behavior in dependence of geometrical variations. Since the results would not change at small variations, polynomial curve fitting is applied to average numerical errors.

As an example the resulting resonant frequency and Q-factor in dependence of h and d are depicted in Figs. 2 and 3. The outer dimensions were set to $H = 24$ mm, $D = 32$ mm and $\sigma = 6.1 \times 10^7 (\Omega\text{m})^{-1}$ (silver) was assumed. Note, that the conductivity as well as resulting Q-factor will be lower than these values, since the manufactured housing will suffer from surface roughness and non-ideal contact of the top cover.

It is obvious that the gap h has to be tuned to keep the frequency f_r constant if d is varied. The optimum inner diameter for maximum Q-factor will be obtained if both arrays of curves hold the same slope as visualized in Fig. 4. As a result, the ratio D/d is approx. 4 % larger than the optimum for coaxial waveguides.

In the same manner simulations have been performed with different outer diameters D . Fig. 5 shows the resulting Q-factor, where the gap h is tuned for $f_r = 2$ GHz. Again, the ratio D/d is slightly larger than 3.59, – especially when the diameter D is larger than the height $H = 24$ mm.

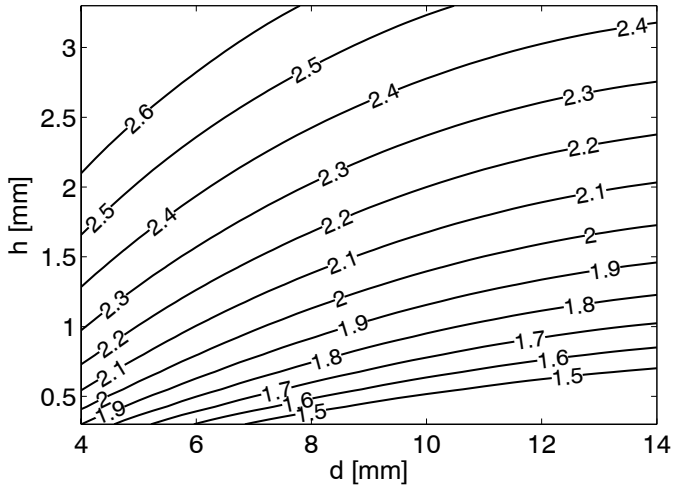


Fig. 2. Frequency [GHz] of a circular combline resonator with $H = 24$ mm and $D = 32$ mm.

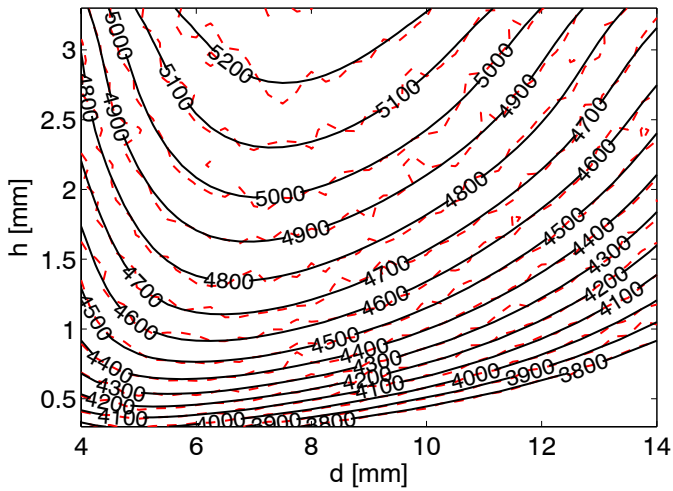


Fig. 3. Q-factor of a circular combline resonator with $H = 24$ mm and $D = 32$ mm (dashed: HFSS results, solid: polynomial curve fitting).

III. COMPARISON: SQUARE AND COAXIAL WAVEGUIDES

Generally, square shaped combline resonators are preferred for filter realization. Their basic shape is sketched in Fig. 6. The radius R_c of the corners is required due to the milling process (in our case: $R_c = 3$ mm). The results of Q-factor calculations which are in correspondence to those of the circular combline resonator are shown in Fig. 7. In this case, the optimal ratio of D/d is slightly larger than 3.59.

To compare the performance of circular and square combline resonators the required base area should be considered. For the square resonators the base area amounts to D^2 . To build compact filters with circular resonators hexagonal packaging is needed. Therefore, the base area calculates to $\sqrt{3}/2 D^2$, which is 1.1 times larger than the circular area. The resulting comparison of the Q-factor is shown in Fig. 8. It arises that the circular resonator shows an almost 1% better Q-factor if the results are related to those base areas. It is interesting to note that the Q-factor is almost equal if the comparison is related to the inner diameter d .

For the design of entire filter panels the available space has to be considered for the choice of the proper resonator type. If the complete base area is square, square resonators have to be

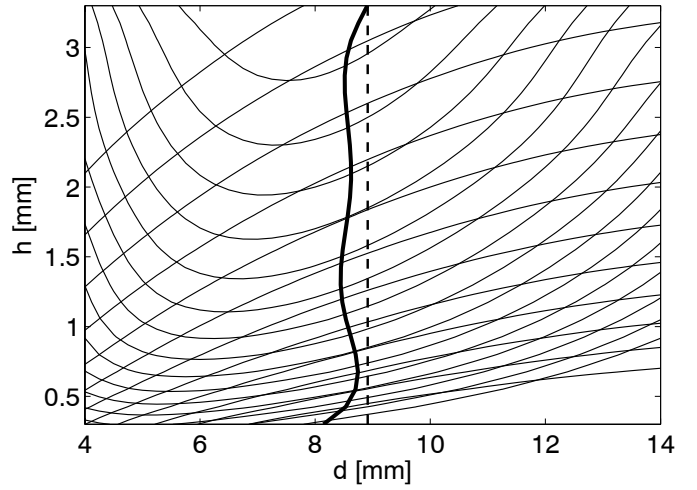


Fig. 4. Thin lines: Frequency and Q-factor from Figs. 2 and 3. Thick line: Optimum inner diameter for maximum Q-factor. Dashed line: $D/d = 3.59$ (lowest coaxial waveguide losses).

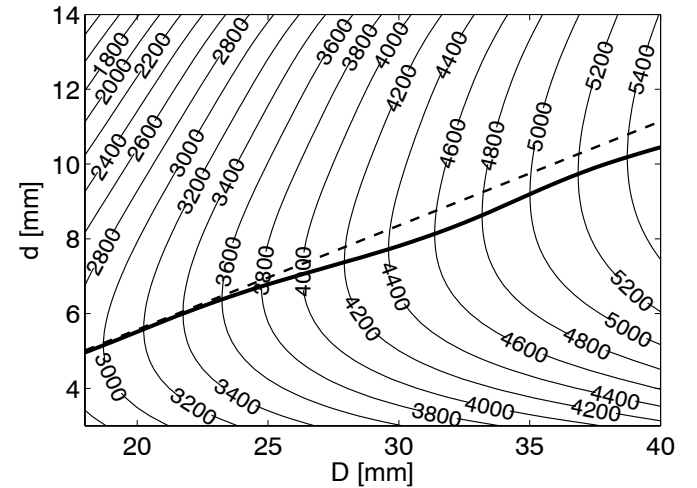


Fig. 5. Thin lines: Q-factor of a circular combline resonator with gap h tuned for $f_r = 2$ GHz. Thick line: Optimum D/d -ration. Dashed line: $D/d = 3.59$.

preferred, since hexagonal packaging of round resonators will waste some space at the corners. But if the complete base area is rectangular and square resonators would not fill the space, circular resonators might be the better choice.

In the latter case, rectangular shaped resonators may also be considered. In our application the available base area for a single resonator is 3.2×4.0 cm². The calculated Q-factor at 2 GHz results to $Q = 5230$. Corresponding square and circular combline resonators with the same base area show $Q = 5340$ and $Q = 5370$, respectively. Square resonators do not fit into the overall base area, while circular ones do.

IV. BASE ROUNDING

The maximum current I_{max} is flowing at the bottom of the resonator, as already depicted in Fig. 1. Since this current contributes a large part of the ohmic losses, we analyzed a modified setup where a base rounding R_b is introduced, as sketched in Fig. 9. Such a base rounding can easily be manufactured by choice of a corresponding milling cutter. Due to this rounding the power loss contribution of the bottom is minimized. In contrast, the inductance is decreased. In Figs. 10 and 11 the results for a circular combline resonator

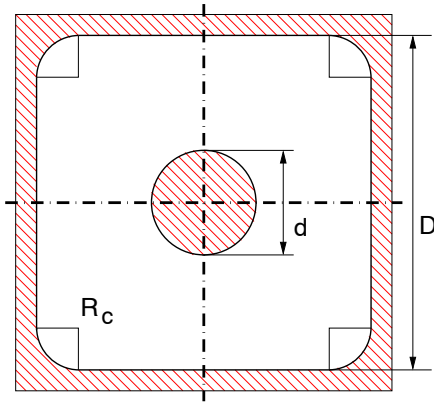


Fig. 6. Base shape of a combline resonator with square waveguide.

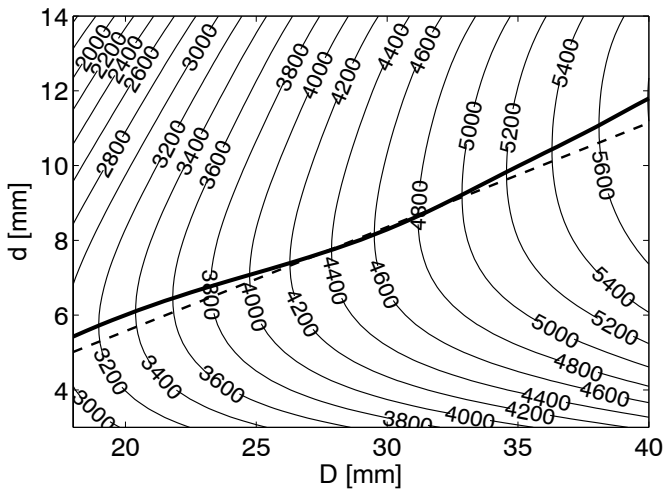


Fig. 7. Thin lines: Q-factor of a square combline resonator with gap h tuned for $f_r = 2$ GHz. Thick line: Optimum D/d -ratio. Dashed line: $D/d = 3.59$.

with $H = 24$ mm and $D = 32$ mm are depicted. Obviously, the power loss minimization outweighs the inductance decrease, which results in an increase of 5% for Q-factor. As shown in Fig. 11, the inner diameter d has to be built slightly smaller.

The introduction of a same rounding at the top corners of the resonator would lead to an additional improvement of the Q-factor, but it would be difficult to manufacture. Note, that the small rounding R_t of the inner conductor is mainly applied to improve high power handling.

V. CONCLUSIONS

Possibilities for increasing the quality factor of combline resonators have been presented. The analysis has been performed with a finite element simulator. To overcome numerical uncertainties of the Q-factor calculation, parametric sweeps and polynomial curve fitting have been applied. Note, that this method can easily be applied for other numerical studies.

The comparison of circular and square shaped resonators show that for the filter design mainly those type should be chosen which will result in a maximum base area of the individual resonators. Furthermore, the Q-factor can be increased by 5% by introduction of a base rounding with almost no additional manufacturing costs. Measurements confirm the predicted improvements.

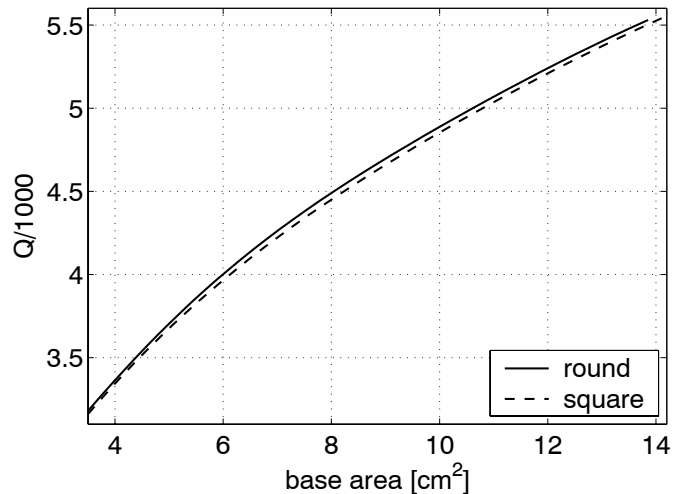


Fig. 8. Comparison of the Q-factor of a square and round combline resonator related to their base area.

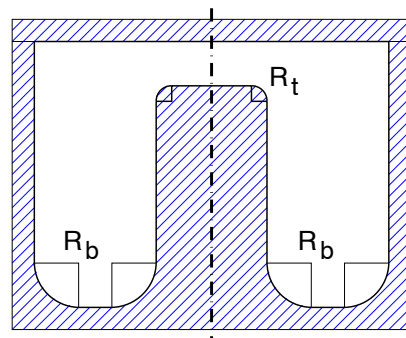


Fig. 9. Cross section of the combline resonator with base rounding R_b .

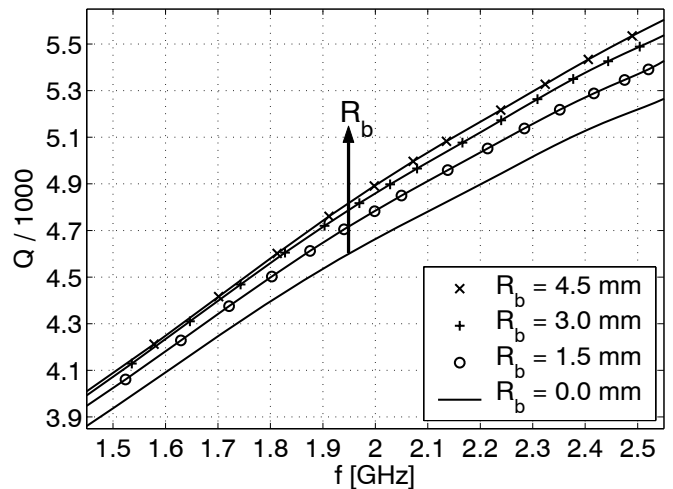


Fig. 10. Maximum Q-factor for different radii of the base rounding R_b .

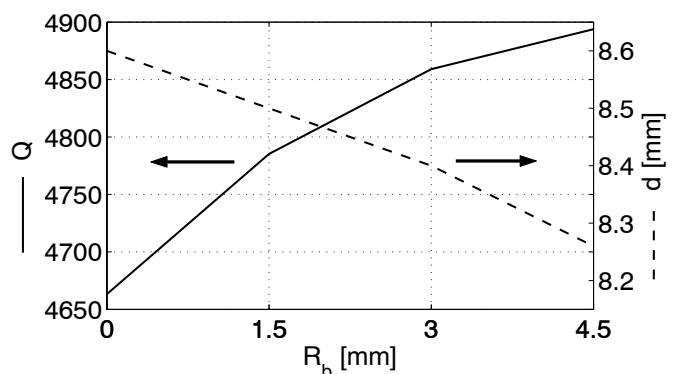


Fig. 11. Q-factor and inner diameter d at 2 GHz.

REFERENCES

- [1] G. Shen, D. Budimir, "Novel Resonator Structures for Compline Filter Applications," *32nd European Microwave Conf.*, Milan, Italy, 23.-27. Sept. 2002, pp. 597-599.
- [2] R.S. Kwok, S.J. Fiedziuszko, "Helical ceramic resonator structures," *IEEE MTT-Symp.*, Anaheim, CA, USA, 13.-19. Jun. 1999, pp. 1033-1036.
- [3] J. Chuma, D. Mirshekar-Syahkal, "Compact Dielectric Loaded Compline Filter with Low Insertion-Loss," *30th European Microwave Conf.*, Paris, France, 2.-6. Oct. 2000.
- [4] O. Bartz, S. Burger, M. Tzortzakakis, "UMTS Filterpanel for European Market," *Matsushita Technical J.*, vol. 48, no. 6, Dec. 2002, pp. 458-463 (http://www.panasonic-eutc.com/support/pdf/MTJ12_2002.pdf).
- [5] O. Zinke, H. Brunswig, *Hochfrequenztechnik 1*, 5th ed., Berlin: Springer, 1995, pp. 93-96.
- [6] M. Amato, P. Marchisio, A. Soverchia, "Dual Tower Mounted Amplifier for UMTS FDD Node B: Prototyping and results" *Conf. on Wireless Techn. 2002*, Milan, Italy, 23.-27. Sept. 2002.

Design of WLAN Filters in LTCC and LCP System-On-Package Technologies

V. Palazzari ¹, S. Pinel ², M. M. Tentzeris ², L. Roselli ¹, J. Laskar ² and F. Alimenti¹

¹Dipartimento di Ingegneria Elettronica e dell'Informazione, Università di Perugia, via G. Duranti 93, 06125 Perugia, Italy, phone:+39-(75)-5853644, e-mail: valeria.palazzari@diei.unipg.it

²Georgia Electronic Design Center, School of Electrical and Computer Engineering Georgia Institute of Technology, Atlanta GA 30332-0269 USA, e-mail: Stephane.Pinel@ece.gatech.edu

Abstract — Electronics packaging evolution involves both architectural and technology considerations. In this paper, we present the design and measurements of Single-Input-Single-Output (SISO) dual-band filters operating at ISM 2.4-2.5 GHz and UNII 5.15-5.85 GHz frequency bands, using the novel "dual behavior resonators" technique. The filters have been fabricated using Low Temperature Co-fired Ceramic (LTCC) and Liquid Crystal Polymer (LCP) multi-layer packaging technologies, enabling a low cost system-on-package (SOP) implementation. Finally an LTCC low-pass filter have been measured and cascaded to the dual-band in order to suppress high-frequency spurious response.

I. INTRODUCTION

Several standards have been approved for operating in the ISM and UNII frequency bands, including Bluetooth, IEEE 802.11a/b/g [1]-[3]. The explosive expansion of the WLAN marketplace has been mostly enhanced by the introduction of dual-band wireless systems. Most of the products that can be found in the market offer a dual path architecture. The reason behind this is to be found in the different power level characterizing the two operating bands and the different modulation scheme adopted with respect to the standard in use. Moreover, the services operating in the 5 GHz have a total available signal bandwidth of 300 MHz (5.15-5.35 and 5.725-5.825 GHz), as compared to the 85 MHz available for 2.4 GHz standards. One notices that the dual-band system is intrinsically asymmetrical. Therefore, this growing WLAN market has raised interest in novel architecture design and new technologies, in order to reduce complexity, costs and space. The goal is to exploit the same RF path providing support to multi-standards and multi-bands on a single platform, reducing the number of components, while maintaining effective performance and compactness.

Miniaturization, portability, cost and performance have been the driving force for the evolution of packaging and system-on-package (SOP) approach in RF, microwave and millimeter wave applications. Few material technologies are able address these considerations simultaneously. LTCC is a technology that has excellent electrical performance, dense multilayer integration, and good barrier properties, but it is relatively expensive compared to standard FR4. Most other substrate and packaging materials do not have low enough water absorption properties in tandem with multilayer construction capabilities to be considered for vertically integrated designs. Liquid crystal polymer (LCP) is a promising material because it has exceptional properties that make it well suited for use as a substrate material [4]. It is extremely attractive as a high frequency circuit substrate and package material due

to its low loss ($\tan\delta < 0.004$) and low dielectric constant (2.9-3) up to mm-wave frequency range. Very good barrier properties make LCP well suited for the use in packaging applications. Moreover, LCP is quite flexible and significantly cheaper (comparable to FR4) than most of the other laminated materials. Superior performance of integrated passives can therefore be achieved using this technology [5].

On the basis of the previous considerations, Single-Input-Single-Output (SISO) WLAN dual-band filters have been synthesized adopting the novel "dual behavior resonator" technique [6]. Exploiting the strong second resonant frequency of resonators to realize the filtering response, allows for achieving the asymmetric shape and the good rejection between the two bands. The filter has been fabricated both in LCP and LTCC and measured performances will be shown. Finally a low-pass filter, designed basing on the "m-derived" method [7] will be cascaded to the dual-band filter to provide a good high frequency spurious response suppression.

II. THE DUAL-BAND FILTER DESIGN

SISO WLAN dual-band filters have been synthesized basing on the novel "dual behavior resonator" technique. The dual behavior resonators (DBRs) technique is based on the parallel association of two open-ended stub resonators [6]. The open-ended stub is, in fact, the simplest realization of a band-stop structure and shows a dual behavior in the band-pass and stop-band regions: using an open-ended shunt stub implies the introduction of a transmission zero (stop-band area), the resonance frequency of which can be easily controlled by adjusting the stub length, plus by playing with the several degrees of freedom that a microwave design offers. If the

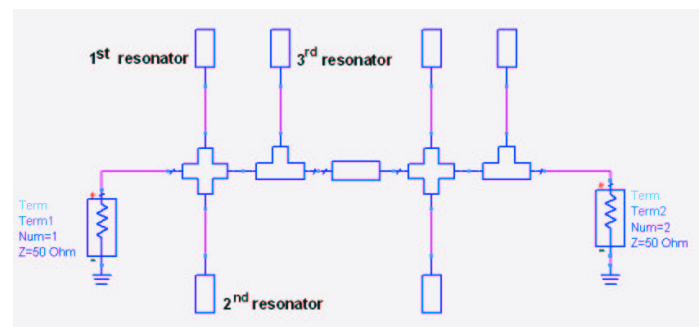


Fig. 1. Dual-band filter schematic

stubs are properly connected under constructive recombination criteria, the result is a band-pass response created between the lower and the upper rejected bands. The same approach has been extended to obtain a dual-band narrow band pass filter, simply adding a third resonator to create a third transmission zero. Choosing the transmission zero frequencies, one can first determine the length of the stubs which is equal to $\lambda/4$. The characteristic impedances of the three stubs are linked by the constructive recombination criterium. Once the central frequencies of band-pass regions are established, all impedances are determined and the full control of the pass-bands is possible, as demonstrated [8]. The values provided by the synthesis procedure, have been used to design an optimized planar compact structure by means of a full wave CAD tool. A second order filter has been considered, to achieve better performance in terms of selectivity. A simple version of the filter schematic is shown in figure 1.

In this case, the location of the transmission zeros has been accurately chosen in order to control the width and the location of the desired bands, successfully exploiting the second resonance frequency. The desired bands, 2.4-2.5 GHz and 5.15-5.85 GHz, are, in fact, very different in terms of width. Moreover the channel spacing is wide and a good rejection is difficult to achieve with the standard technique. On this basis, the stubs have been dimensioned in order to have transmission zeros at 2.2 GHz, 2.93 GHz and 3.14 GHz. To realize the pass-band in the 5 GHz range, the second resonance frequency of the first stub has been successfully exploited, while the close transmission zeros at 2.9 and 3.14 GHz allows a better rejection in the inner stop band.

III. PROTOTYPING AND MEASUREMENTS RESULTS

Multi-layer substrates have been and still are of great interest for research in the area of the 3D integration of RF and millimeter waves functions and module using the System-on-Package (SOP) approach. Our interest has been focused mainly on advanced multi-layer materials such as liquid crystal polymer (LCP) and Low Temperature Co-fired Ceramic (LTCC). LTCC has been widely used for RF and millimeter waves applications because of its process maturity and stability and its relatively low cost. Multi-layer capability up to 20 metal layer makes LTCC very attractive for 3D integrated embedded components such as filter and antenna in a very compact and cost effective manner [9]. LCP (Liquid Crystal Polymer) is a fairly new and promising thermoplastic material [10]. It can be used as a low cost dielectric material for high volume large area processing methods that provides very reliable high performances circuits at low cost. LCP have a unique combination of properties such as excellent electrical properties up to millimeter waves (low dielectric constant of 2.9 @ 20 GHz and low loss tangent of 0.002 @ 20 GHz comparable with ceramics), very good barrier properties, permeability comparable to that of glass and very close to that of ceramic, low coefficient of thermal expansion.

The prototype, shown in figure 2, has been fabricated in LCP and LTCC substrates. The size of the filter is mostly determined by the open-ended shunt stubs length. Folding the shunt stubs by the length of the open end in a sort of spiral shape, alleviates the effect of such excessive lengths and gives the structure a more compact and symmetric shape.

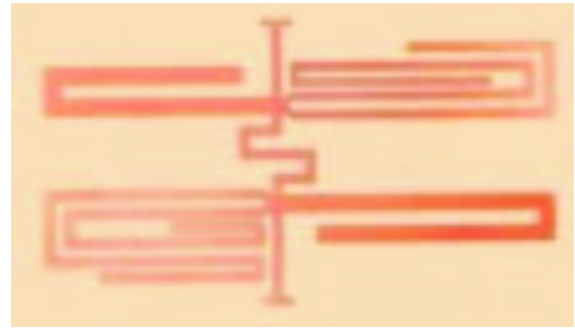


Fig. 2. WLAN Dual-band filter prototype

The LCP substrate is characterized by ϵ_r 2.9, $\tan\delta$ 0.002, substrate thickness 275 μm , conductor thickness 9 μm . The prototype occupies a 8mmx15mm of LCP area. Figure 3 shows the good agreement between IE3D simulation and measurement. The occurrence of a frequency shift, due to substrate dispersion and fabrication uncertainties, has been detected. The insertion loss and return loss at the central frequency are -2.4dB and -15dB for the 2.4 GHz band, respectively, and -1.8dB and -10dB for the 5 GHz band, respectively. Though the lower band is perfectly covered, the upper band is narrower than expected. Nevertheless this parameter can be easily recovered after a further optimization of the design. The filter exhibits also an out-of-band rejection as high as 45 dB between the bands.

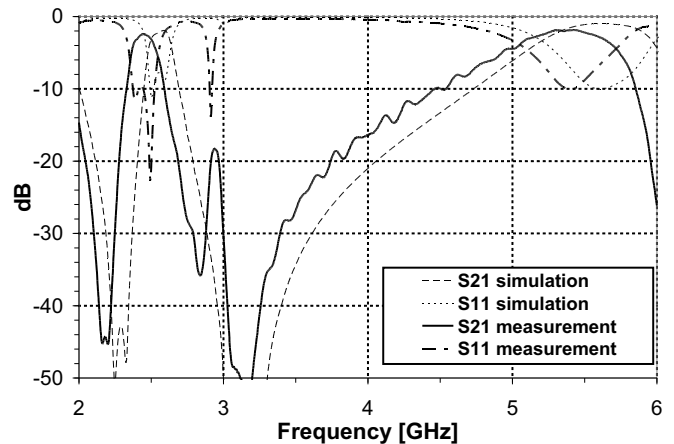


Fig. 3. Comparison between IE3D simulation results and measurements on the LCP prototype

The LTCC substrate is characterized by ϵ_r 5.4, $\tan\delta$ 0.0015, substrate thickness is 600 μm (stacking six layers of 100 μm each), conductor thickness 9 μm . The prototype occupies a 7mmx9mm of LTCC area. Figure 4 shows the comparison between IE3D simulation and measurement. The insertion loss and return loss at the central frequency are -5.8dB and -10dB for the 2.4 GHz band, respectively, and -2.5dB and -20dB for the 5 GHz band. The out-of-band rejection is as high as 45 dB between the bands. The results are poorer than in the LCP case: the occurrence of a frequency shift is present as well, and the lower band is characterized by a high insertion loss. Further optimization is required, but the results shows

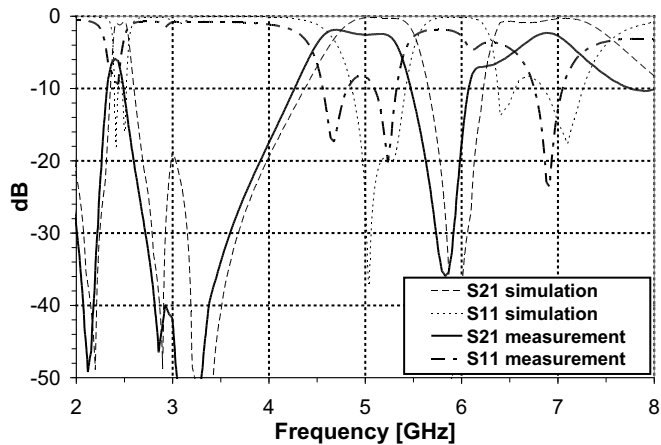


Fig. 4. Comparison between IE3D simulation results and measurements on the LTCC prototype

in both cases (LCP and LTCC) that these substrates are good candidates for microwave filters implementation.

In filter design based on the "dual behavior resonators" technique, the constructive recombination is placed between the intrinsic resonance of each stub and causes the spurious resonances to be closer to the band-pass filter, allowing undesired low and high frequency signals to pass through. Capacitive feeding of the filter will remove the DC, and low pass filtering will remove the high frequency spurious response. This second aspect has been investigated in the case of the LTCC dual-band filter prototype.

A compact low-pass filter showing a cut-off frequency around 6 GHz has been designed basing on the "m-derived" sharp cut-off method [7]. The presence of strong attenuation pole near the cutoff frequency provides a sharp attenuation response, while ensuring good matching properties in the pass-band, making this filter design very attractive for harmonic spurious response suppression. It has been fabricated in LTCC, exploiting 8mmx4mm of substrate area (see figure 5), and measured. Figure 6 shows the comparison between IE3D simulations and experimental results. The agreement is quite satisfactory, despite of a slight frequency shift that has already been observed in the dual-band filters case. Measured performances exhibit rejection of the attenuated pole greater than 40dB while insuring insertion losses below 1 dB in the pass-band.

The low-pass filter has then been cascaded to the LTCC dual-band filter. As can be seen from figure 7 the high frequency spurious response is definitively removed and the return loss improved.

IV. CONCLUSION

In this paper SISO dual-band filters for WLAN applications in ISM 2.4-2.5 GHz and UNII 5.15-5.85 GHz frequency bands fabricated on LCP and LTCC have been shown. The design has been based on the novel "dual behavior resonators" technique and exploits the strong second resonant frequency of resonators to realize the asymmetric filtering response. Moreover, a LTCC compact low-pass filter design for harmonic spurious response suppression at 6 GHz has been detailed.

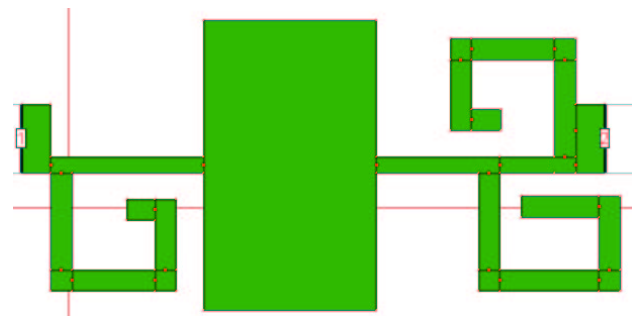


Fig. 5. "m-derived" low-pass filter LTCC prototype

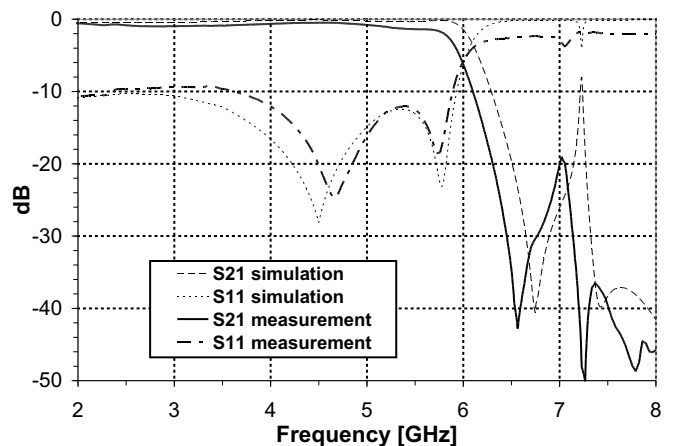


Fig. 6. Comparison between IE3D simulation results and measurements on the LTCC low-pass filter

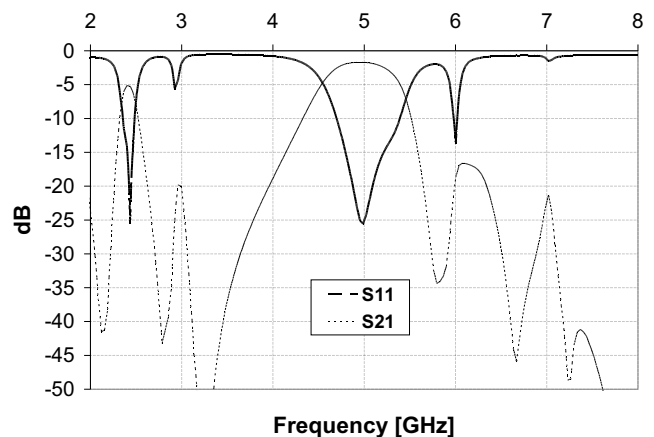


Fig. 7. Measurements results for the LTCC dual-band filter with low-pass filter

In combination with innovative design this paper demonstrates LCP and LTCC potential for very low cost and high performances integrated circuits for RF and mm-wave applications.

ACKNOWLEDGMENT

The authors wish to acknowledge the support of the NSF CAREER, ECS-9984761, the NSF ECS-0313951, the Georgia

Electronics Design Center and the Georgia Tech Packaging Research Center. This work was also partially supported by NASA under contract #NCC3-1015.

REFERENCES

- [1] M. Zargari et al., *A 5-GHz CMOS transceiver for IEEE 802.11a wireless LAN systems*, IEEE Journal of Solid-State Circuits 2002, vol.37, n.12, pp.1688-1694
- [2] J. O. Plouchart, H. Ainspan and M. Soyuer, *A 5.2 GHz 3.3 V I/Q SiGe RF transceiver*, Proc. IEEE Custom Integrated Circuits 1999, pp.217-220
- [3] M. A. Margarit, D. Shih, P. J. Sullivan and F. Ortega, *A 5-GHz BiCMOS RF IC Front-end for IEEE 802.11a/HiperLAN Wireless LAN*, IEEE Journal of Solid-State Circuits 2003, vol.38, n.7, pp.1284-1287
- [4] D. C. Thompson, O. Tantot, H. Jallageas, G. E. Ponchak, M. M. Tentzeris and J. Papapolymerou, *Characterization of Liquid Crystal Polymer (LCP) Material and Transmission Lines on LCP Substrates from 30-110 GHz*, IEEE Transactions on Microwave Theory and Techniques, Vol.52, No.4, pp.1343-1352, April 2004
- [5] M. F. Davis, S.-W. Yoon, S. Pinel, K. Lim and J. Laskar, *Liquid Crystal Polymer-based Integrated Passive Development for RF Applications*, IEEE International Microwave Symposium 2003, vol.2, pp.1155 -1158
- [6] C. Quendo, E. Rius and C. Person, *Narrow bandpass filters using dual-behavior resonators*, IEEE Trans. Microwave Theory Tech. 2003, vol.51, n.3, pp.734-743
- [7] D. M. Pozar, *Microwave engineering*, Addison-Wesley Publishing Company, 1990.
- [8] C. Quendo, E. Rius and C. Person, *An original topology of dual-band filter with transmission zeros*, IEEE International Microwave Symposium 2003, pp.1093-1096
- [9] K. Lim, S. Pinel, M. Davis, A. Sutono, C.-H. Lee, D. Heo, A. Obatoynbo, J. Laskar, M. Tantzeris and R. Tummala, *RF-SOP For Wireless Communications*, Microwave Magazine, March 2002.
- [10] K. Brownlee, S. Bhattacharya, K. Shinotani, C. Wong, R. Tummala, *Liquid Crystal Polymer for High Performance SOP Applications*, 8th International Symposium on Advanced Packaging Materials, pp 249-253, IEEE 2002.

Compact Suspended Stripline Quasi-Elliptic Low-Pass Filters

Wolfgang Menzel, Atallah Balalem

Microwave Techniques, University of Ulm, PO Box, D-89069 Ulm, Germany
Tel.: +49-731-5026350, Fax: +49-731-5026359, E-mail: wolfgang.menzel@ieee.org

Abstract — The design of very compact suspended stripline low-pass filters with additional transmission zeroes is presented. The transmission zeroes are achieved by additional capacitive coupling between different elements of the low-pass filter. Both interdigital as well as broadside coupling is investigated, and single, twofold, and threefold coupling is demonstrated for test filters with edge frequencies between 5 GHz and 6 GHz and order 5. Excellent agreement is achieved between theory and experiment.

I. INTRODUCTION

Suspended stripline (SSL) has proven to be an excellent transmission line system to realize different types of filters with moderate or even low loss. Using both sides of the substrate, very versatile transmission line structures can be realized, e.g. improved end-coupling by overlapping of strips on different sides of the substrate [1, 2]. Using an additional ground metallization on one side of the substrate, microstrip lines can be designed with very low impedance compared to the quite high impedance of a narrow normal SSL line. This enables the realization of very compact low-pass filters with, at the same time, wide stopband [2]. The basic cross section of the SSL as used in this work is shown in Fig. 1.

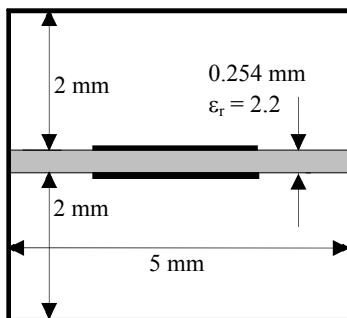


Fig. 1: Cross section of the suspended stripline as used in this work.

Quasi-elliptic low-pass responses can be achieved either by using parallel resonators instead of the series inductances or by series resonators instead of the shunt capacitances (Fig. 2). The first solution may be realized using stub-type elements [3, 4], the second one by placing the capacitive

patches close to each other and using narrow folded lines as inductances [5, 6].

This paper describes a similar approach. As the SSL low-pass filters can be made much more compact, however, some kind of "inline" coupling between the capacitive patches can be achieved.

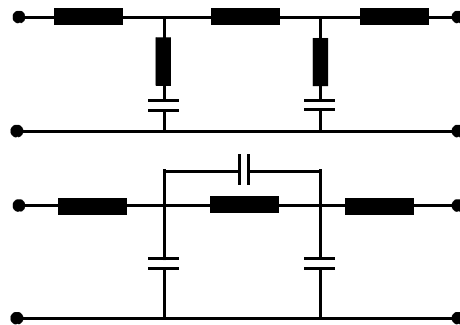


Fig. 2: Equivalent circuits of possible quasi-elliptic low-pass filters.

II. LOW-PASS FILTER WITH INTERDIGITAL COUPLING

As both the inductive and capacitive transmission line segments in a SSL filter are quite short, two neighboring capacitive elements each can be modified in such a way that they, while keeping their capacitance, are made shorter in the center but lengthened at the edges to couple in the form of an interdigital capacitor (Fig. 3). At the same time, the narrow inductive line length has to be increased slightly to maintain the passband filter performance. Details of the design were done using a 2.5D simulator [7]. Modifying the amount of coupling, the position and distance of the transmission zeroes can be adjusted to some extent.

The layout of such a filter of order 5 for a corner frequency of about 6 GHz is displayed in Fig. 3. The capacitive elements consist of wide lines (the same width as the 50 Ω SSL connecting lines) with partly backside metallization. They are coupled to input and output lines by two interdigital structures arranged at the side of the narrow inductive lines.

Together with the inductances for the outer filter elements, this forms two parallel resonators at the input and output of the filter.

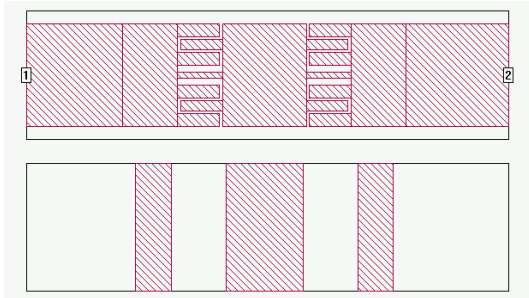


Fig. 3: Front side (top) and back side (bottom) layout of a quasi-elliptic low-pass filter using interdigital coupling.

The substrate is placed in a mount as shown in Fig. 1 (this mount is used for all other filters presented here, too); it is clamped by two 0.5 mm deep grooves at the edges. The low-pass filter itself (without connecting lines) is only 8 mm long. Fig. 4 shows theoretical and experimental results of this filter. Two transmission zeroes can clearly be recognized; however, some frequency shift can be stated. On the one hand, the width of the coupling slots of the interdigital capacitors was 90 μm in reality compared to 100 μm as designed, and the metallization thickness of 17 μm was not taken into account for the design. Therefore, the structure was recalculated using a slot width of only 50 μm to account for both the smaller slot width as well as approximately the effect of the finite metallization thickness (reduction of the slot widths by twice the metallization thickness). This result is included in Fig. 4 with the dash-dotted line, now showing a very close agreement with experiment.

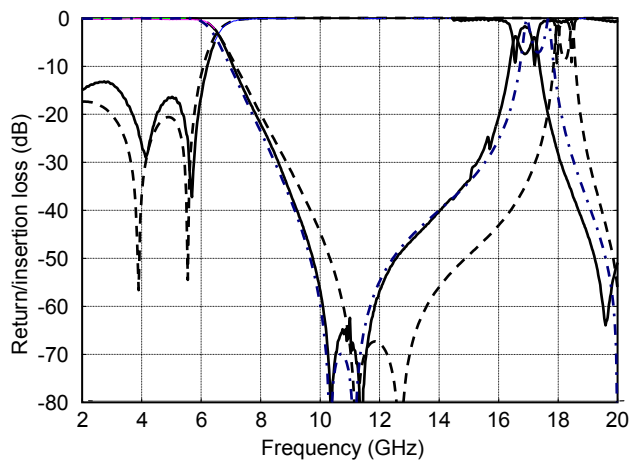


Fig. 4: Return and insertion loss of the low-pass filter according to Fig. 2. (Dashed lines: theory, solid lines: experiment, dash dotted line: theoretical S_{21} with coupling slots reduced to 50 μm).

III. LOW-PASS FILTERS WITH ADDITIONAL BROADSIDE COUPLING

The use of metallization patterns on both sides of the structure allows the realization of broadside capacitive coupling. In the configuration as used here, the lines are on the same side of the structure. Therefore, neighboring low-pass shunt capacitances are brought close together (but not as close as with the previous example), and some small metal patches are placed on the backside of the substrate overlapping with both, resulting in the series connection of two capacitances. This provides an additional coupling between the two capacitive elements (see Fig. 2, bottom). The overlapping areas result in increased coupling without critical narrow slot widths as in the first example. Design examples and experiment were done for single as well as multiple couplings, as shown in the Figs. 5 to 8. In all figures, layout of front and back side is given on top of the figures, and theoretical and experimental results are compared at the bottom.

As expected, a single additional coupling leads to one transmission zero. For a coupling capacitance in the center (Fig. 5), the transmission coefficient shows a zero at about 11 GHz, and a narrow spurious passband at 18 GHz. This is caused by the bigger lengths of both capacitive and inductive elements. With the broadside capacitive coupling as used here, a very good agreement between theory and experiment can be stated.

An interesting effect occurs if a single additional coupling is introduced at one of the edges of the filter, i.e. between one of the capacitive elements and one of the input lines (Fig. 6). A very wide stopband can be observed with a rejection of better than 40 dB up to nearly 25 GHz. Some resonances around 20 GHz and 24 GHz are probably due to some clamping problems of the mount. In addition, in that frequency range, the first waveguide mode may be excited in the channel. An excellent agreement between theory and measurement is found, only the passband return loss is slightly deteriorated by reflections of the transition from the coaxial connector to the SSL.

In the low-pass filter examples of 5th order as investigated here, also a twofold coupling at the two edges and a threefold coupling at the edges and in the center were investigated (Fig. 7 and 8). Different amounts of coupling were adjusted to control the positions of the transmission zeroes. In both cases, a high stopband rejection over a wide frequency range could be realized, and once again, an excellent agreement with experiments can be stated down to -60 dB and even below.

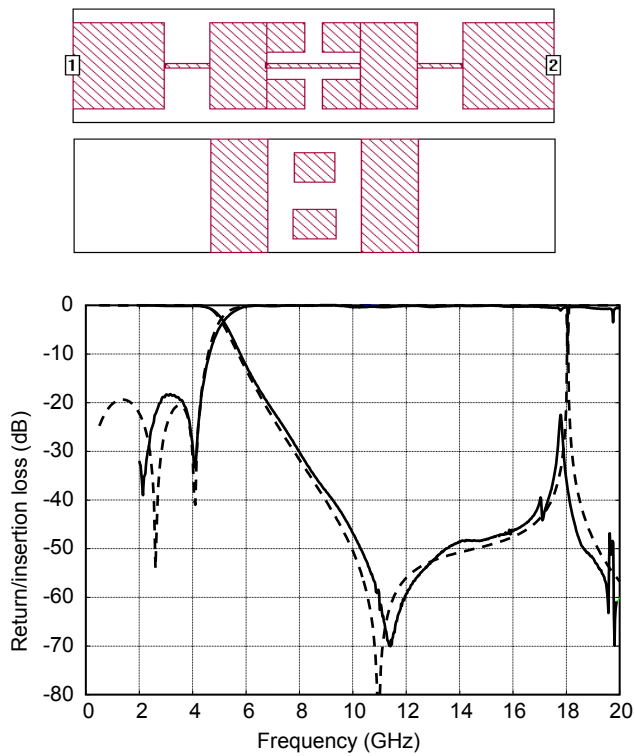


Fig. 5: Front and backside layout and transmission performance of a low-pass filter with a single central capacitive coupling. (Dashed lines: theory, solid lines: experiment).

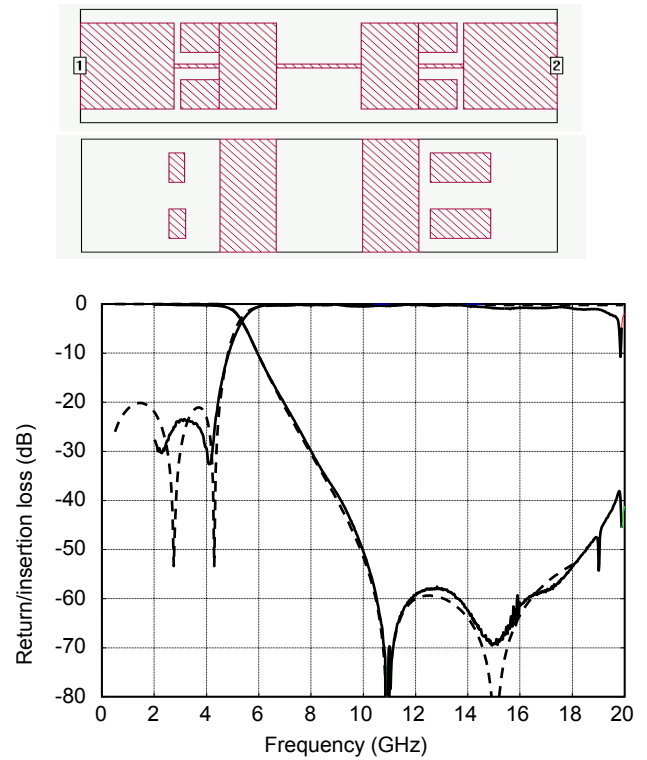


Fig. 7: Front and backside layout and transmission performance of a low-pass filter with a twofold edge capacitive coupling. (Dashed lines: theory, solid lines: experiment).

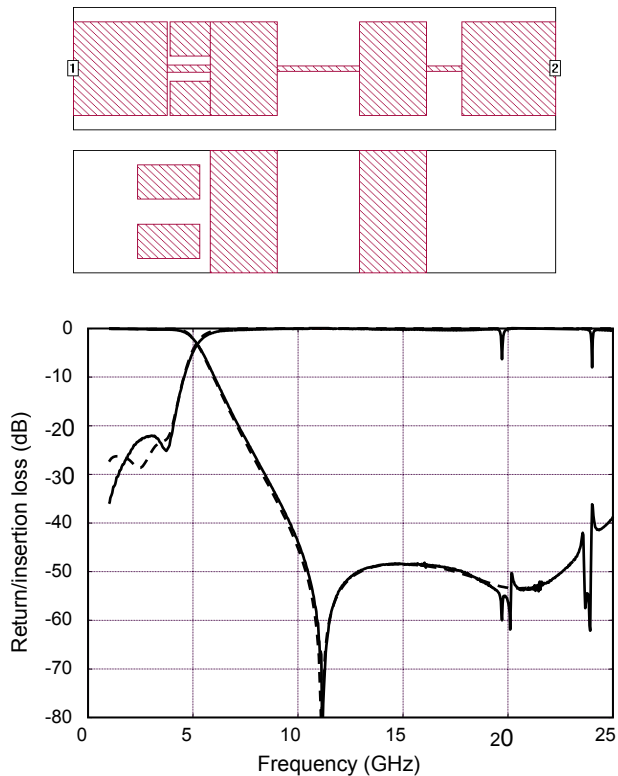


Fig. 6: Front and backside layout and transmission performance of a low-pass filter with a single edge capacitive coupling. (Dashed lines: theory, solid lines: experiment).

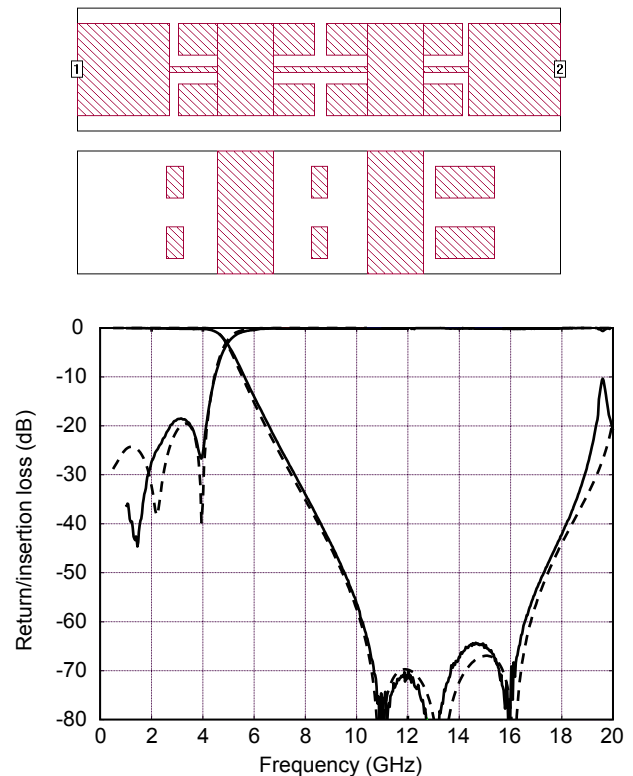


Fig. 8: Front and backside layout and transmission performance of a low-pass filter with a threefold capacitive coupling. (Dashed lines: theory, solid lines: experiment)

IV. LOW-PASS FILTER WITH A MODIFIED CAPACITIVE ELEMENT

Transmission zeroes can be implemented, too, in a way similar to Fig. 1, top. In the example given here, the ground plane metallizations below one of the capacitive elements is replaced by a shunt resonator similar to that used in [8] for bandpass filters (Fig. 9, top). In an approximate equivalent circuit (Fig. 9, bottom), this results in the series connection of this shunt resonator and the capacitive low-pass filter element. This configuration again leads to transmission zeroes of the low-pass filter as shown in Fig. 10.

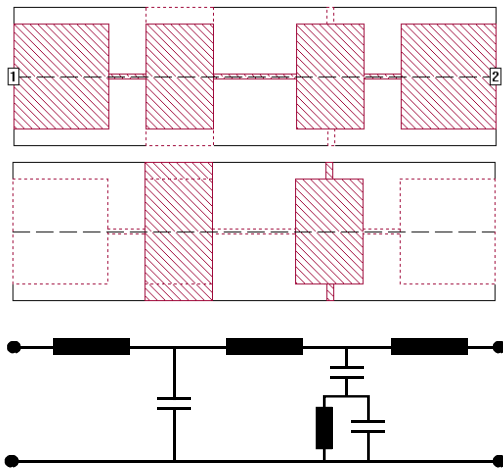


Fig. 9: Layout and equivalent circuit of a low-pass filter with modified capacitance element.

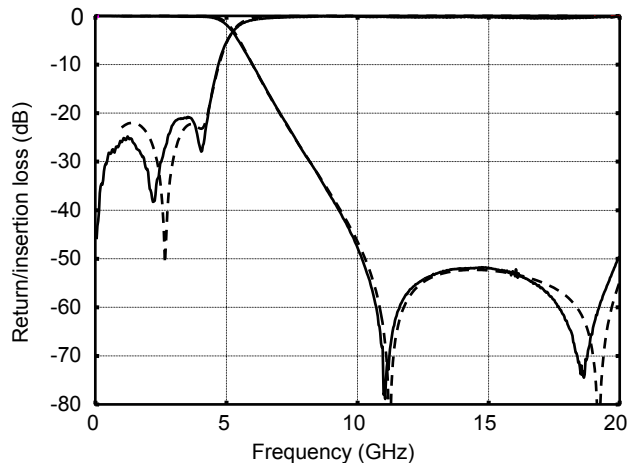


Fig. 10: Transmission performance of a low-pass filter with modified capacitance element. (Dashed lines: theory, solid lines: experiment).

V. CONCLUSION

This contribution has shown that transmission zeroes can easily be added to suspended stripline low-pass filters without major increase in complexity and size. This is simply done by introducing coupling between the shunt capacitances of the low-pass filters which can be achieved on the same substrate side as well as by structures on the backside of the substrate. An additional way to introduce transmission zeroes is demonstrated adding a parallel resonator to one (or more) of the shunt capacitive elements. Simulation and optimization with a commercial 2.5D simulator give results which show an excellent agreement with experiment, and computation time even including optimization is kept reasonably short. The design principle as used here can easily be scaled to other frequencies.

REFERENCES

- [1] P. Bhartia and P. Pramanick, "Computer-Aided Design Models for Broadside-Coupled Striplines and Millimeter-Wave Suspended Substrate Microstrip Lines", *IEEE Transactions on Microwave Theory and Techniques*, Vol. MTT-36 (Nov. 1988), pp. 1476 - 1481.
- [2] Menzel, W., "Broadband Filter Circuits Using an Extended Suspended Substrate Transmission Line Configuration", *22nd Europ. Microw. Conf.*, 1992, Helsinki, Finland, 459 - 463.
- [3] G. T. Roan and K. A. Zaki, "Computer-Aided Design of Microstrip Filters by Iterated Analysis" *IEEE Transactions on Microwave Theory and Techniques*, Vol. MTT-36 (Nov. 1988), pp.1482 - 1487.
- [4] R. N. Martins, H. Abdalla, "Design of Low-Pass Microstrip Filters with Equal-Ripple Passband and Finite Attenuation Poles", *SBMO/IEEE IMOC 2001*, pp. 71 - 74.
- [5] M. Miyazaki, H. Asao and O. Ishida, "A Broadband Dielectric Diplexer Using a Snaked Strip-Line", *1991 IEEE International Microwave Symposium*, Boston, Vol. II, pp. 551 - 554.
- [6] H. Hsieh, K. Chang, "Compact, Broad-Stopband Elliptic Function Lowpass Filters Using Microstrip Stepped Impedance Hairpin Resonators", *2003 IEEE International Microwave Symposium*, Philadelphia, pp. 1775 - 1778.
- [7] SONNET, Version 9, *Sonnet Software Inc.*
- [8] W. Menzel, "A Novel Miniature Suspended Stripline Filter", *33rd European Microwave Conf.*, Munich, Oct. 2003, pp. 1047 - 1050.

Channel Branching Equipment For Outdoor Radio Transceivers Serving High Capacity ($n \times \text{STM-1}$) Short Haul Radio Links

Uwe Rosenberg, Jürgen Ebinger, Michael Knipp

Marconi Communications GmbH, Backnang, D-71522 Germany (e-mail: Uwe.Rosenberg@ieee.org)

Abstract — A novel channel branching approach for STM-1 short haul radio systems is introduced to provide flexible adaptation of link capacity without the need of extra antenna sites and equipment. Moreover, the total system branching loss of the concept is evidently lower compared with 3dB coupler solutions commonly used for short haul applications. The Rx/Tx diplexer used in standard equipment is replaced by a branching filter unit to provide separate access to the transmit and receive paths inside the transceiver. Waveguides are applied for low loss interconnection of the radios. The Rx/Tx branching circulator is directly mounted to the first radio in the chain, which is connected via a feeder waveguide with the respective antenna port. For example, the branching loss for a $2 \times \text{STM-1}$ system (16QAM) at 26GHz is app. 5dB less compared with a conventional coupler solution.

Keywords: Channel Branching, Short Haul Radio, System Branching Loss, High Q Channel Filters

I. INTRODUCTION

The steady growth of mobile services yields continuously upgrading of the GSM base stations for higher data rates. Proceeding this trend, UMTS has started operation recently, providing new services and to overcome limited frequency resources of existing GSM solutions. The access networks for the base stations of these systems are mainly realised by short haul radio links. Up to now, PDH radio equipment, serving up to 34Mbit/s, has been used for many links. But such a capacity will no longer be sufficient for the increasing service demands. Hence, SDH radio solutions are becoming more and more attractive for such access networks. In particular, this holds if they allow transmission of an arbitrary number of STM-1¹ channels via one antenna per station for a dedicated link. The possibility of later upgrading such links according to the individual upcoming transmission demands will further enhance attractiveness of this approach.

So far, high capacity short haul radio equipment has been designed for operation with a single STM-1 channel [1-3]. It commonly consists of an indoor unit that is interconnected via a coaxial cable with an outdoor RF transceiver operating in a frequency band above 15GHz. The transceivers are generally equipped with integrated antenna solutions, which are fed by a diplexer for the combination/separation

of the co-polarised receive (Rx) and transmit (Tx) channel signals (cf.: [1-3]). The remaining ports of the diplexer are directly interconnected with the transmit and low noise (LNA) amplifiers, respectively. Obviously, such compact solutions exhibit lowest possible RF losses between antenna and amplifiers, however, the complete transceiver must be mounted at exposed locations to cope with the line-of-sight requirement for the link. Moreover, if link capacity demands essentially exceed that of a single STM-1 channel, more and more transceiver equipment must be considered at the exposed positions. As a consequence, the base station sites would rapidly be overcrowded with antenna equipment with the need of significant extra expenses for the respective infrastructure. To overcome such problems, a single relocated antenna will be used for a link, serving all dedicated radios. They will be mounted close to the antenna or at shielded areas in the near ambit. In that case, the integrated antennas are removed from the radios and the respective diplexer ports of the equipment are combined by waveguides with 3dB couplers that finally feed the antenna. Evidently, such solutions exhibit high branching loss (e.g. more than 6.5dB extra coupler loss per link for two operated channels) yielding substantially reduced link performance or hop length. Even a possible application of larger antennas with all their drawbacks (e.g., mounting infrastructure, wind loads, public acceptance) may only compensate in part for these losses in most situations.

Thus, this paper introduces a novel channel branching concept for high capacity short haul radios, to defeat the disadvantages of the solutions above. In principle, it is based on the general circulator/filter chain approach as traditionally used for indoor long haul radio equipment [4-5]. However, the adaptation to the existing outdoor radio units yields particular constraints, that are optimally satisfied by integrated Rx/Tx branching filter units each dedicated to one radio. The special trade-off for the overall interconnection between radios and antenna and the inherent design requirements for the branching units are outlined. The application of this approach to an existing high capacity short haul radio product line, using 16 and 128 QAM modulation schemes, prove the salient features. Since the extra branching loss is kept reasonably low, the achievable link performance for all channels is almost comparable with that

¹ Data rate of one STM-1 signal is 155Mbit/s

obtained up to now for a single channel². Standard equipment – that is only capable to serve a single channel per link – can be retrofitted easily by only replacing the diplexer by an Rx/Tx branching filter unit, to obtain the capability for low loss channel branching. In addition the introduced solution allows later extension with extra radios without interruption of service of the operating channels.

II. BASIC COMPONENT DESIGN ASPECTS

A principle block diagram of the approach is depicted in Fig.1. The components in the shadowed boxes are dedicated to the Rx/Tx branching filter units substituting the diplexer of the standard equipment [1]. Due to the application of such a unit the radio will no longer have a common Rx/Tx port as in the diplexer case. The unit provides separate access to Rx and Tx paths inside the equipment with two waveguide ports assigned to each path. One of which is assigned to the interconnection with extra radios (Rx-out and Tx-in ports, respectively) while at the other ports (Rx-in, Tx-out) the channel signals of the dedicated radio and the succeeding extra radios in the chain are served. The latter two ports of the radio near the antenna are directly associated with the branching circulator to feed Rx and Tx signals of all radios to the antenna. The remaining RF ports of the last radio in the chain are terminated by waveguide loads.

A. Branching Filter Unit

The branching filter unit represents the basic building block of the approach. Main requirements result from the previous diplexer application [1]. The unit size and internal interfaces with the LNA and transmit amplifier must fit with those of the diplexer. The complete unit has to comprise, Rx and Tx filters, isolators, harmonic reject filter, and channel branching circulators with separate access to the Rx and Tx signal paths of the equipment. In addition to the required electrical filtering and matching properties, the branching filter unit has to accommodate the multiplexing task of channels with close centre frequency spacing. Hence, narrow band channel filters in combination with Y-junction circulators are considered.

A comparison with narrow band filter designs at frequencies for long haul applications demonstrates the design challenge for the desired application. Considering identical channel bandwidths yields a substantial reduction of the relative filter bandwidth at the high frequency bands. In addition, the unloaded Q-factor of cavities systematically decreases with frequency while the effects caused by tolerances and

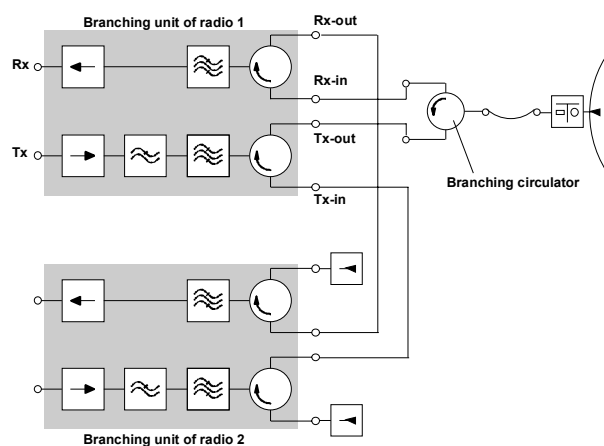


Fig. 1. Principle Block diagram of channel branching network for two SDH short haul radios for 16QAM.

temperature increase. Moreover, the outdoor application has to cope with approx. twice the operating temperature range as occurring for indoor designs. Careful investigation of all these aspects yields a reasonable approach with high-Q narrow band filters.

a. Channel Filters for 16QAM Transceivers. For the 16QAM transceivers a 5-pole filter function with a bandwidth of 65MHz (equiripple 21dB return loss) is optimally suited for the desired application, namely, the combination of channels with a centre frequency spacing of 112(110)MHz. The response provides an asymmetric located transmission zero towards the centre gap to accommodate with increased rejection at the image frequency band of the transceiver and to satisfy the isolation demands for the channels at the centre gap.

For low insertion loss reasons, overmoded rectangular cavities have been considered for the filter realisation. The particular constraints for such a filter design is described in [6]. It should be noted, that the application of an optimised TE_{103} overmoded cavity type at 26GHz yields 57% improvement of the unloaded Q-factor compared with a standard TE_{101} cavity.

The filter is realised from silverplated INVAR sheets to attain high frequency stability of the response at all environmental conditions (outdoor temperature range $-45...55^{\circ}\text{C}$) while maintaining good surface conductivity. The application of proper tuning elements yields a tuning capability for the filter response over the complete lower and upper half band, respectively, without remarkable degradation of the insertion loss. Thus, there is only a sole pair of filters, that is capable to serve arbitrary Rx/Tx channel combinations out of the overall frequency band. For example, the insertion loss of the realised channel filters for the 26GHz band is less than 2.0dB. The measured frequency response of a typical channel filter for the upper band is shown in

² For the same antenna equipment.

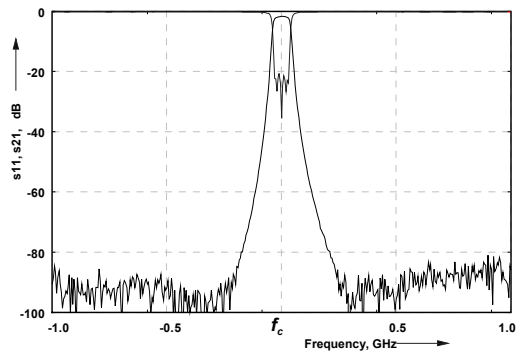


Fig. 2. Measured typical frequency characteristic of an upper half band channel filter for a 16QAM transceiver

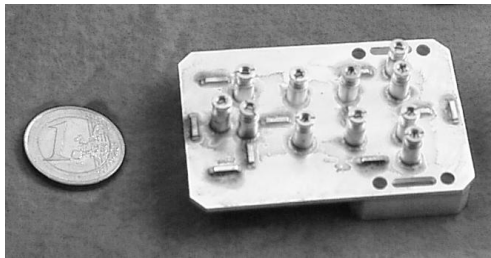


Fig. 3. Photograph of the upper half band channel filter for the 26GHz 16QAM transceiver

Fig. 2. As an example, a photograph of the realised 26GHz filter is depicted in Fig. 3.

b. Channel Filters for 128QAM Transceivers. The challenging aim of combining STM-1 channels with a centre spacing of 56(55)MHz requires rather narrow 5-pole filters providing a chebyshev response with 32MHz bandwidth (equiripple 21dB return loss). Note, the relative filter bandwidth at 26GHz is about 0.12% ! Using the same filter realisation as for the 16QAM transceivers would yield an unacceptable high insertion loss due to the extreme narrow bandwidth. Consequently, another realisation has been considered, which is based on cylindrical high Q dual mode cavities. Owing to the dual-mode design the filter size is also kept in acceptable limits. For example, the realised filters at 26GHz based on TE_{113} mode cavities exhibit an insertion loss of 2.3dB. This value corresponds to a 45% higher unloaded Q-factor as achieved for the already improved TE_{103} mode filter above.

The filter is realised in two parts from INVAR by milling techniques, to accommodate the high frequency stability of the response for the specified outdoor environmental conditions. For high surface conductivity, i.e., low insertion loss, the INVAR parts are silverplated prior to the filter assembly. The particular filter design also considers the tuning capability (app. 1GHz) of the response to arbitrary channel locations in the upper and lower half band, respectively.

Fig. 4 shows a photograph of the realised filter for the 26GHz 128QAM radio. It should be noted, that

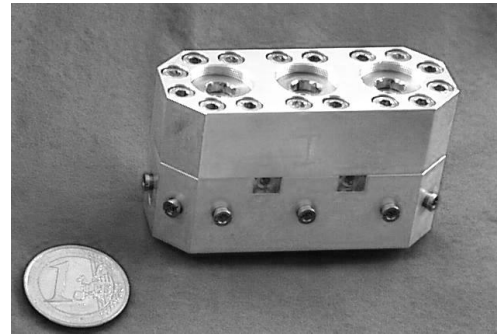


Fig. 4. Photograph of the upper half band channel filter for the 26GHz 128QAM transceiver (dual-mode design)

this filter design is obviously more complex compared with the 'single acting' solution above. However, it satisfies the overall extreme requirements for the channel branching at reasonable cost.

c. Broadband Components. All components assigned to the complete frequency band (isolators, circulators and low pass filter) are integrated in the basic unit which also provides the internal (LNA, transmit amplifier) and external (Rx-in/-out, Tx-in/-out) waveguide interfaces. It is realised in two half shells from silverplated aluminium. The filters are directly mounted into recesses of the aluminium halves which simultaneously provide the respective module interconnections. This advanced integrated concept facilitates a very compact size and high performance properties. A photograph of the complete branching filter unit for the 26GHz 16QAM transceiver is shown in Fig. 5. It comprises Rx and Tx filters, isolators, harmonic reject filter and channel branching circulators. At the four external RF interfaces, the unit is equipped with an adapter plate for the sealed assembly within the transceiver housing. It should be noted, that the insertion loss of this branching unit is only 0.6dB higher compared with the value of the diplexer of the standard transceiver [1].

B. Rx/Tx Branching Circulator

The design of the Rx/Tx branching circulator is based on the well known Y-circulator type. According to the filter branching unit, the design considers direct interfacing of the Tx-out and Rx-in ports without the need of extra interconnecting waveguides. The common port situated at the opposite side of the circulator is interconnected with the dedicated antenna by a feeder waveguide. This branching circulator is realised from two half shells aluminium. Since the circulator is directly exposed all outdoor climatic conditions, the shells are alodined and an O-ring is considered between the mounted halves for appropriate sealing. Despite the need of the alodine surface, the insertion loss between common and Tx (or Rx) ports is less than 0.2dB. At all environmental operating conditions (including the

temperature range of -45 to 55°C) the return loss and isolation properties exceed 23dB. Fig. 6 shows photographs of the Rx/Tx branching circulator from both interfacing sides.

C. Pre-assembled Waveguide Interconnections

To accommodate with proper equipment mounting while keeping the overall branching loss very low, U-shaped waveguide sets are used for the interconnection of the adjacent mounted transceivers. This solution yields an insertion loss improvement of app. 50% as compared with commonly used flexible waveguides. This solution accommodates with the aim of high return loss (typical more than 28dB) and low insertion loss (less than 0.3dB) interconnection of the transceivers.

III. OVERALL CONSTRUCTION

The radios are mounted side by side close to the antenna or at shielded and easy accessible areas of the station, several metres apart from the antenna site. The RF interconnections of the radios are performed by precast waveguide sets. They do not only account for improved insertion loss properties but also facilitate mounting and handling issues. The first radio of the chain which is dedicated to the interconnection with the antenna is associated with the Rx/Tx branching circulator providing the common antenna interface. According to low insertion loss demands, standard or overmoded ALFORM waveguides are used for the interconnection with the assigned antenna port [7]. The introduced branching solution allows arbitrary extension of an existing configuration with extra channels (i.e. transceivers) – without any interruption of service. Owing to the good matching properties for all channels, there will be no impairment of the system by long feeder waveguide runs as e.g. by the long line effect.

It should be noted, that standard transceiver equipment for single channel operation can be retrofitted by only replacing the Rx/Tx diplexer by the branching filter unit for the operated channel.

Despite of the slightly higher insertion loss of the narrow band channel filters applied for the channel branching, the substantial advantages of the introduced approach are obvious. The system needs only one antenna per site and link for the

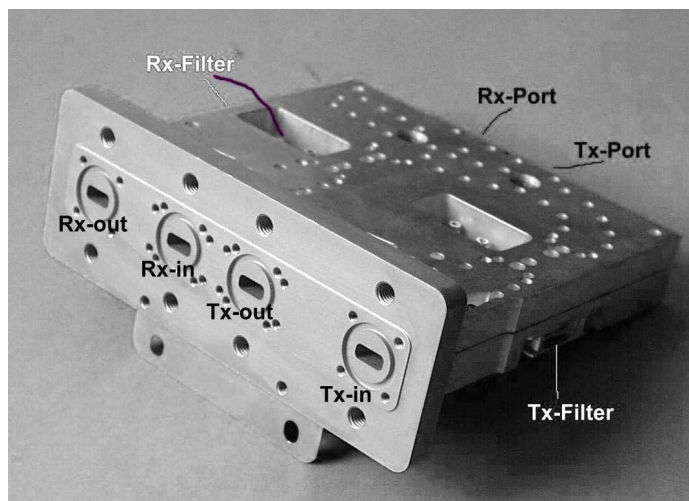


Fig. 5. Complete branching filter unit for a 26GHz 16QAM transceiver (replaces diplexer of standard equipment)

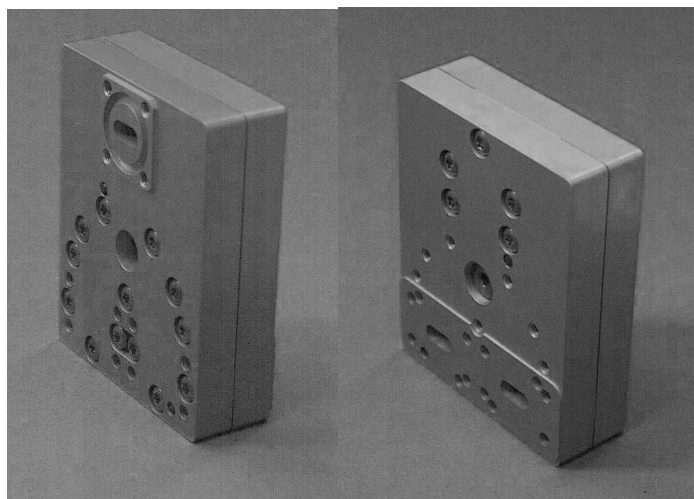


Fig. 6: Photographs of Rx/Tx branching circulator, left: view of antenna interface, right: view of interfaces to branching filter unit

transmission of an arbitrary number of STM-1 channels. The considerable benefit concerning the total system branching loss becomes evidently when comparing the solution with the conventional 3dB coupler branching approach, that is commonly applied to SDH short haul radio systems. As an example, the use of the new approach for a 2xSTM1 system at 26GHz using 16QAM provides app. 5dB less branching loss as the coupler concept with standard radios¹. This improvement increases with the number of operated channels. This is, for a 4xSTM1 channel system sharing the same antenna and polarisation the branching loss advantage is app. 11dB over the coupler concept. Thus, the introduced branching approach provides nearly the same link performance or hop length for all operated channels as up to now only obtained for a single STM-1 channel².

¹ Includes branching loss at both stations

² Considering the same antenna equipment.

IV. CONCLUSION

The introduced channel branching approach for short haul radios provides flexible configuration and arbitrary expansion of link capacity serving several STM-1 channels at a dedicated polarisation. It should be noted, that the utilisation of the orthogonal polarisation with identical or similar radio branching configurations will allow protected transmission equivalent to more than two STM-4 (STM-4 is 4 times STM-1) signals. Standard transceiver equipment for single channel operation can easily be upgraded for the combination with other transceivers. The extra costs for the branching capability are kept reasonably low due to the application of a basic integrated design approach for the key component, namely the branching filter unit. Consequently, this concept will keep pace with the needs of modern access networks, namely the flexible adaptation and increase of transmission capacity to individual sites.

REFERENCES

- [1] Rosenberg, U., Beis, K., Ebinger, J., Martin, S. 'Advanced integrated antenna coupling equipment for millimetre wave radio link systems', *5th ECRR Proceedings*, pp. 249-253, Bologna, Italy, 1996
- [2] Solvaag, T., 'New Technology for 25GHz high capacity radio', *6th ECRR Proceedings*, pp. 105-108, Bergen, Norway, 1998
- [3] Ferrucci, L., Marconi, F., Piloni, M., 'Millimeter wave linear outdoor unit for access radio applications', *7th ECRR Proceedings*, pp. 207-211, Dresden, Germany, 2000
- [4] Uher, J.; Bornemann, J.; Rosenberg, U., 'Waveguide Components for Antenna Feed Systems: Theory and CAD', Artech House, Boston – London, 1993
- [5] Rosenberg, U., Heisen, S., Knipp, M., Martin, S., 'A Novel Channel Branching Network Approach for Contiguous (28 MHz Spacing) and Co-channel Operation in SDH Radios', *7th ECRR European Conference on Fixed Radio Systems and Networks - Proceedings*, pp. 227-232, Dresden, Germany, 2000
- [6] Rosenberg, U., Hägele, W., 'Consideration of Parasitic Bypass Couplings in Overmoded Cavity Filter Designs', *IEEE Transactions on Microwave Theory Tech.*, Vol. 42, No. 7, pp. 1301-1306, 1994
- [7] Rosenberg, U., Knipp, M., Speldrich, W., 'Sophisticated Components for Waveguide and Feed Systems Enhance Attraction on Radio-In-The-Loop Applications', *7th ECRR European Conference on Fixed Radio Systems and Networks -Proceedings*, pp. 227-232, Dresden, Germany, 2000

Session 3b

Antenna Elements

A Matching Technique for Dual-Band Composite Right/Left Handed (CRLH) Transmission Line Resonator Antennas

S. Otto¹, A. Rennings¹, C. Caloz², P. Waldow¹

¹Department of Engineering Duisburg-Essen University, Bismarckstr. 81, D-47048 Duisburg,
Phone: +49 203 379 1058, otto@ate.uni-duisburg.de

²École Polytechnique de Montréal, 3333, ch. Queen Mary, Montréal (Québec), Canada

Abstract — Recently, a novel dual-band Composite Right/Left Handed (CRLH) resonator antenna was introduced. The two operation frequencies f_{-1} and f_{+1} of this antenna correspond to a pair of negative and positive resonance frequencies ($-n, +n$) associated with a left-handed (LH) and right-handed (RH) resonances of the CRLH structure, respectively. Although these resonances exhibit identical field distributions, because they have the same electrical length $|\beta l| = |\pm n \lambda_g|$, they can have significantly different input impedances in general, so that simultaneous good matching at both frequencies can be difficult. This paper provides a rigorous technique for this simultaneous matching of both frequencies to obtain an efficient dual-band antenna. Furthermore, introducing a dual-band CRLH $\lambda/4$ resonator antenna, a more size effective antenna is obtained along with the suppression of undesired spurious modes.

1. INTRODUCTION

CRLH-TLs are artificially designed transmission lines. They have been used for various novel concepts of microwave devices [1]. A CRLH-TL is composed of cascaded CRLH unit cells. The lossless CRLH unit cell is modeled with its four lumped element circuit parameter as they are C_R, L_R, C_L, L_L . The series capacitance C_L and shunt inductance L_L account for the LH propagation (anti-parallel group and phase velocity). This duality of the LH and RH propagation mechanism exhibits unusual phenomena. At lower frequencies the propagation is essential affected by the LH elements C_L, L_L , leading to backward propagation and a proportional relation of frequency and wavelength ($f \sim \lambda$) on the transmission line. With increasing frequency the RH elements are dominating the wave propagation and the usual anti-proportionality of frequency and wavelength is observed ($f \sim 1/\lambda$). This dispersion characteristic provides the same $|\beta|$ for two different frequencies, one located in the LH frequency range with $\beta < 0$ and the other one in the RH frequency range with $\beta > 0$. Such a pair of propagation constants has been exploited in our open ended resonator antenna. In our previous work [2] the main focus has been on the two half-wavelength resonant modes and their qualitatively same voltage and current distribution. The highly dispersive transmission line impedance Z_{CRLH} was not considered and therefore an additional matching circuit was needed to achieve simultaneous matching. The key idea to obtain equivalent dual band behavior is to have the same mode along with the same line

impedance for the two operating frequencies. Qualitative (same mode pair) as well as quantitative (same CRLH line impedances) design will ensure fully equivalent dual frequency operation.

2. THEORY

2.1. Resonant Modes

The upper right corner of Fig. 1 shows the lumped element unit cell model of the CRLH-TL. An N -cell CRLH-TL resonator of physical length $l = Np$ (p : length of the unit cell) has the following resonance condition:

$\beta_n = n\pi/l$ ($n = 0, \pm 1, \pm 2, \pm 3, \dots, \pm(N-1)$) associated with the resonant frequencies [3]

$$\frac{n\pi}{N} = \cos^{-1} \left(1 - \frac{1}{2} \frac{(f^2 - f_{se}^2)(f^2 - f_{sh}^2)}{f^2 f_R^2} \right), \quad (1)$$

$$f_{se} = \frac{1}{2\pi\sqrt{C_L L_R}}, \quad f_{sh} = \frac{1}{2\pi\sqrt{L_L C_R}} \text{ and } f_R = \frac{1}{2\pi\sqrt{C_R L_R}}$$

An N -cell CRLH resonator supports the zeroth order resonance plus $N-1$ resonances in the RH range and $N-1$ resonances in the LH range. Every mode pair has the same voltage/current distribution on the open ended CRLH-TL. The voltage/current distributions at the terminals of the unit cells follow a sinusoidal half wavelength distribution, in the particular case of f_{-1} and f_{+1} . The lower operating frequency f_{-1} is located in LH frequency region of the CRLH dispersion characteristics and the f_{+1} is located in the RH frequency region, respectively.

2.2. Line Impedance

Based on the $ABCD$ -matrix of the symmetrical unit cell depicted in the upper right corner of Fig. 1, the transmission line impedance Z_{CRLH} (Bloch impedance [4]) for a lossless CRLH-TL is calculated:

$$Z_{\text{CRLH}} = \sqrt{\frac{B}{C}} = \sqrt{\frac{Z(4 + ZY)}{4Y}}, \quad (2)$$

with $Z = j(\omega L_R - 1/\omega C_L)$ the series impedance and $Y = j(\omega C_R - 1/\omega L_L)$ the shunt admittance of the unit cell. The lumped element parameters used for the circuit simulations are: $C_L = 1.4\text{pF}$, $L_R = 2.7\text{nH}$ and $C_R = 2\text{pF}$ with the shunt inductance L_L varied in three steps $L_L = 1.6\text{nH}$,

$L_L=1.9\text{nH}$ and $L_L=2.1\text{nH}$. The reason L_L was chosen for the variation is the easily controllable inductance in the later design implementation in microstrip technology. In Fig. 1 the line impedance Z_{CRLH} is plotted for the three different cases: I.) $L_L=2.1\text{nH}$ with $f_{\text{sh}} < f_{\text{se}}$; II.) $L_L=1.9\text{nH}$ the balanced case with $f_{\text{sh}} = f_{\text{se}}$; III.) $L_L=2.1\text{nH}$ with $f_{\text{sh}} > f_{\text{se}}$. It can be observed that with increasing shunt inductance L_L the CRLH-TL impedance in the LH frequency range increases as well. In the RH frequency range the opposite behavior of decreasing impedances with higher inductances is found. The line impedances for the balanced case are equivalent in the RH and LH region around the series resonator frequency $f_{\text{sh}} = f_{\text{se}}$. The shaded regions indicated the transmission band gaps and are associated with imaginary line impedance for the non-balanced cases in I.) and III.).

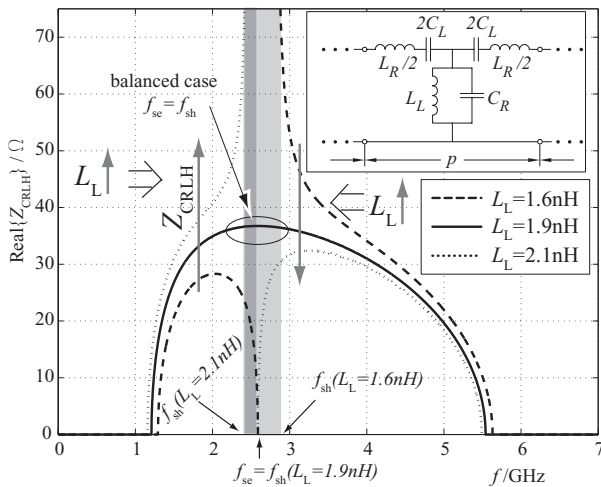


Fig. 1: Transmission line impedance (Bloch impedance) for an infinite CRLH transmission line.

2.3. Circuit Simulation

A 7-cell lumped circuit network, modeling a CRLH resonator, has been investigated. In order to account for losses mainly related to radiation, conductor losses and dielectric losses, a series resistor $R=1\Omega$ and a shunt conductor $G=1/1\text{M}\Omega$ have been introduced. The symmetrical unit cell model is depicted in Fig. 3. In Fig. 2 the overall configuration of 7 cascaded unit cells to form the open-ended resonator is shown. The circuit has been excited with a 50Ω port at the port position 3 as illustrated in Fig. 2. and the s_{11} -parameter has been simulated. In Tab. 1 the $f_{\pm 1}$ resonance frequencies are listed for the three different inductance values. In Fig. 4 the s_{11} -parameter is plotted for the (a) lower f_{-1} and (b) upper f_{+1} half-wavelength resonance frequency with L_L varying. The input impedance at resonance is related to the TL impedance, so that the input impedance increases with higher Z_{CRLH} values.

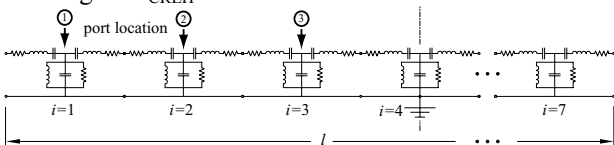


Fig. 2: Lumped circuit model of a 7-cell CRLH open-ended resonator. The symmetrical unit cell with its lumped element parameters of Fig. 3 is cascaded to form the resonator line.

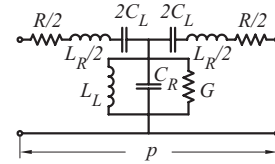
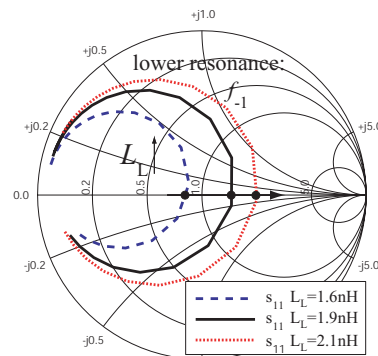


Fig. 3: CRLH unit cell model including losses for the circuit simulation.

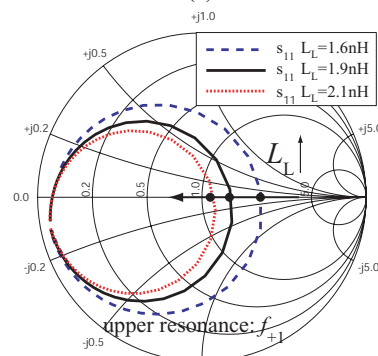
For the balanced case, plotted with solid lines, the input impedance is identical at both frequencies. The reason is the same TL impedance Z_{CRLH} at both resonant frequencies. Three different port locations 1, 2 and 3 (Fig. 2) have been evaluated and plotted in the smith chart. A perfect agreement of the input impedance at the lower resonance f_{-1} and the upper resonance f_{+1} is found. With increasing distance from the center the input impedance enlarges which can be observed in Fig. 4 (c) for the balanced case. Therefore, the concept of the dual-band half wavelength field distribution is totally supported by very simple circuit simulations and a consistent matching strategy to achieve dual-band matching can be proposed.

L_L / nH	f_{-1} / GHz	f_{+1} / GHz	f_{sh} / GHz	f_{se} / GHz
1.6	2.27	3.15	2.81	2.59
1.9	2.18	3.06	2.59	2.59
2.1	2.13	3.02	2.45	2.59

TABLE 1
SIMULATED RESONANCE FREQUENCIES OF THE RESONATOR LINE IN FIG. 2.



(a)



(b)

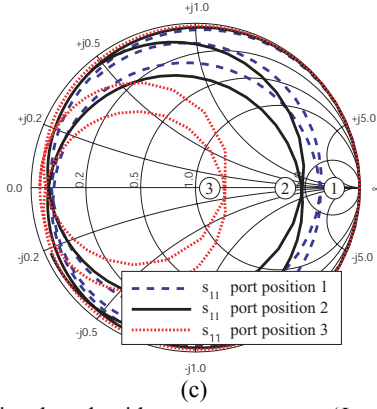


Fig. 4: s_{11} is plotted with two parameters (L_L and the port location) varied. In (a) and (b) the port is located at position 3, while the inductance L_L varied. In (c) the port is shifted to location 2 and 1 with a constant inductance $L_L=1.9\text{nH}$.

3. EM SIMULATION AND MEASUREMENTS

The results from the circuit simulation in 2.3 have been applied to optimize simultaneous matching for a proposed 9-cell resonator antenna. EM simulations with parameter variations corresponding the parameters in the circuit simulation in 2.3 have been performed. In Fig. 5 (a) the prototype of the proposed 9-cell resonator antenna is shown. It is composed of cascaded unit cell of Fig. 5 (b).

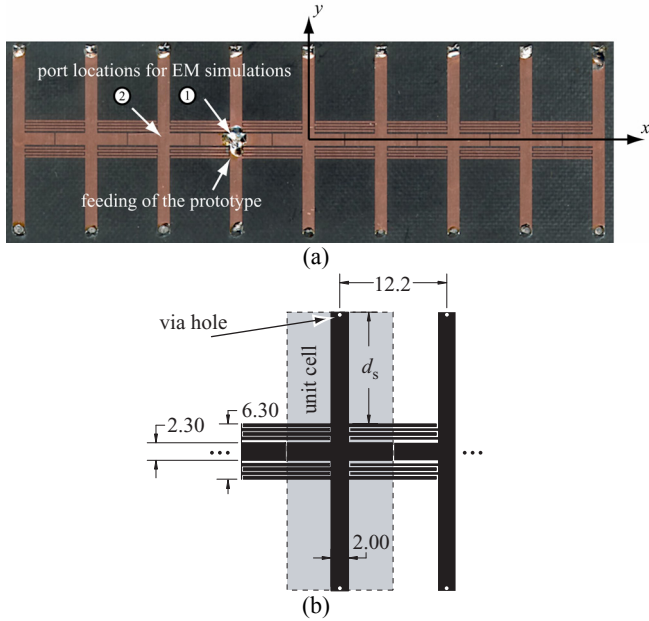


Fig. 5: Picture of the $\lambda/2$ antenna prototype (a). The CRLH unit cell ms metallization layout with its physical dimensions (b). The width of the interdigital fingers is 0.3mm with a gap of 0.2mm between the fingers.

3.1. Matching Optimization

Extensive EM simulations using Ansoft Designer (MoM) have been performed. The model of the prototype shown in Fig. 5 (a) has been simulated with the stub length (Fig. 5 (b)) and the port location varied. The stub length variation d_s has a main effect on the shunt inductance L_L , which can be observed in Tab. 2. In Fig. 6 (a) and (b) s_{11} is plotted for the upper f_{+1} and lower f_{-1} resonance frequency. The real part of the input impedance increases for the lower resonance and

decreases for the upper resonance frequency with longer stubs. For $d_s=12.8\text{mm}$ (solid lines) a simultaneous matching for both frequencies is found. In Fig. 6 (c) it can be observed that a port shift in negative x-direction to the center of the next unit cell (position 2) results in a larger real part of the input impedance for both frequencies. Consequently, the matching strategy is as follows, first find line impedance to have both resonant circles almost congruent and second shift the port along the line to find the desired real input impedance.

d_s / mm	L_L / nH	C_R / pF	f_{-1} / GHz	f_{+1} / GHz
10.8	1.80	2.20	2.32	3.10
12.8	2.20	2.14	2.19	2.99
14.8	2.70	2.03	2.06	2.92

TABLE 2

PARAMETER EXTRACTION FOR THE CRLH UNIT CELL AND SIMULATED RESONANCE FREQUENCIES FOR THE 9-CELL OPEN-ENDED RESONATOR.

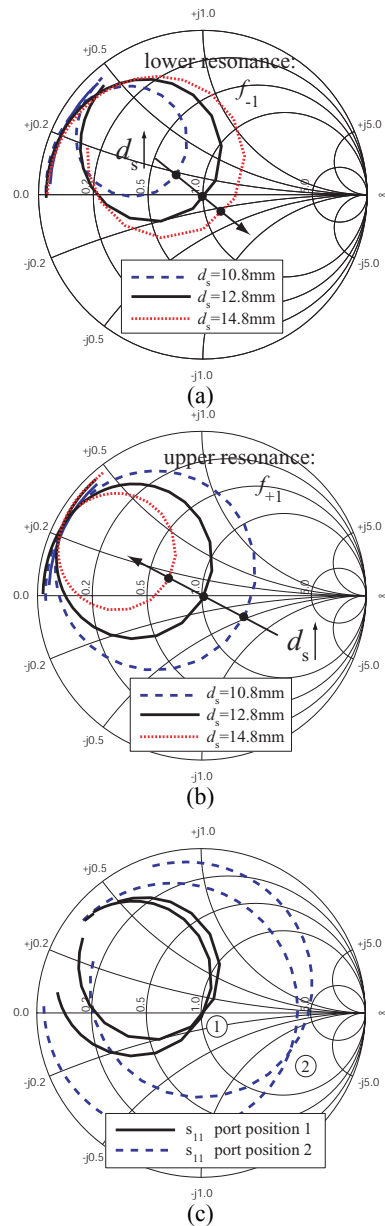


Fig. 6: s_{11} is plotted with two parameters varied. In (a) and (b) the port is located at position 1 while the stub length d_s was varied. In (c) the port is shifted to location 2, with a constant stub length $d_s=12.8\text{mm}$.

3.2 Measurement of the $\lambda/2$ -Resonator Antenna Prototype

The prototype in Fig. 5 (a) was measured and the simulated s_{11} along with the measured s_{11} is plotted in Fig. 7. The measured resonances are shifted by a non-negligible frequency offset to lower frequencies. The reason has to be investigated in detail. Nevertheless, the concept itself is supported by the measurement and the measured resonant frequencies are f_{-1} and f_{+1} . The radiation for the two modes is given in Fig. 8 and is in very good agreement with the simulated radiation. The measured gain is relative and has been normalized to match the maximum simulated gain for each frequency. The cross-polarization was 30dB below the co-polarization level and is not plotted to maintain the shape of the graph. The E-field polarization is in x-direction corresponding to the non compensating current in x-direction on the structure. The aperture size relative to the radiated wavelength for the upper operating frequency is larger even though the same current distribution on the 9-cell antenna is present. This results in a higher directivity for the upper operating frequency.

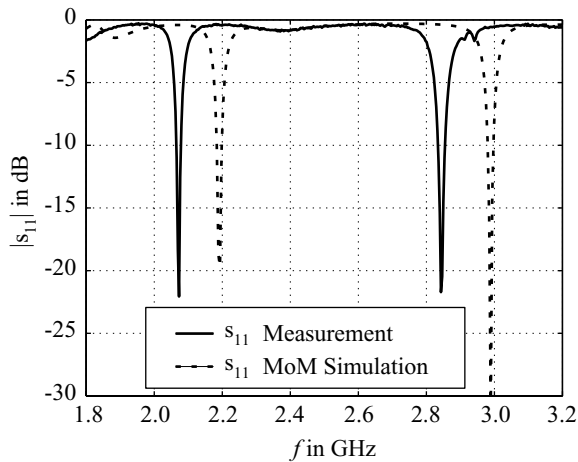


Fig. 7: Comparison of the simulated and measured s_{11} for the EM optimized antenna with the port located at position 1 and $d_s=12.8\text{mm}$.

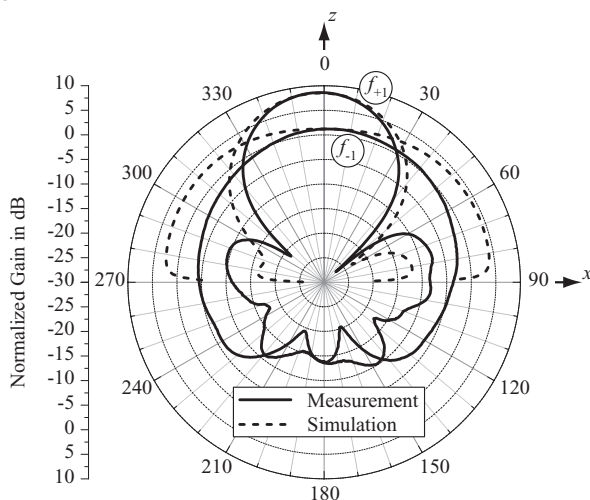


Fig. 8: Measured and simulated far-field co-polarization patterns in the E-plane (x-z) plane for the upper f_{+1} and lower resonance frequency f_{-1} . (The measured data is relative and has been normalized to the maximum simulated gain)

3.3. Simulation model of the $\lambda/4$ resonator antenna

This concept has been directly applied to obtain a $\lambda/4$ dual band resonator antenna (Fig. 9). Here, only the simulated s_{11} is presented and the same resonance behavior as for the $\lambda/2$ antenna has been achieved. An advantage of this proposed resonator is besides the size reduction of 50%, the suppression of undesired modes. The radiation is expected to differ from the initial $\lambda/2$ device. This will be investigated in our further work.

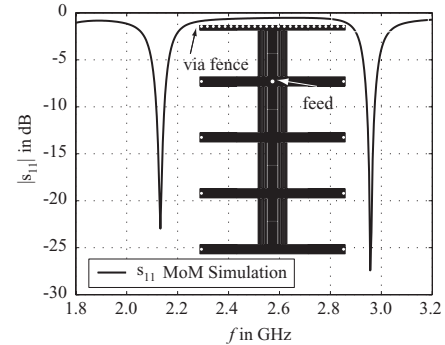


Fig. 9: Simulated s_{11} for the proposed $\lambda/4$ dual frequency resonator antenna displayed in the inset.

4. CONCLUSION AND OUTLOOK

A novel concept of CRLH dual-band antennas has been discussed with the focus on the matching techniques. The main idea here is to exploit the same mode along with the same characteristic impedance on an open-ended resonator line to build dual-band antennas. As far as the matching to the 50 Ohm port impedance was concerned the line impedance was found to be crucial for the matching. Circuit and EM simulations have been performed for a 7-cell/9cell resonator line showing the effect of the line impedance on the input impedance at resonance. The optimized $\lambda/2$ resonator antenna was built and measured. Besides the deviation in the simulated and measured s_{11} (frequency offset) a good agreement of theory and measurement has been observed supporting the conceptual ideas. A new device of a $\lambda/4$ antenna has been proposed and the simulated s_{11} -parameter has been presented. Simulation and measurement of the far-field characteristics will be evaluated in our upcoming work.

REFERENCES

- [1] C. Caloz and T. Itoh, "Novel microwave devices and structures based on the transmission line approach of metamaterials", *IEEE-MTT Int'l Symp.*, vol. 1, pp. 195-198, Philadelphia, PA, June 2003.
- [2] S. Otto, A. Sanada, C. Caloz, and T. Itoh, "A dual-frequency composite right/left-handed half-wavelength resonator antenna", *Asia-Pacific Microwave Conference*, India, December 2004, accepted for presentation.
- [3] A. Sanada, C. Caloz, and T. Itoh, "Novel zeroth-order resonance in composite right/left-handed transmission line resonator," 2003 Asia-Pacific Microwave Conference Proceedings, pp.1588-1591, Nov. 2003.
- [4] Collin, Robert E., "Foundations for Microwave Engineering", 2nd ed. New York: McGraw-Hill, 1992

A Highly Decoupled Dual Antenna Rx/Tx Arrangement Based on LTCC Modules

A. Rennings, M. Vesterling, A. Pimpertz, W. Schroeder¹, M. Leitner², P. Waldow

Duisburg-Essen University, Department of Engineering (ATE), Bismarckstr. 81, D-47048 Duisburg, Germany
Tel: +49-203-379-3183, E-Mail: A.Rennings@ieee.org

¹Siemens Communications, Technology & Innovation, Frankenstr. 2, D-46395 Bocholt, Germany

²EPCOS OHG, Siemensstr. 43, A-8530 Deutschlandsberg, Austria

Abstract — A highly decoupled dual antenna Rx/Tx arrangement based on LTCC chip antennas is presented in this paper. An excellent isolation of more than 25 dB has been measured and is due to the orthogonal field distributions of the dipole and monopole in our setup. Therefore this dual antenna module may be used for polarisation diversity applications. The performance of the antenna test board was simulated using commercial FDTD/FEM tools and validated with measurements on fabricated prototypes.

I. INTRODUCTION

In [1] a Rx/Tx arrangement based on two printed antennas was investigated. A minimal isolation of 14 dB was measured between their ports and is due to the frequency selective behaviour of the dual-band antennas. By using such a pre-filtering of the antennas the requirements on a CDMA duplexer can be reduced. In the present paper LTCC chip antennas on K8 (Table 1) have been used to build a compact, highly decoupled Rx/Tx antenna module. In contrast to the approach in [1], decoupling is achieved here by exploiting the different field symmetries of the two antennas. The general setup is depicted in Fig. 1. The excellent isolation between the two ports is due to the orthogonality of the field distributions of the dipole and monopole. Therefore, this dual antenna module based on LTCC chip antennas may be used in polarisation diversity applications.

Properties of LTCC Modules	Unit	MKE-100
Dielectric strength	kV/mm	>15
Dielectric constant	(1MHz)	7.8
Dissipation factor	(1MHz)	$2 \cdot 10^{-3}$
Volume resistivity	$\Omega \cdot \text{cm}$	$>10^{14}$
Sheet resistance (inner)	$\text{m}\Omega/\square$	Ag:3
Sheet resistance (top)	$\text{m}\Omega/\square$	Ag/Pt:3

TABLE 1
PROPERTIES OF LTCC MODULES

FR-4 substrate has been used for the printed circuit board (PCB). Its size measures 75 x 36 x 1 mm³. The backside metallisation is 20 mm shorter than the substrate as depicted in Fig. 1.

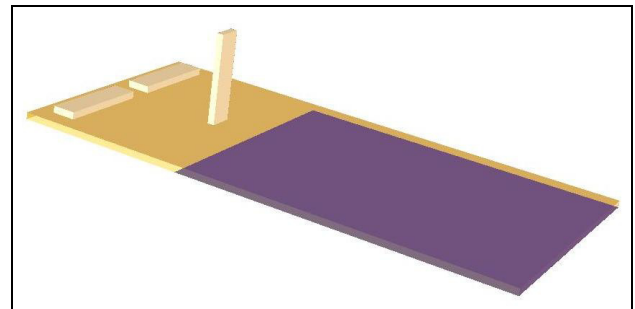


Fig. 1: Setup with dipole and upright mounted monopole

A detailed FDTD model [2] of the used chip antennas shown in Fig. 2 was created by us. It is depicted in Fig. 3. This model has been used for the design of the antenna test board. In the next section some of the design steps of the dipole are mentioned. For lack of space the also interesting design aspects of the upright mounted monopole are skipped.

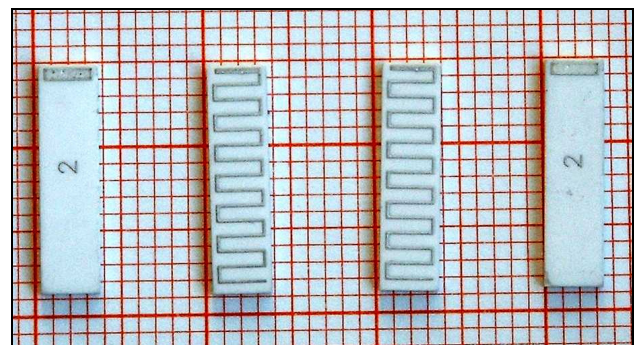


Fig. 2: Used chip antennas on K8 material from EPCOS

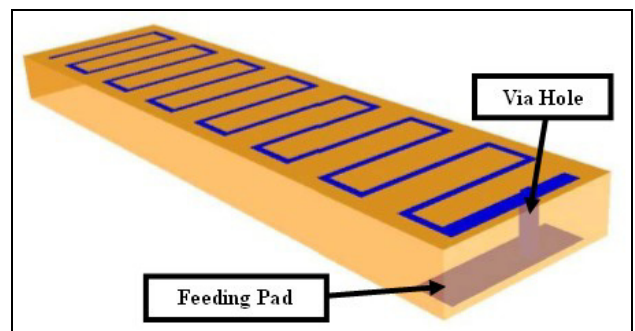


Fig. 3: FDTD model of the chip antennas in Fig. 2

II. DESIGN/MATCHING OF DIPOLE ANTENNA

The dipole antenna is constructed from two LTCC meander-line modules as depicted in Fig. 4. The design process has been started with a lumped port of 100Ω between the two LTCC modules, since the balun we used in the feeding network had a 100Ω balanced output.

One analysis that we carried out is related to the influence of the distance between dipole and ground plane metallisation on return loss. As Fig. 5 indicates, for close distances to the ground plane the matching was not good at all. Since the area of the dual antenna module was limited to $36 \times 20 \text{ mm}^2$ a good matching without additional inductive stubs to compensate the capacitive coupling to the ground plane was not possible.

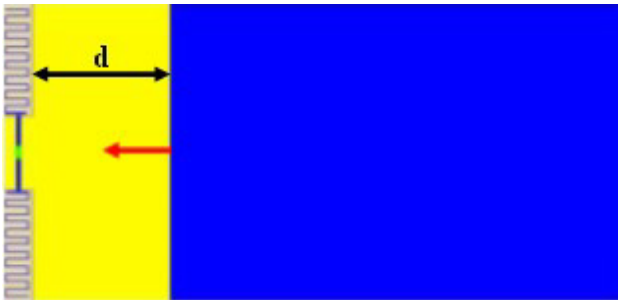


Fig. 4: Dipole formed by two meandered monopoles on K8

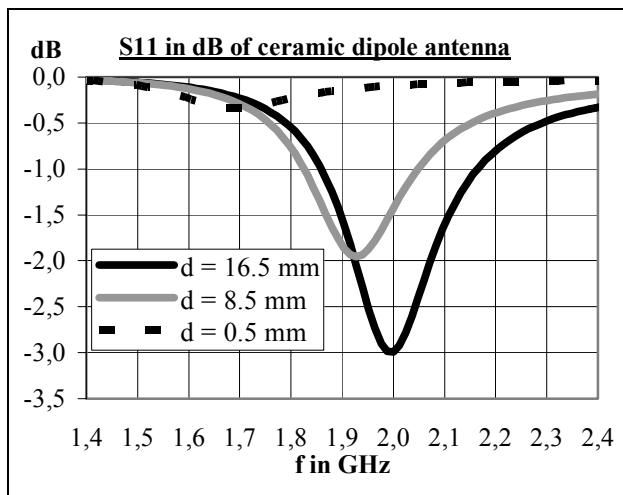


Fig. 5: Return loss while varying distance dipole to ground

With two inductive stubs that are connected to the virtual ground in the symmetry plane of the dipole a good matching was possible. The whole feeding/matching network for the dipole is shown in Fig. 6. The short 100Ω coplanar slotline (CPS) line is connected to the balun. In our simulations we put a balanced 100Ω lumped port at the beginning of the CPS line, since the balun was not part of the simulations. Also in Fig. 6 three geometrical parameters are indicated which have been varied to optimise the feeding/matching of the dipole. Finally a return loss of 25 dB at 2 GHz (without the influence of the balun) was predicted by the simulation.

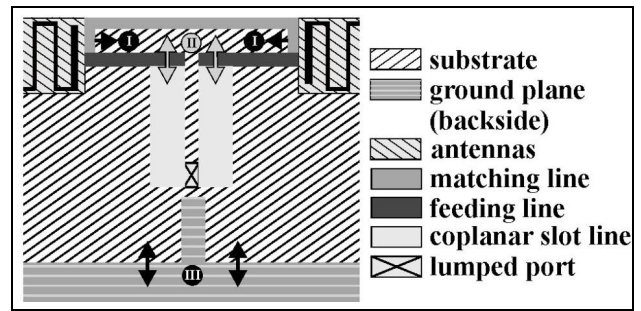


Fig. 6: Feeding/matching network for the dipole antenna

III. FDTD/FEM SIMULATIONS WITH DETAILED MODELS OF THE DUAL ANTENNA ARRANGEMENT

Since the dipole required a balanced feed a balun was needed within the feeding network. The Murata balun LDB20C101A1900 with 50Ω unbalanced input and 100Ω balanced output has been chosen. The pattern (landmark) of the balun depicted in Fig. 7/8 has been included in the simulation models. The full FEM/FDTD model of the two antenna setup including the mentioned balun pattern is shown in Fig. 9. The feeding of the upright mounted monopole is done by the lumped port 1 – the feeding of the dipole by port 2, respectively. The semi rigid cables of the prototype used for feeding are modelled by rectangle PEC tubes within the simulations.

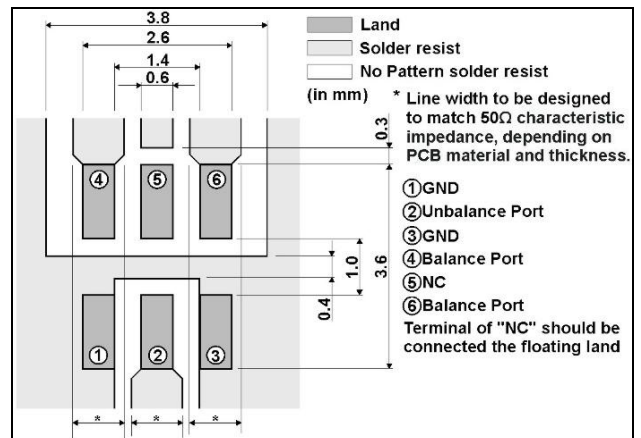


Fig. 7: Pattern of Murata balun LDB20C101A1900

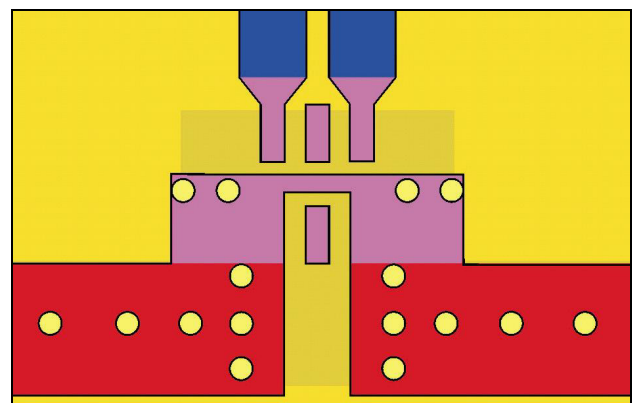


Fig. 8: FDTD model of the balun pattern depicted in Fig. 7

The optimisation of the structure has been done with the FDTD tool EMPIRE™ [2] because of its computational power. The fine-tuning including dielectric and conductor losses has been carried out with the FEM software HFSS™ [3]. Finally, we got the following s-parameters plotted in Fig. 10.

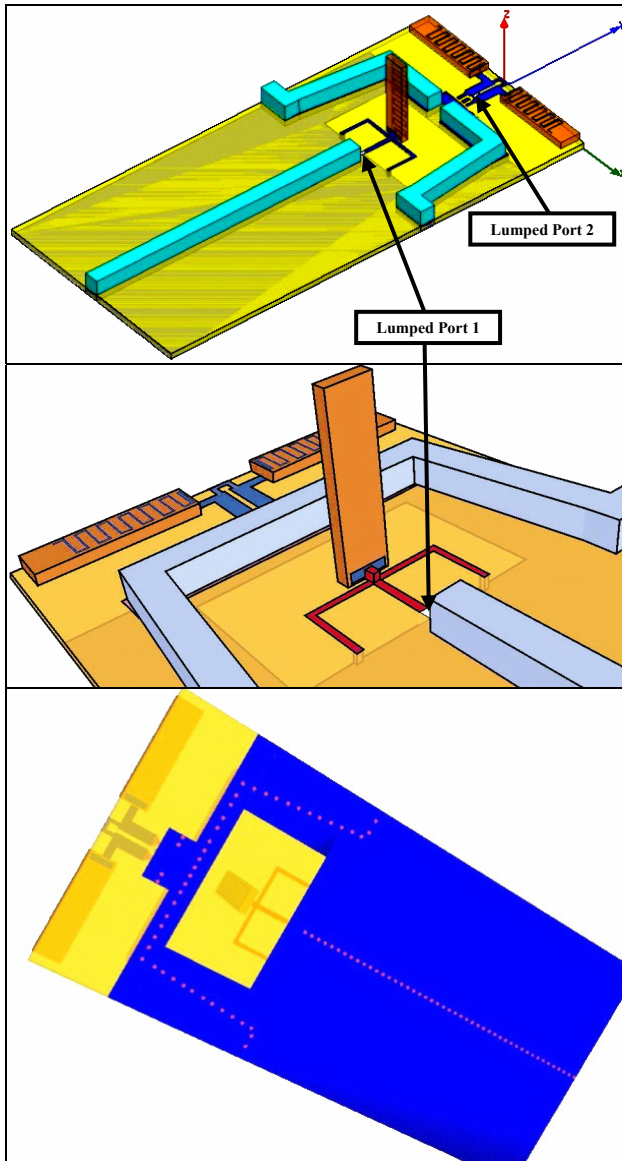


Fig. 9: Detailed FEM model (top) and FDTD model (bottom) of the dual antenna setup

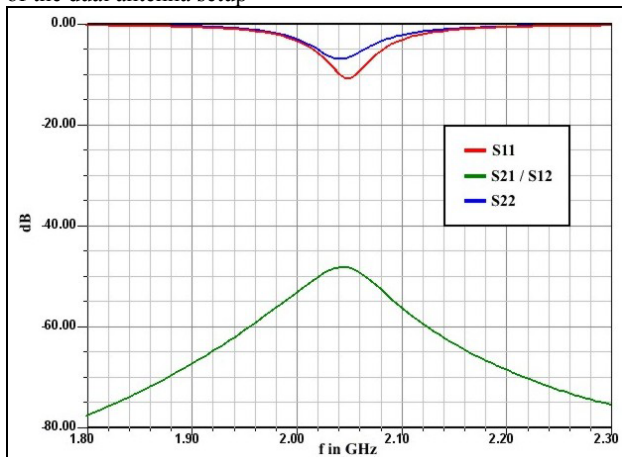


Fig. 10: S-parameter result of the FEM simulation

IV. MEASUREMENT OF PROTOTYPE

A prototype has been built based on the results we got from the simulation series. Two pictures of the antenna test board can be seen in the following figures (Fig. 11/12). The antennas are fed via semi rigid cables that are connected to the monopole and to the unbalanced port of the balun, respectively. The outer conductor of the cable is connected to the backside ground by using vias to prevent unwanted resonances. Additionally, the measurement has been carried out using ferrite beads to suppress resonances on the feed cables. The upright mounted monopole has been fixed with glue to the PCB. The minimal isolation that has been measured with our HP NWA 8722C was 27 dB. The slight deterioration compared to the simulation which predicted an isolation of at least 40 dB may be attributed to deviations from symmetry and imperfectness of the balun. In view of the fact that the two antennas are extremely close to each other, the isolation of 27 dB is considered a good result.

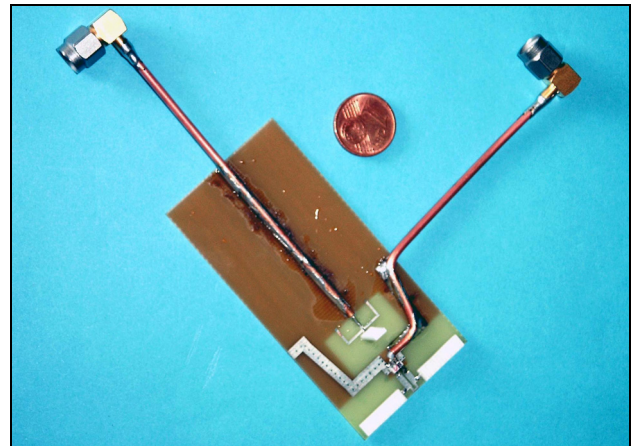


Fig. 11: Prototype of antenna test board (top view)

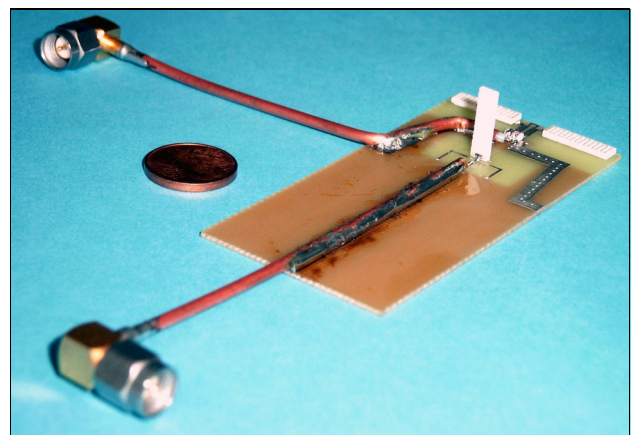


Fig. 12: Prototype of antenna test board (side view)

Since the two antennas radiate at the same frequency, the isolation is exclusively based on field orthogonality and not on some frequency selective effect. The return loss of the two antennas was around 10 dB at slightly below 2 GHz. The whole set of measured s-parameters is plotted in Fig. 13.

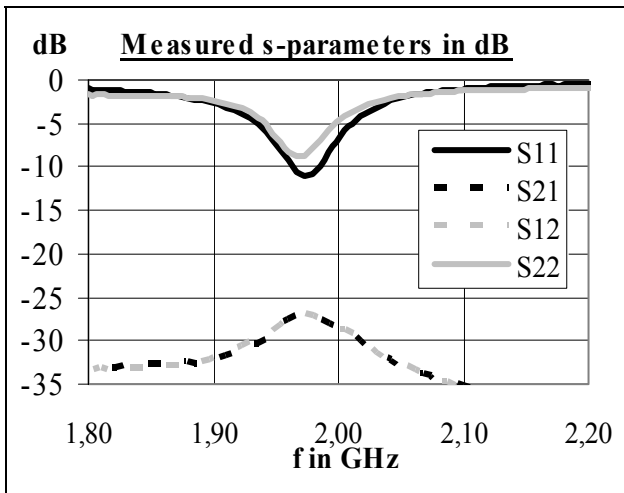


Fig. 13: Measured s-parameters of test board in Fig. 12

V. FINAL TUNING

Since the measured return loss of the two antennas (especially for the dipole) was not that good (around 10 dB), we did some final tuning. The matching lines of the feeding/matching networks of the antennas have been tuned one more time. Again, we will only show the results for the dipole (Fig. 6). In Fig. 14 one can see, that a better matching is possible. The whole s-parameter set of the improved structure is displayed in Fig. 15.

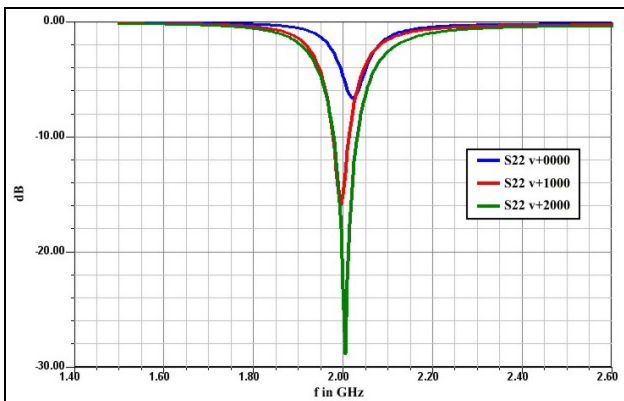


Fig. 14: Matching improvement of dipole antenna

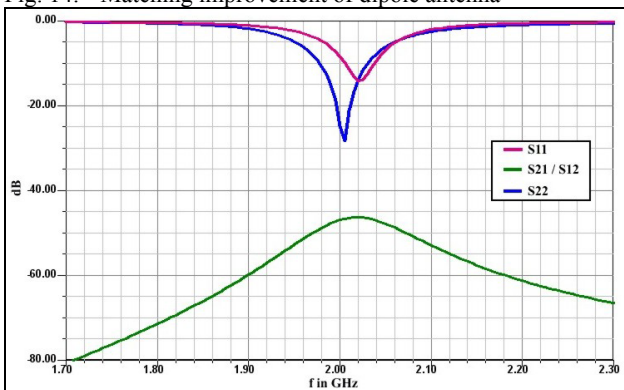


Fig. 15: S-parameters of test board with improved matching

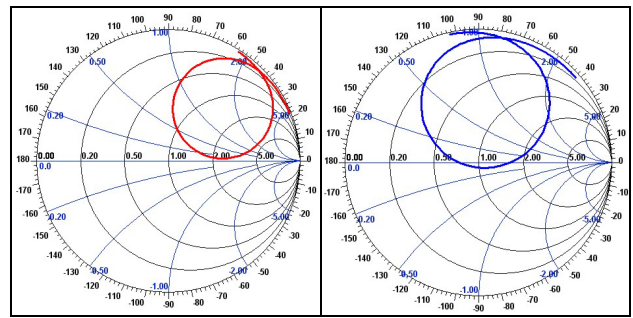


Fig. 16: Return loss behavior for the monopole (left) and for the dipole (right) displayed in Smith chart

The improved return loss performance of the two antennas within the Smith chart is plotted in the Fig. 16.

VI. CONCLUSION

After the isolation principle in [1] that was based on the frequency selective behavior of two printed antennas, here we introduced a highly decoupled dual antenna arrangement that is based on field orthogonality. A measured isolation better than 25 dB has been achieved. The future work in this area will focus on analyses of radiation characteristics and efficiencies of the dual antenna solutions based on LTCC chip antennas. Subsequently, the arrangement will be used as a polarization diversity antenna system for a PCMCIA card for notebook computers. Furthermore, use of a shorter version of the upright mounted LTCC module in K20 material with an relative permittivity of 19.2 will be investigated to arrive at an overall low profile solution.

REFERENCES

- [1] A. Rennings, M. Rauf, P. Waldow, I. Wolff, "A dual-layer printed antenna system for DCS/PCS/UMTS," *Proceedings of 2004 European Microwave Conference*, Amsterdam, The Netherlands, pages 1249 - 1252, October 11 - 15, 2004.
- [2] IMST GmbH, "User manual for the 3D EM time domain simulator Empire", www.empire.de, Jan. 2004.
- [3] Ansoft, "User manual for HFSS", www.ansoft.de

Very Broadband Radiating Element

Eugen Arnold, Ingo Walter

EADS Deutschland GmbH, Woerthstrasse 85, 89077 Ulm /Germany,
e-mail: eugen.arnold@eads.com

Abstract — An antenna is presented with an impedance bandwidth ratio which exceeds 3:1. The dimensions of the base of the antenna are $0.22*\lambda_{low}$ x $0.24*\lambda_{low}$, the antenna height is $0.12*\lambda_{low}$, where λ_{low} denotes the wavelength belonging to the lower frequency limit. The antenna looks similar to a patch antenna. Actually it is an open TEM waveguide whose aperture is shunted by inductors. The lumped elements have only slide inductance. The antenna can be mounted on a metallic plane

I. INTRODUCTION

For future applications small antennas with large bandwidth are required. Bandwidth ratios of 3:1 or 5:1 are desirable, with the bandwidth ratio being defined as the ratio between the upper frequency limit and the lower frequency limit. These antennas can be used for simultaneous reception of signals over large frequency bands, simultaneous transmission of signals of several transmitters or for increased interception security by frequency hopping.

Antennas with very small dimensions compared to the wavelength of the lower frequency limit are well known. Examples are spiral or sinuous antennas, but due to their efficiency of less than 50% they are not suitable as transmit antennas. On the other hand broadband antennas with good efficiency are usually not small. A well known example for a very broadband antenna is the open TEM waveguide – however this antenna is rather large.

In this article an antenna is introduced which is small with a very simple construction. The antenna uses no dielectric or ferrite material.

II. THE ANTENNA AND ITS DEVELOPMENT

Starting point of the development was the open TEM waveguide over a perfect electrically conducting (pec) ground-plane. The aim was to change the design in that way, that the lower frequency limit is shifted down as far as possible. By using inductors, which were connected between the TEM waveguide and the ground-plane, this aim could be achieved successfully. The necessary inductances of the inductors are very low. They can be realized by using a low number of windings of thin wire or by printing them on a substrate. Fig. 1 shows a typical antenna and Fig. 2 shows the VSWR of the antenna as a function of frequency. The antenna was designed for the UHF-Band with a lower frequency limit of 250 MHz. It is trivial that the antenna can be scaled with frequency.

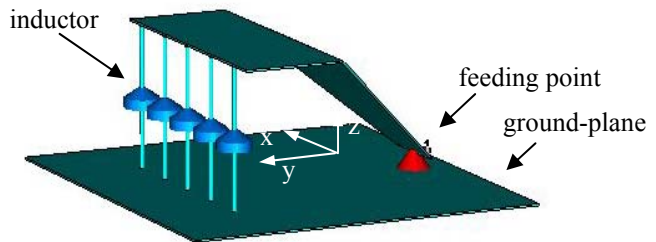


Fig. 1: View to a typical antenna under discussion.

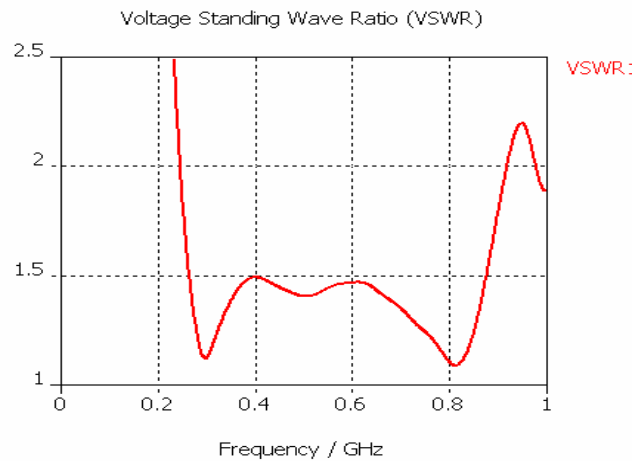


Fig. 2: VSWR of the antenna of Fig. 1.

Beside the VSWR property, the radiation pattern as a function of frequency is a very important property. The radiation patterns are shown in Fig. 5 to Fig. 7.

The dimensions of the antenna are

height	$0.12*\lambda_{low}$,
length (feed to aperture)	$0.22*\lambda_{low}$,
width at the aperture	$0.24*\lambda_{low}$.

In the case of a lower frequency limit of 250 MHz, λ_{low} is 1.2 m, the antenna height is 14.3 cm, the length (from feed to aperture) is 26.7 cm and the width is 29 cm.

The large bandwidth together with the small size of the antenna are astonishing. We can not give a valid physical explanation of this property, even not with the transmission line model shown in Fig. 3. Nevertheless we use this model, because the transmission line model makes the explanation of the antenna construction easier.

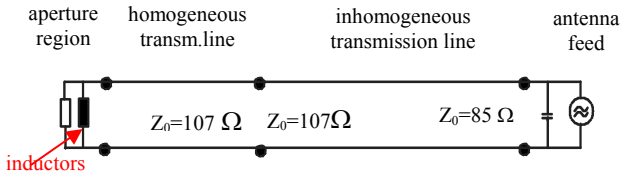


Fig. 3: Transmission line circuit diagram of the antenna.

In Fig. 3 the open TEM waveguide is represented by the transmission line parts of the model. We start at the aperture of the antenna, which is located on the left side of Fig. 3 and move step by step to the feeding point at the right side. The two resistors at the left side, which shunt the transmission line, represent the complex radiation resistance of the aperture and the inductance of the inductors. The adjacent section describes that piece of the TEM waveguide, where its width and its height are constant. This part is represented by the homogeneous transmission line section. Next to the right follows the raising part of the TEM waveguide. That part is represented by the inhomogeneous transmission line section. The characteristic impedance of this line at the aperture side is about 107Ω and at the right side 85Ω . At the right side of Fig. 3 is the feed of the antenna. For fine tuning of the antenna matching a small capacitance is shunted at the feed point. The impedance of the feed point should be 50Ω .

As mentioned above the transmission line model of Fig. 3 cannot describe this good matching shown in Fig. 2. Probably the transmission line model lacks the fact, that only the TEM waveguide mode is taken into consideration. It is trivial that the TEM waveguide carries several modes. A better theoretical model with more modes was not created, because models with more than one mode are rarely synoptic.

To show the effect of the inductors connected to the aperture, we first show the radiation resistance of the aperture with these elements disconnected. Fig. 4a shows the model: A waveguide port feeds a small piece of the TEM-waveguide. Fig. 4b shows the complex radiation resistance plotted into the Smith chart. The reference plane is the aperture. Please notice, that the reference impedance of the diagram is $Z_0=120 \Omega$. The radiation resistance looks very inconvenient. At the lower frequency limit its value is $(107.3-j181.4) \Omega$.

Considering the Smith chart in Fig. 4b the first idea is to improve the impedance of the radiating aperture by an inductor which is connected in series to the aperture. But because no current flows at the open end of the TEM waveguide, the inductive resistor would not be effective. The second idea is, to connect an inductive resistor shunt to the aperture. Fig. 4c shows this result using the set of inductive resistors which lead to the result shown in Fig. 2. The curve of Fig. 4c looks much more convenient than the curve of Fig. 3. Especially at the lower frequencies matching of the antenna feed to 50Ω seems to be possible.

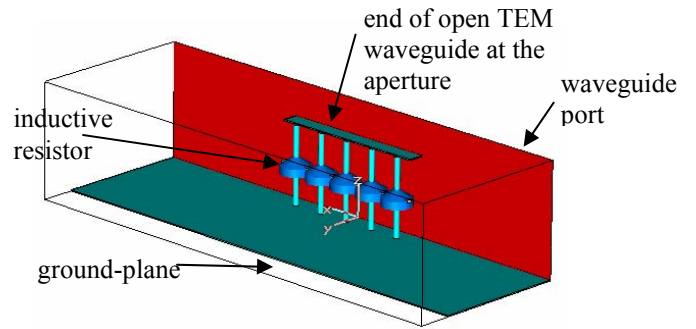


Fig. 4a: Model with 5 inductors for calculation of the complex resistance of the aperture (Fig. 4).

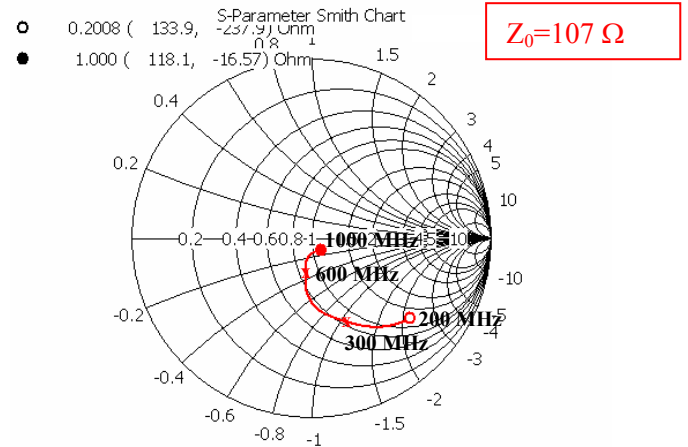


Fig. 4b: Smith Chart showing the complex resistor of the aperture (inductors disconnected), $Z_0=107.3 \Omega$.

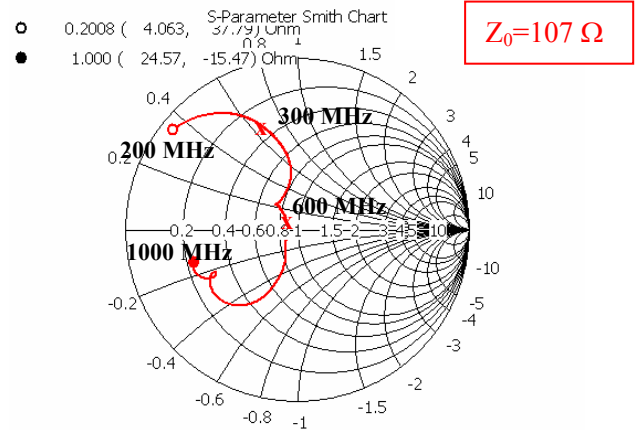


Fig. 4c: Smith Chart showing the complex resistor of the aperture (inductors connected), $Z_0=107.3 \Omega$.

III. INDUCTORS

The inductors are important parts of the antenna. They have different inductances. For frequencies at the lower frequency limit of the antenna, their inductive reactance are as following.

- centre inductor $j 52.0 \Omega$,
- inductors adjacent $j 94.5 \Omega$
- and for the outer inductors $j105.0 \Omega$.

In case of a lower frequency limit at 250 MHz

the centre inductor must have 34 nH,
 each of the 2 adjacent inductors must have 60 nH
 and the 2 outer inductors must have 67 nH.

Calculations showed that 1 winding with radius of 11 mm has an inductance of about 40 nH. Therefore no difficulties are expected using these inductors.

IV. RADIATION PATTERNS

The antenna does not belong to the class of so called frequency independent antennas. Therefore the current distribution on the antenna changes as a function of frequency. Because of the large frequency range we have to expect, that the radiation pattern changes also as a function of frequency. Fig. 5 to Fig. 7 show the function of directivity at frequencies of 250 MHz, 450 MHz and 650 MHz. Beside a 3D-diagram, the diagrams for one cut in elevation and for the 2 main cuts in azimuth are shown. For the definition of elevation and azimuth refer to the coordinate system within Fig. 1. The x-axis points to $az=0^\circ$, the y-axis to $az=90^\circ$ and $el=0^\circ$ is the xy-plane.

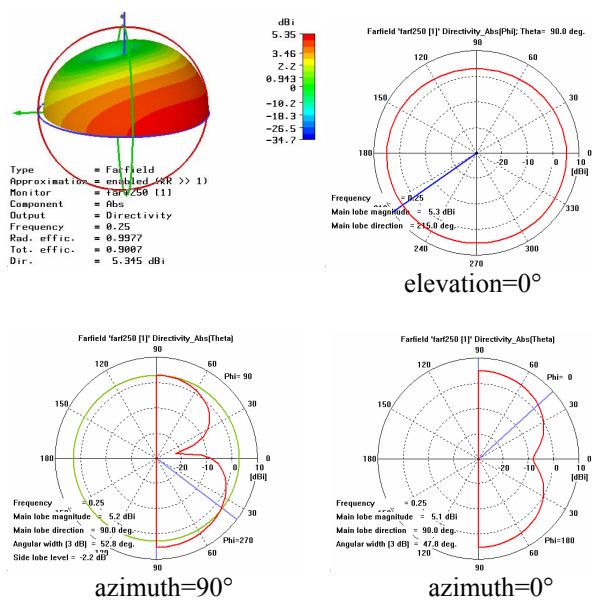


Fig. 5: Farfield pattern (directivity) of the antenna at 250 MHz.

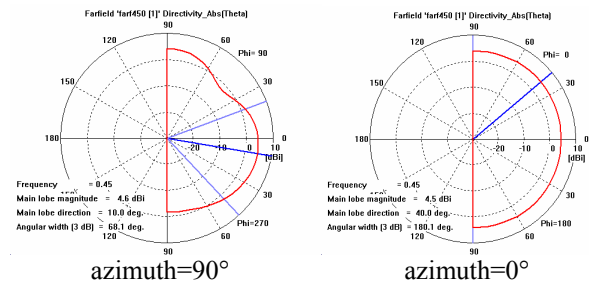
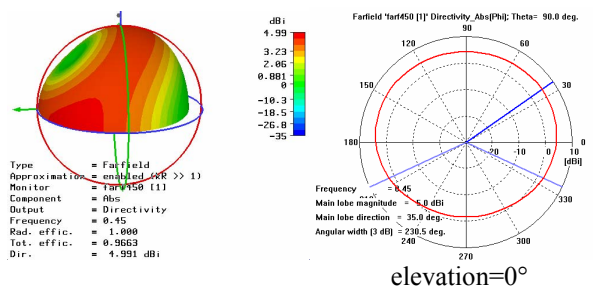


Fig. 6: Farfield pattern (directivity) of the antenna at 450 MHz.

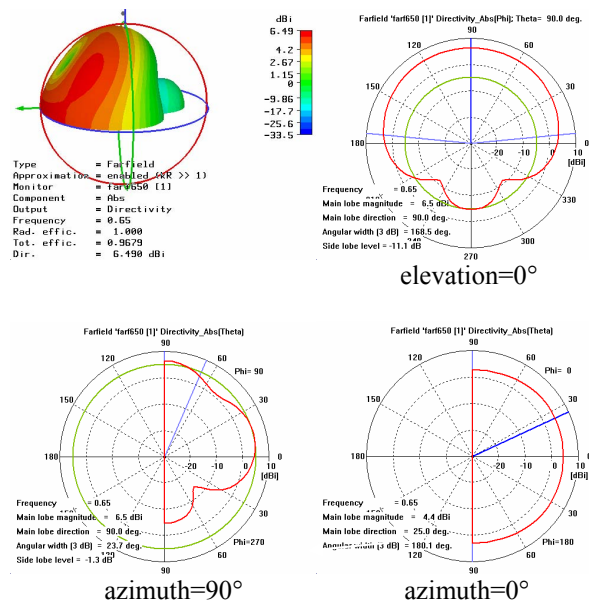


Fig. 7: Farfield pattern (directivity) of the antenna at 650 MHz..

At 250 MHz the pattern looks similar to the pattern of a monopole above a pec-ground-plane (see Fig. 5). If the frequency approaches 450 MHz the zero of the monopole diminishes and the pattern looks similar to the pattern of a patch antenna (see Fig. 6). At frequencies above 550 MHz the pattern changes slightly to the pattern of an open TEM waveguide. For all frequencies up to 1000 MHz the pattern is very broad and covers a large part of the hemisphere surrounding the antenna.

III. A VARIATION OF THE ANTENNA

It is sometimes desirable to have an antenna with a radiation pattern which changes only slightly with frequency over a large frequency range. For this purpose the antenna shown in Fig. 8 has been designed.

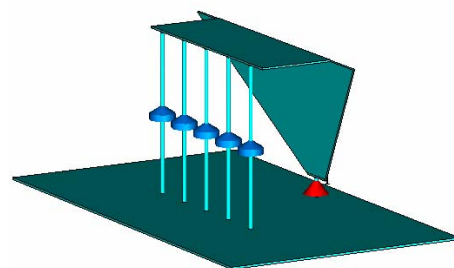


Fig. 8: Variation of the antenna of Fig. 1.

The dimensions of this antenna are
 height $0.123 * \lambda_{low}$,
 length (feed to aperture) $0.094 * \lambda_{low}$,
 width at the aperture $0.230 * \lambda_{low}$.

The antenna in Fig. 8 is still smaller than the antenna in Fig. 1. Nearly the same inductors are used. But the impedance of the feed point is 100Ω instead of 50Ω . Fig. 9 shows the function of the VSWR. It looks as good as that of the 1st antenna, actually the impedance bandwidth is still larger.

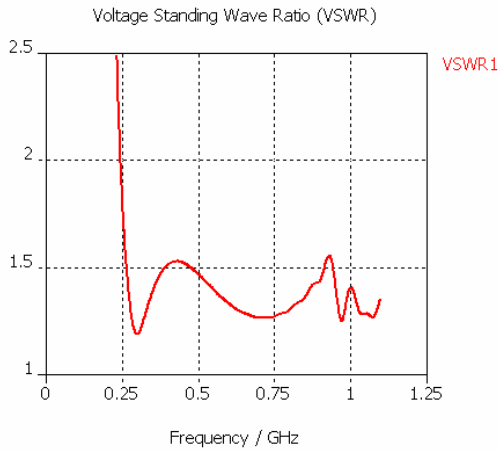


Fig. 9: VSWR of the antenna of Fig. 8.

Fig. 10, Fig. 11 and Fig. 12 show the radiation patterns for frequencies of 250 MHz, 500 MHz and 800 MHz.

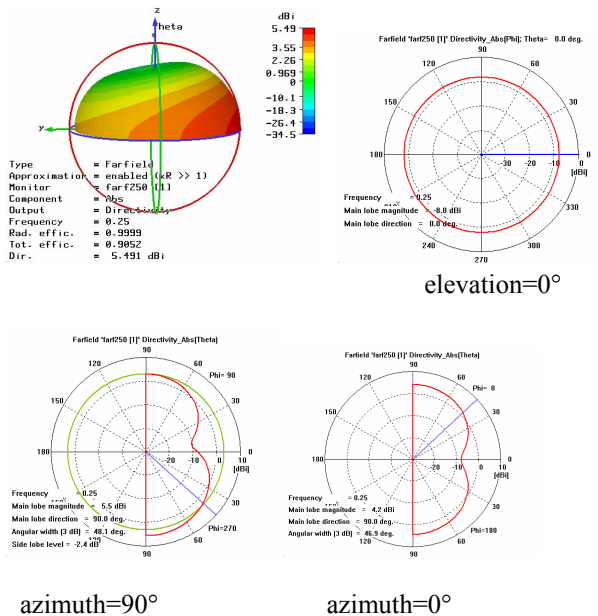


Fig. 10: Farfield pattern (directivity) of the antenna of Fig. 8 at 250 MHz.

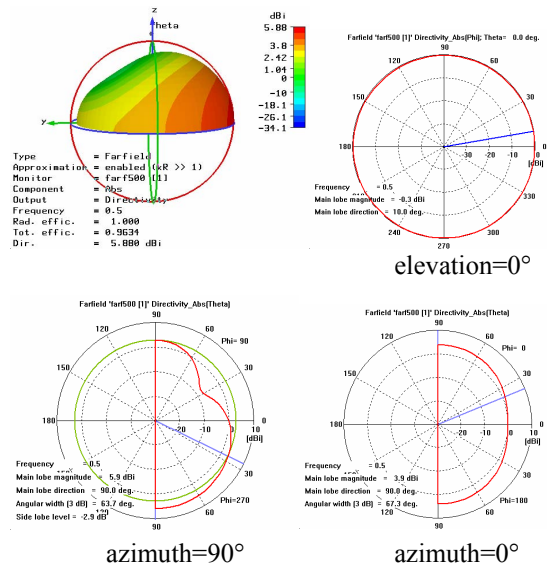


Fig. 11: Farfield pattern (directivity) of the antenna at 500 MHz

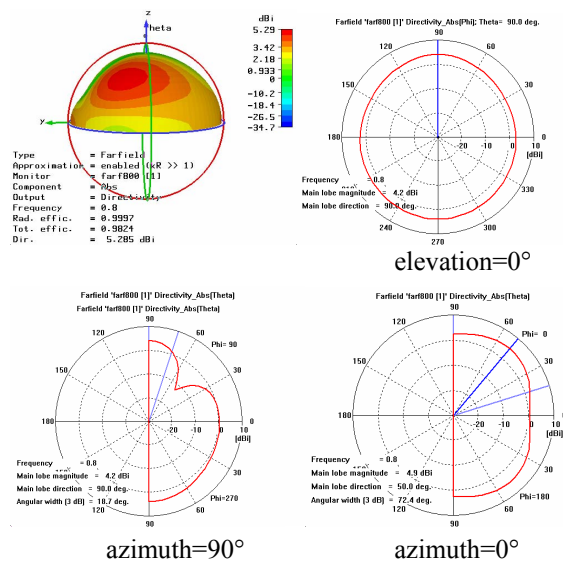


Fig. 12: Farfield pattern (directivity) of the antenna at 800 MHz

The farfield patterns show for all frequencies very good coverage in the elevation=0° plane. The diagrams look similar to the diagram of a monopole.

Focusing Element Aberration Reduction Procedure: Application to Spherical Metal Plate Lenses

E. Jehamy, G. Landrac, M. M. Ney

Laboratory of Electronics and Systems for Telecommunications (LEST, CNRS)
ENST-Bretagne/University of Western Brittany
CS 83818, 29238 Brest Cedex 3, FRANCE, Tel: 0033 2 29 00 13 09

Abstract — A general procedure to reduce aberrations produced by a focusing element of high-gain antenna is presented. The objective is to design such element with minimum phase errors (aberrations) to reduce side lobe level, for relatively large beam tilt angles. The procedure is described in details in the case of a metal-plate lens antenna (constrained lens) with narrow and wide field of view with spherical shapes. The application is intended for automotive radar antenna operating at 76 GHz, in short range operation with relatively wide angle of view. Numerical simulations show that maximum side-lobe level below -18 dB can be obtained by a design based on Geometric Optics (GO) and an optimization procedure using a full-wave model [1] to characterize the source near-field patterns.

I. INTRODUCTION

Third generation of Automatic Cruise Control (ACC) radars, operating at 76-77 GHz have requirements such as compactness, high gain antenna (25-30 dB). It should ensure both a long-range detection within $\pm 7^\circ$ in the main axis and a short-range detection that requires a $\pm 15^\circ$ angle tilt. In addition, side lobe levels should typically be below -20 dB to avoid false detections in any operating detection. Both phase error (aberration) and feeder illuminations are major contributions to increasing side lobe levels. Consequently, optimization procedures should be considered (see for instance [2]). The structure under investigation is a metal plate lens antenna that provides a good trade-off between compactness, low-cost process and performances. It includes parallel metal plates illuminated by a primary source (feeder) whose electric field must be along the z-axis (Fig. 1). The equivalent local refraction index is less than unity to produce a focusing system. The plates are separated by a foam substrate of constant thickness, which was found to have an optimum value $h = 2.4$ mm to minimize ohmic losses and insure TE_1 mode operation between plates [3]. In this paper, some investigation on metal plate lenses with spherical profiles is presented with the objective to minimize aberration effects.

II. ABERRATIONS REDUCTION PROCEDURE

The radius of curvature of the two lens surfaces, is calculated from the basic optic principle:

$$\frac{1}{F} = |n - 1| \left(\frac{1}{R_1} - \frac{1}{R_2} \right) \quad (1)$$

where the geometrical parameters are shown in Fig. 2 and n is the lens refractive index. Once the profiles and the focal distance ($f = 45$ mm) are specified, preliminary simulations determine the far fields at the output of the lens for both short and long-range operations.

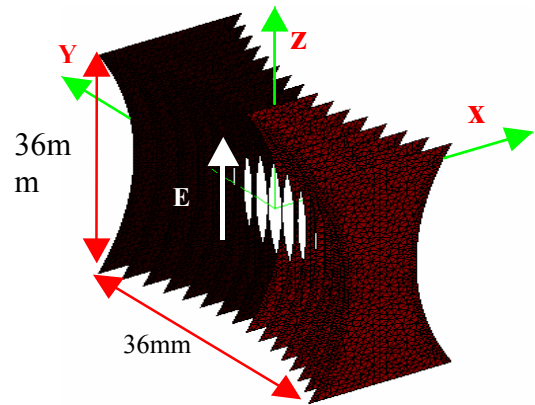


Fig. 1. Metal plate lens.

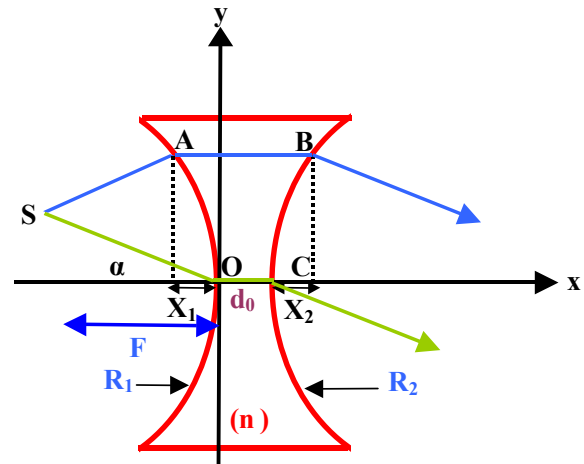


Fig. 2. Ray paths of an offset source.

To reduce the above effects, some optimisation on the lens geometry is performed by choosing the best radius of curvature while maintaining the other lens parameters. To evaluate aberrations, let us calculate the phase change as a function of the radius of curvature, the focal distance, and the index of the medium (Fig.2):

$$\delta = \frac{f}{\cos\alpha} - \sqrt{(f+x_1)^2 + (f \tan\alpha + y)^2} - n_0(x_2 - x_1) + x_2 \cos\alpha + y \sin\alpha \quad (2)$$

where n_0 is the index of the medium, f the focal distance, x_1 and x_2 the inner and outer sphere equations,

respectively, and α the tilt angle. Then, a Taylor development of (2) is performed, yielding:

$$T(\delta) = A y^2 + B y^4 + C y^6 + D \alpha y^3 + E \alpha^3 y^3 + F \alpha y^5 + G \alpha^2 y^2 + H \alpha^2 y^4 + I \alpha^4 y^2 + J \alpha y + K \alpha^3 y \quad (3)$$

in which orders above 6 have been neglected. One can identify in (3) the terms below by their coefficients:

- 1) A, B, C: Spherical aberration (independent on α) that produces deeper zero radiation levels and a broader main lobe.
- 2) D, E, F: Cubic aberration (called also "coma") that introduces a radiation pattern dissymmetry, an increase of the side lobe level on one side only and, finally produces a gain reduction.
- 3) G, H, I: Astigmatism and field curvature producing the same effects as the spherical aberration.
- 4) j, K: Distortion factor (free of aberration) that provokes a tilt of the main lobe.

The above coefficients are aberration coefficients that depends on structure parameters. Note that spherical aberration exists even when $\alpha = 0^\circ$. Thus, it is the only aberration on the optical axis involved in long range operation. Other terms will have effects when the primary source is out of the optical axis. First of all, let us study the aberration behaviour with lens geometrical parameters for $n_0 = 0.569$, a distance of 2.4mm between metal plates, with an outer radius $R_2 = 40\text{mm}$ and $f = 40\text{mm}$.

Figure 3 shows that the spherical (fig. 3a) and the cubic (fig. 3c) aberrations can be minimized with a radius of curvature R_1 around 40mm. On the other hand, one can note that the quadratic aberration requires a radius R_1 of 22mm to be reduced but is negligible as compared to other aberrations (see fig. 3b). Finally, a radius R_1 between 38 to 42 mm with a minimum of coma and spherical phase errors is chosen. The variations of those errors compared to the variable $y(\text{mm})$, show that the paraxial rays give less aberrations than the marginal ones.

III. SELECTION OF THE PRIMARY SOURCE POSITION

After determining the structure parameters, an optimisation of the feeder is performed to further reduce the spherical aberration. The first step is to determine the optimal position of the primary source. To achieve this, the lens is excited with a plane wave and the distribution of the fields around the main axis (optical axis) is computed. One can observe on fig. 4a a focal spot implying some energy concentration while it is more spread out around the main axis on figs. 4b and 4c. It means that, as expected, (1) is no more valid for the optimal choice of the focal distance.

From the field distributions above, one can conclude that we don't have a concentration around a point but, due to the spherical aberration, one has a zone of concentrated energy. To have the best choice for the primary source location, one has to detect the E field maximum magnitude on the optical axis (fig. 5b). This position corresponds to the circle of least confusion (fig. 5a). Preliminary simulations showed that for feeder

positions between 40 and 42mm, the coma's effect is reduced. Assuming that the optimal focal distance will lie within the above range, further full-wave simulations are carried out to evaluate the behavior of other sources of aberrations over that range.

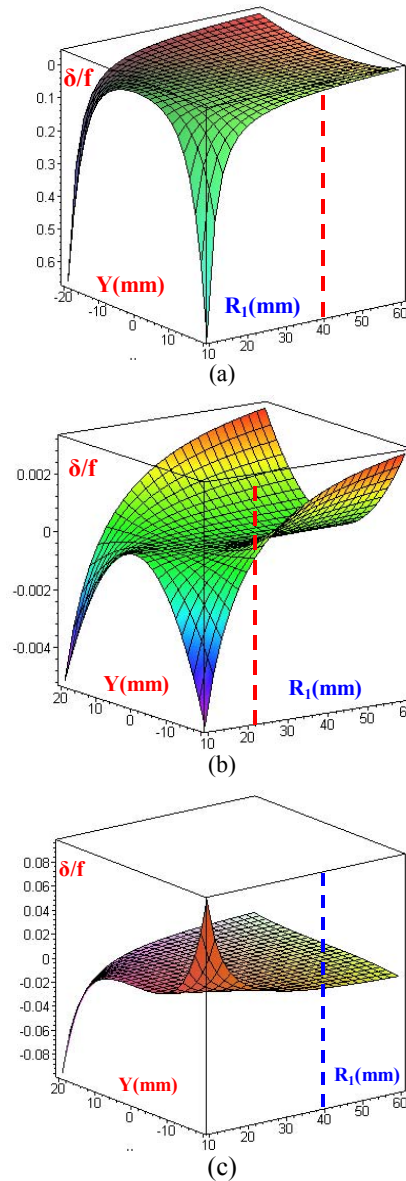


Fig. 3. Aberration behavior: (a) Spherical. (b) Quadratic. (c) Cubic.

IV. FEEDER OPTIMIZATION

After the selection of the optimal feeder position, one has to find the optimal dimensions of the pyramidal horn that is used for primary source (feeder). According to Robieux's theorem [5] illustrated in fig.6, global efficiency (excluding metallic and mismatch losses) of an antenna with a focusing system can be calculated as the coupling factor η between electromagnetic fields (E_2, H_2), radiated by the primary feed located at the focal plane of the lens, and electromagnetic fields (E_1, H_1) issued from an incident plane wave crossing this lens:

$$\eta = \frac{\left| \int_S (\vec{E}_1 \wedge \vec{H}_2 - \vec{E}_2 \wedge \vec{H}_1) \cdot \vec{n} \, dS \right|^2}{16 P_1 P_2} \quad (4)$$

where P_1 et P_2 correspond to the flow of power radiated by the horn across its aperture and the power in the focal plane S of the lens, respectively. Equation (4) mathematically verifies that the efficiency is maximum when the electric and magnetic fields have complex conjugate values. Thus, optimal solution is found when fields in the aperture match perfectly to that in the focal plane of the lens (same amplitude, opposite phase).

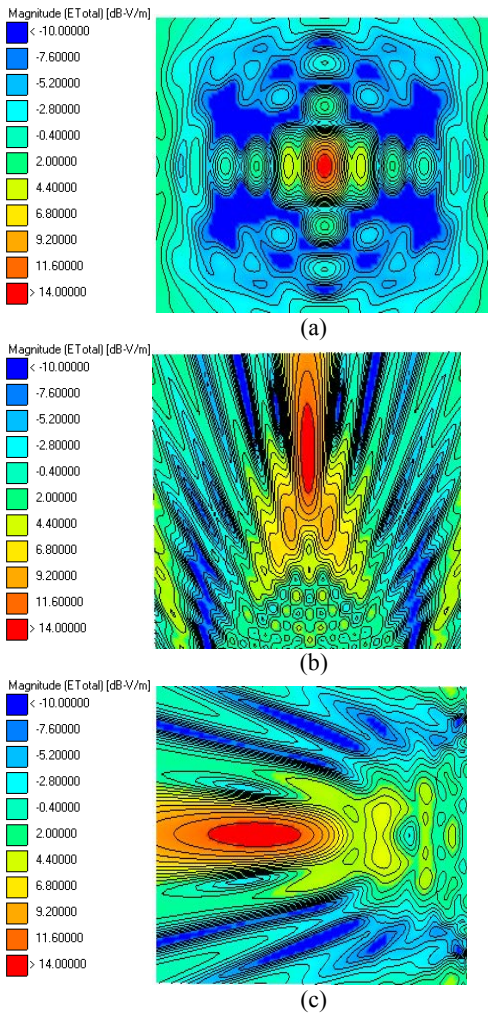


Fig. 4. E-field distribution ($f = 46,5$ mm): (a) Y-z plane. (b) X-y plane. (c) X-z plane.

To enforce those conditions, one has to study first the power distribution in the focal plan (fig. 7). Then, one chooses the zone where 80% of the energy is concentrated to have an idea about the horn aperture dimensions. Both, the amplitude and phase of the E and the H fields in this zone are used to apply matching conditions stated by Robieux's theorem. This is done by carrying out a parametric study on pyramidal horn dimensions (a, b, L in fig.8).

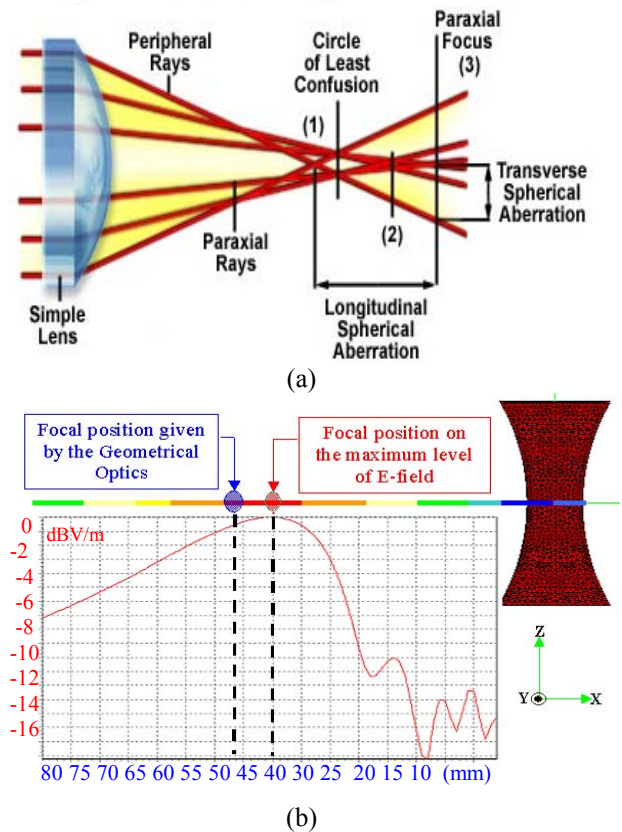


Fig. 5. Illustration of the feeder optimal position: (a) Spherical aberration distribution [4]. (b) E-field magnitude along the optical axis (Ox).

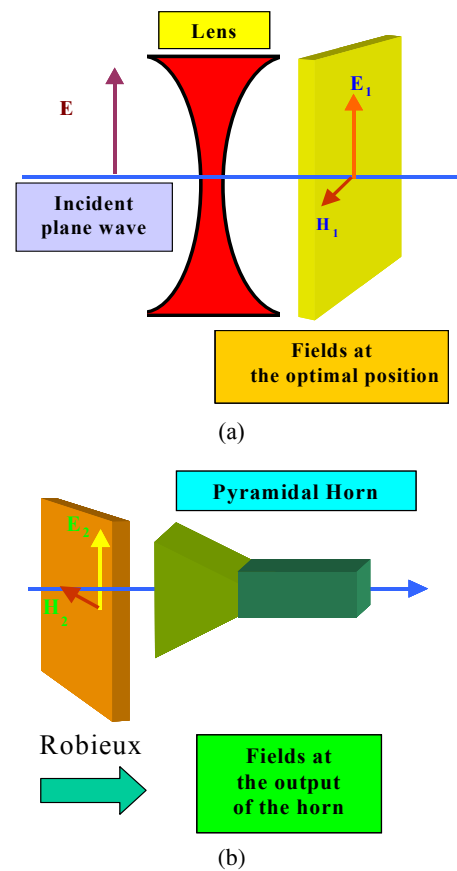


Fig. 6. Illustration of Robieux' theorem: (a) Location of the plane of maximum energy. (b) Complex conjugate feed.
Fig. 7. Power distribution in the focal plane.

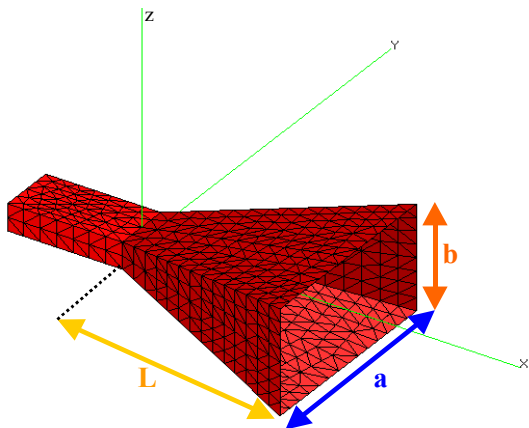
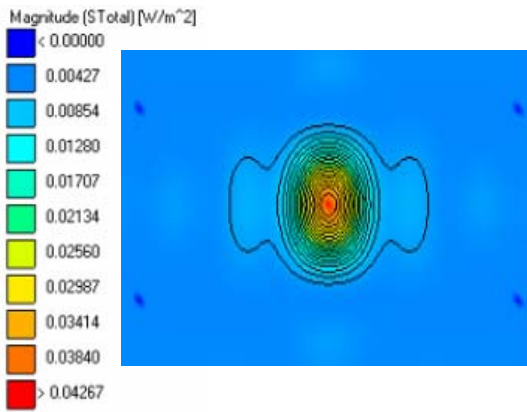


Fig.8. Pyramidal horn dimensions.

V. RESULTS

After the parametric study of the horn, one obtained a lens with a 64% of efficiency, against 52% for a classic lens without optimisation. The rejection of the side lobes is around 22dB in both E and H planes, for the feeding horn at 0° (long range operation). For short-range operation, the position of the horn was modified to obtain

various beam angles (fig. 9). The optimisation procedure yields an average of 18dB of side lobe rejection in the H-plane.

VI. CONCLUSION

An efficient method to reduce aberrations involved in antenna with focusing element designed with classical optics was presented. It is based on lens spherical shape corrections to minimize the deviation function related to ray theory. Then, a full-wave approach was used to determine the optimal position of the feeder and to apply Robieux's principle to obtain maximum matching between the feeder and the lens. The procedure, although general, was applied to a metal plate lens fed by a pyramidal horn for potential application to an ACC radar antenna at 76 GHz. Results show some substantial improvement as compared to non optimised structures. Current work concerns other lens shape optimisation, physical implementation and measurements.

REFERENCES

- [1] www.feko.co.za
- [2] E. Jehamy, M.M. Ney, G. Landrac, "Reduction of Aberrations for Constrained Lenses at 76-77 GHz", *Proceedings of the Mediterranean Microwave Symposium*, Marseille, June 2004, pp 88.
- [3] G. Landrac, M. Ney, F. Gallée, "Monopulse millimeter wave radar antenna with an artificial lens focusing system", *Proceedings of the European Workshop on integrated radio communication systems*, Vol. Angers, May2002, pp. 187-190.
- [4] www.olympusmicro.com/primer/java/aberrations/spherical/
- [5] J.Robieux, "Lois générales de la liaison entre radiateurs d'ondes", *Ann. Radioélectr.*, 1959, Vol.14, pp.187-229.

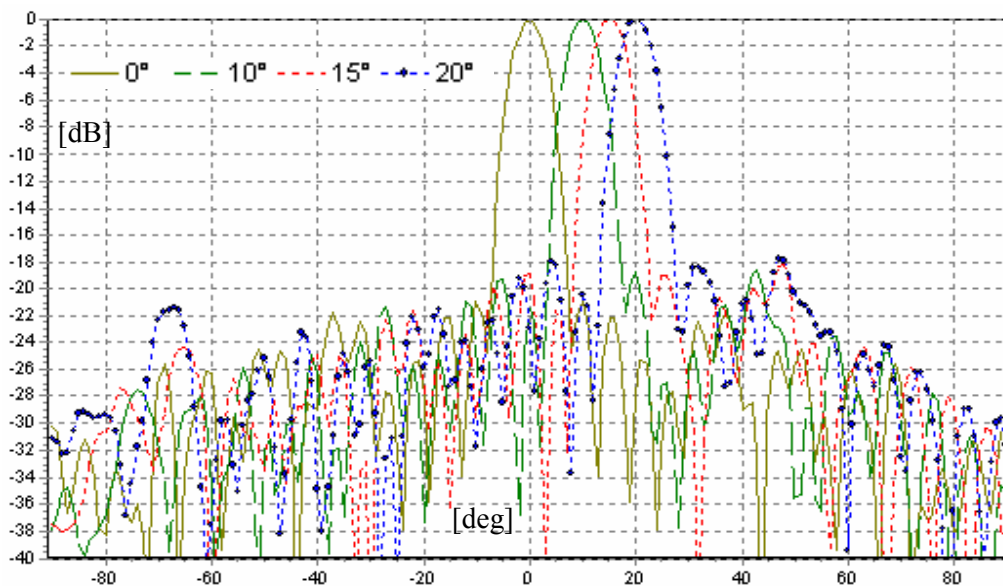


Fig.9. Radiation pattern in the H plane [1].

Meander Antenna with Backside Tuning Stubs

THE NAN Chang and C.C. Kuo

Tatung University, E.E. Department, No.40, Sec.3, Chung Shan N. Road, Taipei, Taiwan

Abstract—In this paper, we discuss a kind of meander antenna which is designed for DAB (Digital Audio Broadcasting) reception in BAND-III upper band (210-240MHz). Three resonators in addition to a driven element were constructed on the topside of a printed circuit board. On the backside of it, several coupling stubs were introduced to tune resonant frequencies to the required pass-band. Resonators with different lengths are resonated at different frequencies and these multiple resonances are responsible for an enhancement in bandwidth. With the help of backside coupling, it is easy to tune multiple frequencies to the required pass-band. It is also found that current density of the associated elements is increased by backside coupling. According to experimental results, the designed antenna reaches a bandwidth around 13.3% (return loss < -10dB) in the range of 210MHz ~ 240MHz.

I. INTRODUCTION

Radio broadcasting is entering the digital era, where services are delivered from the studio to the receiver, entirely in the digital domain. The Digital Audio Broadcasting (DAB) System developed within the Eureka 147 Project and now standardized by the European Telecommunications Standards Institute provides means to deliver high-quality digital radio services to the listener. In Europe, national and regional broadcasts have been allocated frequencies in Band-III and local broadcasts are using L-Band at roughly 1.5 GHz. In Taiwan, we began pilot trials using five channels in upper half of Band-III.

To develop antennas for DAB reception, a new class of meander antenna having both gap and backside coupling is proposed in this paper. Similar to other bent antennas, this antenna resonates at a shorter length than a straight-wire dipole or monopole. In [1], various short antennas such as fractal, helix, and (uniform) meander antennas were studied and it was concluded that their resonant properties will be the same independent of any difference in geometrical configurations. The achievable 2:1 VSWR bandwidth is 2.64% at 691.1MHz which is the closest frequency to that studied in this paper. To enhance the bandwidth, a non-uniform meander antenna was proposed [2]. It was designed by Genetic Algorithm optimization method. 10% band-width has been obtained by tuning both the vertical and horizontal segments. In [3], a bow-tie meander antenna was reported to achieve a 2:1 VSWR bandwidth of 8.6%.

In this paper, a new class of meander antenna having both gap and backside coupling is proposed. Gap coupling with parasitic elements has widely been used in

micro-strip antennas [4]. Multiple resonances are responsible for bandwidth enhancement. The same concept should easily be adopted for meander line antennas. To tune resonant frequencies to the required pass band, we put parasitic stubs on the backside of the PCB. It was observed that the backside coupling will also help increase the current distribution strength of the associated element by allocating the backside parasitic element in a proper position.

II. GAP-COUPLED STRUCTURE

The structure under study is shown in Figs.1 and 2. It is formed on a 1.6mm thick FR4 substrate ($\epsilon=4.6$). On the front side of the substrate, there is a driven element on the up-right position followed by three parasitic elements on the low-right, low-left, and up-left position respectively. They shall be named element A, B, C, and D clockwise starting from the up-right one. On the backside of the substrate, there are several meander stub patterns. The stub located underneath element B is named stub B. The stub located underneath element D is called stub D. There is another stub called by stub AC since it is located underneath both elements of A and C. In this section, we assume that there are no stubs on the backside of the substrate. Therefore, Fig.1 will be referred.

Three feeding methods were studied. They are micro-strip, CPW, and CPW with bottom ground as shown in Fig.3. We found that return loss does not vary significantly by different feeding methods. In case of feeding by CPW and by CPW with bottom ground, the return loss is also not significantly affected by varying S. However, good match can be achieved using larger values of W, and L for these two cases. We choose CPW with bottom ground as our feeding method.

In this topology, we choose $W=3\text{cm}$, and $L=13\text{cm}$. The width of the center conductor is 3mm and spacing of feed line to coplanar ground plane is 0.5 mm. The gap width, G, is chosen to be 0.2mm.

For structure (with no backside stubs) shown in Fig.1, it was studied that there are four resonant frequencies at 215MHz, 228MHz, 260MHz, and 273MHz. The return losses are 10.4dB, 4.0dB, 17.4dB, and 9.5dB respectively. By checking the current density distribution, we see that antenna A is strongly excited and should be the main active antennas responsible for radiations at 215 MHz. For other three frequencies, currents on all antennas are excited at a relatively low level. The reason is that they

are not directly connected to the feed line. We will see in the next section that the current level can easily be boosted up by adding tuning stubs on the backside of the substrate.

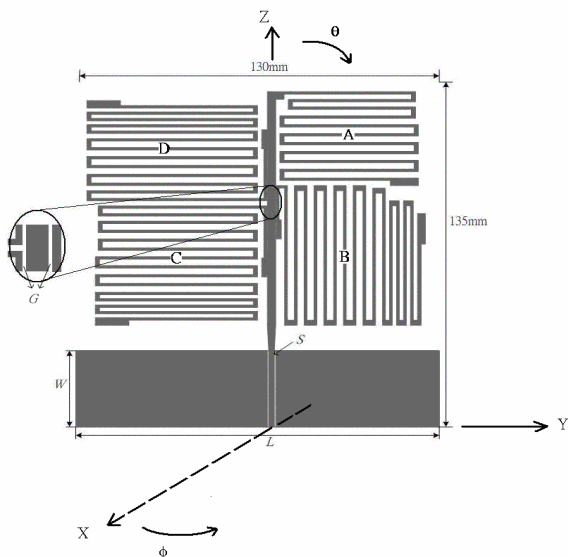


Fig.1 CPW-fed meander antenna with three gap-coupled parasitic elements and three electromagnetically coupled tuning stub

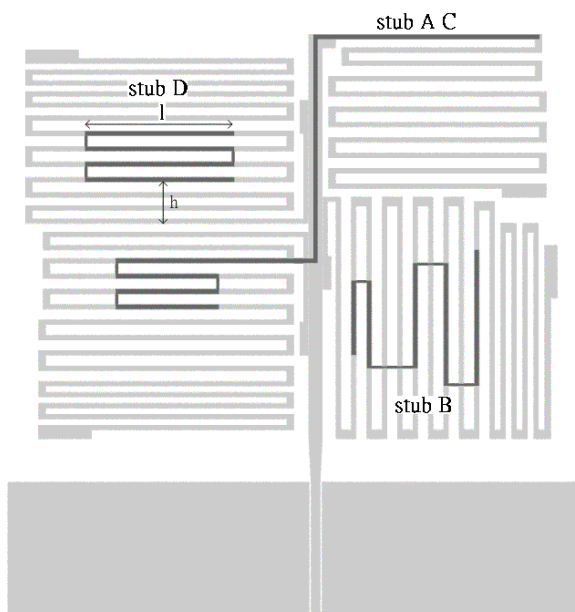


Fig.2 Location of the three electromagnetically coupled stubs on the opposite side of the substrate

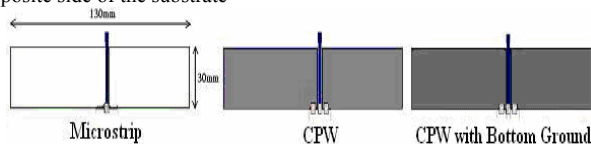


Fig. 3 Three different feeding methods

III. TUNING STUBS ON BACKSIDE OF THE SUBSTRATE

Figure 2 illustrates that some tuning stubs are allocated on the backside of the dielectric substrate. Fig.4 shows the current density distribution of two cases. Trace with “x” signs displays the current distribution at a frequency of 260 MHz for element D in Figure 1. Trace with “+” signs displays the distribution at a frequency of 240 MHz for the same element in Fig.2. The shift in frequency from 260 MHz to 240 MHz for element D in the two cases is confirmed from current distributions of the respective antenna.

In fact, the shift in frequency for antenna element D in Fig.2 can be controlled by varying l and h defined in Fig.2. Generally speaking, the tuning stub should be placed underneath the center area of each associated antenna element. For example, the resonant frequency of antenna element D is reduced as h increases toward the center (or as l increases. The shifts in frequency can be judged from Figures 5 and 6.

The reason why stub AC is underneath both elements A and C is that element C is at a distance far from the driven element. We can see from Fig.1 or Fig.2 that elements B and D are located next door to A, while C is located diagonally. It had been studied that the current on element C can efficiently be boosted up in this way. No stub is placed underneath element A. The reason is that element A is the driven element whose current can be strongly excited. Judging from current distributions shown in Fig.4, we can see that each trace looks like a sinusoidal function especially in the central part of it.

The design procedure is briefly reviewed. We begin with a structure shown in Fig.1. The length of each element (A, B, C, D) is about one half free-space wave length at a center frequency of the desired bandwidth. The return loss plot reveals that some resonant frequencies are beyond the pass-band. By checking the current distribution, we can identify that elements B and D are responsible for resonance at 273MHz and 260MHz respectively. Therefore, we need to bring them inside. We then found that we can lower down resonant frequency by a backside coupling technique. So, we added stub B and stub D to element B and D, respectively. As expected, two resonant frequencies shift inside. However, we found that the other two resonant frequencies of 215MHz and 228MHz caused by element A and C do not change too much. After placing stub AC, we finally get the required result. The function of stub AC also helps increase current distribution of element C

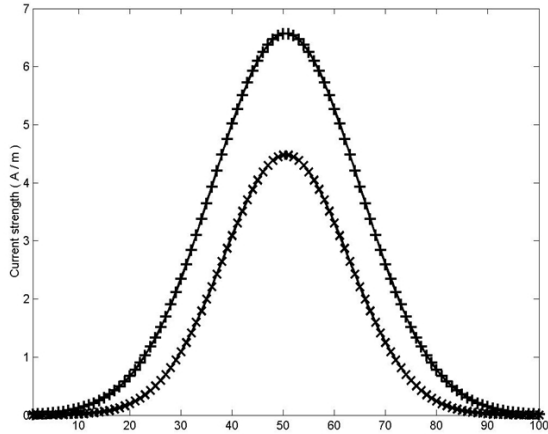


Fig.4 Current density distribution of element D in structures shown in Figs. 1 and 2

IV. EXPERIMENTAL RESULTS

Fig.7 shows the simulated and experimental results of the proposed meander antenna. The experimental results are better than those predicted by theory. Part of the reason may be due to that material loss was not included in the theory. Bandwidth around 13.3% for VSWR=2 over the frequency range from 210MHz to 240MHz can be achieved. There are four resonant points over this range. The multiple resonances do contribute for the overall performances.

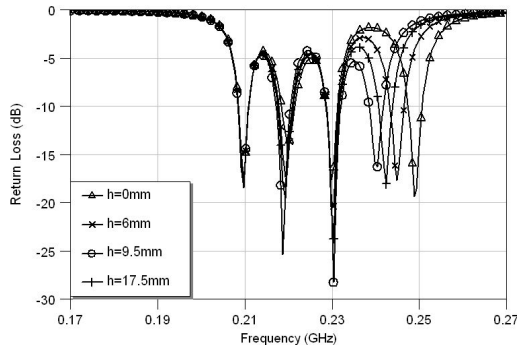


Fig.5 Frequency tuning effect by varying parameter “h”

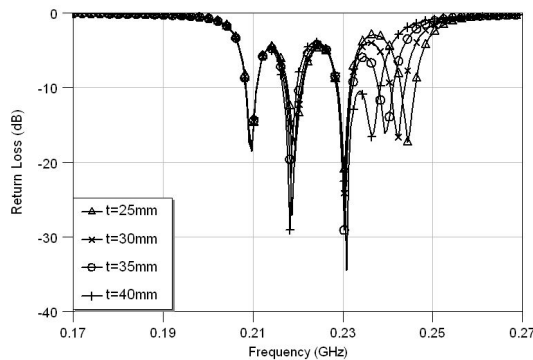


Fig. 6 Frequency tuning effect by varying “t”

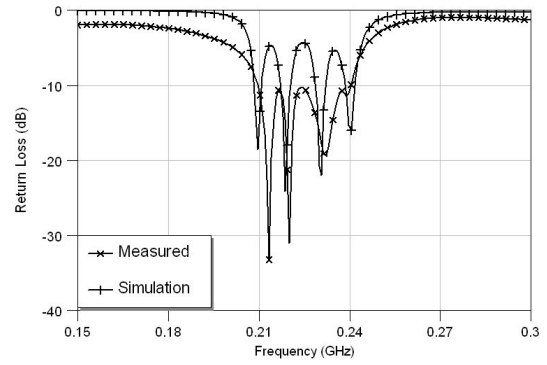
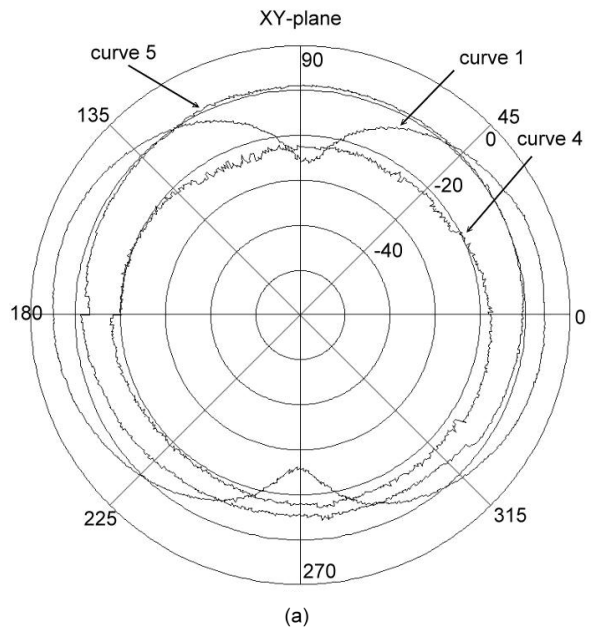


Fig.7 Measured and simulation results of the meander antenna

Fig 8 shows the measured patterns of two principle planes of the present antenna at 225 MHz. For comparison, the xy-plane pattern of a commercially available high-precision half-wave dipole antenna (Rohde & Schwarz HZ-12) is also shown as curve 1. Curve 1 was measured by placing the dipole along y-direction and was used to receive a horizontal polarized (y-polarized) wave. The pattern is easily identified by its shape, which looks like “the figure of eight”. At $\Phi=90^\circ$, it should have a null, actually it is -16dB down compared with the value in main beam. Curves 4 and 5 represent the xy-plane patterns of the present antenna. Curve 4 is for receiving a horizontal polarized wave, while curve 5 is for vertical polarized (z-polarized) wave. Both patterns are close too omni-directional patterns. The vertical polarized reception is dominated within whole azimuth angles.

In DAB reception, we prefer a vertical polarized reception. Therefore, the horizontal polarized reception is considered as the cross-polarization. The cross polarized level ranges from 6 to 12 dB in this plane.



(a)

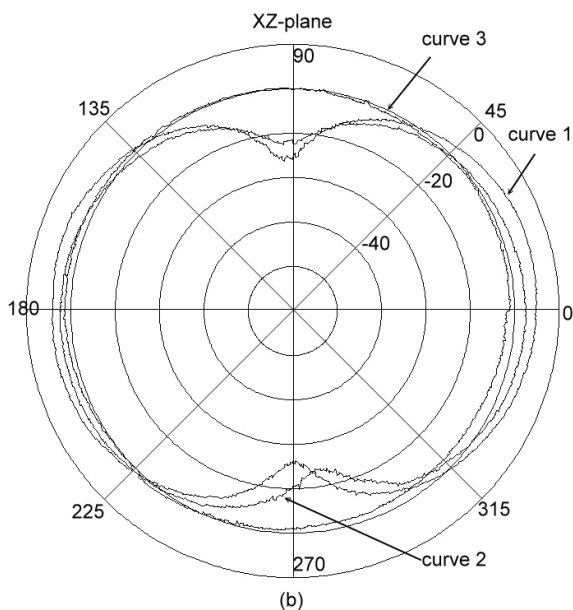


Fig. 8 Measured (a) xy-plane and (b) xz-plane patterns of the proposed meander antenna

Curves 2 and 3 represent the xz-plane patterns of the present antenna. Curve 2 is for receiving a horizontal polarized wave, while curve 3 is for vertical polarized (z-polarized) wave. Horizontal polarized reception is dominated within $-45 < \Phi$ (in degrees) < 45 , while vertical wave is dominated outside this region.

The absolute gain of a dipole is 2.2 dBi. For the adopted dipole, there is 10dB attenuation from the input of the dipole to the plane of measurement. The attenuation is for wideband match. Therefore, the absolute gain at $\Phi=0$ for curve 1 is evaluated as -7.8dBi. By this value, maximum gain for the present antenna is -7.8dBi at 225 MHz. It was studied that variations were within 1dB from 210 to 240 MHz. The simulated return loss (which does not include loss of the substrate) in Figure 5 illustrates that the low gain of the present design is due to a mismatched impedance over the entire band. The achieved bandwidth is directly a result of decreased

antenna efficiency. The measured better return loss comes from the loss of the substrate. The lossy substrate further decreases the gain.

V. CONCLUSION

In this paper, we present a novel meander antenna with an attempt to increase the bandwidth. On the top side of a substrate, resonators with different lengths are responsible for a multi-frequency operation. On the backside of the substrate, several tuning stubs are formed. The backside coupling is introduced to bring multiple frequencies to the required pass-band. The function of each backside stub is to tune frequency flexibly for a particular element, while to keep its influence to other elements' resonant frequencies to a minimum level. By this way, we construct a meander antenna which is designed for DAB (Digital Audio Broadcasting) reception in BAND-III upper band (210-240MHz). A bandwidth around 13.3% (return loss < -10 dB) can be achieved. However, the achieved bandwidth is directly a result of decreased antenna efficiency. Therefore, there is a significant limitation on this design approach. For practical applications, reference [5] can be consulted.

REFERENCES

- [1] [1] Steven, R. Best, "On the resonant properties of the Koch fractal and other wire monopole antennas", *IEEE Antennas and Wireless Communication Letters*, Vol.1, pp.74-77, 2002
- [2] Gaetano Marrocco, Alessandro Fonte, and Fernando Bardati, "Evolutionary design of miniaturized meander-line antennas for RFID applications", *IEEE AP-S international symposium*, pp.362-365, 2002
- [3] M. Ali, and S.S. Stuchly, "A meander line bow-tie antenna", *IEEE AP-S international symposium*, pp.1568-1569, 1996
- [4] C.K. Aanandan, P.Mohanan, and K.G.Nair, "Broad-Band gap coupled microstrip antenna", *IEEE Transactions on Antennas and Propagation*, Vol.48, pp.1452-1460, 2000
- [5] Simon Mason, "Indoor reception of DAB-consequences for planning and implementation", *EBU Technical Review*, July, 2004

Session 4a

Active Filters

2 GHz Tuneable Integrated Differential Active Bandpass Filter on Silicon

Zoheir Sassi¹, Sébastien Darfeuille¹, Bruno Barelaud¹, Laurent Billonnet¹, Bernard Jarry¹
Hervé Marie², Nguyen Tran Luan Le², Patrice Gamand²

¹ IRCOM, University of Limoges, 123 Avenue Albert Thomas, 87060 Limoges Cedex, France

² Innovation Centre RF, Philips Semiconductors, 2 Rue de la girafe, 14079 Caen Cedex, France
E-mail: zoheir.sassi@unilim.fr

Abstract — Improvements of Silicon technology in CMOS and BiCMOS process, is nowadays showing very interesting intrinsic characteristics. Circuit ideas and topologies are improved more and more to fit the industrial needs.

Our design is a 2 GHz BiCMOS process filter based on a LC-Q enhanced topology. With a power supply of 2.7 V, the circuit consumes less than 6.1 mA. It shows at the centre frequency a 20 dB power transmission gain, a noise figure of 4.2 dB, a -35 dBm -1dB input referred compression point and a -3dB bandwidth of 50 MHz.

I. INTRODUCTION

The challenge today is an alternative use of active filtering to replace the combination of external passive filters (SAW filters for example) and amplifiers. Most serious literature comparisons believe on the efficiency of LC-Q enhanced filters [1-6]. Indeed, they are showing the best compromises, especially in terms of power consumption, cost, noise figure and linearity with respect to other topologies, like active inductors and Gm-C filters.

The proposed filter topology is then based on the use of integrated inductors rather than off-chip components to achieve important improvements in terms of cost and die space. Unfortunately, in classical filter topologies, the quality factor Q_0 of inductors is crucial, especially in terms of linearity and bandwidth of the response. On-chip inductors designed by BiCMOS process provide low quality factors due to the high metal to silicon substrate couplings [7]. The best we have done is in the order of 10 for an inductance value of 6-7nH. This approach automatically implies the use of compensation circuits to increase the quality factor of such components, with the inherent problems of possible degradations of the noise figure and the compression point of the circuit.

II. CIRCUIT ARCHITECTURE

The proposed circuit (Fig. 1) is made up of a classical LC resonator associated with a negative resistance, an input differential amplifier, an impedance converting block and an output buffer. For the parallel LC resonator, we use a combination of an integrated square symmetric spiral inductor L_{eff} (8.65 nH) with a quality factor Q_0 of 9.43, and a symmetric set of two series capacitors C_1 , C_2 .

The resonant frequency is:

$$f_0 = \frac{1}{2\pi\sqrt{L_{eff}C_{eff}}}$$

where C_{eff} represents the combination of C_1 , C_2 and the capacitive effect of both the negative resistance and the converting impedance blocks. These blocks have been integrated using MOSFETs.

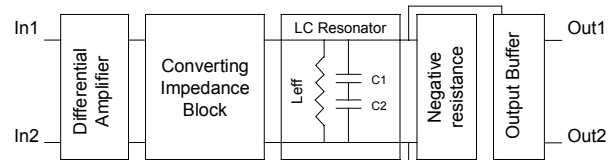


Fig. 1 Simplified schematic of the filter

Note that, when the resonator is loaded, additional impedances must be considered, thus needing a higher compensation level to maintain the required bandwidth of 50 MHz. Even though the value of this negative resistance is rather small, it must be well estimated and controlled to avoid instabilities.

From the filter output point of view, simple buffers composed of MOSFETs are very efficient, since they present high input impedance levels. From the filter input point of view, a classical solution consists of using a combination of series inductors with small grounded capacitors at the input of the amplifier. Unfortunately, this solution implies large inductors and introduces too much noise due to their use at the input of the circuit.

In this circuit, we use a novel impedance converting block, with no more than four transistors just after the amplifier. Thus, the compensated resonator is loaded with a high impedance while the amplifier is loaded with a very small positive impedance. The final result is very efficient in terms of high selectivity of the response, input matching and noise figure.

II-A. IMPEDANCE CONVERTING BLOCK

The impedance converting block (Fig. 2(c)) is composed of two parts. The first one introduces a negative resistance using two NMOS transistors back to back (Fig. 2(a)). The second one increases the impedance level to make both Z_{in} and Z_{out} of this block positive-valued (Fig. 2(b)).

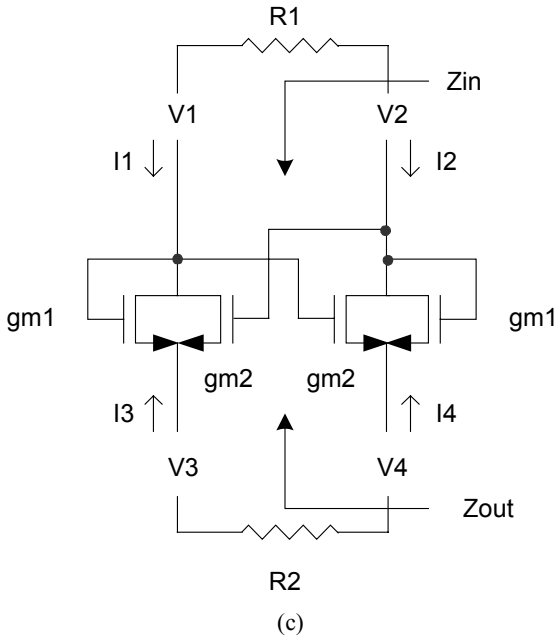
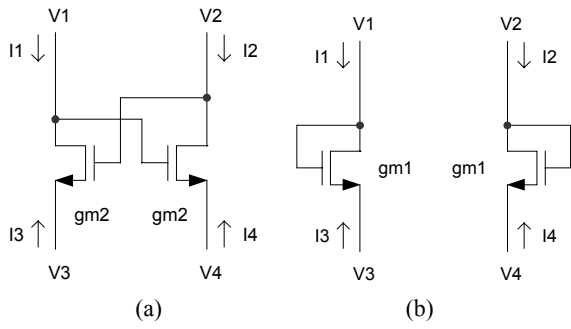


Fig. 2 (a) Negative resistance generator. (b) Positive resistance shifter. (c) Impedance converting block

To evaluate Z_{in} and Z_{out} , we use admittance matrices of the two blocks, Y_n (1) and Y_p (2) respectively. Using the sum matrix $Y_n + Y_p$ (3), the input and output impedances expressions are given by (4) and (5) respectively. Note that transistors are modelled by ideal transconductances.

$$Y_n = \begin{bmatrix} 0 & gm_2 & -gm_2 & 0 \\ gm_2 & 0 & 0 & -gm_2 \\ 0 & -gm_2 & gm_2 & 0 \\ -gm_2 & 0 & 0 & gm_2 \end{bmatrix} \quad (1)$$

$$Y_p = \begin{bmatrix} gm_1 & 0 & -gm_1 & 0 \\ 0 & gm_1 & 0 & gm_1 \\ -gm_1 & 0 & gm_1 & 0 \\ 0 & -gm_1 & 0 & gm_1 \end{bmatrix} \quad (2)$$

$$Y_n + Y_p = \begin{bmatrix} gm_1 & gm_2 & -(gm_1 + gm_2) & 0 \\ gm_2 & gm_1 & 0 & (gm_1 - gm_2) \\ -gm_1 & -gm_2 & (gm_1 + gm_2) & 0 \\ -gm_2 & -gm_1 & 0 & (gm_1 + gm_2) \end{bmatrix} \quad (3)$$

$$Z_{in} = \frac{1 + R_2(gm_1 + gm_2)}{gm_1 - gm_2} \quad (4)$$

$$Z_{out} = \frac{1 + R_2(gm_1 - gm_2)}{gm_1 + gm_2} \quad (5)$$

If the four transistors are scaled to the same size in such way that $gm_1 = gm_2 = gm$, then the input impedance Z_{in} will be very important compared to Z_{out} . The output impedance in this case is independent of R_2 and equal to $1/(2 \cdot gm)$.

II-B. COMPLETE FILTER

As shown in Fig. 3, the differential amplifier block is composed of two BJT transistors Q_1 , Q_2 with two degeneration inductors L_1 , L_2 .

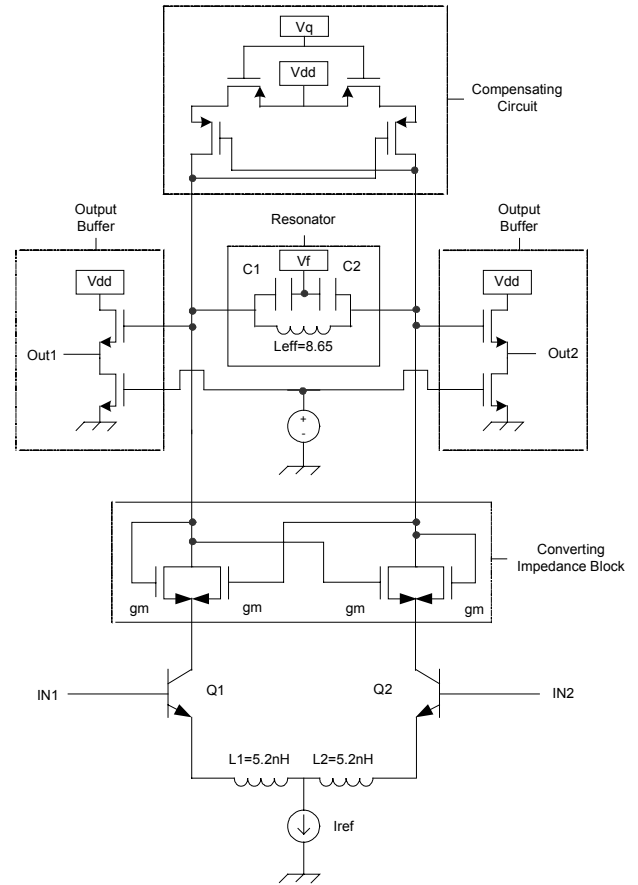


Fig. 3 Global filter circuit

Currents flowing through these transistors have been fixed and optimised for minimum noise generation [2]. For linearity and matching reasons, inductors L_1 and L_2 are designed to be 5.2 nH in order to increase the real part of the input impedance.

PMOS transistors are used in the negative resistance part. to increase the quality factor of the inductors. They are preferred to NMOS transistors because they generate less noise in the circuit [1].

III. CIRCUIT LAYOUT

BiCMOS Philips QUBIC4 0.25 μm Library is used [8]. The final layout is shown in Fig. 4. Dimensions of the chip are 1510 X 1040 μm^2 (1.57 mm^2). Differential pads have been used for input and output differential modes measurements. Control pads have been also added for frequency, quality factor and gain controls.

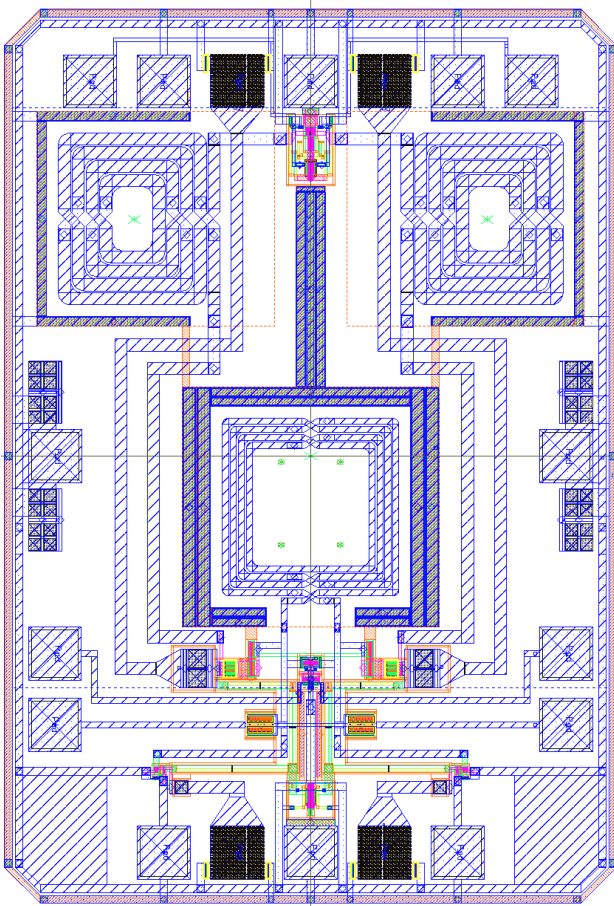


Fig. 4 Complete filter layout

IV. SIMULATION RESULTS

The experimental circuit is being processed at the foundry. Measurements will be available for the conference.

With a power supply of 2.7 V, the circuit consumes less than 6.1 mA (16.47 mW), which is very small compared to other circuits using the same technology. At the centre frequency, the circuit exhibits a S_{21} parameter of 20 dB. Reflection parameters S_{11} and S_{22} are less than -20 dB (Fig. 5).

For a bandwidth of 50 MHz, the noise figure is about 4.2 dB. The -1dB input referred compression point is evaluated at -35 dBm, corresponding to an output compression point of -16 dBm. Table 1 summarises the main characteristics of the final filter.

Summary of the filter performances	
Supply voltage	2.7 V
Current	6.1 mA
Frequency tuning range	1.5 - 2.2 GHz
Q quality factor with adequate input and output matching	20 - 200
Gain S_{21} at centre frequency	20 dB
S_{11} , S_{22}	-20 dB
-3 dB bandwidth	50 MHz
1-dB input compression point	-35 dBm
Noise figure	4.2 dB
Die area	1.57 mm^2

Table. 1 Filter performances summary

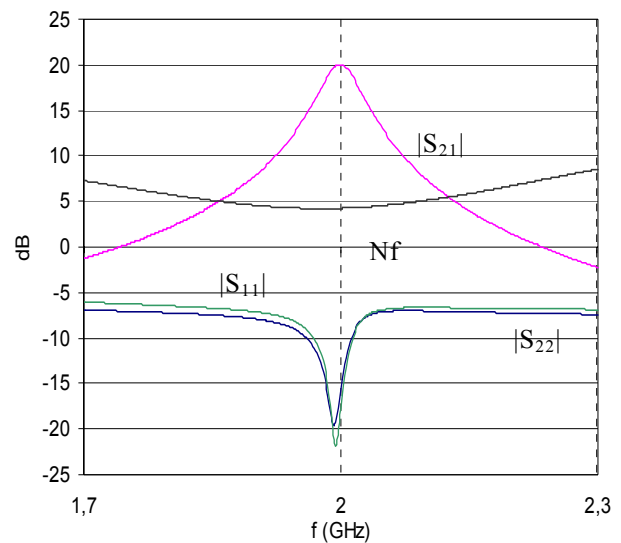


Fig. 5 Scattering parameters and Noise Figure of the circuit

V. TUNEABILITY PERFORMANCES

One of the main advantages of this circuit is the ability to tune the centre frequency from 1.5 GHz to 2.2 GHz by varying the control voltage V_f from 0.9V to 2.2V. Gain can be readjusted if necessary. Centre frequency relative tuneable range is close to 40% (Fig. 6). Reflection parameters are always less than -10 dB in all tuning states (Figs. 7 and 8). Noise figure varies from 3.7 dB to 4.47 dB in the worst case. Quality factor can also be modified from 20 to 200 by choosing V_q from 1.2V to 1.6V (Fig. 9). Only a very small frequency readjustment is then needed to maintain the 2 GHz centre frequency.

VI. CONCLUSION

Using a standard 2.7V power supply, the proposed filter structure can demonstrate good results from 1.5GHz to 2.2GHz. With a current consumption of 6.1 mA, a power transmission gain S_{21} of 20 dB is obtained. Noise figure equals 4.2 dB, and 1-dB input referred compression point is about -35 dBm for a 50 MHz -3dB bandwidth. The topology can be as well generalised to implement higher order filters.

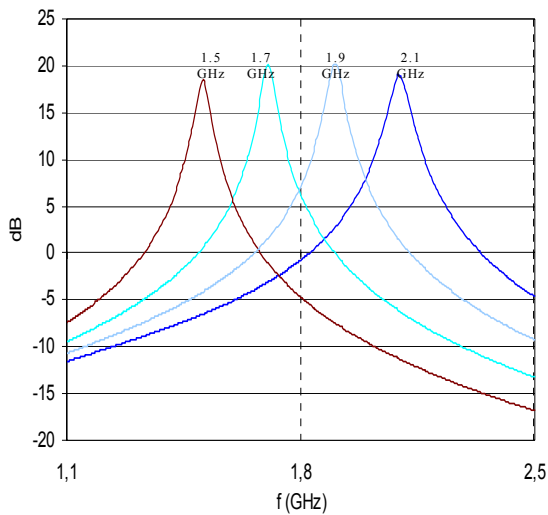


Fig. 6 $|S_{21}|$ response with respect to frequency tuning from 1.5 GHz to 2.1 GHz with $Q \approx 60$.

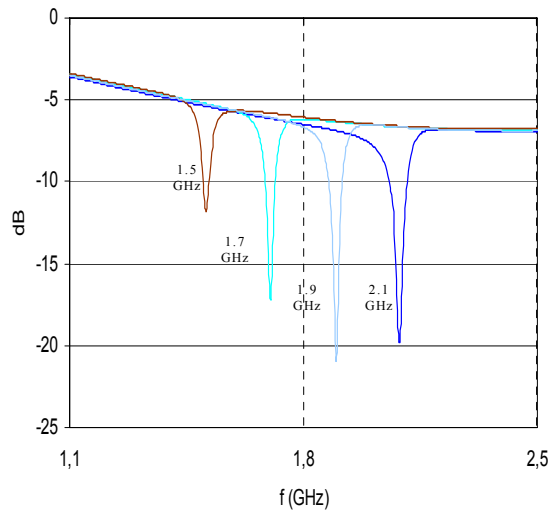


Fig. 7 $|S_{11}|$ response with respect to frequency tuning from 1.5 GHz to 2.1 GHz with $Q \approx 60$.

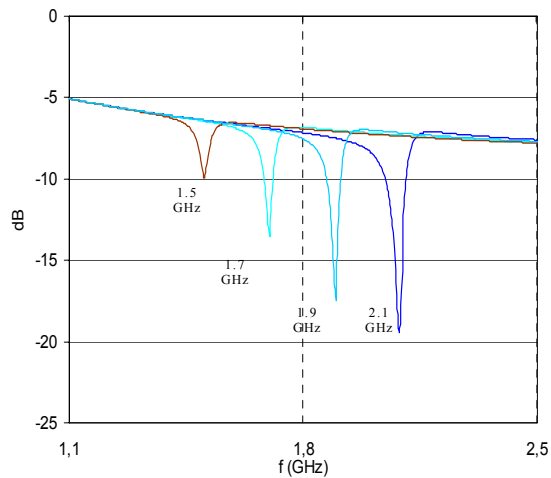


Fig. 8 $|S_{22}|$ response with respect to frequency tuning from 1.5 GHz to 2.1 GHz with $Q \approx 60$.

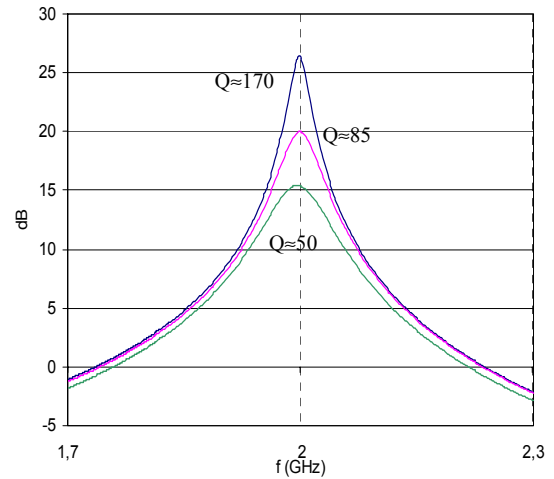


Fig. 9 Quality factor tuning at 2 GHz.

ACKNOWLEDGEMENT

The authors wish to acknowledge R&D department of Philips Company in Caen for their assistance and the realisation of the chip.

REFERENCES

- [1] Xin He, W.B. Kuhn, "A fully integrated Q -enhanced LC filter with 6 dB noise figure at 2.5 GHz in SOI", 2004 RFIC Symposium, pp. 643- 646.
- [2] S.P. Voinescu et al., "A scalable high-frequency noise model for bipolar transistors with application to optimal transistor sizing for low-noise amplifier design", IEEE Journal of Solid-State Circuits, Volume 32, Issue 9, Sept. 1997, pp. 1430-1439.
- [3] W.B. Kuhn et al., "Dynamic range performance of on-chip RF bandpass filters", IEEE Transactions on Circuits and Systems II, Volume 50, Issue 10, Oct. 2003 pp. 685-694.
- [4] W.B. Kuhn et al., "Q-enhanced LC bandpass filters for integrated wireless applications", IEEE Transactions on MTT., Volume 46, Issue 12, Dec. 1998, pp. 2577-2586.
- [5] F. Dulger, E. Sanchez-Sinencio, J. Silva-Martinez, "A 1.3-V 5-mW fully integrated tunable bandpass filter at 2.1 GHz in 0.35- μ m CMOS", IEEE Journal of Solid-State Circuits, Volume 38, Issue 6, June 2003, pp. 918-928.
- [6] Z. Sassi et al., "Fully Differential 2 GHz 2.7V 4th-Order Low-Noise Active Bandpass Filter on Silicon", European Microwave Week 2004 Conference Proceedings 11-15 October 2004. Amsterdam, The Netherlands.
- [7] A.M. Niknejad, R.G. Meyer, "Analysis, design, and optimization of spiral inductors and transformers for Si RF ICs" IEEE Journal of Solid-State Circuits, Volume 33, Issue 10, Oct. 1998, pp. 1470-1481.
- [8] D. Szmyd et al., "QUBICA: a silicon RF-BiCMOS technology for wireless communication ICs", Proceedings of the 2001 bipolar/BiCMOS Circuits and Technology Meeting, pp.60-63.

Selective Tuneable Active Filter with Gain Using Active Impedance Profile Technique

Sébastien Dardillac, Laurent Billonnet and Bernard Jarry

IRCOM UMR CNRS n°6615 - University of Limoges
123, Avenue Albert Thomas - 87060 Limoges Cedex, France
Email : laurent.billonnet@unilim.fr

Abstract — This paper deals with a novel approach for the design of microwave filters. This approach uses the Active Impedance Profile (AIP) technique and can be considered as an extension of the classical loss compensation method with negative resistances. This technique takes benefit of the adequate imaginary part of an active one-port to control the bandwidth and selectivity of a passive filter response, while the real part simultaneously compensates for the losses in the passbands. We first explain this method and then, we apply it to the design of a selective tuneable band-pass filter.

I. INTRODUCTION

In the past years, passive filter structures solutions were mostly of the volumic type. The main drawback of volumic filters is too important dimensions. This problem can be definitely reduced if planar technologies are considered. However, with these technologies, all the passive topologies leads to lossy responses, avoiding highly selective characteristics. Since several years, active filtering solutions have become promising for the design of integrated planar circuits [1] [2]. Using active techniques, improvements classically rely on loss compensation in the passbands, but also on size and weight reductions. Recently, request for new capabilities and applications for telecommunication systems have imposed better performances for example for the front-end receivers. The most popular proposed solutions, generally consist in compensating the filter losses, either with amplifiers, or with negative resistance circuits. With this approach, the objective performance is to design pure negative resistance circuits, with a minimum associated parasitic imaginary impedance. We here explain how to take benefit of the associated imaginary part of the active chips on the filter response shape. We apply the Active Impedance Profile (AIP) method to the design of a selective tuneable band-pass filter. In a first step, we explain the method and show the role of the imaginary part of the active circuit on the response. We then apply this method to the design of a selective band-pass filter using a GaAs process and show measurement results.

II. ACTIVE IMPEDANCE PROFILE PRINCIPLE

Generally, compensation techniques just focus on a mean of compensating losses introduced by passive parts of a circuit. In most cases, the objective is then to improve the transmission level of the filters in the passbands.

The technique then consists either on designing directly perfect active elements (inductances [3] or capacitances) by means of gyrators (or NICs), or on compensating for losses thanks to circuits simulating negative resistance behaviour. In planar passive filters, depending on the technology used, the most degrading elements are either microstrip line -based resonators or integrated spiral inductors. In both cases, the simplest way to compensate for the losses in then to connect in series a negative resistance circuit.

With the Active Impedance Profile technique, an adequate active one-port circuit is added to a passive filter. This active circuit presents a complex impedance $Z(f)=R(f)+X(f)$ for which the imaginary part contributes to a significant improvement of the filter response. The objective is then to determine the characteristics of the active one-port in terms of real and imaginary parts:

- 1) the value of the real part to strictly compensate for the losses of the passive filter in the pass-band,
- 2) the value of the imaginary part to set the central frequency of the global filter (see Fig. 1) [6],
- 3) the slope of the imaginary part in a given frequency band around the central frequency to adjust the filter bandwidth and selectivity.

As an example, we consider here a bandpass filter based on a $\lambda_0/2$ resonator connected at its input and output through $\lambda_0/4$ coupled lines (Fig. 2). The filter response presents insertion losses at its central frequency.

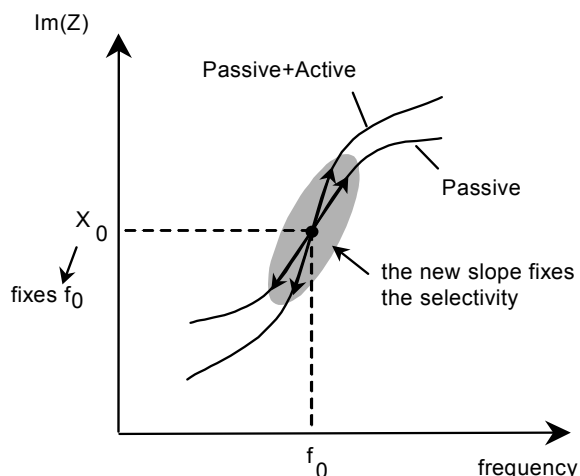


Fig. 1. Active Impedance Profile principle

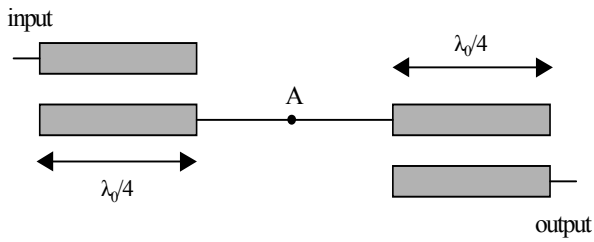


Fig. 2. Passive filter topology

Following the method, it is possible, by inserting the adequate active impedance at point A, to compensate for the losses and to simultaneously modify the values of the central frequency and bandwidth. Figs. 3 and 4 show the influence of an increase respectively of the value of the imaginary part and the slope of this imaginary part on a passive filter response initially centred at 60 GHz.

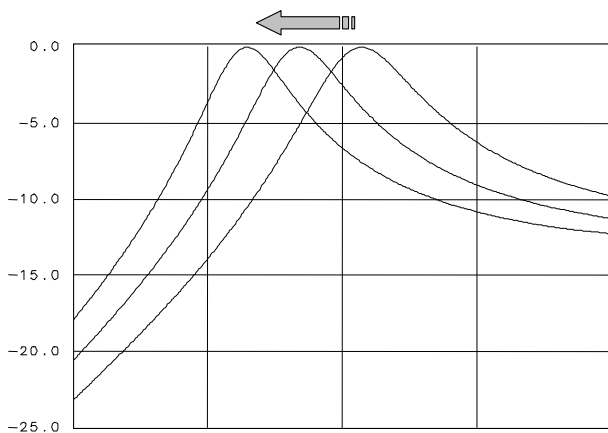


Fig. 3. Frequency shift due to the increase of the value of the imaginary part

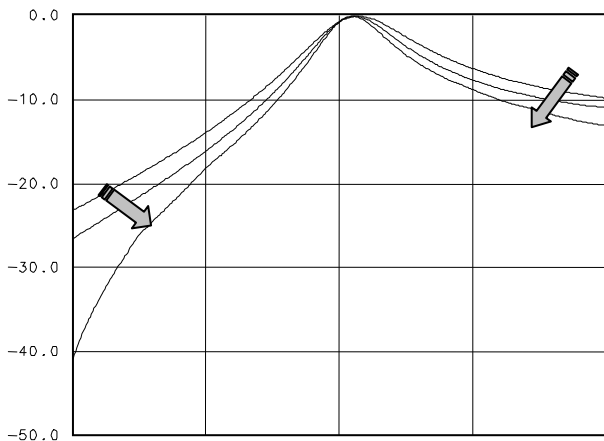


Fig. 4. Bandwidth variations due to the increase of the slope of the imaginary part

For this filter topology, an increase of the value of the imaginary part of the AIP involves a centre frequency decrease. An increase of the slope leads to a narrower bandwidth.

III. APPLICATION OF THE AIP PRINCIPLE

We now apply this technique to the design of a selective bandpass filter. The procedure is described in three steps.

A. Starting point of the design

The objective is to realise a bandpass filter around 15 GHz with a 50 MHz-bandwidth. The initial passive filter is shown in Fig. 5.

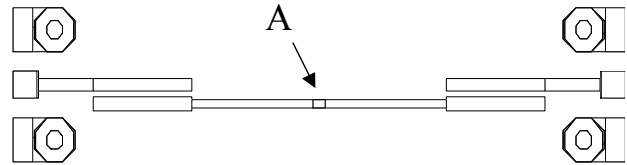


Fig. 5. Initial passive filter topology

The passive filter response is around 35 GHz, with a 4GHz bandwidth and insertion losses around -7 dB.

B. AIP characteristics extraction

The next step is to find, for each frequency point, the real and imaginary parts of the AIP circuit to connect to the passive parts (at point A) to carry out the desired response of the global filter. This impedance is shown in Fig. 6.

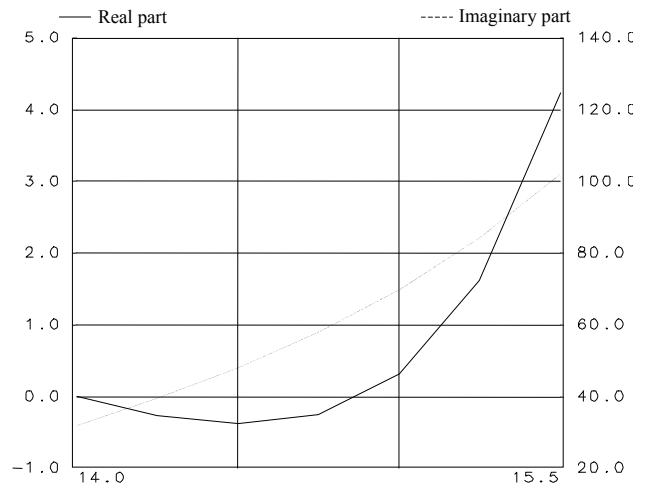


Fig. 6. Active impedance profile

C. AIP design

In a first step, we must determine which topologies are able to realise the desired impedance behaviour. In general, these topologies are based on negative resistance topologies [4], [5]. For our case, the active circuit (Fig. 7) consists of a common-source transistor with series feedback.

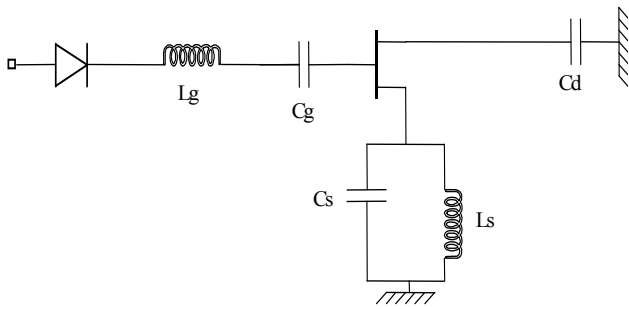


Fig. 7. Active circuit topology

The real part is realised through the LC-shunt tank and the imaginary part through the other elements. A diode is added in series to shift the value of the imaginary part and then to influence the global filter response.

D. Active filter layout

The two parts (active and passive) are associated in a single chip whose dimensions are 2*1.5 mm² (Fig. 8). Simulation results are shown in Fig. 9. This filter achieves a central frequency at 14.62 GHz with 0 dB of insertion losses, a bandwidth of 60 MHz and an isolation at central frequency around 42 dB.

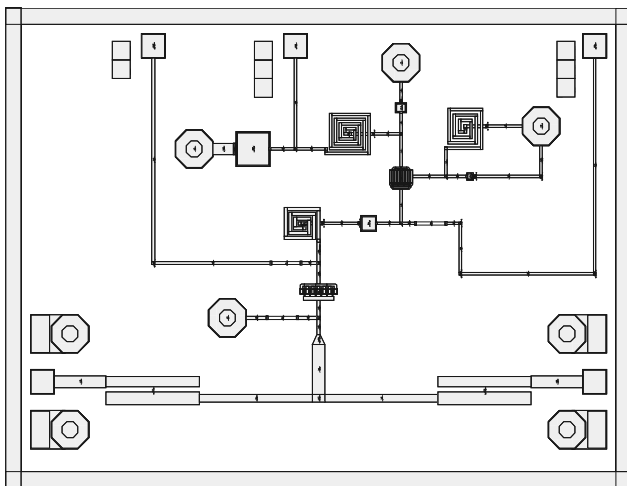


Fig. 8. Active filter layout

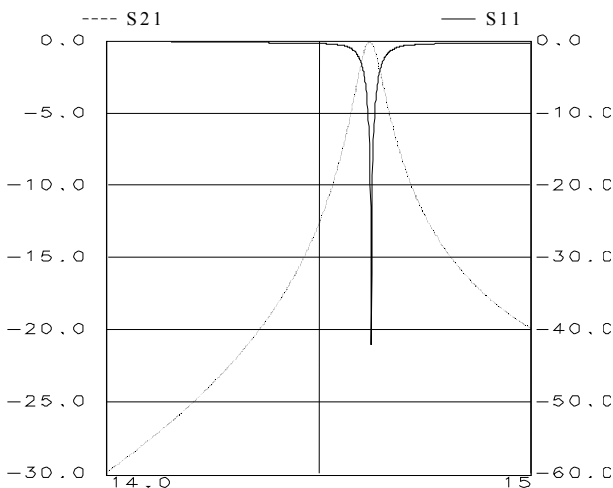


Fig. 9. Simulated results

III. MEASUREMENT RESULTS

The first measurement results have been obtained with the scheduled bias voltages. A comparison between measurements and simulations is shown in Fig. 10. As can be shown, in spite of a frequency shift of 230 MHz, measurements are in good agreement with simulations. There are no losses in the passbands at the centre frequency. The passband is 60 MHz wide.

In a second step, diode bias voltage is tuned to show the effect of the imaginary part of the active circuit on the response. Bias voltages of the transistor are adjusted to maintain the level of the response. Best measurements obtained are shown in Fig. 11.

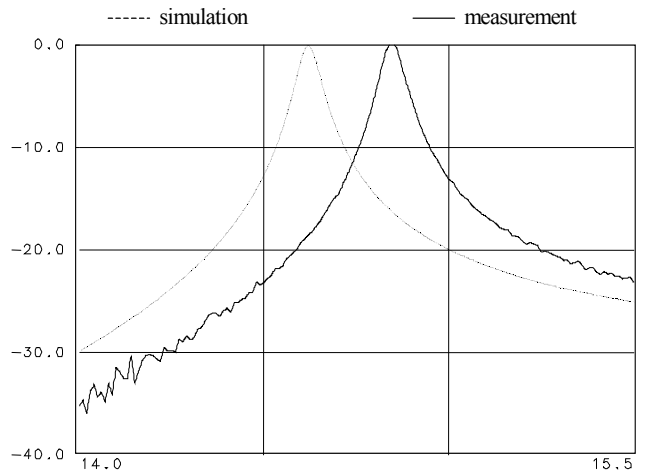


Fig. 10. Comparison between simulations and measurements

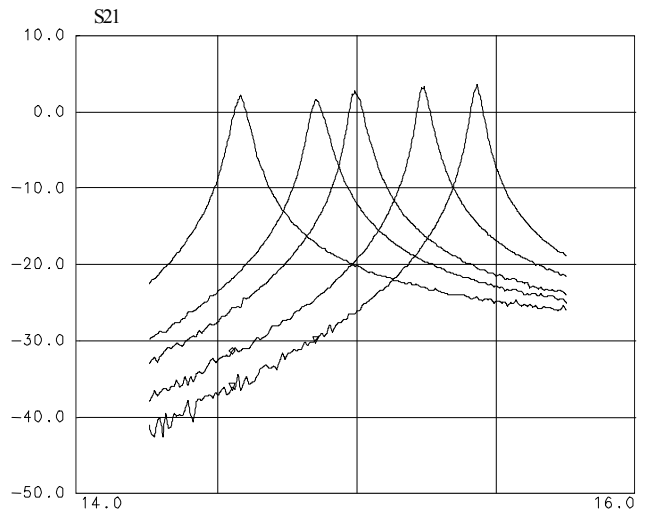


Fig. 11. Measured tuned response of the filter

Measurements show the expected tuneability of the central frequency provided by the imaginary part of the active circuit. The response is tuneable on a 850 MHz wide frequency range. Gain at centre frequency is between 2.2 and 3.6 dB. Bandwidth is around 55 MHz. All these results are in perfect agreement with simulations.

IV. CONCLUSION

The AIP technique is derived from the classical loss compensation approach based upon the use of circuits simulating a negative resistance. By appropriately taking benefit of the associated imaginary part of such circuits, we have shown the effects and improvements performed on the bandwidth and selectivity of a one-pole distributed passive filter response. With this technique, we have designed a tuneable filter with gain in the passband (between 2.2 dB and 3.6 dB) and a narrow bandwidth (55 MHz).

REFERENCES

- [1] A. Brucher, P. Meunier, C. Cenac, B. Jarry, P. Guillon, "Broadband and tuneable negative monolithic circuits for microwave active filters compensation," *1995 IEEE MTT-S Int. Microwave Symp. Dig.*, pp. 213–216, May 1995.
- [2] I. C. Hunter, L. Billonnet, B. Jarry, P. Guillon, "Microwave filters-applications and technology," *IEEE Trans. Microwave Theory & Tech.*, vol. 50, no. 3, pp. 794–805, March 2002.
- [3] S. E. Sussman-Fort, L. Billonnet, "An NIC-based negative capacitance circuit for microwave active filters", *1995 International Journal of Microwave and Millimeter-wave Computer Aided Engineering*, vol. 5, pp. 271-277.
- [4] U. Karacaoglu, I. D. Robertson, "MMIC active bandpass filter using negative resistance elements", *1995 IEEE MTT-S Int. Microwave Symp. Dig.*, vol. 1, pp. 135-138, May 1995.
- [5] R. V. Snyder, D. L. Bozarth, "Analysis and Design of a Microwave Transistor Active Filter", *IEEE Trans. on Microwave Theory & Tech.*, vol. 18, no. 1, pp. 2-9, January 1970.
- [6] F. Biron, D. Denis, J.Ph. Plaze, L. Billonnet, B. Jarry, G. Tanné, E. Rius, "Active Impedance Profile Technique for Size Reduction, Loss Compensation and Selectivity Improvement of Planar Passive Filters", *EuMC'2002, 32nd European Microwave Conference Proceedings*, September 2002, Milan, Italy.

Improved Magnitude Sensitive Detector Structure for Automatically Tuned Filters at Microwave Frequencies

Eckhard Neber¹, Laurent Billonnet², Bernard Jarry², Michael H.W. Hoffmann¹

¹ University of Ulm, Albert-Einstein-Allee 41, 89081 Ulm, Germany

Email: neber@mwt.e-technik.uni-ulm.de

² IRCOM UMR C.N.R.S. 6615, 123 Avenue Albert Thomas, 87060 Limoges Cédex, France

Email: gary@ircom.unilim.fr

Abstract — In this paper an improved detector structure for an automatically tuned filter that is well suited for application at microwave frequencies is proposed. It can be used in a master-slave structure where the amplitude response of a consecutively detuned master filter at one reference frequency is used to derive a control signal that steers a slave filter in the signal path. The improved detector is analysed theoretically and the result is compared to measured values. It provides good performance at reduced complexity.

Index Terms — Frequency control, tunable filters, microwave filters

I. INTRODUCTION

The characteristics of analog filters are vulnerable to fabrication tolerances and temperature drift. Automatic frequency control using the popular master-slave approach is the most feasible solution to control these characteristics [1]. It uses a master device that is embedded in a control loop to generate the tuning signal for the slave *Voltage Controlled Filter (VCF)* in the signal path. A good matching between master and slave is essential for a precise operation.

For microwave filters, this problem has been solved in [2], [3] by using a typical phase locked loop based on a voltage controlled oscillator matched to the slave filter.

Another control scheme that uses identical filters for master and slave was proposed in [4] and analysed in detail in [5]. It utilises a test signal to measure either the magnitude response or the phase response of the filter at one reference frequency. The phase sensitive detector showed good performance at the price of higher complexity due to the necessary mixer. In [6] a novel detector was introduced that requires no mixer at the cost of an additional master filter.

In [7] an approach was presented where the amplitude response of one master filter is measured, sampled and stored at different reference frequencies in a time multiplex scheme. A feedback signal is derived from the sampled amplitude values. The various reference frequencies are generated by a frequency synthesiser.

In this paper the concept of an alternating measurement of the master filter is applied to the structure of [6], thereby eliminating the drawbacks of that method because it needs only one master filter. Additionally only one power detector is required and it is operated at the same input power level so that there are no additional

inaccuracies due to nonlinearities or insufficient matching between the detectors.

In the following chapter the function principle is explained first. On that basis the new structure is derived and analysed in detail. The results are validated by measurements at microwave frequencies.

II. THE FUNCTION PRINCIPLE

A. State of technique

The structure of an automatically tuned filter following the master-slave principle with the detector structure presented in [6] is depicted in Fig. 1. The function is as follows: the control loop in the upper part of the picture adjusts the tuning voltage u_0 of the slave filter in such a way that the centre angular frequency ω_0 of the slave filter is tuned to the angular frequency ω_r of the reference signal. The useful signal of the circuit is filtered by the slave in the lower part.

The crucial component in the control loop is the detector (dashed block in Fig. 1). Its output signal u_d has to reflect the frequency error between the reference angular frequency and the centre angular frequency of the slave filter. It is fed back as the tuning voltage u_0 via the control

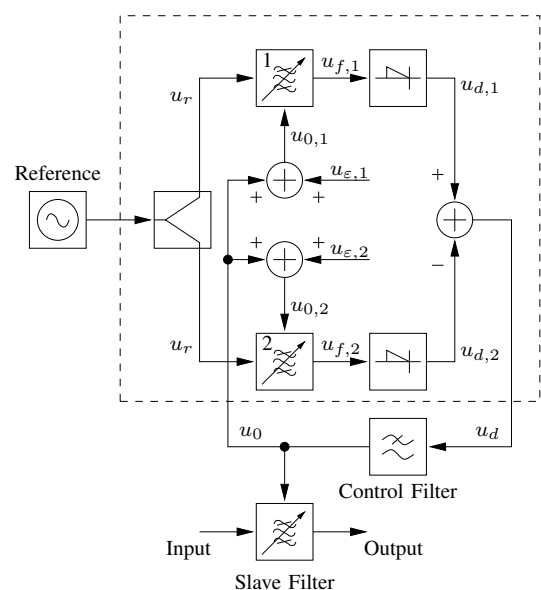


Fig. 1. Structure of the control loop presented in [6]. The circuitry in the dashed box will be called *detector* of the system, the nonlinear blocks represent power detectors.

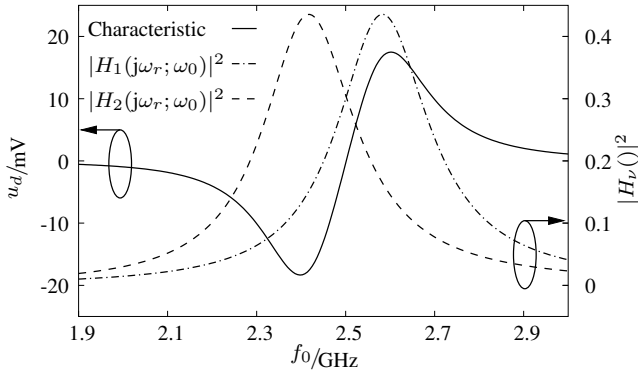


Fig. 2. Magnitude response of the detuned filters and resulting detector characteristic for a linear tuning characteristic of the filter. The passband of the slave filter is around f_0 . Parameters: $f_0 = \omega_0/2\pi$, $f_r = \omega_r/2\pi = 2.5$ GHz, $A = 0.66$, $Q_0 = 10$, $\omega_{0,0} = 2\pi \cdot 2.25$ GHz, $k_f = 1.3 \cdot 10^9$ rad/Vs, $k_p \hat{u}_r^2 = 75$ mV, $u_{\varepsilon,2} = -u_{\varepsilon,1} = 0.4$ V, $H_\nu(j\omega_r; \omega_0) = H(j\omega_r; \omega_0 + \omega_{\varepsilon,\nu})$.

filter to close the loop.

The sinusoidal reference signal $u_r(t) = \hat{u}_r \cos(\omega_r t)$ with angular frequency ω_r is applied to both tunable master filters (1 and 2) that have the same properties as the slave filter. Throughout the analysis a second-order band pass filter will be assumed:

$$H(p; \omega_0) = \frac{A \frac{p}{\omega_0 Q_0}}{1 + \frac{p}{\omega_0 Q_0} + \frac{p^2}{\omega_0^2}} \quad (1)$$

with A being the gain at centre frequency, $Q_0 = \omega_0/\Delta\omega_0$ and $\Delta\omega_0$ (in rad/s) the relative angular frequency bandwidth at -3 dB. The relation between the centre angular frequency and the tuning voltage is assumed to be linear for the moment. It is given by $\omega_0(t) = \omega_{0,0} + k_f u_0(t)$ with the VCF conversion factor k_f (in rad/Vs) and the quiescent angular frequency $\omega_{0,0}$.

The master filters are detuned compared to the slave filter by the voltages $u_{\varepsilon,1}$, $u_{\varepsilon,2}$. For a linear tuning characteristic of the filters the detuning is proportional to the offset voltages:

$$\omega_{0,\nu} = \omega_{0,0} + k_f(u_0 + u_{\varepsilon,\nu}) = \omega_0 + \omega_{\varepsilon,\nu}, \quad (2)$$

$$\omega_{\varepsilon,\nu} = k_f u_{\varepsilon,\nu}, \quad \nu \in \{1, 2\}. \quad (3)$$

The power of the filtered reference signals is converted to proportional DC signals that are subtracted. The power detectors are modelled by $u_{d,\nu} = k_p \hat{u}_{f,\nu}^2$ with k_p (in 1/V) being a proportionality constant of the power detector.

Fig. 2 exemplifies the principle. The characteristic of the detector has the typical S-shape of a phase sensitive detector. The zero crossing is close to the reference frequency.

B. New detector structure

Fig. 3 shows the block circuit diagram of the improved detector structure. Instead of two detuned master filters there is only one filter that is successively detuned to an upper and to a lower passband frequency compared to the slave. The power of the filtered signal is converted to a proportional voltage and stored in the sample and hold circuits S/H. The rest of the control loop is like in Fig. 1.

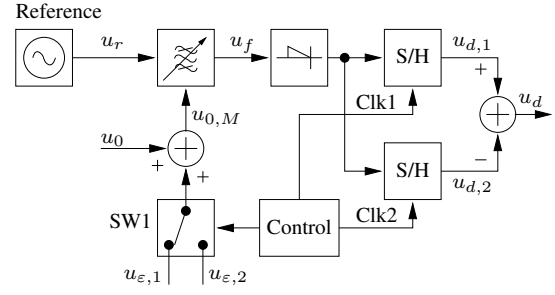


Fig. 3. Block circuit diagram of the improved detector structure.

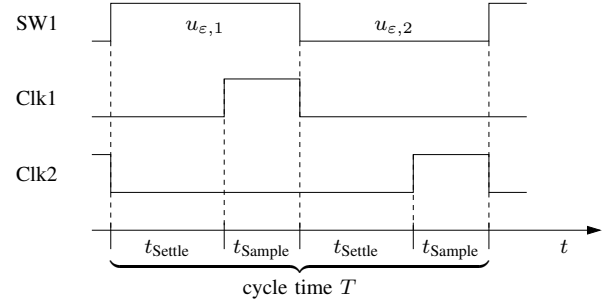


Fig. 4. Timing diagram of the improved detector circuit (Fig. 3). The sample and hold stages are activated with a delay of t_{Settle} after the tuning voltage is switched by SW1 to give the filter, the detector and the baseband signal processing time to settle to the new state.

The timing of the switch and the sample and hold circuits is shown in Fig. 4. After the switch SW1 has changed the control voltage of the filter, there is a short delay t_{Settle} before the data is sampled to give the filter, the detector and the baseband signal processing time to settle to the new state. The delay avoids additional spurious responses in the control loop due to transient terms.

The multiplexed operation of the detector converts the time continuous control system into a sampled system. As long as the sampling frequency is much higher than the bandwidth of the loop it can be expected to operate similar to the analog system. If that condition is not fulfilled it is necessary to take the time discrete behaviour into account.

C. Time discrete system

Fig. 5 shows a simplified baseband model of the time discrete control system. It is simplified as compared to Fig. 3 insofar as the interleaved sampling of the two sample and hold circuits is modelled as a sampling at the same time instance.

In the following analysis all variables and functions of the discrete time μ will be denoted by a tilde. The

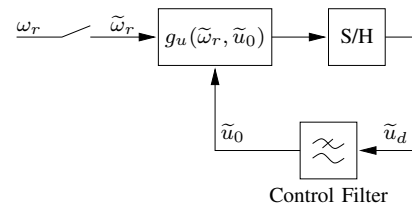


Fig. 5. Baseband model of the time discrete system. The block labelled by $g_u(\tilde{\omega}_r, \tilde{u}_0)$ models the detector circuit.

conjunction to the time continuous quantities is given by

$$\tilde{u}(\mu) = u(t = \mu T). \quad (4)$$

The function block $g_u(\tilde{\omega}_r, \tilde{u}_0)$ models the baseband behaviour of the detector in the dashed box of Fig. 1. Its input quantities are the sampled reference angular frequency $\tilde{\omega}_r$ and the tuning voltage \tilde{u}_0 . This relation holds true, no matter if the signals are time discrete or time-continuous, as long as the settling of the master filter can be neglected. The detector output signal is sampled at equally spaced time intervals T and held constant for the rest of the interval. Even though the control filter is still a time continuous filter, the loop can be analysed as a time discrete system [8].

The analysis follows the procedure described in [5]. Again the tuning characteristic of the filter is approximated by a square root function

$$\omega_0 = v(u_0) = 2\pi \cdot 10^9 \frac{1}{s} \left(c_0 + c_1 \sqrt{\frac{u_0}{V}} \right). \quad (5)$$

For the control filter, an ideal integrator is assumed with the transfer function

$$H_{\text{RF}}(p) = \frac{b_0}{p} \quad (6)$$

in the Laplace domain.

All the signals in the baseband model are constant in the steady state. The sampling does not alter the static behaviour in any way, hence the results of the time continuous analysis hold true here as well.

It has been shown previously that the steady states, also called *operating points (OP)* of the control system, are given by the zero crossings of the characteristic $g_u(\omega_r, u_0)$.

The stability behaviour of the steady states is determined using a model that is linearised in the vicinity of the operating point, in which

$$K_v = \left. \frac{\partial g_u}{\partial u_0} \right|_{\text{OP}} \quad (7)$$

is the slope of the characteristic in the OP.

The z-transform of the time discrete impulse response of the system is given by

$$\tilde{H}_s(z) = \frac{K_v \tilde{H}_{\text{RF}}(z)}{1 - K_v \tilde{H}_{\text{RF}}(z)} = \frac{K_v b_0 T}{z - 1 - K_v b_0 T}, \quad (8)$$

hence a stable operating point is achieved for

$$-2 < K_v b_0 T < 0. \quad (9)$$

In the time continuous case the stability condition was $K_v b_0 < 0$. The sampling adds an upper limit to the gain in the loop.

A vivid interpretation of the stability boundaries is given by the time discrete step response of the linearised system:

$$\tilde{h}_s(\mu) * \tilde{\varepsilon}(\mu) = \left((1 + K_v b_0 T)^\mu - 1 \right) \tilde{\varepsilon}(\mu) \quad (10)$$

with $\tilde{\varepsilon}(\mu)$ being the unit step function.

For $-1 < K_v b_0 T < 0$ the sequence approaches the final value monotonously, while for $-2 < K_v b_0 T < -1$ it is an alternating sequence. The shortest settling could be achieved for $K_v b_0 T = -1$, but as the parameter K_v

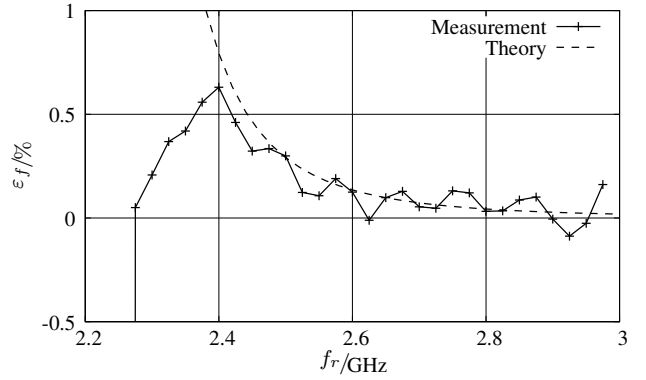


Fig. 6. Relative frequency error in the steady state. Comparison between the analytical and the measured results. Below the reference frequency $f_r = 2.35$ GHz the system does not operate correctly as the tuning voltage of the filter is negative for parts of the cycle. Parameters: $f_0 = \omega_0/2\pi$, $f_r = \omega_r/2\pi$, $\varepsilon_f = f_0/f_r - 1$, $A = 0.66$, $Q_0 = 10$, $k_p \hat{u}_r^2 = 75$ mV, $b_0 = -3.1 \cdot 10^4$ s $^{-1}$, $T = 18$ μ s, $u_{\varepsilon,2} = -u_{\varepsilon,1} = 0.4$ V, $c_0 = 2.1561$, $c_1 = 0.3392$.

slightly depends on the operating point the condition cannot be met exactly in every point. Nevertheless it is a good value for the loop gain.

The results of the theoretical analysis were confirmed in a simulation using Matlab/Simulink[®]. Additionally the time-interleaved sampling that was not considered in the theoretical analysis was also included in the simulations. The system showed stable behaviour within the predicted range of values. It stayed even stable for slightly larger values of $|K_v b_0 T|$.

III. MEASUREMENTS

A system was implemented to validate the analytical results. The filter was built up as a first order parallel coupled filter with a varactor diode in the middle of the resonator using microstrip technology.

The filter is tunable in a range from 2.2 GHz to 3 GHz. It has a quality factor of $Q_0 = 10$ and 3.6 dB attenuation in the passband at 2.5 GHz.

The parameter $k_p \hat{u}_r^2 = 75$ mV that was used in the analysis was derived from the realised system at an input power level of -7 dBm with $f_r = 2.5$ GHz. It was $u_{\varepsilon,2} = -u_{\varepsilon,1} = 0.4$ V resulting in a detuning of the filters by 140 MHz.

The power detector was built up using a zero bias Schottky diode and a transmission line matching network.

The minimum cycle time T was primarily dictated by the speed of the operational amplifiers and the sample and hold circuit in the baseband signal processing. It was chosen to $T = 18$ μ s, the parameter b_0 was chosen in order to obtain $K_v b_0 T \approx -1$.

Fig. 6 shows the relative frequency deviation

$$\varepsilon_f = \frac{f_0 - f_r}{f_r} \quad (11)$$

of the measurement together with the results of the theoretical analysis. Above of the reference frequency $f_r = 2.4$ GHz theory and measurement are in good agreement. The deviations at lower frequencies have two reasons. First, the simple square root approximation from

eq. (5) does not reflect the behaviour of the filter well enough for small tuning voltages u_0 . Secondly, below $f_r = 2.35$ GHz the tuning voltage of the master filter becomes negative during parts of the cycle due to the offset voltage $u_{\varepsilon,1}$. Operation is not useful in that region because the varactor diode is biased in forward direction.

The tuning voltage u_0 is used to steer the centre frequency of the slave filter. Some attention has to be paid to the proper rejection of spurious clock signals as they could interact with the wanted filtered signal.

IV. CONCLUSION

In this paper an improved magnitude sensitive detector structure for an automatic frequency control system for tunable filters was proposed. It provides the same properties as the system presented in [6] with reduced complexity. It requires only one master filter and one power detector at microwave frequencies, the rest of the control loop operates at baseband frequencies.

During normal operation there is always the same power level applied to the power detector. Hence nonlinearities in its conversion behaviour do not affect the precision of the control system. Furthermore, its behaviour does not have to be matched to a second device.

The analysis predicts a good performance of the system. Measurements at microwave frequencies confirm the theoretical results.

REFERENCES

- [1] Y. P. Tsividis and J. O. Voorman, Eds., *Integrated continuous-time filters*. IEEE press, New York, 1993.
- [2] P. Katzin, B. Bedard, and Y. Ayasli, "Narrow-band MMIC filters with automatic tuning and Q-factor control," in *IEEE MTT-S International Microwave Symposium Digest 93*, 1993, pp. 403–406.
- [3] V. Aparin and P. Katzin, "Active GaAs MMIC band-pass filter with automatic frequency tuning and insertion loss control," *IEEE Journal of Solid-State Circuits*, vol. 30, no. 10, pp. 1068–1073, 1995.
- [4] S. Quintanel, H. Serhan, L. Billonnet, B. Jarry, and P. Guillon, "Theoretical and experimental analysis of automatic frequency control techniques for microwave active filters," in *EuMC Conference Proceedings*, October 2000, pp. 47–50.
- [5] E. Neber, S. Quintanel, L. Billonnet, B. Jarry, and M. H. W. Hoffmann, "Analysis of an automatically tuned filter and its application at microwave frequencies," in *EuMC Conference Proceedings*, October 2003, pp. 915–18.
- [6] E. Neber, L. Billonnet, B. Jarry, and M. H. W. Hoffmann, "Novel detector structure for automatically tuned filters at microwave frequencies," in *IEEE Transactions on Microwave Theory and Techniques Symposium*, 2004, pp. 1963–66.
- [7] H. Liu and A. İ. Karşıluyan, "An accurate automatic tuning scheme for high-Q continuous-time bandpass filters based on amplitude comparison," *IEEE Transactions on Circuits and Systems – II: Analog and Digital Signal Processing*, 2003.
- [8] J. van de Vegte, *Feedback Control Systems*. Prentice-Hall, 1986.

A Fully-Differential 2 GHz Tunable Recursive Bandpass Filter on Silicon

Sébastien Darfeuille¹, Zoheir Sassi¹, Bruno Barelaud¹, Laurent Billonnet¹, Bernard Jarry¹,
Hervé Marie², Nguyen Tran Luan Le², Patrice Gamand²

¹IRCOM, UMR CNRS 6615, University of Limoges, 123 Avenue Albert Thomas, 87060 Limoges cedex, France

²Innovation Centre RF, Philips Semiconductors, 2 Rue de la girafe, 14079 Caen cedex, France

Email : sebastien.darfeuille@ircom.unilim.fr

Abstract — In this paper, we present a novel fully-differential active integrated bandpass filter employing recursive principles. This circuit, based upon the cascade of two elementary recursive stages, can be tuned independently in terms of centre frequency, selectivity and gain. The chip surface is less than 1.4 mm². Centre frequency can be tuned in the 1.7 to 2.4 GHz range, bandwidth can be set to less than 60 MHz and gain can be up to 20 dB. This chip has been implemented using Philips QUBIC4 Si BiCMOS technology [1].

I. INTRODUCTION

Off-chip passive filters are nowadays the most frequently implemented solution in RF receivers front-ends. However, the main drawback with that kind of filters is that they are often expensive and occupy an important surface.

An interesting alternative could be the use of active filters associating in a single circuit a bandpass filter and a low-noise amplifier, thus leading to more compact and lower cost circuits. Another advantage is that, as they are realised with the same technology, these filters can be easily integrated with the other functions of the transceivers (mixer, ...). Moreover, they often exhibit a frequency tunability that could help to reduce the number of required elements in multi-standard equipments that are being generalised more and more each day. This aspect is also interesting to realise automatically tuned structures [2]. In this article, we propose an original tunable recursive filter integrated using a silicon MMIC process and based on the cascade of two elementary recursive stages.

II. THEORETICAL BACKGROUND

The concept of recursive filters has been mainly developed at low frequencies for digital applications. However, as demonstrated in [3], it can also be applied to microwave analogue filters.

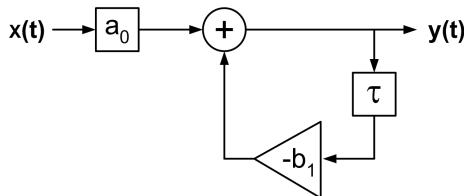


Fig. 1. Block diagram of a first-order recursive filter

Fig. 1 presents the flow graph of a first-order recursive filter, driven by the following time-domain equation :

$$y(t) = a_0 x(t) - b_1 y(t - \tau) \quad (1)$$

which leads to the corresponding transfer function :

$$H(f) = \frac{a_0}{1 + b_1 e^{-j2\pi f\tau}} \quad (2)$$

The topology proposed here relies on the cascade of two first-order recursive cells, as can be seen in Fig. 2.

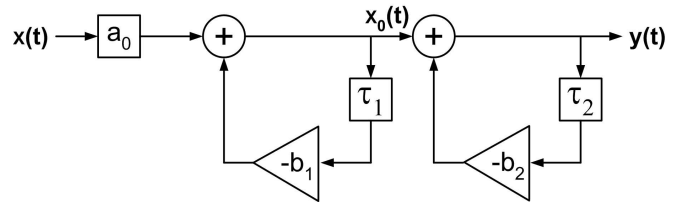


Fig. 2. Block diagram of the cascaded recursive filter

The main advantage of this kind of structure is that it permits to realise, with only two branches, a recursive filter that would require three branches with a more classical ladder implementation, as can be seen in Fig. 3.

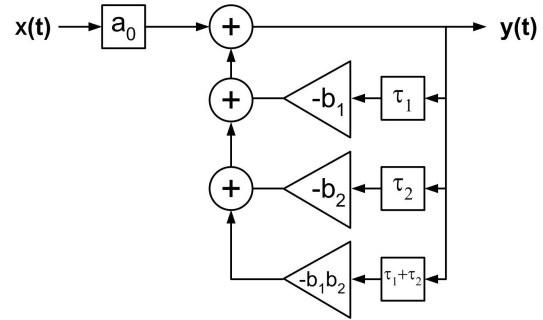


Fig. 3. Block diagram of the equivalent ladder configuration

The obtained transfer function is depicted by [4] :

$$H(f) = \frac{a_0}{1 + b_1 e^{-j2\pi f\tau_1} + b_2 e^{-j2\pi f\tau_2} + b_1 b_2 e^{-j2\pi f(\tau_1 + \tau_2)}} \quad (3)$$

Then, if the delay times are chosen identical ($\tau_1 = \tau_2 = \tau$), it is possible to achieve a typical second-order recursive filter response with amplifiers of respective gains $b_1 + b_2$ and $b_1 b_2$.

$$H(f) = \frac{a_0}{1 + (b_1 + b_2) e^{-j2\pi f\tau} + b_1 b_2 e^{-j4\pi f\tau}} \quad (4)$$

III. IMPLEMENTATION

The chosen topology for the differential first-order cells is derived from [5], with the delay cell inserted within the feedback branch.

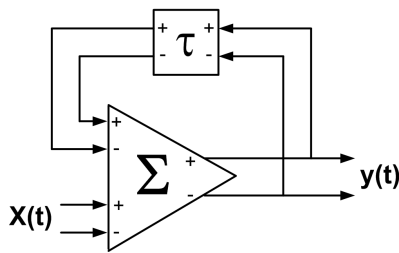


Fig. 4. Principle scheme of an elementary stage

The use of a passive delay section achieving a 180° phase shift has been preferred to an active solution - even considering the important size of the inductors - as it allows to reduce the global power consumption which is a critical point in our application where two of these delays are required. Varactor diodes controlled by two independent voltages allow to control the objective delay in each cell.

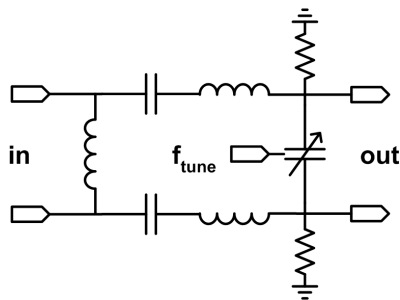


Fig. 5. Tunable passive delay electrical scheme

The circuit used for amplification and summation is derived from the adders presented in [5] and [6] and is presented in Fig. 6. The use of a cascode topology for the direct input (in_1 in Fig. 6) exhibits better noise performances than a common-base one, whereas for feedback input (in_2 in Fig. 6) a classical differential amplifier topology including a gain control with a current-mirror is used.

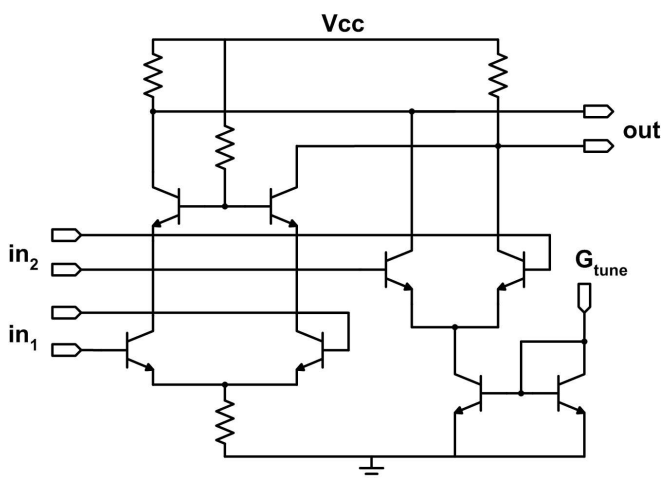


Fig. 6. Simplified electrical scheme of the amplifier/adder

Finally, a buffer stage (see Fig. 7) derived from the cascode amplifier of the adder is cascaded at the output. It permits to set the global gain of the structure. Indeed, the base resistance of the cascode transistors of the adder has here been replaced with a PMOS transistor. Thus, by controlling the gate voltage, it is possible to set the gain of this stage and, as a consequence, of the whole filter.

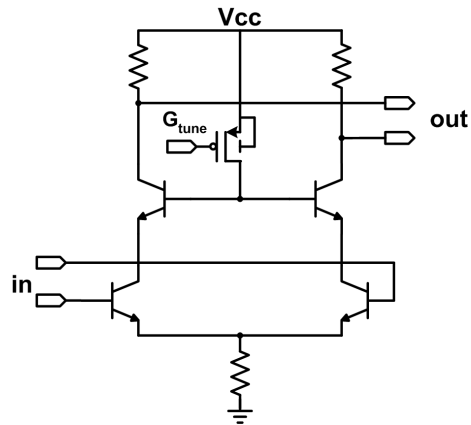


Fig. 7. Simplified electrical scheme of the output buffer

The use of tunable structures for all the elements in the circuit gives more flexibility in the response shape. Indeed, it is possible to control independently the centre frequency (by acting on the delay elements), the bandwidth (by acting on the gain of the feedback input of the adders), and finally the global gain (with the output buffer).

The chip surface is $1.05 \times 1.3 \text{ mm}^2$. On the layout presented in Fig. 8, the two passive delays can be easily identified at the top-left and bottom-right as they are the most space consuming components due to the use of inductors (each delay occupies a surface of about $600 \times 550 \mu\text{m}^2$). In general, chip dimensions is a highly critical point due to the price of the substrate. Here, to keep an acceptable surface for the global circuit, the other parts (adder and buffer) are inductorless.

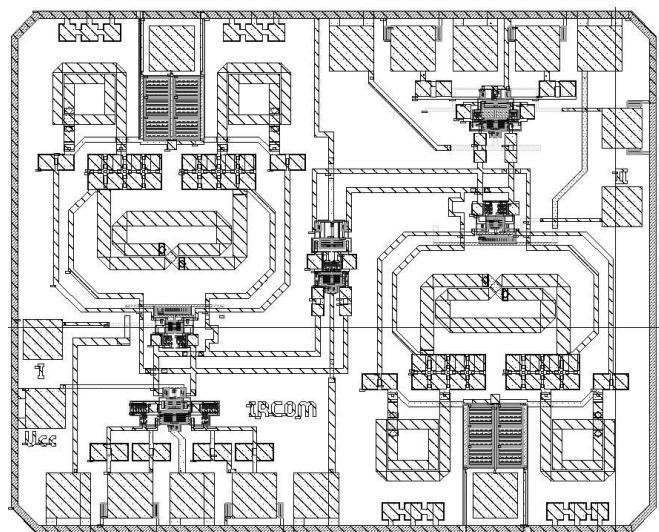


Fig. 8. Layout of the circuit

IV. SIMULATION RESULTS

The circuit is being processed at the foundry. Measurements will be available at the conference.

As can be seen in Fig. 9, this filter can be tuned in the 1.7 to 2.4 GHz range.

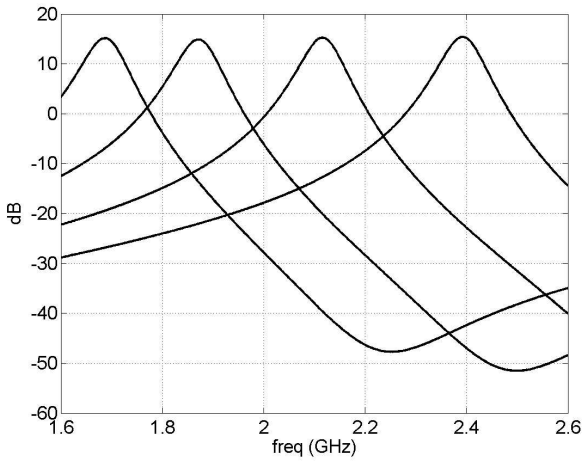


Fig. 9. Simulated gain

For all the centre-frequencies, it is possible to obtain a gain of 15 dB and a 60 MHz bandwidth. These values of gain and selectivity are not the best achievable and can still be decreased or increased to fit specific performances. Moreover, as illustrated in Fig. 10, it is possible, by setting different delays for the two subcircuits ($\tau_1 \neq \tau_2$), to obtain a different response shape (for example if a flatter response is desired in the bandwidth). However, in this case, selectivity is generally worse than when the delays are chosen identical ($\tau_1 = \tau_2$).

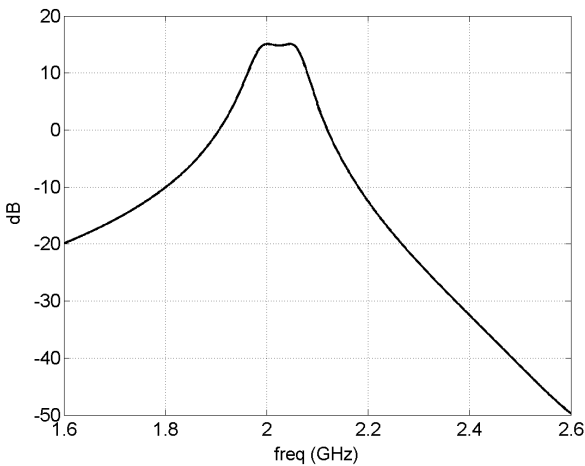


Fig. 10. Simulated gain with a quasi-flat response shape

Depending on the centre frequency, and for a typical 15 dB gain and 60 MHz bandwidth, noise figure varies between 3.6 and 5.5 dB, and output-referred -1 dB compression point between -36 and -26 dBm. This last parameter is the main drawback of this circuit and is due to the important number of active cascaded sub-cells.

For a nominal 2.7 V biasing and in the same conditions as previously, power consumption varies between 35 and 50 mW.

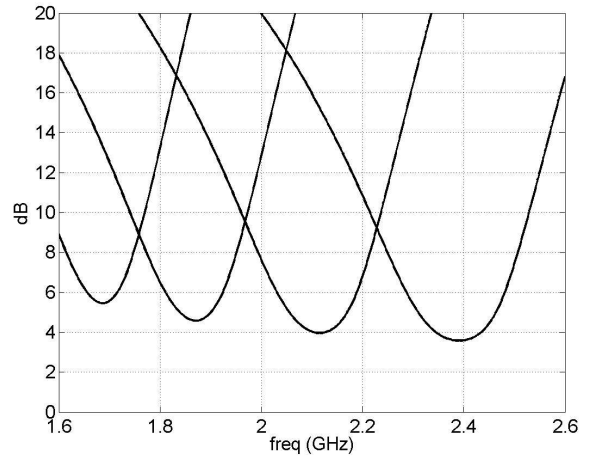


Fig. 11. Simulated noise figure for various centre frequencies

Thanks to the presence of the amplifier at the input and of the buffer at the output of the circuit, S_{11} and S_{22} responses are quasi-independent of the different tuning parameters. In any case, in the 1.7 - 2.4 GHz range, they are less than -9.5 dB for S_{11} and -14.5 dB for S_{22} . This value of S_{11} can be explained by the fact that, for the chosen inductorless adder topology, it is impossible to obtain simultaneously noise and power matching over a wide frequency band [7]. A compromise has thus been made between these two parameters. Concerning S_{22} , the value is directly driven by the value of the resistances placed between the collectors of the output buffer cascode transistors and the global bias V_{cc} (see Fig. 7).

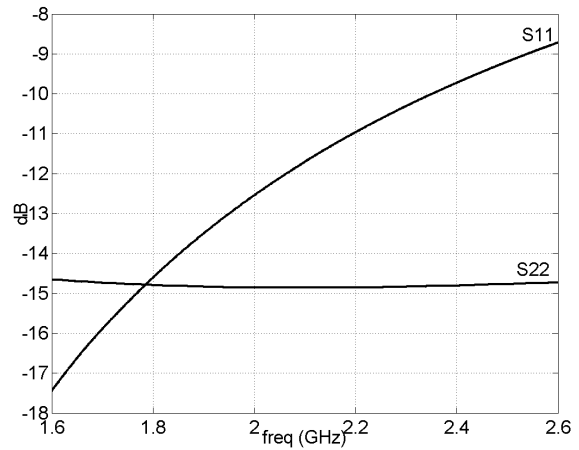


Fig. 12. Simulated matching parameters

All the S -parameters presented here are fully-differential mode S -parameters obtained using mixed-mode analysis method [8]. They correspond to the results that would be obtained if 50 Ω -baluns were used at the input and output of the circuit.

As can be seen in Fig. 13, common-mode gain is always lower than -20 dB, which leads to a more than 35 dB common-mode rejection ratio at the centre frequency. All

V. CONCLUSION

In this article, we have presented an original differential tunable recursive filter. This circuit performs a simulated gain of 15 dB with a 60 MHz bandwidth at centre frequencies ranging between 1.7 and 2.4 GHz. In these conditions and depending on the centre frequency chosen, power consumption ranges between 35 and 50 mW for a supply voltage of 2.7 V. Simulated noise figure is about 3.6 to 5.5 dB at the centre frequency. P_{-1dB} is reached for an output power of -36 to -26 dBm. Chip dimensions are $1.05 \times 1.30 \text{ mm}^2$.

ACKNOWLEDGEMENT

The authors wish to acknowledge R&D Department of Philips Semiconductors Caen for their assistance during the conception of the circuit, and the realisation of the chip.

REFERENCES

- [1] D. Szymd, R. Brock, N. Bell, S. Harker, G. Patrizi, J. Fraser and R. Dondero, "QUBIC4 : a silicon RF-BiCMOS technology for wireless communication ICs", *Proceedings of the 2001 bipolar/BiCMOS Circuits and Technology Meeting*, pp. 60–63.
- [2] E. Neber, L. Billonnet, B. Jarry and M. H. W. Hoffmann, "Novel detector structure for automatically tuned filters at microwave frequencies", *2004 IEEE MTT-S International Microwave Symposium Digest*, vol. 3, pp. 1963–1966.
- [3] C. Rauscher, "Microwave active filter based on transversal and recursive principles", *IEEE Transactions on Microwave Theory and Techniques*, vol. 33, no 12, dec. 1985, pp. 1350–1360.
- [4] M. Delmond, L. Billonnet, B. Jarry and P. Guillon, "High-Order Monolithic Active Recursive Filter Based Upon Multicellular Approach", *IEEE MTT-S International Microwave Symposium Digest*, 17-21 June 1996, vol. 2, pp. 623–626.
- [5] S. Andersson, P. Caputa and C. Svensson, "A Tuned, Inductorless, Recursive Filter LNA in CMOS", *Proceedings of the ESSCIRC 2002 conference*, Florence, Italy, 24-26 Sep 2002, pp. 351–354.
- [6] R. Tao and M. Berroth, "Monolithically Integrated 5Gb/s CMOS Duobinary Transmitter for Optical Communication Systems", *2004 IEEE Radio Frequency Integrated Circuits (RFIC) Symposium*, Digest of papers, pp. 21–24.
- [7] T. K. Nguyen, C. H. Kim, G. J. Ihm, M. S. Yang and S. G. Lee, "CMOS Low-Noise Amplifier Design Optimization Techniques", *IEEE Transactions on Microwave Theory and Techniques*, vol. 52, no. 5, May 2004, pp. 1433–1441.
- [8] D. Bockelman and W. Eisenstadt, "Combined differential and common-mode scattering parameters: theory and simulation", *IEEE Transactions on Microwave Theory and Techniques*, vol. 43, no. 7, July 1995, pp. 1530–1539.

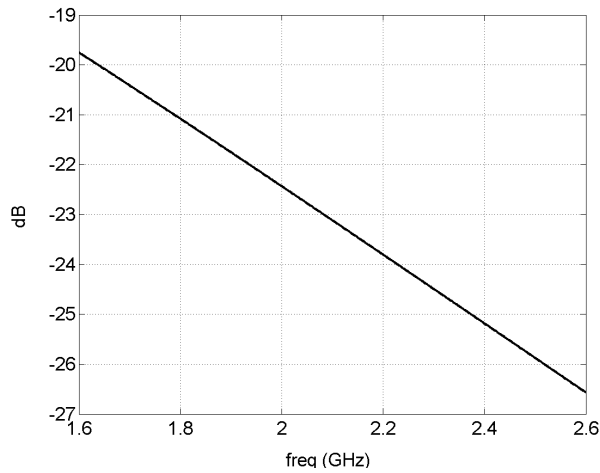


Fig. 13. Simulated common-mode gain

Conversion modes (i.e. differential-to-common and common-to-differential modes) S -parameters were found to be lower than -40 dB at any frequency, meaning that the topology is quite insensitive to electromagnetic interferences (which are typically of the common-mode type).

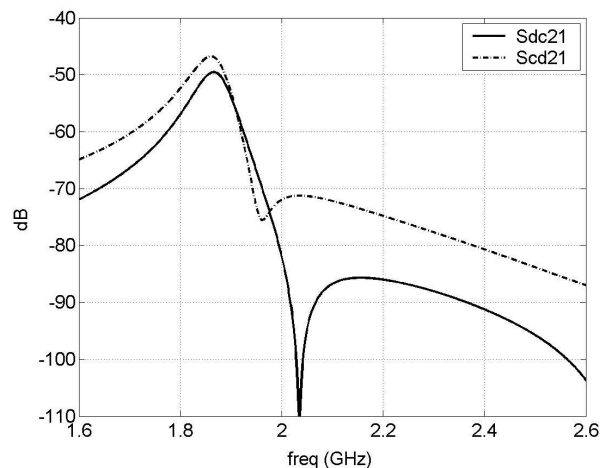


Fig. 14. Simulated common-to-differential and differential-to-common gains

Transversal Notch Filter Design using Recursive Principles in MMIC Technology

B. Albert, L. Billonnet and B. Jarry

IRCOM – UMR CNRS 6615 - University of Limoges
123, Albert Thomas - 87060 Limoges Cedex - FRANCE
e-mail : benoit.albert@ircom.unilim.fr

Abstract — In this paper, a new transversal active notch filter is presented. Basic principle consists in combining the signals coming from two branches, one of which includes a band-pass active filter. The transversal combination leads to a bandstop response. The use of a passive branch enables a minimum noise power in the passbands. For the band-pass filter, we have chosen a recursive topology that uses the same weighting and power combination/division principles. We first present the theoretical background of the transversal filter. We show how, with analytical tools, the response can be achieved while optimising the noise performance of the global filter.

Index Terms — transversal filter, recursive filter, power combiners/dividers, notch filter, noise optimisation.

I. INTRODUCTION

Compared to passive structure, active filters provide many advantages among which, small size with high selectivity response. Another positive aspect is that most of the topologies can provide frequency tuneable responses. Nevertheless, when introducing active elements, new parameters must be taken into account [1] such as electrical stability, power handling behaviour, and noise performances. In most cases, active techniques have been recently applied to band-pass filtering functions. The objective here is to design a notch filter using a transversal approach [2][3]. In comparison to previous studies, response and noise figure are derived by analytical means using the noise-wave formalism [4].

II. TRANSVERSAL NOTCH FILTER PRINCIPLE

A. Theoretical background

Our work is derived from the circuits presented in [2] and [3] by Rauscher (Fig. 1). The chosen topology uses two power dividers, to combine the signals coming from a low-noise passive branch and from an active band-pass filter branch.

Notch response at a desired centre frequency is obtained by a destructive transversal combination of signals from the two branches (Fig. 2).

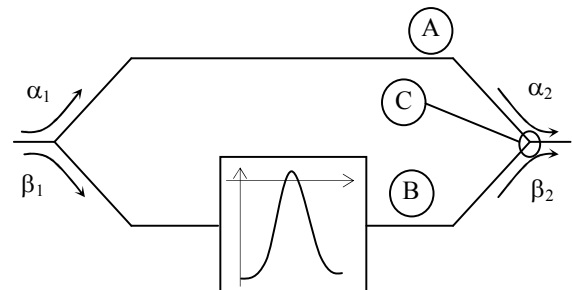


Figure 1. Stop-band filter topology

Relative phase and magnitude levels of the two branches are analytically calculated to perform a zero at centre frequency f_0 in the transmission response.

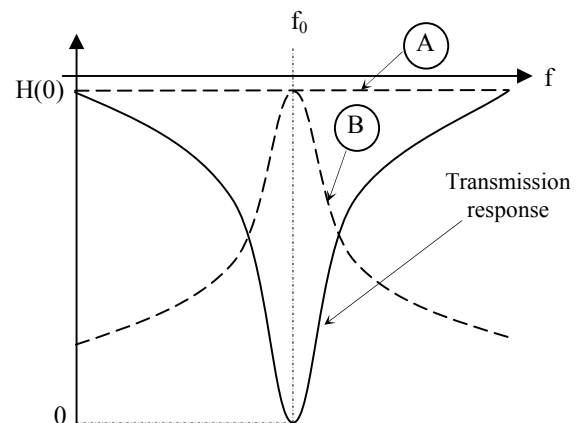


Figure 2. Notch response principle

In the passbands of the global transversal filter response (i.e. apart from the centre frequency), noise contribution is mainly due to the noise generated in the passive branch, thus leading to a low noise figure. In the rejected frequency band (at centre frequency), noise at the output of the filter is mainly due to the active band-

pass filter but for a frequency where the transmission level of the filter response is minimum.

Thanks to the use of the noise wave formalism introduced by Wedge in [4], the analytical expression of noise figure enables an easy numerical optimisation of the combiners/dividers values of the structure to achieve a minimum noise figure in the passbands.

B. Analytical study of the active notch filter

A critical step in the design has been to choose an adequate band-pass filter topology. Keeping in mind the transversal approach of the global filter, we then use here a first-order recursive filter for the band-pass filter. This filter can then use the same power divider/combiner elements in association to a low-noise amplifier. Global filter structure is presented in Fig. 3.

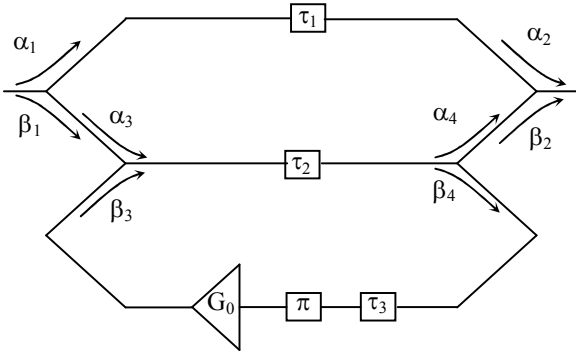


Figure 3. Topology of the active notch filter

Corresponding filter response $H(f)$, where V characterises the selectivity of the recursive filter response, is:

$$H(f) = \alpha_1 \alpha_2 e^{-2j\pi f \tau_1} + \frac{\alpha_3 \alpha_4 \beta_1 \beta_2 e^{-2j\pi f \tau_2}}{1 + G_0 \beta_3 \beta_4 e^{-2j\pi f (\tau_2 + \tau_3)}} \quad (1)$$

$$= e^{-2j\pi f \tau_2} \left(\alpha_1 \alpha_2 e^{-2j\pi f \tau} + \frac{\alpha_3 \alpha_4 \beta_1 \beta_2}{1 + V e^{-2j\pi f \tau}} \right)$$

Due to the passband behaviour of the response at $f=0$, the periodicity of the transversal response is set to:

$$\Delta f = 2f_0 = \frac{1}{\tau}$$

At this step, the design process consists in imposing the notch depth and the rejected bandwidth of the transversal filter. To perform a zero at the centre frequency, expression (1) is used at $f = f_0$ as:

$$|H(f_0)| = -\alpha_1 \alpha_2 + \frac{\alpha_3 \alpha_4 \beta_1 \beta_2}{1 - V} = 0 \quad (2)$$

$$\text{with } \beta_i = \sqrt{1 - \alpha_i^2}$$

From (2), a first coupling value can be extracted, for example α_1 , as an expression of the other filter parameters:

$$\alpha_1 = \text{fn}(\alpha_3, \alpha_4, \alpha_2, \beta_2, V) \quad (3)$$

Then, by imposing the desired rejected bandwidth S , the selectivity of the recursive part can be numerically found. Considering that $V = \beta_3 \beta_4 G_0$ (1), another coupling expression can be extracted. For example:

$$\beta_3 = \frac{V}{\beta_4 G_0} \quad (4)$$

At this step, the only unknowns are the two last coupling values that can be scanned by numerical means to achieve the smallest noise figure of the structure.

As an example, we try to design a low-noise bandstop filter of rejected bandwidth $S=1\%$ of f_0 . The LNA used for the active recursive filter branch performs a gain $G_0=12.3$ dB at the centre frequency of the filter with an associated noise figure $NF=2.2$ dB. The passive branch is chosen as a simple passive transmission line achieving the adequate delay-time in the upper branch (Fig. 3). Synthesis process then gives the following coupling values:

$$\alpha_1 = -2.853 \text{ dB} \quad \alpha_2 = -.087 \text{ dB} \quad (5)$$

$$\alpha_3 = -.259 \text{ dB} \quad \alpha_4 = -19.17 \text{ dB}$$

Corresponding transfer function, and noise figure results are :

$$|H(0)| = -2.88 \text{ dB} \quad |H(f_{-3\text{dB}})| = -5.89 \text{ dB} \quad (6)$$

$$|NF(0)| = 2.88 \text{ dB} \quad |NF(f_{-3\text{dB}})| = 8.50 \text{ dB}$$

III. MMIC IMPLEMENTATION

To validate the theoretical approach, we have implemented a low-noise notch transversal filter in MMIC technology, using the OMMIC ED02AH process [5]. Layout of the filter is presented in Fig. 4. Lange couplers of adequate length and coupling values are used to realise the combination/division components.

Fig. 5 presents the simulated S_{21} parameter and noise figure of the transversal notch filter response.

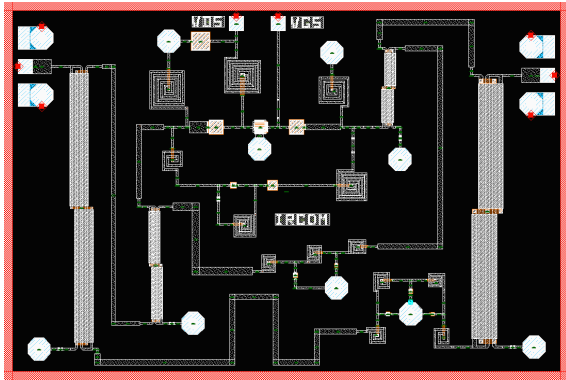


Figure 4. Layout of the transversal filter

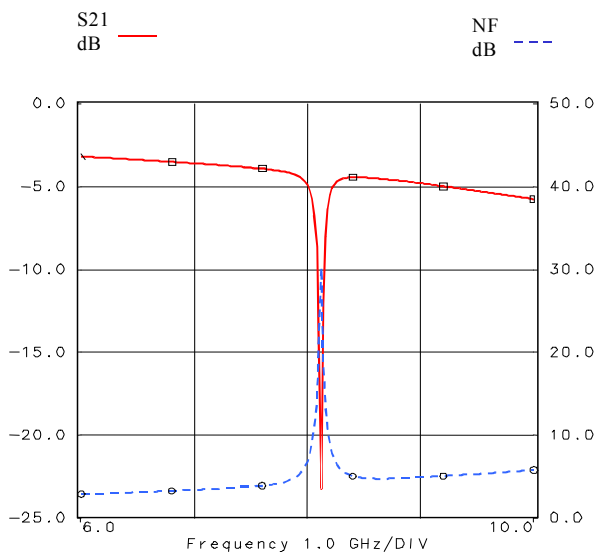


Figure 5. Simulated S_{21} and noise figure

Transmission level at 6 GHz is around -3.17dB . Noise figure at the same frequency is around 2.92dB , clearly showing that, in the passbands, noise is mainly due to the passive branch. At $f_{3\text{dB}}$, transmission level is around -6.17dB with an associated noise figure around 9.9dB . The rejected bandwidth is around 130MHz ($S=1.6\%$ of f_0). Even if differences are observed at $f_{3\text{dB}}$, in terms of transmission and noise figure levels, the performances are as scheduled at notch frequency. These differences are simply due to the frequency response of the Lange couplers that performs non-constant coupling levels as used in the theoretical approach. The immediate consequence is that it is not possible to evaluate the maximum level of the response, and then, to evaluate the frequencies that define the rejected band. Moreover, whereas lossless components were considered in the analytical approach, differences can also arise from losses in the transmission lines and the couplers modifying both the recursive and transversal combination levels.

Fig. 6 presents the S_{11} and S_{22} parameters which, are less than -10dB in the 6 to 10 GHz range.

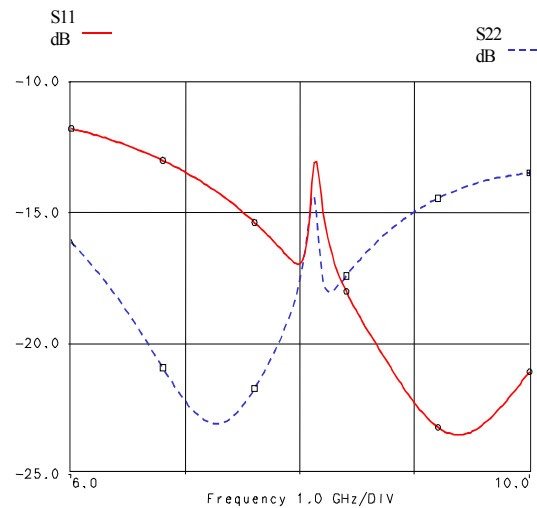


Figure 6. Simulated S_{11} and S_{22} parameters.

Stability conditions have been verified with both plots of K and B in the frequency range from 0 to 30 GHz and with the NDF plot.

IV. EXTENDED TRANSVERSAL FILTER STRUCTURE

To extend the concept of the transversal filter, a second LNA is added in the upper branch (Fig. 7), in order to obtain gain in the band pass. A theoretical optimisation of the new structure is performed. The objective is to improve the noise figure of the circuit for the same selectivity. Fig. 7 presents the new notch filter topology with two LNAs within the structure.

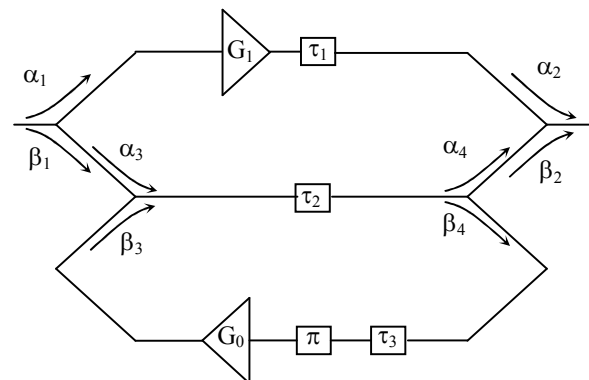


Figure 7. Active notch filter topology with two LNAs

A numerical optimisation is done to achieve a relative rejected bandwidth of $S=1\%$ of f_0 , with the lowest noise figure in the passbands. LNAs used in the recursive filter branch, and in the upper branch of the transversal part perform a gain of $G_i=12.3\text{dB}$ with an associated noise

figure $NF_i=2.2\text{dB}$. Synthesis process gives the following coupling values:

$$\begin{aligned} \alpha_1 &= -2.32\text{dB} & \alpha_2 &= -1.01\text{dB} \\ \alpha_3 &= -.28\text{dB} & \alpha_4 &= -17.08\text{dB} \end{aligned} \quad (7)$$

Fig. 8 presents the simulated transfer function and noise figure of the two-LNA topology.

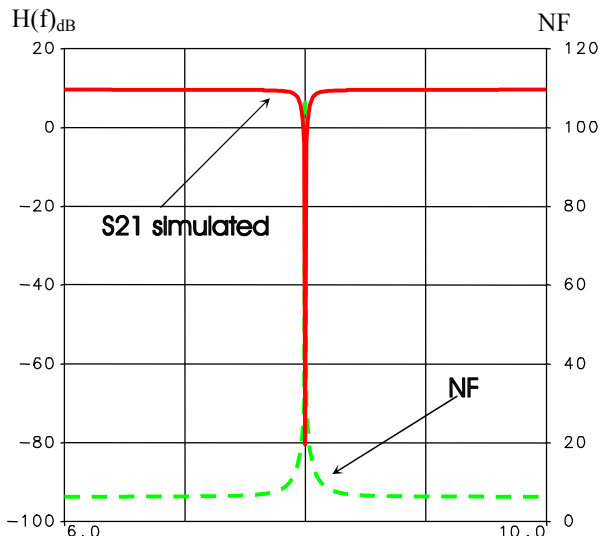


Figure 8. Simulated S_{21} and NF parameters of the two LNA transversal filter.

Transmission level is around 8.51dB at 6GHz with an associated noise around 4.5 dB. At $f_{3\text{dB}}$ frequency, transmission level is around 5.72 dB with an associated noise figure of 9.53 dB.

In order to implement this notch filter structure in MMIC technology, the size of each element has to be optimised, particularly the size of the power combiners/dividers. Active power combiners/dividers could then be used. Moreover, these new active couplers could include the amplification function.

V. CONCLUSION

A new procedure to synthesise a MMIC bandstop filter based on transversal combination filter principle is described. A bandpass filter is used within the structure to obtain the notch effect. The recursive and transversal coupling values are extracted by a mixed analytical /numerical procedure to obtain the desired rejected bandwidth, and the minimum noise figure in the passbands. Simulated performances are very close to the theory even when considering non-ideal couplers.

A second topology of notch filter is synthesised in order to obtain gain in the passbands, with the lowest noise figure.

REFERENCES

- [1] S.E. SUSSMAN-FORT, "Design concepts for microwave GaAs FET active filters", *IEEE Trans. on MTT*, vol. 37, n°9, Sept. 1989, pp. 1418-1424
- [2] C. RAUSCHER, "Varactor-tuned active notch filter with low passband noise and signal distortion", *IEEE Trans. on MTT*, vol. 49, n°8, Aug. 2001
- [3] C. RAUSCHER, "Microwave channelized active filters- a new modular approach to achieving compactness and high selectivity", *IEEE Trans. on MTT*, vol. 44, n°1, Jan. 1996
- [4] S. WEDGE and D. RUTLEDGE, "Wave technique for noise modeling and measurement", *IEEE Trans. on MTT*, vol. 40, pp. 2004-2012, Nov. 1992
- [5] ED02AH monolithic process, OMMIC, ED02AH design manual, GaAs Foundry and ASIC Design Center, <http://www.ommic.fr>

Microwave Analogue FIR-Filter

Klaus Solbach, Taleb Ould Mohamed, Markus Neinhüs, Michael Tekloth

University Duisburg-Essen, Hochfrequenztechnik, Bismarckstr.81, 47048 Duisburg, Email: hft@uni-duisburg.de

Abstract — Analogue FIR-filters have been proposed for the realization of wideband array antennas, where they replace conventional amplitude/phase control and true-time-delay sections. The filter concept presented in this contribution employs one input and one output transmission line supporting traveling waves. The design has to be different to the traveling wave amplifier design because the signals fed through the bi-phase amplitude controls (attenuator, coefficients a_i) to the output line are not in-phase! We thus need high impedance at input and output ports of the attenuator circuits.

A proof-of-concept circuit was designed and tested which employs three transistors and which operates at a “scaled-down” frequency band (VHF). A full FIR-filter structure with $N = 4$ sections was built and tested and will be compared to theoretical predictions.

I. INTRODUCTION

Finite Impulse Response (FIR) filter structures, Fig. 1, are widely used in digital signal processing for the realization of filter responses with prescribed frequency behaviour, e.g. as equalizers, correlators and matched filters in communications and recently also as element signal weight controls in smart antenna arrays, see overview [1]. In our companion paper [2], we present the concept of electronic steered microwave array antennas using analogue FIR-filters at each element with the aim of realizing wideband, frequency independent pattern characteristics.

The aim of this paper is to present the concept for broadband analogue FIR filter circuits for the microwave frequency range and discuss proof-of-concept circuit design and results.

II. CONCEPT OF MICROWAVE FIR-FILTER

The principle design of FIR-filter due to Fig. 1 combines time delay sections with amplitude control (attenuator) circuits. While the amplitude control circuits

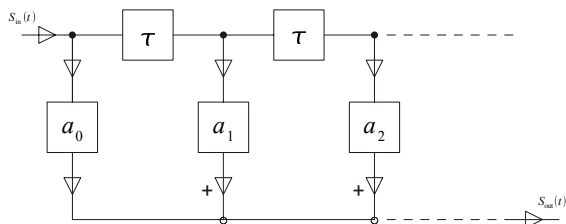


Fig. 1. Finite Impulse Response filter principle design

realize the real amplitude coefficients a_i , Microwave realizations have to take into consideration the inherent

delays, parasitic elements and wideband impedance transformation properties of circuits and their connections. Therefore, our circuit is based on the traveling wave concept, similar (but not identical) to the design of distributed amplifiers, e.g. [3].

Our circuit concept is shown in Fig. 2: The input signal $s_{in}(t)$ is fed to an input transmission line and a traveling wave is created propagating towards the

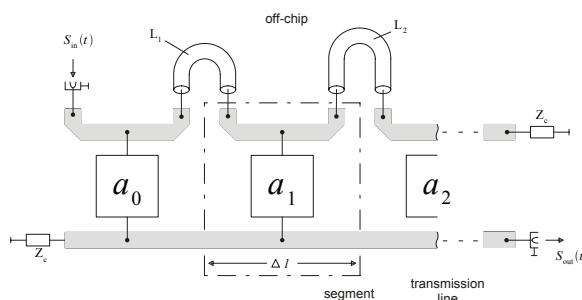


Fig. 2. Circuit concept for a microwave analogue FIR filter

matched end termination. The transmission line is segmented with interconnecting extra transmission lines representing the time delay units (in the circuit diagram with lengths L_i) which may be realized off-chip in order to keep the circuit size low; they may also be realized on-chip as lumped LC networks, a similar approach as used in a microwave equalizer circuit recently published [4]. Within each segment of the transmission line, there is one bi-phase variable attenuator connected to the input signal transmission line with the weight factor ideally between -1 and $+1$ ($-1 < a_i < 1$). The input impedance of the attenuator has to be high in order not to disturb the forward traveling wave on the input-line, thus we assume this port to be realized by the gate / source terminals of a FET. The attenuated signal is coupled to the output transmission line on the other side, where we also terminate by a matched load at one end while the other port supplies the output signal $s_{out}(t)$ to a matched load. Signal injection from each segment has to sum up on the output transmission line which can be achieved by the creation of a traveling wave on the output transmission line and assuming superposition of contributions from each segment. Note the difference with respect to a traveling wave amplifier: The output signal contributions are not in-phase in our case! Note also that each current source will set-up a wave in either direction, while only those waves traveling towards the output port are used for $s_{out}(t)$.

We thus require high source impedance for the attenuator output terminals making the attenuator act as a

current source (rather than an impedance-matched generator) and thereby avoiding heavy resistive loading of the output transmission line. We may describe our attenuator circuit also as voltage controlled current source, or bi-phase transconductance amplifier, and we therefore find the drain / source terminals pair of a saturated GaAs FET to be a viable solution for this purpose. In principle, we could imagine a single FET connected with its gate to the input line and with its drain to the output line, Fig. 3.

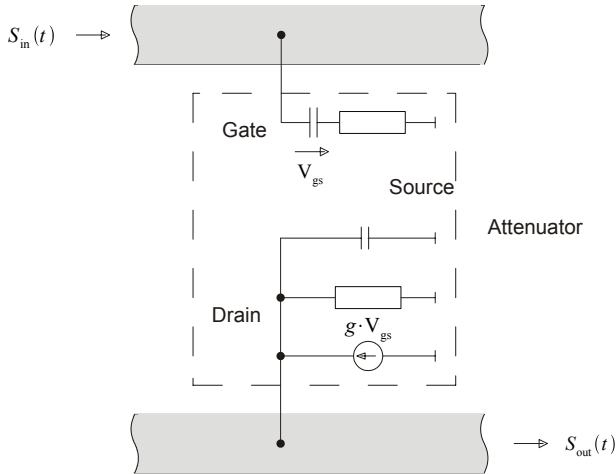


Fig. 3: RF equivalent circuit of a high input impedance / high output impedance attenuator circuit

However, the full circuit developed in our project uses three transistors in order to realize the bi-phase characteristics instead of just one transistor. The first transistor functions as an unbalanced-to-balanced circuit with in-phase and anti-phase outputs driving the two second stages. By application of appropriate bias to the second stage transistors, either a signal from the in-phase second stage or from the anti-phase second stage feed into the output transmission line.

All segments in our circuit are constrained to be realized by the same pitch Δl in the input- and output transmission lines. In that case we can condense the net-effect of the N segments of the FIR-circuit to one single transmission line of length $N\Delta l$ and consider the remaining circuit as ideal, concentrated FIR-circuit (including the required delay lines) plus a fixed average time delay τ_g due to the bi-phase attenuator group delay (which is around 2 ns), see Fig. 4.

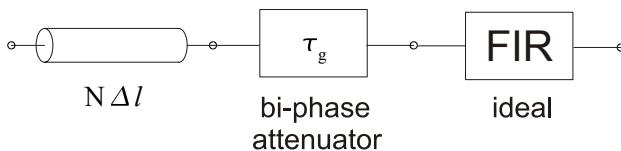


Fig. 4. Block diagram representation of microwave FIR-filter circuit

The total extra delay from the transmission lines and the group delay applies to all possible signal paths through the filter and all possible filter settings and to all

individual filters in the same way, e.g. in an antenna array, so that we may neglect it or subtract it completely in most applications. The frequency domain response of the FIR structure therefore can be written as

$$H(f) = e^{-j2\pi f(N\Delta l/v_{ph} + \tau_g)} \cdot \sum_{i=0}^{N-1} a_i e^{-j2\pi f \cdot i\tau}$$

where the first factor is due to the constant delay and the second factor characterizes an ideal FIR-filter.

The size of the required delay per stage is discussed in our companion paper [2] for the antenna array application: In an example array design, we would need 20 antenna elements, each connected to one FIR-filter and each filter consisting of about 10 stages. The delay per stage was chosen to be equivalent to the propagation delay in free space from one element to the next d/c_0 . For an antenna array operating up to 10 GHz, this would require $d = 15$ mm and $\tau = 50$ ps.

III. PROOF-OF-CONCEPT

The critical component of the FIR-filter circuit is readily identified as the bi-phase attenuator. It is required to have high input and output impedances and flat amplitude and group delay transfer characteristic over a broad band and over the dynamic range. Such circuits presently are not available commercially (only 50 Ω -impedance matched attenuators and modulators are available) so that we had to develop a suitable attenuator circuit before implementing the FIR filter circuit. Since, in an ultimate microwave circuit realization for e.g. 3 to 10 GHz (as for UWB-pulse applications) expensive monolithic integration would be applicable, a proof-of-concept circuit was designed for a scaled-down “model” frequency range of a few 100 MHz compatible with conventional PCB technology and the use of surface mount devices. Our bi-phase attenuator lab-model as shown in Fig. 5 uses a first stage (input) configured as an unbalanced-to-balanced source follower stage while the second stage (output) of the circuit employs two transistors in common source configuration; we use CF739 dual-gate FETs which have the advantage of particularly high output impedance, high transconductance and the availability of a second gate for gain control. The two output stage transistors’ drain R.F. currents are combined (shunt connection) at the output transmission line, but under operating conditions, only one transistor is conducting at a time, making the weight factor a_i either positive or negative.

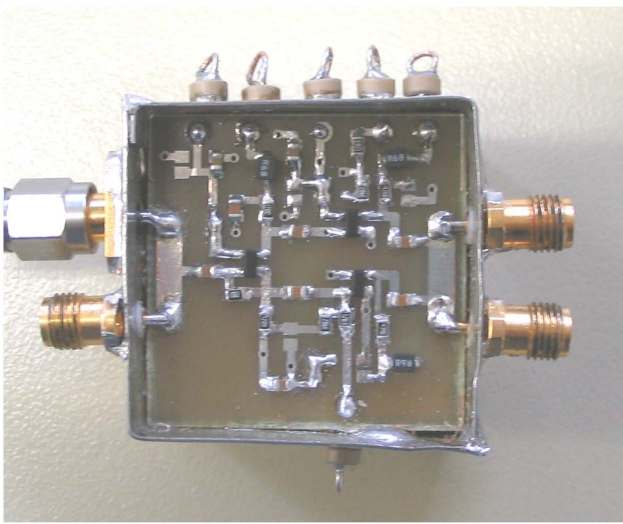


Fig. 5(a) Photograph of experimental bi-phase attenuator circuit

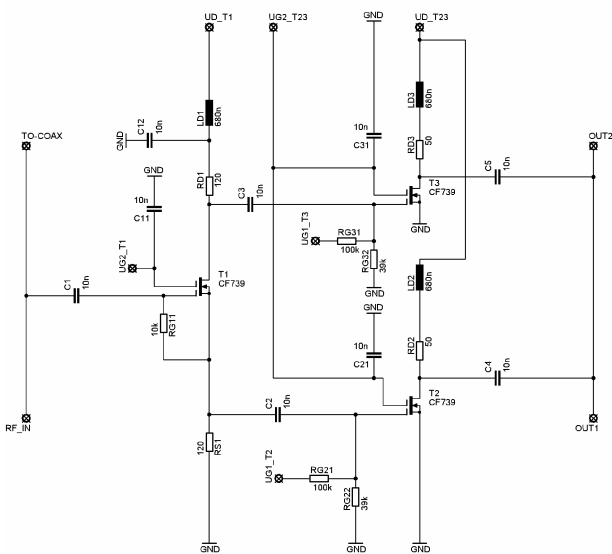


Fig. 5 (b) Schematic of the realized bi-phase attenuator using three transistors

First measurements of the scattering parameters of the lab-model have shown wide dynamic range, flat amplitude response and only little group delay dispersion over frequency as shown in Fig. 6. The measurement of the transmission scattering parameter $|S_{21}|$ was done loading the second input-port and the second output port by an extra 50 Ω -termination in order to mimic the traveling wave environment of the ultimate filter circuit. We can realize that the attenuator circuit can be steered to a few dB of amplification ($a > 1$) and exhibits a dynamic range of more than 30 dB.

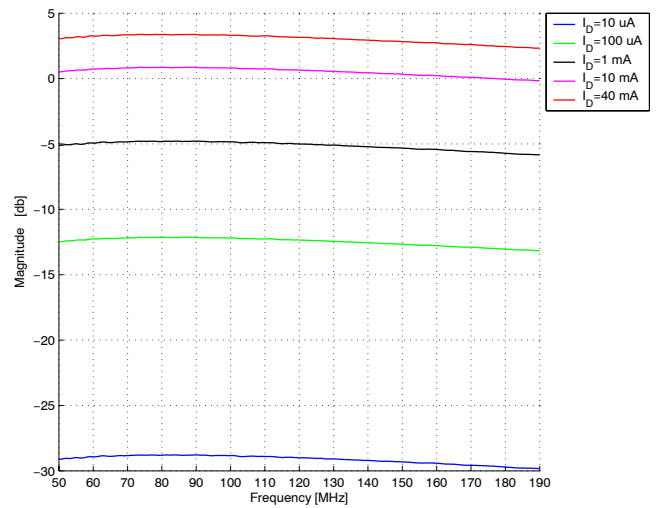


Fig. 6 Insertion loss of bi-phase attenuator as a function of second stage drain current

A full FIR filter circuit lab-model using four sections based on the present attenuator design and coaxial delay lines was built and tested. Results of this experiment and comparison with theoretical predictions will be reported at the conference.

IV. CONCLUSION

The concept of an analogue microwave FIR-filter was discussed and a proof-of-concept experiment at VHF presented. Future work will be directed towards improving insertion loss- and group delay- flatness and toward the realization of filter-circuits at microwave frequencies, including the consideration of monolithic fabrication.

REFERENCES

- [1] Tuan Do-Hong, Peter Russer, "Signal Processing for Wideband Smart Antenna Array Applications", *IEEE Microwave Magazine*, March 2004, 57-67
- [2] M. Neinhüs, K. Solbach, S. Held, "Concept of Microwave Electronic Steered Array using Analogue FIR-Filter", *German Microwave Conference (GeMiC) 2005*, session 4b, Ulm, April 2005.
- [3] James B. Beyer et al., "MESFET Distributed Amplifier Design Guidelines", *IEEE Trans. MTT*, vol. 32, March 1984, 268-275
- [4] Y.Hur, et al., "Equalization and Near-End Crosstalk (NEXT) Noise Cancellation for 20 Gb/s 4-PAM Backplane Serial I/O Interconnections", *IEEE Trans. MTT*, vol.53, no.1, Jan.2005, 246-255

Session 4b

Antenna Arrays and Frequency Selective Surfaces

Phased Array Technology: Trends & Developments

Rens Baggen ⁽¹⁾, Sybille Holzwarth ⁽²⁾, Martin Böttcher ⁽³⁾, Michael Eube ⁽⁴⁾

*IMST GmbH, Carl-Friedrich-Gauss Str. 2 D-47475 Kamp-Lintfort, Germany
Tel. +49-2842-981-326*

⁽¹⁾ baggen@imst.de, ⁽²⁾ holzwarth@imst.de, ⁽³⁾ boettcher@imst.de, ⁽⁴⁾ eube@imst.de

Abstract — This paper gives an overview of developments and projects in the area of electronically steerable antennas at IMST, also commonly called phased arrays. This type of antenna has become a key area since the last years and various projects have been conducted in the past, and are currently ongoing. Phased array antennas incorporate in general active components for performing beam steering, and have achieved ever more popularity during the last years, mainly driven by mobile multimedia applications. The design of phased arrays involves different areas of expertise such as antenna design, feeding networks, beamforming/steering hard/software, RF-components design, signal processing, prototyping and complex measurements. At IMST various R&D projects reflect the broad spectrum of activities with respect to design and development of phased arrays. It is intended to give here an overview of the work performed, and a global technical description.

I. INTRODUCTION

Steerable antennas, whether mechanically, electronically, or any hybrid combination, are nowadays becoming more and more attractive for a broader audience such as for mobile telecommunication services, e.g. mobile satellite terminals for land mobile, maritime or aeronautical applications.

Latter systems must be able to track one or more satellites and provide sufficient bandwidth. Multimedia is here the driving force to develop small intelligent terminals, eventual at low-cost, for applications such as general or customised broad-casting or communication services, e.g. in-flight entertainment (internet in the sky).

Most of the conventional antenna systems realise the satellite tracking functions by the use of mechanical steering: the antenna is mounted on a two-axis steering system adjusting the antenna's orientation in such a way that the main beam is continuously re-directed towards the satellite. However, systems with mechanically moving parts are maintenance intensive, heavy and/or bulky, and sensitive to G-forces. These issues do not make this type of antenna very well suited for automotive or aeronautical applications. So, there is an increasing demand for fully electronically steerable solutions. With respect to the commercial sector, one of the major limitations and biggest design challenges of this type of phased array is the relatively high price due to its complexity.

The range of steerable antenna systems, developed at IMST, varies from small arrays with switchable elements, and partially mechanically and electronically steerable arrays (hybrid systems) to fully electronically steerable antenna arrays. Such systems can be equipped with RF-phase and -amplitude shifters for each element or the design can be based on Digital BeamForming (DBF). This technique, in which the steering is performed directly on a digital level, allows the most flexible and powerful control of the antenna beam (forming & tracking).

Designing phased arrays involves expertise from many different areas such as antennas, RF-networks & electronics, steering software, signal processing, prototyping and sophisticated measurement scenarios. Also, the low-cost aspect has to be taken into account in order to be commercially successful. At IMST, a large number of R&D projects focuses on the design of phased arrays. Various projects have been conducted since the last 6 years which all differ in topic, application and frequency range (from L-band up to Ka-band). Three typical R&D projects out of our phased array spectrum will be presented in this paper. Their application is discussed, and global technical specifications are given. This will be followed by an outlook on future activities.

II. ALCANT

The focus of the project ALCANT - Active Low Cost steering ANTenna - was on the development & prototyping of a transmit-/receive array for maritime applications in L-band. This antenna employs the hybrid steering approach: steering is performed electronically in elevation and mechanically in azimuth. The project was supported by the German Ministry of Education and Research - BMBF- in the ALCANT-SATCOM project, contract number 01AK007G/8. The antenna architecture was designed by the University of Karlsruhe (Germany), and the feeding network by IMST. The final prototype is depicted in fig. 1.

The design is based on a classical phased array approach where RF-amplitude and phase shifters are used to steer the antenna beam in elevation.

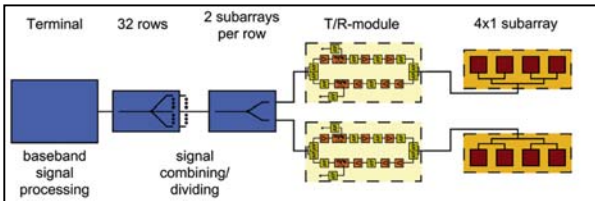
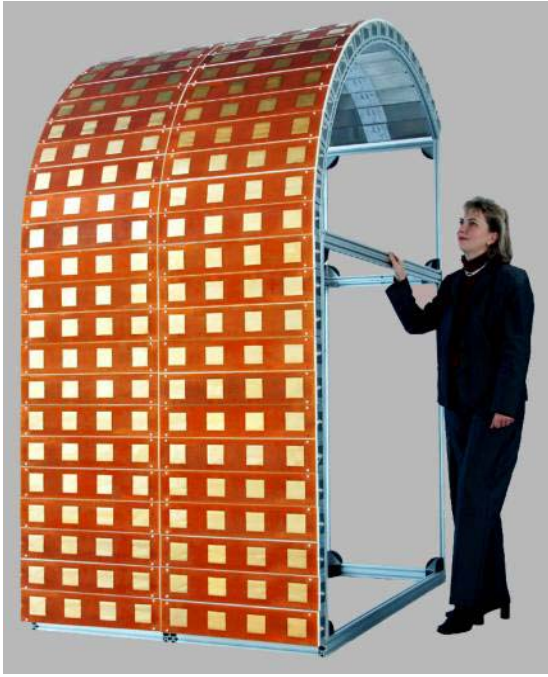


Fig. 1.: Prototype of the ALCANT antenna (above), schematic overview of number of rows and patches (below).

The antenna consists of 256 patches, and each row of 2x4 patches has its own RF-phase and -amplitude circuit. The system is also equipped with a separate calibration network. The size of the antenna is the consequence of the very stringent G/T requirement (Figure of Merit) for this type of application. The specifications of the prototype are listed in table I.

Frequency range	1.5 – 1.7 GHz
Bandwidth	8.5 %
Polarisation	Circular
G/T	-4 dBK
Beam steering: elevation azimuth	-10° to 100° (electrical) 4° (electrical) 360° (mechanical)

TABLE I. Specifications of the ALCANT antenna

For a more detailed description is referred to [1].

III. INES

A complete other type of antenna is being developed in the framework of the **In**expensive **E**arth **S**tation project (INES), supported by the ESA.

The scope of this activity is to develop a solution for land mobile terminals (cars, trains, trucks) as shown in fig. 2. The systems considered here are medium data rates applications like the future Inmarsat BGAN system. The satellites used for latter system (L-Band) transmit high power signals so that the G/T requirements for the terminal are not very stringent.

Low cost is the major issue here, thus the concept has been analysed thoroughly with respect to this aspect, assisted by experienced manufacturers from industry. As a result, the antenna is based on an optimised combination of both phased array and beam switching concepts.



Fig. 2.: INES antenna demonstrator on top of a van (composite picture).

The prototype currently developed is depicted in fig. 3. It consists of an array of 8 stacked patch elements that can be combined in different configurations: the single elements can be used stand-alone, or a combination of paired patches, each pair formed by the zenith element and one of the low elevation elements can be used. Latter pairs are equipped with amplitude and phase shifters. Depending on the position of the mobile terminal with respect to the satellite, the signal of one of the 8 elements or one of the element combinations - is used for transmitting/receiving. The relative position of the satellite is estimated on bases of gyro, compass and GPS.

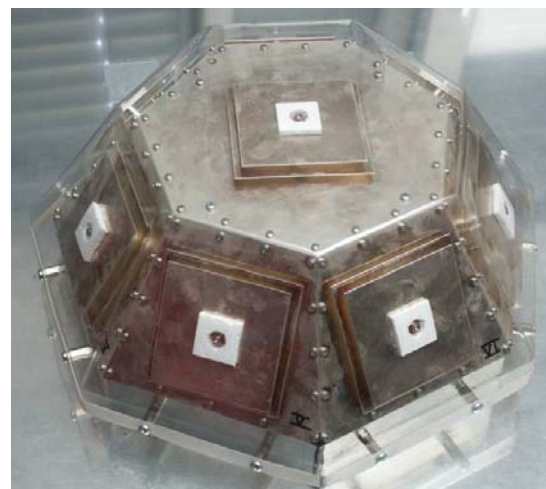


Fig. 3.: The INES antenna.

Thus, in total 15 different states – beams - can be distinguished. For the low elevation angles and the zenith direction, the coverage of one single patch suffices. For a certain region in between, a correct combination of two patches is required.

For a more detailed technical background of this concept is referred to [2], [3], and [4].

IV. SANTANA

This project stands for **Smart ANTenna terminal**, and focuses on the high-end of phased array technology, namely DBF antennas. Each antenna element is equipped with a complete down-/upconverting circuit, and the received/transmitted element signal is digitalised and directly handled by a digital processing unit (e.g. a DSP). This is not only the most complex system, but also the most flexible one. Because of the fact that the complete beam forming is performed within the DSP, all kind of signal processing operations and algorithms can be performed.

The application focussed on here is an air borne Ka-band satellite terminal for broadband multimedia services like internet in the sky. The terminal is divided into a separate transmit - 30 GHz - and receive - 20 GHz - antenna array. These frequency bands are based on future satellite multimedia applications.

The Tx/Rx antennas are composed of 4x4 array modules, which are used as basic building blocks to realise DBF arrays of large element numbers. In fig. 4 the prototype of a Tx-4x4 patch array is depicted. The basic element design is based on circularly polarised patches. Currently a new Tx antenna layout, based on a highly integrated LTCC (Low Temperature Co-fired Ceramics) multilayer structure, featuring hybrid couplers, shielding cavities and a calibration network is developed.

The project goal is the construction of an 8x8 element high data rate communication system consisting of 4 basic building blocks.

This project is supported and funded by the German Ministry of Education and Research (BMBF/DLR) under research contracts 50YB0101 and 50YB0311, in cooperation with the Technical University of Hamburg, DLR and Astrium. For more elaborate description of the technical details is referred to [5], [6], and [7].

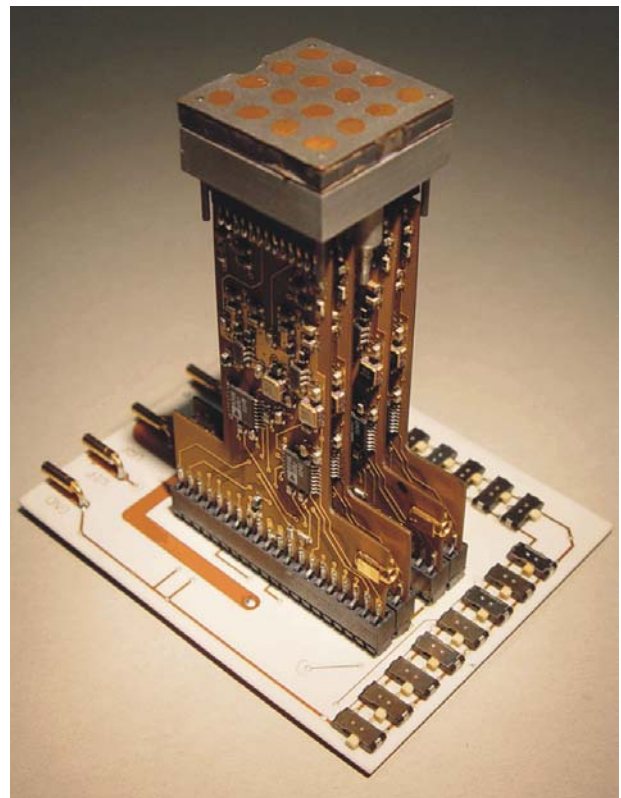
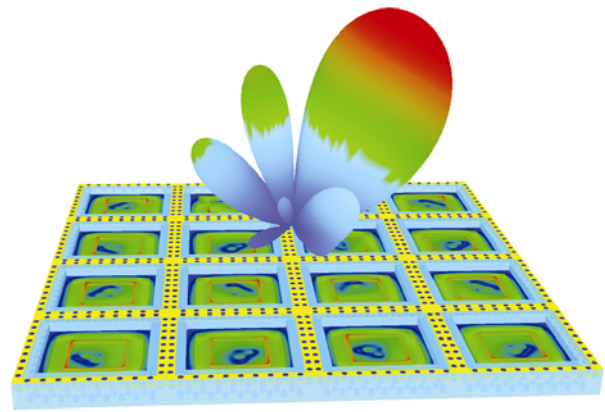


Fig. 4. Tx-Demonstrator 4x4 patch array: simulation scanning (above), prototype (below).

V. OUTLOOK

The short overview of the projects presented here gives an impression of the work performed by IMST in the area of phased array technology. Projects like SANTANA and INES are at the moment in the prototyping phase and experiments with mobile platforms are planned in near future. Also, new projects are on the horizon, one just has been initiated and will focus on low-cost terminals in Ku-band for automotive applications. This project is characterised by the fact the design will be performed in close cooperation with the car industry, taking into account their specific requirements especially the low-cost aspect.

REFERENCES

- [1] D. Löffler, W. Wiesbeck, M. Eube, K. Schad, E. Ohnmacht, "Low Cost Conformal Phased Array Antenna Using High Integrated, SiGe-Technology", IEEE A&P International Symposium, Boston, USA, pp. 334-337, July 2001.
- [2] Q. Wang, M. Lecours, and C. Vergnolle, "Optimization of Switches for Radial Satellite Antenna Array Applications", Sixth Int. Mobile Satellite Conference, Ottawa, Canada, pp. 393-397, June 1999.
- [3] N. Karmakar, M. Bialkowski, "A Low Cost Switched Beam Array Antenna For L-Band Land Mobile Satellite Communications in Australia", Proc. IEEE Vehicular Technology Conf. 1997, pp. 2226-29, 1997.
- [4] S. Jellet, M. Bialkowski, and R. Varnes, "An L-band vehicle mounted cylindrical array for satellite communications", IEEE ICCS, pp. 710-14, Singapore, India, 1994.
- [5] A. Dreher, D. Heberling, S. Holzwarth, C. Hunscher, A.F. Jacob, N. Niklasch, H. Pawlak, L. Richard, A. Schroth, L.C. Stange, and M. Thiel, "Ka-band DBF terminal concepts for broadband satellite communications", 25th ESA Antenna Workshop on Satellite Antenna Technology, Noordwijk, The Netherlands, pp. 95-102, Sept. 2002.
- [6] L.C. Stange, H. Pawlak, A. Dreher, S. Holzwarth, A.F. Jacob, O. Litschke, M. Thiel, "Components of a Highly Integrated DBF Terminal Antenna for Mobile Ka-Band Satellite Communications", IEEE MTT-S, Microwave Symposium Digest, Philadelphia, USA, vol. I, pp. 583-586, June 2003.
- [7] H. Pawlak, L.C. Stange, A. Molke, A.F. Jacob, O. Litschke, S. Holzwarth: "Miniaturized 30 GHz DBF Transmitter Module for Broadband Mobile Satellite Communications", 34th European Microwave Conference, Amsterdam, The Netherlands, Oct. 2004.

Proceeding for Calculating Large Arrays

Eugen Arnold

EADS Deutschland GmbH, Woerthstrasse 85, 89077 Ulm, Germany
e-mail: eugen.arnold@eads.com

Abstract — The article presents a proceeding for calculating S-matrix and radiation patterns of arrays. Even very large arrays can be calculated. The advantage of the proceeding is the short calculation time. By using a commercially available 3D-em-simulator a single radiating element located in free space or above the ground is analysed in the transmit and receive case. With an eigenmode solver, which is part of the em-simulator, about 10 Eigenfunctions of the radiating element located inside a box with perfect boundaries are calculated. These Eigenfunctions are used as basis functions. From the results of the analysis of the single radiating element a linear equation system is created involving the coupling between all radiating elements. By inverting the matrix the excitations of the basis functions of every radiating element is calculated.

I. INTRODUCTION

Usually large plane arrays with equidistant radiating element spacing are designed by calculating a unit cell, determine the scan reflection coefficient as a function of scan angle and use this coefficient for all radiating elements. Additionally all radiating elements are defined to have the same embedded radiation pattern. This procedure works quite well for active array antennas and for antennas with decoupled feeding structures, because this type of feeding structure suppresses internal coupling between the radiating elements. In reality the scan reflection coefficient and the embedded farfield pattern of every radiating element is dependent on its location inside the array environment. To design an antenna without a decoupled feeding network and to calculate accurately the farfield pattern of this antenna, the scan reflection coefficient and the embedded single element farfield pattern of every radiating element should be known.

With the proceeding, which is described below, the S-matrix between the radiating elements of an antenna, the embedded single element radiation patterns, the radiation patterns of the whole antenna and the RCS of the antenna can be calculated.

II. THE STRUCTURE OF THE LINEAR EQUATION SYSTEM

The basis of the calculation procedure is similar to the basis of the moment method. The current distribution of every radiating element is approximated by a linear combination of very powerful basis functions. A linear equation system (1a) is constructed. The excitations of the basis functions are achieved as the solution of the equation system.

A. Assumptions:

The Antenna consists of N radiating elements. The volume current density of every radiating element is represented by a linear combination of elements of a basis of functions consisting of M basis functions. In the transmit case the array is excited by sources located at the end of the feeding lines. In the receive case the excitation is an incidenting plane wave.

B. Equations describing the Coupling:

The complex amplitude of the l^{th} basis function of the k^{th} radiating element will be designated by u_{kl} . u_{kl} can be represented by

$$u_{kl} = u_{kl}^p + u_{kl}^c.$$

u_{kl}^p is the primary excitement at the feeding point of the radiating element or an incidenting plane wave and u_{kl}^c is the contribution of the coupling among the radiating elements.

The primary excitement u_{kl}^p of the k^{th} radiating element is the excitement of the l^{th} basis function of the k^{th} radiating element, if the k^{th} radiating element is located alone in free space. In the transmit case

u_{kl}^p is a linear function of the complex amplitude of the travelling wave feeding the k^{th} radiating element and in the receive case

u_{kl}^p is the sum of the contribution of the co- and of the cross polarized component of the incidenting plane wave at the location of the k^{th} radiating element.

u_{kl}^p is discussed in more detail in chapter V, section D.

The coupling contribution u_{kl}^c of the k^{th} radiating element is a linear function of the excitations of all basis functions on all radiating elements excluding these of the k^{th} radiating element. From this the equation follows:

$$\begin{aligned} u_{kl} &= u_{kl}^p + u_{kl}^c \\ &= u_{kl}^p + \alpha_{k,1,1} * u_{1,1} + \dots + \alpha_{k,1,M} * u_{1,M} \\ &\quad + \alpha_{k,2,1} * u_{2,1} + \dots + \alpha_{k,2,M} * u_{2,M} \\ &\quad + \dots \\ &\quad + \alpha_{k,N,1} * u_{N,1} + \dots + \alpha_{k,N,M} * u_{N,M} \text{ with } \alpha_{k,l,k,j} = 0. \end{aligned} \quad (1)$$

In equation (1) u_{kl} is the complex amplitude of the l^{th} basis function of the k^{th} radiating element in the case, when the other radiating elements are present and $\alpha_{k,l,i,j}$ are scalar coefficients describing the coupling of the j^{th} basis function of the i^{th} radiating element (transmitter) to the l^{th} basis function of the k^{th} radiating element (receiver), $i \neq k$. The coupling among the basis functions belonging to the same radiating element is 0.

If we arrange the terms of (1) in a different way, we achieve

$$-u_{kl}^p = \sum_{i=1}^N \sum_{j=1}^M \beta_{k,l,i,j} * u_{ij} \quad (1a)$$

$$\text{with } \beta_{k,l,k,l} = -1, \beta_{k,l,k,j} = 0 \\ \text{for } k=1,\dots,N, j,l=1,\dots,M, j \neq l$$

Formula (1a) is valid for the transmit and the receive case. It is referred later as the equation for the l^{th} basis function of the k^{th} radiating element. For every basis function of every radiating element an equation of type (1a) exists. All equations (1a) represent a linear equation system with the complex basis function amplitudes u_{ij} as solution.

III. CALCULATION OF THE BASIS FUNCTIONS

The volume current density \vec{j} of the whole antenna is the set union of the volume current densities \vec{j}_k , $k=1,\dots,N$, of all N radiating elements. The volume current density of the k^{th} radiating element is approximated by a linear combination of elements of a function basis $\{\vec{j}_{kl}, l=1,\dots,M\}$. Therefore

$$\vec{j}_k = \sum_{l=1}^M u_{kl} * \vec{j}_{kl} \quad (3)$$

The function basis belonging to the k^{th} radiating element and the function basis belonging to the n^{th} radiating element, $k \neq n$, are in principle identical but distinguish in their definition ranges. The ranges differ by the translation vector from the location of the k^{th} radiating element to the location of the n^{th} radiating element.

The main property of the functions \vec{j}_{kl} of the selected basis is the possibility to approximate the current distribution of the radiating elements sufficiently well with a minimal number of functions. To create this set of functions we use the eigenfunction solver of a program working with the finite integrals technology. For this purpose we place one single radiating element, which has no ohmic loss in a closed box with magnetic and electric boundaries. The box must be large enough to have sufficient free space between the radiating element and the boundaries. This space is needed to calculate the farfield characteristic of the basis functions, as described in chapter V, section B. Then the resonant frequencies and the eigenfunctions of the radiating element inside the box are calculated. Every eigenfunction is represented by a pair of functions, consisting of an E-field distribution and an H-field distribution. Few of the eigenfunctions are strongly related to the shape of the box and its boundary conditions, the others are mainly related to the radiating element. From those, who are related to the radiating element, we select these M Eigenfunctions, whose resonant frequency is closest to the mid frequency of the array antenna. They will be used as members of the basis.

Because of the large number of radiating elements the number M of basis functions must be relatively small (\leq

20), so that the resulting equation system gets not too large. It is clear that this basis is not complete. This is one of the approximations used in this method.

IV. THE RELATION OF THE BASIS FUNCTIONS TO MAXWELLS EQUATIONS

We define the volume current density \vec{j} of the radiating elements by Maxwell's Equations in the following form:

$$\nabla \times \vec{H} - j\omega\epsilon_0 \vec{E} = \vec{j} \quad (2) \\ \nabla \times \vec{E} + j\omega\mu_0 \vec{H} = 0$$

$$(\vec{j} = (\sigma + j\omega(\epsilon - \epsilon_0))\vec{E} + \vec{j}_s, \\ \vec{j}_s \text{ impressed source current})$$

The equations (2) assume that the total space is homogen with the properties of vacuum ($\epsilon=\epsilon_0, \mu=\mu_0$). The effects of the material are replaced by the fictive electrical volume current density \vec{j} . We consider \vec{j} to consist of current sources which we can control. The sources create outside of the radiating elements the same electromagnetic field as the radiating elements. Additionally it is assumed in (2), that the radiating elements do not have magnetic material. The enlargement to include magnetic material is trivial.

To achieve the volume current distribution belonging to an Eigenfunction we have to insert the E- and the H-field distribution of the Eigenfunction into the left side of the 1st equation of (2). One part of the resulting current density (right side of equation (2)) flows as surface current density on the inner surface of the box, the other part flows within the volume of the radiating element. Only the latter part is used for the function basis.

V. CALCULATION OF THE COEFFICIENTS OF THE EQUATION SYSTEM

A. Preparing Calculations With One Single Radiating Element Using A 3D-EM-Simulator

The calculation of the coefficients of the linear equation system (1a) is based on an intensive investigation of the properties of a single radiating element located in free space or above the ground. The calculations are performed with a 3D-Solver based on the FITD-method. The results of these calculations are

- reflection coefficient at the feeding line,
- farfield characteristic,
- backscatter farfield characteristic of the radiating element at a sufficiently large set of directions of incidenting co-polarized plane waves,
- backscatter farfield characteristic of the radiating element at a sufficiently large set of directions of incidenting cross-polarized plane waves.

For every direction and polarization of the incidenting plane wave the backscatter farfield characteristic are approximated by a linear combination of the farfield characteristics of the basis functions. The set of directions must be large enough to enable the interpolation of every coefficient of the linear combination about the whole unit sphere. This interpolation will deliver the contributions of the farfield characteristic of the basis functions at the backscattered farfield characteristic, which is created by a plane wave incidenting with arbitrary polarization from an arbitrary direction. The contributions are used for the calculation of the coupling coefficients β_{klj} . The calculation is described in chapter V, section E.

B. CALCULATION OF THE FARFIELD CHARACTERISTIC OF THE BASIS FUNCTIONS

The basis functions defined in chapter III are not directly used to calculate the coefficients of the linear equation system (1a). Instead of them we use the farfield characteristic of the basis functions. These characteristics are calculated according to Huygens principle:

Inside the box, used for calculating the Eigenfunctions in chapter III, we define a subvolume enclosing the radiating element. On its surface we define the magnetic and electric surface current densities $\vec{n} \times \vec{E}$ and $-\vec{n} \times \vec{H}$ and calculate the farfield characteristic. \vec{n} is the unit vector orthogonal to the surface of the subvolume, directing to its outer side. \vec{E} and \vec{H} is the electric and the magnetic field strength of the Eigenfunction. That this calculation takes into account only the volume current density used for the basis function (inside the radiating elements), can be seen from [1].

C. DECOMPOSITION OF A FARFIELD CHARACTERISTIC INTO A LINEAR COMBINATION OF FARFIELD CHARACTERISTICS OF THE BASIS FUNCTIONS

We denote by $\vec{c}_l(\vartheta, \varphi)$, $l=1, \dots, M$, the farfield characteristics of the M basis functions of a radiating element. To approximate a farfield characteristic $\vec{C}(\vartheta, \varphi)$ of this radiating element by a linear combination of $\vec{c}_l(\vartheta, \varphi)$, $l=1, \dots, M$, we define the "Ansatz"

$$\vec{C}(\vartheta, \varphi) = \sum_{l=1}^M a_l * \vec{c}_l(\vartheta, \varphi) \quad (4)$$

To determine the coefficients a_l , $l=1, \dots, M$, we calculate the scalar product of both sides of equation (4) with the function $\vec{c}_i(\vartheta, \varphi)$, $i=1, \dots, M$. This leads to M equations of the form

$$(\vec{C}, \vec{c}_i) = \sum_{l=1}^M a_l * (\vec{c}_l, \vec{c}_i), \quad i=1, \dots, M \quad (5)$$

(5) represents a small linear equation system from which the coefficients a_i can be determined. The scalar product between two farfield characteristics \vec{C}_1 and \vec{C}_2 is chosen to be

$$(\vec{C}_1, \vec{C}_2) = \int_{unit\ sphere} \vec{C}_1(\vartheta, \varphi) * \vec{C}_2(\vartheta, \varphi)^{\otimes} dS$$

$\vec{C}_2(\vartheta, \varphi)^{\otimes}$ denotes the conjugate complex function of $\vec{C}_2(\vartheta, \varphi)$.

D. CALCULATION OF U_{KL}^P

Transmit Case:

In the transmit case a voltage wave with the complex amplitude u_k^p is travelling from a source located at the termination of the feeding line of the k^{th} radiating element to the radiating element. Because of the definition of u_k^p only the k^{th} radiating element is present. The complex amplitudes u_{kl}^p of all l basis functions must be linear functions of u_k^p . Therefore a complex number α_{kl}^p exists with

$$u_{kl}^p = \alpha_{kl}^p * u_k^p \quad (6)$$

The coefficients α_{kl}^p are calculated according to the procedure described in chapter V, section C. A travelling wave with voltage $u_k^p=1V$ is excited in the feeding line of the k^{th} radiating element. The radiating element creates a farfield characteristic, which is decomposed into the farfield characteristics of his basis functions. One calculation delivers the coefficients α_{kl}^p for all l , $l=1 \dots M$, basis functions of the k^{th} radiating element.

Receive Case:

In the receive case a plane wave

$$\vec{E}^{inc}(x) = (u_{co} * \vec{e}_{co} + u_{cross} * \vec{e}_{cross}) * e^{j\vec{k} * \vec{x}}$$

incidents from the direction defined by the wave vector \vec{k} upon the k^{th} radiating element. x denotes the location of a point and \vec{x} the vector from the origin to the point x .

\vec{e}_{co} and \vec{e}_{cross} are unit vectors in the direction of the co-polarization and the cross-polarization. The k^{th} radiating element is located alone in free space, therefore no coupling occurs. The co-polarized part of the plane wave creates a backscatter farfield characteristic which is decomposed into the farfield characteristics of the basis functions according to the proceeding of chapter V, section C. The same is done with the cross polarized part. If β_{kl}^{co} denotes the contribution of the l^{th} basis function to the co-polarized characteristic and β_{kl}^{cross} the contribution of the cross-polarized characteristic, then

$$u_{kl}^p = \beta_{kl}^{co} * u_{co} + \beta_{kl}^{cross} * u_{cross} \quad (7)$$

E. CALCULATION OF THE COEFFICIENT β_{KLJ}

The equation system (1a) is valid for arbitrarily chosen complex amplitudes u_{kl} , $k=1, \dots, N$, $l=1, \dots, M$. If we insert a complete set of arbitrarily chosen amplitudes at the right side of (1a), the system delivers the voltages of the forward travelling waves in the feeding lines of the

radiating elements, which are necessary to excite the basis functions with the prescribed amplitudes. Therefore we can use the equation system to calculate the coefficients.

To calculate the coefficient β_{klj} we choose the complex amplitudes of all basis functions on all radiating elements to be zero except the l^{th} basis function of the k^{th} radiating element and the j^{th} basis function of the i^{th} radiating element, $k \neq i$. Furthermore we terminate all feeding lines of the radiating elements with ideal absorbers so that the amplitudes of all forward travelling waves are zero. Then from equation (1a) for the l^{th} basis function of the k^{th} radiating element we receive

$$0 = \beta_{klj} * u_{ij} + \beta_{kkl} * u_{kl} \quad \text{with } \beta_{kkl} = -1 \rightarrow \beta_{klj} = \frac{u_{kl}}{u_{ij}} \quad (8)$$

According to (8) we receive β_{klj} if we excite the j^{th} basis function of the i^{th} radiating element with the complex amplitude u_{ij} and calculate the complex amplitude u_{kl} of the l^{th} basis function of the k^{th} radiating element. For this calculation only the i^{th} and the k^{th} radiating element is present, because the excitations of all other radiating elements were chosen to be zero. This is only possible if they are absent.

If the distance between the two considered radiating elements is larger than 1 wavelength the coupling calculation can be based on farfield approximations: The k^{th} radiating element is hit by an incident field created by the j^{th} basis function of the i^{th} radiating element, which is excited with the complex amplitude u_{ij} . The field is easily calculated from the farfield characteristic of the basis function. At the location of the k^{th} radiating element it can be approximated by a plane wave. The plane wave excites the basis function of the k^{th} radiating element and creates a backscatter farfield characteristic. This farfield is decomposed into the contributions (complex amplitudes) of the basis functions of the k^{th} radiating element, using the interpolation function mentioned in chapter V, section A. With one calculation the whole set of coefficients β_{klj} , $l=1, \dots, M$, is received from (8).

Also for neighbouring radiating elements the error, resulting from this farfield approximation, is mostly negligible. If the error is too large, it is possible to extract the coupling coefficients between two adjacent radiating elements from additional calculations with the 3D-emulator.

IV. TEST OF THE PROCEEDING

The presented proceeding was developed to determine the properties of large aperiodic volume arrays. The verification of the proceeding has been done by calculating and measuring the aperiodic volume array shown in Fig. 1. It consists of 32 radiating elements. Some of these test results are shown here. For the calculations 10 Eigen- functions were used.



Fig. 1: Test array

The embedded single element farfield patterns of the radiating elements is very important, because they reflect the directivity function of the antenna. At aperiodic arrays these patterns show much larger variation than at periodic arrays. Fig 2 shows the calculated pattern of radiating element no. 2.

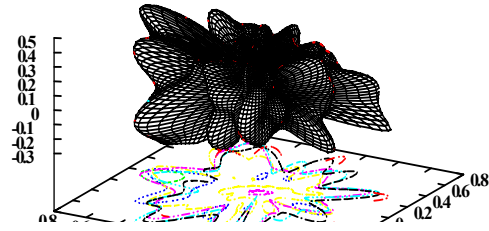


Fig. 2: Calculated embedded farfield pattern of radiating element no. 2

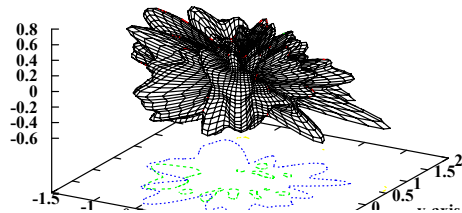


Fig. 3: Measured embedded farfield pattern of radiating element no. 2

Fig. 3 shows for comparison the measured pattern. Fig. 4 shows calculation and measurement of the scan reflection coefficient of radiating element no. 15. The offset between the results of Fig. 4 is due to the attenuation of the coaxial cables connected to the radiating elements which is not involved in the simulation.

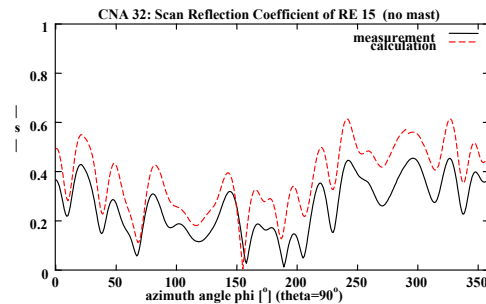


Fig. 4: Scan reflection coefficient while scanning the array in azimuth ($\theta=90^\circ$)

ACKNOWLEDGEMENT

The author want to acknowledge the work of his colleagues at FGAN, who developed the radiating element and made available the data of the s-parameter measurements.

REFERENCES

- [1] Claus Müller, "Grundprobleme der mathematischen Theorie elektromagnetischer Schwingungen", Springer Verlag Berlin-Göttingen-Heidelberg, 1957
- [2] FGAN: Neuenahrerstr. 20, 53343 Wachtberg-Werthoven

Concept of Microwave Electronic Steered Array using Analogue FIR-Filter

M. Neinhüs, K. Solbach, S. Held

Universität Duisburg-Essen, Hochfrequenztechnik, Bismarckstr. 81, 47048 Duisburg, Germany
Phone: +49 (203) 379-3439, E-Mail: m.neinhues@uni-duisburg.de

Abstract — A concept for wideband electronic steered array using analogue FIR-filters has been formulated. This paper focuses on microwave applications, e.g. wideband antenna radiation pattern, where we explain the design of a desired radiation pattern for bandwidth 2:1. Therefore we consider a linear narrowband radiation pattern and expand it to a wideband array synthesis. The requirements for higher bandwidth, e.g. 3:1 in ultra wideband (UWB) communication systems, w.r.t. different design parameters are obtained. Finally, we propose the requirements for practical realization at microwave signal level.

I. INTRODUCTION

Recently, interest for very wideband antennas has grown, e.g. in applications for Pulse Radar [1], Synthetic Aperture Radar and for UWB-pulse communication systems [2]. Requirements for antenna pattern characteristics have been established going beyond those for conventional array antennas and active phased array antennas designed for radar and communication systems: Instantaneous bandwidth of e.g. 3:1 is required with wide angle beam scan, side-lobe control, control of nulls and with constant beamwidth and constant beam pointing and null-direction over frequency [3]. Such goals currently drive many workers in the field of signal processing and smart antennas, where it is assumed that the signals from the elements of an array can be processed digitally in a computer (digital signal processing) and beams are formed digitally [4]. However, digital beamforming seems to be improper for microwave applications in the GHz-range due to extremely high sampling rate. Looking at the beamforming concepts being employed, it is seen that frequency dependent weighting coefficients must be used in order to make antenna patterns frequency independent and that some concepts use the Finite Impulse Response (FIR) filter structure to realize such responses [5]. The aim of this paper is to propose the use of analogue FIR-filter structures (at microwave signal level) for the design of wideband electronic steered array antennas.

II. MICROWAVE CONTROL CONCEPTS

In conventional microwave electronic steered arrays (ESA) we make use of phase shifters (PS), amplitude shifters (AS) and true time delay-elements (TTD) in order to control the weighting factor of elemental signals before summation [6], Fig. 1. Typical characteristics of the phase shifters are the frequency independent phase shift, Fig. 2a, which results in a squint of the main beam with frequency. In broadband (instantaneous bandwidth) array antennas, we use TTD-elements [7] with linear phase variation versus frequency, Fig. 2b, in order to keep the beam constant with frequency. However, both techniques result in a shift of nulls and in a widening of

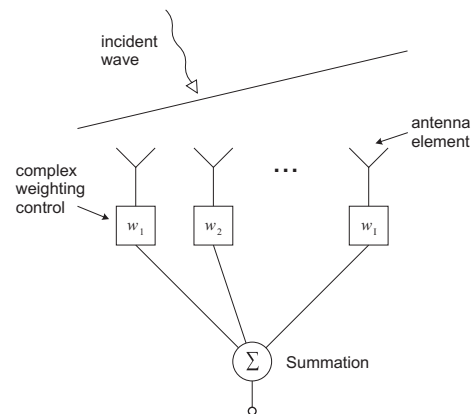


Fig. 1. Principle of narrowband electronic array steering with complex weighting control

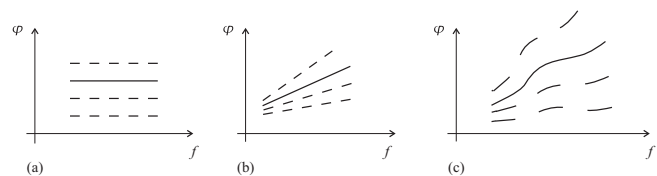


Fig. 2. Phase characteristic of electronic array control elements: (a) phase shifters, (b) true time delay elements, (c) FIR-filter

the beam with frequency. Amplitude control is employed usually to set the side-lobes at low levels but can in principle be employed also to reduce the active length of the array, resulting in wider beams; phase spoiling has also been used for that purpose. However, both techniques would require either frequency dependent amplitude control or phase control, both non-linear with frequency in a rather complex pattern, e.g. as shown in Fig. 2c, which can be realized, e.g. by a FIR-filter.

A. FIR-Control Elements

In principle, the frequency dependence of phase and amplitude at each antenna element, as required from array theory, can be realized by a number of filter types. One particularly appropriate type is the FIR-filter, because it can be thought of as an extension of the TTD-control element with integrated amplitude control and the additional freedom of inserting several different delays at the same time, see Fig. 3. On each antenna element, the FIR-filter causes a phase response that varies with frequency. So, spatial phase shifts due to different frequencies are temporally equalized by the FIR-filters.

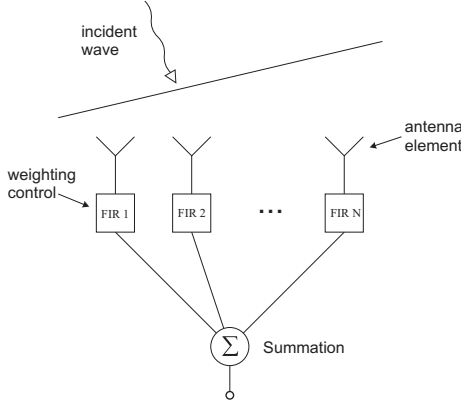


Fig. 3. Principle of wideband electronic array control using N FIR-filter at each antenna element

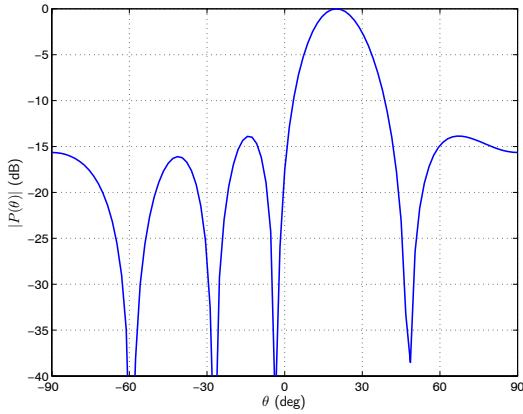


Fig. 4. Normalized desired narrowband radiation pattern with $I = 5$ uniformly weighted antenna elements and $\lambda/2$ spatial spacing. The main beam direction is $\theta_0 = 20^\circ$

III. DESIGN PROCEDURE OF A WIDEBAND ANTENNA RADIATION PATTERN

The design procedure for the wideband radiation pattern begins with the design of a narrowband radiation pattern. Here, all known synthesis techniques can be applied, e.g. uniform weighting or windowing methods [8], [9] in order to reduce sidelobe level. This design step delivers the required number of narrowband antenna elements I and (complex) weighting coefficients w_i .

Using these results, a frequency independent spatio-temporal response function is obtained [10], [11], from which the FIR-filter coefficients can be determined. In order to demonstrate the viability of our concept, we consider the narrowband radiation pattern of $I = 5$ element antenna array with equal spacing of $\lambda/2$ between the elements and uniform antenna weighting $|w_i| = 1$. The main beam direction or steering angle should be $\theta_0 = 20^\circ$; the resulting radiation pattern is shown in Fig. 4.

We design this radiation pattern to be constant over a bandwidth 2:1 using the array-FIR structure shown in Fig. 5. A linear array is assumed to have N antenna elements; the spatial distance d between the antenna elements is $\lambda/2$ for the highest frequency f_h . Each element is connected to an M th order FIR-filter with the real weighting coefficients a_{nm} and delay lines of time delay τ . The input signal $x(t)$ is obliquely incident under an angle θ . The resulting output signal $y(t)$ can be

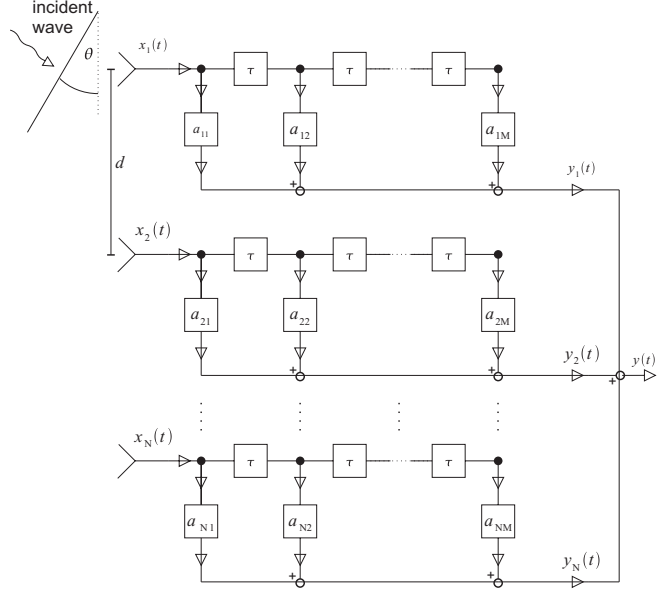


Fig. 5. Principle of array-FIR structure with N antenna elements and M th order FIR-filter

obtained in time-domain as

$$y(t) = \sum_{n=1}^N \sum_{m=1}^M a_{nm} x(t - (n-1)T_0 - (m-1)\tau) \quad (1)$$

A delay time T_0 exists between the antenna elements and is obtained by

$$T_0 = \frac{d}{c_0} \sin \theta, \quad (2)$$

where c_0 is the velocity of light. Eqn. (1) can be transformed to frequency domain, yielding the frequency response of the system as a function of frequency f and incident angle θ as follows

$$\begin{aligned} H(f, \theta) &= \frac{Y(f, \theta)}{X(f)} \\ &= \sum_{n=1}^N \sum_{m=1}^M a_{nm} e^{-j2\pi f((n-1)\frac{d}{c_0} \sin \theta + (m-1)\tau)} \end{aligned} \quad (3)$$

The real filter coefficients a_{nm} can be obtained by performing the 2D inverse discrete Fourier transformation (IDFT) on the frequency response $H(f, \theta)$ [8]. The resulting wideband antenna radiation pattern for three different frequencies in the band 2:1 is shown in Fig. 6. For the simulation, the delay time τ is assumed to be d/c_0 . It can be seen that the wideband radiation pattern does not match exactly with the desired radiation pattern. The latter is an envelope, containing the main beam and sidelobe level of the wideband pattern. The smaller main beamwidth of the wideband pattern compared to the desired one, is due to the higher number of antenna elements $N > I$. However, in main beam direction, the wideband patterns coincide in the investigated frequency band between $0.45f_h$ and $0.9f_h$, where f_h is the highest frequency and serves as a reference for the interelement spacing d . It should be mentioned that the frequency f_h is chosen to be greater than what is required for the frequency band. Since we use a limited

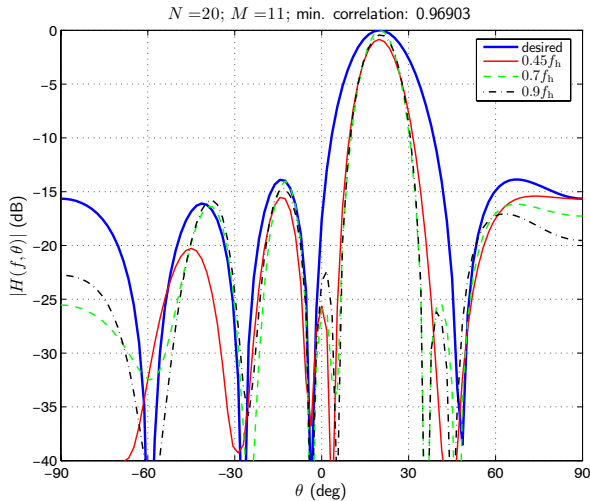


Fig. 6. Normalized desired narrowband radiation pattern (thick blue line) and resulting wideband radiation patterns for a bandwidth 2:1

number of weighting elements, the frequency response $H(f, \theta)$ strongly varies at the frequency band boundaries. However, in the chosen frequency band 2:1, also the nulls are constant (up to a signal level of -32 dB) and the sidelobe levels are below the envelope.

A. Required number of antenna elements and filter-order

The required number of antenna elements N and the FIR-filter order M depend on various design parameters: The desired beam pattern, bandwidth and main beam direction θ_0 . Theoretically, an infinite number of antenna elements and infinite filter order would result in an ideal frequency independent beam pattern. But in practice, the maximum viable array element number and filter order are limited. Ref. [10] concludes that the number of antenna elements and the filter order should be more than three times the numbers of the desired narrowband array. But this assumption neglects the desired bandwidth and main beam direction θ_0 . In addition, ref. [11] presents an expression taking into account the main beam direction θ_0 in the determination of the array size.

Nevertheless, we can check the congruence of our wideband radiation patterns by calculating their correlation; ideally, the correlation should be equal to one. For a given finite number of array and filter-elements, the correlation is lower than one. The worst congruence or the minimum correlation is between the radiation pattern of the lowest and highest frequency in the desired band. In our design example, Fig. 6, the minimum correlation is $x_{\text{cor}} = 0.97$, which indicates good congruence. We arbitrarily assume that the congruence in the frequency band is suitable, if the minimum correlation is greater than $x_{\text{cor}} = 0.97$.

Fig. 7 shows a plot of the minimum correlation as a function of the array element number N and the filter order M for the desired wideband radiation pattern. We can conclude from this simulation that a minimum antenna element number of $N = 20$ and a filter order of $M = 11$ should be chosen. It can be shown that the optimal ratio of array element number and filter order varies as a function of the main beam direction θ_0 . Angles close to $\theta_0 = 0$ require lower filter order and greater array size. With increasing angle θ_0 this ratio changes, up to $\theta_0 = 90^\circ$, where the maximum filter order and the minimum

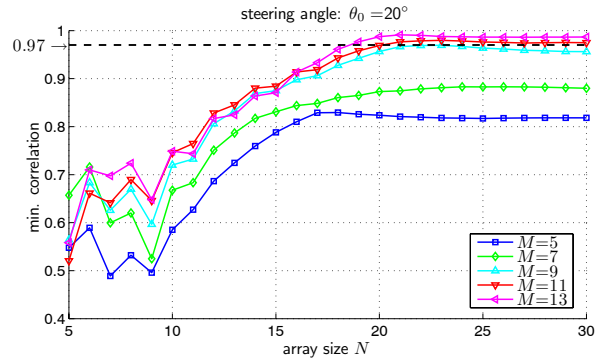


Fig. 7. Correlation of the wideband radiation patterns as a function of the array element number N and filter order M for the design example. A correlation of 1 means a perfect congruence for all frequencies in the desired frequency band 2:1

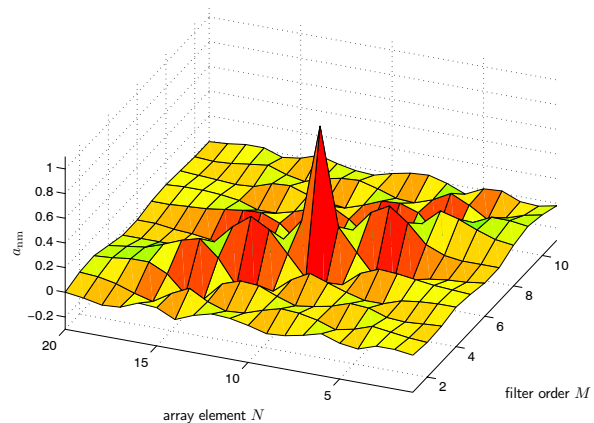


Fig. 8. Normalized weighting coefficients for a $N = 20$ and $M = 11$ array-FIR-structure for bandwidth 2:1. The main beam direction is $\theta_0 = 20^\circ$

array element number is required.

Fig. 8 shows a plot of the normalized weighting coefficients a_{nm} , resulting from our design example. The major weights are located on a diagonal line, whose angle is a function of the steering angle θ_0 . This can be explained by considering a simple TTD-beamformer: The signal $x_1(t)$, reaching the first antenna element, has to be delayed maximum in order to equalize the spatial phase-shift. The required delay decreases from antenna element to element. The higher the steering angle, the higher is the required delay. So, the line of major weights rotates as a function of the steering angle.

B. Requirements for different bandwidths

It is clear that the requirements for the array element number N and the filter order M varies w.r.t. the desired bandwidth and the narrowband synthesis target, e.g. the required beamwidth, number of nulls, etc. Table I summarizes the results for various bandwidths and steering angles, using the above correlation method. The angle $\theta_0 = 0^\circ$ requires the largest array size, whereas the angle $\theta_0 = 90^\circ$ requires the highest filter order. In addition to the five-element uniform narrowband weighting, a Tschebyscheff-windowing was used with 30 dB sidelobe attenuation.

It can be seen that both the antenna element number and the filter order increase with the bandwidth. Furthermore, the Tschebyscheff-windowing yields a relief of the requirements.

TABLE I

REQUIRED NUMBER OF ANTENNA ELEMENTS N AND FILTER ORDER M

bandw.	narrowband pattern	$\theta_0 = 0^\circ$	$\theta_0 = 90^\circ$
1.5:1	$I = 5$ (uniform weighting)	$N = 15$ $M = 5$	$N = 14$ $M = 9$
	$I = 5$ (Tscheb. windowing)	$N = 12$ $M = 5$	$N = 10$ $M = 7$
2:1	$I = 5$ (uniform weighting)	$N = 20$ $M = 7$	$N = 16$ $M = 13$
	$I = 5$ (Tscheb. windowing)	$N = 16$ $M = 5$	$N = 13$ $M = 11$
3:1	$I = 5$ (uniform weighting)	$N = 30$ $M = 15$	$N = 21$ $M = 21$
	$I = 5$ (Tscheb. windowing)	$N = 25$ $M = 7$	$N = 20$ $M = 15$

This is because the Tschebyscheff-windowing increases the narrowband beamwidth. Thus, the requirements for the wideband radiation pattern are reduced, resulting in a lower number of required antenna elements and lower filter order.

So, for the 2:1 bandwidth, a minimum array element number of $N = 16$ elements and a FIR-filter of 10 ($M - 1$) incremental steps is required in order to steer all angles θ_0 , assuming $I = 5$ narrowband elements with Tschebyscheff-windowing. For uniform element spacing of $\lambda/2$ (at highest frequency), the total array length becomes $(N - 1) \cdot \lambda/2 = 15\lambda/2$ and main beamwidth of 12.6° .

IV. CONCEPT FOR PRACTICAL REALIZATION

The amplitude weighting factors a_{nm} of the FIR-filter requires bi-phase variable attenuators ($-1 \leq a_{nm} \leq 1$), which can be realized broadband and as integrated circuits. Practical problems of realization of microwave FIR-filter structures will therefore arise mainly from the spacious delay lines which have to fit in a predictably limited volume and which have to be connected to the attenuator (integrated) circuit.

The variability of the filter response in practical realizations must be limited due to the limitations on the total length of the delay possible and the size of increments τ . In general, time delay increments can be realized at microwave frequencies by using sections of transmission line, either on-chip as lumped LC-networks [12] or off-chip.

Nevertheless, the principle setup of the single FIR-elements, Fig. 9, reminds of a traveling wave amplifier [13]. The weightings a_{nm} are realized by FET-amplifiers, which are distributed along microstrip-lines, realizing the true-time delays τ . By biasing the FET-gates, the amplification of each transistor can be varied according to the required weighting coefficients.

This simple concept neglects the need for both positive and negative weighting coefficients. In [14] we present a modified concept, providing in-phase and out-phase amplification.

Using the traveling wave concept, our design example in practice, for a frequency band from 2 GHz to 4 GHz, would require a total array width of 64 cm ($f_h = 4.45$ GHz, $d = \frac{c_0}{2f_h}$). Realizing the time delays $\tau = \frac{d}{c_0}$ of each FIR-filter in microstrip-line techniques with effective dielectric constant $\epsilon_{r,\text{eff}} = 2.3$, the total length of the transmission lines shrinks to 22 cm. This length should be reduced dramatically, if the transmission lines are coiled, as indicated in Fig. 9. Such array-FIR structure size should be acceptable, e.g. in access point applications.

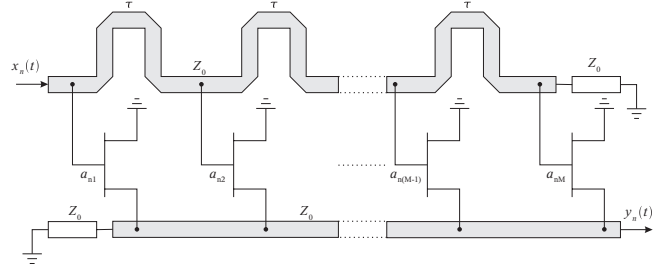


Fig. 9. Concept of a traveling-wave amplifier with M cascaded FETs, connected to transmission lines

V. CONCLUSION

The design procedure of a FIR-filter controlled antenna array for wideband radiation pattern and some trade-off considerations have been presented in this paper. On a concrete design example, we proposed that the required number of antenna elements is between 2 and 6 times that of the narrowband element number, the filter order is between 5 and 15, both depending on the desired bandwidth and steering angle. Our concept for practical realization at microwave signal level is promising due to the use of standard RF-components.

Our future research will focus on the robustness of the wideband radiation pattern design. We will investigate the results in view of systematical and statistical variation of the design parameters due to practical tolerance problems. This could be the non-ideal variation of interelement spacing, time-delay, weighting coefficients, non-uniform gain of the antenna elements, influence of mutual coupling between antenna elements, etc.

REFERENCES

- [1] C. E. Baum, E. G. Farr, "Impulse radiating antennas," pp. 139-147 in H. L. Bertoni et al (eds.), *Ultra Wideband/Short-Pulse Electromagnetics*, Plenum Press, New York, 1993.
- [2] H. G. Schantz, "Introduction to ultra wideband antennas," *IEEE UWBST Conference*, pp. 1-9, Nov., 2003
- [3] S. Ries, T. Kaiser, "Towards beamforming for UWB signals," *EUSIPCO*, Sep. 2004
- [4] T. Do-Hong, P. Russer, "Signal processing for wideband smart antenna array applications," *IEEE Microwave Magazine*, pp. 57-67, March. 2004.
- [5] L. C. Godara, "Application of antenna arrays to mobile communications, part II: beam-forming and direction-of-arrival considerations," *IEEE Proc.*, vol. 85, no. 8, pp. 1195-1245, Aug. 1997
- [6] S. Drabowitch, A. Papiernik, H. Griffiths, J. Encinas, B. L. Smith, *Modern antennas*, Chapman & Hall, 1998
- [7] M. Ghavami, L. B. Michael, R. Kohno, *Ultra Wideband - Signals and systems in communication engineering*, John Wiley & Sons, Inc., 2004
- [8] H. L. van Trees, *Optimum array processing - part IV of detection, estimation and modulation theory*, John Wiley & Sons, Inc., 2002
- [9] C. A. Balanis, *Antenna theory - analysis and design*, 2nd ed. John Wiley & Sons, Inc., 1997
- [10] T. Sekiguchi, Y. Karasawa, "Wideband beamspace adaptive array utilizing FIR FAN filters for multibeam forming," *IEEE Trans. Signal Processing*, vol. 48, no. 1, pp. 277-284, Jan. 2000
- [11] M. Ghavami, "Wideband smart antenna theory using rectangular array structures," *IEEE Trans. Signal Processing*, vol. 50, no. 9, pp. 2143-2151, Sept. 2002
- [12] M. Maeng, F. Bien, Y. Hur, S. Chandramouli, H. Kim, Y. Kumar, C. Chun, E. Gebara, J. Laskar, "A 0.18um CMOS equalizer with an improved multiplier for 4-PAM/20Gbps throughput over 20-inch FR-4 backplane channels," *IEEE MTT-S Digest*, vol. 1, pp. 105-108, June. 2004
- [13] D. M. Pozar, *Microwave engineering*, 3rd ed. John Wiley & Sons, Inc., 2005
- [14] K. Solbach, T. Ould Mohamed, M. Neinhüs, M. Tekloth, "Microwave analogue FIR-filter," *German Microwave Conference*, Ulm, April 2005.

94 GHz Zonal rings reflector for helicopter collision avoidance

B.D. Nguyen, C. Migliaccio, C. Pichot

Laboratoire d'Electronique, Antennes et Télécommunications (LEAT), Université de Nice- Sophia Antipolis,

CNRS-UMR 6071, 250 rue A.Einstein, 06560 Valbonne, France. Tel:+33.4.92.94.28.00

Abstract — A single-layer reflector antenna combining eight and four correcting Fresnel zones is presented. The progressive phase shift is achieved by circular and annular patches. The choice of a quarter-wavelength thickness substrate provides naturally 0° and 180° correcting zones that simplifies the reflector design. A prototype of reflector antenna working at 94 GHz has been designed, built and measured. Measurement results show 70% improvement of antenna aperture efficiency compared to the half-wave Fresnel zone plate reflector [1].

I. Introduction

Millimeter-wave radars are commonly used as complementary systems for preventing helicopters crashes. The antenna of the radar requires high gain. Recently, printed reflectors or reflectarrays [1-5] have become competitive solutions against parabolic reflectors or lenses, due to their low cost, low profile and fabrication facilities. The critical point in their design is to obtain a reflection phase range varying over 360°. It might be achieved by using rectangular or annular patches elements combined with multilayer structures [3, 5], but is not easy to fabricate at millimetre wavelengths. A single-layer alternative solution is the use of a concentric ring array structure [5]. Nevertheless, dimensions are still critical for classical printed circuit fabrication techniques at high frequencies because of fabrication tolerances and limited number of possible correcting zones.

In this paper, we present a single-layer ring reflector using circular, annular or combined patches placed in classical Fresnel zones. Furthermore, a quarter-wavelength substrate was used to simplify the design. The aperture radiation efficiency at 94 GHz is of 34%. Two zonal ring reflectors were made, measured and compared with the classical half-wave Fresnel zone plate reflector (FZP) showing an improvement of 50% aperture radiation efficiency for the smallest one (four correcting Fresnel zones) and 70% for the largest (combined eight and four correcting Fresnel zones).

II. Design of the reflector

Fig.1 shows the design principle of a quarter-wave zonal ring reflector from the substrate top side. The other side of the substrate is a ground plane. The radius of each zone is calculated with the classical Fresnel formula, where f is the focal length, n the order of the zone, λ the wavelength and P the number of correcting zones (here $P=4$).

$$r_n = (nf\lambda + n\lambda/P)^{1/2} \quad (1)$$

The dedicated space for each zone is given by $(r_n - r_{n-1})$. The use of a quarter-wavelength substrate provides naturally 0° and 180° zones. Zones of 90° and 270° are filled with three basic elements (a), (b) and (c) described in Fig 2. As an example to show the reflection phase range, we choose to fix the external radius r_e of (b) and (c) and to vary r (Fig. 3). Reflection phase range -180°/180° is covered. Simulations were made by means of HFSS software using the periodic structure module. As the space for each zone decreases when n increases, the external radius r_e in (b) and (c) has to be recalculated. Internal radius r is then adjusted in order to provide the desired reflection phase. The 270° zone of Fig.1 is achieved with (c) and r about 0.33mm. The choice of the type of basic element on several factors, the priority is given to the easiest to etch (e.g. (a), circular patch). It is suitable for up to the 90° zone but has to be replaced by (b) or (c) for higher phases. The $\lambda/8$ -wave zonal rings reflector is based on the same principle with $P=8$. It is important to note that an increase in P is possible only by using element (c) that provides phases between 180° and 360° in a limited space. Owing to computation limits, only 23 mm diameter with $P=4$ was simulated using HFSS to verify the improvement in antenna aperture radiation efficiency compared to classical FZP.

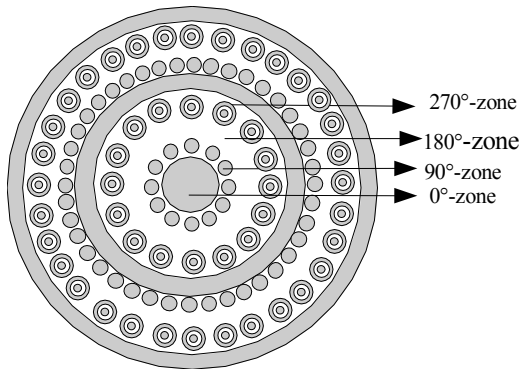


Fig.1 Design and geometry of quarter-wave zonal rings reflector of 9 zones

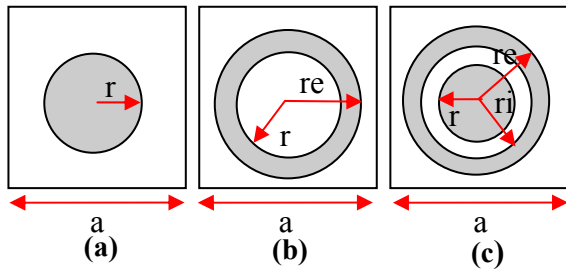


Fig. 2 Basic elements used for the zonal ring reflector
 (a) circular patch element.
 (b) annular patch element
 (c) combined circular and annular patch element

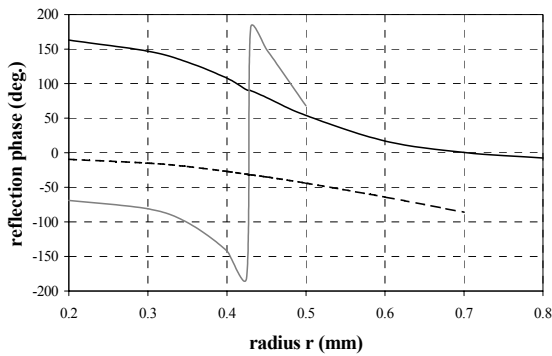


Fig. 3 Reflection phase from each basic element versus the inner radius r at $f=94$ GHz with $a=1.8$ mm.
 (a) — circular patch element
 (b) --- annular patch element, $r_e = 0.8$ mm.
 (c) — combined circular and annular patch element, $r_e = 0.8$ mm and $r_i = 0.6$ mm

III. Measurements

Two different rings reflectors were fabricated. The first one, 56 mm in diameter, focal length of 35 mm, is a quarter-wave zonal ring reflector with 13 zones. The second one, 130 mm in diameter, focal length of 72 mm is a combination of $\lambda/8$ -wave zonal rings reflector in its center and a quarter-wave zonal ring reflector when n increases. Indeed when n increases the space for each zone with $P=8$ becomes too short to achieve the desired

reflection phase. We have to reduce $P = 4$. Therefore, the fabricated reflector has 9 zones with $P=8$ and 24 with $P=4$. For performance comparisons, half-wave FZP reflectors of the same diameters were fabricated. All reflectors are made on Duroid of dielectric constant 2.2 and 0.508mm thickness. The primary source is a standard open ended WR-10 waveguide. The design frequency is 94 GHz. In Fig. 4, E- and H-planes radiation patterns are plotted for the largest zonal rings reflector antenna. Beamwidth at -3 dB is 1.5° in both planes and side lobes levels are of -18 dB in the E-plane and -19 dB in H-plane. Figure 5 shows measured gain against frequency. It is 3 dB higher than FZP for the small zonal ring reflector and 4.5 dB higher for the largest one at 94 GHz. Table. 1 gives performances in terms of gain and antenna aperture efficiency (η) for the four investigated reflectors. We note that η is the same for the 56 and 130 mm zonal rings' reflectors. This is due to inadequate measurement conditions for the largest reflector in our anechoic chamber. Indeed, dimensions of the chamber limit the distance used for measurements to 4.65 m whereas the minimum distance required for far-field measurements is about 10 m at 94 GHz for a 130 mm diameter antenna. Gain and radiation pattern measurements are affected, i.e, real gain and h should be higher [6]. Nevertheless, half-wave FZP of 130 mm diameter was measured under the same conditions. Antenna aperture efficiency improvement is of 70%.

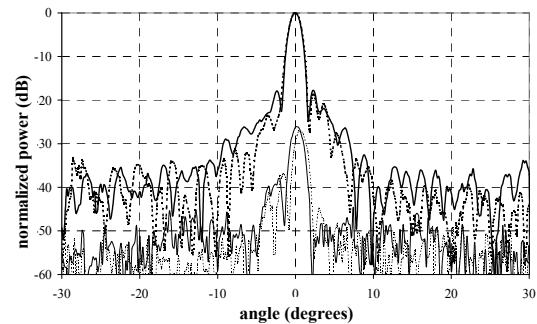


Fig. 4 Measured radiation pattern at 94 GHz
 — E-plane, co and cross polarizations
 --- H-plane, co and cross polarizations

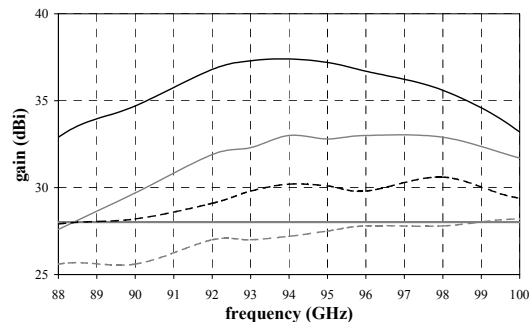


Fig. 5 Measured gain versus frequency
 — zonal rings reflector, 130 mm diameter
 --- FZP, 130 mm of diameter
 -.- zonal rings reflector, 56 mm diameter
 ... FZP, 56 mm of diameter

Type of reflector	Gain (dBi)	η (%)
Rings reflector (56 mm)	30.2	34
Half-wave FZP (56 mm)	27.4	17.3
Rings reflector (130 mm)	37.5	34
Half-wave FZP (130 mm)	33	12.3

TABLE I
GAIN AND APERTURE EFFICIENT OF REFLECTORS AT 94 GHZ

IV. CONCLUSION

We have developed a reflector antenna combining metallic correcting zones with smaller circular or annular patches providing up to 8-Fresnel correcting zones. The choice of the substrate thickness corresponding to a quarter-wavelength provides naturally 0° and 180° zones. It reduces the sensitivity to manufacturing tolerances and simplifies the design. Furthermore, the phase correction has been increased up to 360° by using three types of basic elements. Preliminary measurements show a good performances and an improvement of 70% comparing to half-wave zonal reflector antenna.

References

- [1] B. Huder and W. Menzel, "Flat printed reflector antenna for mm-wave applications", *Electron. Lett.*, vol. 24, pp. 318-319, Mar. 1988.
- [2] Pozar, S.D. Targonski, and H.D. Syrigos, "Design of millimeter wave microstrip reflectarrays", *IEEE Trans. Antennas Propagat.* Vol. 45, pp. 287-295, Feb.1997.
- [3] A. Encinar, "Design of two-layer printed reflectarrays using patches of variable size", *IEEE Trans. Antennas Propagat.* Vol.49, pp 1403-1410, October 2001.
- [4] Y.Jay Guo and S.K. Barton, "Phase correcting zonal reflector incorporating rings", *IEEE Trans. Antennas Propagat.* Vol. 43, pp 350-355, April 1995.
- [5] N.Misran, R.Cahill and V.F.Fusco, "Design optimisation of ring elements for broadband reflectarray antenna", *IEE Proc.-Microw. Antennas Propag.*, Vol.150, No. 6, pp. 440-444, December June 2003.
- [6] W. Menzel and B. Huder, "Compact range for millimeter-Wave frequencies using a dielectric lens", *Electron. Lett.*, vol.20, pp. 768-769, September 1984.

Multi-layered Submillimetre FSS of Shifted Crossed Slot Elements for Applications in Radio Astronomy

Ge Wu¹, Volkert Hansen¹, Hans-Peter Gemuend² and Ernst Kreysa²

¹Chair of Electromagnetic Theory, University of Wuppertal,
Rainer-Gruenter-Str. 21, 42119 Wuppertal, Germany,
Tel: +49-202-439-1935, E-Mail: ge.wu@uni-wuppertal.de

²Max Planck Institute for Radioastronomy, Bonn, Germany

Abstract — This paper deals with the designs and performances of the multi-layered FSS structures proposed as band-pass filters in space applications. The so called shifted crossed slot elements are utilized as resonant meshes, with the help of which two types of 4-resonant-mesh-filters are realized either with air spacers or dielectric separations, possessing a sharp roll-off frequency response. The method of moment (MoM) used in a spectral domain analysis and some numerical results are presented. The production technology is also described.

I. INTRODUCTION

The advances in frequency selective surfaces (FSS) technology have led to their use as high-grade filters for submillimetre wave applications [1], [2]. In this paper, we report on the designs and performances of FSS band-pass filters which fulfill the special requirement of bolometer systems for radio astronomy. The proposed filters shall, on the one hand, exhibit a selectivity as high as possible, so it is often necessary to have a frequency separation ratio of 1.05:1 or less; on the other hand possess a broad stop band - a good attenuation is necessary particularly at higher frequencies because of the thermal radiation rising with f^2 , from telescope and atmosphere at ambient temperature [3], [4].

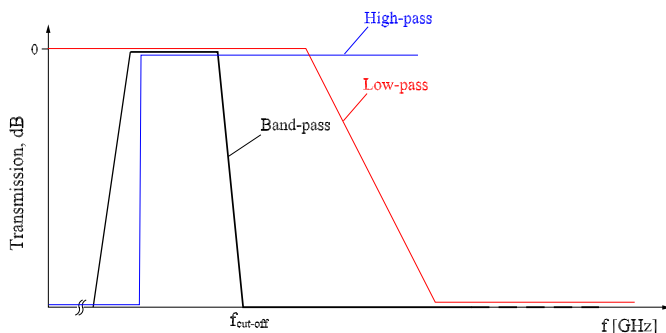


Fig. 1. Cascading of a high-pass, a low-pass and a band-pass

A sharp roll-off frequency response can only be achieved by making use of the interference effects between two or more FSS screens. We present one 4-resonant-mesh-filter with air spacer at a cut-off frequency of 290 GHz, and one with 4 mesh layers embedded in dielectric material (polypropylene), at a cut-off frequency of 370 GHz. The so called shifted crossed slot elements are applied as resonant mesh structure.

To suppress the high order propagating modes, a low-pass filter consisting of layers of metallic square patches is applied for making a sufficient wide stop band. On the other hand, a circular waveguide is employed as a high-pass which cuts out the undesired low frequency band to meet the required

bandwidth. Fig. 1 indicates schematically this combination. It is easy to realize these types of low-pass and high-pass filters, therefore, the entire problem is led to the essential task of developing the band-pass filters with a sharp roll-off on the edge of interest (cut-off).

II. DESIGN OF FSS BAND-PASS FILTERS

In simple mesh filters, metal meshes (either free-standing or supported by dielectric sheets) are mounted with separating distances typically less than one wavelength. The distances between these meshes provide the resonant elements. More advanced designs use meshes that are resonant in themselves thus reducing the accuracy of spacing required [5], [6]. Fig. 2 shows a capacitive mesh, an inductive mesh and a resonant mesh of crossed slot structure.

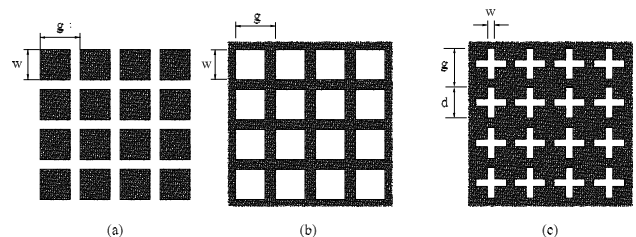


Fig. 2. (a) Capacitive mesh, (b) Inductive mesh and (c) Resonant Mesh

In this study, we take advantage of the so called shifted crossed slot elements to realize the band-pass filters because of their excellent resonant behavior. Fig. 3 illustrates the geometry of this resonant mesh and its equivalent circuit from lumped elements.

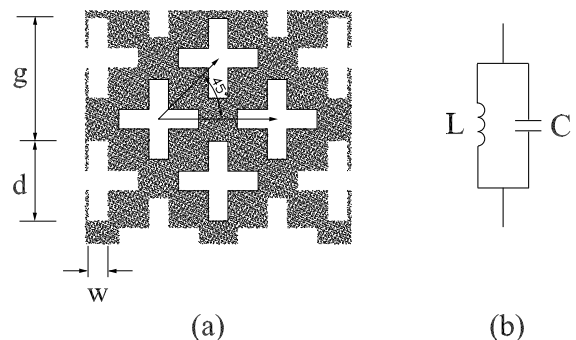


Fig. 3. (a) Shifted crossed slots elements and (b) Equivalent circuit

It has to be taken into account during the design process that compared to the normal crossed slots elements (Fig. 2.

(c)), the densely packed shifted crossed slots elements cause a frequency shift towards higher frequencies. Furthermore, they possess a broader bandwidth that leads to more stability according to the frequency response. This has been confirmed by many measurements.

The multi-layered FSS band-pass filters are first approximated by an equivalent circuit model, which represents the FSS layers and their separations (air or dielectric) by LC resonant circuits and transmission lines, respectively (Fig. 4).

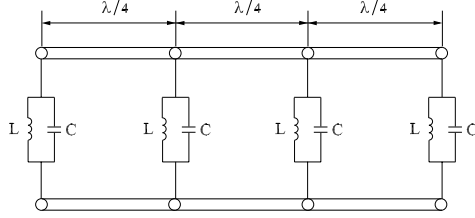


Fig. 4. Equivalent circuit model consisting of LC resonant circuits connected by $l = \lambda/4$ transmission lines

The analysis of the equivalent circuit model is carried out with the help of the classical filter theory [7], [8]. The transmission characteristics of the equivalent circuits are evaluated recursively starting from the end of the circuit applying the formulas of transmission-line. This first order analysis shows that the roll-off rate is optimized by making the length of the transmission lines $l = \lambda/4$, where λ is the peak wavelength of the individual resonant circuits. The transmission lines then act as the so called impedance inverters leading to high peak transmission in the pass band, but away from the center wavelength leading to a sharp cut-off and excellent out of band rejection.

For the realization of the filters with FSSs, a 4-resonant-mesh-filter design is selected - 4 identical resonant meshes are placed one on top of the other with an equal spacing layer of $l = \lambda/4$. The performances of the designed filters are further analyzed and the transmission characteristics are exactly calculated with the help of the below mentioned numerical code.

III. COMPUTATION OF THE TRANSMISSION FACTORS

The computation of the FSS filter is based on a spectral domain analysis, which solves the electromagnetic field problem with the help the spectral Green's function of layered media [9].

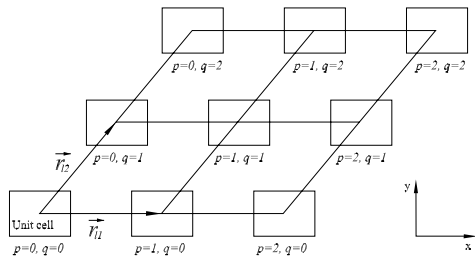


Fig. 5. General grid array consisting of a double periodic arrangement of elementary cells

Fig. 5 shows a general grid array, which consists of a infinite double periodic arrangement of elementary cells. In this study, they are apertures in a conducting surface. In the l th layer, the position of the pq th cell compared to that of the unit cell is

described by

$$\vec{r}_{lpq} = p\vec{r}_{l1} + q\vec{r}_{l2}, \quad (1)$$

where l denotes the layer number. And the pq th cell is move by

$$\Delta x_{lpq} = p \cdot r_{l1x} + q \cdot r_{l2x}, \quad \Delta y_{lpq} = p \cdot r_{l1y} + q \cdot r_{l2y} \quad (2)$$

from the unit cell located in the origin. Applying the Floquet theorem, the magnetic current distribution is formulated:

$$\vec{M}(x, y, z) = \sum_{l=1}^L \sum_{p=-\infty}^{+\infty} \sum_{q=-\infty}^{+\infty} \sum_{n=1}^{N_l} U_{ln} \cdot \vec{f}_{ln}(x - \Delta x_{lpq}, y - \Delta y_{lpq}) \cdot e^{j(k_{ex} \Delta x_{lpq} + k_{ey} \Delta y_{lpq})} \delta(z - z_l), \quad (3)$$

where $\vec{f}_{ln}(x, y)$ are the basis functions, k_{ex} and k_{ey} are the wave numbers of the incident plane wave, and U_{ln} are the unknown amplitudes of magnetic currents, respectively.

Using the 2-D Fourier transformation, the magnetic field is obtained as

$$\vec{H}(x, y, z) = \sum_{l=1}^L \frac{1}{|r_{l1x} \cdot r_{l2y} - r_{l2x} \cdot r_{l1y}|} \cdot \sum_{n=1}^{N_l} \sum_{p=-\infty}^{\infty} \sum_{q=-\infty}^{\infty} U_{ln} \cdot \vec{G}_M^H(k_x(l, p, q), k_y(l, p, q), z, z' = z_l) \cdot \vec{F}_{ln}^H(k_x(l, p, q), k_y(l, p, q)) \cdot e^{j(k_x(l, p, q)x + k_y(l, p, q)y)}, \quad (4)$$

where \vec{G}_M^H denotes the spectral Green's function for the magnetic field, \vec{F}_{ln}^H are the Fourier transforms of the basis functions \vec{f}_{ln} and the discrete wave numbers

$$k_x(l, p, q) = k_{ex} + \frac{2\pi}{|r_{l1x} \cdot r_{l2y} - r_{l2x} \cdot r_{l1y}|} \cdot (r_{l2y} \cdot p - r_{l1y} \cdot q) \quad (5)$$

and

$$k_y(l, p, q) = k_{ey} + \frac{2\pi}{|r_{l1x} \cdot r_{l2y} - r_{l2x} \cdot r_{l1y}|} \cdot (r_{l2x} \cdot p - r_{l1x} \cdot q) \quad (6)$$

are in context with the Floquet theorem.

An integral equation for the magnetic currents can be formulated by substituting the spectral domain representation of the magnetic field (eq. 4) into the remaining boundary condition at the surfaces. The integral equation is solved by the Galerkin MoM, leading to a linear system of equations with the system matrix $[Z]$ and the matrix elements

$$Z_{mn}(l, l') = \frac{1}{|r_{l'1x} \cdot r_{l'2y} - r_{l'2x} \cdot r_{l'1y}|} \cdot \sum_{p=-\infty}^{\infty} \sum_{q=-\infty}^{\infty} \vec{G}_M^H(k_x(l', p, q), k_y(l', p, q), z = z_l, z' = z_{l'}) \cdot \vec{F}_{ln}^H(k_x(l', p, q), k_y(l', p, q)) \cdot \vec{F}_{lm}^H(-k_x(l, p, q), -k_y(l, p, q)). \quad (7)$$

A computer program on the basis of this theory has been developed. A lot of FSS structures have been calculated and a large number of measurements have been made, yielding a rather good agreement between the measured and the calculated values [4], [9].

IV. FABRICATION

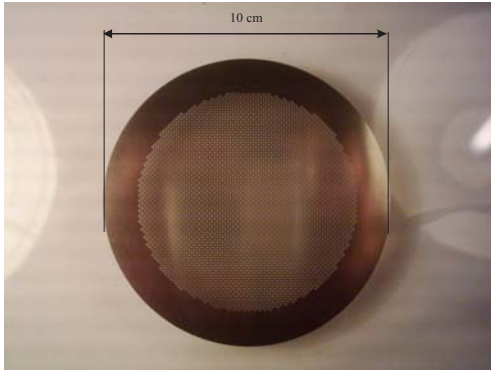


Fig. 6. Basic resonant mesh filter

Basic parts of the filters are the meshes which are galvano formed high-precision parts (Fig. 6). They consist of approximately 15 micron thick Ni-foils holding an appropriate array of apertures (in our case the array consists of a dense packing of cross-shaped apertures). Even for structured regions of 100 mm diameter or more the thin foils exhibit an excellent flatness and at the same time a high mechanical stability. Both are necessary for the embedding in a polymer. Up to four meshes were stacked together in well-defined distances and embedded in a polypropylene matrix.

The idea behind the embedding is the following: Knowing the spectral behaviour of a single mesh, it is possible to match a desired spectral profile by stacking several meshes with specific spacers between them. This can be done with help of annuli between freestanding plane meshes: the thickness of the distance-ring is equal to the air-gap between two adjacent meshes. The spectral performance of such filters is strongly depending on the dimension of the spacer, so it is not wonder that small changes in the distance between the meshes cause severe changes (typically degradations) of the achieved spectral profile.

We are considering filters of large diameter, and these filters are to be used in cryogenic systems. Consequently, the filters have to withstand repeated vacuum cycles and repeated thermal cycles. Considering large filters of freestanding meshes with air-spacers between them, already a single vacuum cycle (air-vacuum-air) is a substantial load at least onto the outer meshes of the stack. During cryogenic cycles the large meshes are cooled or warmed radially, accordingly different regions of the meshes have different temperatures and hence different thermal contractions. Especially when repeated, both cycles result in a degradation of the evenness of the meshes, and this is equivalent with a loss in the optical performance.

Embedding the meshes into an appropriate medium is a way to make the filters so robust that they withstand vacuum cycles as well as thermal cycles. For this purpose we use commercial PP-foils which are available in a large variety of thickness. The desired PP-spacer thickness can be realized by combination of several thin foils. Then beginning with a thin PP-foil the stack starts with the first mesh, then the first PP-spacer in form of several foils follows, then the second mesh and so on. The single meshes are (more or less) aligned to each other. After the last mesh a last thin foil is added as top

layer. Then the complete stack is put between two heating plates which are transferred into a vacuum chamber. Here the stack of many foils is gently heated above the melting temperature of the polypropylene. After cooling all single foils have combined into a flat monolithic block of polypropylene incorporating several meshes in well-defined distances. The resulting filters are very plane, at room-temperature as well as at low temperatures. When cooling to temperatures around 4 K the composite filter might deform due to differences in the thermal expansion coefficients of its components. Because most of the integral thermal contraction has happened already at 77 K, we therefore performed thermal cycles by dropping the filters into liquid nitrogen and bringing them back to room-temperature. In spite of this rough method the filters showed no change (visual inspection) or degradation (spectral measurement) over 40 cycles. Thus, embedding these particular meshes into polypropylene results in rigid and robust filters for cryogenic application and provides stable optical performance over a long lifetime.

V. NUMERICAL AND EXPERIMENTAL RESULTS

Numerical and measured results of two types of band-pass filters composed of the shifted crossed slot elements are presented. The element sizes and the free-standing mesh resonant characters of the two different types are displayed in Fig. 7 and Fig. 9, respectively. Fig. 8 shows the 4-resonant-mesh-filter in air, i.e. type 1, designed for $f_c = 290GHz$, and Fig. 10 the type 2 of $f_c = 370GHz$ with dielectric separations. A good agreement is achieved between the measured and computed values. The filter type 1 gives an edge of band frequency roll-off rate of $\sim 1.05:1$. However, due to the attenuation in the pass band of the filter type 2, the absorption loss of the substrate material has been shown to be a limiting factor in the performance.

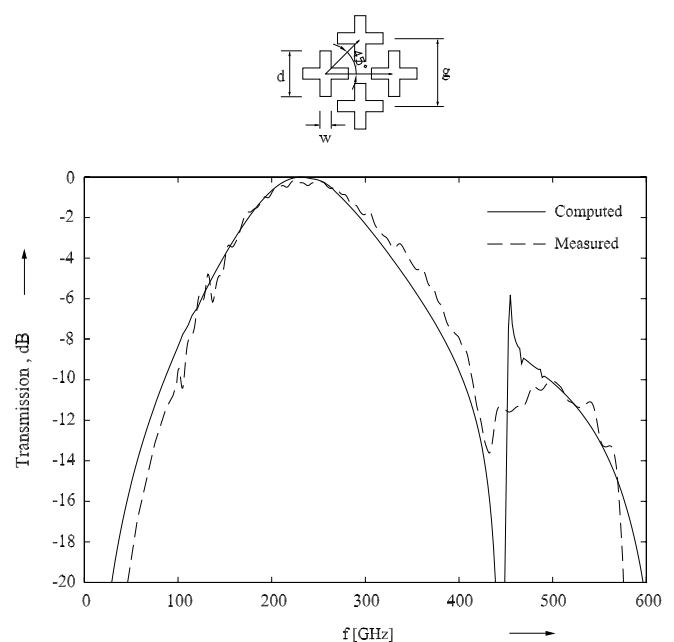


Fig. 7. Computed and measured transmission of one free-standing resonant mesh of type 1.

Grid parameters are: $g = 935\mu m$, $d = 760\mu m$, $w = 99\mu m$.

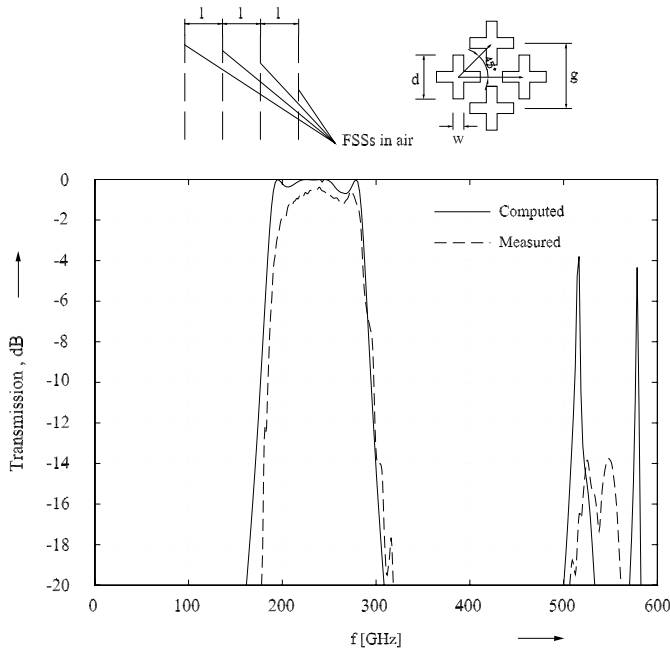


Fig. 8. Computed and measured transmission of the 4-resonant-mesh-filter (type 1).

Air separation: $l = 300\mu\text{m}$. Grid parameters are:
 $g = 935\mu\text{m}$, $d = 760\mu\text{m}$, $w = 99\mu\text{m}$.

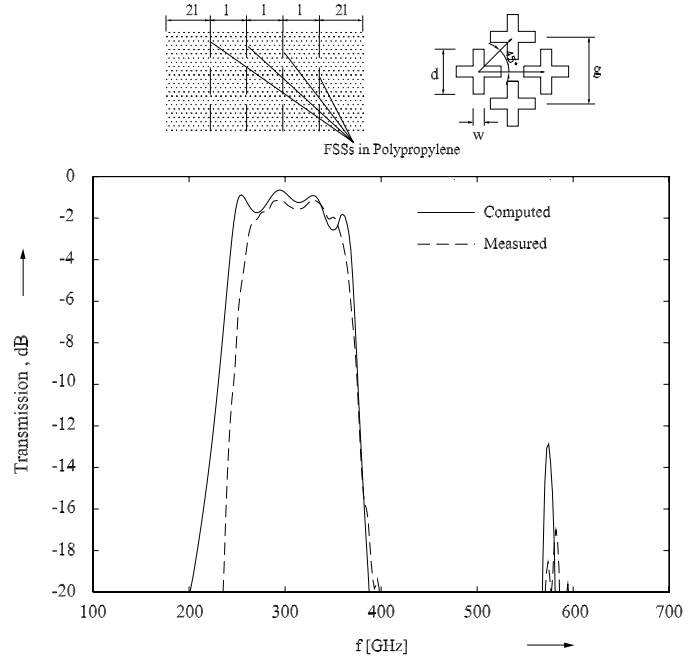


Fig. 10. Computed and measured transmission of the 4-resonant-mesh-filter (type 2).

Dielectric separation: $l = 133\mu\text{m}$. Grid parameters are:
 $g = 492\mu\text{m}$, $d = 400\mu\text{m}$, $w = 52\mu\text{m}$.

VI. CONCLUSION

The work presented in this paper describes design and performance of submillimetre band-pass filters, which are realized by shifted crossed slot elements meshes. Some numerical results are presented, which agree quiet well with the experimental measurements. The performance of a multi-layered FSS with dielectric spacer material is limited by the insertion loss, which has negative influence on the transmission roll-off rate. Further developments are in progress to reduce this loss component.

REFERENCES

- [1] Hook, M., Vardaxoglou, J.C., Ward, K. Applications of Frequency Selective Surfaces, *27th ESA-WPP-222*, pp. 299-309 2004.
- [2] Irwin, P.G.J., Ade, P.A.R., Calcutt, S.B. Taylor, F.W., Seeley, J.S., Hunneman, R. and Walton, L. Investigation of dielectric spaced resonant mesh filter designs for PMIRR, *Infrared Physics*, Vol. 34, pp. 549-563 1993.
- [3] Aroudaki, H., Hansen, V., Gemuend, H.P., Kreysa, E. Analysis of Low-pass Filters Consisting of Multiple Stacked FSS's of Different Periodicities with Applications in the Submillimeter Radioastronomy, *IEEE Trans. Antennas Propagat.*, vol. 43, pp. 1486 - 1491, December 1995.
- [4] Wu, G., Hansen, V., Kreysa, E., Gemuend, H.P., Combination of Classical Filter Theory and Spectral Domain Analysis for the Design of Multi-layered Filters in the Submillimetre Wave Range, *URSI EMTS* 2004.
- [5] Munk, B.A. Frequency Selective Surfaces, Theory and Design, *John Wiley & Sons, Canada* 2000.
- [6] Wu, T.K. Frequency Selective Surfaces and grid array, *John Wiley & Sons, Canada* 1995.
- [7] Matthaei, G., Young, L., Jones, E.M.T. Microwave filters, impedance-matching networks, and coupling structures, *Artech House Books, Dedham, MA*, 1964.
- [8] Saal, R. Handbook of Filter Design, *AEG-Telefunken, Berlin und Frankfurt am Main*, 1979.
- [9] Aroudaki, Spektralbereichsanalyse von mehrlagigen planaren Schaltungen mit dreidimensionalen Diskontinuitäten, *Dissertation, Universität Wuppertal* 1996.

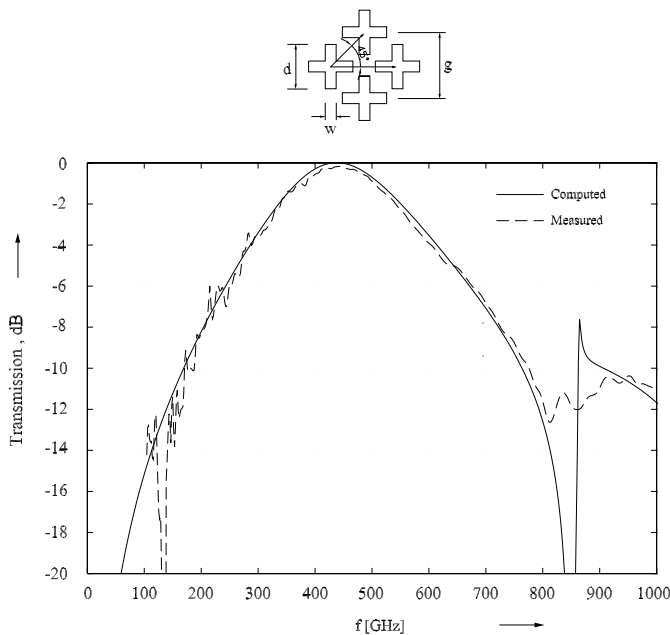


Fig. 9. Computed and measured transmission of one free-standing resonant mesh of type 2.

Grid parameters are: $g = 492\mu\text{m}$, $d = 400\mu\text{m}$, $w = 52\mu\text{m}$.

A Frequency Selective Surface for Harmonic Suppression in THz-Multipliers

S. Biber¹, O. Günther¹, M. Bozzi², L. Perregrini², B. M. Fischer³, A. Hofmann¹,
P. U. Jepsen⁴, H. Helm³, L.-P. Schmidt¹,

Contact: Stephan Biber, stephan@lhft.de, Institute for Microwave Technology,
Cauerstr. 9, 91058 Erlangen, Germany, fax: (49) 9131 8527212

Abstract—A quasi-optical filter for harmonic suppression in THz multipliers with a pass-band at 300 GHz and a stop-band at 450 GHz was developed. The filter consists of a 2-dimensional slot array, and is made from microstructured aluminium on an electrically thick, high-resistivity silicon substrate. The filter therefore have a very good mechanical stability and can be manufactured by using reliable processes available from the semiconductor industries. The design of the filter was based on the MoM/BI-RME method. The frequency response of the filter was optimized for a plane wave with oblique incidence angle and it was shown that fine-tuning of the stop-band can be accomplished by small changes of that angle. Measurements relying on THz-time-domain spectroscopy as well as CW-measurements show an insertion loss smaller than 1.6 dB at 300 GHz and a stop-band attenuation larger than 20 dB at 450 GHz.

Index Terms—Filter-Design, Frequency-Selective Surface, Quasi-Optics, THz-Technology.

I. INTRODUCTION

IN the course of increasing interest in the millimeter and sub-millimeter wave domain, powerful and compact semiconductor based sources have been developed. This motivated the development of a broad variety of different technologies including Gunn-oscillators, waveguide and quasi-optically coupled multipliers based on Schottky-diodes or varactors [1]-[4]. As thermal failure limits the maximum output power of single devices, sources with output-power levels larger than 100 mW use quasi-optically coupled distributed elements and spatial power combining to generate a single strong beam [5]. A problem of all systems based on multiplier concepts is the generation of undesired harmonics. To generate a beam consisting of a single frequency it is necessary to suppress the unwanted lower and higher harmonics. While lower harmonics can be eliminated on the detector-side using the cut-off-frequency of a rectangular waveguide in front of the mixer, higher harmonics can be eliminated by using frequency selective surfaces (FSSs). For this kind of applications, FSSs usually consist of a single or double metal screen, perforated periodically with holes and possible supported by a dielectric substrate.

¹Institute for Microwave Technology, University of Erlangen-Nuremberg, Germany.

²Department of Electronics, University of Pavia, Italy.

³Institute for Molecular and Optical Physics, University of Freiburg, Germany.

⁴COM Research Center, Nanophotonics, Technical University of Denmark.

In this paper, we propose the design of FSSs on thick high-resistivity silicon substrates, in order to overcome the major disadvantages of the technologies developed so far. The silicon substrate with a thickness in the 200-1000 μm mechanically supports the FSS and prevents damage as well as changes of the frequency-characteristics due to cooling or mechanical deformation of the FSS, as it often happens for free standing structures. Its mechanical stability would also allow for the application of such a device as a window material with integrated filter for vacuum shielding of cryogenic receivers/transmitters. High-resistivity silicon is one of the very few materials with extremely low dielectric loss even at higher millimeter and sub-millimeter wave frequencies. Using silicon as a substrate also enables to use highly developed and extremely reliable technologies for structuring metal on silicon, which are available from semiconductor foundries. This is the major advantage compared to other approaches [6], [7], which all require to develop a new specialized technology, resulting in very time-consuming and costly fabrication processes.

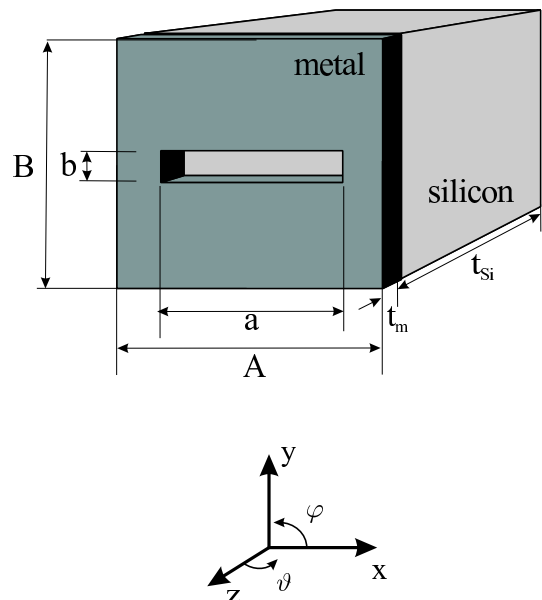


Fig. 1. Unit cell of the FSS with a rectangular aperture. The filter was designed for an incident plane wave at $\vartheta = 20^\circ$, $\phi = 90^\circ$, in TM-polarization.

II. DESIGN OF THE FILTER

The filter presented here is intended for transmitting the second harmonic generated by a quasi-optical multiplier array pumped at 150 GHz, and suppressing the signal at the 3rd harmonic. Therefore, to satisfy the design specs, the FSS should exhibit minimum insertion loss at 300 GHz, and present a stop-band attenuation larger than 20 dB at 450 GHz.

The structure of the filter consists of a 2 μm aluminium layer, perforated periodically with rectangular slots and mechanically stabilized by an electrically thick silicon wafer, with relative dielectric permittivity $\varepsilon_r = 11.8$ (Fig. 1). The design was performed for an incidence angle of $\vartheta = 20^\circ$, in order to prevent standing waves in the quasi-optical setup.

Since the thickness of the silicon wafer is in the order of the wavelength, the structure behaves like a Fabry-Perot resonator. Therefore, in order to get maximum transmission at 300 GHz, it is necessary to align the resonance of the metal grid—depending on the slot length—and the resonance of the Fabry-Perot, which is defined by the thickness of the silicon layer. Conversely, the stop-band frequency at 450 GHz can be set by properly choosing the spacing between the slots (A and B in Fig. 1).

On the bases of these physical concepts, it is possible to select the tentative values of the geometrical dimensions of the structure. In particular, three parameters have to be set:

- the thickness t_{Si} of the silicon substrate;
- the length a of the rectangular slot;
- the size of the unit cell (A and B).

The thickness t_{Si} of the dielectric substrate has to satisfy the Fabry-Perot resonance condition at $f = 300$ GHz:

$$t_{Si} = k \cdot \frac{c}{2f\sqrt{\varepsilon_r}} \cdot \cos \left[\arcsin \left(\frac{1}{\sqrt{\varepsilon_r}} \sin \vartheta \right) \right] \quad (1)$$

where $k = 1, 2, \dots$, and c is the speed of light in vacuum. For an oblique incidence angle at $\vartheta = 20^\circ$ and by choosing $k = 2$, the required thickness results $t_{Si} = 289.7 \mu\text{m}$. The design presented here is based on wafers with $t_{Si} = 302 \mu\text{m}$, because wafers with that thickness have been easily available.

Under the hypothesis $b \ll a$, the length a can be determined by using the resonance condition:

$$a = \frac{\lambda}{2} = \frac{c}{2f\sqrt{\varepsilon_a}} \quad (2)$$

where ε_a is the effective dielectric permittivity, approximately given by $\varepsilon_a = (1 + \varepsilon_r)/2$. For a resonance at 300 GHz, equation (2) gives a slot length of $a = 197 \mu\text{m}$. Moreover, the initial value of the slot width was set to $b = 30 \mu\text{m}$.

The size $A = B$ of the square unit cell can be used to define the stop-band frequency of the filter. Due to [11], the first minimum in the transmission spectrum can occur when higher order modes can propagate. The onset of propagating higher order modes therefore coincides with the stop-band frequency of $f_{\text{stop}} = 450$ GHz. According to [12] the required size of the unit cell is given by:

$$A = B = \frac{c}{f_{\text{stop}}(\sqrt{\varepsilon_r} + \sin \vartheta \sin \varphi)} \quad (3)$$

Equation 3 yields a periodicity of $A = B = 176 \mu\text{m}$ for a stopband frequency of 450 GHz. As this is smaller than the desired slot length a , $A = B = 176 \mu\text{m}$ is not a possible solution of the design problem. The stopband can therefore not coincide with the first minimum in the transmission spectrum of the FSS. In order to design the stopband properly the MoM-BI-RME simulation method was used to realize a minimum in the transmission spectrum at the stopband frequency. As the initial parameters could not be derived directly from equation 3, they were set to be about 25 % larger than the slot size a ($A = B = 250 \mu\text{m}$).

Starting from these initial parameters, the filter was optimized for minimum insertion loss at 300 GHz and stop-band attenuation at 450 GHz, by using a full-wave analysis tool based on the MoM/Bi-RME method [8]. This method applies to the analysis of FSSs, consisting of single/multiple thick metal screens, perforated periodically with arbitrarily shaped apertures and possibly supported by a dielectric layer. This technique is based on the use of the Method of Moments (MoM) with entire-domain basis functions. In the case of apertures with an arbitrary shape, the basis functions are calculated numerically by using the Boundary Integral-Resonant Mode Expansion (BI-RME) method. The MoM/Bi-RME method has been used for the design of FSSs operating in the microwave region [9], and in the millimeter and sub-millimeter wave range [10]. In all cases, it proved very accurate and fast (it requires few seconds for a wide-band analysis on a standard PC). Due to its rapidity, this analysis tool is particularly suited for wide-band optimization purposes.

In the optimization process based on the MoM/Bi-RME method, the optimization variables were the dimensions A and B of the unit cell and the length a of the slot, while keeping constant all other geometrical dimensions. This process permitted to obtain a filter that fulfills the design specifications. The dimensions of the optimized filter resulted: $a = 175 \mu\text{m}$, $b = 30 \mu\text{m}$, $A = B = 236 \mu\text{m}$, $t_{Si} = 302 \mu\text{m}$ and $t_m = 2 \mu\text{m}$.

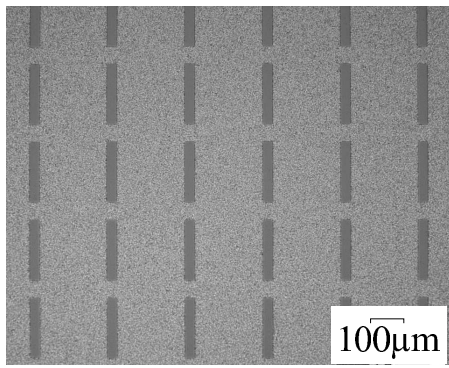
III. MANUFACTURING TECHNOLOGY

The filter was machined using modern semiconductor manufacturing technologies. An aluminum layer with a thickness of $t_m = 2 \mu\text{m}$ and a titanium layer of 20 nm thickness was sputtered on the front side of the wafer and then structured using a dry etching process. Fig. 2 shows photos of the filter structure taken by an optical microscope. One can see that there is only a small rounding of the inner corners. Optical inspection of the structure showed that all the dimensions could be machined within an accuracy better than $2 \mu\text{m}$. As we were using 100 mm wafers, there was enough space on the wafer to manufacture several 300 GHz filters with slightly varying geometric parameters and therefore slightly varying pass-band frequencies. This ensures even in the case of larger manufacturing tolerances that there will be at least one filter with the desired properties in the first run.

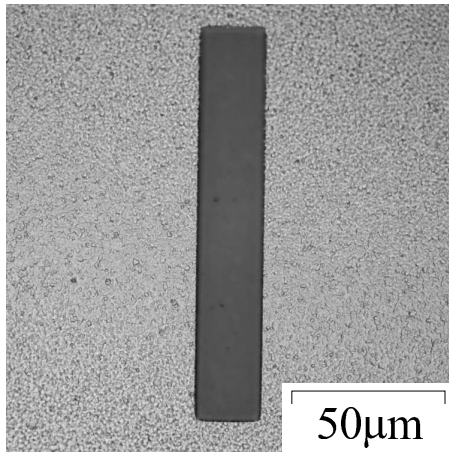
IV. EXPERIMENTAL RESULTS

A. Filter Characteristics

The filter spectrum was first characterized in a broad frequency range by using THz time domain (TD) spectroscopy



(a)



(b)

Fig. 2. (a) Photo of the FSS with rectangular slots; (b) Zoom in of a single slot.

and application of FFT on the time signals. The optical setup used for this investigation allowed a frequency resolution of 8 GHz and a dynamic range > 40 dB between 100 GHz and 1000 GHz. Afterwards, a CW measurement using a backward wave oscillator (BWO) was performed to characterize the filter spectrum between 290 GHz and 305 GHz. Fig. 3 shows all results of simulation and measurement. It can be seen, that there is very good agreement between both measurement results in the pass-band of the filter. The minimum insertion loss is better than 1.6 dB. Comparing the simulation and the measurement it turned out that the filters with the measured pass-band maximum at 300 GHz were those, whose resonance frequency was predicted to be 292 GHz by the simulation. The small frequency shift (about 3 %) between predicted and measured resonance frequency is very likely due to the influence of the ohmic losses on the aluminum which were not considered in the simulation. According to Fig. 3 the pass-band of the filter at 450 GHz is not situated in the first minimum of the transmission spectrum due to the comparatively large size of the unit cell. The stop-band attenuation is about 17 dB and has to be improved in order to fit the specification of an insertion loss better than 20 dB. This can be done by changing the incidence angle of the FSS as shown in the next section.

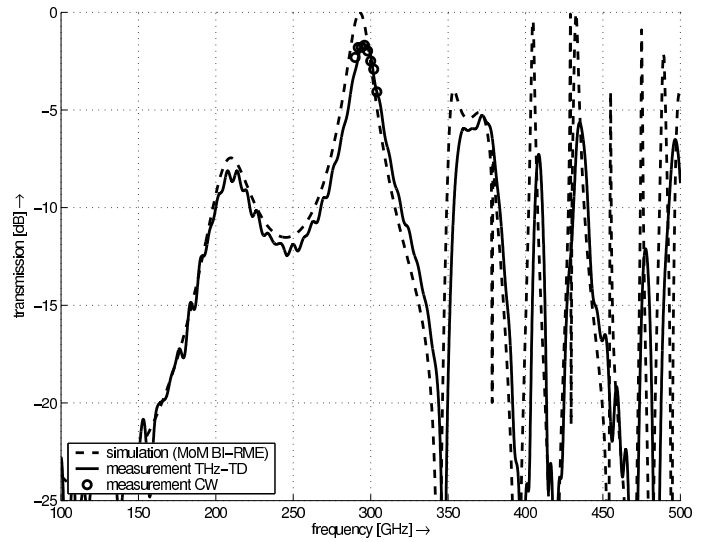


Fig. 3. Frequency response of the 300 GHz pass-band filter: comparison of the MoM/BI-RME simulation, TD-measurement and CW-measurement.

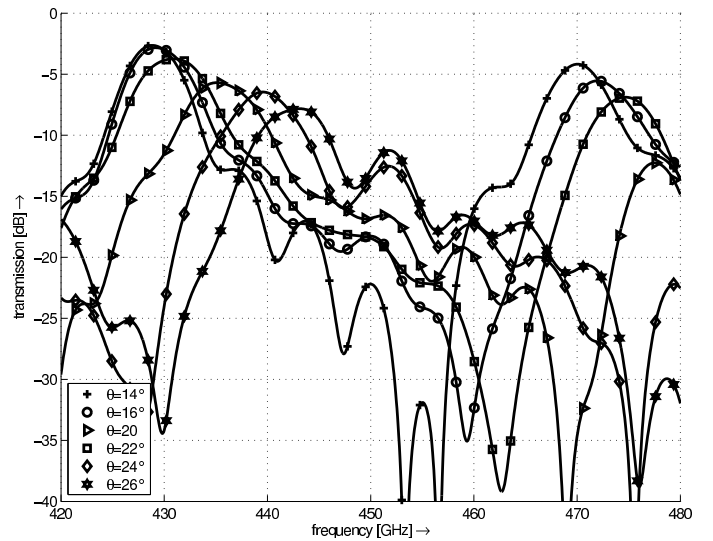


Fig. 4. Change of transmission minimum as a function of the incidence angle ϑ .

B. Fine Tuning of Stopband

After the manufacturing of the filter, the only remaining free parameter which allows to modify the filter characteristics is the incidence angle. The major advantage of this approach is the fact that the stop-band frequency can be changed by varying the incidence angle while the pass-band remains nearly unaffected. Using TD-spectroscopy we have measured the exact position of the stop-band as a function of the incidence angle. The change of the transmission in the stop-band is shown in Fig. 4 as a function of the incidence angle. A decrease of the incident angle from $\vartheta = 20^\circ$ to 14° enhances the stop-band attenuation to more than 20 dB.

V. RESULTS

A frequency selective surface has been applied to design a filter for harmonic suppression with a pass-band frequency at 300 GHz and a stop-band frequency at 450 GHz. The

FSS consists of an array of simple slot apertures which were realized on an aluminium layer deposited on an electrically thick silicon substrate. Initial values for the geometry of the filter structure were found and used for the optimization with the MoM/BI-RME method. Subsequently the filter was machined by modern semiconductor manufacturing technologies. Time domain spectroscopy as well as CW transmission measurement of the filter have demonstrated good agreement with simulation results. A minimum insertion loss better than 1.6 dB was achieved for the pass-band of the filter. It was found that the stop-band attenuation can be fine tuned after the manufacturing process by changing the incidence angle of the FSS. An improvement of the frequency characteristics of the FSS will be published elsewhere [13].

VI. ACKNOWLEDGEMENTS

This work was partly supported by the DAAD/Vigoni project 2004.

REFERENCES

- [1] S. Martin, B. Nakamura, A. Fung, P. Smith, J. Bruston, A. Maestrini, F. Maiwald, P. Siegel, E. Schlecht, and I. Mehdi, "Fabrication of 200 to 2700 GHz multiplier devices using gaas and metal membranes," *IEEE Microwave Theory and Techniques Symposium*, May 20-25 2001.
- [2] M. Shalaan, M. Bozzi, J. Weinzierl, K. Beilenhoff, G. Conciauro, H. Brand, and H. L. Hartnagel, "A 300 GHz quasioptical schottky frequency doubler," *International Journal of Infrared and Millimeter Waves*, Vol. 18, pp. 2277–2294, December 1997.
- [3] P. Arcioni, M. Bozzi, M. Shaalan, J. Weinzierl, L. Perregrini, G. Conciauro, and H. L. Hartnagel, "Design and optimisation of quasi-optical frequency multipliers," *Conference Digest of the 23rd Int. Conf. on Infrared and Millimeter Waves*, (University of Essex, Colchester, U.K.), September 1998.
- [4] G. Schoenthal, W. Bishop, X. Haiyong, J. Hesler, R. Weikle, and T. Crowe, "Fabrication of integrated THz sources," *Infrared and Millimeter Waves, Conference Digest*, vol. 127-128, 22-26 Sept. 2002.
- [5] B. Schumann, M. Höft, and R. Judaschke, "A multi-element 150/300 GHz spatial power dividing/combining doubler," *IEEE Microwave Theory and Techniques Symposium*, pp. 1539–1542, 2002.
- [6] P. A. Chen, "The performance of dielectric coated mesh filter," *International Journal of Infrared and Millimeter Waves*, Vol. 8, No. 1, pp. 29–33, 1987.
- [7] D. W. Porterfield, J. L. Hesler, R. Densing, E. R. Mueller, T. W. Crowe, and R. Weikle, "Resonant metal-mesh bandpass filters for the far infrared," *Applied Optics*, Vol. 33, pp. 6046–6052, September 1994.
- [8] M. Bozzi, L. Perregrini, J. Weinzierl, and C. Winnewisser, "Efficient analysis of quasi-optical filters by a hybrid MoM/BI-RME method," *IEEE Trans. Antennas & Propagat.*, Vol. AP-48, No. 7, pp. 1054–1064, July 2001.
- [9] P. Besso, M. Bozzi, L. Perregrini, L. Salghetti Drioli, and W. Nickerson, "Deep Space Antenna for Rosetta Mission: Design and Testing of the S/X-Band Dichroic Mirror," *IEEE Trans. Antennas & Propagat.*, Vol. AP-51, No. 3, pp. 388–394, March 2003.
- [10] M. Bozzi, L. Perregrini, J. Weinzierl, and C. Winnewisser, "Design, Fabrication, and Measurement of Frequency Selective Surfaces," *Optical Engineering*, Vol. 39, No. 8, pp. 2263–2269, Aug. 2000.
- [11] N. Amitay, V. Galindo, and C. Wu, *Theory and Analysis of Phased Array Antennas*. Wiley-Interscience, New York, 1972.
- [12] J. Reed, *Frequency selective surfaces with multiple periodic elements*. Ph.D. Thesis, University of Texas at Dallas, Dec. 1997.
- [13] S. Biber, M. Bozzi, O. Günther, L. Perregrini, L.-P. Schmidt "Low-Loss Quasi-Optical Filters with Thick Silicon Substrates for Sub-mmWaves Frequency Multipliers," accepted for *International Symposium on Microwave Theory and Techniques*, IMS 2005, Long Beach, USA .

Session 5

Plenary Session II

Microwave Photonics – From Concepts to Applications

Dieter Jäger and Andreas Stöhr

Universität Duisburg-Essen, Fachbereich Ingenieurwissenschaften, Zentrum für Halbleitertechnik und Optoelektronik,
Lotharstrasse 55, D-47048 Duisburg, Germany, Tel.: +49 203 379 2341, E-Mail: d.jaeger@uni-duisburg.de

Abstract - Microwave photonics can be generally defined as the study of high-speed photonic devices operating at microwave or millimeter wave frequencies and their use in microwave or photonic systems. In this multidisciplinary field at the interface between microwave techniques, ultra fast electronics and photonic technologies, typical investigations include, for example, high-speed and microwave signal generation, processing and conversion as well as the distribution and transmission of microwave signals via broadband optical links. From pioneering experiments in the 70's, this field of microwave photonics has paved the way for an enabling novel technology with a number of commercially important applications. This paper is intended to give an overview on this multidisciplinary field of microwave and millimeter wave photonics.

I. INTRODUCTION

Within the last decade the field of microwave photonics has attracted growing interest worldwide. The term of microwave photonics was introduced in 1991 and used to describe novel optoelectronic components based upon the interaction of traveling optical and microwaves [1, 2]. In the following, the merging of microwave and photonic technologies was foreseen to be a new approach for future fiber radio communication systems where the RF signal is transmitted over optical carriers [3]. Since then the field of RF optoelectronics and photonics rapidly broadened: Since 1996 International Topical Meetings on Microwave Photonics (MWP) are being held annually [4] and 1995 was the first year of an IEEE MTT Special Issue on Microwave Photonics now being published regularly [5].

Microwave photonics [6] is an innovative multi- and interdisciplinary field combining and transferring different technologies. In particular, microwave technologies are used and employed in photonics and photonic technologies are utilized in microwave techniques. Moreover, in specific areas novel synergistic concepts have been developed by merging both technologies which particularly holds for the field of optoelectronics as their interface. As a result of ever increasing frequencies the term microwave stands here for GHz or THz frequencies in the frequency and equivalently for ps- or fs-time scales in the time domain.

This paper is intended to give an overview on this field of microwave photonics together with recent results ranging from devices and technologies to specific

systems under investigation. In particular, the following topics will be addressed by way of key examples for the synergetic mixture of the two technologies involved: (i) Ultra fast photonic components such as optical modulators and detectors with special emphasis on traveling wave devices, (ii) Broadband analog optical links for high-speed interconnects, (iii) Microwave photonic systems based upon the merging of microwave and optical technologies.

II. MICROWAVE PHOTONIC COMPONENTS

For high-speed operation electronic devices are usually scaled down with respect to the lateral dimensions in order to decrease the device capacitance and to decrease the RC time constant. A solution of this problem is the use of propagation effects, i. e. to employ wave propagation phenomena in the design of the electronic device as has been described in [7] and already used in the design of high-speed integrated circuits such as RFICs and MMICs (cf. Traveling wave amplifiers). Moreover, at high frequencies the packaging of high-speed devices or circuits has basically to include wave propagation effects, for example the characteristic impedance of the electrical interconnect. Finally, the transit time and wave propagation effects of space charges have also to be regarded in the development of the high-speed device.

In optics on the other hand, wave propagation is the fundamental physical basis and no lumped elements exist up to now. As a consequence, the design of optical and photonic components usually includes optical waveguides and element dimensions large with respect to the wavelengths in optics.

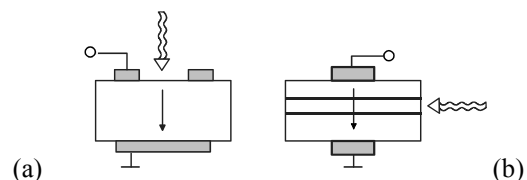


Fig.1. Microwave optical interaction devices with vertical (a) and horizontal (b) light wave propagation.

In microwave photonic components an interaction between electrons, electrical fields and photons take place which can be regarded as microwave-optical interactions (Fig. 1). Consequently, different

technologies meet and may - in a synergetic mixture - be merged in order to develop novel concepts with great advantages. A key example is the traveling wave (TW) device (Fig. 2) where wave propagation effects in the electrical as well in the optical domain are utilized. The concept is based on the fundamentals of nonlinear optics where interaction takes place during wave propagation. Obviously, the bandwidths of these elements are not limited by „RC time constants“, see Fig. 3.

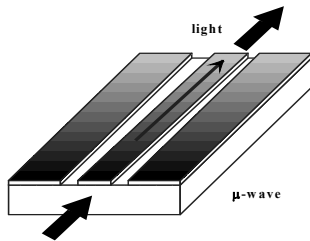


Fig.2. Traveling wave (TW) concept, [8, 9].

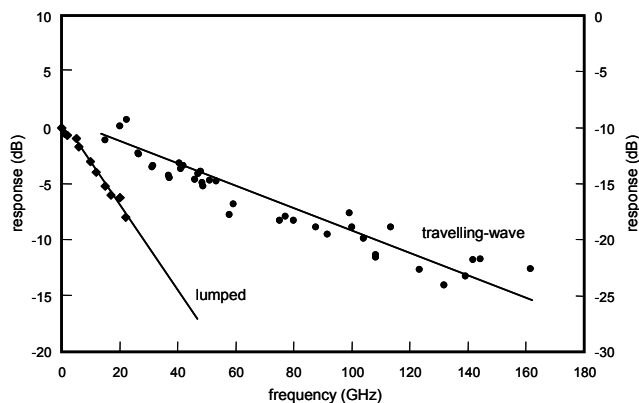


Fig.3. Frequency response of a lumped and a TW device.

In an optoelectronic TW device [8, 9] an optical waveguide is used for optical wave propagation and an electrical transmission line (e. g. microstrip or coplanar waveguide) for guiding the microwave, usually in the same direction. In the region where the electrical fields overlap, the optoelectronic interaction occur. Note that a dc bias may additionally be applied to control the operating point. From a physical point of view the interaction is a nonlinear or active process. The photodetector and the laser diode are basic examples of two-port devices where optical power is converted into electrical power and vice versa. Typical three-port devices are electrically controlled optical modulators/switches or optically controlled microwave modulators/switches. Due to the inherent nonlinearity these devices are further used for optoelectronic mixing of input electrical and/or optical signals where the output signal can be electrical or optical. For next generation broadband photonic communication networks, the electroabsorption modulator (EAM) will be a key element because it can be used also as an electroabsorption detector (EAD). As a result, this element is a multifunctional device [8, 9] which has been called electroabsorption transceiver (EAT) because of its applications in full-duplex optical communication links [10]. An EAT can further be used to generate artificial

optical nonlinearities such as optical bistability [11] which gives rise to switching, logic and memory effects and may be useful for multiple-GHz A/D conversion. In Fig. 3, a comparison is made between a lumped EAM and a TW EAD with comparable cross sections. As can be seen, the lumped element exhibits a RC time constant corresponding to about 10 GHz whereas the TW device shows a clear response beyond 160 GHz. Obviously, the use of microwave technologies can drastically improve the bandwidth of such photonic devices.

III. BROADBAND FIBER OPTICAL LINKS

An analog optical link consists of an optical transmission medium (preferably a fiber) and optoelectronic converters on both sides [12]. The great advantage is that due to the broadband low-loss transmission capability the optical fiber (see Fig. 4) can ideally be used to transmit microwave signals and therefore replace other lossy metallic waveguides, e. g. X-band WG or coax. Here different techniques have been explored. For example, on the transmitting side a cw laser diode and an external modulator (electrooptic or EAM) and on the receiving side an optoelectronic photodetector can be used. Besides the bandwidth a key parameter of such a link is the link loss which depends on the conversion efficiencies of the optoelectronic elements, the optical coupling efficiencies and the attenuation and dispersion of the transmission medium [9, 12]. Note that a link gain can easily be achieved when an optical amplifier (EDFA) and/or external modulators, preferably on both sides, are being used [9]. For high-speed and broadband operation the a. m. TW microwave photonic devices can successfully be employed.

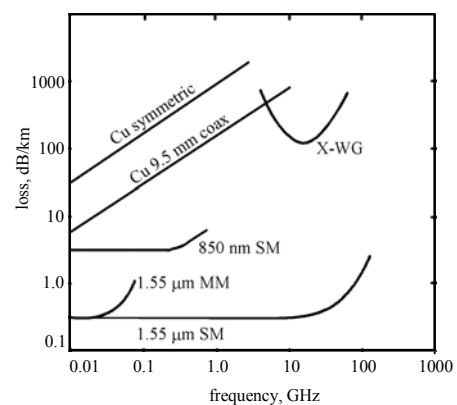


Fig.4. Propagation loss of different transmission media, SM = single mode and MM = multimode glass fiber.

For bidirectional communications, the link would require a duplication of the elements on both sides in order to provide uplink and downlink transmission. This is the conventional system architecture. In an advanced system the base station contains only one optoelectronic element, the transceiver, as realized by an EAT [10]. Given that due to the basic physical mechanisms the electrical bandwidth of the EAT is the same for the

detection and the modulation process, a bandwidth of more than 160 GHz can be achieved using an TW EAT.

IV. MICROWAVE PHOTONIC SYSTEMS

Broadband fiber optic links are regarded to be basic building blocks for different microwave systems.

(a) Photonic signal generation and local oscillators: Fig. 5 shows the concept of UWB signal generation using a microstrip resonator with an optoelectronic switch as an RF mirror integrated with a broadband antenna [13-15]. Further, mixing two optical wavelengths from two frequency locked lasers or a two mode laser in a photodetector emulates a microwave local oscillator where the difference frequency is photonically generated by heterodyne techniques (Fig. 6) and where wavelength tuning provides a bandwidth of several THz depending on the bandwidth of the detector [16, 17].

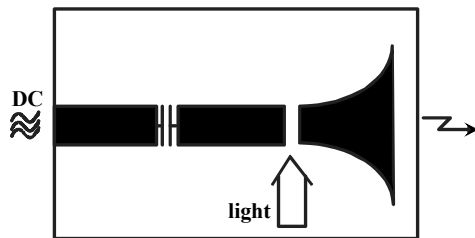


Fig.5. Optoelectronic generation of UWB signals.

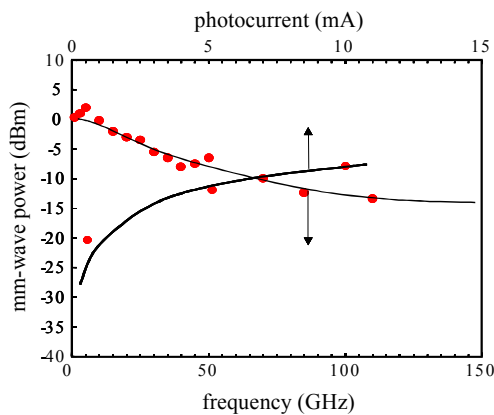


Fig.6 Heterodyne RF generation using a TW-PD and generated power versus photocurrent at 110GHz.

(b) EMC sensor: When the modulator at the end of a fiber is driven by an electrical input signal at the given position, the received optical signal can be used to measure the electrical signal quantitatively at the transmitter side and a field sensor results. Note that an electrical dc power required at the sensor side can also be transmitted optically by employing a photovoltaic cell at the receiver side [18].

(c) Optoelectronic testing: A microminiaturized modulator chip working in reflection mode and coupled to the end of a fiber can be applied to measure electrical fields in free space with high spatial resolution [19]. This is also the basic concept for contactless high-speed testing of integrated circuits, well-known as the electrooptic sampling principle of Fig. 7, [20, 21].

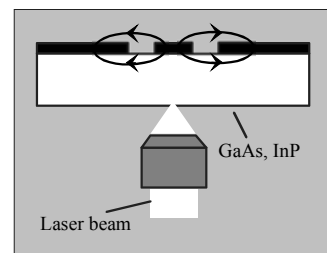


Fig. 7 Principle of electrooptic sampling, [20, 21].

(d) Hybrid fiber-coax systems: In cable TV (CATV) the signals received from TV satellites can be converted into the optical domain and fed into a fiber to be transmitted over long distances with only small attenuation. The optical signals being transmitted are converted back into the electrical domain and guided to the customer via coaxial cable.

(e) Fiber-radio systems: It is agreed that fiber-radio access [22] will provide a solution to the demands for a wireless connection to the customer („last or first mile problem“). For broadband services the frequencies are in the millimeter wave range. Such a concept is based upon an optical link between the central station (CS) and the base station (BS) in a pico cellular structure. Recently, 60 GHz fiber radio links have been demonstrated providing 155 Mbps using EAMs for half-duplex and EATs for full-duplex transmission in a WDM ring network [23]. Fig. 8 shows a novel architecture of a 60 GHz fiber-radio

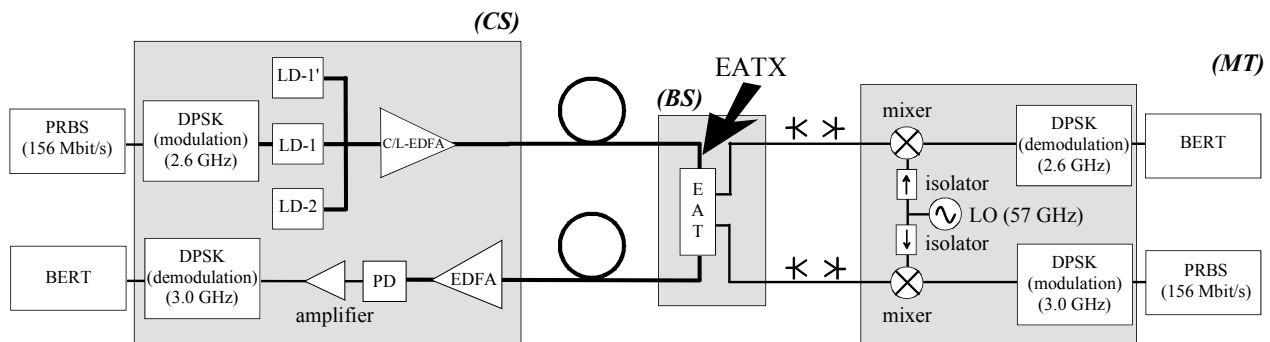


Fig. 8 Architecture for a 60 GHz fiber-radio access system [23]. LD denotes a laser diode, PD a photodetector, and EAT-X an EAT – mixer. MT is the mobile terminal.

system using an EAT, (i) to generate the 57 GHz carrier frequency from LD1 and LD1' where LD1 is directly modulated by the downlink IF signal at 2.6 GHz, and (ii) to mix the photonic LO signal directly with the IF signal. LD2 provides the uplink signal to be modulated at the BS with the uplink signal.

(f) Antenna systems: A major application of optical link technology is the remoting of antenna systems and, particularly, the optical control of array antennas, see for example Refs. [4] and [5]. A millimeter wave or THz camera with photonic interconnection is foreseen.

V. CONCLUSIONS

In the past decade the field of microwave and millimeter wave photonics has become a key technology extending from components and modules to systems with important applications. The driver has been twofold: On one hand the broadband low-loss and high-speed transmission capability of optical fibers has led to a considerable interest in their use for distributing and controlling micro- and millimeter wave signals. On the other hand the breakthrough in the design and demonstration of several ultra-broadband photonic components has paved the way for wideband and high efficiency optoelectronic converters being important building blocks for microwave optical links. As a result, it can be foreseen that this multidisciplinary field of microwave photonics will continuously be expanded and lead to further novel concepts due to the synergetic merging of different technologies as has been done similarly in the area of MEMS, for example.

ACKNOWLEDGEMENT

The authors wish to thank Professor K. Kitayama, Osaka University, and T. Kuri, Communications Research Laboratory, Tokyo, for their contributions to this work. The authors are further grateful to the cooperation in the framework of the European Networks of Excellence NEFERTITI, e-Photon/ONE and e-PIX.

REFERENCES

[1] D. Jäger, „Traveling-Wave Optoelectronic Devices for Microwave and Optical Applications“, *Proc. of Progress in Electromagnetic Research Symposium [PIERS]*, p. 327, 1991.

[2] D. Jäger, „Microwave Photonics“, in „*Optical Information Technology*“, S.D. Smith and R.F. Neale [Eds.], Springer Press, 1993, pp. 328-333.

[3] D. Polifko and H. Ogawa, „The Merging of Photonic and Microwave Technologies“, *Microwave Journal*, pp. 75-80, March 1992.

[4] „*International Topical Meeting on Microwave Photonics*“, Techn. Digest, Kyoto 1996, Duisburg 1997, Princeton 1998, Melbourne 1999, Oxford 2000, Long Beach 2001, Awaji 2002, Budapest 2003, Ogunquit 2004.

[5] *IEEE Trans. Microwave Theory and Techn.*, Special Issues on Microwave and Millimeter Wave Photonics, Sept. 1995, Sept. 1997, July 1999, Dec. 2001, and *IEEE J. Lightw. Techn.*, Dec. 2003.

[6] A. Vilcot, B. Cabon, and J. Chazelas (Eds), „*Microwave Photonics*“, Kluwer, 2003.

[7] D. Jäger, „Characteristics of traveling waves along nonlinear transmission lines for monolithic integrated circuits – A review“, *Int. J. Electron.*, vol. 58, pp. 649-669, 1985.

[8] D. Jäger, R. Kremer, and A. Stöhr, „Traveling wave optoelectronic devices for microwave applications“, 1995, in *IEEE Int. Microw. Symp. Digest*, vol. 1, pp 163-166.

[9] D. Jäger, A. Stöhr, and R. Heinzelmann, „Advanced microwave photonic devices for analog optical links“, 1998, in *Int. Top. Meet. Microwave Photonics, Techn. Digest*, Princeton, pp. 153-156.

[10] K. Kitayama, A. Stöhr, T. Kuri, R. Heinzelmann, D. Jäger, and Y. Takahashi, „An approach to single optical component antenna base stations for broadband millimeter wave fiber-radio access systems“, *IEEE Trans. Microw. Th. Techn*, vol 48, pp 2588-2595, 2000.

[11] D. Jäger, „Large optical nonlinearities in hybrid semiconductor devices“, *J. Opt. Soc. Am. B*, vol. 6, pp.588-594, 1989.

[12] C. Cox, III, „*Analog Optical Links*“, Cambridge, 2004

[13] R. Heidemann, Th. Pfeiffer, and D. Jäger, „Optoelectronically pulsed slot line antennas“, *Electron. Lett.* vol. 19, pp. 316-317, 1983.

[14] P. Paulus, W. Brinker, and D. Jäger, „Generation of microwave pulses by optoelectronically switched resonators“, *IEEE J. Quantum Electron.* vol. QE-22, pp. 108-111, 1986.

[15] P. Paulus, L. Stoll, and D. Jäger, „Optoelectronic pulse compression of microwave signals“, *IEEE Trans. Microw. Theory Techn.*, vol. MTT-35, pp. 1014-1018, 1987.

[16] A. Stöhr, R. Heinzelmann, K. Hagedorn, R. Güsten, F. Schäfer, H. Stüer, F. Siebe, P. van der Wal, V. Krozer, M. Feiginov and D. Jäger, „Integrated 460 GHz photonic transmitter module“, *Electr. Lett.*, vol. 37, No. 22, , pp. 1347-1348, 2001.

[17] A. Malcoci, A. Stöhr, A. Sauerwald, S. Schulz, D. Jäger, "Waveguide and antenna coupled traveling-wave 1.55- μm photodetectors for optical (sub)millimeter-wave generation", in *Proc. SPIE Photonics Europe, Microwave and Terahertz Photonics*, 2004, Strasbourg, France, pp. 202-209.

[18] R. Heinzelmann, A. Stöhr, M. Groß, D. Kalinowski, T. Alder, M. Schmidt, and D. Jäger, „Optically powered remote optical field sensor system using an electrobabsorption modulator“, 1998, in *IEEE Int Microw. Symp. Digest* pp. 1225-1228.

[19] D. Kalinowski, S. Redlich, and D. Jäger, „Novel micromachined fiber-optic E-field sensor“, in *Proc. LEOS Annual Meeting*, LEOS'99, 1999, pp. 385-386.

[20] G. David, R. Tempel, I. Wolff, and D. Jäger, „Analysis of Microwave Propagation Effects using 2D Electro-Optic Field Mapping techniques“, *Optical Quantum Electron., Special Issue*, pp. 919-931, 1996.

[21] G. David, P. Bussek, U. Auer, F.-J. Tegude, and D. Jäger, „Electro-Optic Probing of RF-Signals in Sub- μm MMIC-Devices“, *Electron. Lett.*, vol. 31, no. 25, pp. 2188-2189, 1995.

[22] H. Al-Raweshidy and S. Komaki (Eds), „*Radio Over Fiber Technologies*“, Artech House, 2002.

[23] Stöhr, T. Kuri, K. Kitayama, R. Heinzelmann, and D. Jäger, „Full-Duplex 60GHz fiber optic transmission“, *Electron. Lett.*, vol. 35, no. 19, pp. 1653-1655, 1999.

RF-Payload of TerraSAR-X

Dietmar Pilz¹, Peter Feldle²

¹EADS Deutschland GmbH, Defence Electronics, Synthetic Aperture RADAR, 88039 Friedrichshafen, Germany

²EADS Deutschland GmbH, Defence Electronics, Analogue Hardware, 89070 Ulm, Germany

Abstract — TerraSAR-X is a Low Altitude-Earth Observation Satellite carrying a high resolution X-Band SAR-Sensor. An overview of the RF-System and its respective requirements is given. Furthermore key elements such as the X-band T/R Frontend and the RF-part of the Core Electronics (CE) are described in detail: The RF-part of the CE comprises an ultra stable oscillators a programmable 300MHz chirp generator, X-Band transmitter and receiver and an advanced calibration scheme. The T/R-Frontend hybrid module consists of a standardized T/R module, the RF Frontend Electronics, and the related Control Electronics. The architecture and measurement results of this X-band T/R Frontend and related subunits are described in detail with reference to advanced SAR system requirements.

reception.

Specific modes like Spotlight-, Stripmap- and ScanSAR mode with selectable polarization and for special missions MTI mode are supported by the active phased array to fulfill the required performance and flexibility in complex observation and reconnaissance missions

The core-element of the earth observation instrument is the RF-sensor. This paper will give an overview of the architecture of the RF-System. Two key elements, the RF- Core Electronics and the T/R Frontend are described in detail.

I. INTRODUCTION

TerraSAR-X is a German national SAR-satellite system [1]. The TerraSAR-X-satellite features an advanced high-resolution X-Band Synthetic Aperture RADAR sensor, which enables operation in Spotlight-, Stripmap- and ScanSAR Mode. In addition, experimental modes like the Dual Receive Antenna Mode will allow polarimetric imaging as well as along track interferometry. Furthermore, the architecture of the RF-System features fully flexibility in terms of pulse generation and pulse

II. THE RF-SYSTEM

The RF-System is required to enable numerous advanced SAR-System features such as

- High Resolution (in experimental. Spotlight Mode 1m)
- High Pulse Parameter Flexibility
- Spotlight, StripMap, ScanSAR Modes
- Polarimetric Imaging

A block diagram of the architecture of the RF-System is shown in Fig. 1. A Digital Chirp-Generator generates a

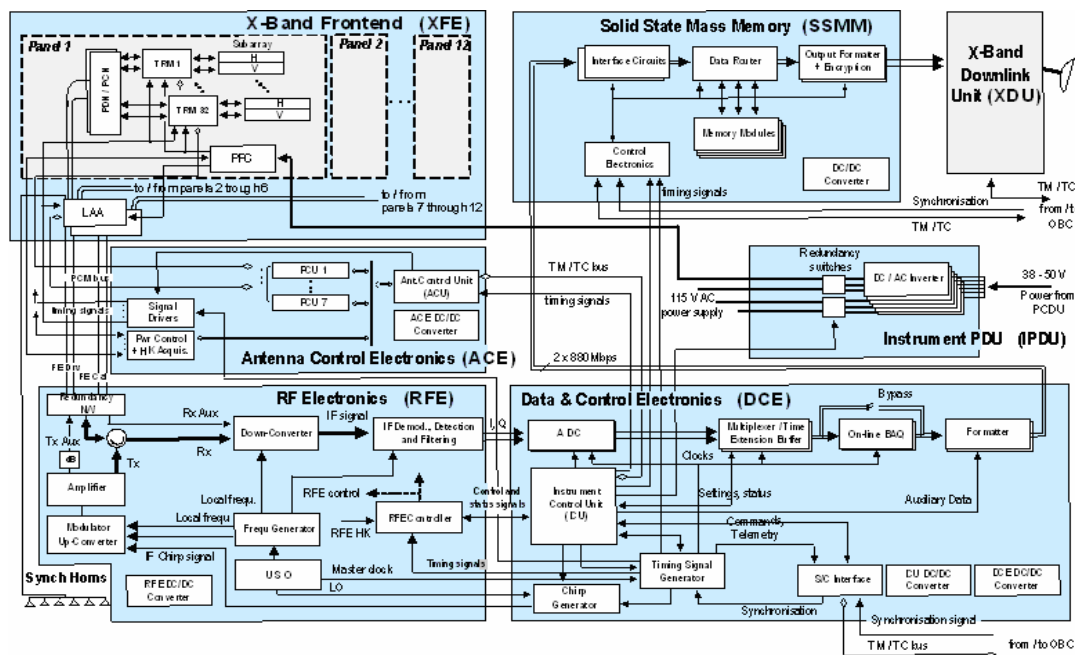


Figure 1 Block Diagram of the RF System of TerraSAR-X (Courtesy of EADS Astrium GmbH)

flexible transmit base band signal in I and Q. After I/Q-

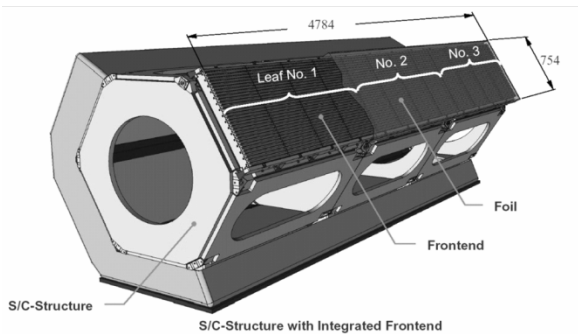


Figure 2 Picture of the satellite structure including the antenna leaves of the RF-sensor.

Modulation the signal is multiplied and up converted. The X-Band signal is amplitude limited before a gain-controlled driver amplifier feeds the antenna network.

A stripline network including several leaf amplifiers distributes the power. Several hundred T/R Frontends amplify the RF-signal and shift the respective phase according to an antenna control unit. Transmission and reception is realized by respective slotted waveguide antenna arrays [2]. Circulators are used to separate transmitted and received signals inside the T/R-modules.

The received echo signal is amplified by an LNA in the T/R Frontends and combined by the LAA network. Down conversion, I/Q-Demodulation and Baseband filtering is realized in the RFE. A picture of the satellite structure including the antenna leaves of the RF sensor is shown in Figure 2.

III. RADIO FREQUENCY ELECTRONICS

The Radio Frequency Electronics (RFE) is part of the Central Electronics (CE) of TerraSAR-X. The design of the CE is based on the successful X-SAR-SRTM shuttle mission.



Figure 3 Photograph of the integrated Radio Frequency Electronics.

The Core Electronics of TerraSAR-X receives commands from the ground station, prepares and executes the timing control, generates the chirp sequences, passes the RF transmitter signals on to the X-Band Instrument Frontend (XFE), receives the RF radar returns, preprocesses and compresses the received data stream and passes the SAR

data on to a Solid State Mass Memory (SSMM) for on-board buffering and data dumps. This paper focuses on the RF-part only.

The RFE consists of several functional slices, which fulfill respective tasks in the transmit and receive chain. The functional blocks are: Transmitter Up Stage (TUS), Intermediate Frequency Section (IFS) Frequency Generator (FRG), Calibration and Redundancy Network (CRN), Power Supply (PSR). Coaxial connectors are used as well to concatenate the modules as well as to interconnect SMA-components inside the modules. Where necessary, hybrid components have been designed and fabricated in house. However, most of the components are bought-in parts. A photography of the integrated RFE can be seen in Fig. 3.

In Table 1 key requirements and its realization are listed.

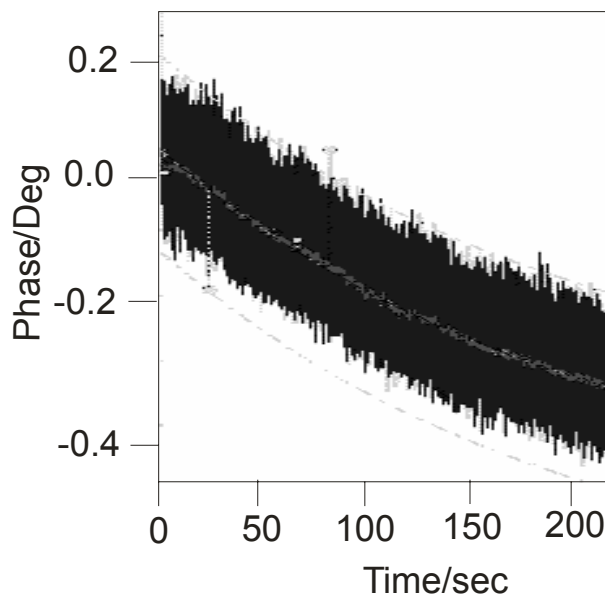


Figure 2 Phase Drift versus Time of the CE.

Requirement	Realization
RF Bandwidth	I/Q-Modulator followed by two Frequency Multiplier stages
TX Output Power Stability	Gain-Controlled transmit driver Amplifier
Overall phase stability	Similar design of Up- and Down-Converter
Accurate Calibration Process	Entirely passive Calibration and Redundancy Network

Table 1 Key Requirements and addressed measures

The RFE is assembled, integrated, tested and the qualification process is currently ongoing. Test results of the Flight Model are now available (compare to [3]). Figure 4 shows the test results for the phase stability of the RFE at estimated satellite temperature. The absolute value for the phase drift over a period of 220 sec is only 0.7° Deg. Using the built-in calibration scheme the unknown error of the phase drift can even be reduced to less than 0.1° deg, here.

IV. X-BAND T/R FRONTEND

The TerraSAR-X antenna subsystem consists of several hundreds of T/R Frontends which are one of the key elements and determine the overall system performance of this SAR instrument. Technical risks, mass and cost of the active SAR antenna are limited using these T/R Frontends with matured and proven technology [5]. Each T/R Frontend includes a standardized modular T/R Module (SMTR module [6]), the RF Frontend Electronics, and the related Control Electronics.

Driver for the architecture and technologies of this X-Band T/R Frontend were the following cardinal requirements:

- full polarimetry of operation (HH, VV, HV, VH) and switching of polarization from pulse to pulse,
- high precision of amplitude and phase adjustment over a wide temperature range,
- high overall efficiency,
- calibration and temperature compensation,
- high reliability,
- low mass,
- affordable cost.

Each T/R Frontend (Figure 5, [7]) includes a standardized modular T/R Module (SMTR module [6]), the

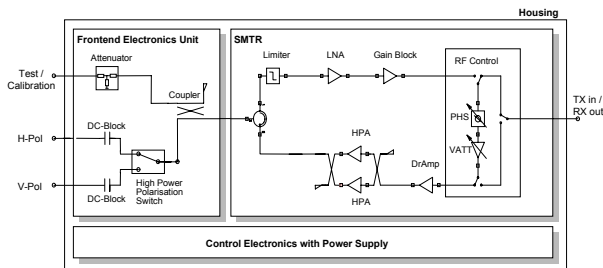


Figure 5: RF Architecture of the TerraSAR-X T/R Frontend

RF Frontend Electronics, and the related Control Electronics in a common housing. The T/R Frontend will be directly connected to two waveguide radiators for H&V polarization. A special RF port for calibration and built-in-test is part of the architecture. Figure 6 shows the top view of the TerraSAR-X T/R Frontend without lid.

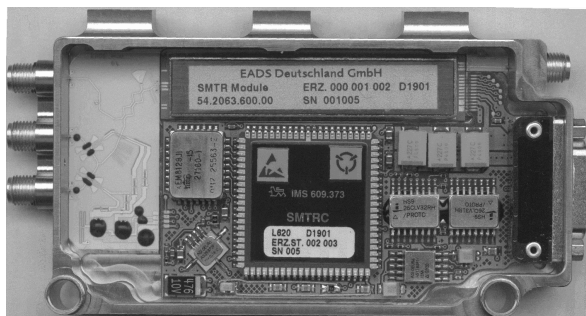


Figure 6: TerraSAR-X T/R Frontend (top view without lid)

Besides the generation of the required transmit power, prime task of each frontend is the adjustment of the RF signal phase during the transmission and the phase and amplitude during the receive of the RF signals with highest precision.

Main part of the X-band T/R Frontend is the SMTR module [5] with a very small size (64.5 x 13.5 x 4.5 mm³) and low mass (less than 15 grams). Topics of this module are low noise operation in receive mode, high power amplification in transmit mode, accurate phase and gain setting, and high overall power added efficiency. Interface between the SMTR module and antenna radiating elements is the RF Frontend Electronics [4]. Key features of this unit are high power polarization switching from PRI to PRI between the antenna ports and a monitor port for test and calibration purposes. A special design of a SPDT switch with PIN diodes provides the required very low insertion loss and high isolation, respectively.

Essential tasks of the Control Electronics Unit (mainly implemented in an ASIC and an E²PROM) are communication with the Antenna Panel Controller, control of the SMTR module and RF Frontend Electronics unit during transmit and receive operation, autonomous temperature compensation according to the T/R frontend temperature, and power conditioning control and monitoring.

Some of the chosen technologies have been proven by the successfully flown X-SAR/SRTM mission [5] (Figure 7).

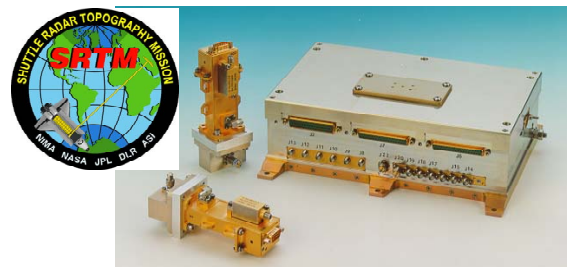


Figure 7: RF Frontend for the X-SAR/SRTM Mission

The T/R Frontend operates within the TerraSAR-X specific frequency range from 9.5 to 9.8 GHz and the large temperature range from -20°C to +60°C. Therefore, a special calibration and temperature compensation procedure has been developed to guarantee stable and accurate RF performance over a wide temperature range. The outstanding performance of the T/R Frontend (Figure 8) is demonstrated

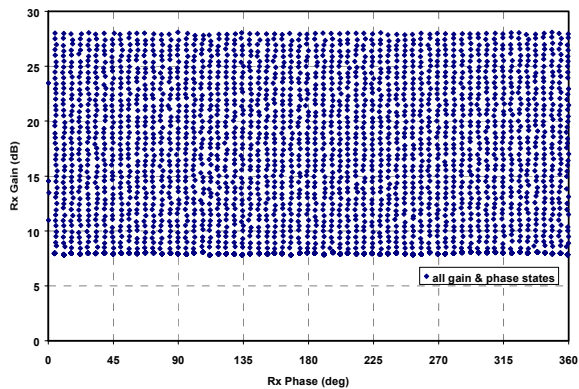


Figure 8: Gain-phase map in Rx mode at center frequency

by the corrected gain-phase map in Rx operation (64 phase states covering a nominal range from 0 to 360 deg times 41 gain states covering a nominal range from 8 to 28 dB). The described correction is done applying a nearest state algorithm which leads to an amplitude error of less than 0.1 dB RMS and to a phase error of less than 1.0 deg RMS at room temperature. A noise figure of less than 4.3 dB was measured for maximum Rx gain of 28 dB over the given frequency band.

In transmit mode the output power versus all 64 phase states is demonstrated in Figure 9. Measurement results show a remarkable flat characteristic at the output power of typ. 38 dBm (approx. 6.3 W).

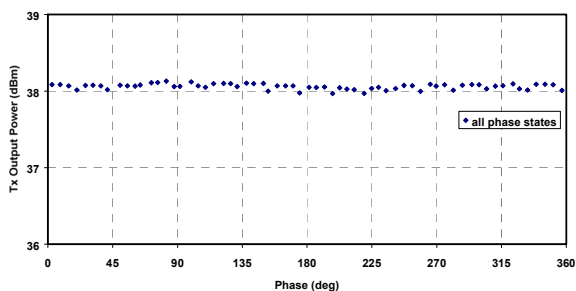


Figure 9: Phase map in Tx mode at center frequency

Channel isolation between the two antenna ports (H&V) of the T/R Frontend is another critical parameter with respect to the system performance. The isolation of minimum 35 dB was measured in the required frequency range.

V. CONCLUSION

The concept and the architecture of the RF-System of TerraSAR-X has been characterized. Two key components, the Radio Frequency Electronics and the T/R-Frontend, have been described in detail. Outstanding results on phase stability at the RFE on one hand and on high gain, phase accuracy and low noise figure of the T/R-Frontend on the other hand have been shown.

ACKNOWLEDGEMENT

The authors wish to thank their colleagues of DLR, EADS ASTRIUM, EADS Deutschland GmbH.

This work has been supported by DLR in co-operation with EADS Astrium.

REFERENCES

- [1] R. Werninghaus, W. Balzer, S. Buckreuss, P. Mühlbauer, W. Pitz "The TerraSAR-X Mission" *Proceedings of EUSAR 2004*, vol. 1, pp. 21-22, May 2004.
- [2] M. Brandfass, "Latest Real SAR Data Performance Evaluations of the TerraSAR-X Central Electronic" *Proceedings of EUSAR 2004*, vol 2, Neu-Ulm pp. 509-512, May 2004.
- [3] A. Herschlein, H. Braumann, M. Stangl, W. Pitz, "Development and Measurement Results for TerraSAR-X Phased Array" *Proceedings of EUSAR 2004*, vol 2, Neu-Ulm, pp. 505-508, May 2004.
- [4] M. Suess, S. Rieger, W. Pitz, R. Werninghaus; "TerraSAR-X – Design and Performance"; *Proceed. EUSAR 2002*; Cologne; June 2002; pp. 49-52.
- [5] M. Ludwig, R. Biskupek, W. Bösch, G. Höfer, J. Knödlstorfer, M. Lörcher, R. Reber; "RF Front-End for the X-SAR/SRTM Mission with Electronic Beam Steering Capability"; *Proceedings of EUSAR 2000*; Munich; May 2003; pp. 95-98.
- [6] R. Rieger, B. Schweizer, H. Dreher, R. Reber, M. Adolph, H.-P. Feldle; "Highly Integrated Cost-effective Standard X-Band T/R Moduzle Using LTTC Housing Concept for Autometed Production"; *Proceedings of EUSAR 2002*; Cologne; June 2002; pp. 303-306.
- [7] U. Hackenberg, M. Adolph, H. Dreher, H. Ott, R. Reber, R. Rieger, B. Schweizer; "T/R-Module for Synthetic Aperture Radar wih Polarisation Agility"; *Proceedings EUSAR 2004*; vol. 2, Neu-Ulm; pp. 477-480.

Automotive Radar – Status and Trends

Martin Schneider

Robert Bosch GmbH, Corporate Research, PO box 77 77 77, D-31132 Hildesheim, Germany, +49 5121 49 2543,
Schneider.Martin@de.bosch.com

Abstract — The paper gives a brief overview of automotive radar. The status of the frequency regulation for short and long range radar is summarized because of its importance for car manufacturers and their sensor suppliers. Front end concepts and antenna techniques of 24 GHz and 77 GHz sensors are briefly described. Their impact on the sensor's field of view and on the angular measurement capability is discussed. Esp. digital beamforming concepts are considered and promising results are presented.

I. INTRODUCTION

First experiments in the field of automotive radar took place already in the late 50's. In the 70's, more or less intensive radar developments started at microwave frequencies. The activities of the last decades were concentrated mainly on developments at 17 GHz, 24 GHz, 35 GHz, 49 GHz, 60 GHz, and 77 GHz. Even from the early beginning in automotive radar the key driver of all these investigations has been the idea of collision avoidance; this idea has spent enormous motivation for many engineers all over the world to develop smart vehicular radar units. During this quite long period a lot of know-how has been gained in the field of microwaves and in radar signal processing. Accompanied by the remarkable progress in semiconductor microwave sources (esp. Gunn sources and GaAs MMICs) and in available computing power of microcontrollers and digital signal processing units, the commercialization of automotive radar became feasible in the 90's.

Competing and complementing technologies in vehicular surround sensing and surveillance are Lidar, ultrasonics, and video cameras (based on CCD or CMOS chips including near-infrared sensitivity). Car manufacturers and suppliers are developing optimized sensor configurations for comfort and safety functions wrt. functionality, robustness, reliability, dependence on adverse weather conditions etc. Last but not least the total system costs have to meet the marketing targets to be attractive for the end customers. First applications with surround sensing technologies were parking aid (based on ultrasonics), collision warning, and Adaptive Cruise Control (ACC). For instance, collision warning systems were successfully introduced in the US in the 90's. Greyhound installed more than 1600 radar systems (24 GHz) in their bus lines yielding a reduction of accidents of 21 percent in 1993 compared to the year before.

ACC was commercialized for the first time in Japan in 1995. Whereas Lidar-ACC has been favored esp. in Japan, European and US companies have been focused mainly on radar based ACC. In 1999, Mercedes introduced the 77 GHz "Distronic" into the S class, followed

by other premium models equipped optionally with an ACC, such as BMW 7 series, Jaguar (XKR, XK6), Cadillac (STS, XLR), Audi A8, and VW Phaeton. ACC is also available in Mercedes E, CL, CLK, SL class, BMW 5 and 6 series, Audi A6, Nissan (Cima, Primera), Toyota (Harrier, Celsior), Lexus (LS, GS), and Honda (Accord, Inspire, Odyssey). Furthermore, ACC will become an option in the new BMW 3 series and in the new VW Passat, both with start of production in 2005.

Whereas European car manufacturers offer 77 GHz systems only for ACC systems so far, their Japanese competitors Honda and Toyota already introduced an active brake assist for collision mitigation (additionally to ACC) in 2003 based on 77 GHz long range radar (LRR) technology. In contrast to the only smooth deceleration capability of an ACC system (because ACC is only marketed as a comfort feature), the active brake assist provides much higher braking forces for deceleration, when a threatening situation is identified and the driver starts braking, but maybe not as strong as it would be necessary to avoid a crash.

This shows the trend from "comfort only" functions to active safety systems with radar sensing technologies that serve both the comfort and the safety domain. Within the next few years these active safety systems will be introduced in Europe. Mercedes started with the first generation of their Presafe system in the S class in 2003, which isn't based on surround sensing techniques yet but (only) on the data of the electronic stability program (ESP) and the antilock braking system (ABS). If these control units identify an imminent accident due to the car's dynamics, electronic seat belt tensioners will be activated, seat orientations will be adapted, and the sunroof will be closed.

The next step in this evolutionary process will be to gain some more milliseconds in advance for reaction and for automatic activation of suitable protection measures. Bosch names this system "Predictive Safety System (PSS)", which will have mainly three stages. The first one (PSS1, to be introduced in 2005) is a preset of the brake system. As soon as a threat will be identified by the 77 GHz LRR, the brake system will be pre-filled, but this won't be noticed by the driver. But when the driver pushes the brake pedal in such a situation, maximum braking forces will be available without any latency. In the second stage (PSS2, 2006) the driver will be notified in a hazardous situation with an automatic, very short but intensive brake activation, accompanied by optical or acoustic signals. In the third stage (PSS3) an automatic emergency brake will be initiated if otherwise a crash couldn't be avoided. Bosch was recently awarded for its PSS with the "Gelber Engel (Yellow Angel)" from the

German auto club ADAC (similar to AAA in the US) in the category “Innovation”.

Short range radar (SRR) sensors for passenger cars will be mounted first in premium class models for pre-crash sensing, ACC support, parking assistance, and blind spot surveillance. Preferred microwave technology is 24 GHz in ultra wideband (UWB) operation with high range resolution in the range of cm.

II. FREQUENCY REGULATION

A lot of progress has been made during the last years in the frequency regulation for automotive radar. The 76 – 77 GHz band was regulated already in the 90’s followed by a standardization in Europe (ETSI EN 301 091). Now, this band is allocated for Intelligent Transport Services (ITS) in Europe, North America, and Japan.

For short range applications UWB sensors are widely preferred because of their low cost perspectives and their high resolution in the range cm. The Federal Communications Commission (FCC) regulated UWB for the North American market (NAFTA) already in 2002. For automotive UWB short range radar systems the FCC allocated the band 22 – 29 GHz with a maximum mean power density of -41.3 dBm/MHz.

In 2002, more than 30 mainly European car manufacturers and suppliers founded the Short range Automotive Radar frequency Allocation consortium (SARA). SARA’s main objective is to support UWB regulation for automotive radar in the 24 GHz range in Europe. Because of strong objections of the telecom industry and earth observation institutions, a lot of effort was dedicated to find a compromise and to enable automotive UWB radar systems. On 17 January 2005 the commission of the European Community finally decided to allocate the range of 21.65 – 26.65 GHz for UWB short range radar. The marketing of these systems is allowed from 07/2005 till 06/2013. The penetration rate is restricted to 7 percent of all cars in each country of the European Community. It is expected that this time frame of eight years will be sufficient to develop inexpensive short range radar sensors operating at a new frequency without impairing other commercial, scientific or military systems and services. Hence, in March 2004 the European commission allocated the frequency range 77 – 81 GHz for UWB SRR with permitted usage from 2005 onwards. Anticipating the allocation of this band also in Japan and North America, the SRR suppliers will probably shift their UWB developments from 24 GHz to 79 GHz in the medium term.

III. FRONT END TECHNIQUES AND ANTENNA CONCEPTS

Functional requirements, limited space for the sensors’ mounting, regulatory issues, components’ and fabrication costs, and marketing schedules mainly determine the choice of sensor concepts. One main requirement for long range radar is a range capability up to 150 .. 200m. With regard to the radar equation of a monostatic radar

$$R_{\max} = 4 \sqrt{\frac{P_{Tx} \cdot A^2 \cdot \sigma}{P_{\min} \cdot 4\pi \cdot \lambda^2}}, \quad (1)$$

we have in mind that the maximum range R_{\max} is proportional to the square root of the effective antenna aperture size A and to the square root of the frequency. σ denotes the reflectivity of the target, P_{Tx} the transmitted power and P_{\min} the minimum power necessary for detection. Therefore, highest frequencies should be preferred to get small box volumes. But this demand is contrary to the availability of cost saving microwave technologies. The antenna size of 77 GHz LRR sensors may decrease to approx. 50 x 50 mm². But even when the sensitivity would be sufficient, high antenna directivity and low sidelobes would still be necessary to cope with the effects of guard rails and irrelevant surroundings besides the road lanes.

A. 24 GHz Sensors

SRR sensors do not require long range capability. Hence, lower frequencies are preferred, enabling the use of available microwave components also used in the telecom industry. The 24 GHz technology seems to be the best compromise between today’s component costs and sensor size. Typically, SRR sensors do not measure the angle of detected objects and they have a very broad lateral coverage. Therefore, single antenna elements are sufficient. Only vertically the beams are directed to increase antenna gain and to minimize clutter effects from the road surface [1]. SRR sensors are typically operated in pulsed mode (pulse, pulse Doppler) or in continuous wave mode (CW, FMCW, FSK, FMCW & FSK). Also coded radar with spread spectrum techniques (pulsed, CW, pseudo-noise) is a common technique. For instance, Delphi’s 17 GHz radar is a phase coded CW radar with a pseudo-noise (PN) BPSK modulation. The M/A-Com sensor is a pulsed radar. Hella is developing a 24 GHz UWB radar for short range applications and a narrow-band FMCW radar operating in the license free 24 GHz ISM band with a maximum range of 70m [2].

To measure not only targets’ distances but also their angular positions, several adjacent sensors can be used. Their measurements of the targets’ distances are fused in a trilateration algorithm yielding also the angular positions. Valeo-Raytheon is developing a multibeam phased array SRR that provides angular information itself.

B. 77 GHz Sensors

Main manufacturers of 77 GHz LRR sensors are ADC (subsidiary of Continental Temic in cooperation with M/A-Com), Bosch, Delphi, Denso, TRW (Autocruise), Fujitsu Ten, and Hitachi. Fig. 1 shows Bosch’s LRR in its 2nd generation, production has been started in 2004. The system has a box size of only 74 x 70 x 58 mm³ (H x W x D) and contains all sensing and ACC functionality. The 77 GHz circuitry contains 4 feeding elements (poly-rods) directly attached to 4 patch elements on the RF board, illuminating a dielectric lens. The monostatic analog beamforming approach results in a broad illuminating transmit beam and four single receiving beams which partially overlap in azimuth yielding a total azimuthal coverage of ±8 degrees, see Fig. 2. The modulation is FMCW with a triangular shape [3].



Fig. 1. Bosch ACC, 2nd generation

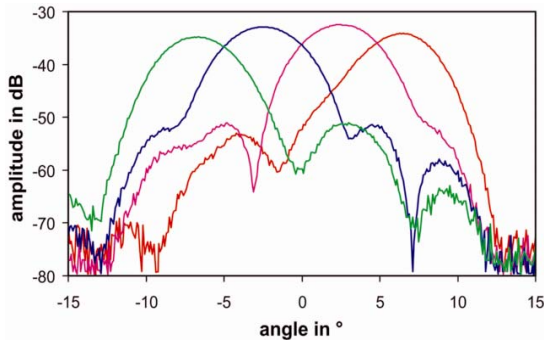


Fig. 2. Receive beam pattern of Bosch ACC, 2nd generation

TRW also uses the dielectric lens concept whereas ADC (resp. M/A-Com) takes advantage of a folded structure with a very low profile resulting in a sensor depth of 5cm. Other companies (Delphi, Fujitsu Ten, Mitsubishi electric, Celsius Tech) use mechanical mechanisms to steer the beam in azimuth. Although mechanical radar scanners yield quite good detection performance, they might be sensitive in their mechanical reliability over lifetime. Moreover, they are limited concerning further miniaturization. Delphi's and Fujitsu Ten's mechanical radar are in series production.

IV. DIGITAL BEAMFORMING CONCEPTS

77 GHz radar sensors with digital beamforming (DBF) front ends were introduced into the market by Japanese companies in 2003. Denso built a bistatic LRR with planar patch antennas with a range capability up to 150m and a field of view of approx. ± 10 degrees [4]. The nine receiving antennas are multiplexed with four 77 GHz SP3T switches to only one base band channel, see Fig. 3.

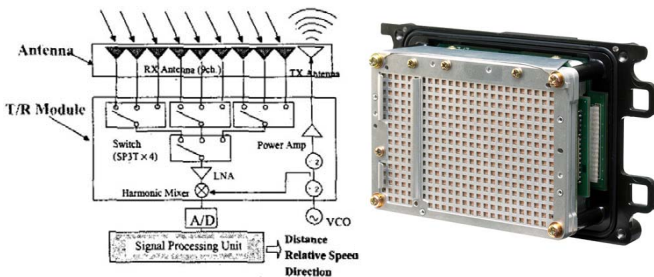


Fig. 3. Denso's 77 GHz DBF sensor [4]

The Toyota CRDL 77GHz LRR radar (Fig. 4, [5]) switches 3 equal transmitting antennas and 3 receiving antennas resulting also in one base band channel, and, after demultiplexing in the digital domain, nine digital receiver channels for DBF.

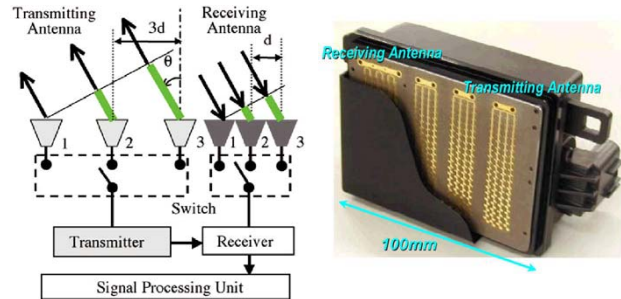


Fig. 4. Toyota CRDL Radar with DBF, 77 GHz, [5]

A. Direction of Arrival Estimation

All conventional direction of arrival (DOA) estimation methods as monopulse techniques (comparison of the received signals in partially overlapping beams) or spatial power spectrum measurement techniques (mechanical scanning, phased array) do have an angular resolution in the range of the half-power beamwidth. Hence, the angular resolution directly depends on the aperture size, because the 3 dB beamwidth of an antenna with diameter D and constant illumination is approx.

$$\theta_{3dB} \approx 59^\circ \frac{\lambda}{D}. \quad (2)$$

Therefore, the angular resolution of long range 77 GHz sensors is typically in the range of 2 .. 5 degrees. To overcome this limitation, parameter estimation methods based on subspace techniques can be applied. These methods rely on a subspace decomposition of the noisy received signals of an array of multiple antenna elements. With an eigenvalue decomposition of the autocorrelation matrix of the received signals of a uniform linear array (ULA) the noise and the signal subspace can be determined. Knowing these subspaces, the DOA's of the targets can be estimated. Well known in array signal processing theory are the Music and Esprit algorithms [6, 7]. We applied these techniques to a 24 GHz SRR with digital beamforming and published very promising results in 2002 [8].

In our further work we started to transfer this approach to the 77 GHz domain. The main objectives of our current research activities are to gain know-how about 77 GHz DBF concepts and their benefits in combination with parameter estimation techniques and to investigate their impact on development efforts. Fig. 5 shows one of our 77 GHz DBF front ends with a ULA consisting of eight parallel receiving columns. The transmit antenna consists out of 4 columns with a tapered power distribution yielding a low sidelobe level of approx. -27 dB. The 3 dB beamwidth of the transmit antenna is approx. 26 degrees and the antenna gain is 20.5 dB.

V. CONCLUSION

Short range radar in ultra wideband operation at 24 GHz and at 79 GHz from 2013 at the latest will be used first in premium and later on in upper class models. Main applications will be ACC support, pre-crash detection, parking assistance, and blind spot surveillance. Market introduction of 24 GHz SRR will start in 2005. SRR sensors won't have angular measurement capabilities in the first generation (except the Valeo-Raytheon sensor), but future generations will also be able to provide angular information. Although these sensors will be more expensive, they will contribute to the minimization of the total number of sensors and therefore they will reduce overall system costs.

77 GHz ACC systems will be extended to be operational at low speeds including full stop capability. This will provide increased customer benefits and it will contribute significantly to the market success of ACC systems. In the same manner the 77 GHz sensor will be used not only for comfortable driving (ACC stop & go) but also for predictive and active safety systems. Active safety systems up to an automatic emergency braking in unavoidable crash situations will be the key for a considerable reduction of the total number of crashes and fatalities.

The detection performance of 77 GHz sensors will be further improved, for instance wrt. false alarm rate and reaction time. Also sensor costs will be lowered. Planar antennas in combination with digital beamforming provide interesting front end concepts for 77 GHz radar. These techniques might become feasible for high volume production as far as costs of 77 GHz components and powerful digital signal processing units will further decrease.

REFERENCES

- [1] I. Gresham, A. Jenkins, "Ultra-wideband radar: Regulations, Applications, and Challenges," *Int. Microwave Symposium 2003*, Philadelphia, Penn., June 2003
- [2] Th. Wixforth, W. Ritschel, "Multimode-Radar-Technologie für 24 GHz," *auto & elektronik*, vol. 3/2004, pp. 56-58
- [3] G. Kühnle, H. Mayer, H. Olbrich et al, "Low-Cost Long-Range Radar for Future Driver Assistance Systems," *Auto Technology*, vol. 4/2003, pp. 2-5, 2003
- [4] A. Kawakubo, S. Tokoro et al., "Electronically-Scanning Millimeter-Wave RADAR for Forward Objects detection," *SAE Congress 2004*, pp. 127-134, Detroit, 2004
- [5] Y. Asano, S. Ohshima et al, "Proposal of Millimeter-Wave Holographic Radar with Antenna Switching," *Int. Microwave Symposium 2001*, Phoenix, Az, May 2001
- [6] R. O. Schmidt, "Multiple emitter location and signal parameter estimation," *Proc. RADC Spectrum Estimation Workshop*, RADC-TR-79-63, Rome Air Development Center, Rome, NY, Oct. 1979, p. 243 (reprinted in *IEEE Trans. Antennas Propag.*, vol. AP-34, pp. 276-280, 1986)
- [7] R. Roy and T. Kailath, "ESPRIT - Estimation of signal parameters via rotation invariance techniques," *IEEE Trans. Acoust., Speech, Signal Processing*, vol. 37, pp. 984-995, July 1989
- [8] M. Schneider, V. Groß et al, "Automotive 24 GHz Short Range Radar Sensors with Smart Antennas," *German Radar Symposium 2002*, Bonn, September 2002

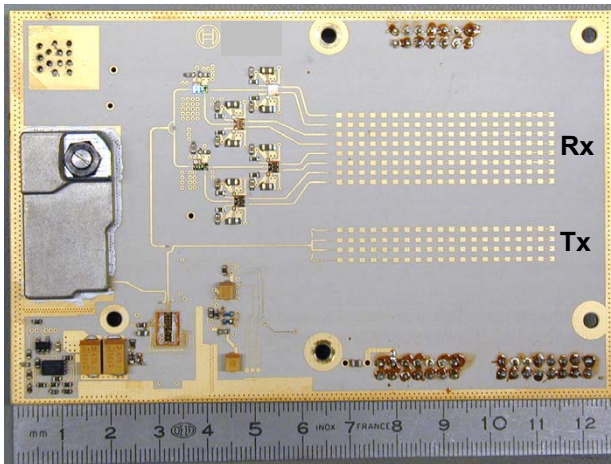


Fig. 5. Bistatic 77 GHz DBF front end with 8 patch antenna columns for receive and 4 columns (fed by a power splitter) for transmit

Another front end with extended arrays for long range operation was put into a water-resistant housing and was mounted on our test vehicle, see Fig 6. First results of our implementation of parameter estimation techniques on a 77 GHz DBF demonstrator are shown in Fig. 7. The markings no. 1 and 2 indicate the estimation of the Esprit algorithm. Although the half power beamwidth of the virtual beams of the DBF sensor is approx. 8.5 degrees, both cars with their angular separation of less than 4 degrees are detected and no ghost target between both objects does appear.



Fig. 6. Test vehicle with 77 GHz DBF demonstrator (also insert in right bottom corner)

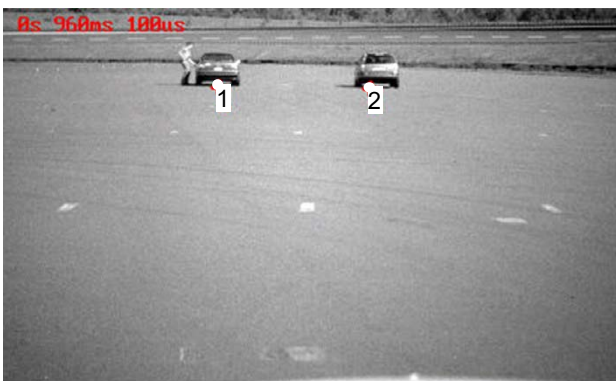


Fig. 7. Angular measurement of two cars at the same distance (60 m radial distance and 4 m lateral separation)

Trends in Automotive RF Wireless Applications and their Electromagnetic Spectrum Requirements

Hans Ludwig Blöcher¹, Gerhard Rollmann², Steffen Gärtner²

¹DaimlerChrysler AG, Research & Technology, D-89081 Ulm, Germany

²DaimlerChrysler AG, D-71059 Sindelfingen, Germany

Hans-Ludwig.Bloecher@daimlerchrysler.com

Gerhard.Rollmann@daimlerchrysler.com

Steffen.Gaertner@daimlerchrysler.com

Abstract — During the next years, the number of wireless sensor and communication systems used in cars will increase significantly. The operational frequencies will span from the LF to the MMW range. In particular, Ultra-Wideband (UWB) systems will be introduced, due to the expected low costs of these systems and their technical advantages. This contribution gives an overview on actual and planned wireless systems used in cars and on the necessary spectrum resources of the technologies to be applied. Furthermore, the spectrum engineering, technical standardization and regulatory body processes involved are shown by the example of the 24/79GHz UWB automotive short range radar (SRR) regulatory activities.

I. AUTOMOTIVE WIRELESS RF SYSTEMS

In the (near) future, a variety of wireless RF automotive communication and sensor applications is expected to be integrated in cars (Figs. 1, 2). These systems will be realized using conventional and Ultra-Wideband (UWB) technology approaches. The planned operational frequencies cover a range from e.g. 9 KHz (RFID) to e.g. 79 GHz (UWB automotive short range radar (SRR)).

Careful spectrum engineering and regulation is required, in order to ensure the coexistence with other existing services (commercial, military, government).

II. ULTRA-WIDE-BAND (UWB) SYSTEMS

Ultra-wideband signals are commonly defined as electromagnetic waves with an instantaneous bandwidth greater than 25% of the centre operating frequency, or which have an absolute bandwidth of at least 1.5 GHz (US FCC: 20%, 500MHz). The “classical” UWB approach uses carrier-free nano- and picosecond pulses with a bandwidth up to 11 GHz, but e.g. 24 GHz automotive radar with a bandwidth of up to 5 GHz is also an UWB system by definition.

Some UWB systems characteristics are listed in the following:

- very low emitted spectral power density, near the noise floor (Fig. 3)
- large bandwidth and therefore spectrum sharing with other services

- UWB chip mass production possible, low target prices (up to 11 GHz)
- high timing and detection accuracy and resolution precision
- immunity to multipath fading.

UWB systems first have been used by the military, in particular for “low probability of intercept (LPI)” applications. There is still a variety of commercial applications, e.g.:

- communications equipment used as “cable replacement system” in high speed wireless networks (50-100 Mb/s) e.g. for downloading streaming video from camcorder to a television set
- imaging systems such as ground penetrating radar, motion detectors for security and surveillance applications, medical imaging
- automotive radar sensors for active and passive safety applications (e.g. around 24/77/79 GHz)
- inventory tracking tags e.g. anti-theft tags, tags for lost pets
- identification systems e.g. for implementing motorway tolls
- breathing monitors e.g. to prevent cradle death.

Due to their particular properties, ultra-wide band devices offer a special challenge to spectrum management and regulation. There are still R&D activities going on, dealing with the development and standardization of UWB systems (e. g. the EC FP6 project “PULSERS”).

III. UWB REGULATORY EXAMPLE: 24 GHz AUTOMOTIVE UWB SHORT RANGE RADAR - EUROPE

The European Commission defined the task to reduce road fatalities by 50 % until 2010. The objective and focus of “The EC Approach to Road Safety and Intelligent Transport systems” (ITS, Intelligent Vehicle Systems) are defined as to “Improve Safety, Security, Comfort and Efficiency in all Transport modes” and “Focusing on Advanced Pilot/Driver Assistance Systems”.

The industry has responded to the European Commission programs and has developed new, efficient 24 GHz UWB short range radar (SRR) solutions for road



Fig. 1. (Expected) automotive wireless RF communication applications (Expl.).

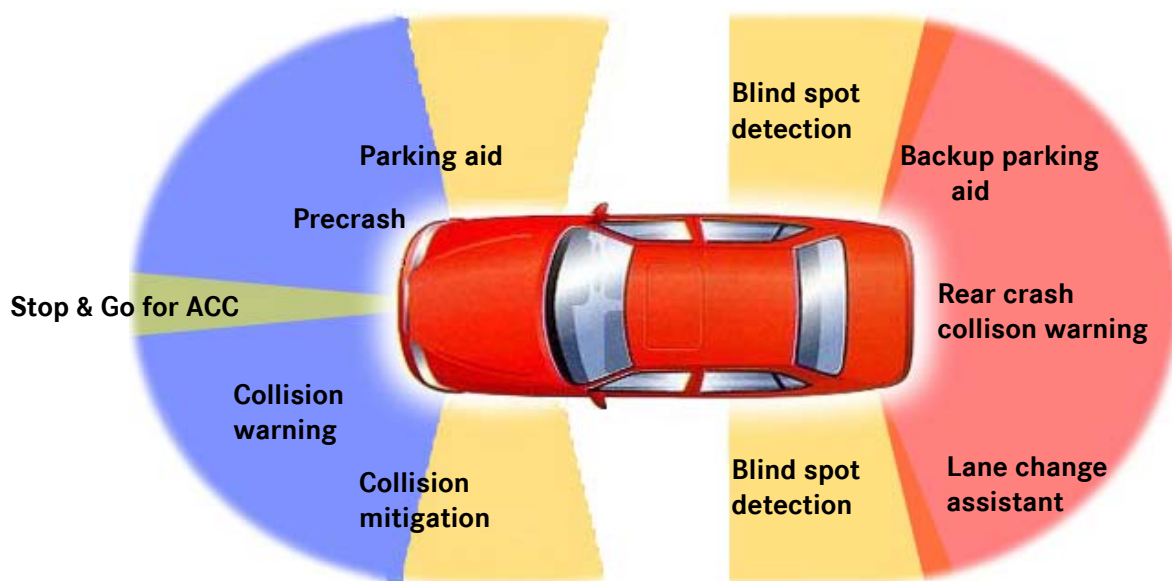


Fig. 2. (Expected) automotive wireless RF (radar-) sensor applications (Expl.).

safety and intelligent transport systems. The operational bandwidth of 5 GHz, due to the required high resolution of 3 cm, causes emissions into frequency bands of other services. SRR's at 24 GHz are mature and ready for deployment today and not limited to high end cars.

Intensive sharing studies have been performed e.g. with fixed services, earth exploration satellite services, radio astronomy services, and radio amateur services [1]-[4]. The sharing study results have been published as Repts. 23 and 56 of the CEPT ECC [5].

In order to achieve the necessary regulatory and standardization issues, an ad hoc grouping of automotive manufacturers, suppliers and institutions (SARA - short range automotive radar frequency allocation) has been founded. SARA found that the activities necessary for getting a frequency allocation are time consuming (in particular the coexistence studies). Moreover, the decisions of the regulatory administrations can have a serious bearing on the market introduction and cause further efforts.

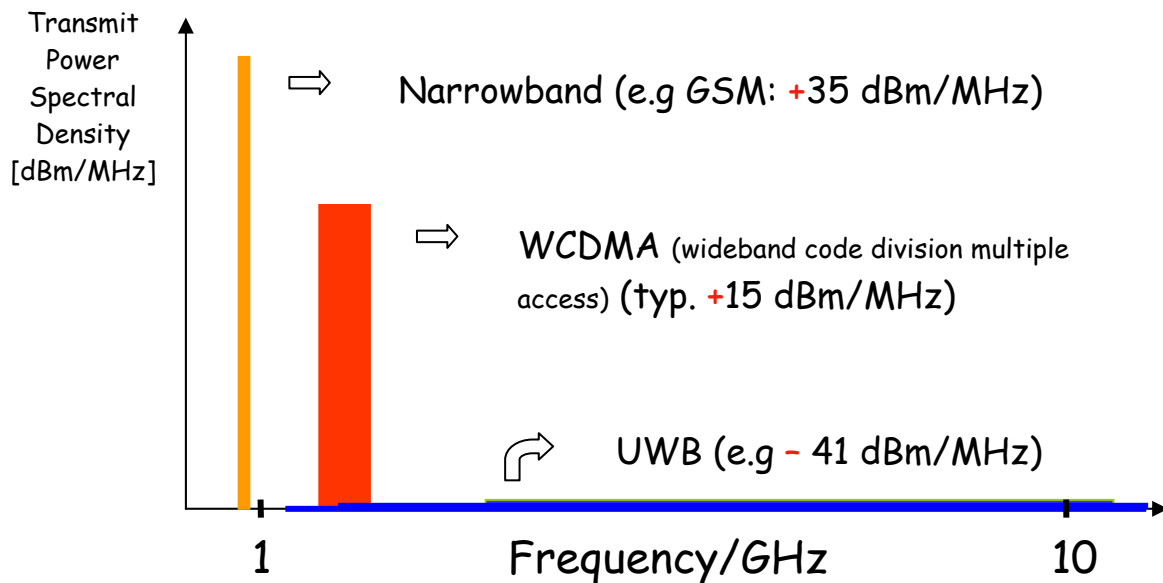


Fig. 3. Comparison UWB spectrum – spectra of conventional wireless RF systems.

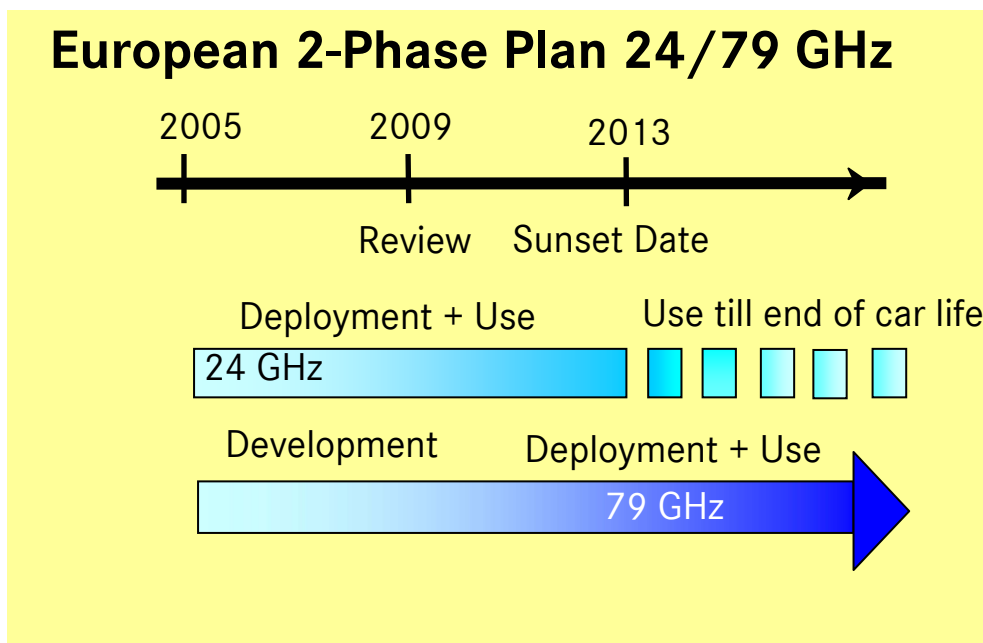


Fig. 4. “Package Solution” for automotive short range radar in Europe.

As result of the regulatory process, in Europe a “Package Solution” for the SRR (Fig. 4) has been adopted with a transition from 24 GHz to 79 GHz from 2013 on:

- 24 GHz interim technology
 - until mid of 2013
 - max. car parc penetration 7%
 - deactivation near radioastronmoy sites
- 79 GHz long term solution.

As a consequence, a strong effort in R&D activities towards the provision of 79 GHz technology is

necessary, in order to achieve the availability of this successor technology in time.

Until end of 2004, decisions of the EC (obligatory for the 25 EC countries) and the CEPT ECC (recommendation for the 46 european countries, incl. the EC countries) have been adopted. These decisions deal with an interim allocation of the 24 GHz range for SRR (documents: 2005-50-EC [9] and ECC/DEC(04)10 [8]) and the new 79 GHz SRR allocation (documents: 2004-545-EC [9] and ECC/DEC(04)03 [8]). The national implementation in the EC countries has to be carried out

until end of June 2005. In Germany, up to now the 79 GHz SRR allocation has been adopted (document: ABl. 25/04, VfG 59 of the RegTP [7]).

An european 24 GHz SRR standard (document: ETSI EN 302 288 [6]) has been completed recently, the drafting process of the european 79 GHz SRR standard (document: ETSI EN 302 264 [6]) has started and is still ongoing.

IV. CONCLUSION

In the future, the use of automotive wireless RF communication and sensor applications will increase, using the frequency range from the LF band up to the MMW band.

Within an electromagnetic scenario of increasing complexity, frequency sharing is an important topic to be considered. In this context, UWB systems require a special care and attention. Thus, in parallel to the pure development of technologies, spectrum engineering, frequency allocation and standardization processes should become an integral part of the product development chain.

REFERENCES

- [1] R. Makanaboyina, M. Sadashivaiah, H. H. Bloecher, G. Rollmann and K. Gopalakrishnan, „Compatibility Study of 24 GHz Short Range Radar with fixed Satellite and Broadcasting Satellite Services,” in *Proc. MIKON 2004*, Warsaw, Poland, May 2004.
- [2] M. Younis, J. Maurer, J. Fortuny-Guasch, R. Schneider, W. Wiesbeck and A. J. Gasiewski, „Interference from 24-GHz Automotive Radars to Passive Microwave Earth Remote Sensing Satellites,” *IEEE Trans. Geoscience and Remote Sensing*, Vol. 42, S. 1387-1398, July 2004.
- [3] H. L. Blöcher and G. Rollmann, „Coexistence Study of Automotive Short Range Radar operating in the W-Band,” in *Proc. EuMC 2004*, Amsterdam, Netherlands, October 2004.
- [4] G. Rollmann, P. Knoll, M. Mekhaïel, V. Schmid and H. L. Blöcher, „Short-Range-Radar-System for Automotive Applications,” published in the Internet: on the Homepage of the IEEE MTT/AP German Chapter (<http://ewh.ieee.org/r8/germany/mtt-ap>), June 2004.
- [5] The SE24-Sharing-Study-Reports ECC Rept. 23 (Compatibility 24 GHz SRR) and ECC Rept. 56 (Compatibility 79 GHz SRR) are available in the Internet: ERO-Homepage (<http://www.ero.dk/deliverables/reports>).
- [6] The European Product-Standards EN 302 288 Parts 1 and 2 (24 GHz SRR) and EN 302 264 Parts 1 and 2 (79 GHz SRR) are after completion available in the Internet: ETSI-Homepage (<http://www.etsi.org>).
- [7] The German General Frequency Assignment dealing with the SRR application of the frequency range 77-81 GHz, ABl. 25/04, VfG 59, is available in the Internet: RegTP-Homepage (http://www.regtp.de/reg_tele/02881/00/).
- [8] The ECC Decisions ECC/DEC(04)10 (24 GHz SRR) and ECC/DEC(04)03 (79 GHz SRR) are available in the Internet: ERO-Homepage (<http://www.ero.dk/deliverables/decisions>).
- [9] The EC Decisions 2005-50-EC (24 GHz SRR) and 2004-545-EC (79 GHz SRR) are available in the Internet: EC-Homepage: (<http://www.europa.eu.int/eur-lex>).

Session 6a

High Speed Digital Circuits

Sensitivity Matched Static Frequency Divider Using A $0.8 \mu\text{m}$ SiGe HBT Technology

Ertugrul Sönmez, Sébastien Chartier, Peter Abele, Andreas Trasser, and Hermann Schumacher
Dept. of Electron Devices and circuits
University of Ulm, Germany
Email: esoenmez@ebs.e-technik.uni-ulm.de
Phone : +49 731 50 31584
Fax : +49 731 50 31599

Abstract — In this paper, the authors present a static frequency divider designed for the 24 GHz ISM band, with a divide ratio of 16, using an innovative sensitivity matching concept between the first and the second stages. The divider is using a master-slave toggle flip-flop topology and implemented in a $0.8 \mu\text{m}$ SiGe HBT process with a maximum f_T of 80 GHz. The circuit operates up to 25 GHz and consumes 240 mW at 4 V supply voltage.

I. INTRODUCTION

Frequency and phase-locking of oscillators are essential requirements for 24 GHz automotive radars. To provide this functions within the system, frequency dividers are essentials. We present in this paper, a static frequency divider using the master-slave toggle flip-flop topology. The circuit operates up to 25 GHz and consumes 240 mW at 4 V supply voltage. The divider uses a novel innovative sensitivity match concept. The chip, pads included has a size on-chip of $870 \times 340 \mu\text{m}^2$.

II. THE SiGe HBT TECHNOLOGY

The circuit was implemented in the second generation of the commercially available Si/SiGe HBT process of Atmel GmbH (Germany) [1] which provides 3 aluminium metal layers and transistors with an effective emitter width of $0.5 \mu\text{m}$. Selective collector implants offers devices with $f_T=80$ GHz. The divider was realized on a wafer with a $20 \Omega\text{cm}$ substrate resistivity.

III. DESIGN PHILOSOPHY

A. Frequency divider topology

1) *Various design approaches:* There are different approaches to achieve frequency division by 2. A first topology is an analog dynamic frequency divider. Recent applications of this concept exhibit performance up to 110 GHz, like reported in [2]. However, the analog dynamic frequency division has a low operation bandwidth, and for broadband applications such as the 24 GHz ISM band, a circuit with a wider frequency range of operation is preferable. A second approach is a digital frequency divider, also called static frequency dividers. The most popular and well balanced representative is the master-slave toggle flip-flop (MS-TFF) circuit, which was used here.

2) *2:1 static frequency divider topology:* The MS-TFF presented in this paper is fully differential. It consists of two D-latches, implemented in standard Emitter-Coupled-Logic (ECL). The ECL (see Fig. 1) is using single feedback emitter

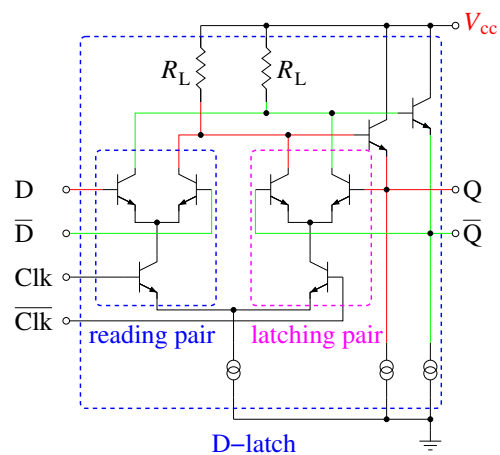


Fig. 1. Emitter-Coupled-Logic schematic

followers instead of two or more, like widely used in literature [3] [4] [5], to reduce the supply voltage level below 5V.

The block diagram and the chip photography of the complete static frequency divider are depicted in Fig. 2 and Fig. 3, respectively. For a simple single-ended on-wafer measurement setup, the complementary input port is short-circuited to ground by a capacitor. The inverted output port is kept floating in layout. The complete circuit schematic of the frequency divider is depicted in Fig. 4.

The divider itself needs a chip-area of $95 \times 73 \mu\text{m}^2$, defined by minimum device and metal layer distances. The overall chip size is $360 \times 330 \mu\text{m}^2$ with the contact pad extensions. To save voltage headroom, and because of the wide band operation, the current sources have been realized by high ohmic resistors instead of current mirrors.

To optimize the circuit performances, the individual delay contribution of the circuit elements to the overall time delay must be analyzed. From [6] it can be summarized, that the smallest available transistor is optimal for high speed operation.

Therefore, a transistor with an emitter length of $1.4 \mu\text{m}$ has been chosen. In addition to the time constants, discussed in [6], the low-pass filter made up with the load resistance

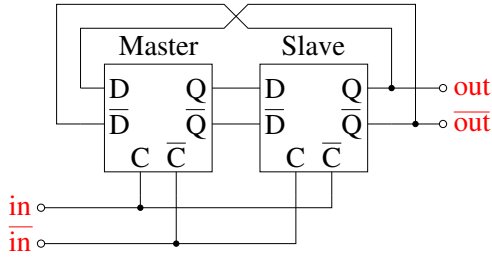


Fig. 2. Block diagram of the 2:1 static frequency divider

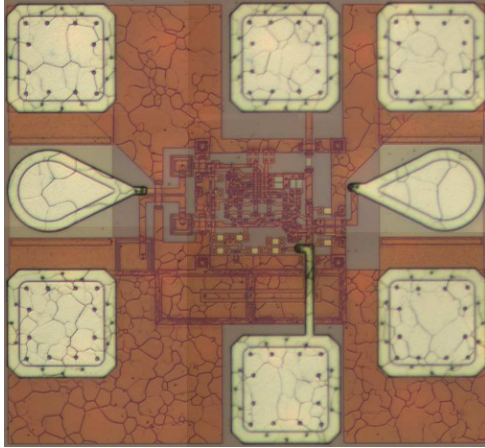


Fig. 3. Chip photography of the 2:1 static frequency divider

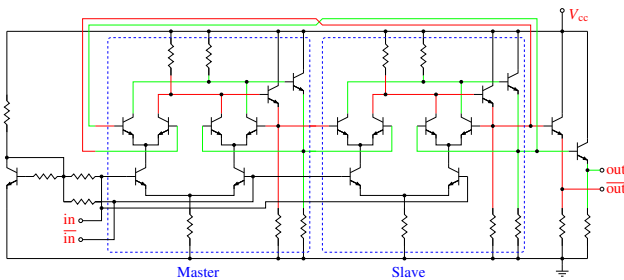


Fig. 4. Schematic of the complete 2 by 1 static frequency divider

R_L and the collector-substrate depletion capacitance C_{js} is limiting the upper operation frequency of the circuit. The smallest substrate parasitic (C_{js}) is obtained with a transistor with a collector/emitter/base (ceb) electrode configuration. The collector-substrate depletion capacitance C_{js} of a transistor with a ceb electrode configuration as a function of the laid out emitter length is shown in Fig. 5.

Additionally, a parasitic direct sub-collector to sub-collector coupling contributes to the $R_L C$ -filter. The reading pair and latching pair transistors collectors, which are connected to a single load resistance R_L , are connected through an uninterrupted buried layer to each other.

The two sub-collector strips of the 4 upper-level current-switching transistors are facing one another in a distance of $8 \mu\text{m}$. The coupling between them is measured to be 5fF . As the signals at the sub-collector strips are differential, their coupling capacitance is contributing to the low-pass filter with twice its value. Therefore, an $R_L C$ -filter with a corner

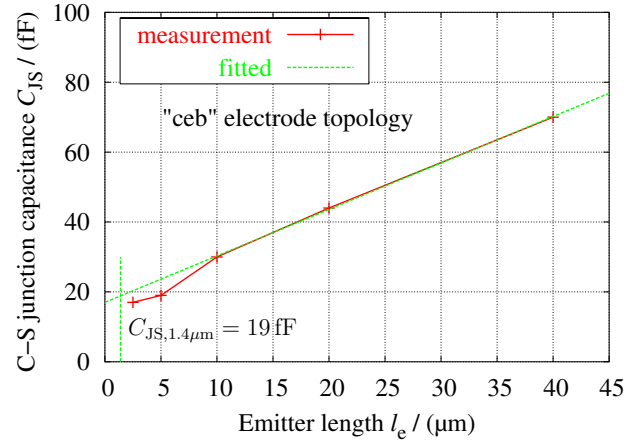


Fig. 5. The Collector-Substrate depletion capacitance C_{js} of a transistor with a ceb electrode configuration as a function of the laid out emitter length

frequency of 24GHz would occur, deteriorating the dividers performance significantly, if the value for the load resistance is chosen to be 230Ω by these simple estimations already. The R_L value range is, to the lower end the limit of self-oscillations due to loop-gain dropping below 1 and to the upper end the shift of the self-oscillation frequency to lower frequencies, consequently not being able to lock the divider to the clock frequency anymore. Together with the switched part of the biasing, R_L is controlling the self-oscillation frequency and thereby, the upper operation frequency of the divider, very sensitively.

The feedback emitter followers are not only providing a high load impedance at the collectors of the latching pair, but also delivering the base charging current of the next stages reading pair. Therefore, the minimization of the current level of this stage would deteriorate the performance of the divider.

3) 16:1 static frequency divider topology: The 16:1 divider is realized by cascading 4 of the static 2:1 dividers, basically. Due to the optimization of the first divider for highest possible operation frequencies, its output signal amplitude is too low to drive the clock port of the next divider stage. Instead of a buffer amplifier between the first stage and the second, a sensitivity matching concept has been used. The self oscillation frequency of the second divider can be designed to be shifted towards the first dividers output frequency. This shift has been performed by increasing the load resistors value from 150Ω to 250Ω and reducing the biasing current. These actions increase at the same time the output signal amplitude of the second stage making the design of the third stage uncritical.

The chip photography of the 16:1 is depicted in Fig. 6, in which the arrangement of the 2:1 dividers, of the capacitive DC decoupling between the stages and of the distributed Vcc-filter network can be taken from. The overall chip, pads included, consumes an area of $870 \times 340 \mu\text{m}^2$.

B. DC distribution filter network

1) Stage to stage isolation: The supply voltage port of each single stage of the divider is blocked by an efficient RC filter (see Fig. 7). In order to decrease the interconnection parasitics, the placement of the capacitor C_{block} has to be in

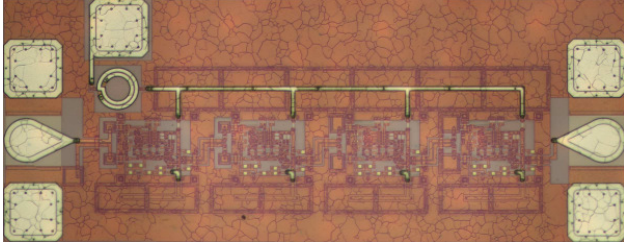


Fig. 6. Chip photography of the 16:1 static frequency divider

close vicinity to the circuit elements which are supplied by an ideal voltage source. The design criteria of these passive components are as follows: the capacitor needs to provide a low impedance to the $V_{CC,stage}$ -port and a compromise must be found for the R_{filter} between minimum necessary isolation and the introduced voltage drop at the $V_{CC,stage}$ -port.

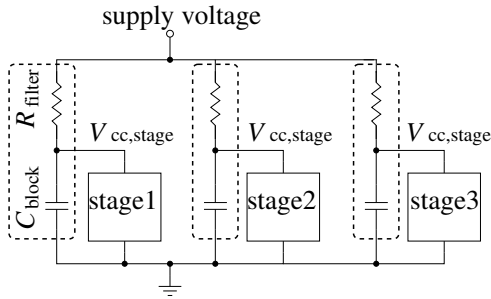


Fig. 7. Schematic of the RC filtering network

2) *Function block to function block isolation:* Two or more function-blocks (for example: an oscillator and a divider) can be interconnected to a common supply voltage. However, this connection may create a path for signal cross-talk. To avoid this problem an LC low-pass filter is provided. The schematic and the layout of the filter network are depicted in Fig. 8 and Fig. 9, respectively. The inductor L_{filter} used for the filtering is an on-chip stacked inductor (using the 3 available metal layers of the technology) of 1nH and the capacitor is obtained by connecting several capacitor in parallel. The overall value of the C_{filter} network is 30 pF.

In order to estimate the isolation provided between the function-block supply voltage line and the V_{CC} -port of a single stage, a test structure combining both LC and RC DC-filtering network techniques was used (see Fig. 10). The provided isolation is better than 40 dB between 9 GHz and 50 GHz.

IV. MEASUREMENTS

The first stage and the second stage of the 16:1 static divider was laid out individually to characterize the input sensitivity gain at $f_{LO}/2$ for the second stage. For these both stages and the complete 16:1 static frequency divider the input sensitivity is plotted versus the clock frequency in

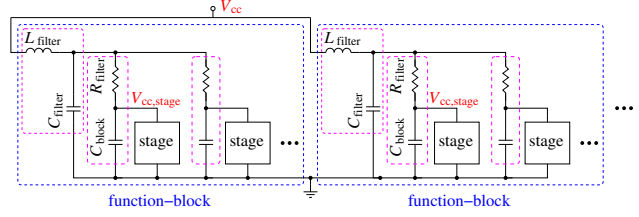


Fig. 8. Schematic of the function block to function block filtering

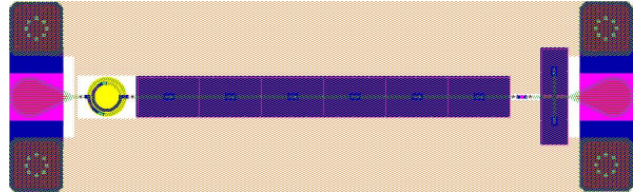


Fig. 9. Layout of the function block to function block filtering

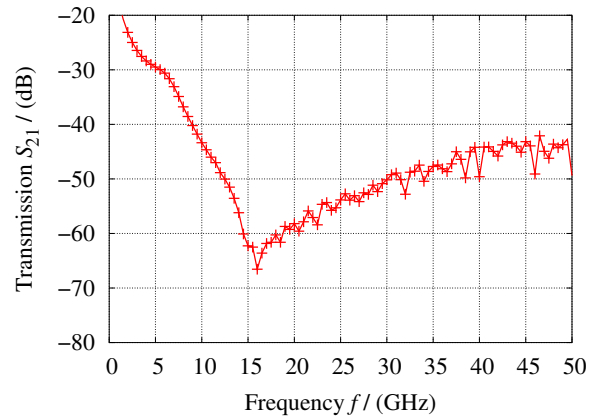


Fig. 10. Measurement of the isolation between V_{CC} -port and $V_{CC,stage}$ -port provided by the filter

Fig. 11. The characterization is performed on-wafer, driving the single-ended clock-port by an external signal generator. The divided signal is detected by a spectrum analyzer. The reduced sensitivity to lower frequencies is caused by the limited slew rate of the sinusoidal input signal. A square wave signal should be applied to the input to determine the maximal operation bandwidth. The input sensitivity of the second stage is increased compared to the first stage operated at 12 GHz. By comparing the self-oscillation frequency and the input sensitivity of the first stage alone and the complete 16:1 divider, a shift of both to higher values can be observed. Both shifts are induced by changed load conditions of the first divider. Within the 16:1 frequency divider the first stage is differentially loaded by the bases of the minimal sized switching transistors of the second stage through a DC-block capacitor (100 fF). Within its separate test-structure, the output is loaded single-ended by the bonding pad parasitics and the 50 Ω measurement port. For the 16:1 static frequency divider, the input sensitivity is about -2 dBm at the design frequency of 24 GHz and the DC power consumption is 240 mW at 4 V supply voltage.

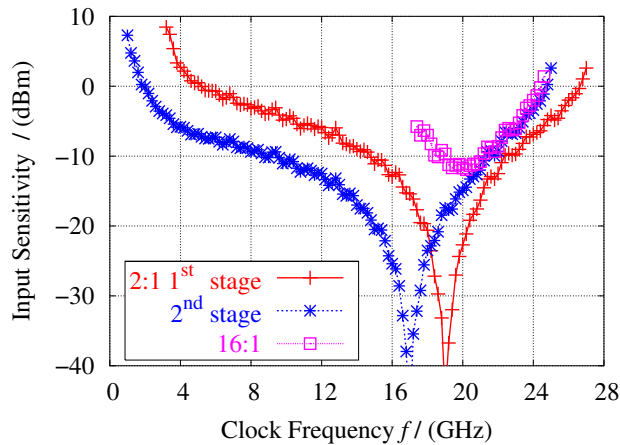


Fig. 11. Single-ended measured input sensitivities of the first stage, second stage and the complete 16:1 static divider

V. CONCLUSION

In this paper, we have presented a 16:1 static frequency divider designed for 24 GHz automotive radar applications. The circuit is using an innovative sensitivity matching concept between the first and the second stage to avoid to use a buffer amplifier and therefore, reduces DC consumption. The circuit operates up to 25 GHz and consumes 240 mW at 4 V supply voltage. The size of the circuit, with its pads, is $870 \times 340 \mu\text{m}^2$

ACKNOWLEDGMENT

The 16:1 static frequency divider realization was supported by the European Commission by the means of the IST project ARTEMIS. The authors wish also to thank Atmel GmbH for their support.

REFERENCES

- [1] A. Schüppen, J. Berntgen, P. Maier, M. Tortschanoff, W. Kraus and M. Averweg "An 80 GHz SiGe Production Technology", III-V Review, Vol. 14, pp 42-46, August 2001.
- [2] H. Knapp, M. Wurzer, T. F. Meister, J. Böck, K. Aufinger, S. Boguth, H. Schäfer "86 GHz Static and 110 GHz Dynamic Frequency Dividers in SiGe Bipolar Technology", Proc. International Microwave Symposium (IMS), Philadelphia, Pennsylvania, USA, pp 1067-1070, June 2003.
- [3] K. Ishii, H. Ichino, M. Togashi, Y. Kobayashi, and C. Yamaguchi "Very-High-Speed Si Bipolar Static Frequency Dividers with New T-Type Flip-Flops", IEEE Journal of Solid-State Circuits, Vol. 30, pp 19-24, January 1995.
- [4] A. Felder, M. Moller, J. Popp, J. Bock, and H.-M. Rein "46 Gb/s DEMUX, 50 Gb/s MUX, and 30 GHz static Frequency Divider in Silicon Bipolar Technology", IEEE Journal of Solid-State Circuits, Vol. 31, pp 481-486, April 1996.
- [5] M. Wurzer, T.F. Meister, H. Schäfer, H. Knapp, J. Böck, R. Stendl, K. Aufinger, M. Franosch, M. Rest, M. Möller, H.-M. Rein, and A. Felder "42GHz Static Frequency Divider in a Si/SiGe Bipolar Technology", Proc. International Solid-State Circuits Conference (ISSCC), IEEE, pp 122-123, 1997.
- [6] K. Ishii, H. Ichino, C. Yamaguchi "Maximum operating frequency in Si bipolar master-slave toggle flip-flop circuit", IEEE Journal of Solid-State Circuits, IEEE, Vol. 29, pp 754-760, July 1994.

Bias Dependent Boolean Multivalued Logic Application of Resonant Tunneling Bipolar Transistors

A. Matiss, J. Driesen, S. Ehrich, W. Prost, F.-J. Tegude

Department of Solid State Electronics, University Duisburg-Essen
Lotharstrasse 55 (ZHO), D-47057 Duisburg, Germany
matiss@hlt.uni-duisburg.de

Abstract — Resonant tunneling diodes (RTD) are well suited for future digital circuit components. Their negative differential resistance (NDR) allows to reduce the logic depth and the number of devices required for logic circuits. The resonant tunneling bipolar transistor (RTBT) is a concept that exploits the NDR-property of the RTD and the functionality of a single heterostructure bipolar transistor (SHBT). The nonlinear behavior allows the realization of up to six different Boolean functions by using a single device only. The diversity of the Boolean functions is based on the DC offset of the input voltage applied to the RTBT.

an AIX200-system with rf-heating at $p_{\text{tot}} = 50$ mbar reactor pressure using N_2 carrier gas. A non-gaseous-sources (ngs-) configuration is used based on TBAs/TBP/TMAAs as group-V, DitBuSi/CBr₄ as group-IV n-/p-type dopant sources, and the metalorganics TMIIn/TEGa. [7].

I. INTRODUCTION

III-V semiconductor devices have distinct advantages concerning very high frequency digital and analog applications, e.g. the high carrier mobility and the compatibility to widely used optical wavelengths for combined optical and electronic applications.

The Resonant Tunneling Diode (RTD) has demonstrated high potential regarding high speed, multiple-valued digital applications [1,3]. This device allows to build up rather complex digital gates with quite a small number of elements, and therefore with a minimum of space on the die [6].

Well known RTD circuits are the MOBILE (Monostable Bistable Transition Logic Element) structures where at least two RTDs are combined, together with switching elements like HFET, MODFET or HBT devices [5]. The combination of switching transistors and RTD results in monolithically integrated devices, where the transistor and the RTD have been merged into a new device. One of these results is the Resonant Tunneling Bipolar Transistor, RTBT [2].

The investigations described in the subsequent sections concern the modeling and measurement of the most simple gate circuit possible with these devices. Especially the bias dependent gate functionality is demonstrated and the DC and RF model of the device is validated by comparing not only single device characteristics but also time domain gate measurements with corresponding simulations.

II. DEVICE TECHNOLOGY

Basically the RTBT consists of a HBT with a RTD incorporated in the HBT emitter. We started the fabrication of the demonstrator circuits with the growth of the RTD/SHBT layer stack by metal-organic vapor phase epitaxy (MOVPE). The experiments were done on (001)±0.5° orientated s.i. InP:Fe epi-ready substrates in

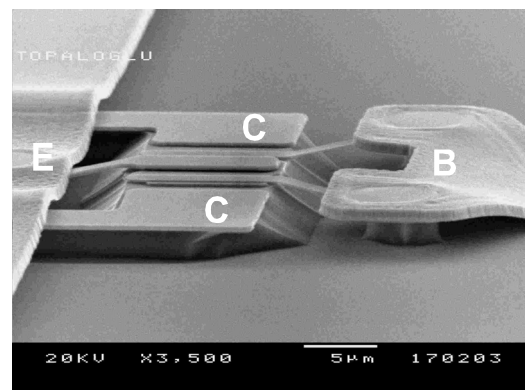


Fig. 1: SEM image of RTBT

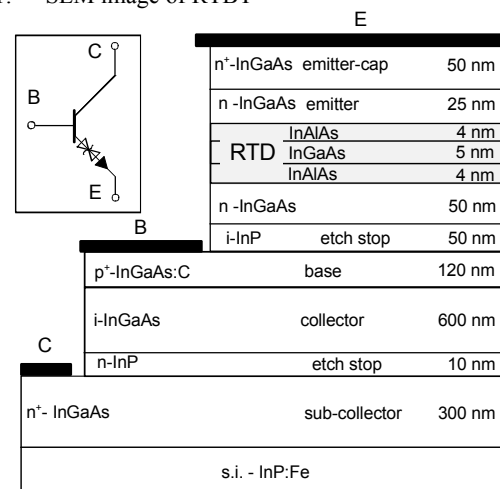


Fig. 2: Layer system of the used RTBT

A mesa technology is applied using wet chemical etching. Non-alloyed ohmic contacts are realized with Ti/Au metallizations for emitter and collector and Pt/Ti/Pt/Au for the base. To reduce parasitic capacitances the contacts of the devices are placed on extra mesas connected to the inner devices via underetched airbridges. Further details on RTD/HBT processing are described by W. Otten et al. [4].

III. DEVICE CHARACTERIZATION

All measurements have been performed using an on-wafer measurement setup. First of all, the Single

Heterojunction Bipolartransistor has been characterized by measuring the DC and RF characteristics. The standard I-V-curves (output characteristics, Gummel plots, diodes and more) have been used to extract the bulk resistances, saturation currents, ideality factors and current gains.

For the RTBT, the additional RTD characteristic in the BE diode has to be taken into account. This results in a negative differential resistance regime in the output characteristics as shown in Fig. 3. Therefore, V_{BE} voltages in excess of 1.3 V have to be applied to extract the R_E bulk resistance. In order to analyze the specific properties of the RTBT, separate SHBT and RTD as reference structures have been realized.

The figures of merit for high frequency performance are the transit frequency f_T and the maximum frequency of oscillation f_{max} . These values are $f_T = 70$ GHz and $f_{max} = 83$ GHz in case of the SHBT at $V_{CE} = 1.8$ V and $I_B = 250$ μ A, and $f_T = 45$ GHz and $f_{max} = 40$ GHz for the RTBT at the same bias conditions.

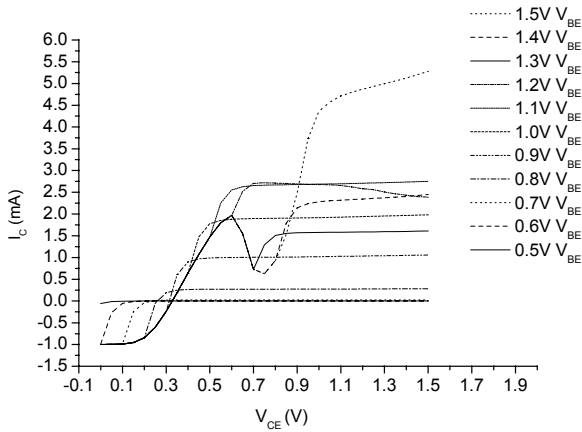


Fig. 3: Measured V_{BE} -controlled output-characteristic of one RTBT showing the envelope of the RTD-I/V characteristic

IV. RTBT-MODELING

The RTBT model used in this investigation is a series connection of the SHBT model and the additional RTD model in the emitter. Furthermore, parasitic elements have been added. The complete model is shown in fig. 4.

For the HBT the standard Gummel-Poon model is used. The equivalent circuit describing the RTD is given in fig. 5. The mathematical description of the voltage controlled current source is based on five currents, each switched on and off in the specific regions of the I-V curves using the tanh function. The parameters are all fitted to the measured curves.

$$I_{RTD}(U_{RTD}) = F \cdot (i_{peak} \cdot I_p(U_{RTD}) + r_p(U_{RTD}) - I_n(U_{RTD}) - r_n(U_{RTD}) + i_{therm} \cdot idt(U_{RTD}))$$

$$I_p(U_{RTD}) = \frac{1}{2} \cdot \exp\left(\frac{-(U_{RTD} - U_{resp})^2}{W_{rl}^2}\right) \cdot (1 - \tanh(10(U_{RTD} - U_{resp})))$$

$$r_p(U_{RTD}) = \frac{1}{2} \cdot \exp\left(\frac{-(U_{RTD} - U_{resp})^2}{W_{rr}^2}\right) \cdot (1 - \tanh(10(U_{RTD} - U_{resp})))$$

$$I_n(U_{RTD}) = \frac{1}{2} \cdot \exp\left(\frac{-(-U_{RTD} + U_{resn})^2}{W_{rn}^2}\right) \cdot (1 - \tanh(10(-U_{RTD} + U_{resn})))$$

$$r_n(U_{RTD}) = \frac{1}{2} \cdot \exp\left(\frac{-(-U_{RTD} + U_{resn})^2}{W_{rn}^2}\right) \cdot (1 + \tanh(10(-U_{RTD} + U_{resn})))$$

$$idt(U_{RTD}) = \exp(de \cdot U_{RTD}) - \exp(-de \cdot U_{RTD})$$

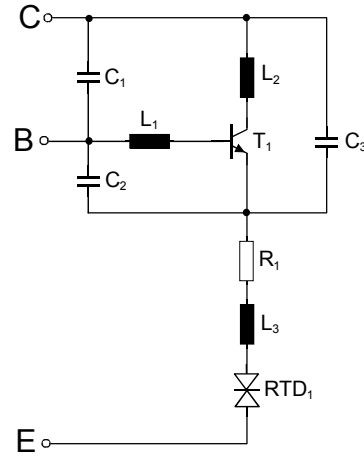


Fig. 4: Equivalent circuit of the RTBT consisting of the rf-environment (C_1 , C_2 , C_3 , L_1 , L_2 , and L_3) the transistor T_1 and the RTD

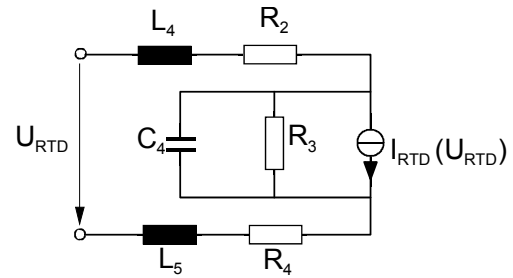


Fig. 5: Equivalent circuit of the RTD consisting of the rf-environment (L_4 , L_5 , C_4 , R_2 , R_3 and R_4) and the voltage controlled current-source I_{RTD}

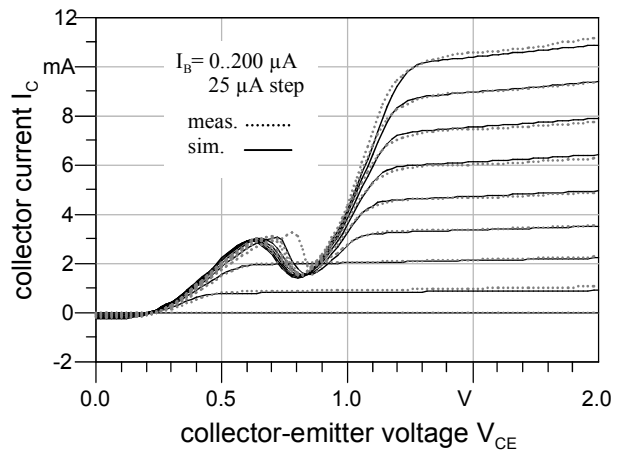


Fig. 6: Simulated and measured common emitter output characteristic.

Good agreement between measured and modeled data in case of the common emitter output characteristics is achieved, as well as acceptable agreement for the RF behavior, represented by the s-parameters near "peak-current" (fig. 7) and well above the NDR regime (fig. 8).

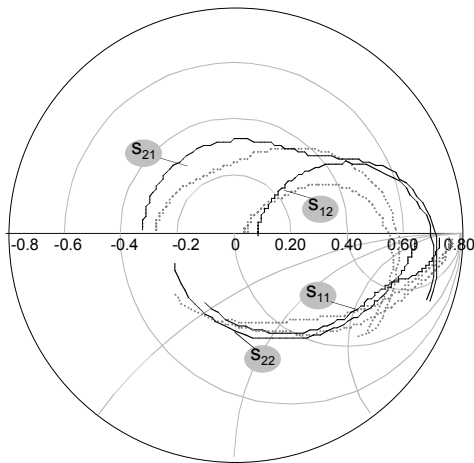


Fig. 7: Measured (dotted) and modeled (solid) s-parameters at $V_{CE} = 0.6V$ and $I_B = 50\mu A$, at the peak current.

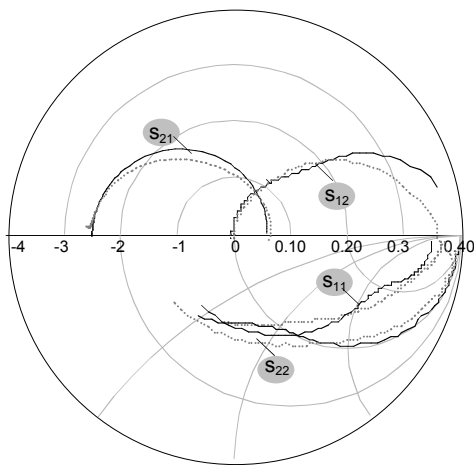


Fig. 8: Measured (dotted) and modeled (solid) s-parameters at $V_{CE} = 1.8V$ and $I_B = 250\mu A$, above the NDR regime.

MULTIFUNCTIONAL BOOLEAN LOGIC

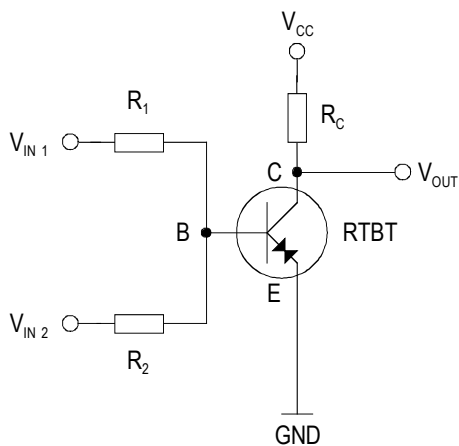


Fig. 9 Schematic circuit of the multivalued logic gate

The RTBT forms a the multiple valued logic gate with a resistive network R_1 , R_2 and a load resistor R_C . Two binary inputs with equal high/low voltages allow the realization of up to three different voltage levels at the base terminal of the RTBT. This results in up to six different logic functions if both inputs are driven with equal signal levels. The load resistor defines the output

signal levels. The V_{CC} bias voltage adjusts the output offset level.

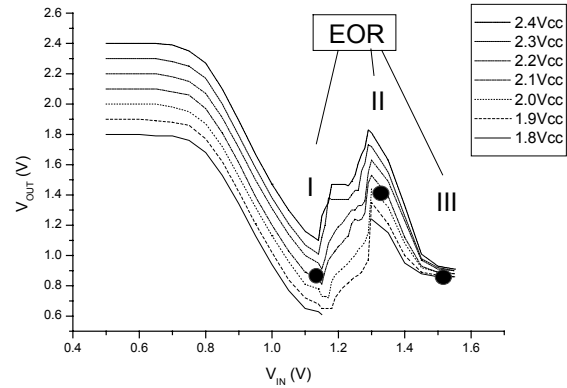


Fig. 10 Transfer characteristic of the gate for different bias voltages V_{CC} (EOR operation points are marked)

The gate transfer characteristic can be adjusted by V_{CC} to achieve a sufficient output voltage level necessary to drive a next stage in a logic circuit.

The logic function is set by an offset voltage additional to the signal voltage amplitude of the two input terminals. V_{CC} has to be adjusted to exploit the negative differential region of the RTD. For $V_{CC} > 1.8V$ the NDR property is valid. Above this level six logical functions can be realized (Fig. 10, Tab. 1). By choosing the proper bias voltage V_{CC} and load resistor R_C the output voltage V_{out} will maintain the same voltage level for two different input voltages (e.g. I and III; see. Fig. 10). These operation points are usually located around the peak (I) or valley (II) currents of the RTD and four logic functions can be realized (NAND, NOR, EOR, ENOR). Two more functions have an operation point in the negative resistance region to achieve a constant output voltage for two input voltages. These are the AND and the OR function.

V. MEASUREMENT SETUP

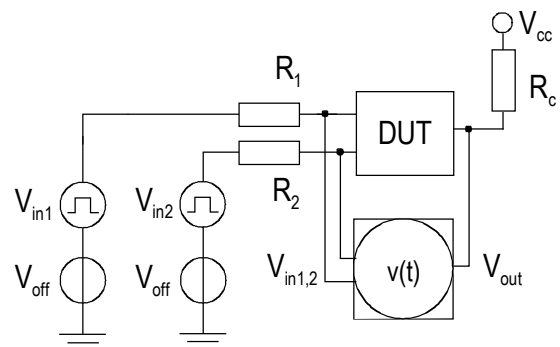


Fig. 11 Measurement setup for the verification of logical functions with a single resonant tunneling bipolar transistor

For the verification of the logic functions the measurement setup presented in fig.11 is used. To perform measurements on devices without any buffer stages, a low-frequency real-time oscilloscope (DC to 500MHz) with an input impedance of $1 M\Omega$ has been employed to record the input and output voltages. To provide the proper input voltages, a 3.35 GHz pulse/square generator with two outputs is connected to

an on-wafer resistance network. One channel is phase shifted by 90° to provide all possible combinations of the two input signal during one period. The resistance network R_1 and R_2 consists of two 100Ω resistors as shown in fig. 11. A Microwave probe station provides a coaxial to co-planar conversion to create a connection to the input and output of the RTBT-circuit on the wafer. An additional third probe applies the bias V_{CC} to the load resistance R_C in the collector branch. The recorded signals are the output signals of the generator, which shows the two resulting phase-shifted signals, and the output voltage at the collector. The frequency range was limited by the circuit-design and also by the oscilloscope bandwidth, so measurements have been performed up to 150 MHz source frequency. The different measurements are made by only adjusting the input voltage levels and offsets to fit the requirements of the respective logic function. The bias voltage as well as the resistances are kept constant ($R_C = 100\Omega$, $R_{1,2} = 100\Omega$, $V_{CC} = 2.1$ V).

VI. MEASUREMENT RESULTS

This section presents the measurement results with a detailed table of all Boolean functions verified with the previously described circuitry.

Function	$V_{in,2}$		V_{out}		
	(L)ow	(H)igh	$V_{in1,L}=V_{in2,L}$	$V_{in1} \neq V_{in2}$	$V_{in1,H}=V_{in2,H}$
NAND	0.3V	1.1V	H (2.1V)	H (2.1V)	L (1.2V)
NOR	0.7V	1.5V	H (1.9V)	L (1.0V)	L (1.0V)
EOR	1.1V	1.5V	L (0.95V)	H (1.4V)	L (0.95V)
ENOR	0.9V	1.3V	H (1.3V)	L (1.0V)	H (1.3V)
AND	1.03V	1.33V	L (1.1V)	L (1.1V)	H (1.4V)
OR	1.1V	1.4V	L (0.95V)	H (1.2V)	H (1.2V)

Tab. 1 Boolean operation voltages of input and output for different functions. ($R_C=100$ Ohm, $R_{1,2}=100$ Ohm, $V_{CC}=2.1$ V)

The functions have been verified for different bias conditions (Tab. 1). Two of the six time-domain signals are shown in fig. 12 and 13 demonstrating the two functions AND and EOR.

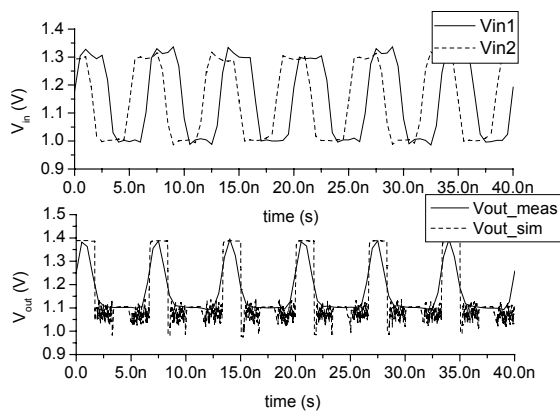


Fig. 12 Comparison of simulated and measured results for the AND-function

In the simulation, the AND function shows oscillating behavior in the NDR operation point as observed in fig. 12. The oscillation could not be observed during the

measurement due to the limited bandwidth of the oscilloscope of 500 MHz. Therefore the output voltage appears to be constant for the low-level within the measurement range. A good agreement for the EOR function between the simulated results and the measurement results is presented in fig. 13. Small variations between the simulated and measured plots are partly due to the limited amount of obtained measurement points which do not allow a good interpolation of the real waveform at the investigated frequency.

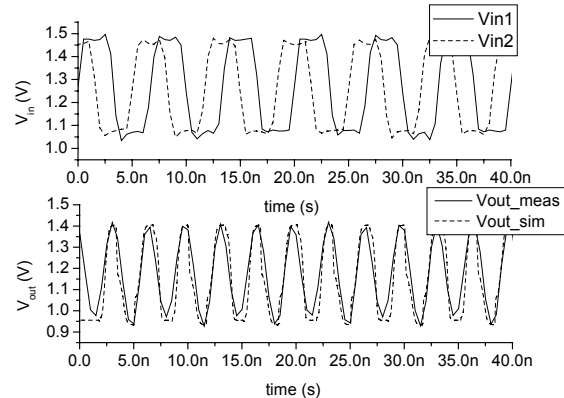


Fig. 13 Simulated and measured results of the EOR function

VII. CONCLUSION

The combination of the resonant tunneling diode in the emitter branch of a heterostructure bipolar transistor yields advantages in device count per function for future logic design. Based on Boolean input and output logic, six different logic function have been verified using a single device and only adjusting the DC-bias voltages, which makes them suitable for digital applications.

REFERENCES

- [1] P. Mazumder, S. Kulkarni, M. Bhattacharya, J. Ping Sun, G. I. Haddad: *Digital Circuit Applications of Resonant Tunneling Devices*, Proceedings of the IEEE, VOL. 86, NO. 4, April 1998
- [2] F. Capasso, et Al.: *Quantum Functional Devices: Resonant-Tunneling Transistors, Circuits with Reduced Complexity, and Multiple-Valued Logic*, IEEE Transactions on Electron Devices, VOL. 36, NO. 10, October 1989
- [3] H. I. Chan, S. Mohan, P. Mazumder, G. I. Haddad: *Compact Multiple-Valued Multiplexers Using Negative Differential Resistance Devices*, IEEE Journal of Solid-State Circuits, VOL. 31, NO. 8, August 1996
- [4] W. Otten, P. Glösekötter, P. Velling, A. Brennemann, W. Prost, K.F. Gosser, F.J. Tegude: *InP-based monolithically integrated RTD/HBT MOBILE for logic circuits*, Proc. 13th InP & Related Materials Conf., pp. 232-235, 2001.
- [5] S. Choi, B. Lee, T. Kim and K. Yang: *CML-type Monostable Bistable logic element (MOBILE) using InP-based monolithic RTD/HBT technology*, Electronic Letters, VOL. 40, NO. 13, 24th June 2004
- [6] C.H. Lin, K. Yang, et Al.: *Monolithically Integrated InP-based Minority Logic Gate Using an RTD/HBT Heterostructure*, 10th Intern. Conf. On Indium Phosphide and Related Materials, 11-15 May, 1998, Tsukuba, Japan
- [7] P. Velling, M. Agethen, W. Prost, F.J. Tegude: *InAlAs/InGaAs/InP Heterostructures for RTD and HBT Device Applications Grown by LP-MOVPE Using Non-Gaseous Sources*, Journal of Crystal Growth, Japan, June 2000, pp. 722-729

PERFORMANCE ESTIMATE FOR HIGH-SPEED CMOS-CURRENT-MODE-LOGIC CIRCUITS BASED ON OUTPUT VOLTAGE SWING CONSIDERATIONS

Niels Christoffers, Renee Lerch, Bedrich J. Hosticka, Stephan Kolnsberg, Rainer Kokozinski

Fraunhofer Institute for Microelectronic Circuits and Systems
Finkenstraße 61
47058 Duisburg, Germany
niels.christoffers@ims.fhg.de

ABSTRACT

Current-mode-logic circuits play an important role in the design of CMOS frequency synthesizers for modern wireless digital communication systems. They provide the building blocks for frequency dividers with input frequencies in the range of the desired carrier frequencies. In this communication we estimate the upper limit frequency as a function of the gate length using voltage swing considerations.

1. INTRODUCTION

High-speed digital circuitry, i.e. gates and flipflops, plays a substantial role in PLL-based frequency synthesizers used in modern wireless digital communication systems. The output frequency f_{out} of the synthesizer shown in Figure 1 is generated by a VCO that is exposed to strong component value variations. It is required to be a known multiple M of the accurate reference frequency f_{ref} produced by a crystal oscillator and therefore has to be controlled using negative feedback. A frequency divider is employed to obtain a signal the frequency $f_d = f_{out}/M$ of which can be compared with the reference frequency by means of a Phase- and Frequency Detector (PFD) that produces a corrective signal for the VCO via charge pump and loop filter. [3]

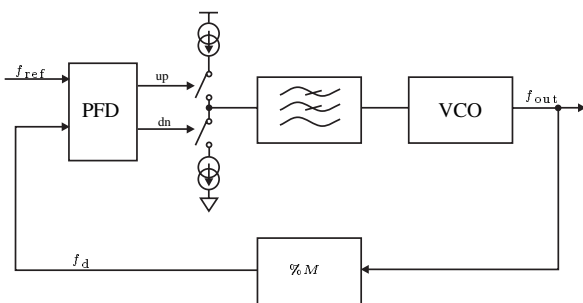


Figure 1: Block level schematic of a frequency synthesizer

The divider is a digital counter. It has to be designed for a bandwidth at least as high as the output frequency of the synthesizer. Current-mode-logic (CML) building-blocks [5] are often proposed as solution to meet such requirements using easily available and cost-saving CMOS processes [1, 4].

In this communication we present several insights into the design of current-mode flipflops and gates. Using a simplified formula for the drain current of short channel MOSFETS presented in [6], a simplified definition of delay and considerations of the necessary DC-gain we establish fundamental limitations for the output voltage swing of CML building blocks and relate it to the minimum gate length of the employed transistors. We show that for low VCO frequencies the current drawn from the supply is proportional to the square of the frequency and the cube of the gate length, but can increase faster for sufficiently high frequencies.

In Section 2 we present the block level schematic of a prescaler used in a frequency divider of a synthesizer and compute the delay requirements of the employed gates. In Section 3 the circuits realizing high-speed gates and flipflops are presented. Their design, especially the necessary output voltage swing, is discussed in Section 4: The results allow prediction of available gain and delay of the flipflops and gates for a given technology. A summary is given in Section 5.

2. A PRESCALER USING CML BUILDING BLOCKS

One possible block level schematic for a frequency divider is given in Figure 2[1]. The depicted divider comprises a prescaler that divides by $N + 1$ or N , depending on whether MC is high or low, a program counter with modulus P , and the swallow counter that will output an overflow indication to MC after S input impulses and afterwards stop operation until it is restarted by a reset impulse from the program

counter. The complete circuit generates a division

$$M = PN + S. \quad (1)$$

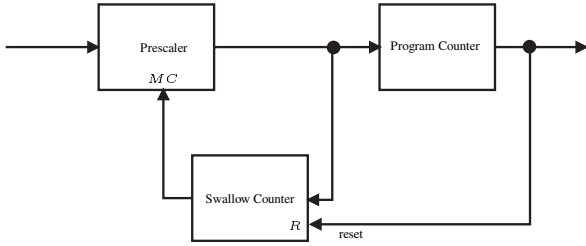


Figure 2: Block level schematic of a frequency divider

The building block with the highest input frequency $f_{CLK} = f_{out}$ is the prescaler. The schematic of it in case of $N = 15$ is given in Figure 3. Consider a situation when the output state of the flipflops is $(Q_1, Q_2, Q_3, Q_4) = (0, 1, 0, 1)$ and MC is low. A rising edge of the clock causes Q_3 to go low after the delay $\tau_{FF2} + \tau_{FF3}$ of FF_2 and FF_3 . Now, the information that both \bar{Q}_3 and \bar{Q}_4 are low propagates through the gates G_1, G_2 , and G_3 with their delays τ_{G1}, τ_{G2} , and τ_{G3} , respectively, to the input of FF_2 . It has to arrive before the next rising edge triggers the prescaler to compute the next state based on the inputs of the flipflops. If not

$$\tau_{FF2} + \tau_{FF3} + \tau_{G1} + \tau_{G2} + \tau_{G3} < \frac{1}{f_{CLK}} \quad (2)$$

the circuit will malfunction [1].

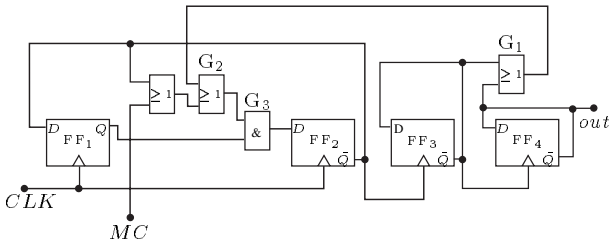


Figure 3: Block level schematic of the prescaler within the divider

3. CML LATCHES AND GATES

The schematic of a current-mode-logic latch is given in Figure 4. It contains a differential pair M_4/M_5 and a pair of cross coupled MOSFETS M_6/M_7 . If the clock input is high

current flows through the first while the latter is off. The output is directly controlled by the input. A falling edge of the clock turns the differential pair off and lets I_{BIAS} flow through the cross coupled pair. Having two stable states, namely $I_6 = I_{BIAS}$ and $I_7 = 0$ or $I_6 = 0$ and $I_7 = I_{BIAS}$ it holds the output of the latch in that state observed in the immediate instant before the transition of the clock. A flipflop is realized using two latches in a master-slave configuration.

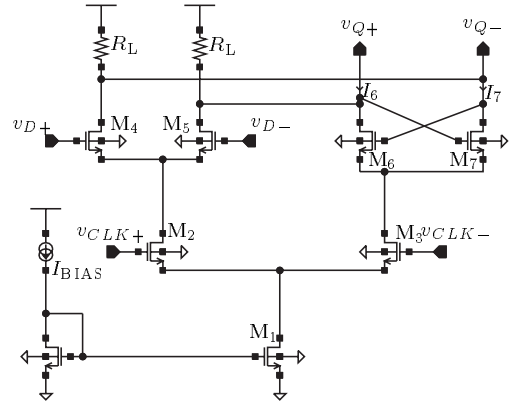


Figure 4: Current-Mode Latch.

The current-mode-gate depicted in Figure 5 realizes the AND-function. However, since inverters can easily be realized by interchanging the two lines of a differential signal path it can act as an OR- NAND- or NOR-gate as well if the DeMorgan-rules are exploited.

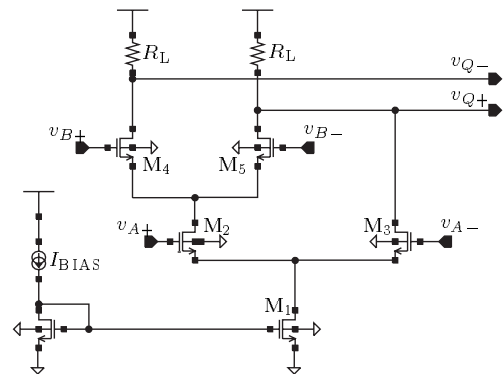


Figure 5: Current-Mode Gate

4. DESIGN CONSTRAINTS FOR CML-CIRCUITS

In order to rate CML-circuits in terms of their high-frequency behaviour we first estimate the delay through the input differential pair of either latch or gate to be

$$\tau \approx R_L C_L = \frac{\hat{v}}{I_{\text{BIAS}}} C_L, \quad (3)$$

where C_L is the total capacitance connected to one of the two differential output nodes and \hat{v} the single ended output voltage swing. Assuming n identical input stages are connected we obtain

$$\tau = n\tau_0, \quad (4)$$

where $\tau_0 = R_L C_{\text{ox}} W L$, C_{ox} is the specific oxide capacitance, and W and L are the width and the length of the input transistors, respectively. Note that according to (2) τ_0 must be inversely proportional to the input frequency f_{CLK} .

During the design of CML building blocks a proper setting of the output voltage swing \hat{v} is indispensable for two reasons discussed in the following.

Note that the transistor M_1 in both latch and gate must be kept in saturation. Therefore the voltage drop across the load resistance and the transistor pairs M_2/M_3 , M_4/M_5 in latch and gate and additionally across M_6/M_7 in the latch is limited. We assume that an upper bound for the voltage drop across the transistors is defined:

$$I_{\text{BIAS}} R_{\text{ON},M_x} < V_{\text{ON},\text{max}} \quad (5)$$

where R_{ON,M_x} is the ON-resistance of a transistor M_x . If this requirement is met for $M_4/M_5/M_6/M_7$ it is met for M_2/M_3 , too, since their gate source voltage in ON-state is higher and hence their ON-resistance lower.

The ON-resistance of the transistors M_4 and M_5 is [2]

$$R_{\text{ON}} = \frac{L}{W} \frac{1}{\mu_e C_{\text{ox}} (V_{\text{DD}} - \hat{v} - R_{\text{ON}} I_{\text{BIAS}} - V_{\text{T}})} \quad (6)$$

where $\mu_e \approx 0.04 \text{m}^2/(\text{vs})$ is the electron mobility. We can find an upper bound for the output voltage swing multiplying (6) by I_{BIAS} , solving for $I_{\text{BIAS}} R_{\text{ON}}$ and afterwards solving (5) for \hat{v} . We obtain:

$$\hat{v} < \mu_e \frac{V_{\text{ON},\text{max}} (V_{\text{DD}} - V_{\text{T}} - V_{\text{ON},\text{max}})}{L^2/\tau_0 + \mu_e V_{\text{ON},\text{max}}} \quad (7)$$

The upper bound for the voltage swing is nearly independent of τ_0 for very high delays. However, it will fall linearly when τ_0 is much smaller than $L^2/(\mu_e V_{\text{ON},\text{max}})$

To establish a lower bound for the output voltage swing we observe the output signal of a differential pair after a change of the input voltage from $-\hat{v}$ to $+\hat{v}$. After the subsequent settling process has finished we require the output

voltage to be identical to the input voltage. However, it cannot be higher than the input voltage times the DC-gain of the differential pair. We demand

$$A_{\text{DC}} = g_m R_L > A_{\text{min}} > 1 \quad (8)$$

The transconductance of the MOSFETs in the differential pair can be expressed in terms of the current using a simplified formula for the drain current in short channel MOSFETS proposed in [6]:

$$I_{\text{D}} \approx \frac{\mu_e C_{\text{ox}} W}{2} \frac{(V_{\text{GS}} - V_{\text{T}})^2 L E_{\text{sat}}}{V_{\text{GS}} - V_{\text{T}} + L E_{\text{sat}}} \quad (9)$$

where $E_{\text{sat}} \approx 4 \cdot 10^6 \text{V/m}$ is the field strength for velocity saturation. Solving (9) for $V_{\text{GS}} - V_{\text{T}}$ and computing the derivative $\partial V_{\text{GS}}/\partial I_{\text{D}}$ we find

$$\frac{1}{g_m} = \frac{1}{\mu_e C_{\text{ox}} W E_{\text{sat}}} + \frac{I_{\text{D}} / (\mu_e C_{\text{ox}} E_{\text{sat}})^2 + L / (W \mu C_{\text{ox}})}{\sqrt{I_{\text{D}}^2 / (\mu_e C_{\text{ox}} E_{\text{sat}})^2 + 2 I_{\text{D}} L / (W \mu C_{\text{ox}})}} \quad (10)$$

Substituting the delay, the load capacitance, the output voltage swing we require from (8)

$$\hat{v} > 2\mu\tau_0 E_{\text{sat}}^2 \cdot \left(-1 + \sqrt{1 + \frac{A_{\text{min}}^2 L^2}{\mu_e \tau_0 E_{\text{sat}} (\mu_e \tau_0 E_{\text{sat}} - 2 A_{\text{min}} L)}} \right) \quad (11)$$

Using a the Taylor series based approximation $\sqrt{1+x} \approx 1+x/2$ we find that for long delays τ_0 the voltage swing \hat{v} is inversely proportional with τ_0 and grows linearly with L^2 . The minimum current $I_{\text{BIAS}} = \hat{v} C_L / \tau_0$ therefore grows with the square of the input frequency f_{CLK} and with the cube of the gate length L if the transistor width W remains unchanged. If τ_0 approaches $2A_{\text{min}}L/(\mu_e E_{\text{sat}})$ the output swing and the current theoretically even become infinite. For that reason a decrease of the gate length L has a tremendous impact on the power consumption of CML frequency dividers for high input frequencies.

Still, the question of the necessary DC-gain remains to be answered: One typical output signal of the positive output node of FF₃ obtained by circuit simulations for an input frequency of 1.5GHz is depicted in Figure 6. The disturbances highlighted by circles stem from the fact that the output signal of FF₂ has no perfect rectangular shape. Therefore, during its transitions with finite slope the current I_{BIAS} is shared by the differential pair M_4/M_5 and the cross coupled pair M_6/M_7 so that both possess less than I_{BIAS} . The total gain from the input to the output therefore drops and causes the output to decrease. To prevent the output from reaching the trip point between High and Low a sufficient margin must be added to the DC-gain. From simulations we

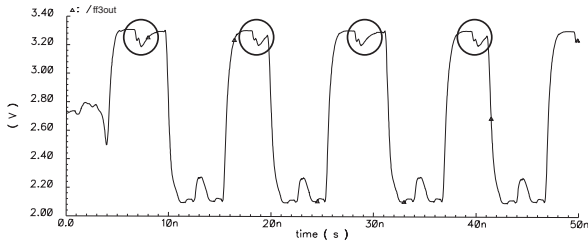


Figure 6: Output signal at the positive node of FF₃ (from simulations)

infer that $A_{DC} \approx 3$ allows robust operation of the circuits. However, it should be increased if disturbances are expected in addition to that discussed above.

Having established an upper and lower bound for the output voltage swing of current-mode latches and gates we are now in the position to determine the minimum delay given the gate length and the necessary DC-gain. For sufficiently low τ_0 it is impossible to find \hat{u} in such a way that both requirements (7) and (11) are met. In Figure 7 the maximum available DC-gain is displayed versus $1/\tau_0$ for a maximum voltage drop $V_{ON,max} = 0.25 V$ and several gate lengths L . The higher the DC-gain the more robust to disturbances the circuits will be. We can see that for a transistor length $L = 0.6 \mu m$ and a minimum DC-gain of $A_{DC} = 3$ $1/\tau_0$ can be no higher than $13 \cdot 10^9/s$. For the prescaler we find the critical delay of (2) to be $7\tau_0$ if the delays of the single blocks are computed using (4). The maximum input frequency to the divider would therefore be in the vicinity of 1.7 GHz which is slightly higher than the maximum input frequency of the divider used for circuit simulations.

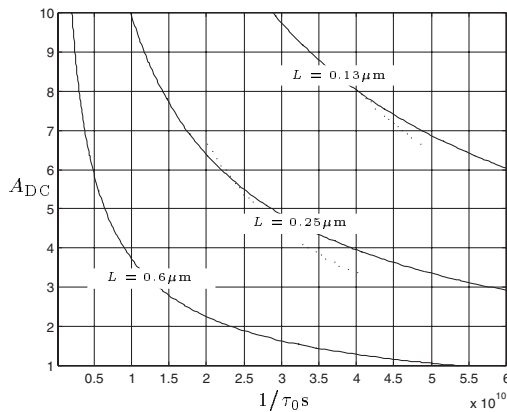


Figure 7: Maximum DC-gain versus inverse delay for different gate lengths.

5. SUMMARY

In the preceding sections we have provided insights into the design of frequency dividers using current-mode-logic with input frequencies in the vicinity of theoretical limits. These limits have been estimated by finding requirements for the output voltage swing as a function of the delay requirement for the gates and latches.

Simulations indicate that the performance estimates are very helpful at finding the maximum possible performance of a current-mode-logic circuit. However deviations must be accepted since the transconductances found by simulations are slightly (approximately 10%) lower than those predicted by (10). Also, the foregoing discussion neglects parasitic capacitances arising from the interconnects between the transistors and the resistors.

Nevertheless it has been shown that a lower and upper bound for the output voltage swing exist and approach each other for increasing frequencies. For sufficiently high frequencies the output voltage swing cannot meet both requirements. The current consumed by the circuits increases with the square rather than linearly with the frequency.

6. REFERENCES

- [1] Razavi B. *RF Microelectronics*. Prentice-Hall Inc., Upper Saddle River, 1st edition, 1997.
- [2] Allen P.E. Holberg D.R. *CMOS Analog Circuit Design*. Oxford University Press. Inc, New York, 1st edition, 1987.
- [3] Egan W. F. *Frequency Synthesis by Phase Lock*. John Wiley and Sons, INC., New York, Chichester, Brisbane, Toronto, 1. edition, 1981.
- [4] Craninckx J. Steyaert M. *Wireless CMOS Frequency Synthesizer Design*. Kluwer Academic Publishing, Boston, Dordrecht, London, 1. edition, 1998.
- [5] J. Musicer J.M. Rabaey. MOS Current Mode Logic for Low Power, Low Noise CORDIC Computation in Mixed-Signal Environment. In *Proc. ISLPED*, pages 102–107, 2000.
- [6] Lee T.H. *The Design of CMOS Radio-Frequency Integrated Circuits*. Cambridge University Press. Inc, New York, 1st edition, 1998.

Session 6b

Antenna Systems & Propagation

New Internal Beam-Forming Mirror System for a Multi-Frequency 1 MW F-Band Gyrotron

X.Yang¹, A.Arnold^{1,2}, E.Borie¹, G.Dammertz¹, O. Drumm²,

K.Koppenburg¹, O.Prinz^{1,2}, D.Wagner³, M.Thumm^{1,2}

¹ Forschungszentrum Karlsruhe, Association EURATOM-FZK, IHM, D-76021 Karlsruhe, Germany

² also Universitaet Karlsruhe, IHE, Kaiserstr. 12, D-76128 Karlsruhe, Germany

³ Max-Planck-Institut fuer Plasmaphysik, Association EURATOM-IPP, D-85748 Garching, Germany
e-mail: xiaokang.yang@ihm.fzk.de . Tel: (49) 07247-822455

Abstract — Due to the requirement of a newly designed ultra-broadband CVD-diamond window for a multi-frequency 1 MW F-Band gyrotron at Forschungszentrum Karlsruhe (FZK), the existing beam-forming mirror system inside the gyrotron tube has to be modified. This paper describes the design scheme for shaping the output beams from the launching antenna waveguide into the desired Gaussian profile by using adapted phase-correcting mirrors with non-quadratic surface contour function. Simulation results show these phase-correcting mirrors can be used for broadband operation of a frequency step-tunable gyrotron, which operates in nine modes from the TE_{17,6} mode at the frequency of 105 GHz to the TE_{23,8} mode at 143 GHz. Further calculations show that efficiencies of more than 94% have been achieved for converting the high-order cylindrical cavity modes into the usable fundamental Gaussian mode.

I. INTRODUCTION

In nuclear fusion devices, the availability of MW gyrotrons with fast frequency step tunability permits the use of a simple fixed, non-steerable mirror antenna for local electron cyclotron resonance heating and current drive at different magnetic fields, as well as gives more flexibility for the stabilization of neo-classical tearing modes (NTM) through the possibility of current drive without changing the magnetic field. For plasma stabilization in the ASDEX-Upgrade tokamak, there is great interest in step-tunable gyrotrons operating at frequencies between 105 GHz and 140 GHz [1]. For this purpose a multi-frequency test gyrotron is under construction at FZK in a cooperative parallel development with the Institute of Applied Physics in Nizhny Novgorod, Russia [2-5]. The complementary key tasks for FZK are: a cavity operating in wide range of magnetic fields and with proper choice of a set of operating modes with the same direction of rotation; a broadband quasi-optical mode converter transforming all operating modes into fundamental Gaussian beam with low diffraction losses; development of ultra-broadband CVD-diamond Brewster window; a low power measurement set-up.

Due to the large Brewster angle of 67.2°, the maximum effective window diameter for currently available CVD-diamond disks (140 mm diameter) is about 50 mm, and the length of the waveguide to house the disk is 149 mm

[6]. As shown in Fig.1, this window configuration adds a strict requirement for the gyrotron output beams with different frequencies. The central position of a Brewster window along the axis of the output beam should also be optimized to minimize the RF power screened by window aperture, this can be done by choosing optimal RF beam radii for the nine modes with low power reflections at the input and output of the waveguide. So the existing beam-forming mirror system has to be optimized to minimize the demand of the window aperture by optimizing the gyrotron output beam parameters. Intensive calculations have been done for this purpose in this paper.

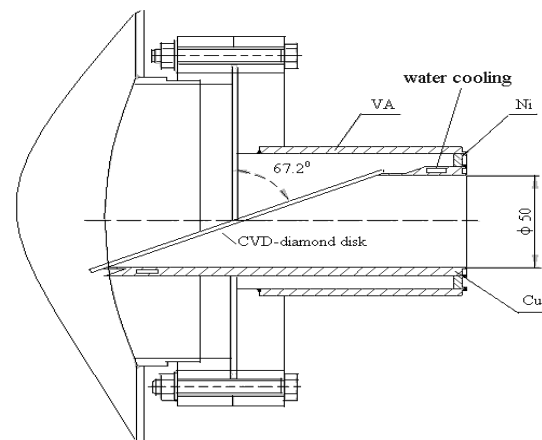


Fig. 1. Technical drawing of the CVD-diamond disk Brewster window.

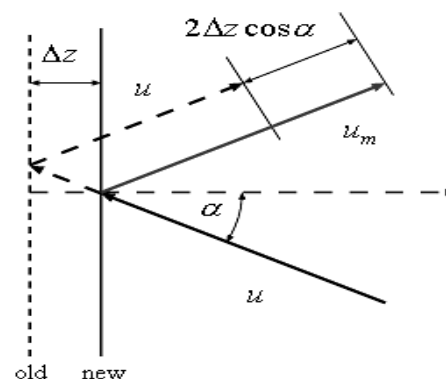


Fig. 2. Reflection of a plane wave at different planes.

II. DESIGN SCHEME OF THE PHASE-CORRECTING MIRRORS

The output beams from the launcher are directed by the beam-shaping mirror system in order to obtain the desired beam patterns, which are transmitted with low diffraction losses through the output window and which can be easily handled by the subsequent quasi-optical transmission line. For a frequency step-tunable high power gyrotron, this mirror system will also guide the RF beams with high efficiency and minimal frequency dependence through the gyrotron output window. The beam-shaping mirror system consists of three mirrors. The first mirror is a large quasi-elliptical one; it is used to focus the divergent beams radiating from the launcher. The second and third mirrors are adapted phase-correcting mirrors with a complicated non-quadratic shape function of the surface; they are designed to produce the desired beam on the gyrotron output window.

By means of the phase-correcting mirrors the RF beam is adjusted in its phase distribution to model the field. There are small altitude changes of the surface on these phase-forming adaptive mirrors, which modify the phase of the local plane wave and leave the amplitude of the reflected field at a plane mirror unchanged (see Fig.2). To obtain the phase corrected and adjusted field $u_m(\vec{r})$, the original incident beam field $u(\vec{r})$ at the mirror is multiplied by a phase term,

$$u_m(\vec{r}) = u(\vec{r}) e^{j2k_0 \Delta z(\vec{r}) \cos \alpha} \quad (1)$$

where k_0 is the wave number of free space, \vec{r} the position vector of the mirror surface, $\Delta z(\vec{r})$ the surface deformation of the mirror, and α the angle of the wave incidence or reflection.

With the help of Kirchhoff's diffraction integral evaluated over the reflected two-dimensional field distribution, the field on an arbitrary reference plane at z_0 can be obtained by:

$$u_r(\vec{r}_0) = 2 \int_{-\infty-\infty}^{\infty \infty} u_m(\vec{r}) \frac{\partial}{\partial z} g(\vec{r}_0 - \vec{r}) dA_0 \quad (2)$$

$$\text{Green's function: } g(\vec{r} - \vec{r}_0) = \frac{e^{-jk_0 |\vec{r}_0 - \vec{r}|}}{4\pi |\vec{r}_0 - \vec{r}|} \quad (3)$$

A numerical solution utilizes the Fast Fourier Transformation (FFT) [7]. With appropriate altitude changes $\Delta z(\vec{r})$ on the mirror, it is possible to obtain almost any reflected field distribution $u_r(\vec{r})$ on the reference plane.

After choosing a contour for a mirror surface, the evaluation has to compare the calculated field $u_r(\vec{r})$ with the desired field $u_d(\vec{r})$ on the reference plane, as shown in Fig 3. There are two evaluation criteria. The

first criterion is to decide about the agreement between the amplitude distributions of $u_r(\vec{r})$ and $u_d(\vec{r})$. For a single frequency, the following correlation can be used:

$$I^1(\Delta z) = \frac{\iint u_r \|u_d\| dA_0}{\sqrt{\iint |u_r|^2 dA \iint |u_d|^2 dA_0}} \quad (4)$$

The correlation I^1 varies between 0 and 1, and approaches the maximum value 1 if there is a good agreement between $u_r(\vec{r})$ and $u_d(\vec{r})$.

Another criterion is the integral over the squared error differences:

$$I^2(\Delta z, \theta) = \iint |u_r - u_d|^2 dA_0 \quad (5)$$

This criterion approaches a minimum value of 0 if both distributions are in good agreement. Here θ is the phase of the mirror surface.

Both criteria depend on the function Δz of the mirror contour. In addition, the criterion of the error differences compares the phase of both field distributions and therefore it depends also on the phase of the desired field.

III. DESIGN AND SIMULATION RESULTS

To match the requirement of the newly designed ultra-broadband CVD-diamond window, the optimal waist of the fundamental Gaussian beam on the gyrotron window is 10.7 mm. With this parameter, the optimized mirror surfaces of two phase-correcting mirrors can be determined by the methods described in Section 2.

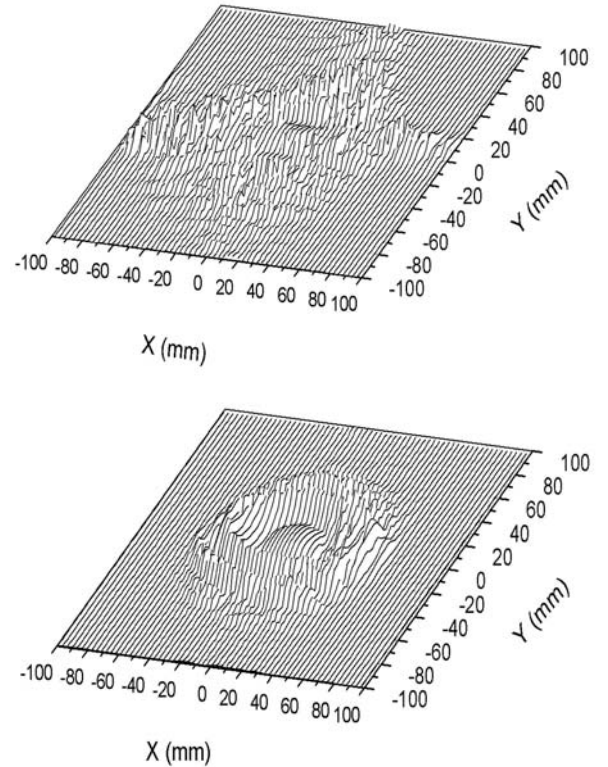


Fig. 3. Mirror surface of adapted phase-correcting mirror1 (upper) and phase-correcting mirror2 (lower).

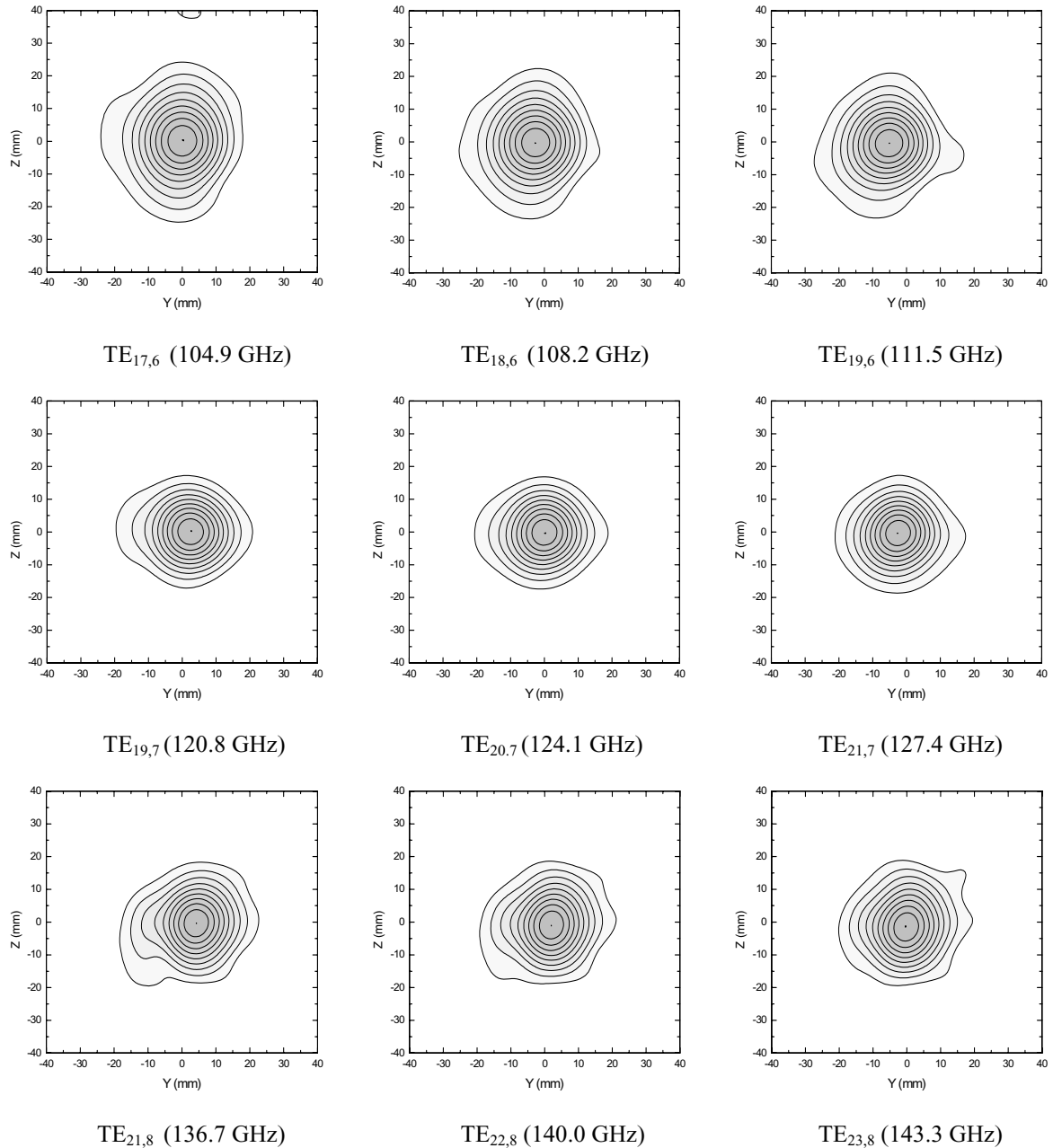


Fig. 4. Calculated power density distribution at the output window plane. Normalized power contours are shown in linear scale with 0.1 increments from the peak.

Fig.3 shows the calculated contour map of mirror surfaces for the first (upper) and the second (lower) phase-correcting mirror. Due to the limited space inside the gyrotron tube, the actual sizes of the designed phase-correcting mirrors are 200 mm × 140 mm for the first one, and 200 mm × 150 mm for the second one. Nevertheless, calculations show that there is no pronounced power loss on the first phase-correcting mirror.

Fig.4 shows the power density distribution at the gyrotron window plane for 9 operating modes from TE_{17,6} at 105 GHz to TE_{23,8} at 143 GHz. It is obvious that every mode has a nearly fundamental Gaussian distribution at the window. Meanwhile, due to the

different caustic radii, different modes have different angles of emission and thus different beam positions on the window plane; the beams shift by ±5 mm in horizontal direction around the center of the window plane (Fig.4).

Further calculations show that using the two optimized adapted phase-correcting mirrors, the quasi-optical mode converter has achieved efficiencies of 94%-98% for converting the high-order cylindrical cavity modes into the usable fundamental Gaussian mode. These two phase-correcting mirrors have been fabricated employing a numerically controlled milling machine at FZK.

IV. LOW POWER MEASUREMENT SET-UP

A broadband low power test facility [8] has been built to check the performance of the quasi-optical mode converter system, which includes a dimpled launcher and a beam-forming mirror system. The transmission measurement device consists of a home-made vector network analyser (VNWA), a broadband low power mode generator, the mode converter system as device under test, and a pick-up antenna to measure the E-field distribution in a defined linear polarization (horizontal or vertical) (Fig.5). The upper block shows the VNWA, which provides a phase lock loop (PLL) stabilized microwave signal within the whole D-band (110-170 GHz) at a power level of about 20 mW. The VNWA output signal feeds the broadband quasi-optical mode generator which excites the considered nine $TE_{m,n}$ modes. The pick-up antenna is fixed on a programmable 3-dimensional movable table in order to scan the distribution at an arbitrary position.

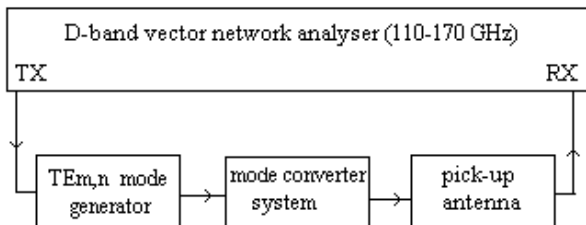


Fig. 5 Block diagram of the cold measurement set-up.

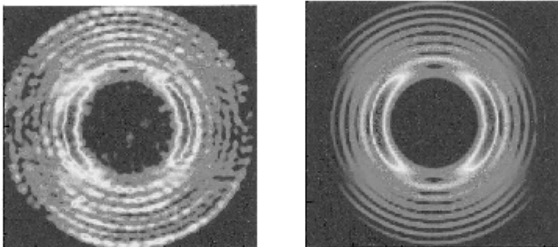


Fig. 6 Measured (left) and calculated (right) horizontal plane field distribution of the $TE_{22,8}$ mode excited at 140 GHz by the new mode generator. The total scale for vertical and horizontal axis is 60 mm for each picture.

First measurements of the output field pattern of the mode generator showed a very good performance at most of the gyrotron output frequencies; as shown in Fig. 6, more than 99% of the power in the right rotating direction has been achieved [9]. Since all operating modes of a step-tunable gyrotron have a similar structure, with their caustic radius being approximately half the cavity radius,

only one set of resonator and lenses are required. During the process of cold measurement, only a minor readjustment of the quasi-optical components is needed for generation of different modes.

Two identical beam-forming mirror systems have been manufactured at FZK. The purpose is to use a set of mirrors for cold measurement while the other set is installed inside the gyrotron. Cold measurements will be carried out soon to compare with theoretical predictions.

V. CONCLUSION

In order to match the requirement of a newly designed CVD-diamond disk Brewster window for a multi-frequency 1 MW F-band gyrotron, the existing beam-forming mirror system has been modified and designed. Simulation results show that the two phase-correcting mirrors can be used for broadband operation of the gyrotron from the $TE_{17,6}$ mode at 105 GHz to the $TE_{23,8}$ mode at 143.3 GHz; nearly fundamental Gaussian output beams have been obtained. Cold measurements will be carried out soon to verify the theoretical predictions.

REFERENCES

- [1] F. Leuterer, et al., "Plans for a new ECRH system at ASDEX-Upgrade", *Fusion Engineering and Design*, vol. 66-68, pp.537-542, 2003.
- [2] V. Zapevalov, et al., "Optimization of the frequency step tunable 105-170 GHz 1 MW gyrotron prototype," *Proc. 27th Int. Conf. on Infrared and Millimeter Waves*, San Diego, USA, 2002, pp.1-2.
- [3] V. Zapevalov, et al., "Development of a Prototype of a 1 MW 105-156 GHz Multifrequency gyrotron," *Radiophysics and Quantum Electronics*, vol. 47, pp.396-404, 2004.
- [4] E. Borie, et al., "Possibilities for Multifrequency Operation of a Gyrotron at FZK," *IEEE Trans. Plasma Science*, vol. 30, pp.828-835, 2002.
- [5] K. Koppenburg, et al., "Fast Frequency-Step-Tunable High-Power Gyrotron with Hybrid-Magnet-System", *IEEE Trans. Electron Devices*, vol. 48, pp.101-107, 2001.
- [6] X. Yang, et al., "Design of an Ultra-Broadband Single-Disk Output Window for a Frequency Step-tunable 1 MW Gyrotron," *23th Symposium on Fusion Technology (SOFT)*, Venice, Italy, September 20-24, 2004, B25.
- [7] G. Michel and M. Thumm, "Spectral domain techniques for field pattern analysis and synthesis," *Surveys on Mathematics for Industry*, vol.8, pp.259-270, Springer, 1999.
- [8] D. Wagner, M. Thumm and A. Arnold, "Mode Generator for the Cold Test of Step-Tunable gyrotrons," *Proc. 27th Int. Conf. on Infrared and Millimeter Waves*, San Diego, USA, 2002, TH1.6.
- [9] A. Arnold et al., "Low Power Measurements on a Mode Converter System of Step-Tunable Gyrotrons," *Proc. 28th Int. Conf. on Infrared and Millimeter Waves*, Otsu, Japan, 2003, pp.125-126.

Radiation-Based Alignment Method for Millimetre-Wave Antennas

Robert Schneider

DaimlerChrysler Research and Technology, Radar Systems (REI/AU),
Wilhelm-Runge-Str. 11, D-89081 Ulm, Germany, Phone: (+49)731-505-2037

Abstract — The paper describes a new method for the angular adjustment of aperture type millimetre-wave antennas. It is applicable directly in the near-field and therefore especially useful for the alignment of highly directive antennas. A practical implementation in the form of a low-cost adjustment device for automotive long range radar sensors is presented, which achieves accuracies better than 0.1 deg.

Kurzfassung — Dieser Beitrag beschreibt ein neues Verfahren zur Winkelausrichtung von Apertur-Antennen im Millimeterwellen-Bereich. Es kann im unmittelbaren Nahfeld eingesetzt werden und ist daher besonders nützlich zur Ausrichtung hoch bündelnder Antennen. Als praktische Anwendung wird eine kostengünstige Justagevorrichtung für Weitbereichs-Radarsensoren im Automobil vorgestellt, mit der sich Genauigkeiten von besser als 0,1° erzielen lassen.

I. INTRODUCTION

Narrow-beam antenna applications like communication links, satellite receivers, or radar sensors require a careful angular adjustment. This is usually performed by localising the far-field main lobe in transmit or receive mode [1], or relating the antenna pointing direction to the housing (typically boresight). The first requires a large space without any interferences, the latter implies low tolerances of the antenna pattern with respect to the housing.

Hence it would be helpful to have a tool to be placed close in front of the antenna under test (AUT), which is able to determine its pointing direction and to bring it in congruence with a desired one.

Such a tool can be realized by a simple and compact quasi-optical configuration, which has been investigated theoretically, prototypically realized, and specified in its performance.

II. FUNCTIONAL PRINCIPLE BASED ON QUASI-OPTICS

Millimetre-wave antennas for the above mentioned applications mostly consist of a beam forming or phase correcting element (lens or reflector) with a primary feed in its focus. According to Huygens' Principle the wave-fronts of the radiation are approximately plane inside a tube formed by the cross section of the aperture even in the close part of the Fresnel zone (see Fig. 1). At the edges of the tube the wave fronts are increasingly bended.

A second focusing lens (or reflector) placed within this tube will focus the plane waves again at a caustic point, which is dependent on the direction of the incoming wave front and widely independent of the exact position relative to the AUT (laterally and longitudinally). Fig. 2 visualises both situations, when the AUT transmits correctly in boresight (Fig. 2a), or with an angular offset θ_{err} (Fig. 2b).

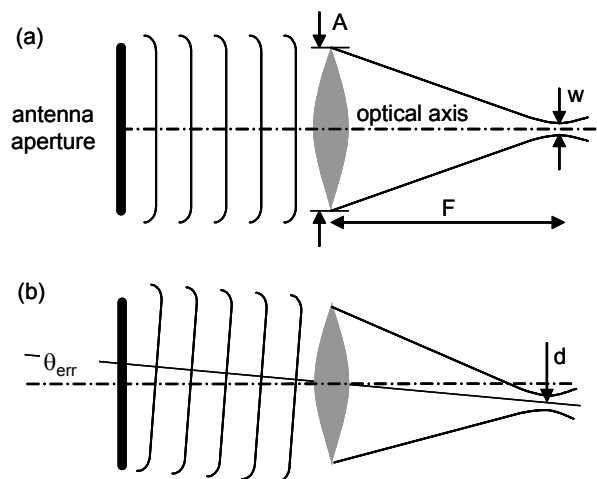


Fig.2. Quasi-optical configuration transforming incoming wave-fronts into caustic locations for the antenna beam pointing boresight (a) and with an angular offset θ_{err} (b).

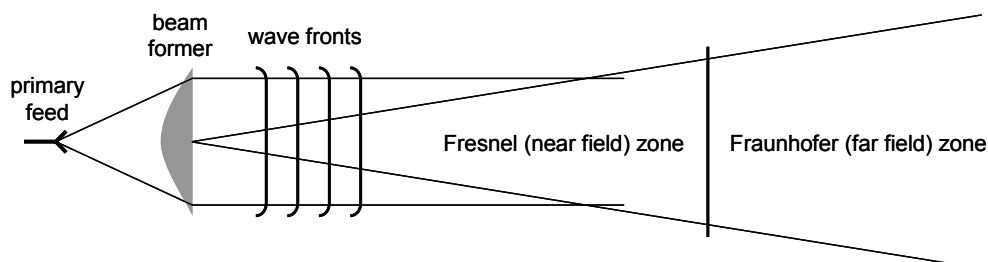


Fig. 1. Radiation field of a phase corrected aperture antenna.

In the focal plane of the lens power detecting means can be provided, which localise the caustic and thus deliver information about the pointing direction of the AUT. For the adjustment procedure the optical axis of the configuration has to be oriented in parallel to the desired pointing direction.

The lateral shift of the caustic in the focal plane depending on the angular pointing error θ_{err} in first order approximation equals

$$d = F \cdot \tan(\theta_{err}) \quad (1)$$

The extension w of the caustic in its lateral 3 dB-limits can be estimated as a function of the geometrical dimensions A (diameter of the focusing lens), F (its focal length), and the wavelength λ according to

$$w \approx \lambda \cdot \frac{F}{A} \quad (2)$$

[2]. For the values $\lambda = 4\text{mm}$, $F = 200\text{mm}$, $A = 100\text{mm}$, the resulting lateral caustic spot diameter is $w = 8\text{mm}$. This is a good trade-off in order to be found easily in the focal plane and to be localized in its exact position. For smaller caustics close side lobes may cause ambiguities. The extension of the caustic in transversal direction is about five times larger, which makes the positioning of the power detector uncritical and tolerates lens aberrations (for example by dispersion).

In the following the influence of a lateral shift of the AUT relatively to the lens will be demonstrated. Fig. 3 visualizes real measured power distributions of the caustic in the focal plane for the above mentioned lens configuration with $\theta_{err} = 0\text{ deg}$ and the phase centre placed on the optical axis (Fig. 3a) and with a horizontal lateral shift of 1 cm (Fig. 3b). The black lines denote a 3 dB power descent from the maximum. In the on-axis case a rotationally symmetric Gaussian profile results showing an extension in good agreement with (2). When considering the off-axis case, the symmetry is deteriorated clearly with the maximum of the lobe moving slightly to the left, but its -3 dB points remaining nearly unchanged. Obviously a moderate lateral positioning uncertainty of the AUT relatively to the lens is tolerable, as it is mandatory for the underlying functional principle.

In a first approach the caustic localisation could be performed by a single power detector at the intersection of the optical axis with the focal plane and the AUT adjusting for maximum value at the detector, but much more accurately by difference measurements of two sensors symmetrically to the optical axis, as can be concluded from Fig. 3.

A configuration for antenna adjustment in azimuth and elevation then would require four power detectors in a cross hairs arrangement.

III. LOW COST MILLIMETER-WAVE POWER DETECTION WITH PYROELECTRIC SENSORS

The power detection in the focal plane can be performed with conventional diode detectors connected

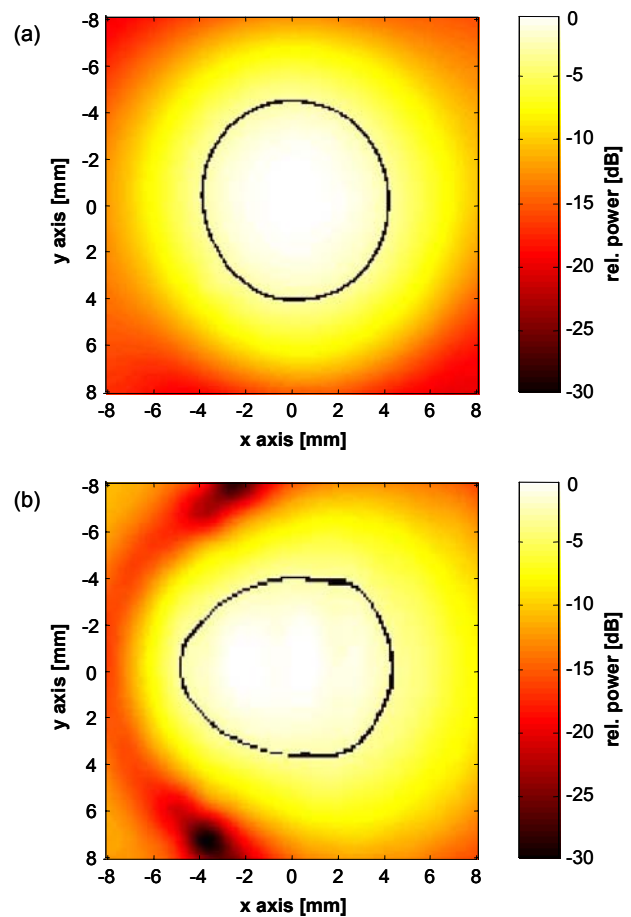


Fig. 3. Power distribution in the focal plane of the lens for the AUT phase centre on the optical axis (a) and with a horizontal offset of 1 cm (b). The black lines denote a 3 dB power descent from the maximum.

to open waveguide field-probes. Much more cost effective, however, is the use of pyroelectric power detectors (PDs), as they are commonly used for laser beam measurements [3]. These sensors respond with a voltage signal on variations of impinging thermal radiation in a very broad-band wavelength range. Maximum sensitivity is reached by variation frequencies in the region of 1...10 Hz. For millimetre-wave radiation the sensitivity isn't specified but was measured at 77 GHz to be about 100 mV per mW power modulation at 10 Hz, which is fully sufficient for the described application.

PDs contain a ceramic crystal typically sized $(2.5\text{ mm})^2$ and are commercially available in TO-5 transistor cans with specific windows or just a cut-out in the top of the housing. This metallic housing isn't well suited for millimetre-wave applications, as it forms a cavity resonator with polarisation dependent coupling. Hence the sensor elements should be exposed directly to the radiation, or at least the surrounding area properly covered with absorbing material. Customized solutions are available.

Another peculiarity of PDs is their extremely high output impedance of several $T\Omega$, which requires proper LF amplification circuitry as well as shielding and filtering of interfering signals, but doesn't cause any critical or expensive measures.

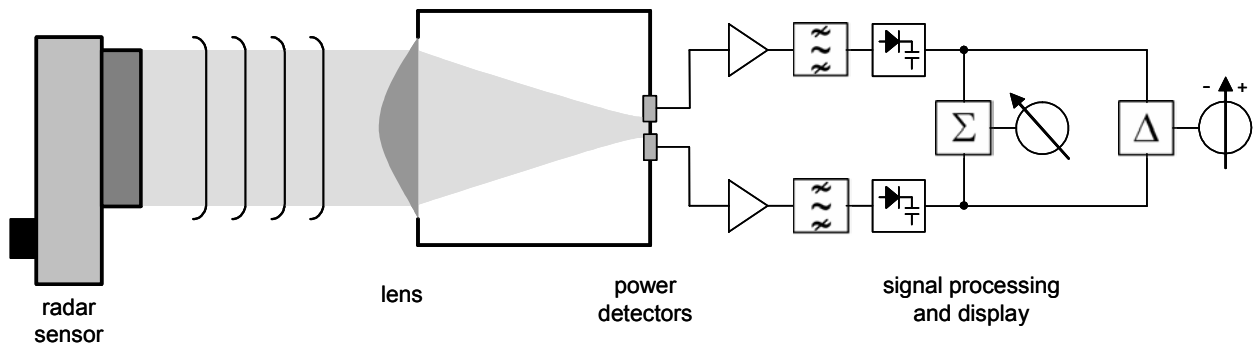


Fig. 4. Schematic diagram of a radar sensor alignment tool.

As PDs are only sensitive against power variations, the AUT needs to be connected to an amplitude modulated source, or in the quasi-optical signal path a modulating element has to be inserted (for example a rotating polarisation grid in front of the power detector). If the alignment of a radar sensor has to be performed, its transmitter could be set directly into a proper modulation mode (either CW on-off or pulse bursts with about 10 Hz repetition frequency).

IV. PRACTICAL APPLICATION: AN ALIGNMENT DEVICE FOR AUTOMOTIVE RADAR SENSORS

Based on the above described method, a prototypical device for the alignment of far range automotive radar sensors, as they are used for autonomous cruise control (ACC), was realised and tested.

The concept is very related to that one used for headlight adjustment well known from car workshops. The alignment device is arranged in front of the radar sensor with its optical axis parallel to the vehicle's longitudinal axis and illuminated by the radiated field. In practice one could combine both tools favourably.

Fig. 4 depicts a schematic diagram of the overall configuration. The prototype was realised just for the alignment in a single axis (azimuth). In the focus of the dielectric lens a dual-channel PD power detector is located and connected to an analogue signal processing electronics (amplifier, band-pass filter, full wave rectifier, low-pass filter). As the PD exhibits a very broadband sensitivity, the band-pass filter is required to suppress interfering AC power components in IR and optical wavelengths. The output signals of both channels are combined in sum and difference and displayed at two gauges. The sum indicator is used for proper positioning of the tool in front of the antenna (which is especially helpful, when the antenna isn't directly visible behind a cover or radome). The difference indicator serves for the actual manual mechanical alignment, which is successful, when zero value is displayed.

In Fig. 5 photographs of the prototype and its practical application are shown. Fig. 5a depicts the set-up with all components of the block diagram in Fig. 4 arranged on a base plate, which is mounted on a two-axis sliding table. In Fig. 5b the lens tube has been detached from the power detector, which is realized by two commercial PD elements. They are covered by absorber material around

the sensitive area in order to reduce resonance effects by reflections from the metallic housing. See Figures 5c and 5d for detailed views. The cut-out in the housing is sealed with a thin polyethylene film in order to avoid pollution. Additionally this measure eliminates the sensitivity of the power detectors against ambient air flow. Fig. 4e shows the complete tool integrated with the headlight adjustment equipment in a car workshop.



Fig.5. Prototype of an alignment tool for automotive radar sensors (a), with dismounted lens tube (b), detailed views of the dual-channel power detector (c) and the PD elements (d), and field test in a car workshop (e).

Comprehensive tests using the tool for the adjustment of an ACC radar sensor have shown excellent results. A special operation mode of the radar sensor merely had to be implemented by software, which performs a transmit power on-off modulation of about 10 Hz at a duty cycle of 50 %. The radar antenna has a circular aperture with 10 cm diameter and about 3 deg symmetrical beam width. Its folded reflector beam forming concept [4] ensures approximately plane wave fronts even in the very close near field.

For the adjustment procedure the distance between the AUT and the tool may vary between a few mm and 30 cm. Within these limits angular adjustment accuracies of better than 0.1 deg can be achieved, when the misalignment of the AUT at the beginning of the procedure doesn't exceed about 2...3 deg. For greater misalignments, a second cycle consisting of positioning the tool in front of the AUT (searching for maximum reading of the sum gauge) and adjusting the antenna azimuth angle for zero reading of the difference gauge should be performed in order to maintain maximum accuracy.

Interfering effects due to power emissions of lamps or car engine components weren't observed during extensive tests, although the lens was manufactured of optical transparent polycarbonate. It has a plano-convex profile with its hyperboloidal contour outside in order to minimize standing waves between the AUT and the lens surface.

V. ADDITIONAL APPLICATIONS

Beyond the application described in section 4 various implementations of the principle are possible:

1. For angular adjustment in two axes simultaneously, the power sensor has to be replaced by a quadruple configuration and extended by suited signal processing and visualization. Here manifold detail solutions for the user interface are imaginable.

2. Especially for the adjustment of radar sensors the power detector in the focal plane could be replaced by a small reflector on the optical axis, which is transformed by the lens into a virtual far-field target at boresight. The angular reading of the radar sensor then can be used for alignment.

3. In order to separate the target echo from other reflections, the reflector of 2 can perform mechanical oscillations (amplitude in the order of 100 μm) at a frequency f_{mod} causing a narrowband FM of the receive signal. The resulting frequency spectrum features two

lines symmetrically to the carrier f_c at $f_c \pm f_{mod}$. This virtual Doppler shift simulates moving targets with a velocity

$$v = \pm \frac{c_0}{2} \cdot \frac{f_{mod}}{f_c}, \quad (3)$$

which have to be handled in the subsequent signal processing. The mechanically modulating element can be formed by the moving coil of a miniature sonic transformer.

4. When a receive antenna has to be aligned, a point source can be placed in the focal plane of the lens, which simulates the incidence of a plane wave front from boresight or any other desired direction.

5. Finally the alignment process could be automated, when the signals are evaluated numerically and a closed loop with a motor driven mechanical adjustment mechanism is formed.

VI. CONCLUSION

A new approach for the radiation-based alignment of high directivity millimetre-wave antennas has been suggested and practically verified. It can be employed in all cases where the antenna has to be aligned with respect to a given reference axis and combines a very compact set-up with high accuracy and the potential of extremely low cost. A very attractive application is the alignment of automotive radar sensors.

ACKNOWLEDGEMENT

The author acknowledges the assistance of M. Oertel, who realized the test setups during his student internship, acquired, and evaluated an immense amount of measurement data underlying the results presented in this paper.

REFERENCES

- [1] M. Grace, R. Abou-Jaoude, K. Noujeim, D. Bradley, "76 GHz Radar Antenna Alignment System", in *Proceedings of the 30th European Microwave Conference*, Paris, France, October 2000.
- [2] H. D. Hristov, *Fresnel Zones in Wireless Links, Zone Plate Lenses and Antennas*; Artech House, Boston, 2000.
- [3] D. Cima, "Introduction to IR Pyroelectric Detectors", in *Sensors*, vol. 10, no. 3, pp. 70-75, March 1993.
- [4] W. Menzel, D. Pilz, M. Al-Tikriti, "Millimeter-Wave Folded Reflector Antennas with High Gain, Low Loss, and Low Profile", in *IEEE Antennas and Propagation Magazine*, vol. 44, no. 3, pp. 24-29, June 2002.

Antenna Coupling on Electromagnetic Large Objects

I. Walter¹, E. Arnold¹, C. Holtzhausen¹, M. Sabelny¹

¹EADS Germany, Woerthstrasse 85, 89077 Ulm, ##49 731 392-3429, ingo.walter@eads.com

Abstract — This paper contains in a rather tutorial style a brief summary about problems which occur during the process of antenna integration. The expression "electromagnetic large objects" usually means that the objects have geometric dimensions which are several times larger than the considered wavelength. Therefore ships and aircrafts can be electromagnetically large. The designer tackling the task to place antennas appropriately along such structures can often experience problems in carrying out electromagnetic simulations. This can either be down to the applied methods or limitations of the hardware platform. Therefore it is essential to consider the use of approximative methods in order to be able to carry out the analysis of large geometries while being aware of their limitations.

I. INTRODUCTION

There are numerous wireless systems which need to be considered during the process of antenna integration. Over the last decades there has been a tremendous increase of wireless on-board units independently whether the vehicle is supposed to be for civilian or military use. In order to get an idea about past and present challenges of antenna placement it is worthwhile referring to [1] and [2]. There can be easily somewhere over a hundred different antennas distributed across a whole aircraft or ship. Although one might assume that there is plenty of space available on large objects to accommodate various antennas it can be rather difficult to find an appropriate placement along the structure.

For naval ships and military aircrafts the amount of wireless systems depends very much on the operational tasks and missions a vehicle has to carry out and what kind of support it has to provide within specific scenarios.

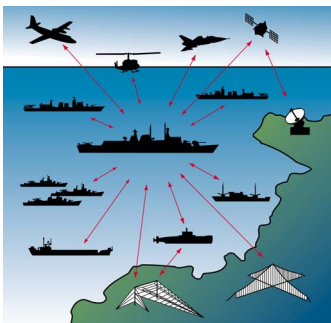


Fig. 1. Operative scenario of a naval ship.

Figure 1 shows an example of a naval ship which participates in a convoy operating and administering various simultaneous communication lines via voice or data channels to other ships, aircrafts or on-shore bases. Depending whether there is a need of just line of sight or wide range communication bridging thousands of

nautical miles to reach the home base it is necessary to use different appropriate frequency bands and antennas. During specific operational tasks there can also be requirements to employ electronic sensors or countermeasures for surveillance or protection respectively. The growing demand to provide different wireless simultaneous communication services goes hand in hand with an increasing number of antenna structures which have to be located within a limited space due to the finite size and other design requirements of the vehicle.

Sometimes it can be necessary to place additional antenna structures due to hardware upgrades either because additional or new equipment is needed. There can be restrictions in place due to stealth performance, mechanical or electrical reasons, which lead to a significant reduction of possible places where an antenna can be mounted. Before the installation of additional systems can be carried out it has to be confirmed whether there will be potential interference problems which might lead to a compromise in expected performance.

To understand the present changes of requirements for antenna siting it is helpful to consider the current on-going trends of antenna integration.

The conservative approach has been to pursue distributed antenna systems. This means that single antennas have been placed along the structure to achieve sufficient isolation between them. For simultaneous use within the same frequency band the number of antennas had to be increased corresponding to the number of wireless systems needed. At higher frequencies sufficient decoupling could be achieved by locating the antennas if possible just far enough from each other. Problems can occur at lower frequencies where the whole structure becomes comparable to the considered wavelength and can be at resonance supporting coupling effects from antennas in lower frequency bands to higher frequency bands even stronger. A significant problem is to provide simultaneous use in the HF-band where antennas usually have a quite narrow bandwidth and a relatively high coupling across the structure. The coupling between antennas for lower frequencies to antennas for higher frequencies is in particular an issue as the power for HF-band systems can be up to one or two orders of magnitude higher. This is to overcome the lower antenna efficiency which is caused by their relative short length in comparison to the wavelength. How quickly one can run out of available space shows just another aspect like necessary safety clearances which have to be obeyed to avoid radiation hazard due to high power. A disadvantage of distributed antennas can also be a significant deterioration of the radar signature for the vehicle.

The present trend moves towards integrated and centralised antenna systems. It can save a lot of space and volume through the use of broadband antennas which allow to combine several wireless units onto a single antenna structure via multicoupler equipment. Once the coupling between the antennas has been optimised the integrated antenna system can be utilised on other vehicles as well. Another positive aspect is the possibility to minimise the radar signature of the ship or aircraft due to the ability to integrate as much as possible under a single radom.

Broadband radiating elements for integrated antenna systems are also useful for new digital communication equipment. Digital communication systems these days can use spread spectrum techniques like direct sequence or frequency hopping to become resistant against jamming and interference both from inside and outside. A trade-off is that they require more bandwidth than conventional analogue systems which means that they need antennas with sufficient bandwidth.

As antennas move closer together within integrated antenna systems coupling effects have to be carefully considered and analysed beforehand. Unless all units run synchronous in time several transmitter and receiver cannot be just combined to a single broadband antenna as there would be a lack of isolation. Therefore transmit and receive antennas are usually separated within integrated antenna concepts.

The following part will briefly summarise the typical onboard systems which have to be considered during the antenna integration process. Further it presents an explanatory summary about the analysis and methods being used for an antenna siting process on electromagnetic large objects. It also highlights problems which arise during the simulation process due to size of objects. The dimensions of objects in comparison to the considered wavelength requires an amount of memory during computation which is often the bottleneck to carry out the analysis of a complete model. Alternative methods with less computational effort often bear other trade-offs which might make the simplification of the model necessary in order to analyse the coupling effects between antennas.

II. TYPICAL ONBOARD SYSTEMS

To show the task which is involved during the antenna integration it is worthwhile to generate an overview by classifying the systems into functional groups and show their frequency allocation. As it can easily be seen from figure 2 the functional groups radar, civil and military communication, electronic warfare and identification systems utilise the whole available frequency spectrum which stretches from LF- right up to the EHF-band.

Radar depending whether they are used for wide or middle range applications can be within the L- or S-Band whereas mid to short range applications usually operate within C-, X- or Ku-band. Some over the horizon search radars even operate within the HF-band. Whether it is an

aircraft or ship it carries at least an S- or X-band navigation radar on board.

The group civil and military communication usually operates within the HF-, VHF-, UHF- up to the SHF-bands. Out of all groups civil and military communication contains the largest number of wireless systems occupying similar frequency bands. Civil communication with approximately 10 to 15 systems includes air traffic, TETRA, radio, TV, Inmarsat and many others. Military communication with up to around 40 systems includes numerous dedicated tactical links where there are usually for specific links more than a single unit on board.

Satcom communication within the group of civil and military communication lies within SHF band except for UHF-Satcom.

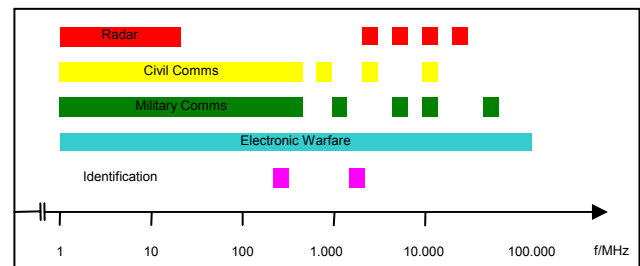


Fig. 2. Frequency allocation of on-board systems.

Electronic surveillance and countermeasure equipment usually covers the whole frequency range and are used to pick up and analyse possible transmissions of others and to apply specific protective means.

The group of identification systems usually contain IFF- or AIS-units which both operate within the UHF- and VHF-band respectively.

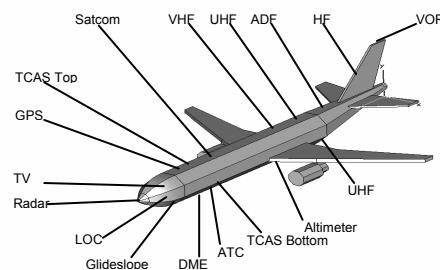


Fig. 3. Antenna locations along aircraft fuselage.

Figure 3 shows just a few basic systems and their possible location around a conventional aircraft. The HF antenna which requires rather long structures to obtain a tolerable efficiency is usually integrated within the vertical stabiliser or tail wing of an aircraft. The antennas for higher frequency ranges are usually blade antennas which are located at various different locations around the outer shell. Although it may appear that there are not too many antennas around the aircraft many of them are placed more than once at different locations to ensure simultaneous operation within the same frequency band.

Figure 4 shows a ship with two masts carrying most of the antenna structures and sensors within the masts. A

more detailed view on just how many antennas there can be located on the mast is shown in figure 5.

Despite all analysis and minimisation of antenna coupling, there has to be a certain amount of frequency assignment and planning to avoid interferences for simultaneous operation under real conditions.

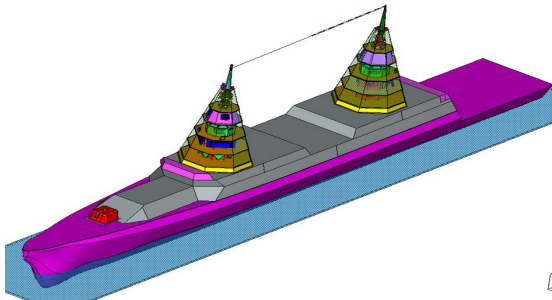


Fig. 4. Antenna locations on ship.

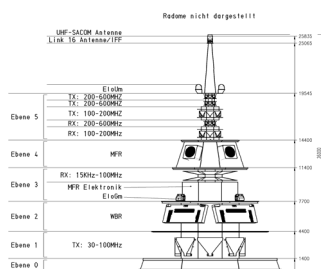


Fig. 5. Antenna placement along mast.

III. METHODS FOR ANALYSIS

At present there are numerous different simulation tools available which can be utilised to analyse electromagnetic behaviour of three dimensional structures. Unfortunately and quite often it is the sheer size of the geometries which pushes those tools and computational hardware right up to their limits.

Analysing the antenna coupling performance using brute force is not a problem if there is parallel computing, sufficient memory and time available. If it is not the computational memory which is the limit most likely the time which is required to calculate large scale models puts a limit on the size or the upper frequency range of the models. Taking the model of an aeroplane like it is shown in figure 3 at a frequency of 1 GHz which is approximately 120 wavelength in length and 17 wavelength in diameter is already quite difficult to be simulated on just a single PC.

A. Exact Methods

There is a wide variety of methods available at present for the analysis of antenna coupling problems. Exact methods like method of moments (MoM), finite element (FE), finite difference (FD) are very useful and work very well for models which have a dimension of just a few wavelengths. Recent developments like the fast multipole method (FMM) or multilevel fast multipole method (MLFMM) allow the computation of electromagnetically even larger problems within tolerable computation time. Still when being restricted by the available hardware, memory or time for the calculation at

high frequencies it can become necessary to consider still alternative methods. It is also worth mentioning that not in all circumstances parallel computing licenses and hardware are around to perform large scale computation.

B. Approximative Methods

PO which is an asymptotic method can offer a significant reduction during the computational process but it has its trade-offs when calculations within the shadowed region have to be carried out. Even using Fock currents does not always lead to satisfactory results when trying to analyse the coupling between two antennas e.g. on each side of a cylindrical shape.

Ray based asymptotic methods like UTD allow the simulation of even larger geometries but often there are other limitations which put further restrictions on the calculation.

Knowing your tools and their capabilities is another quite important issue when facing the task to analyse coupling between different antenna locations. Providing the given circumstances like distance between the antennas, size of the model, far-field condition allows to use UTD it might still be a problem to get a result.

With some UTD tools the number of hops for ray propagation is restricted. This can be a disadvantage if an object consists of several cylindrical and polygonal shapes which have to be considered for ray propagation.

Take the aircraft in figure 3 which consists of cylindrical shapes like the fuselage and turbines and polygons for the wings. Depending on the antenna siting which has to be considered there can be multiple subsequent diffractions called hops along cylindrical and polygonal shapes within the path of propagation. It is sensible to check whether the applied tool supports multiple hops and whether it also allows multiple canonical shapes and combinations of canonical objects and polygonal plates within a model. If this is not the case restrictions like these can either make it impossible to carry out simulations or makes it necessary to create models with appropriate and sometimes extensive simplifications.

IV. ANTENNA COUPLING ANALYSIS

A. Reduction of the model

Due the above mentioned problem of computational resources it is important if possible to reduce the computational size of models which allows an efficient analysis of antenna structures.

Take the coupling of antennas along a fuselage of a large aircraft. Considering this example it is not really necessary to include every tiny detail for simulation. When analysing the coupling effects between antennas on the top side of the fuselage it has to be questioned whether it requires to consider wings, turbines, cockpit, etc. Also shapes can be simplified. The fuselage e.g. can be reduced to just a cylinder if only the direct coupling effects between antennas are dominant like in figure 6.



Fig. 6. Simplified fuselage model for verification of method.

How accuracy can still be maintained even using rather simplistic models can also be seen in [3] where various calculations have been carried out for antennas on aircrafts and ships which have subsequently been verified by measurements using scaled brass models. Although brass models to scale like shown in [1], [2] and [3] are still being used as one possible alternative method to carry out analysis and verification of antenna coupling and siting, it has to be said that it is a quite time consuming and expensive method as well.

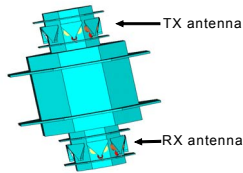


Fig. 7. Model for antenna coupling.

Figure 7 shows how the calculation of antenna coupling for ship antennas mounted on top of the mast as shown in figure 4 and 5 can be simplified. For the coupling effects it is rather the coupling of near field and surface currents along the mast causing unwanted interaction than reflections from the opposite mast or the hull.

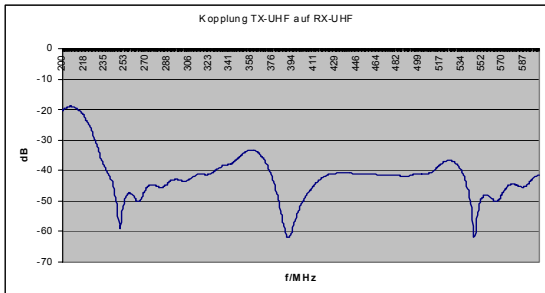


Fig. 8. Antenna coupling for antennas in figure 7.

For the calculation of two blade antennas positioned along the upper shell of an aircraft it might not be necessary to consider the lower shell as well, providing the frequencies are high enough to do so and direct and reflected path are dominant. Even the simulation of coupling for the HF-band ship antenna does not automatically require to model the complete hull.

B. Verification of applied method

After setting up a model for the analysis of the antenna coupling like in figure 6 it is advisable to cross check the validity of assumptions to apply approximative methods. Some CAD tools provide approximative and exact methods in a single bundle. Therefore it is sensible to

benchmark whether the results are correct and converging by applying both exact and approximative methods to the same model if it is possible. This can be done in a first step by using simple models as described above. Figure 9 shows the results for the simulation of the two antennas in figure 6 which are assembled on the top and bottom side of the fuselage of an aircraft. The upper three curves show the scenario that both antennas are on the same side of the fuselage whereas the lower three curves show the results for the antennas being mounted on opposite sides.

For the first case exact and approximative methods agree quite well with each other over the whole frequency range. For the second case the results for UTD are like an envelope over the results of MoM and PO. There are single frequencies where the results agree with each other but there are also frequencies with quite different values for coupling.

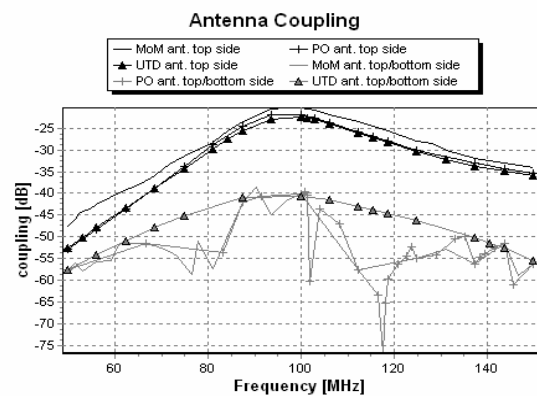


Fig. 9. Comparison of different methods.

V. CONCLUSIONS

The analysis of antenna coupling can still be a quite cumbersome task for large objects. The use of approximative methods is often the only way to calculate the problem. Before applying any approximative method it is always advisable to validate results if possible with exact methods and to reduce the geometrical complexity of the model.

ACKNOWLEDGEMENT

The authors wish to acknowledge the support of all co-workers Dr. U. Fuchs, B. Michael, Dr. H. Bleichrodt, Dr. W. Carl, W. Kredel, J. Voge and all who made valuable contributions to the investigation of an integrated antenna system.

REFERENCES

- [1] Preston E. Law, Shipboard Antennas, Artech House, 1987
- [2] Preston E. Law, Shipboard Electromagnetics, Artech House, 1986
- [3] Y.T.Lo, S.W. Lee, Antenna Handbook Theory, Application and Design, Van Nostrand Reinhold Company, 1988, chapter 20.

Dominant Path Prediction Model for Indoor Scenarios

Gerd Wölfle¹⁾, René Wahl¹⁾, Philipp Wertz²⁾, Pascal Wildbolz¹⁾, Friedrich Landstorfer²⁾

¹⁾AWE Communications GmbH, Otto-Lilienthal-Str. 36, 71034 Boeblingen, Germany, www.awe-communications.com

²⁾Institut für Hochfrequenztechnik, University of Stuttgart, Pfaffenwaldring 47, 70569 Stuttgart, Germany

Abstract— Currently, for the planning of wireless networks (e.g. WLAN) in indoor scenarios either empirical (direct ray) or ray-optical (ray tracing) propagation models are used. In this paper both approaches are compared to one another and to measurements in different (multi-floor) buildings. Additionally a new concept - which is called Dominant Path Model - is presented in this paper. This new concept does not focus only on the direct ray (like empirical models) and it does not consider hundreds of rays for a single pixel (like ray tracing), but it focuses on the dominant path(s) between transmitter and receiver. The parameters of these dominant paths are determined (e.g. path length, number and type of interactions, material properties of objects along the path, etc.) and are used for the prediction of the path loss between transmitter and receiver. Thus the computational effort is far below ray tracing and in the range of empirical models. But the accuracy of the new model in very complex environments (where multiple interactions occur) is even higher than the accuracy of ray tracing models (because of their limitations in the number of interactions considered). This very high accuracy is shown with the comparison to measurements in different buildings.

Keywords—wave propagation, indoor, ray tracing, dominant paths, measurements.

I. INTRODUCTION

The planning of wireless communication networks in indoor scenarios must be based on accurate propagation models for the prediction of the path loss between fixed base station antennas (e.g. WLAN access points) and mobile terminals. Many different approaches have been investigated during the last years to obtain accurate and fast propagation models. Today either statistical/empirical models or ray-optical models are used. For the ray-optical models significant accelerations are available [1].

Nowadays 3D vector databases of buildings are available and can be used without any restrictions. These databases provide a high accuracy, but errors in the material definitions or in the coordinates lead to significant errors if ray-optical propagation models are used (see figure 3). So there is a demand for models which are fast and consider multiple interactions (e.g. diffractions) – but which are not relying on each detail of the vector database. In this paper such an approach is presented and compared to empirical and ray-optical propagation models as well as measurements.

II. INDOOR DOMINANT PATH MODEL

A. Current status

Figure 1 shows the problem of empirical propagation models in indoor scenarios. They are based on the direct ray between transmitter and receiver. However, this ray is not always dominant and very often this path is highly attenuated.

Focusing a model on this path must lead to errors in nearly all scenarios where this path has only a minor contribution to the total received signal power.

In figure 2 the principle of a ray-optical propagation model is shown. Up to many hundreds of rays are computed for each receiver

location. The contributions of each ray are superposed to obtain the received power. In most cases only 2 or 3 rays are contributing more than 95% of the energy, i.e. by focusing on these dominant rays the accuracy would be sufficient.

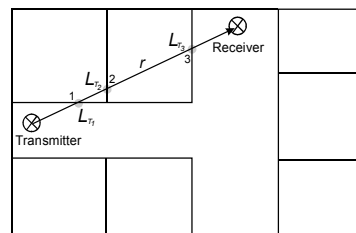


Figure 1. Empirical propagation models in indoor scenarios

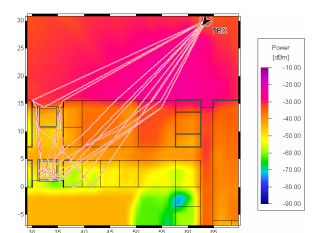


Figure 2. Ray-optical propagation models in a university office building

A second disadvantage of ray-optical models is shown in figure 3. Small inaccuracies in the databases lead to totally different prediction results. As angular criteria are evaluated during the ray-optical prediction, the orientation of walls is extremely important. Unfortunately building databases with this very high accuracy incl. a very detailed description of the material properties are very difficult to obtain at reasonable costs.

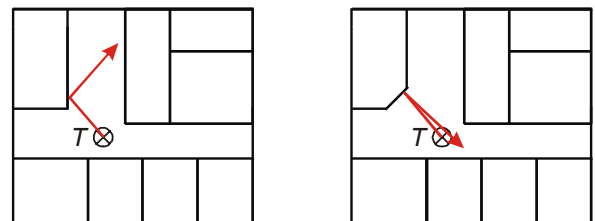


Figure 3. Accuracy of building databases

B. Requirements for a new model

After analyzing the status of the models currently available, the requirements for a new model can be defined:

- Model should not depend on each micro-detail in the vector database (see figure 3).
- Focusing on the dominant paths (see figure 4) and not computing hundreds of irrelevant paths.
- Simple calibration possible with reference data (e.g. measurements).

With these requirements the dominant path model was defined.

C. The Dominant Path Model

The Dominant Path Model can be subdivided into two steps:

- Determination of the dominant paths (geometry)
- Prediction of the path loss along the paths

Determining the dominant paths is a very complex task [2], [3]. Figure 4 shows an example for dominant paths in indoor scenarios.

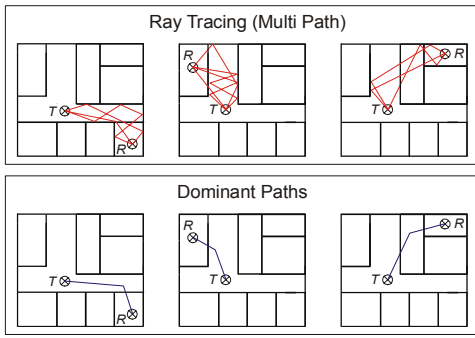


Figure 4. Dominant paths in indoor scenarios

By adjusting the weights described in [3], different paths can be obtained (small number of interactions, short paths, small number of transmissions, etc.). Obviously more than one path can be computed for each pixel if several runs with different weighting factors are computed and the contributions of the paths are superposed. In this paper the single path approach is used, i.e. only one path is determined per pixel. This reduces the computation time as each new set of weighting factors leads to a new computation of the paths, i.e. 5 different sets lead to a 5 times longer computation time compared to the single path approach.

It should also be mentioned that the path search algorithm works either in 2D or in 3D. In multi floor indoor environments the model can work in rigorous 3D. 2D is sufficient for most single floor applications.

The prediction of the path loss along the path is done with the following equation:

$$L = 20 \cdot p \cdot \log(d) + \sum_{i=1}^n f(\varphi, i) + \sum_{j=1}^m t_j - \alpha$$

L is the path loss in dB after a path length of d (in meters). α is the waveguiding factor (see below). $f(\varphi, i)$ is a function which determines the loss in dB due to an interaction, i.e. changing the direction of propagation. The angle between the former direction and the new direction of propagation is φ_i . The loss for an interaction increases linearly with the angle, beginning with an offset β_1 . The linearity ends at angle φ_2 and the loss will be constant at β_2 for the remaining angles larger than φ_1 . i is the number of the interaction, i.e. $i=2$ means the second interaction on this propagation path. The number of the current interaction is important, because not all interactions are weighted in the same way. Interactions with higher indices i lead to smaller losses in contrast to interactions with smaller indices i . This is reasonable because after multiple interactions the wave is very diffuse and so multiple options for interactions occur and thus the loss is not so high.

The waveguiding factor α is described in [4]. The reflection loss of the walls along the path as well as their distance to the path influence the value. The smaller the reflection loss and the closer the wall to the path, the higher the waveguiding factor will be. As described in [4], the factor is determined in dB. Figure 5 shows an example for the waveguiding factor in a university building [2].

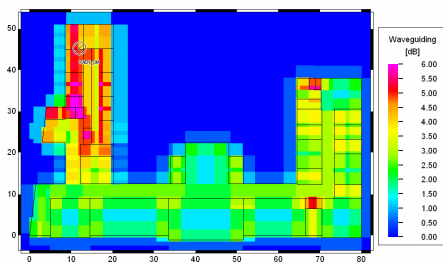


Figure 5. Waveguiding factor in a university building

The model could be improved with more details to increase the accuracy. But if an automatic calibration (e.g. linear regression) of the parameters should be possible, the dependency should not be too complex – otherwise the automatic calibration will not be feasible.

The exponent p for the path loss is set to fit the indoor requirements (i.e. this factor is higher than the value in the urban case). In addition to that, the factor is adapted to the current state of the propagating wave, thus different factors for LOS, OLOS (obstructed LOS) and NLOS (non-LOS) areas can be realized.

For the determination of the path loss, transmissions through walls have to be considered. t_j means the transmission loss for wall number j , i.e. t_2 is the transmission loss of the second wall, which was penetrated by the propagating wave.

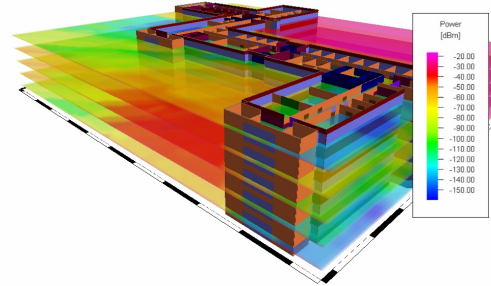


Figure 6. Prediction of received Power with multiple layers

As mentioned above, the algorithm works also in a 3D mode, which is very useful for multi floor buildings (see figure 6). If the rigorous 3D algorithm is used for computation, the dominant paths are determined over several layers, which leads to very accurate results especially in multi floor buildings.

III. BENCHMARKS

A. General

To demonstrate the performance of the Dominant Path Model in indoor environments, measurement campaigns in different types of buildings were used. New office buildings like the University of Stuttgart [5], older office buildings like the University of Vienna [2], [6] as well as buildings with multiple floors like the Instituto de Telecomunicações in Lisbon [7] were used for the comparison. The results concerning accuracy were compared to a 3D ray tracing model (IRT) and the well known Multi Wall model (MW).

B. Modern office building

One measurement campaign was conducted in a modern office building at the University of Stuttgart, which is mainly built of concrete and glass. The database of a single floor of the building contains 108 planar objects with more than 130 subdivisions (windows, doors...).

The campaign includes 20 different transmitter locations and many measurement routes for each location. Two of the transmitter locations are presented in this paper. The comparison of further measurement routes and transmitter locations can be found in [5]. The results of the prediction for transmitter site 8 with different prediction models are presented in figures 7 to 9. The path loss measurements obtained in this building were performed with a CW signal. The carrier frequency was 1800 MHz and the transmitter output power was 20 dBm.

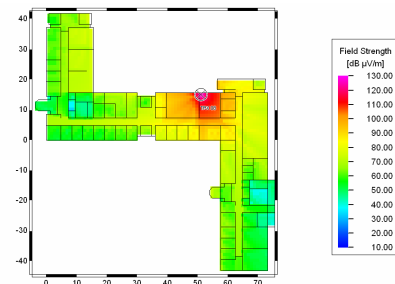


Figure 7. Prediction for site 8 with Dominant Path Model

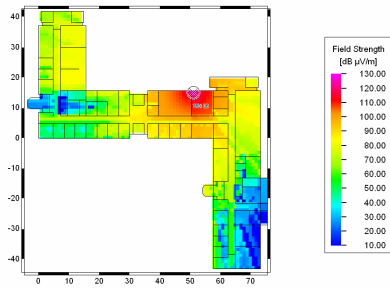


Figure 8. Prediction for site 8 with the 3D ray tracing (IRT) model [1] with 6 transmissions, 4 diffractions and 5 reflections in multiple combinations

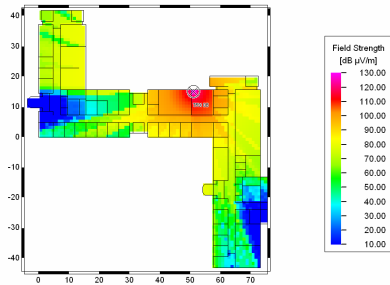


Figure 9. Prediction for site 8 with Multi-Wall Model

The results of the prediction with the Dominant Path Model are more realistic compared to the results of the other two models. Especially after multiple diffractions and large distances, the fieldstrength of the ray tracing and the Multi-Wall Model are too pessimistic (table I and figures 8 and 9). This can be explained with the fact, that the ray tracing considers 4 diffractions and 5 reflections in this case, in contrast to the Dominant Path Model, which has no limit for the number of interactions. The accuracy of the Multi-Wall Model is even worse, which is obviously a consequence of the fact that it considers only the direct ray and does not consider reflections and diffractions.

Figures 10 and 11 show the difference between predictions performed with the Dominant Path Model and measurements for transmitter sites 2, 6, 8, and 12. The differences between prediction and measurement are good as shown in table I.

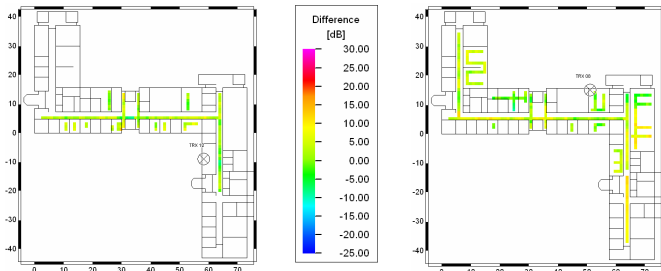


Figure 10. Difference between prediction and measurement for the Dominant Path Model, Site 12 (left) and Site 8 (right)

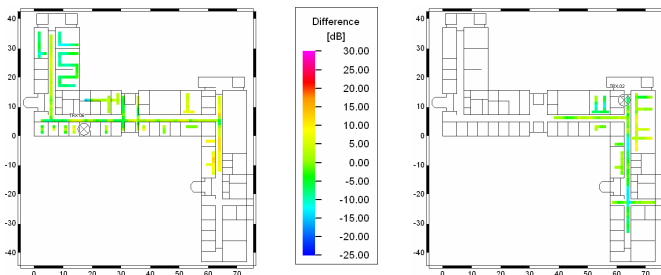


Figure 11. Difference between prediction and measurement for the Dominant Path Model, Site 6 (left) and Site 2 (right)

Table I shows the difference between predictions and measurements for the Dominant Path Model as well as for the ray tracing and Multi Wall models.

TABLE I. COMPARISON TO MEASUREMENTS

Site	Difference (Predictions – Measurements) in dB					
	IRT		Dominant Path		Multi Wall	
	Mean value	Std. Dev.	Mean value	Std. Dev.	Mean value	Std. Dev.
TRX 2	1.25	6.04	-1.73	5.12	-4.31	5.82
TRX 6	-2.94	11.31	-0.19	5.81	-9.62	16.86
TRX 8	3.99	9.30	3.69	4.39	1.54	16.55
TRX 12	6.68	7.13	2.42	3.48	3.21	8.97

C. Old office building

Figures 12 and 13 show the predictions for two transmitter locations in a building of the Institute of Communications and Radio-Frequency Engineering in Vienna [2], [6]. This building is mainly built of brick and wood – so it represents the older office buildings. The database of a single floor of the building contains 107 planar objects.

The carrier frequency for the measurements was 1800 MHz. A detailed description of the measurement equipment and campaign can be found in [2].

In figure 13 some propagation paths are presented. For each receiver location only one set of weighting factors for the determination of the paths is used. Each diffraction and each transmission causes an additional attenuation along the propagation path. The computation is made in 2D as the transmitter and the receiver are located on the same floor.

The comparison between the predictions of the different models and measurements can be found in table II. Also in this scenario the Dominant Path Model shows a very good accuracy.

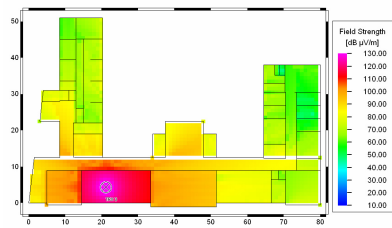


Figure 12. Prediction for Dominant Path Model, Site 3

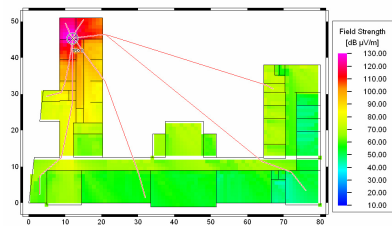


Figure 13. Prediction for Dominant Path Model with some propagation paths, Site 0

TABLE II. COMPARISON TO MEASUREMENTS

Site	Difference (Predictions – Measurements) in dB					
	IRT		Dominant Path		Multi Wall	
	Mean value	Std. Dev.	Mean value	Std. Dev.	Mean value	Std. Dev.
TRX 0	-0.85	12.11	-3.11	5.85	-1.93	11.39
TRX 3	2.18	7.23	-0.87	6.36	-3.96	9.83
TRX 7	-0.85	9.76	-2.86	5.64	0.60	6.04

D. Multi-floor building

The considered multi-floor building is the office building of the Instituto de Telecomunicações (Instituto Superior Técnico, IST) in Lisbon, Portugal. It is mainly built of concrete and glass – so it represents a typical modern office building. The multi floor building database of this building contains 355 planar objects. A three dimensional view (without external walls) of this scenario is given in figure 14.

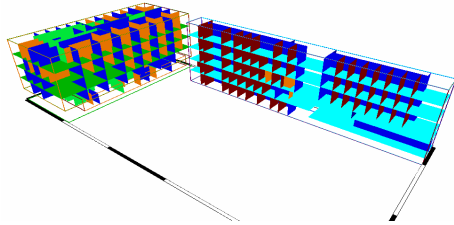


Figure 14. Three dimensional view of modern multi-floor office building in Lisbon

In this scenario the transmitting antenna is located on the top of the building [7]. Measurements and predictions were made in the building below the antenna and in an adjacent building (see figures 15 and 16).

The carrier frequency for the measurements was 950 MHz. As in this scenario the mobile station and the base station antenna are located on different floors (height of antenna: 20.5 m, height of prediction: 15.4 m, 5th floor), the 3D mode of the Dominant Path Model was used for the computation. When using the 3D Dominant Path Model, not only one prediction plane (at receiver height) is used, but several layers between transmitter and receiver are used in order to improve the result. The differences between predictions and measurements are presented in table III. All measurements together with a detailed description of the equipment can be found in [7].

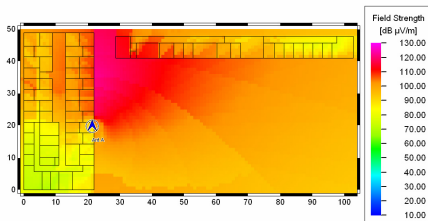


Figure 15. Prediction for Dominant Path Model (3D mode), Site A

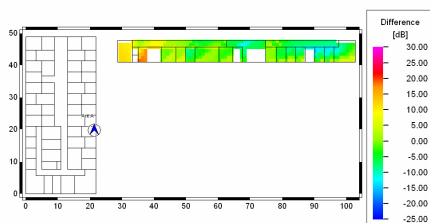


Figure 16. Difference between prediction and measurement for Dominant Path Model (3D mode), Site A

The result of the Dominant Path Model for this scenario is good (considering the complexity of the scenario). Table III shows the difference to measurements for the compared prediction models.

TABLE III. COMPARISON TO MEASUREMENTS

Site	Difference (Predictions – Measurements) in dB					
	IRT		Dominant Path		Multi Wall	
	Mean value	Std. Dev.	Mean value	Std. Dev.	Mean value	Std. Dev.
Antenna A, Building 2, Floor 5	2.79	5.37	-1.25	6.45	0.68	8.46

E. Computation times

The computation times of the Dominant Path Model are in the range of those of the Multi Wall Model, i.e. less than 1 s on standard PCs (AMD Athlon 2800+ CPU) for the scenarios described in sections III.B and III.C.

For the scenario described in section III.D, the 3D mode of the Dominant Path model was used as multiple floors had to be considered (see also section II.C). Therefore, the computation time for this scenario was longer (31 s) on the PC described above.

Ray tracing models have much longer computation times, especially if a sufficient number of interactions is computed. Even the accelerated Intelligent Ray Tracing Model [8] based on the preprocessing of the building data [1] does not reach the computation times of the Dominant Path Model. Additionally, the time for preprocessing that is needed for these Ray Tracing Models has to be considered.

IV. CONCLUSIONS

A new approach for propagation modeling in indoor scenarios based on vector databases is presented in this paper. The approach is based on the fact that not all rays between transmitter and receiver contribute a similar part of the energy. Some paths are dominant and by determining only these dominant paths, the computation time is reduced without influencing the accuracy.

The new indoor propagation model is compared to measurements performed in different indoor environments. In comparison to results of ray tracing predictions it is shown that the new propagation model reaches the accuracy of ray tracing models or even exceeds it. The computation times are in the range of empirical models and therefore very short, especially compared to those of ray tracing models. No preprocessing of the building data is needed.

As the models compute the dominant ray paths, also wideband properties of the channels (channel impulse response, delay spread) could be computed with statistical channel models. This will be the object of further studies.

REFERENCES

- [1] R. Hoppe, P. Wertz, F. M. Landstorfer, and G. Woelfle: *Advanced ray-optical wave propagation modelling for urban and indoor scenarios including wideband properties*, European Transactions on Telecommunications 2003; 14:61-69.
- [2] R. Gahleitner: *Radio wave propagation in and into urban buildings*, PhD Thesis, Technical University of Vienna, 1994.
- [3] G. Woelfle and F.M. Landstorfer: *Dominant paths for the field strength prediction*, 48th IEEE Vehicular Technology Conference (VTC) 1998, Ottawa, Ontario, Canada, May 1998, pp 552-556
- [4] G. Woelfle and F.M. Landstorfer: *Field strength prediction with dominant paths and neural networks for indoor mobile communications* MIOP 1997, 22.-24. April 1997, Sindelfingen, Germany, pp. 216-220, Apr. 1997.
- [5] G. Woelfle, P. Wertz, F.M. Landstorfer: *Performance, accuracy and generalization capability of indoor propagation models in different types of buildings*, 10th IEEE Internat. Symposium on Personal, Indoor and Mobile Radio Communications (PIMRC) 1999, Sept. 1999, Osaka, Japan F5-2
- [6] G. Woelfle, F.M. Landstorfer, R. Gahleitner, E. Bonek: *Extensions to the field strength prediction technique based on dominant paths between transmitter and receiver in indoor wireless communications.*, 2nd European Personal and Mobile Communications Conference (EPMCC) 1997, Bonn, Germany, pp. 29-36, Sept 1997.
- [7] G. C. Angelo, I. Neto, L. M. Correia: *Health and penetration issues in buildings with GSM base station antennas on top.*, 48th IEEE Vehicular Technology Conference (VTC) 1998, Ottawa, Ontario, Canada, May 1998
- [8] AWE Communications, Germany, Software tool WinProp for the planning of mobile communication networks (incl. demo-version), www.awe-communications.com, March 2003.

Propagation Effekte beim Übergang von See auf Land und ihre Auswirkung auf ein RADAR

B. Michael, Dr. S. Ban
EADS GmbH
Defence Electronics
Wörthstr. 85
89077 Ulm

Abstract

Das Einsatzgebiet moderner maritimer Radarsysteme verlagert sich aufgrund geänderter Aufgabenstellungen der Marine immer mehr in Richtung küstennaher Gebiete (litorale Umgebung). Hier stellen sich die Anforderungen an Radare zum Teil wesentlich anders dar als unter klassischen Einsatzprofilen auf offener See oder an Land.

Von besonderem Interesse sind dabei aber sehr niedrig fliegende, kleine Objekte, oder kleine Boote, die sich vor einem dichten Hintergrund von grossen Objekten (z.B. Handelsschiffe) oder urbanen Küstenregionen auf ein Schiff zu bewegen.

Auch in diesem Fall muss ein Marine-Radar in der Lage sein, jederzeit und unter allen Witterungsbedingungen, alle potentiell gefährlichen Objekte schnell und zuverlässig zu detektieren und zu verfolgen.

Die komplexen atmosphärischen Bedingungen (z.B. Inversionsschichten, Nebel) im heterogenen See-Land-Übergang stellen eine grosse Herausforderung für das Radar dar.

Die Kenntnis des Ausbreitungsverhaltens von elektromagnetischen Wellen (Mikro- und Millimeterwellen) in der Atmosphäre spielt dabei eine sehr wichtige Rolle, und ist nicht nur für Verteidigungsanwendungen, sondern auch für zivile Anwendungen (Wetterradar, Kommunikation) von großem Interesse.

In diesem Vortrag werden einige Auswirkungen von anomalen Propagationseffekten auf die Fähigkeiten unterschiedlicher Marine-Radare an Bord eines Schiffes präsentiert.

Als Grundlage der folgenden Darstellungen zur Ausbreitung elektromagnetischer Wellen, dient die modifizierte Brechzahl [1]

$$M = \frac{77,6}{T} \left\{ P + \frac{4807 \cdot e}{T} \right\} + 0,157h \quad . \quad (1)$$

Eine einfache Bestimmung der Brechzahl kann durch direkte Messung der Temperatur T , des atmosphärischen Drucks P , und des partiellen Wasserdampfdruckes erfolgen. Der Wasserdampfdruck steht in direkter Beziehung zur Taupunkttemperatur T_d und kann durch die empirische Beziehung

$$e = 6.1078 \times 10^{\left\{ \frac{A T_d}{B + T_d} \right\}} \quad (2)$$

mit $A=7,5$ und $B=237,3$ beschrieben werden..

Dieser einfache formale Zusammenhang zeigt, wie räumliche Inhomogenitäten der atmosphärischen Zustandsvariablen die Ausbreitung elektromagnetischer Wellen beeinflussen (Brechung).

In diesem Beitrag soll der Focus nicht auf der Standardpropagation sondern auf anomalen Propagationsmechanismen gerichtet sein (**Abb. 1**), wie sie zum Beispiel subrefractive und superrefractive Schichten und atmosphärische Ducts darstellen.

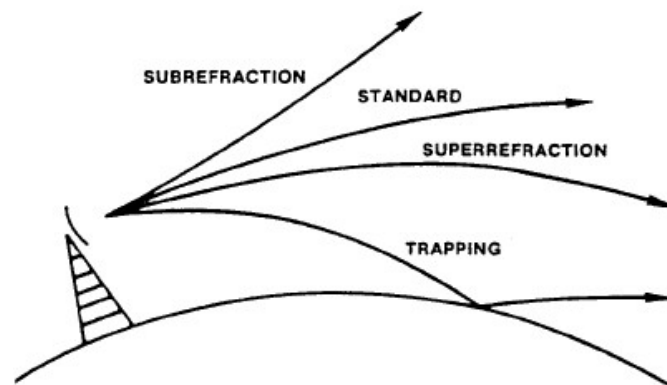


Abb. 1: Brechungsmöglichkeiten

Ausschlaggebend für das Auftreten der verschiedenen Mechanismen von Brechung und Ducting ist dabei eine bestimmte Verteilung von Luftfeuchtigkeit und Temperatur in der Atmosphäre.

Beschreibt Brechung die Eigenschaft eines Mediums eine elektromagnetische Welle bei ihrem Weg durch dieses hindurch abzulenken, so wird unter einem Duct ein Kanal verstanden, in dem zum Beispiel die Propagation der elektromagnetische Energie über eine große Entfernung erfolgen kann. Auch treten z.B. im Fall von Ducting spezielle Ducts nur in begrenzten Zeiträumen auf. Die Dauer und Ausprägung ihres Auftretens wird dabei sowohl von den Atmosphärischen Bedingungen als auch von der Jahres- und Tageszeit bestimmt.

Auf die Performance von Schiffsradaren haben besonders die in niedrigen Höhen der Atmosphäre vorkommenden Brechungsbedingungen einen starken Einfluß. Die hierbei auftretenden anomalen Propagationen können durch den Evaporation Duct [3] oder den Surface Duct hervorgerufen werden [4].

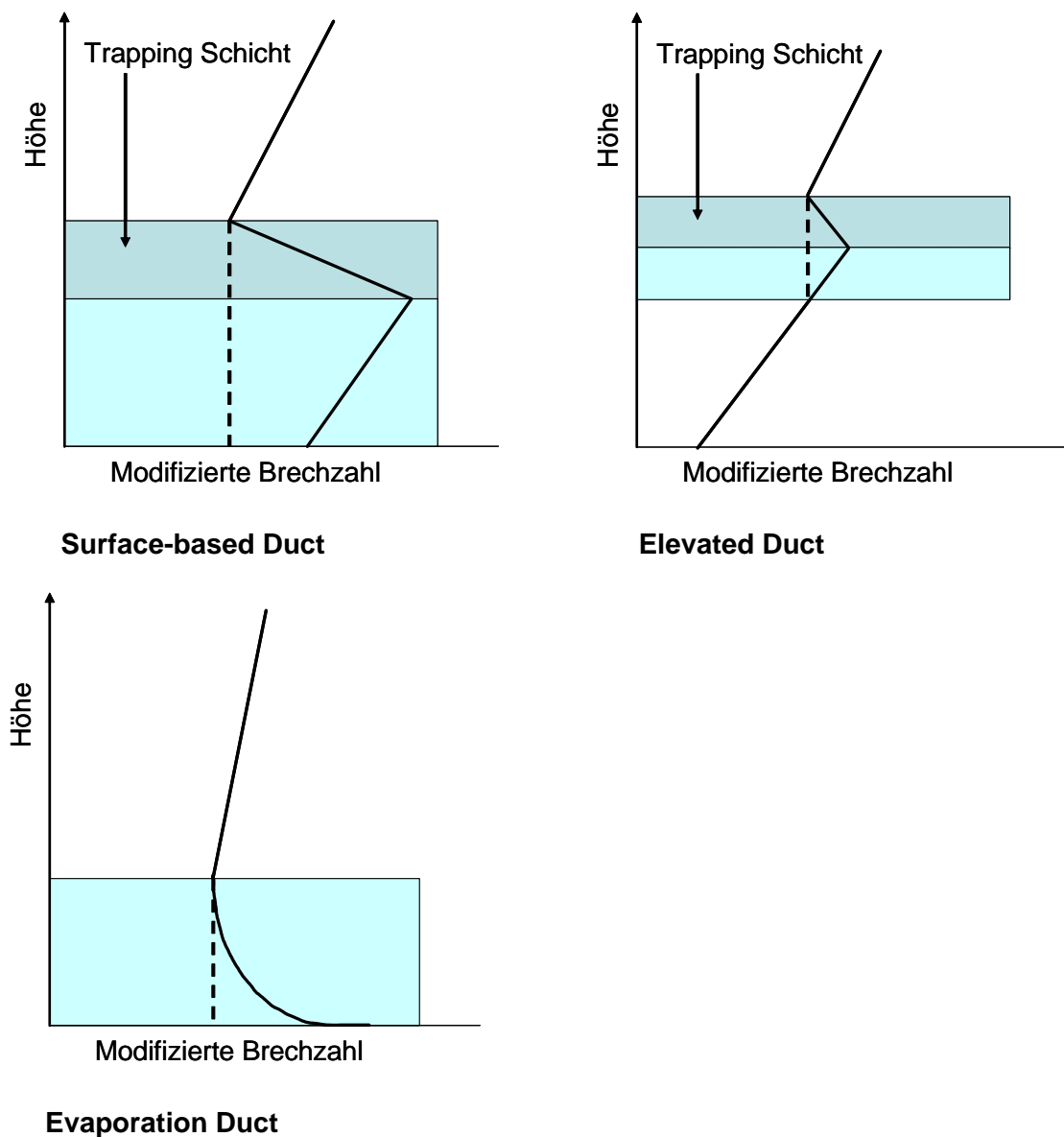


Abb. 2: Duct durch modifizierte Brechungsanzahl in Beziehung zur Höhe

Eine schematische Darstellung der Ducts wird in **Abb. 2** gezeigt. Surface-based Ducts treten im allgemeinen weniger häufig auf als Evaporation Ducts, doch ist ihre Auswirkung auf die Propagation wesentlich stärker.

Durch anomale Propagation kann es vorkommen, dass Objekte an anderen Orten als den tatsächlichen gesehen werden. Im Falle von 3D-Radaren kann es dadurch durchaus zu bedeutenden Fehlern in der Höhenbestimmung von Objekten kommen.

Dies macht die Notwendigkeit einer möglichst genauen Abschätzung der Brechungsanzahl deutlich, um die Genauigkeiten eines Radars in solch einer Umgebung zu bestimmen.

Die Abschätzung der atmosphärischen Brechungsanzahl kann zum einen durch die Betrachtung der See-Clutter-Daten, aber auch durch Messung der Verluste erfolgen.

Um Aussagen für die Performance eines See-Radars zu einer bestimmten Zeit und an einem bestimmten Ort mit bestimmten meteorologischen Daten machen zu können, gibt es heute die Möglichkeit moderne Tools zum Einsatz zu bringen. Die Tools beinhalten

Mikrowellen-Propagationsmodelle wie das der troposphärischen elektromagnetischen Parabolgleichung oder Raytracing.

Für die hier in dieser Arbeit zu betrachtenden Radare mit verschiedenen Operationsbedingungen wird das Tool AREPS (Advanced Refractive Index Prediction System) eingesetzt. AREPS beinhaltet beide zuvor erwähnten Propagationsmodelle. Um die notwendigen meteorologischen realen Verhältnisse eines bestimmten Ortes in die Berechnungen einfließen lassen zu können, werden die Daten für die Berechnung den entsprechenden Zellen einer Marsden Square Map, wie in **Abb. 3** gezeigt, entnommen.

Anhand generischer Radare in unterschiedlichen Frequenzbändern, wird bei einer fester Anbringungshöhe der Antenne, an unterschiedlichen geographischen Orten der Erde der Einfluss der Atmosphäre auf die Fähigkeiten eines Radars zur Detektion gezeigt.

Im Mittelpunkt der Betrachtungen steht dabei die Küstenregion mit urbanen Gelände, sodass nicht nur wie in einem Großteil der Literatur der vertikale Brechungs-Gradient, sondern auch der azimuthale Gradient einbezogen werden muß.

Es wird vorgestellt, welche Rückschlüsse für den operationellen Einsatz in Bezug auf z.B. die Entdeckungswahrscheinlichkeit aus den Abdeckungsdiagrammen gezogen werden müssen.

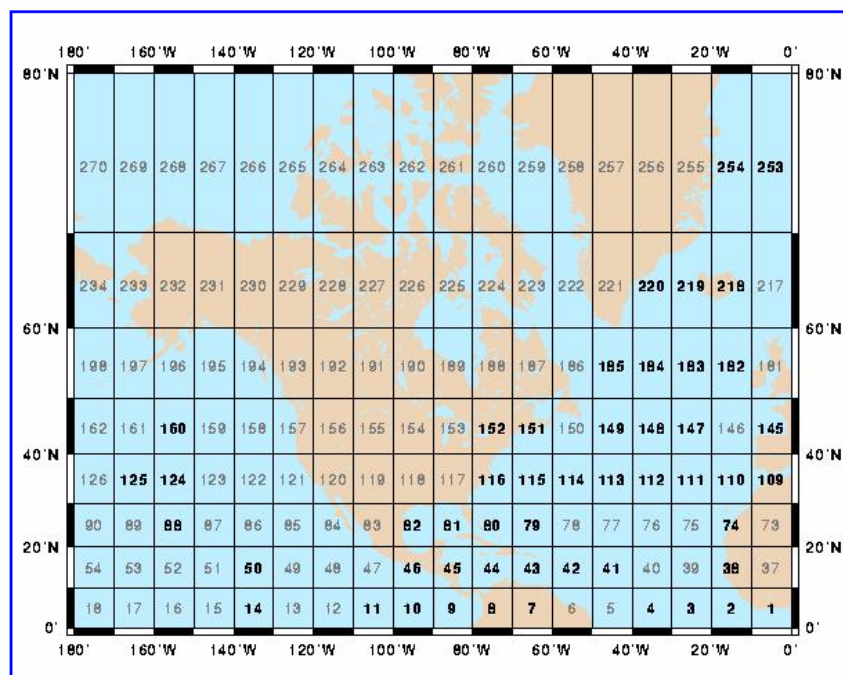


Abb. 3: Beispiel einer Marsden Square Map

Literatur

- [1] J.A. Hermann; A.S. Kulesa; C. Lucas; R.A. Vincent; J.M. Hacker; C.M. Ewenz: Impact of elevated atmospheric structures upon radio-refractivity and propagation
- [2] S.M. Babin; G. S. Young; J. A. Carton: A New Model of the Oceanic Evaporation Duct, Journal of Applied Meteorology, Vol. 36., March 1997, S. 193-204

— FINAL PAPER NOT AVAILABLE AT TIME OF PROCEEDINGS PRODUCTION —

- [3] P. Gerstoft; L.T. Rogers; L. J. Wagner; W. S. Hodgkiss: Estimation of radio refractivity structure using radar clutter, IEEE Oceans conference, Hawaii (2001)
- [4] J.K. Stapleton; V. R. Wiss; R.E. Marshall: MEASURED ANOMALOUS RADAR PROPAGATION AND OCEAN BACKSCATTER IN THE VIRGINIA COASTEL REGION.
- [5] D.R. Cayan: Regimes and events in recent climatic variables. CalCOFI Rep., Vol. XX1, 1980, S. 90-101

Session 7a

Active Devices

10 W Broadband Load-Pull for GaN/AlGaN Characterization

M. Gamal El Din (student member, IEEE), Bernd Bunz (member, IEEE), Günter Kompa (member, IEEE)

University of Kassel, Fachgebiet Hochfrequenztechnik
Wilhelmshöher Allee 73, D-34121 Kassel, Germany, Tel:+49-561-804-6535, Fax:-6529
m.gamal.el.din@ieee.org, bbunz@uni-kassel.de

Abstract — In this paper we will discuss different load-pull techniques under two tone excitation with wide bandwidth (10 MHz). In our measurements a two tone signal with 10 MHz separation will be used with different load configurations. Due to the large bandwidth of the excitation signal each tone as well as the IMD (intermodulation distortion) products will have a different load condition. In the following experiments 4 load configurations will be used and the results will be compared also a load configuration which gives identical load condition at each of the two tones and terminates the IMD products with 50Ω will be demonstrated.

I. INTRODUCTION

GaN/AlGaN material system is a strong candidate for manufacturing high-power high-efficiency and high-linearity RF power transistors for 3G base stations due to its superior electrical properties. The high saturation electron velocity (1.5×10^7 cm/s), wide bandgap (3.4 eV), and high breakdown field strength (35×10^5 V/cm) of the GaN/AlGaN system result in record power densities [1]. In 3G networks WCDMA air interface is used with a carrier bandwidth of approximately 5 MHz. The base station can use up to 4 carriers, where they are combined and amplified together by a common power amplifier. Characterizing GaN HEMTs excited with broadband complex modulated signals requires the use of two-tone signals with broad bandwidth. Performing load-pull on high power transistors services two purposes. The first is to find the optimum impedance required to achieve the required performance characteristics such as output power level, efficiency and IMD level. The second purpose is creating large signal behavioural models [2]. Performing load-pull requires a load whose impedance can be varied in a controllable way. In previous studies [3] two tone load-pull was performed with frequency spacing of 5 MHz but the reflection coefficient was assumed to be same as for the center frequency. In [4] multi tone load-pull was performed with maximum bandwidth of 3.2 MHz. In all of the cases the reflection coefficient was assumed to be identical for all the signal components. In this paper the effect of variation of reflection coefficient in relation to the load configuration will be demonstrated.

II. SYSTEM REALIZATION

The system used in performing the measurements is shown in Fig. 6. This system was first reported in [5] is extended to be able to perform harmonic load-pull and also the power capability is raised to 10 W in [6]. It is based around MTA (microwave transition analyzer), the MTA is a 2 channel high speed sampling scope, through the MUX unit and the bidirectional couplers fitted at the input port and the output port the incident and reflected waves at at both ports can

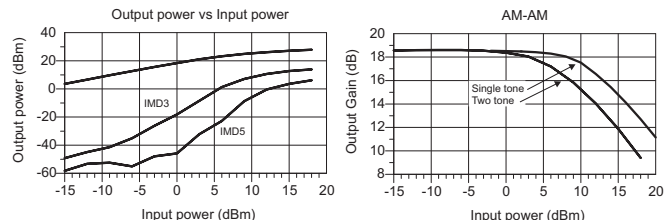


Fig. 1. Output power of the main tones as well as the output power at the 3rd and 5th order IMD at the left side Power gain under single and two tone excitation at the right side.

be measured also the MTA can measure the relative phase between the input port and the output port as well as the harmonics at each port enabling complete measurement of phase and magnitude for nonlinear devices. The bidirectional couplers are fitted with 20 dB attenuators at the coupling ports providing a total attenuation of 40 dB. For linear operation of the MTA the input at any of its 2 channels should be limited to 0 dBm. In this way this setup is capable of measuring signals up to 40 dBm (10 W). The measurement system sensitivity is -50 dBm and it has a dynamic range of -50 dB. Fig. 1 shows the result of a power sweep on the GaN HEMT used in the following experiments. The Device is terminated with a 50Ω termination and operating at class B with supply voltage of 20 V and bias current of 150 mA.

III. LOAD-PULL CONFIGURATIONS

The load configuration used in load-pull measurements determines the phase and magnitude of the load reflection coefficient at each component of the output signal. Load configurations can be divided into two main categories passive loads and active loads. In case of single tone load-pull the magnitude of the reflection coefficient that can be achieved using passive tuners is limited by losses to be less than 1. This limitation can be overcome by using active loads. Active loads can achieve magnitudes for the reflection coefficient greater than 1 by arbitrarily generating the reflected wave. Performing load-pull using two tone signals especially with large tone separation (> 5 MHz) is critical because the load configuration affects the phase of the reflection coefficient seen by each signal component since each signal component has a different phase velocity. In the following sections load-pull will be performed using four configurations under two tone signal with tone separation of 10 MHz. To compare between the different configurations a target impedance is specified and the load configuration is tuned to achieve this target impedance at one tone. At the same time the levels of the

signal components (the main two tones and the 3rd and 5th order IMD) are measured as well as the reflection coefficient at these components. The first target reflection coefficient is $0.41\angle 105^\circ$, the same measurements will be repeated with another target reflection coefficient of $0.27\angle 19^\circ$. The Device is biased for class B operation with supply voltage of 20 V and bias current of 150 mA. Not all configurations can achieve the same reflection coefficient for both tones, leading to variation in IMD levels and main tones levels. Having the same reflection coefficient for both tones is important for modelling purposes to isolate the effect of the termination impedance from the effects associated with the transistor's nonlinear capacitances. To get a true picture of the output levels of the two tones as well as the levels of the IMD products at large bandwidth, software power levelling for the input tones is used to ensure the same level for the input tones, any difference of the output levels of the output tones will be due to the transistor.

A. Passive Tuner

In this configuration a passive tuner from Maury is used. Fig. 3 shows that at large frequency spacing the phase shift between the two reflection coefficients is inevitable because of the length of the tuner (although the tuner is mounted directly without cables to the setup). At the same time the magnitudes of the reflection coefficients of the two tones are identical (the tuner is of high quality and has a very low S_{11}).

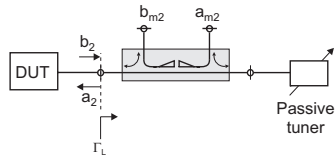


Fig. 2. Passive tuner load configuration.

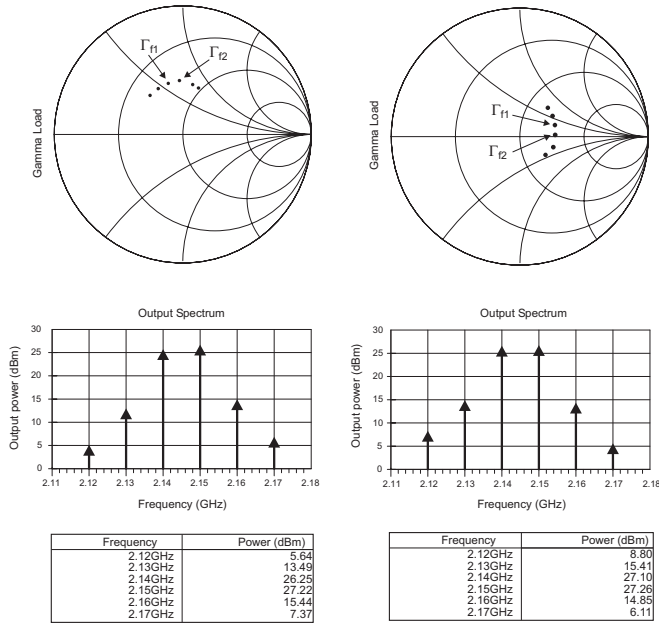


Fig. 3. Load reflection coefficient at each signal component and output power at each signal component for load-pull using passive tuner.

$$\Delta\phi = j2\Delta\beta l = j2\pi l \left(\frac{1}{\lambda_1} - \frac{1}{\lambda_2} \right) \quad (1)$$

Equation 1 gives an estimate of the reflection coefficients phase difference between the two tones. For the first target reflection coefficient (left side of Fig. 3) we have $\Gamma_{f1} = 0.413\angle 105.9^\circ$ and for the other tone $\Gamma_{f2} = 0.42\angle 93.67^\circ$ and the output power of the tones differ by 1 dB.

B. Active Closed Loop

To overcome the problem of losses and inability to cover the whole range of passive loads an active closed loop is used. In this load configuration shown in Fig. 4 a part of the output power is coupled out then amplified, phase shifted and then feed again to the output of the DUT.

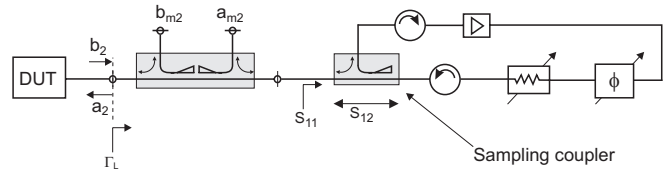


Fig. 4. Active closed loop load configuration

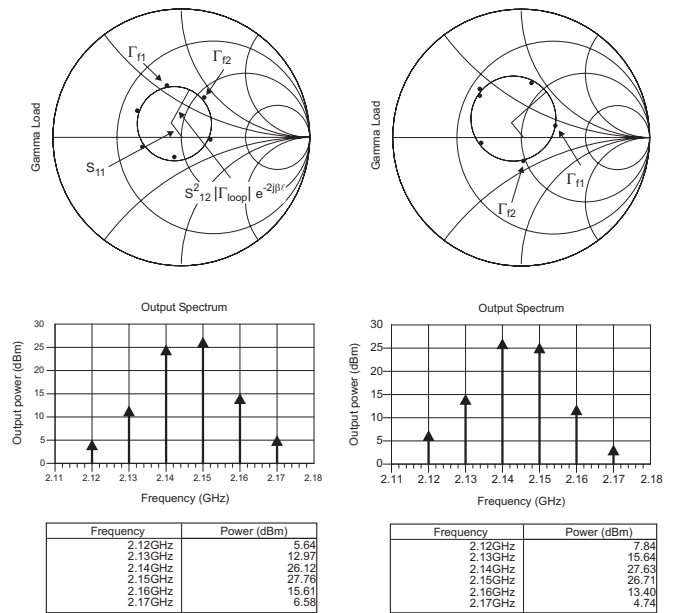


Fig. 5. Load reflection coefficient at each signal component and output power at each signal component for load-pull using active closed loop.

In this setup we have a total reflection coefficient equals to

$$\Gamma_l = S_{11} + \frac{S_{12}S_{21}\Gamma_{loop}}{1 - S_{22}\Gamma_{loop}} \quad (2)$$

S_{11} is the eigen reflection coefficient of the sampling coupler, $S_{12} = S_{21}$ (reciprocity) is the transmission coefficient of the sampling coupler and $|S_{22}| \ll 1$ because of the circulator between the attenuator and the sampling coupler, as a result we have

$$\Gamma_l = S_{11} + S_{12}^2 |\Gamma_{loop}| e^{-2j\beta l} \quad (3)$$

here l represents the length of the loop. As can be seen from equation 3 that the phase of the reflection coefficient is a function of the length of the loop and phase velocity of the wave. For the first target reflection coefficient (left side of Fig. 5) we have $\Gamma_{f1} = 0.42\angle 105.5^\circ$ and for the other tone

$\Gamma_{f_2} = 0.36 \angle 60.15^\circ$ and the output power of the tones differ by 1.64 dB here the difference is bigger than the case of passive tuner due to magnitude and phase variation.

C. Single ALM

In this setup shown in Fig. 6 a single ALM is used to control the reflection coefficient of both tones. ALM is an Automatic load module, it is an IQ modulator which receives a signal split it into I (In phase) and Q (Quadrature phase) components. By varying the amplitude of the inphase and quadrature phase components the phase and amplitude of the signal can be changed independently. These ALM modules are based around Siemens chip PMB 2202.

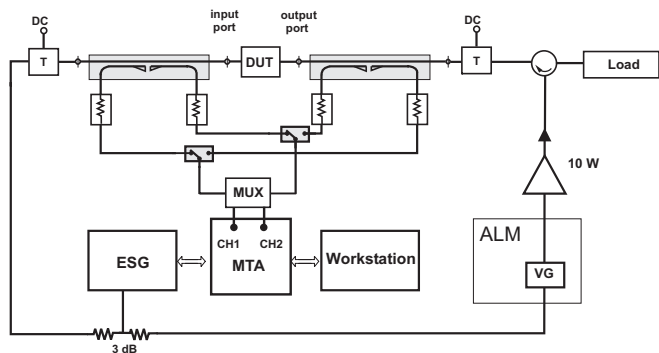


Fig. 6. Single ALM module load configuration

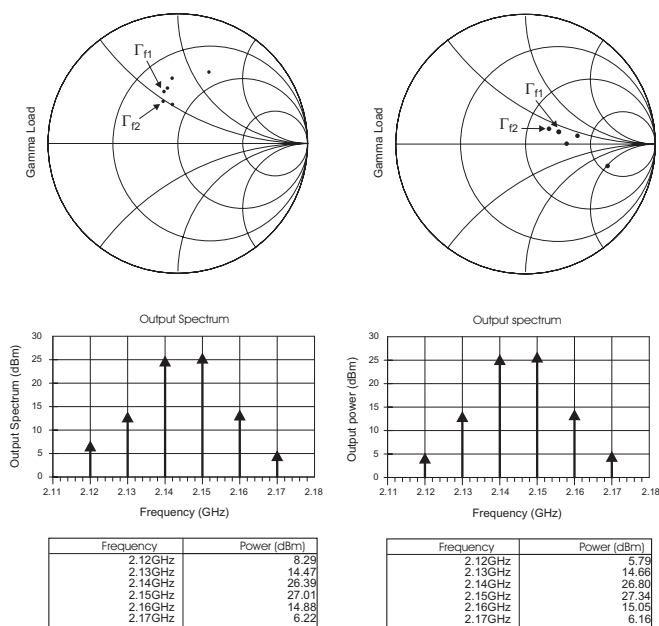


Fig. 7. Load reflection coefficient at each signal component and output power at each signal component for load-pull using a single ALM module.

In our experiment the control voltage which controls the vector generator (VG) is optimized to get a certain reflection coefficient at one tone and then levels and reflection coefficients at the other tone and the IMD products are measured. Because of the varying envelop of the two tone signal the IQ modulator suffers from internal distortion and produces 3rd and 5th order IMD products, Producing reflected waves at these products and thus terminating these products at the output with an impedance other than 50 Ω. For the first target reflection

coefficient (left side of Fig. 7) we have $\Gamma_{f_1} = 0.414 \angle 104.9^\circ$ and for the other tone $\Gamma_{f_2} = 0.34 \angle 109.15^\circ$ and the output power of the tones differ by 1.4 dB.

D. Double ALM

Using two ALM modules, one for each tone as shown in Fig. 8 we can control each tone independently from the other tone. This configuration allows us to obtain arbitrary termination for each tone, also terminating the IMD products with a match. Fig. 9 shows that the reflection coefficients of

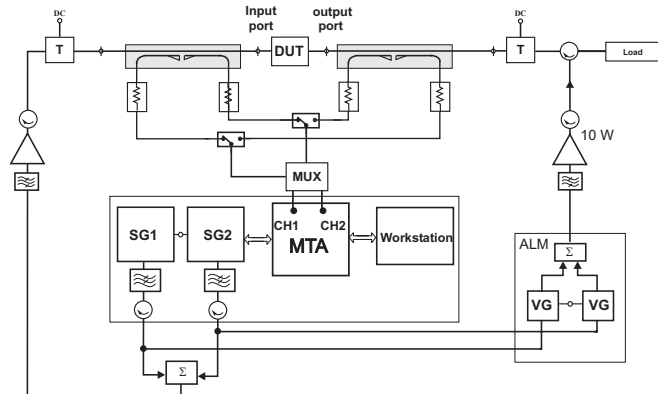


Fig. 8. Double ALM module load configuration

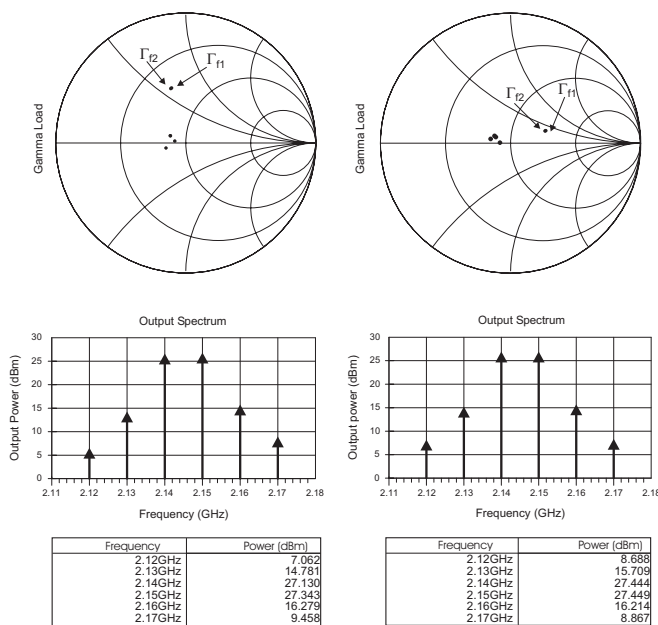


Fig. 9. Load reflection coefficient at each signal component and output power at each signal component for load-pull using two ALM modules.

the two tones are identical in both cases of $\Gamma = 0.41 \angle 105^\circ$ (left side) and $\Gamma = 0.27 \angle 19^\circ$ (right side) and also the output power for the two tones are identical. The IMD products in this setup are terminated with a match. It can be seen that terminating the IMD products with a match results in the highest IMD level in all the previous configurations.

IV. NARROW BAND LOAD-PULL

A conventional load-pull with a passive tuner under two tone signal with frequency separation of 100 kHz ($f_1 = 2.13995$ GHz, $f_2 = 2.14005$ GHz) is performed. The device is biased

for class B operation and the input power is 3 dBm which is equivalent to 3 dB backoff (1 dB compression is at 6 dBm Fig. 1). Fig 10 shows the impedance seen by each tone on the smith chart as well as the output power levels and the C/IMD (carrier to intermodulation ratio) levels. in case of narrow frequency spacing the impedance contours coincide over each others also the power levels are the same for the two tones. $\Gamma_{C/IMD}$ and $\Gamma_{P_{out}}$ shows the reflection coefficients equivalent to maximum C/IMD and output power level respectively.

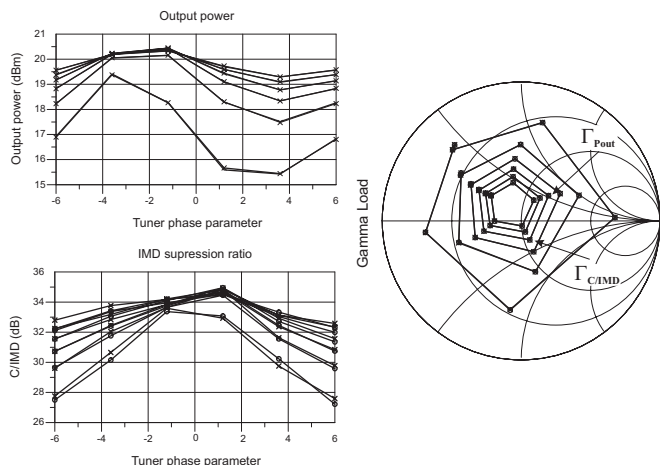


Fig. 10. Load reflection coefficient (Smith chart left). Output power (top right), C/IMD (bottom right) with respect to tuner parameters

Fig. 11 shows constant power and IMD contours. The point Γ_{Opt} is the optimum reflection coefficient which gives 20 dBm of output power and 34 dB of C/IMD. For the same transistor under 50 Ω termination the output power is 20 dBm and the C/IMD is 30 dB.

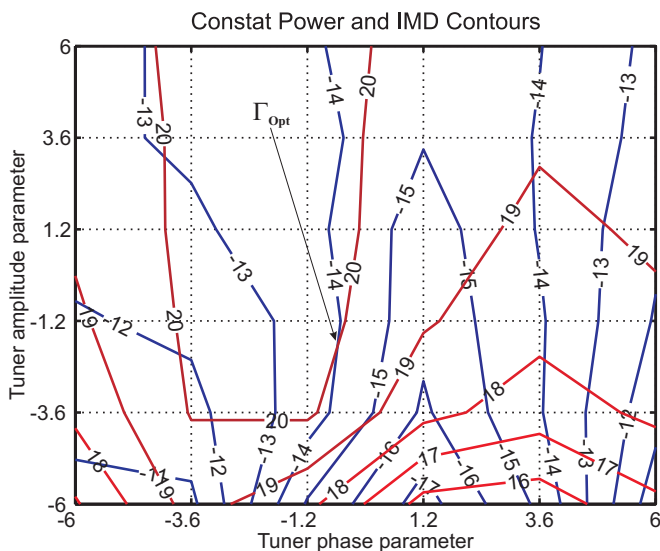


Fig. 11. Constant power and IMD contours with respect to tuner parameters

ACKNOWLEDGEMENT

The authors would like to gratefully acknowledged *Ferdinand-Braun-Institut für Höchstfrequenztechnik in Berlin* for providing the GaN HEMT devices used in this paper, also the authors would like to acknowledge the generous

sponsoring of both BMBF (Bundesministerium für Bildung und Forschung) and EU Project: TARGET.

REFERENCES

- [1] M. Golio, *RF and Microwave semiconductor Device Handbook*. CRC Press, 1999.
- [2] J. Olah and S. Gupta, "Power amplifier design using measured load pull data," *Microwave Engineering Europe*, pp. 23–30, August/September 2003.
- [3] G. Z. F. M. Ghannouchi and F. Beaugard, "Simultaneous load-pull of intermodulation and output power under two-tone excitation for accurate SSPA's designs," *IEEE Trans. Microwave Theory Tech.*, vol. 43, no. 6, pp. 929–934, June 1994.
- [4] F. G. R. Hajji, F. Beaugard, "Multitone power and intermodulation load-pull characterization of microwave transistors suitable for linear SSPA," *IEEE Trans. Microwave Theory Tech.*, vol. 45, no. 7, pp. 1093–1099, July 1997.
- [5] F. van Raay and G. Kompa, "A new on-wafer large-signal waveform measurement system with 40 GHz harmonic bandwidth," *IEEE MTT-S Int. Microwave Symp. Digest*, no. 6, pp. 1435–1438, 1992.
- [6] B. Bunz, *Entwurfsverfahren von breitbandigen Frequenzvielfachern für ein multiharmonisches Source- und Load-Pull System*, "Doktorarbeit. Universität Kassel, Juni 2004.

Modeling of SiC MESFETs for Broadband PA Applications

Ahmed Sayed and Georg Boeck

Technische Universitaet Berlin, Microwave Engineering Group, HFT 5-1, Einsteinufer 25, 10587 Berlin, Germany, sayed@mwt.ee.tu-berlin.de, Tel. +49 30 314 268 95, Fax. +49 30 314 268 93

Abstract — In this paper, a new empirical model for SiC MESFET is proposed. A commercial packaged high power MESFET device (CREE CRF24010) is adopted for the model development. Both hot and cold bias condition measurements are performed to derive equations and parameters. Cold FET technique is used to extract the parasitic extrinsic elements whereas the bias-dependent model elements are extracted analytically in multiple bias points. Nonlinear equations for the bias dependent elements are derived, too. A single stage amplifier is designed to verify the derived model. Simulation and measurement results of small and large signal behavior are compared. A good agreement is obtained.

I. INTRODUCTION

The strong interest in silicon carbide (SiC) MESFET technology for RF and power applications (due to its high breakdown voltage, high saturation velocity and high thermal conductivity) leads to a high demand for an accurate nonlinear RF model primarily for power amplifier design [1]. The investigations in this paper start with small-signal characterization and modeling using cold FET and normal bias point operation. Measurements in the pinch-off and forward bias regime have been applied for the development of the linear model [2]-[4]. This approach leads to physically based model elements well defined and determinable with high accuracy and reliability. DC and multi bias S-parameter characterization have been considered towards large signal modeling. Sec. II introduces an accurate small signal parameter extraction procedure. Extrinsic parameters in both pinch-off and forward bias modes are extracted using cold FET technique whereas the intrinsic parameters are being extracted analytically at multiple bias points. The large signal SiC-MESFET model which can accurately predict both, power and linearity performance of the device is derived in Sec. III. Improved formulas for the bias dependence of the nonlinear elements are given. Simulated and measured inter-modulation distortion of a single stage wideband power amplifier are presented and compared in Sec. III. Finally, Sec. IV summarizes the work.

II. SMALL SIGNAL MODELING

Fig.1 shows the most common MESFET model at normal bias conditions. The model can be divided into two sections: the extrinsic element section and the intrinsic part. The extrinsic section includes all extrinsic elements: C_{PG} , C_{PD} , C_{PGD} , R_G , R_D , R_S , L_G , L_D , and L_S . The

intrinsic section includes all the intrinsic elements: C_{gs} , R_{gs} , C_{gd} , R_{gd} , g_m , τ , R_{ds} , and C_{ds} . The resistance R_{gd} has been added to ensure smooth transition from the symmetric cold model ($V_{ds} = 0$) to operating points in the saturation region [4]. Although this element has little effect on the performance of the model and many authors neglect it, it was included here to present full analytical expressions.

The main concept of the extraction process, which is employed by many researchers, is to remove the extrinsic element section from the measurements to end up with Y-parameters of the intrinsic section. The Y-parameters are the most convenient parameters since the intrinsic section exhibits PI topology. The simple analytical expressions of the Y-parameters can be used to calculate the intrinsic elements.

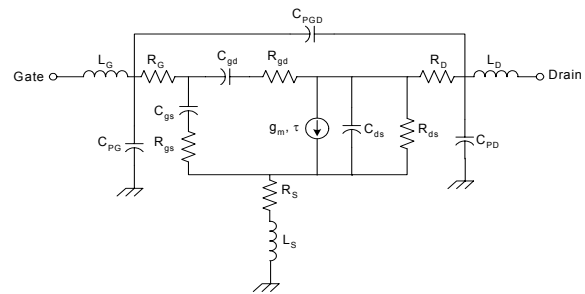


Fig. 1. Small signal equivalent circuit of SiC MESFET.

A. Cold FET Measurements at Pinch-off

In this section, we will provide a much simpler analysis of a SiC MESFET model at a gate-source bias voltage less than or equal to the pinch-off voltage V_p of the device. At the same time zero drain-source bias voltage is applied. Under these conditions, the topology (not the elements) shown in Fig. 1 becomes symmetric, consequently, the associated analysis becomes much easier. At and below pinch-off voltage, the channel is strongly depleted and therefore it exhibits high resistance between drain and source. As a result, the dominant element between drain and source is C_{ds} .

There is no current flowing from drain to source and g_m should be equal to zero. At pinch-off voltage, both gate-source and gate-drain junctions are deeply reverse biased which leads to small values of C_{gs} and C_{gd} . Therefore, both R_{gs} and R_{gd} can be neglected. Fig. 2 shows the simplified model of the considered SiC MESFET at pinch-off state with $V_{ds} = 0$ and $V_{GS} = V_p$ [2].

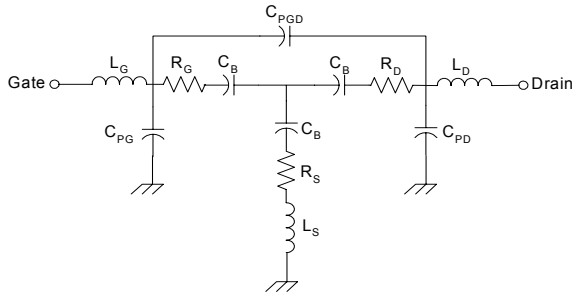


Fig. 2. Simplified equivalent circuit at pinch-off mode.

From the equivalent circuit in Fig. 2 the analytical equations for the Y-parameters can be determined very easily. As a first order approach, the parasitic series resistances and inductances can be neglected at low frequencies. Then, the imaginary part of the Y-parameters can be given as

$$\text{Im}(Y_{11}) = \omega (C_{PG} + 2C_B/3 + C_{PGD}) \quad (1-a)$$

$$\text{Im}(Y_{12}) = \omega (-C_B/3 - C_{PGD}) \quad (1-b)$$

$$\text{Im}(Y_{22}) = \omega (C_{PD} + 2C_B/3 + C_{PGD}) \quad (1-c)$$

Unfortunately, direct analytical extraction of all parasitic capacitances from Eq. (1) is not possible. Therefore, we neglect C_{PGD} for the first time and determine C_{PG} and C_{PD} as starting values for a subsequent optimization process. During this procedure, the square of the difference between simulated and measured Y-parameters is minimized which leads to a very robust and reliable determination of all parasitic capacitance element values. Fig. 3 shows both the simulated and measured imaginary parts of Y-parameters. A good agreement can be observed. The measurements show at the high frequency end a slight deviation of a straight line which is a consequence of neglecting the parasitic series elements.

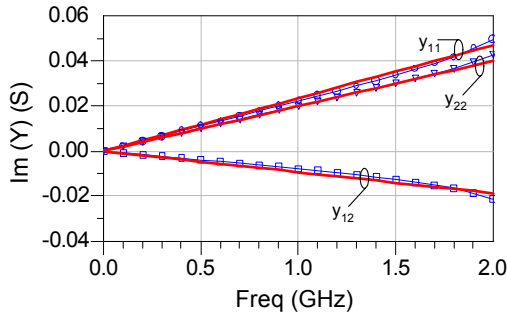


Fig. 3. Simulated (solid lines) and measured imaginary part of Y-parameters after optimization process.

B. Cold FET Measurements at Forward Bias

This case occurs when $V_{DS} = 0$ and $I_G \gg 0$. Under this bias condition, the intrinsic FET is a nonlinear symmetric device with respect to drain source. The intrinsic FET model is replaced by an appropriate diode model that depends on the external gate voltage. Fig. 4 shows the simplified circuit diagram in this mode. The parasitic inductances L_G , L_D and L_S as well as the parasitic resistances R_G , R_S and R_D can be determined. At this bias point, the following simplified equations given in [3], are valid:

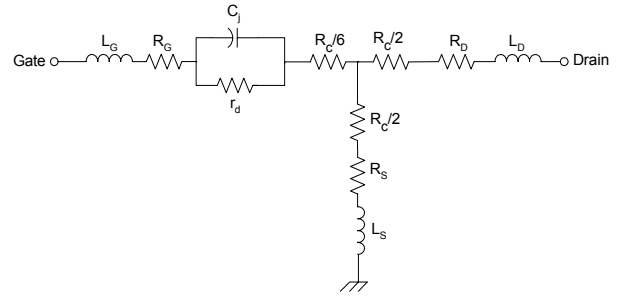


Fig. 4. Simplified equivalent circuit at forward bias.

$$Z_{11} = R_G + R_S + \frac{R_C}{3} + \frac{r_d}{1 + (\omega r_d c_j)^2} + j\omega \left(L_G + L_S - \frac{c_j r_d^2}{1 + (\omega r_d c_j)^2} \right) \quad (2-a)$$

$$Z_{12} = Z_{21} = R_S + \frac{R_C}{2} + j\omega L_S \quad (2-b)$$

$$Z_{22} = R_D + R_C + R_S + j\omega (L_S + L_D) \quad (2-c)$$

If the gate current increases, r_d decreases and c_j increases and the exponential behavior of r_d versus V_{gs} is the dominant factor; consequently the term $(r_d c_j \omega)$ tends to zero. In this case, we have:

$$r_d = \frac{nkT}{q} \frac{1}{I_g} \quad (3)$$

For such gate current, the capacitive effect of the gate disappears:

$$\text{Re}(Z_{11}) = f\left(\frac{1}{I_g}\right) = R_G + R_S + \frac{R_C}{3} + r_d = R_G + R_S + \frac{R_C}{3} + \frac{nkT}{q} \frac{1}{I_g} \quad (4)$$

$$\text{Im}(Z_{11}) = f\left(\frac{1}{I_g^2}\right) = \omega (L_G + L_S - c_j r_d^2) = \omega \left(L_G + L_S - c_j \left(\frac{nkT}{q} \right)^2 \frac{1}{I_g^2} \right) \quad (5)$$

The source inductance L_S can be simply determined from the imaginary part of Z_{12} or Z_{21} . The drain inductance L_D can be then obtained from the equation

$$L_D = \frac{1}{\omega} (Z_{22} - Z_{12}) \quad (6)$$

For the extraction of the parasitic gate inductance L_G , the linear behavior of Eq. (5) against $(1/I_g^2)$ is used. Rearranging (5) as $Y = mX + C$, where

$$m = -c_j \left(\frac{nkT}{q} \right)^2 \quad \text{and} \quad C = L_G + L_S \quad (7)$$

leads to a straight line for $\text{Im}(Z_{11})$ versus $1/I_g^2$. Using linear regression technique, the sum of L_S and L_G can be extracted from the intercept point of the extrapolated straight line with the ordinary axis as shown in Fig. 5. At this point, $1/I_g^2$ tends to infinity.

Similar to the case of the parasitic inductances, the linear relation between $\text{Re}(Z_{11})$ versus $1/I_g$ has to be used additionally for the determination of the four unknowns R_G , R_S , R_D and R_C . At different gate currents, the real part of Z_{11} is plotted versus $(1/I_g)$ and linear regression is applied again. Extrapolation of the regression line and determination of the intercept point with the ordinary axis delivers $R_G + R_S + R_C/3$. Fig. 6 depicts the

dependency of $\text{Re}(Z_{11})$ on the inverse gate current ($1/I_g$). From the intercept point of the regression line with the ordinary axis the sum of the extrinsic resistances R_G , R_S and the channel resistance $R_C/3$ can be extracted.

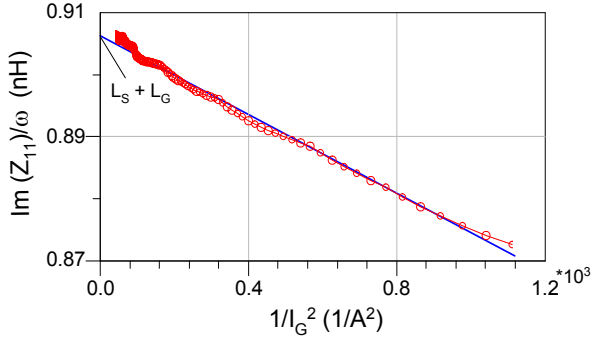


Fig. 5. Dependency of $\text{Im}(Z_{11})$ versus $(1/I_g^2)$, circles: measurements

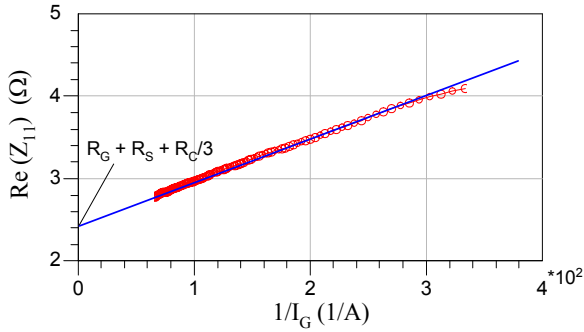


Fig. 6. Dependency of $\text{Re}(Z_{11})$ on gate current ($1/I_g$), circles: measurements

Dependency of channel resistance R_C on gate-source voltage (V_{GS}) has been studied. Hower and Bechtel [3] have estimated the sum of $R_D + R_S$ at $V_{DS} = 0$. Equation (4) is first modified as

$$\text{Re}(Z_{22}) = R_S + R_D + \frac{R_{C0}}{1 - \sqrt{\frac{V_{GS} - V_{bi}}{V_p}}} \quad (8)$$

The procedure of Hower and Bechtel is accomplished as follows:

1. The measured S-parameters (converted into Z-parameters) are given at different V_{GS} values between V_p and V_{bi} .
2. The real parts of Z_{22} are then plotted versus frequency and the average values for different V_{GS} values were extracted. These values are plotted versus V_{GS} , as shown in Fig. 7.

The difference between R_D and R_S , which is defined by many authors as ΔR_{DS} can be simply obtained by solving equations (2-a, 2-b) resulting in

$$\Delta R_{DS} = |R_D - R_S| = |\text{Re}(Z_{22}) - 2 \text{Re}(Z_{12})| \quad (9)$$

Table 1 summarizes all extracted values for the parasitic SiC MESFET equivalent circuit elements. Extraction of the intrinsic small signal elements is based on the procedure given by Dambrine *et al* [4].

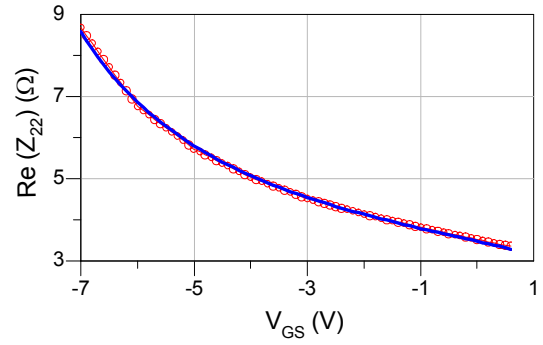


Fig. 7. Extracted values of $\text{Re}(Z_{22})$ as a function of V_{GS} ($V_p < V_{GS} < V_{bi}$; circles: measured, solid line: fitted).

C_{PG}	1 (pF)	R_G	1.2 Ω	L_G	0.88 (nH)
C_{PD}	0.6 (pF)	R_D	1.6 Ω	L_D	1 (nH)
C_{PGD}	0.2 (pF)	R_S	1 Ω	L_S	11 (pH)

Table 1. Extracted extrinsic SiC MESFET equivalent circuit elements.

C. SiC MESFET Intrinsic Parameters Extraction

These elements are determined from measured small signal parameters (as a function of frequency) at a given operating point V_{gs} , V_{ds} . All extracted elements are average values over all measured frequency points.

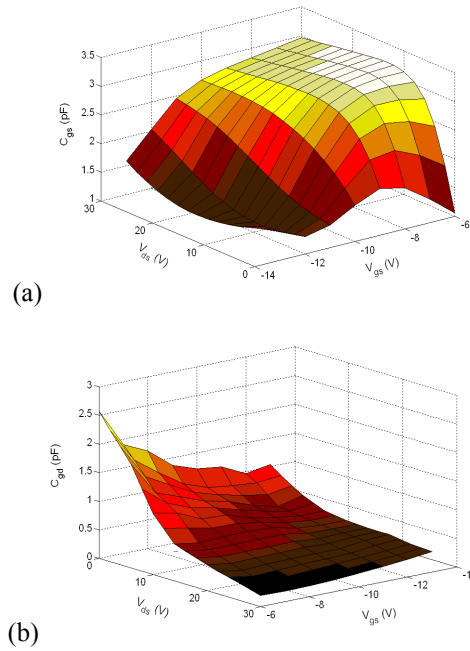


Fig. 8. Modeled C_{gs} (a) and C_{gd} (b) as a function of internal control voltages.

To get accurate and reliable values of the intrinsic parameters, the extracted values may be considered as starting values within an optimization process using Advanced Design System (ADS) of Agilent. The extraction technique was applied to the measured S-parameters of the device at multiple V_{gs} and V_{ds} bias voltages. Fig. 8 shows the extracted nonlinear gate-source and gate-drain capacitances at multiple bias points, respectively.

Simulated small signal gain and stability factor of a designed ultra broadband amplifier [6] based on this model are compared with measurements in Fig. 9. A good agreement has been obtained. The slight differences in Fig. 9 are primarily caused by the insufficient modeling of the losses of SMD-devices, matching and bias networks.

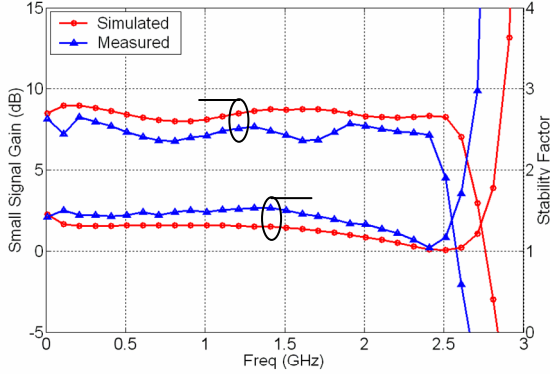


Fig. 9. Simulated and measured small signal gain and stability factor of the designed amplifier.

III. LARGE SIGNAL MODELING

The nonlinear model proposed by Angelov *et al* [5] is improved in this paper to meet both conductive and capacitance nonlinear behavior. The bias dependent parameter P_{1m} of the power series ψ is modified to fit the measured DC nonlinearities:

$$P_{1m} = P_{1s} (1 + B_1 / \cosh(B_2 V_{ds}^2)), \quad B_1 = P_{10} / P_{1s} \quad (10)$$

where P_{10} , P_{1s} and B_2 are constants. On the other hand, the capacitive model given in [5] should also be improved to characterize the extracted bias dependent nonlinear capacitances C_{gs} and C_{gd} . An extra formulation is derived to fit the nonlinear drain-source capacitance, C_{ds} . Taking into consideration the charge conversation conditions, the capacitance equations can be written in the following form:

$$C_{gs} = C_{gsp} + C_{gso} (p_0 + \tanh(\psi_1)) (p_1 + \tanh(\psi_2)) \quad (11-a)$$

$$C_{gd} = C_{gdp} + C_{gdo} (p_2 + \tanh(\psi_3)) (p_3 + \tanh(\psi_4)) \quad (11-b)$$

$$C_{ds} = C_{dsp} + C_{dso} (1 + \tanh(\psi_5)) \exp(\psi_6) \quad (11-c)$$

$p_0 \dots p_3$ are constants whereas $\psi_1 \dots \psi_6$ are bias dependent power series. $\psi_1 \dots \psi_4$ are second order approximations as given by [5] while ψ_5 and ψ_6 are considered first order bias dependent series in the following form:

$$\psi_5 = 1 + p_5 V_{ds} + p_6 V_{gs} \quad (12-a)$$

$$\psi_6 = 1 + p_7 V_{ds} - p_8 V_{gs} \quad (12-b)$$

p_5 , p_6 , p_7 and p_8 are constants. The topology of the large signal SiC-MESFET model is shown in Fig. 10.

Measured and simulated third-order intercept points of the developed single stage SiC amplifier based on the derived model are depicted in Fig. 11 as a sample of harmonic balance simulation using ADS. Typically, the predicted $OIP2$ and $OIP3$ are too optimistic by a few dBm.

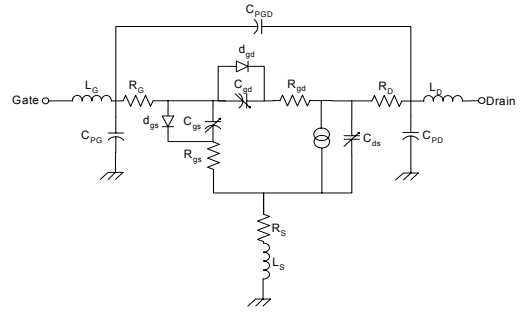


Fig. 10. Large signal model of SiC MESFET.

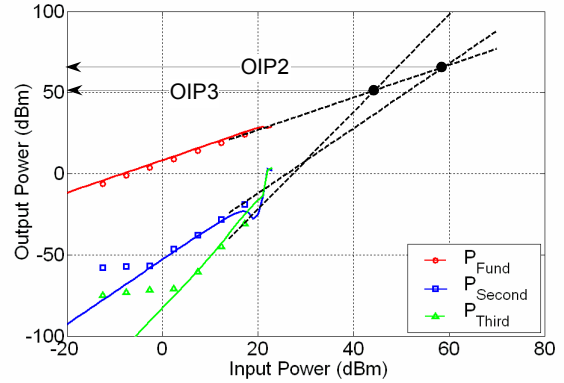


Fig. 11. Measured (symbols) and simulated (solid lines) single stage linearity performance.

IV. CONCLUSION

A new nonlinear SiC MESFET RF-model has been developed. Small signal extrinsic parameters were extracted based on Cold FET technique while the intrinsic parameters were derived analytically at multiple bias points. Towards large signal modeling, an Angelov based model was used as a first step and improved towards SiC MESFETs. Small signal and large signal performances of the derived model were verified. Good agreements between simulated and measured results of designed single stage ultra broadband 5 W amplifier based on this model were achieved.

REFERENCES

- [1] S. T. Allen *et al* "Progress in high power SiC microwave MESFETs," in *1999 IEEE MTT-S Int. Microwave Symp. Dig.*, Vol. 1, Anaheim, CA, June 1999, pp. 321-324.
- [2] P. M. White *et al*, "Improved equivalent circuit for determination of MESFET and HEMT parasitic capacitances from "Cold FET" measurements", *IEEE Microwave and Guided letters*, vol. 3, no. 12, Dec. 1993.
- [3] P. L. Hower *et al*, "Current saturation and small signal characteristics of GaAs field effect transistors", *IEEE Trans. on Electron devices*, vol. 20, March 1973.
- [4] Dambrine *et al*, "A new method for determining the FET small signal equivalent circuit", *IEEE Tans. MTT-S*, vol. 36, no. 7, July 1988.
- [5] I. Angelov *et al*, "An empirical table-based FET model," *IEEE Trans. Microwave Theory and Tech.*, vol. 47, pp. 2350-2357, Dec. 1999.
- [6] A. Sayed, S. von der Mark and G. Boeck, "An ultra wideband power amplifier using SiC MESFETs," in *Proc. 34th European Microwave Conf.*, Amsterdam, Nederland, Oct. 2004.

Key Issues of Compact Models for GaAs Heterojunction Bipolar Transistors

M. Rudolph, R. Doerner

Ferdinand-Braun-Institut für Höchstfrequenztechnik (FBH)

Gustav-Kirchhoff-Str. 4, D-12489 Berlin, Germany, (e-mail: rudolph@fbh-berlin.de)

Abstract—The GaAs-HBT technology nowadays is a standard technology, which is readily available to circuit designers. However, while at least three highly accurate models are available for Si-based HBTs, good models for the GaAs world are rare. This paper highlights the main challenges in the modeling of GaAs-HBTs for circuit design.

I. INTRODUCTION

In recent years, heterobipolar transistors became available in commercial GaAs MMIC technology. Due to their ability to operate at high current densities they are the devices of choice for power amplifiers, e.g. in mobile phones. The lower $1/f$ noise compared to HEMTs also qualifies the devices for oscillator applications. While technology is mature and industry already ships large numbers of HBT-based MMICs, the model development for circuit design lacks behind.

The designer has the choice between about a dozen built-in models for GaAs-based FETs in standard circuit simulators. But for bipolars, most circuit simulators account only for the basic SPICE Gummel-Poon (SGP) model, or additionally for sophisticated models specified for Si-based transistors, like VBIC, MEXTRAM and HICUM.

However, the situation improves. The UCSD model [1] is now available in approximately half a dozen circuit simulators. Moreover, Agilent now provides a dedicated HBT model with its ADS circuit simulation software [2]. This model is based on the UCSD model, with enhancements in order to overcome some critical implementation issues. Finally, also the authors developed a model [3], [4], which can be obtained either as a compiled design kit for ADS or in the highly portable Verilog-A language.

It is the aim of this paper to summarize the model features required to describe the specific behavior of GaAs-based HBTs.

It first is necessary to point out that state-of-the-art GaAs-based HBTs are quite ‘ideal’ devices. Dedicated HBT models, therefore, can be formulated as extensions of the basic SGP model, or even based on a simplified version of it.

1. The semi-insulating substrate prevents parasitic substrate effects that have to be accounted for on silicon.
2. In a state-of-the-art technology, surface or interface related problems such as parasitic currents are negligible.
3. Even thermal runaway can be suppressed by proper emitter feedback or thermal shunt technology.
4. Due to high base doping and high emitter efficiency, Early, Webster, and current crowding effects usually are negligible.
5. Also quasi-saturation usually is not observed.

It remains a quite simple equivalent-circuit topology as shown in Fig. 1.

Due to the mesa structure of the HBTs, the total base-collector junction separates into an active part below the emitter, and a parasitic part under the base contacts. Since the

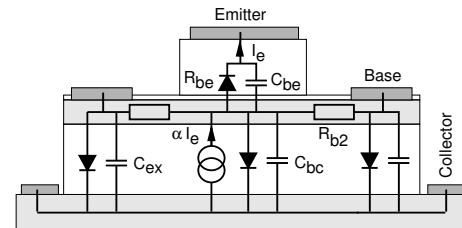


Fig. 1. Schematic cross section of a single finger HBT, with intrinsic T-topology equivalent circuit. The diode symbols represent nonlinear resistors with diode characteristics.

current flows almost vertically from emitter to sub-collector, the parasitic part can be seen as an additional pn diode that is reverse biased in usual operation.

Two effects, however, are most important to simulate HBTs. The first one is self-heating, the second one is the current dependence of the transit frequency, caused by velocity modulation and high current injection into the collector. The latter effect is specific to III-V based HBTs. It has been proven to be an important source of nonlinear distortion [5], [6], and therefore cannot be considered to be negligible. Since the thermal effects are often described in the literature, this point will be reviewed only briefly here, and the paper focuses on modeling of the collector charge.

All examples in this paper are measured on GaInP/GaAs HBTs fabricated on the 4'' process line of the Ferdinand-Braun-Institut [7].

II. THERMAL EFFECTS

Since HBTs are operated usually at high power densities, self-heating plays an important role. Temperature affects the electrical behaviour of an HBT mainly in two ways: Firstly, current gain β decreases almost linearly with increasing temperature. This leads to a decreasing I_C in an output I-V plot with I_B held constant as a parameter, as shown in Fig. 2a for a $3 \times 30 \mu\text{m}^2$ HBT. Secondly, at constant I_B , V_{BE} decreases linearly as temperature is increased, as shown in Fig. 2b. This is caused by the exponential dependence of the base-emitter diode's current on both voltage and temperature.

$$I = I_s e^{V_g/V_{th,0} - V_g/V_{th}} \left(e^{V_{be}/(nV_{th})} - 1 \right) \quad (1)$$

with saturation current I_s , an activation energy $E_g = V_g/q$, the thermal voltage at junction temperature V_{th} and that at an arbitrarily chosen reference temperature $V_{th,0}$, and ideality factor n .

Fig. 3 shows the relevance of a proper thermal model for the normally reverse biased base-collector diode. Since the saturation region is determined by the mutual relationship between the base-emitter and base-collector diodes, both have

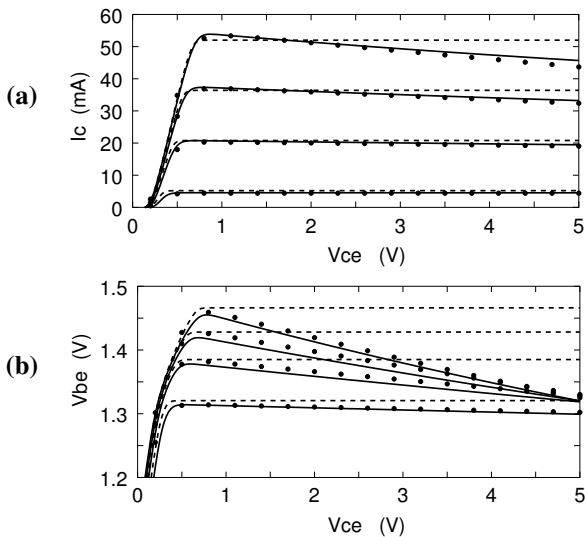


Fig. 2. (a) Output IV curves of HBT with constant I_B , (b) V_{be} measured at same conditions. Symbols: measured $3 \times 30 \mu\text{m}^2$ HBT from FBH foundry. Solid lines: electro-thermal model, broken lines: isothermal model

to be modeled carefully in order to achieve good model performance at low voltages.

From the HBT modeling point of view, a simple thermal model describing the dependence of the internal temperature on the dissipated power by a thermal resistance parameter R_{th} by $\Delta T = P_{diss} R_{th}$, and modeling the slope of β and the diode current's thermal activation energies is sufficient.

Self heating is only caused by slowly varying signals, with time constants usually about $1 \mu\text{s}$. Additionally to the DC parameters discussed so far, temperature has an impact on the base transit time, which increases proportionally with temperature [3]. The temperature dependence of the other parameters, such as the extrinsic resistances, can be neglected without significantly affecting accuracy.

In contrast, accounting for the temperature dependence of many parameters can be expected to be dangerous with respect to the model's numerical stability. Since self-heating introduces a feedback-loop into the model, instability, multiple solutions, or a significantly increased simulation time can be observed. There is a trade-off between model accuracy, or versatility, and numerical robustness. Presumably, this is also the reason why the Agilent HBT model [2] in its first version did not account for thermal effects.

III. CAPACITANCE AND TRANSIT-TIME

The transit frequency f_t of GaAs-based HBTs shows a different bias dependence than in case of silicon. This is shown in Fig. 4. At medium current densities, inside the dashed box, f_t still increases with current, while it decreases with collector-emitter voltage V_{ce} . The current dependence is clearly not caused by the emitter charging time $\tau_{be} = R_{be} C_{be}$, which is observed at lower current densities. The reason for this bias-dependence of f_t is that, beyond a certain critical field-strength, the electron velocity decreases with increasing electric field. Also the profile of the electric field and electron velocity through the collector depletion region plays a role. Already at quite low current densities, the charge of the electrons in the collector depletion region cannot be ne-

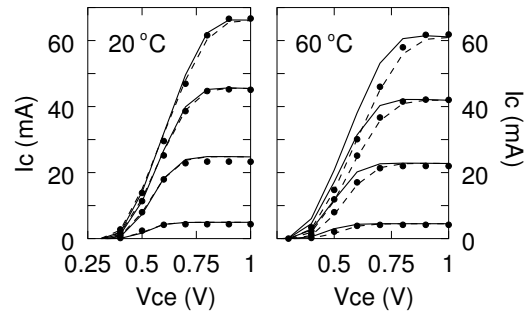


Fig. 3. Output IV curves of HBT with constant I_B , at ambient temperatures 20°C and 60°C . Symbols: measured $3 \times 30 \mu\text{m}^2$ HBT from FBH foundry. Solid lines: electro-thermal model, broken lines: electro-thermal model neglecting temperature dependence of the base-collector current.

glected. This has an impact on transit time τ , as well as on base-collector capacitance C_{bc} [8].

Without going into detail, it has to be stated that the collector transit time dominates the transit frequency. The total transit-time of the device is shown in Fig. 5. The values give the time constant determined for the current gain α of the intrinsic transistor, which is obtained from small-signal parameter extraction. The same effect also alters C_{bc} , as mentioned before. The base-collector capacitance is shown in Fig. 6. At $I_c = 0$, the common depletion capacitance behavior is observed. But, additionally, C_{bc} decreases as I_c increases.

The SGP model does not account for either effect. The transit-time is modeled by a single parameter TF , while the base-collector capacitance is described by the common pn-capacitance formula.

It is the merit of the UCSD model that it put the focus on these effects already ten years ago, even before the devices came to market. At that time, it was not as obvious as today that this is a key feature in HBT modeling. Also a detailed analysis of the effect was published [8].

However, the implementation in the UCSD model has significant drawbacks. The first one is that the transit-times are formulated in the same fashion as in the SGP model. This model uses the time constant of the base-emitter RC branch to describe the time-delay. The parameter TF is multiplied with the forward current I_{cf} , in order to obtain a charge $Q_{f,diff} = TF I_{cf}$. In the UCSD model, however, the transit-time is not constant, but defined as a function of bias and temperature, $T_F(I_{cf}, V_{bc}, T_j)$. Now, this formula is multiplied with the forward current I_{cf} , which then is placed partly at the base-emitter and partly at the base-collector junction. However, the multiplication leads to inconsistency between large- and small-signal model. In order to get back from the large-signal $Q_{f,diff}$ to the small-signal time constant, it is necessary to differentiate:

$$\begin{aligned} \tau_f(I_{cf}, V_{bc}, T_j) &= \frac{\partial Q_{f,diff}}{\partial I_{cf}} = \frac{\partial(T_F I_{cf})}{\partial I_{cf}} \\ &= T_F + \frac{\partial T_F}{\partial I_{cf}} I_{cf} \\ &\neq T_F(I_{cf}, V_{bc}, T_j) \end{aligned} \quad (2)$$

The function still might be able to describe the large- and small-signal behavior of the device. However, parameter extraction is significantly impeded by the fact that the function T_F does not represent the small-signal transit-times.

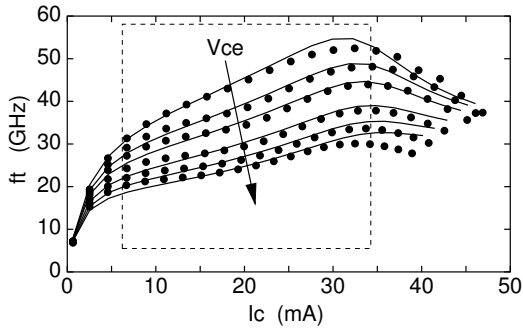


Fig. 4. Typical bias dependence of transit frequency, for $3 \times 30 \mu\text{m}^2$ HBT, Symbols: Measurement, lines: model. $V_{ce} = 1 \dots 5$ V.

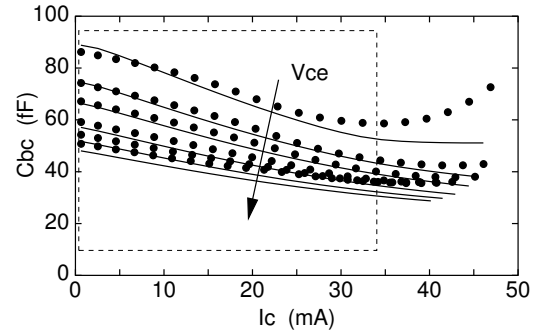


Fig. 6. Typical bias dependence of base-collector capacitance, for $3 \times 30 \mu\text{m}^2$ HBT, Symbols: Measurement, lines: model. $V_{ce} = 1 \dots 5$ V.

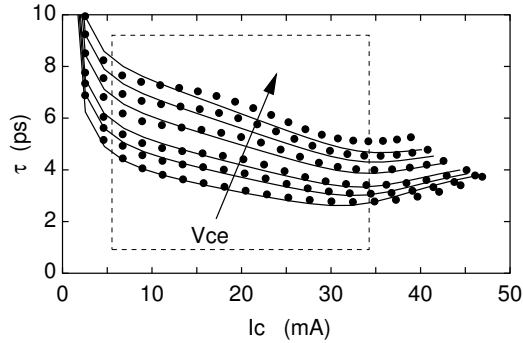


Fig. 5. Typical bias dependence of transit times, for $3 \times 30 \mu\text{m}^2$ HBT, Symbols: Measurement, lines: model. $V_{ce} = 1 \dots 5$ V.

Another problem directly linked with this one is the fact, that there is a second formula that allows to influence the collector capacitance. As seen in Fig. 6, C_{bc} decreases with current. The UCSD model provides a parameter in the formula for the collector charge Q_c to account for this effect on C_{bc} . However, such a definition leads to a transcapacitance C_{tr} :

$$\begin{aligned}
 C_{bc} &= f(V_{bc}, I_c(V_{bc}, V_{be})) \\
 &\Updownarrow \\
 C_{bc} &= f(V_{bc}, V_{be}) \\
 &\Downarrow \\
 Q_c &= \int C_{bc} dV_{bc} = f(V_{bc}, V_{be}) \\
 &\swarrow \searrow \\
 C_{bc} &= \frac{\partial Q_c}{\partial V_{bc}} \quad C_{tr} = \frac{\partial Q_c}{\partial V_{be}}
 \end{aligned}$$

The transcapacitance acts like a voltage-driven current source in parallel with the current source α in the small-signal equivalent circuit, as shown in Fig. 7. Both current sources can be summed and interpreted as the effective current gain α' :

$$\begin{aligned}
 \alpha' &= \frac{\alpha_0 - j\omega C_{tr}/G_{be}}{1 + j\omega \tau_f} \\
 &\approx \frac{\alpha_0}{1 + j\omega(\tau_f + C_{tr}/G_{be})} = \frac{\alpha_0}{1 + j\omega \tau_{eff}} \quad (3)
 \end{aligned}$$

with $\tau_f = R_{be} C_{be}$. The resulting transit-time τ_{eff} is therefore determined by transcapacitance and the time constant τ_f . Consequently, the models of C_{bc} and τ are interdependent. It is not possible to tune one without affecting the other. Additionally, also the definition of $T_F = f(I_{cf}, V_{bc}, T_j)$ yields

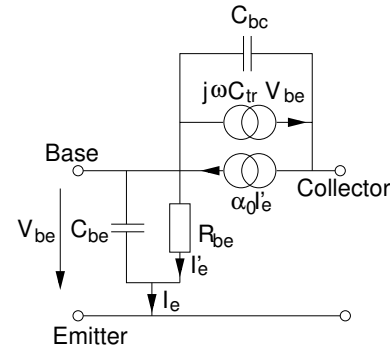


Fig. 7. Generic small-signal equivalent circuit in T-topology. Obtained from large-signal circuit with a base-collector charge source $Q_c = f(V_{be}, V_{bc})$.

a transcapacitance term, since the derivative $\partial T_F / \partial V_{bc}$ exists. Its contribution, too, leads to additional deviation of the large-signal implementation with respect to the small-signal case. Probably these difficulties in the model topology led to the conclusion that even a HBT model that perfectly fits the small-signal parameters is not capable to predict f_t with reasonable accuracy [9].

It was, however, shown that an appropriate charge-function Q_c is capable to describe the bias-dependent part of τ , and C_{bc} as well [4]. This reflects the fact that the collector charge is responsible for both [8]. The small-signal quantities then are obtained from

$$\tau_c = \frac{\partial Q_c}{\partial I_c} \quad C_{bc} = \frac{\partial Q_c}{\partial V_{bc}} \quad (4)$$

With this approach, the small-signal and large-signal implementations are consistent again.

The simulations shown in Figs. 4–6 are obtained with the FBH model. S-parameters were simulated, and then evaluated by the same algorithms as the measured data, in order to get the values. While f_t was extrapolated, C_{bc} and τ were determined by a small-signal parameter extraction algorithm. The formula employed for Q_c is slightly varied compared to the previously published one in [4] in order to gain higher flexibility:

$$\begin{aligned}
 Q_c &= [1 - \tanh(\xi)] \cdot [Q'_c + (1 - X_{J0})C_{\min}V_{bc}] + \\
 &\quad + X_{J0}C_{\min}V_{bc} \quad (5)
 \end{aligned}$$

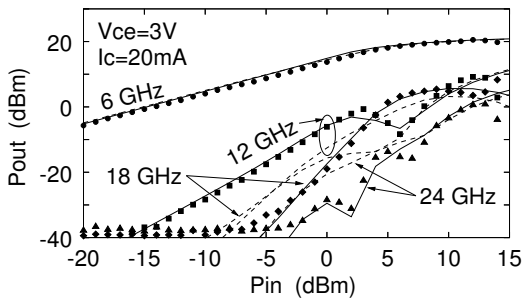


Fig. 8. Power-spectral measurement and simulation of $3 \times 30 \mu\text{m}^2$ HBT. Symbols: Measurement, solid lines: FBH model, broken lines: electro-thermal model neglecting bias-dependence of f_t .

with

$$Q'_c = -(C_{jc0} - C_{\min}) \phi \frac{(1 - V_{bc}/\phi)^{1-m}}{1-m}, \quad (6)$$

$$\xi = \frac{I_c}{2I_0} + \left(\frac{I_c}{2I_0} \right)^{k_{jc}}. \quad (7)$$

with the parameters C_{jc0} , ϕ , m , C_{\min} , I_0 , k_{jc} , and X_{J0} . Compared to the traditional base-collector charge of the SGP model, only four parameters, C_{\min} , I_0 , k_{jc} , and X_{J0} , are introduced. Setting $k_{jc} = 1$ and $X_{J0} = 1$ yields a description as seen in Fig. 6, with C_{bc} decreasing linearly with current, and finally reaching C_{\min} at the current $I_c = I_0$.

The same approach, albeit a different formula, is employed in the Agilent model. Additionally, it allows to distribute the charge Q_c between the base-emitter and base-collector junction.

The reduction of f_t beyond a certain collector current is due to base push-out, which is not specific to GaAs HBTs. Therefore, formulas developed for Si devices can be borrowed, for example from the HICUM model [10], as in the present case.

The relevance of proper modeling of the bias-dependence of the transit-times is not as obvious as in case of the thermal model. In the small-signal and weakly nonlinear case, matching and output power can be simulated for a specific bias condition by tuning the capacitance and transit-time coefficients. This approach might even work in nonlinear operation, when mean values of transit-times and capacitances are used in the model. However, it has been shown that it will not be possible to predict the linearity with such a simplified model [5], [6].

Fig. 8 gives an example. Shown is a power-spectral measurement. The input signal at 6 GHz is continuously increased in power, and the harmonics generated by the HBT are measured. The measurement starts under quasi-linear condition, and finally the HBT is driven into compression. The measurement was performed in a 50Ω environment, which is highly mismatched for the present device. The bias point was determined by a constant base-emitter voltage V_{be} , therefore the collector current was allowed to increase due to self-biasing as the device is driven into saturation. This happens for the measurement shown for input powers larger than -5 dBm, leading to a maximum current beyond 60 mA at 15 dBm.

The simulations shown are performed with the FBH model (solid lines) and a simplified one that accounts for the self-heating, but keeps the transit-time constant (broken lines). Consequently, C_{bc} is independent of I_c in the latter case. It can be observed that the fundamental output power is predicted well for both models. The simulations are comparable,

since the same also holds true with respect to self-heating and self-biasing effects. However, as long as the device is not saturated, the simplified model grossly overestimates the linearity of the transistor. As also shown in [5] by intermodulation analysis, it also can be seen here that the bias-dependence of Q_c is the main contributor to the device's nonlinearities.

IV. CONCLUSIONS

In this paper, the most critical features of compact models for GaAs-based HBTs are identified, and model implementation issues are discussed. The background is that today GaAs-HBT processes are available in standard technologies. Therefore, designers need a reliable model in order to do circuit design. However, there are, to the author's knowledge, only three models open to the public, which are available only in a few circuit simulators.

Two effects are identified to be of prime importance.

The first one is self-heating. This is obvious already from optical inspection of output IV-curves. However, the attempt to describe the thermal properties in great detail can yield a model with poor convergence properties. Therefore, it is shown that a relatively simple model, accounting only for the temperature-dependence of the diode currents and the forward transit-time, is sufficient.

The second effect is the bias-dependence of transit-times and base-collector capacitance. It determines the linearity of the device and must therefore be accounted for in the model. Since this effect is specific to GaAs based HBTs, it makes dedicated models necessary. An improper implementation can impair the meaning of model formulas and parameters, leading to differences between the small- and large-signal model. Therefore, this paper presents how the effect can be implemented consistently.

REFERENCES

- [1] UCSD HBT Model Equations, available at <http://hbt.ucsd.edu/>
- [2] Agilent Technologies, "A Nonlinear Circuit Simulation Model for GaAs And InP Heterojunction Bipolar Transistors" *Microwave Journal*, pp. 126-134 Dec. 2003.
- [3] M. Rudolph, R. Doerner, K. Beilenhoff, P. Heymann, "Scalable GaInP/GaAs HBT Large-Signal Model," *IEEE Trans. Microwave Theory Tech.*, vol. 48, pp. 2370 - 2376, Dec. 2000.
- [4] M. Rudolph, R. Doerner, K. Beilenhoff, P. Heymann, "Unified Model for Collector Charge in Heterojunction Bipolar Transistors," *IEEE Trans. Microwave Theory Tech.*, vol. 50, pp. 1747 - 1751, July 2002. The FBH HBT Model is available at <http://www.fbh-berlin.de/modeling.html>
- [5] M. Iwamoto, P. M. Asbeck, T. S. Low, C. P. Hutchinson, J. B. Scott, A. Cognata, X. Qin, L. H. Camnitz, D. C. D'Avanzo, "Linearity Characteristics of GaAs HBTs and the Influence of Collector Design," *IEEE Trans. Microwave Theory Tech.*, vol. 48, pp. 2377 - 2388, Dec. 2000.
- [6] M. Rudolph, R. Doerner, "Large-Signal HBT Model Requirements to Predict Nonlinear Behaviour" in *IEEE MTT-S Int. Microwave Symp. Dig.*, 2004, 43 - 46.
- [7] J. Hilsenbeck, F. Lenk, W. Heinrich J. Würfl, "Low Phase Noise MMIC VCOs for Ka-Band Applications with Improved GaInP/GaAs-HBT Technology," in *IEEE GaAs-IC Symp. Dig.*, 2003, 223 - 226.
- [8] L.H. Camnitz, N. Moll, "An Analysis of the Behaviour of Microwave Heterostructure Bipolar Transistors," in *Compound Semiconductor Transistors - Physics and Technology*, S. Tiwari, Ed. New York: IEEE Press, 1993, pp. 21 - 45.
- [9] J. Scott, "Nonlinear III-V HBT Compact Models: Do We Have What We Want?" in *IEEE MTT-S Int. Microwave Symp. Dig.*, 2001, 663 - 666.
- [10] M. Schröter, T.-Y. Lee, "Physics-Based Minority Charge and Transit Time Modeling for Bipolar Transistors," *IEEE Trans. Electron Dev.*, vol. 46, pp. 288 - 300, Feb. 1999.

Large Signal Bias Dependent Modeling of Avalanche Photodiode Based on Pulsed RF Measurement

A. Ghose, B. Bunz, J. Weide and G. Kompa

Dept. of High Frequency Engineering, University of Kassel, Wilhelmshöher Allee 73, D-34121, Kassel, Germany,
Tel: +49-561 804 6528, Fax: +49-561 804 6529, Email: ag@hfm.e-technik.uni-kassel.de

Abstract — This work presents a method for large signal characterization of avalanche photodiode (APD) where measurements were carried out using pulsed RF signal at different DC bias points to extract dispersive parameters of the avalanche photodiode. Pulsed optical excitation on the photodiode were synchronized with the pulsed RF signal using a synchronization circuit and in this way characterization of the photodiode was possible up to 1.3 mW of peak optical power whereas using CW measurement, device heating restricts the characterization up to 0.1 mW of optical input power. A comparison was made between the reflection measurements using CW RF excitation and APD model based on pulsed RF signal to establish the present approach for large signal characterization of the photodiode.

Index Terms — Pulse measurement, reflection coefficient measurement, scattering parameters, nonlinearities.

I. INTRODUCTION

High speed optoelectronic devices are of growing interest for its use in analog to digital communication systems and also for industrial and medical sensor applications. Reliability of the observed high speed (pico second) pulses are often affected by the phenomena of jitter, time base distortion, impedance mismatches distortion and waveform or nonlinearity distortion. An accurate nonlinear model of the optoelectronic devices are needed which can be implemented in commercial CAD software to predict and correct the device behavior in such cases. In this work we will consider the Si avalanche photodiode (Silicon Sensor GmbH) as DUT. For microwave characterization of photodiodes it is necessary to regard the photodiode as two-port network with optical port related to electrical port through a nonlinear transfer function according to [1]. Nonlinear dispersive electrical parameters of the large signal photodiode model and the parasitic are extracted by RF reflection measurement through its electrical port. Now, using CW RF measurement together with CW optical input, device thermal resistance increases and restricts the measurement range up to even moderate power optical power of 0.1 mW. Therefore pulsed RF characterization was performed to extract the dispersive parameters of the device at isothermal conditions and in this way characterization was possible up to 1.3 mW of pulsed optical power (average <0.065 mW). During pulsed RF measurement optical input is pulsed and synchronized with the square wave RF envelope through an external synchronization circuit [2]. Resistive electrothermal parameters were extracted using quasi-DC measurements

with pulsed optical input at different DC bias conditions [3].

To extract device parameters at isothermal conditions pulsed RF measurements have been reported for large signal characterization of power microwave devices using pulsed vector network analyzers. Here in this alternative approach, large signal model of the avalanche photodiode was transformed to small signal linear model and Microwave Transition Analyzer (HP 70820A) was used in pulsed RF mode to measure small signal vector reflection coefficients of the avalanche photodiode.

II. AVALANCHE PHOTODIODE MODEL

Nonlinear model of the photodiode was reported by Stolze et al. [1]. The large signal model is divided into two parts, one is optoelectronic converter and electrical equivalent circuit part as shown in Fig. 1. Optical to electrical conversion can be represented with the matrix relation given below.

$$\begin{bmatrix} P_{opt,refl}(f) \\ b_2 / \sqrt{Z_1} \end{bmatrix} = \begin{bmatrix} R_{opt} & 0 \\ S & R_{el} \end{bmatrix} \cdot \begin{bmatrix} P_{opt}(f) \\ a_2 / \sqrt{Z_1} \end{bmatrix} \quad (1)$$

Where P_{opt} is the optical power which penetrates the surface of the photodiode and a small amount will be reflected, denoted as $P_{opt, refl}$ due to complex reflection coefficient R_{opt} . S characterizes the optical to electrical conversion, which is extracted by impulse measurement using a laser excitation of rise time 12 ps. The electrical to optical conversion can be ignored, as the photodiode does not radiate optical power during electrical stimulus. The reflection of the electrical wave (a_2 being incident and b_2 being reflected wave) is characterized by the electrical complex reflection coefficient R_{el} .

It is necessary to transform the large signal model to small signal linear model, which can be readily modeled by commercial circuit simulators (e.g. Advanced Design System, Agilent Technologies) and based on small signal scattering parameter measurement. Optoelectronic converter is the transfer function matrix defined by three measurable time constants (t_1, t_2, t_3). I_0 represents the internal current source of the diode, Q represents the charge source for photodiode conductance and Q_1 is the charge source, which accounts for delay in the avalanche multiplication. G_r is the conductance for diode dark current. C_m and C_p are parasitic capacitance of the diode

bond pad. R_m and L_m are bond wire resistance and inductance respectively. The large signal model describes the nonlinear dependence of internal photocurrent I_2 to the diode current I_1 by the current source I_0 and charge source Q . R_s being the internal series resistance of the photodiode is a nonlinear element dependent on I_2 and V_2 .

In Fig. 2 linearized photodiode model is shown with charge sources replaced by diode conductance G_0 and diode capacitance C_0 . Delay charge source is represented by time constant of the series R_1 and C_1 . Control current I_1 is delayed by the delay coefficient t_{p1} . Electrothermal parameters were measured by quasi-DC I-V characteristic of the diode and dispersive parameters were extracted by pulsed RF measurements.

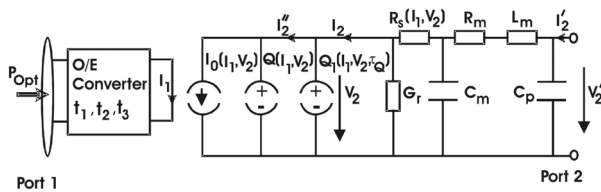


Fig. 1. Large signal model of the avalanche photodiode

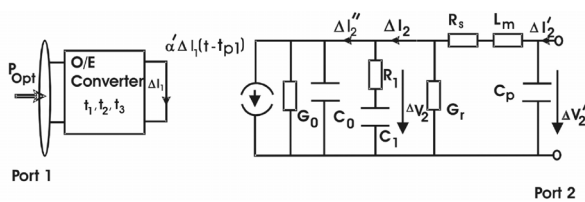


Fig. 2. Derived small signal model of the avalanche photodiode [2]

III. MEASUREMENT TECHNIQUE

In Fig. 3 Schematic of the principle of the used pulsed RF measurement is shown. Optical pulses are synchronized with the pulse envelope of the RF excitation. A safe limit of about 1 micro second was left to perform the measurement at relatively ripple free region of the pulse.

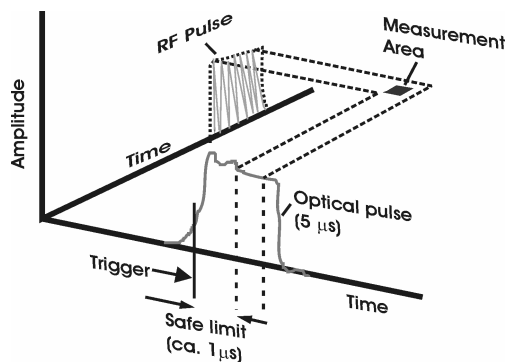


Fig. 3. Pulsed (RF and opt.) measurement principle

The set up was built around Microwave Transition Analyzer (HP70820A) with synthesized signal generator (HP 8360B) as shown in Fig. 4. RF pulses were provided by synthesized source through bias decouple circuit followed by a directional coupler and 23 dB attenuator to the DUT (avalanche photodiode). Reflected pulses were coupled from the forward RF signal by the directional coupler (3 dB). Low frequency components of the electrical pulse from the photodiode (5 micro second pulse width, 5 kHz PRF) were filtered by the bias decoupling circuit. Pulsed RF measurement was carried out from 1 GHz to 30 GHz. Synthesized sweeper was controlled by Microwave Transition Analyzer in the pulsed RF mode. Optical stimulus on the photodiode was synchronized with a synchronization circuit having adjustable amplitude, pulse width and delay. TTL pulses from the Microwave Transition Analyzer trigger the input of the synchronization circuit and output pulses from the synchronization circuit drives a low noise voltage to current converter (LDX3620) for the laser diode (LQ6-780-4a/OECA). Optical power was measured at the output of the optical fiber. Establishment of the measurement point over the pulse is done by placing the microwave transition analyzer in time sweep mode and then a time delay is set between the trigger point (leading edge of the pulse) and measurement point. Measurement point was set near the end of the pulse to avoid overshoot of the pulse [5]. The vector reflection measurement of the device at a specific input pulsed RF power yields a set of raw measurement vectors. S parameters of the directional coupler were measured separately using a HP8510 vector network analyzer and vector error correction was done of the measured reflection coefficients.

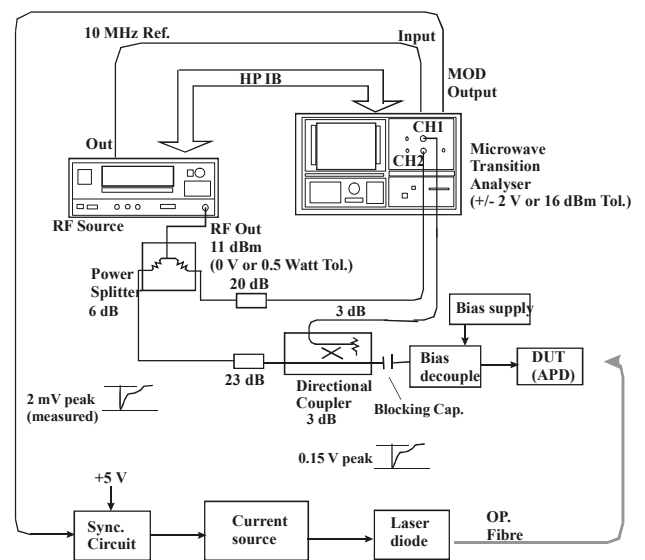


Fig. 4. Set up for pulsed RF characterization

IV. EXTRACTED PARAMETERS

Intrinsic parameters of the photodiode were extracted after de-embedding the extrinsic parameters L_m and C_p from the measured Y parameters. Extrinsic parameters are bias independent and also independent of optical power.

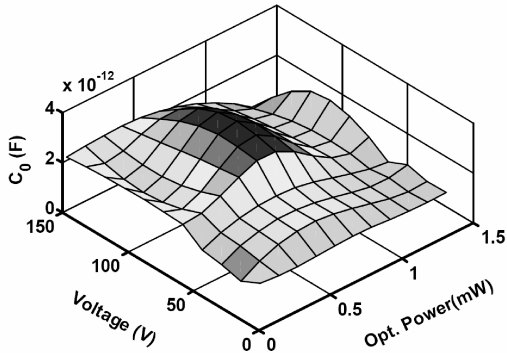


Fig. 5. Measured photodiode capacitance using pulsed RF signal and its variation with optical power and bias voltage

L_m is found to be 276 nH and C_p , the pad capacitance is 0.020 pF. Fig. 5 shows the extracted nonlinear diode capacitance with change in bias voltage and optical conditions using above method of pulsed RF measurement. From Fig. 5, it is evident that the diode capacitance is nearly 2 pF over the bias region of 50 Volt to 148 Volt and a slight decrease to 1 pF is noticed at optical power higher than 1 mW. This is because of increased diode conductance at the reverse bias in the breakdown region (measured breakdown voltage 148.5 V) and optical power of more than 1 mW.

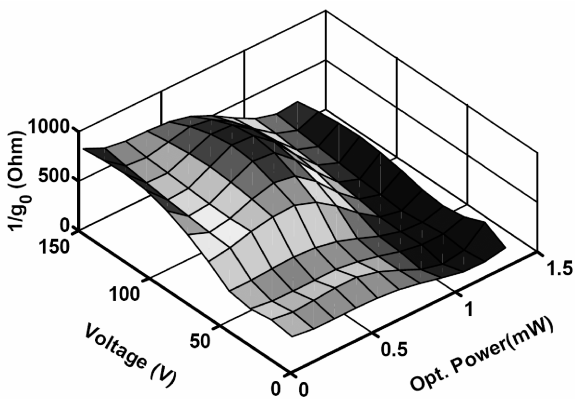


Fig. 6. Measured (pulsed RF) diode conductance

Fig. 6, $[1/g_0]_{RF}$ (diode conductance: g_0) shows slight monotonous variation at the bias region of 50 Volt to 100 Volt and rapid decrease is noticed with optical power input of more than 1 mW. This indicates a decreased gain and simultaneously increased thermal resistance of the device [3].

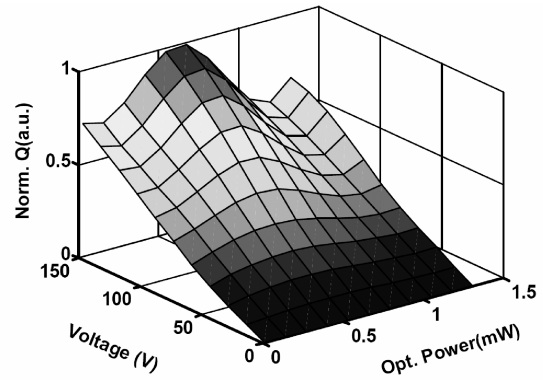


Fig. 7. Extracted Q from pulsed RF measurement

In Fig. 7, charge stored at the depletion region of the photodiode is plotted with photodiode bias and optical power input. Charge stored in the depletion region increases steadily with increase in optical power and bias voltage. Slight variation is noticed at break down region of more than 100 volt due to variation of capacitance at that region (Fig. 5).

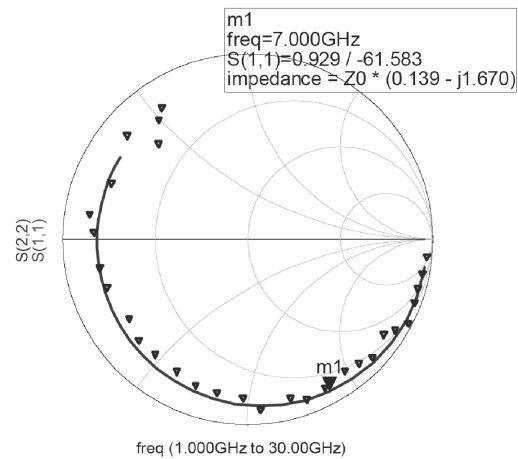


Fig. 8a. Magnitude of measured (triangle) reflection coefficient using Vector Network Analyzer (HP 8510) and modeled (solid) based on pulsed RF measurement

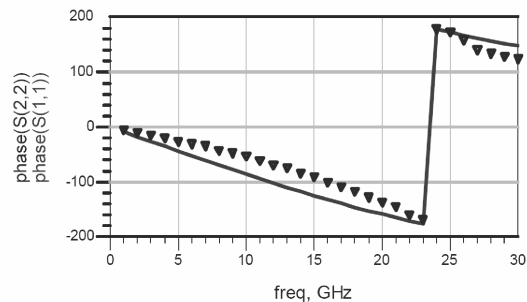


Fig. 8b. Measured phase response of reflection coefficients using Vector Network Analyzer (HP 8510) (triangle) and modeled (solid) based on pulsed RF measurement

Fig. 8a and Fig. 8b shows the comparison of measured reflection coefficient using Vector Network Analyzer (HP 8510) [4] and modeled photodiode based on pulsed RF measurement at the similar optical conditions. Slight deviation (Fig. 8a) is observed after 28 GHz due to increased loss at the bias network.

V. CONCLUSION

It was confirmed that the pulsed RF measurement, which is generally used for power microwave devices to measure low frequency dispersion etc. can also be used for optoelectronic devices like avalanche photodiode to characterize optical power dependent nonlinearities of the photodiode. Avalanche gain is very sensitive to device temperature, therefore present approach allows near isothermal characterization of the device. It was possible to characterize the device up to 1.3 mW of peak optical power, which covers the dynamics of the signal at which it is exposed in practical use e.g. pulsed laser radar system. Photodiode model was implemented by a harmonic balance simulator and modeled reflection coefficients were compared with standard reflection measurement using CW RF signal by Vector Network Analyzer for confirmation at the low optical power level.

ACKNOWLEDGEMENT

This work was performed within the European research project (INTAS 51615009). Financial support is greatly acknowledged.

REFERENCES

- [1] Stolze, A., and Kompa, G., "Nonlinear modeling of dispersive photodiodes based on frequency and time-domain measurements", *26th European microwave conference. Proc., Prague, Czech Republ.*, pp. 379-382, September 9-12, 1996.
- [2] Ghose, A., Bunz, B., Weide, J., and Kompa, G., "Measurement of nonlinear dispersive parameters of avalanche photodiode using pulsed RF signal and quasi-DC optical stimulus," *34th European Microwave Conf., Proc., Amsterdam, The Netherlands*, pp. 925-928, November 11-15, 2004.
- [3] Ghose, A., and Kompa, G., "Electrothermal parameter extraction of avalanche photodiode using quasi-DC optical pulses," *10th IEEE International Symposium on Electron Devices for Microwave and Optoelectronic Applications, Proc., Manchester, UK*, pp. 69-74, November 18-19, 2002.
- [4] Ghose, A., Ring, M., and Kompa, G., "Simultaneous gain and noise matching of a wideband optical receiver front end," *2003 Asia Pacific Microwave Conference, Proc., Seoul Korea*, pp. 431-434, November 4-7, 2003.
- [5] Baylis, C. P., and Dunleavy, L. P., "Performing and analyzing pulsed current-voltage measurements," *High Frequency Electronics*, pp. 64-69, May 2004.

Session 7b

Field Theory & EMC

Full-Wave Simulations and Extraction of Effective Material Parameters for Left-Handed Metamaterials

Rolf Schuhmann, Grzegorz Lubkowski, and Thomas Weiland

Technische Universität Darmstadt, Institut für Theorie Elektromagnetischer Felder,
Schlossgartenstraße 8, 64289 Darmstadt, Germany, (+49) 6151 16 4661, schuhmann@temf.tu-darmstadt.de

Abstract — The simulation of Left-Handed Metamaterials (LHM) with grid-based methods is proposed, with a focus on the calculation of microscopic fields in each array element and the subsequent extraction of effective material parameters. The fields in single cells of an LHM array are determined using either an eigenvalue formulation with periodic boundaries or a multi-port model in time domain. A comparison of different techniques to extract effective material parameters from the simulated field solutions shows that a careful choice of parameters in this extraction process is mandatory. Finally a macroscopic simulation of the famous LHM wedge experiment is presented.

Key words: Left-Handed Metamaterials, Finite Integration Technique, Material Averaging

I. INTRODUCTION

In contrary to standard materials occurring in nature, so-called ‘Left-Handed Metamaterials’ (LHM) show simultaneously a negative permeability and permittivity within a certain frequency range. Some of the surprising properties of such LHM include the left-handed system out of electric and magnetic field and the wave vector (hence their name), or the reversal of signs in Snell’s law. Fig. 1 shows a famous concept of LHM – the Split Ring Resonator (SRR), which was first proposed in [1] and first measured in a wedge experiment in [2]. It consists of periodic metallic structures, which are used to control the electromagnetic properties on a macroscopic scale.



Fig. 1. Left-Handed Metamaterial: Array of metallic Split Ring Resonators (SRR) and wires.

We discuss some approaches to model such LHM by 3D electromagnetic field simulation, with a focus on the accurate analysis of the basic LHM properties rather than on specific applications. This involves the geometric modeling of the LHM structures with CAD methods, where we apply the Finite Integration Technique (FIT, [3,4]) as a general and highly accurate volume-grid based method. Since most realizations of LHM structures are periodic arrays, we have to solve a two-scale problem: On the small, microscopic scale the local fields in the SRR structure are governed by the geometric details within each array element. The desired left-handed waves effects, however, are related to macroscopic waves with wavelengths on a larger scale (typically by more than one order of magnitude), and thus are a property of the complete array. The transition between these two regimes is given by the so-called effective material coefficients [1], the accurate and robust evaluation of which is the main goal of this contribution.

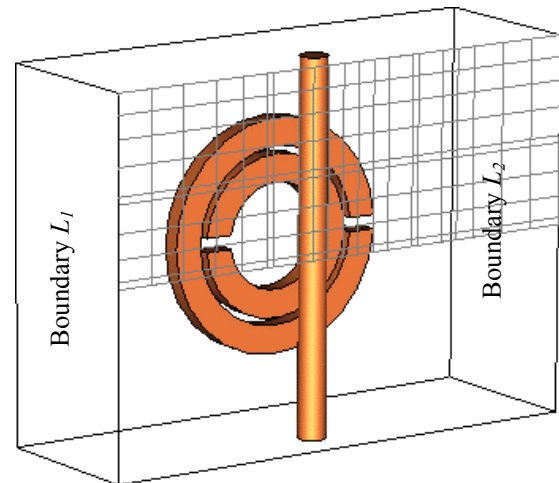


Fig. 2. Simulation model of one element of the array and computational grid. The propagation direction of the macroscopic waves is given by boundaries L_1 and L_2 .

II. MICROSCOPIC MODELING

We restrict our analysis to only a few or even one single element of the array (Fig. 2) which can be modeled using a computational grid with a moderate number of mesh cells (typically some 10,000 cells at a spatial resolution of min. 20 mesh lines per microscopic wavelength). Note that the circular shape of the SRR is

accurately represented in an Cartesian computational mesh using the advanced modeling strategies of FIT which are implemented in a commercial software tool [4]. As a first approximation, the transversal terminations of this single-cell model are set to closed boundary conditions (perfect electric or magnetic conducting – PEC, or PMC, respectively). For the longitudinal dependency (boundaries L_1 and L_2 in Fig. 2) either periodic boundaries can be applied leading to an eigenvalue problem, or a multi-port analysis can be performed in time or frequency domain. In all simulations so far material and radiation losses are neglected.

A. Eigenmode Simulations with Periodic Boundaries

The periodic boundary condition establishes a fixed, pre-determined phase relation between the two longitudinal boundaries, which defines the phase shift and thus (together with the cell size) the wavelength of the macroscopic wave in the array:

$$\vec{E}(L_2) = \vec{E}(L_1) \cdot e^{-j\varphi} \Rightarrow k = \frac{\varphi}{|L_2 - L_1|} \quad (1)$$

Since there is no other excitation, this approach leads to a complex Hermitian eigenvalue formulation. Solving it several times for the unknown eigenfrequencies yields a number of modes, each depending on the phase shift φ . Finally, we obtain so-called dispersion curves describing the relation between frequency and wave number of the macroscopic wave [5], as well as the (microscopic) field patterns within the cell for each eigensolution.

B. Multi-port Analysis

Alternatively, we can reinterpret the single cell model as a two-port system, where now the longitudinal boundary planes L_1 and L_2 define the input and output ports of a standard S-parameter calculation [3,6]. For the transversal boundaries chosen as discussed above, the fundamental mode of each port is a plane-wave like TEM mode, but there is also a possibly large number of higher port modes with cutoff-frequencies above the frequency range of interest. Neglecting all these modes is another simplification of the analysis, but the extension to a multi-mode representation of each port is straightforward. (In current investigations we found that a number of 5 modes at each port is sufficient in this case.)

As a benefit, we can perform an S-parameter analysis in time domain to obtain broadband results from one single simulation run. The result is the complete set of scattering parameters as well as a number of field solutions (using so-called DFT-monitors [4]), which are related to the excitation of the structure by an incoming wave at one of the ports. To construct a periodic solution, comparable to the eigenmode approach above, these field patterns have to be properly superposed to meet the requirement

$$b_2 = a_1 \cdot e^{-j\varphi}, \quad b_1 = a_2 \cdot e^{+j\varphi}, \quad (2a)$$

where a_1, a_2 and b_1, b_2 are the amplitudes of incoming and outgoing waves at ports L_1, L_2 , respectively, and

$$\begin{pmatrix} b_1 \\ b_2 \end{pmatrix} = \mathbf{S} \begin{pmatrix} a_1 \\ a_2 \end{pmatrix}, \quad \mathbf{S} = \begin{pmatrix} S_{11} & S_{12} \\ S_{21} & S_{22} \end{pmatrix} \quad (2b)$$

with the scattering matrix \mathbf{S} obtained from the field simulation. Since the phase angle φ in (2a) is also a result of this post-processing step, the dispersion curves discussed above can also be calculated from this method.

An even more efficient variant of a modal approach, adapted to the special requirements of this project, has been proposed in [6] and produces equivalent results. It is based on the fact that the microscopic fields in the SRR are in strong resonance and dominated by one (or a small number of) eigenmodes of the structure. After the electric fields and the eigenfrequencies of these modes have been computed once (for closed boundaries), they can be combined with the TEM field patterns at the ports, yielding the S-parameters and fields for the open structure (e.g. with periodic excitation) with an arbitrary resolution of the frequency axis.

C. Extraction of Effective Material Parameters

As the final post-processing step after the three-dimensional field simulation, effective material parameters can be extracted.

Again, two alternative approaches are possible: First, with a full-wave field solution at hand, we can easily average field components along ‘characteristic’ lines and facets of the cell as proposed in [1,5],

$$\begin{aligned} \langle E_i \rangle &= \frac{1}{d} \int \vec{E} \cdot d\vec{x}_i \\ \langle D_i \rangle &= \frac{1}{S} \int \varepsilon_o \vec{E} \cdot d\vec{s}_i \end{aligned} \Rightarrow \varepsilon_{eff}^{i,j} = \frac{\langle D_i \rangle}{\langle E_j \rangle} \quad (3)$$

and analogously for the magnetic field components and the effective permeability. Here, the basis must be the periodic field solution as constructed before either in the eigenvalue simulation or in the multi-port analysis.

Simulation results show that care must be taken in this homogenization process to have the proper choice of the coordinates of the averaging lines and planes involved. Typically the integration path d for the field quantities is one edge of the array’s unit cell, and the integration area S for the flux quantities is chosen as one outer face of the cell. It turns out, that especially for the permittivity (which depends on the periodic system of wires) the results are very sensitive to these and some other parameters. Additionally, this approach requires a correction step, if (like given here) the ratio between the two scales (microscopic dimensions and macroscopic wavelength) is only one order of magnitude: Whereas the line integral in (3) is evaluated at one specific phase value (e.g. $\varphi=0$ if the left boundary L_1 is chosen), the area integral includes a specific range of phase values (the full phase shift as specified in the periodic boundary approach). This phase error can lead to considerable quantitative and even qualitative deviations – especially in the frequency range where the resonance effects take

place and the material parameters are changing rapidly in frequency.

In a second strategy, following the idea in [5], we can extract effective parameters also from other ‘global’ quantities such as the dispersion curves of the eigenmode analysis or the S-parameter of the time domain analysis in combination with the wave impedances at the port. At first sight, this approach seems to be the more reliable one, since it is these global quantities which refer directly to the searched quantities of the macroscopic model. However, the numerical results in the next section show that also these ‘global’ methods exhibit a certain sensitivity on the chosen parameters.

III. NUMERICAL RESULTS

A. Effective Material Parameters

Some results of the simulations described above are shown in Fig. 3 (dispersion curve: resonance frequencies as function of phase angle in periodic boundaries) and Fig. 4,5 (effective permeability of the SRR structure after material averaging).

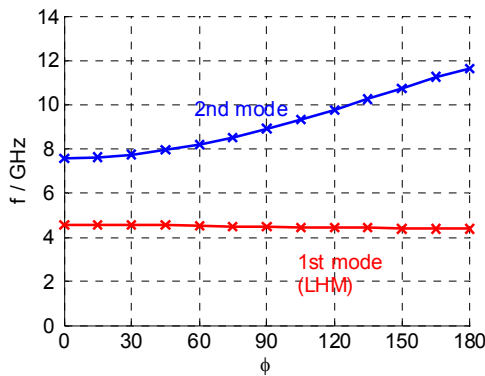


Fig. 3. Dispersion diagram from eigenmode analysis with periodic boundary conditions: The first mode (negative slope) shows left-handed behavior.

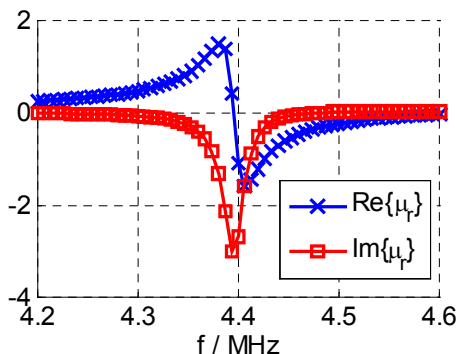


Fig. 4. Result from material averaging: Complex permeability in SRR with negative real parts for some frequencies.

From both curves we can exhibit the desired left-handed behavior for the medium under investigation: The dispersion curve of the 1st mode in Fig. 3 shows a

negative slope, which is a hint for its negative phase velocity. In the permeability curve in Fig. 4 we can see a frequency range with negative real part of μ_r , which together with the negative permittivity (not shown here) also results in the LHM properties of this medium.

A result plot showing a typical comparison between the different extraction approaches is shown in Fig. 5, again for the case of an effective permeability (real part only). One of the curves has been calculated by the described field averaging process, the other curves origin from two different ‘global’ approaches (more details will be given in the conference presentation). It is obvious that only the qualitative behavior is in good agreement, whereas the deviation between the alternative methods (also between the two global ones) is still unsatisfactory. (Imagine to extract the frequency band of LHM behavior from these curves.) This had to be expected due to the fact that different approximations have been made – such as neglecting higher (attenuated) port modes in the time domain approach.

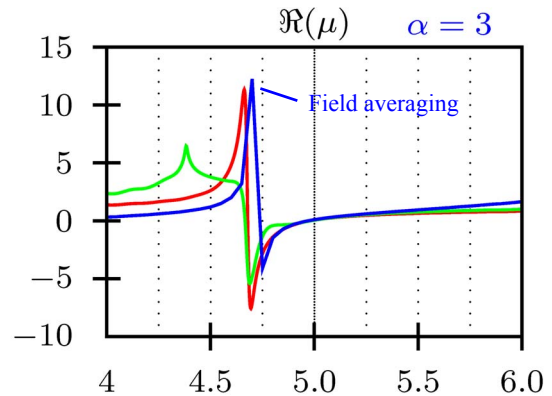


Fig. 5. Effective permeability of an SRR-Wire medium (slightly different geometry), calculated by field averaging and two ‘global’ approaches.

B. Macroscopic Simulation

Finally Fig. 6 shows a first application of the extracted material parameters. In a macroscopic simulation the complete array of SRR/wire cells has been replaced by a homogenized medium with dispersive material characteristics. Such media can be simulated within the Finite Integration Technique using special techniques in time domain, including material models and time integration schemes for Lorentz- and Drude-type dispersion characteristics [7]. Note that a simulation in frequency domain with (constant) negative material parameters may lead to a non-causal model.

The setup of the simulation is analogous to the experiment performed in [2]: A plane wave hits a prism-shaped wedge made of an LHM medium, and the angle of refraction of the transmitted wave is observed.

The first simulation (Fig. 6a) is for validation purpose only: With a standard material (teflon) the wave shows the expected positive angle of refraction at the second interface between the media (wave travels from left to right). In the second simulation (Fig. 6b) the teflon is replaced by the LHM material (in macroscopic modeling

technique). Clearly the angle of refraction is now negative which is the expected consequence of the simultaneously negative permittivity and permeability at this specific frequency. Additionally, in both cases the reduction of the wavelength in the medium can be observed.

Comparing both simulations, a typical shortcoming of the LHM becomes obvious, affecting both simulation and application: Since the SRR shows a strong resonant behavior at the frequency of interest, the simulation needs many periods to establish a steady state field solution. Some parasitic effects (like back-scattering from the boundaries) had to be suppressed in the visualization by a logarithmic scaling of the electric field strength. In practice, the corresponding problems are the small usable bandwidth as well as the possibly high dielectric loss due to the large local field strengths near the SRR.

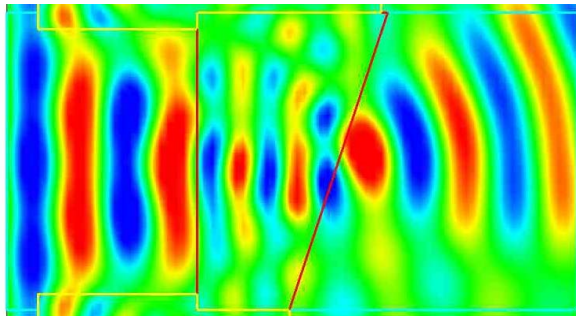


Fig. 6a. Macroscopic simulation using the setup of the experiment in [2]. First case (validation) with a prism-shaped wedge made of a standard material (teflon). The plot (electric field strength for a wave traveling from left to right) shows the expected refraction behavior.

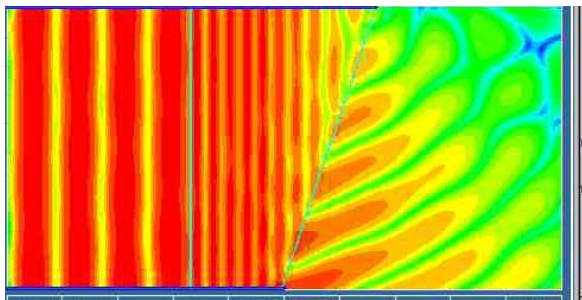


Fig. 6b. Second case: Wedge made of LHM material, simulated using dispersive material models. (Electric field strength, logarithmically scaled). The sign in Snell's law is reversed.

IV. CONCLUSION AND DISCUSSION

The analysis of LHM can be nicely performed with 3D full-wave field simulation of single elements of the array. Whereas the field calculation itself is not critical using modern simulation techniques, the extraction of effective

material parameters is still a difficult task. The comparison of the results of different methods show that the parameters of each approach must be carefully chosen to obtain reliable results.

However, such effective material parameters are essential for the design of LHM-based applications, since for larger arrays the microscopic modeling of the geometric details becomes infeasible. As an example for such an application the simulation of the famous wedge experiment from [2] has been presented. Here the LHM is represented by homogenized dispersive material models and some of the postulated LHM properties can be nicely verified.

The next steps in our research will be devoted to a more robust extraction process for the effective material parameters using the field averaging process. Here also some more physical effects need to be incorporated in the simulation such as dielectric and radiation losses or the coupling of the fields in the unit cell to its neighbors. Finally a number of alternative concepts for LHM has been proposed during the last years covering a variety of frequency bands, and a rigorous field-based analysis and optimization of their properties is still a challenge.

ACKNOWLEDGEMENT

The work of G. Lubkowski is supported by DFG (GRK 1037/1-04).

REFERENCES

- [1] J.B. Pendry, A.J. Holden, D.J. Robbins, W.J. Stewart, "Magnetism from Conductors and Enhanced Nonlinear Phenomena," *IEEE Transactions on Microwave Theory and Techniques*, vol. 47, no. 11, pp. 2075-2084, November 1999.
- [2] R.A. Shelby, D.R. Smith, S. Schultz, "Experimental Verification of a Negative Index of Refraction," *Science*, vol. 292, no. 6, pp. 77-79, April 2001.
- [3] T. Weiland, "Time Domain Electromagnetic Field Computation with Finite Difference Methods," *International Journal of Numerical Modelling, Electronic Networks, Devices and Fields*, vol. 9, pp. 295-319, 1996.
- [4] CST Microwave Studio™: Info at www.cst.de.
- [5] D.R. Smith, D.C. Vier, N. Kroll, S. Schultz, "Direct Calculation of Permeability and Permittivity for a Left-Handed Metamaterial," *Applied Physics Letters*, vol. 77, no. 14, pp. 2246-2248, 2000.
- [6] R. Schuhmann, T. Weiland, "Efficient Calculation of Effective Material Parameters in Metamaterials Using FDTD and a Modal Approach," in *Digest of the IEEE International Microwave Symposium (IMS)*, vol. 3, Seattle, USA, June 2002, pp. 2037-2040.
- [7] S. Gutschling, H. Krüger, T. Weiland, "Time Domain Simulation of Dispersive Media with the Finite Integration Technique," *International Journal of Numerical Modelling, Electronic Networks, Devices and Fields*, vol. 13, no. 4, pp. 329-348, 2000.

Appropriate Wavelets with Compact Support for the Compression of FDTD Calculated Electromagnetic Fields

W. Bilgic, A. Rennings, P. Waldow

Duisburg-Essen University, Department of Engineering (ATE), Bismarckstr. 81, D-47048 Duisburg, Germany,
Tel: +49-203-379-2812, E-Mail: wbilgic@ate.uni-duisburg.de

Abstract — In this paper an investigation on appropriate wavelets with compact support to compress FDTD calculated electromagnetic fields is presented. It turned out that the filter of the used discrete wavelet transform does not need to be as complex as for example the filters used in the image compression standard JPEG 2000. The reason for that is the fact, that in general the distribution of an electromagnetic field is smoother than some sampled image. Additionally, images are two-dimensional data whereas the fields are three-dimensional, including low energy regions with nearly no field strength.

I. INTRODUCTION

Currently, we are developing a multi-scale simulation technique based on a wavelet-transformed finite-difference time-domain scheme (WT-FDTD). In this approach the linear FDTD update equations are transformed by using a discrete wavelet transform (DWT). By neglecting small wavelet coefficients the electromagnetic field is represented in an efficient multi-resolution manner [1]. Some general questions occur concerning the type of the transform, the choice of the wavelet and the number of scales in each direction. In Fig. 1 the structure of two well-known types of wavelet-transforms are shown.

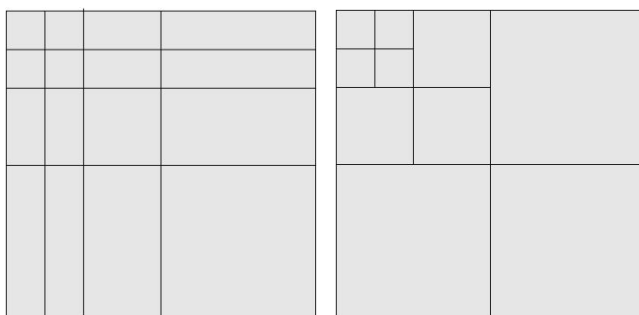


Fig. 1: Type of transform: tensor based (left) and isotropic transformation (right) both with four resolution levels

The two different types have advantages and also disadvantages. The tensor based one can be used with different number of scales in each direction as depicted in Fig. 2 (left) – an important feature for our objective. But there are a lot of different sub-scales and a so-called mixture of scales (some of the sub-scales have another shape than the original domain – here quadratic). The

isotropic one carries out what is called a pure multi-scale analysis (all sub-scales have the shape of the original). A novel approach has been chosen by us. In our approach basically the isotropic one is chosen, but as depicted in Fig. 2 (right) a different number of scales in each direction is possible. Only in the low pass scales in the left upper corner we have the mentioned mixture of scales, but in these resolution levels nearly all wavelet coefficients are updated anyway.

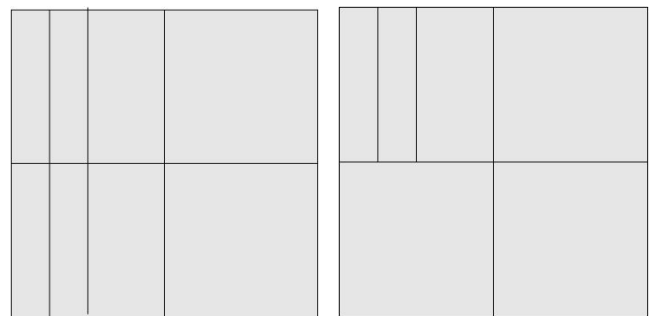


Fig. 2: Type of transform: tensor based (left) and quasi-isotropic transformation (right) with three transformations in x- and just one transform in y-direction

The choice of the wavelet filters is the main topic of this paper. In the field of image processing everybody knows the JPEG 2000 wavelet based compression standard [2, 3]. Within this standard wavelet filters are used to compress images (two-dimensional sampled data). To be more specific, the bi-orthogonal CDF wavelets (Cohen-Daubechies-Feauveau), e.g. the symmetric CDF 9/7 with 9 and 7 filter coefficients, respectively, is used for compression. The question, if a JPEG 2000 wavelet filter used for image compression is a reasonable filter to compress a three-dimensional electromagnetic field calculated by FDTD, should be answered in this paper. In general a digital image has a higher complexity than the distribution of an electromagnetic field. Therefore one may expect, that for the compression of the EM field a shorter filter should be sufficient.

II. ANALYSIS TECHNIQUE

All the wavelets that have been used in our analysis have a compact support and are either orthogonal or bi-orthogonal. The used wavelet type together with the

number of corresponding coefficients of the low and high pass filters are listed in Table 1.

Table 1: Used wavelets	No. of coeffs for low pass filter	No. of coeffs for high pass filter
Haar	2	2
Daubechies 4	4	4
Daubechies 6	6	6
Coiflet 6	6	6
CDF 1/3	2	6
CDF 1/5	2	10
CDF 2/2	3	5
CDF 2/4	3	9
CDF 3/1	4	4
CDF 5/3	5	3

TABLE 1
USED WAVELETS TOGETHER WITH NO. OF COEFFICIENTS

All possible combinations of the above filters have been tested to find the optimum in terms of minimal error for a given compression rate. The number of resolution levels in each direction have been limited to two, i.e. either one or no transformations have been done, since otherwise the analysis would have been last to long. In the future we will try to include a number of up to four different scales in each direction in our testing, maybe with a reduced number of different wavelets.

The analysis of the field data has been carried out by using the following steps:

1. Simulations of several microwave structures (antennas, filters, transitions etc.) have been done with the FDTD method in slightly graded meshes (this mesh is indicated by the lines in the top and right so-called disc bars in the frame of Fig. 6).
2. For each simulation the electric field is saved for approx. 50 equidistant time steps. The saving starts at the beginning of the simulation and ends when the energy is nearly absorbed (20 dB decay of max. energy) by absorbing boundary conditions or by the ports.
3. A copy of all the field distributions is made on the hard disc (HDD). Such a copy is transformed into the wavelet domain (WD) by using the possible combinations of the filters in Table 1.
4. The smallest wavelet coefficients are set to zero until the desired compression rate (30% up to 90%) is reached.
5. A back-transform into the original domain (OD) of the compressed field is carried out.
6. The difference between original data and compressed field (mean square error) is determined.
7. The wavelet filter combination with the lowest error is considered the most suitable choice for the investigated field distribution.

III. ANALYSED EXAMPLES

After explaining the general procedure the results of four chosen examples are presented. The printed patch antenna depicted in Fig. 3 is the first structure. The size of the graded FDTD grid was $33 \times 33 \times 23$ Yee cells. The result of this analysis is summarized in Tab. 2. It turned out that the wavelet combination “HAAR in x, CDF 1/3 in y and no transformation in z-direction” yields the smallest error for a given compression of 70%. That means quite simple (short filter length) wavelets, compared to the ones used in image processing, give the minimal error. Especially the field distribution above the patch in the air region (Fig. 3) is so smooth that a longer transforming filter is not necessary. Since the complexity of our WT-FDTD simulation scheme is highly dependent on the length of the wavelet filters used for the transformation, the above is an encouraging result.

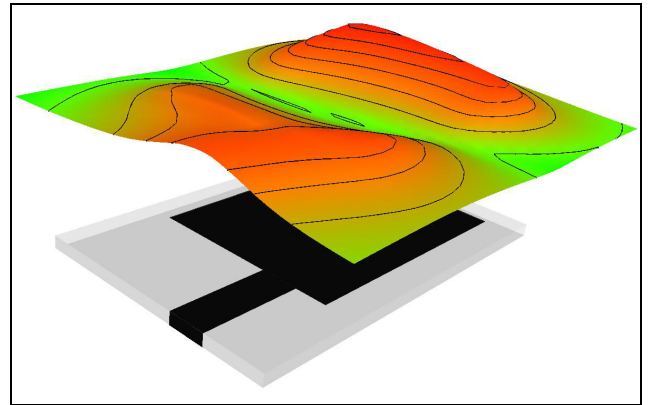


Fig. 3: Patch antenna with electric field 2 mm above the top layer

The second example is also an antenna structure, but not a layered one. To be more specific, it is the thick dipole antenna depicted in Fig. 4. Here the field distribution is so smooth that the combination “HAAR in x, HAAR in y and no transform in z-direction” (along the dipole) yields the minimal error for 70% compression (Tab. 3).

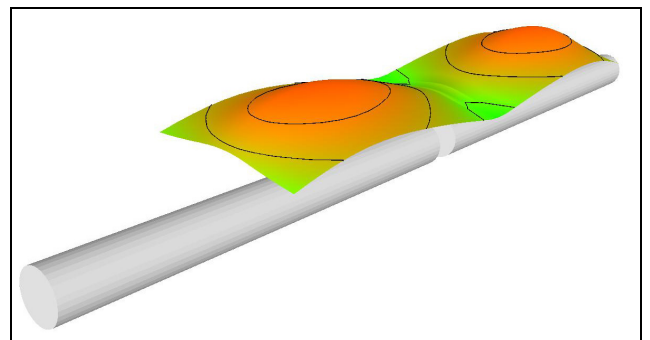


Fig. 4: Thick dipole antenna with electric field above

The third example has a higher complexity. The mobile phone with a folded PIFA depicted in Fig. 5 has been simulated with FDTD and the fields at equidistant time

steps have been analysed with different wavelet combinations. The result presented in Tab. 4 is similar to the dipole one before. The reason for that is the similar near field especially for the lower GSM band, where mainly the printed circuit board (PCB) radiates like a dipole (Fig. 5).

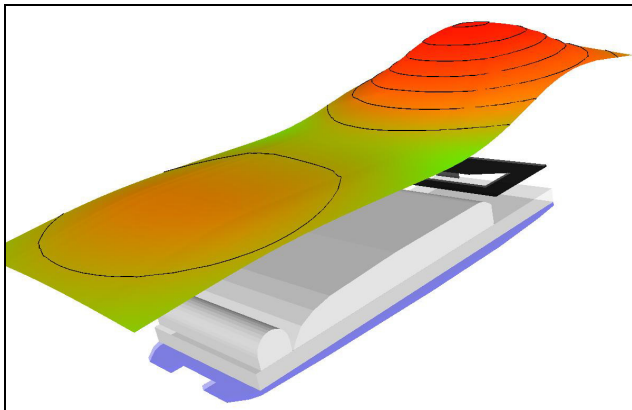


Fig. 5: Mobile phone with folded PIFA and electric near field

Finally, the field around the interdigital capacitor depicted in Fig. 6 has been transformed. The result summarized in Tab. 5 confirms the impression we got from the other three examples.

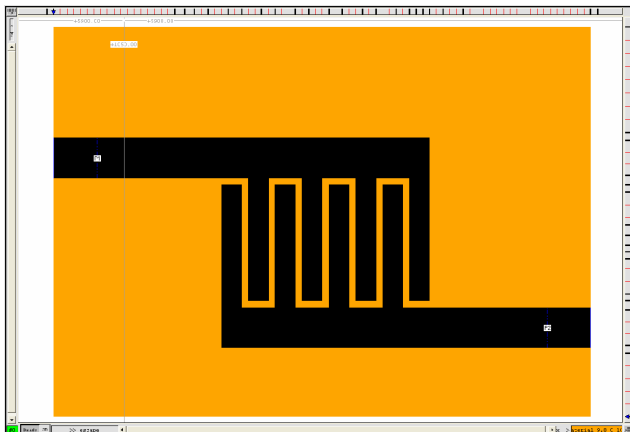


Fig. 6: Interdigital capacitor with graded mesh indicated by the top and right disc bars for the x- and y-direction

IV. CONCLUSION

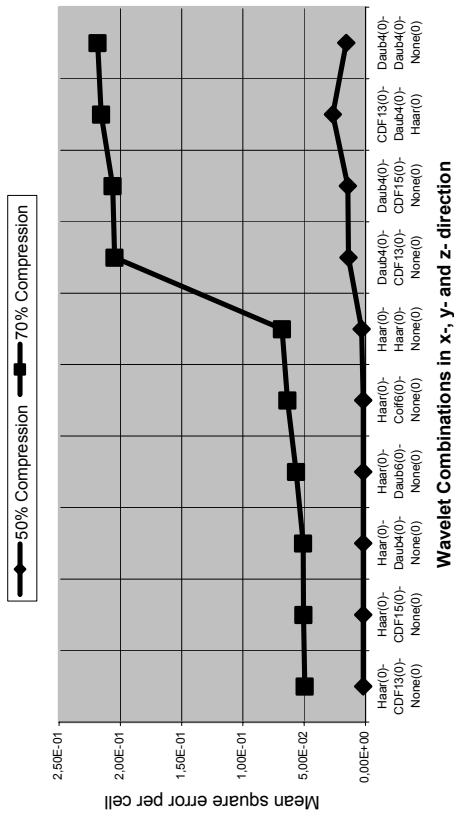
A lot more than the four structures presented in this paper have been investigated by us. All of them support the general idea we got: For the efficient compression of an electromagnetic field calculated by FDTD there is no need for a complex wavelet filter used in JPEG 2000. Wavelets with a shorter filter length, e.g. HAAR, DAUB4, CDF1/3, yield a smaller error for a given compression rate (mostly 50% or 70% in our examples). This statement can currently be made only for two resolution levels. In the future we will investigate also transformations with up to four scales. But in this case we

probably have to reduce the set of possible wavelet filters to a few promising, since otherwise there are just too many combinations possible. Finally we would like to note that on the one hand saving electromagnetic fields to mass storage devices can be compressed by 50% (Tab. 2 to 4) without losing any important field information. And on the other hand by transforming the FDTD algorithm in the wavelet domain one can leave out more than 50% of the wavelet coefficients. This is an encouraging result for future research in the field of wavelet-based field simulation techniques, like the mentioned WT-FDTD scheme.

REFERENCES

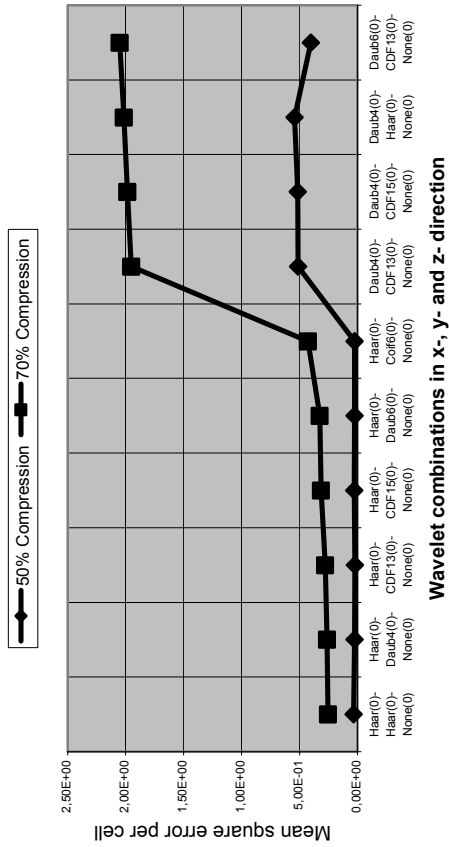
- [1] A. Rennings, F. Wittmann, M. Walter, P. Waldow, I. Wolff, "A wavelet-transformed FDTD scheme with a static multi-resolution grid", *2003 IEEE MTT-S International Microwave Symposium Digest*, Philadelphia, PA, Vol. 3, pages 2089 – 2092, June 8 – 13, 2003.
- [2] ISO/IEC FCD 15444-1, "Information technology – JPEG 2000 Image Coding System.", JPEG 2000 Part I, Final Commite Draft Version 1.0, www.jpeg.org, 16. March 2000.
- [3] ISO/IEC JTC1/SC29/WG11 N1890, "Information technology – JPEG 2000 Image Coding System.", JPEG 2000 Part I, Final Draft International Standard 15444, 25. Sept. 2000.

Patch Antenne (nx,ny,nz) = (34,34,24)



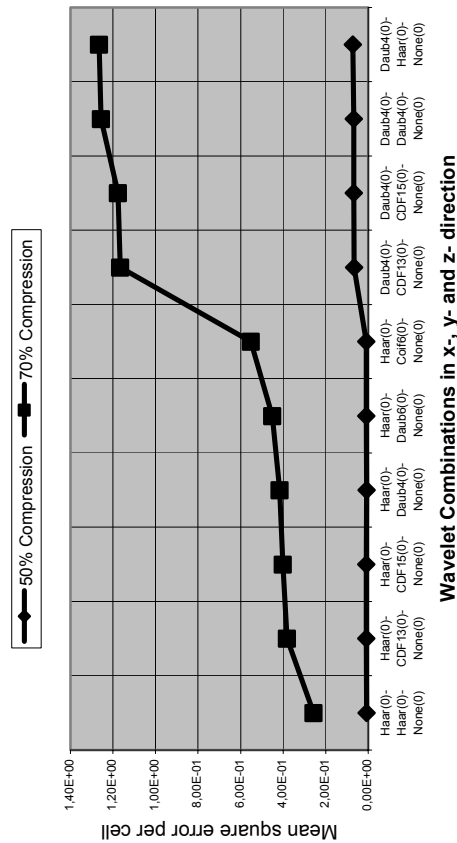
Tab. 2: The ten wavelet combinations yielding lowest error for 70% compression

Thick Dipole Antenna: (nx,ny,nz) = (32,32,64)



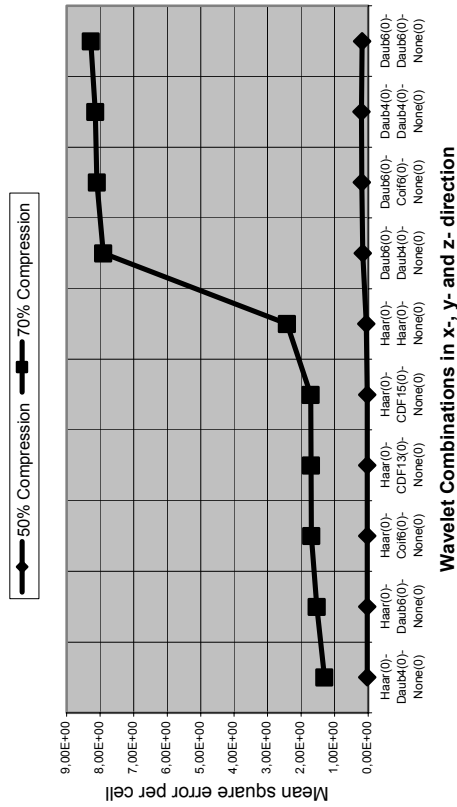
Tab. 3: The ten wavelet combinations yielding lowest error for 70% compression

Mobile with PIFA: (nx,ny,nz) = (54,22,28)



Tab. 4: The ten wavelet combinations yielding lowest error for 70% compression

Interdigital Capacitor: (nx,ny,nz) = (82,36,36)



Tab. 5: The ten wavelet combinations yielding lowest error for 70% compression

Convergence of the Finite Integration Technique on Various Mesh Types

Irina Munteanu¹, Franz Hirtenfelder¹

¹ CST GmbH, Bad Nauheimerstr. 19, 64289 Darmstadt, Germany, Tel. +49-6151-73030

Abstract — The paper presents a comparison between three widely-used mesh types for 3D electromagnetic simulation, in terms of accuracy, computing speed and memory requirements. Although the numerical technique used here was the Finite Integration Technique, the conclusions can be extrapolated to other numerical methods such as FDTD or FEM.

$$\mathbf{C}\hat{\mathbf{e}} = -\frac{d}{dt}\hat{\mathbf{b}}, \quad \tilde{\mathbf{C}}\hat{\mathbf{h}} = \frac{d}{dt}\hat{\mathbf{d}} + \hat{\mathbf{j}} \quad (2)$$

The material property relations become, after discretization:

$$\hat{\mathbf{d}} = \mathbf{M}_\epsilon \hat{\mathbf{e}}; \quad \hat{\mathbf{b}} = \mathbf{M}_\mu \hat{\mathbf{h}}; \quad \hat{\mathbf{j}} = \mathbf{M}_\sigma \hat{\mathbf{e}} + \hat{\mathbf{j}}_s \quad (3)$$

I. THE FINITE INTEGRATION TECHNIQUE

In order to cope with the geometrical and functional diversity of high frequency structures, a variety of methods are used, such as Finite Difference Time Domain – FDTD, finite elements – FEM, integral methods such as the method of moments, etc. Last but not least, the Finite Integration Technique – FIT, first proposed by Weiland in 1977 [1] can be considered as a generalization of the FDTD method and also has tight links to the FEM. It discretizes the integral form of Maxwell's equations (1), rather than the differential one, on a pair of dual interlaced discretization grids.

$$\oint_{\partial A} \vec{E} \cdot d\vec{s} = -\frac{\partial}{\partial t} \iint_A \vec{B} \cdot d\vec{A}; \quad \oint_{\partial \tilde{A}} \vec{H} \cdot d\vec{s} = \iint_{\tilde{A}} \left(\frac{\partial \vec{D}}{\partial t} + \vec{J} \right) \cdot d\vec{A} \quad (1)$$

The degrees of freedom are also of integral type: electrical voltages and magnetic fluxes, defined on the edges and facets of the primary grid, magnetic voltages and electric fluxes, defined on the edges and facets of the secondary grid (Figure 1).

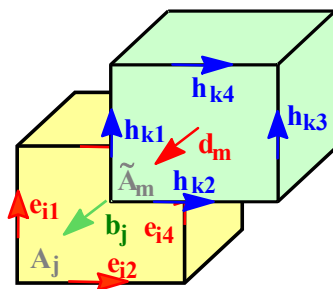


Fig. 1. Dual discretization grids: the grids are interlaced by one-half spatial step. On the primary grid, electric voltages and magnetic fluxes are located.

By writing the integrals on the left sides of (1) as sums of voltages, and by defining the discrete curl-operators (topological matrices) and for the primary and the dual grid respectively, Faraday's and Ampère's Grid Equations become:

Relations (2) have purely topological character and are exact – on a given mesh, while the metric properties and the approximations are contained in the relations (3). This separation has important theoretical, numerical and algorithmic consequences [2].

The FIT can be applied not only to different frequency ranges, from DC to THz, but also on different mesh types (Fig. 2). On Cartesian grids, the time-domain FIT can be shown to be equivalent to FDTD. However, whereas the classical FDTD has the disadvantage of the staircase approximation of complex boundaries, the Perfect Boundary Approximation (PBA)® [3] technique applied in conjunction with FIT maintains all the advantages of the structured Cartesian grids, while allowing an accurate modeling of curved boundaries. Last but not least, the FIT can also be applied on tetrahedral meshes, and it is well known now that the FEM itself (“the” tetrahedron-method) is characterized by equations of the same type, (2) and (3).

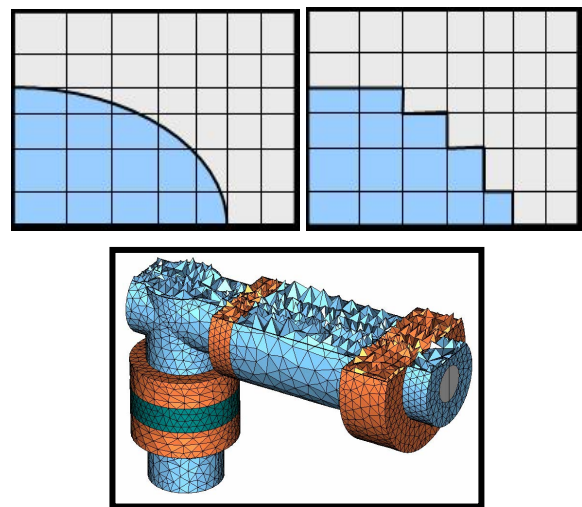


Fig. 2. Examples of PBA, staircase and tetrahedral meshes.

Using the advantage of FIT's applicability on 3 types of meshes, in the present paper we will try to estimate, based on numerical experiments, how much accuracy,

memory efficiency and speed can be expected from a simulation based on each of the 3 meshtypes.

II. NUMERICAL INVESTIGATION OF CONVERGENCE PROPERTIES

To study convergence, the procedure is well-known and simple: discretize the structure with an increasing number of mesh cells, perform the simulation for each mesh, plot the result (e.g. the error, or the computing time) versus the number of mesh cells, in double-logarithmic scales.

All the simulations presented below were performed with the commercial software package CST MICROWAVE STUDIO® [4].

A. Problem with Analytical Solution

The first test case is a very simple one, with known analytic solution: calculation of the line impedance of a coaxial cable.

A short piece of coax with analytical impedance of 50 Ohm has been modelled and discretized with an increasing number of mesh cells. The error of the line impedance vs. number of mesh cells is shown in Fig. 3.

The plot shows that, in order to reach an impedance accuracy of 1%, the number of necessary mesh cells is of about 700 for the PBA mesh, 250 for the tetrahedral mesh, and 38,000 for the staircase mesh, i.e. 50 times more than PBA !

The final meshes are shown in Fig. 4. A strong refinement in the rounded part of the dielectric, especially at the interior contour, can be noticed in the staircase mesh.

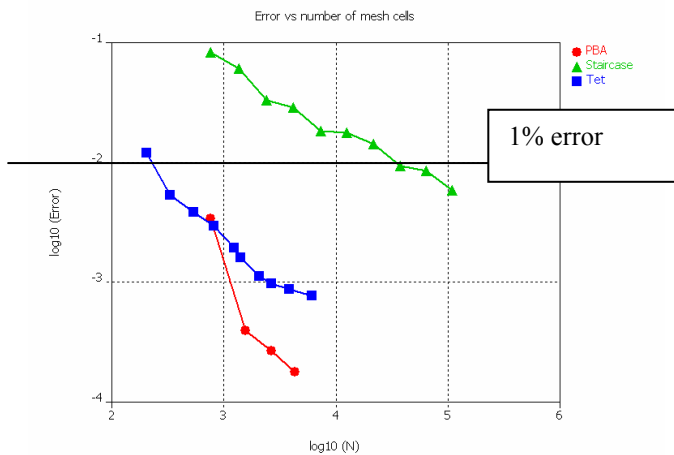


Fig. 3. Error of the line impedance of a coaxial cable vs the number of mesh cells.

B. Coaxial Connector (Moderate-Size Problem)

The second test case was a coaxial connector, shown in Fig. 5. Although the structure looks quite simple, it is a good test vehicle, because it has many rounded parts, both dielectric and metallic, and it exhibits multiple reflections.

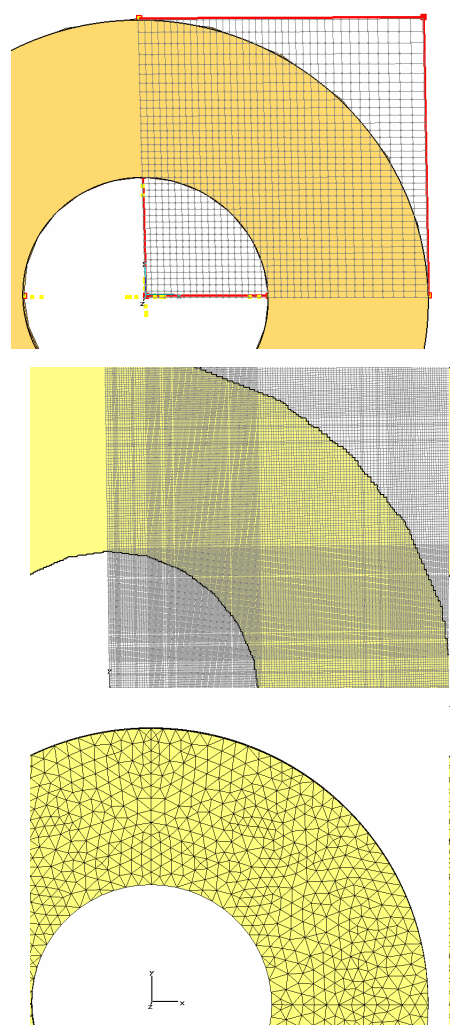


Fig. 4. Coaxial cable impedance simulation: Final mesh at the end of the convergence study, for PBA (4300 meshcells), staircase (110,000 meshcells) and tetrahedral (6175 meshcells) meshes.

The simulation consisted in an adaptive meshing, having as stop criterion a difference of less than 0.01 of the S-parameters between two successive runs.

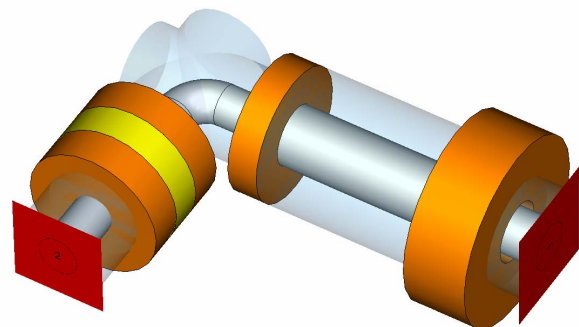


Fig. 5. Coaxial connector test structure.

Fig. 6 shows the variation of the S-parameters' correction and of the computing time with the number of mesh cells. Some interesting things can be noticed:

- The “convergence” for the staircase mesh is very irregular; a large number of mesh cells is necessary

for an acceptable solution; as will be shown in the final paper, the staircase mesh did NOT even reach an acceptable solution within this number of passes.

- Although, as expected, the correction varies in an identical manner for both the direct and the iterative solvers on the tetrahedral mesh, the computing time is *substantially* larger when a direct solver is used.

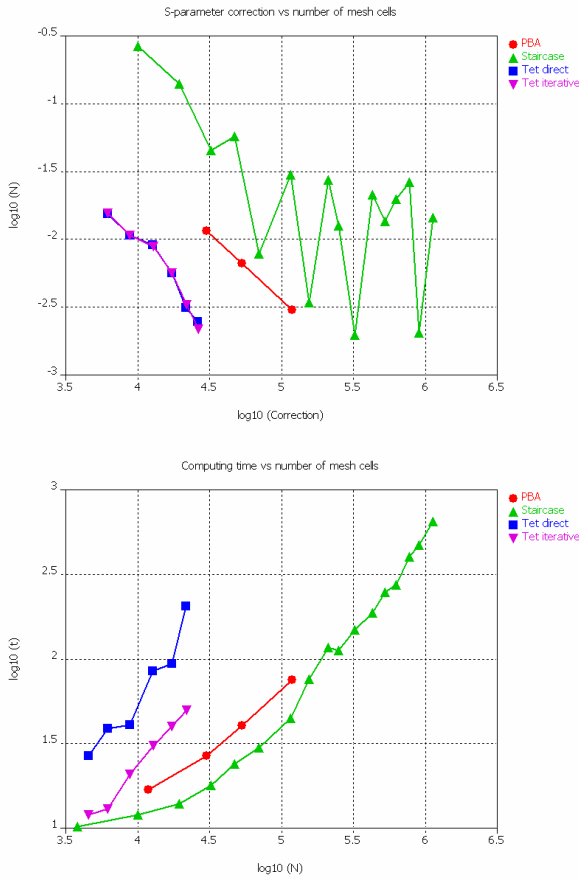


Fig. 6. Coaxial connector results. Upper plot: S-parameter correction vs number of mesh cells; Lower plot: computing time vs number of mesh cells

III. REAL LIFE APPLICATIONS

Real-life applications are often large or require a large number of simulations (e.g. in an optimization process). In this section, two such application examples are presented. Simulations on various mesh types were performed, and the results, as well as the computing time and the necessary memory are compared.

A. 16-Port Divider (Large Problem)

This structure is a relatively large one, a 16-port power divider whose spatial dimensions are about $16 \lambda \times 14 \lambda \times 0.4 \lambda$ (note that this is not yet a *very* large structure!). The geometry of the problem is shown in Fig. 7.

The simulation was performed on the standard mesh (e.g. 10 meshcells / wavelength for PBA and staircase meshes). The purpose of the simulations was to assess the computing time and the necessary memory for large structures. The electric field at 24.76 GHz is shown in Fig. 7, whereas the simulated S-parameters (for excitation at port 1) are shown in Fig. 8.

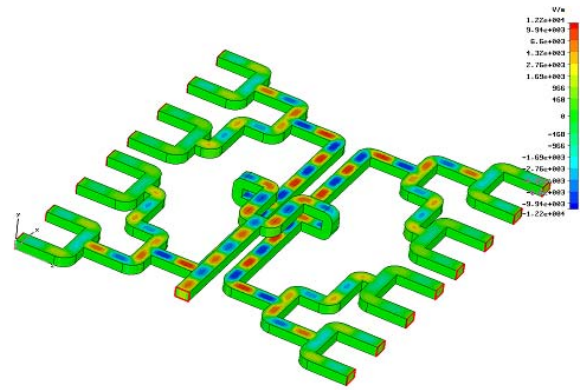


Fig. 7. 16-port power divider

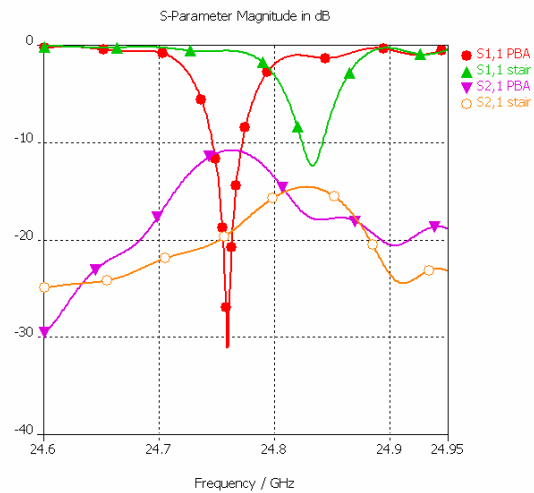


Fig. 8. Simulated S-parameters of the 16-port power divider, for PBA and staircase meshes

The computing time and the necessary memory are summarized in Table 1. Again, the PBA and staircase meshes require the least memory and provide the solution in the shortest time. However, whereas the PBA and the tetrahedral mesh solutions were in good correlation, the results on the staircase mesh did not prove to be satisfactory: a finer mesh is necessary in order to correctly represent the curved details of the structure.

Mesh type	Mesh cells	Comp. time	Memory
PBA	634000	40 ⁷	110 MB
Staircase	634000	41 ⁷	104 MB
Tet-direct solver	65700	97 ⁷	350 MB
Tet-iter. solver	65700	80 ⁷	1.1 GB

TABLE I

SIMULATION OF A RELATIVELY LARGE STRUCTURE:
COMPUTING TIME AND NECESSARY MEMORY

B. Pass-Band Filter

The structure, shown in Fig. 9 is a pass-band, 4-post filter. The purpose of the simulations was to numerically tune (optimize) the filter, finding the dimensions which ensure the prescribed filter characteristics. The tuning procedure is the one described in [5] and is also often used in practice for the final tuning of the filters. Two mesh types were compared, namely PBA and staircase.

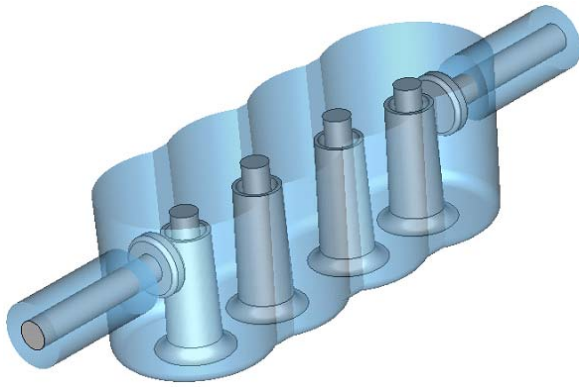


Fig. 9. 4-post pass-band filter. Model courtesy of the company Spinner GmbH, Westerham, Germany.

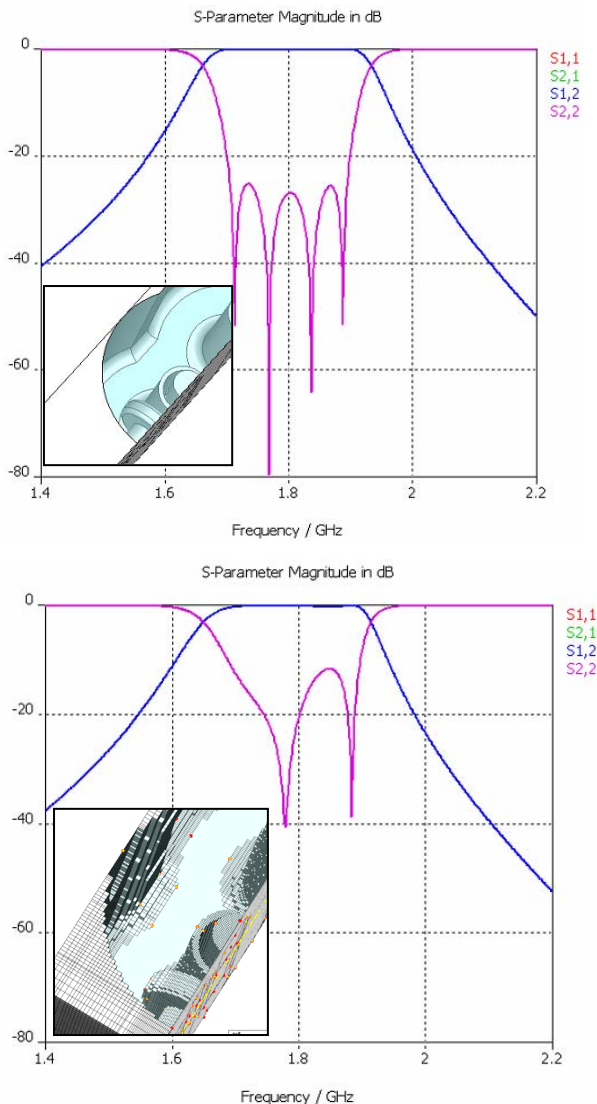


Fig.10. Simulated S-parameters for the 4-post pass-band filter. Upper plot: PBA mesh; lower plot: staircase mesh.

The PBA mesh (obtained based on an adaptive mesh refinement) contained about 50,000 mesh cells and the time needed for one simulation was of 5 minutes. The final S-parameters are shown in the upper plot of Fig. 10.

For the staircase mesh, the number of mesh cells needed was much higher, of about 1 million, and thus the computing time 5 times larger than in the PBA case – 25 minutes. However, the simulated results for the tuned

filter's dimensions, shown in the lower plot of Fig. 10, are very different from the required ones.

The explanation of this fact is that, due to the poor approximation of the curved geometry, the coupling between the cylindrical cavities / posts cannot be correctly represented in the mesh. With a staircase mesh a filter can thus be “untunable” numerically, despite the excellent properties of the real structure.

IV. CONCLUSION

A few practical conclusions can be drawn based on the results presented in this paper.

The **staircase mesh** can be very good on structures without curved or slanted boundaries/interfaces and without thin metallic details. Otherwise, it can be said that the solution practically does not converge, or it doesn't converge in a reasonable amount of computing time.

The **PBA mesh** has excellent convergence properties, and allows obtaining a solution in a very short time. The algorithm used in the simulations is an explicit, first-order one, having very low memory requirements, thus allowing the simulation of very large structures.

The **tetrahedral mesh** also exhibits excellent convergence properties. However, even for moderate structures, both the computing time and the memory needed by the direct solver may become prohibitive. For larger structures, an iterative solver is a must.

For very large structures, of tens of wavelengths dimension, the only viable solution can be obtained with the **PBA mesh**.

Note that the conclusions drawn for the staircase mesh are fully valid also for the **FDTD method**, while the ones for the tetrahedral meshes also apply to the **FE method**.

REFERENCES

- [1] T. Weiland, “A discretization method for the solution of Maxwell's equations for six-component fields”, *Electronics and Communication (AEÜ)*, vol. 31, p. 116, 1977.
- [2] T. Weiland, “Time Domain Electromagnetic Field Computation with Finite Difference Methods”, *International Journal of Numerical Modelling*, vol. 9, pp. 295-319, 1996.
- [3] B. Krietenstein, R. Schuhmann, P. Thoma, and T. Weiland, “The Perfect Boundary Approximation technique facing the challenge of high precision field computation”, in *Proceedings of the XIX International Linear Accelerator Conference (LINAC'98)*, Chicago, USA, 1998, pp. 860-862.
- [4] CST MICROWAVE STUDIO ® 5 User's Manual; see also www.cst.com
- [5] J. B. Ness, “A Unified Approach to the Design, Measurement, and Tuning of Coupled-Resonator Filters”, *IEEE Trans on Microwave Theory and Tech*, vol. 46, no. 4, April 1998.

A FPGA based TDEMI measurement system for quasi-peak detection and disturbance analysis

Stephan Braun, Peter Russer

Lehrstuhl für Hochfrequenztechnik Technische Universität München

München, Germany 80333

Email: stephan.braun@tum.de, russer@tum.de

Abstract — Measurement equipment that allows to measure electromagnetic interference (EMI) in short measurement time allows to reduce the costs and the time-to-market. By a time-domain EMI (TDEMI) measurement the measurement time can be reduced by several orders of magnitude. In the following a novel trigger unit and recording algorithm for a TDEMI measurement system is described. The trigger unit triggers on signal parts that have a maximum amplitude between a certain preselected interval. The maximum detector unit allows to measure and store the maximum amplitude of the signal within a preselected time interval. The maxima of consecutive time intervals are stored. The signal is processed in real-time for several seconds.

Recorded signal parts are assigned according to their maximum amplitude to a certain point in time. The original signal is reconstructed. A time-dependent spectrum for several seconds is calculated. The signal corresponding to the envelope of the IF-signal of an EMI Receiver is extracted at each discrete spectral value. An analysis with the Quasi-Peak-Detector as well as the Disturbance Analyzer is now possible. Measurements were performed in the Quasi-Peak-Detector mode and compared with results obtained by an EMI-Receiver. Also the demodulated IF-Signal of the EMI-Receiver is compared with the reconstructed IF-Signal of the TDEMI measurement system.

I. INTRODUCTION

A time-domain EMI measurement (TDEMI) system that performs a Quasi-Peak-Detection has been presented in [1]. The system generates a time-dependent spectrum statistically equivalent to the original signal. The time intervals between pulses as well as the pulse positions are statistically equivalent to the original signal. One drawback of this method is that it is not possible to perform an analysis of the IF-signal at each frequency as performed with by a disturbance analyzer.

In the following a trigger unit and an algorithm are described that allow to reconstruct the original pulse train of the original signal. The input signal is sampled into several intervals. Within each time interval the maximum of the signal amplitude is recorded. A signal consisting of the stored consecutive maxima is created. A discretization according to the number of selected amplitude intervals is performed. This discretized signal describes at which point in time a signal with a certain maximum amplitude has occurred.

Single shot measurements of individual samples are performed. The samples are assigned to certain amplitude intervals according to their calculated maximum amplitude. The original signal is reconstructed by placing the recorded samples according to their maximum amplitude at that point of time, where it corresponds to the discretized signal of the consecutive maxima.

II. TDEMI MEASUREMENT SYSTEM

In Fig. 1 the block diagram of the TDEMI measurement system is shown. The EMI signal is received by an antenna or Line Impedance Stabilization Network (LISN), amplified by a low noise amplifier (LNA) and low-pass filtered by an anti-aliasing filter. The input signal is digitized by an analog-to-digital converter (ADC). The recording unit, the maximum detector as well as the trigger unit are implemented on a Field Programmable Gate Array (FPGA). In the recording mode individual samples are stored temporarily in the Static Random Access Memory (SRAM). In the maximum detection mode the signal is sampled into several consecutive intervals. The maximum of the amplitude of each interval is calculated and stored into the SRAM. The FPGA is connected via a 16-Bit

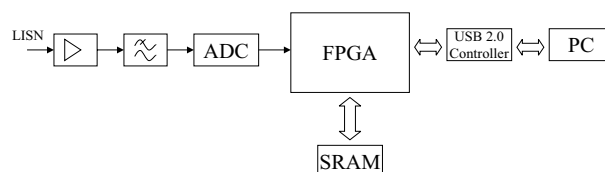


Fig. 1. Time-domain EMI Measurement System

Bus Interface to a microcontroller with integrated USB 2.0 Interface. The microcontroller is controlled by a conventional PC via USB. Stored data is transferred in high-speed mode to the PC for post processing. In Fig. 2 the picture of the realized system is shown.

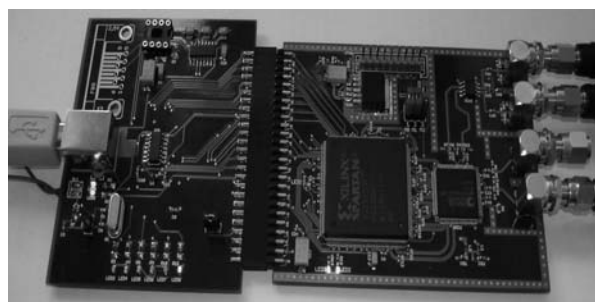


Fig. 2. Time-domain EMI Measurement System

III. ANALOG-TO-DIGITAL CONVERSION

Analog-to-digital conversion is performed by a 12-Bit Analog-to-Digital Converter (ADC) at 200 MS/s. The FPGA has to process a data stream of 400 MByte/s in realtime. The used ADC is a flash-type ADC. The ADC is connected via Low Voltage Differential Signalling (LVDS) to the FPGA. Differential signalling with matched transmission lines and

termination is used to minimize crosstalk between the analog and digital section of the Printed Circuit Board (PCB). In the following the performance of the implemented ADC unit is investigated and characterized.

A. Noise Floor

In Fig. 3 the spectrum of the noise floor with a modelled IF-Bandwidth of 9 kHz and 120 kHz is shown. The measurement was performed without a low-pass filter and a pre-amplifier. The spectrum is evaluated under the peak- and quasi-peak-detector modes for a scantime of 2 s. The spectrum shown in

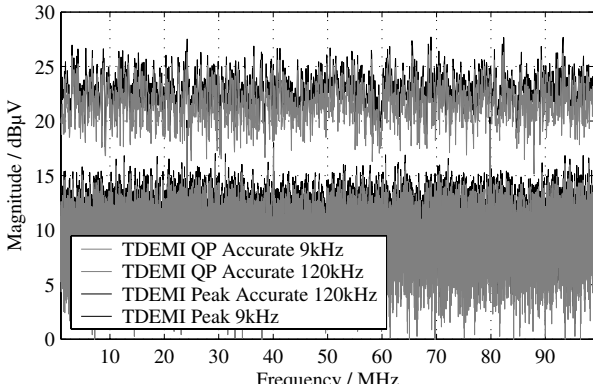


Fig. 3. Noise Floor

Fig. 3 is completely uniform over the whole frequency range.

B. Spurious Signals

Spurious Signals are crucial for EMI measurements. According to CISPR 16-1 [2] spurious signals may only contribute to a maximum measurement error of 1 dB. Thus any spurious signal has to be below 1 dB of the total measurement range. Commercial available oscilloscopes show spurious signals that are up to 15 dB above the noise floor. In Fig. 3 no spurious signals can be seen over the whole frequency range.

IV. SIGNAL-TO-NOISE RATIO

In the following the signal-to-noise ratio (SNR) of the TDEMI Measurement System is investigated.

A. Short-time fast Fourier transform

In order to obtain a time dependent spectrum the STFFT [3] is applied. A time dependent spectrum can be described as consecutive spectra. These spectra are calculated by the DFT, using a time interval smaller than the total record length. T_{sBB} corresponds with the increment used in the STFFT [3].

$$T_{sBB} = \frac{1}{f_{sBB}} \quad (1)$$

f_{sBB} is the baseband sampling frequency, that is used to simulate peak-, average-, rms-, and quasi-peak-detector.

B. Signal-to-noise ratio

For a general signal the SNR is given by [4]:

$$SNR = \frac{P_{Signal}}{P_{Noise}} \quad (2)$$

while the power of the signal is given by (3):

$$P_{Signal} = \sigma_s^2 = \langle (x(t) - \langle x(t) \rangle)^2 \rangle \quad (3)$$

The power of the quantization noise is given by (4)

$$P_{Noise} = \sigma_e^2 = \frac{\Delta^2}{12} \quad (4)$$

with Δ as the quantization step of the analog-to-digital-converter (ADC).

1) *Window function*: The digitized signal $\hat{x}[n]$ is the result of the superposition of the original signal $x[n]$ and the quantization noise $e[n]$. We obtain:

$$z[n] = x[n] w[n] = \hat{x}[n] w[n] + e[n] w[n] \quad (5)$$

$e[n]$ is described as a statistical signal with constant probability density function in the interval $[-\frac{\Delta}{2}; +\frac{\Delta}{2}]$ according to a midriser quantization [4]. Applying (2) and (3) we obtain a SNR for each calculated spectrum:

$$SNR = \frac{\frac{1}{N} \sum_{n=1}^N (\hat{x}[n] w[n] - \frac{1}{N} \sum_{k=1}^N \hat{x}[k] w[k])^2}{\frac{1}{N} \sum_{n=1}^N (e[n] w[n] - \frac{1}{N} \sum_{k=1}^N e[k] w[k])^2} \quad (6)$$

For $e[n] \ll x[n]$ we can replace $\hat{x}[n]$ by $x[n]$ and obtain with (6):

$$SNR \approx \frac{\frac{1}{N} \sum_{n=1}^N (x[n] w[n] - \frac{1}{N} \sum_{k=1}^N x[k] w[k])^2}{\frac{1}{N} \sum_{n=1}^N (e[n] w[n] - \frac{1}{N} \sum_{k=1}^N e[k] w[k])^2} \quad (7)$$

C. Stationary signal

During the last sections the SNR and dynamic range for transient signal was investigated. In the following the SNR for stationary signal is presented.

1) *Signal-to-noise ratio*: Stationary signal has a constant power over the time. Thus the SNR is constant. With (3) and (4) we obtain a constant signal to noise ratio of:

$$SNR = 12 \frac{\langle (x(t) - \langle x(t) \rangle)^2 \rangle}{\Delta^2} \quad (8)$$

2) *Dynamic range*: With the modelled IF-filter we get at each discrete spectral value a SNR according to (9).

$$SNR_{IF} = SNR \frac{B_s}{B_{IF}} \quad (9)$$

B_s is the total bandwidth of the measurement system and B_{IF} is the equivalent noise bandwidth [5] of the IF-Filter.

V. DIGITAL INTERFACE

A. Field Programmable Gate Array

A Field Programmable Gate Array (FPGA) was used to implement the digital interface as well as digital signal processing. The used FPGA provides 150 000 logic gates. For the actual Implementation only 10 percent of the logic gates were used. Thus we have the possibility to add further features via updates.

B. Universal Serial Bus

The the High Speed Universal Serial Bus (USB) interface was implemented with a microcontroller with integrated USB 2.0 interface. The High Speed Mode provides a maximum data rate of 480 Mbps. The microcontroller of the used interface uses the instruction set of a 8051 microcontroller.

For this microcontroller a controlling software (firmware) was developed that allows to perform the high-speed data transfers of recorded samples from the Analog-to-Digital Converter system to the PC. The different modes of the Analog-to-Digital Converter system are controlled by the microcontroller.

The firmware is stored onto an EEPROM and is booted during the power on.

An estimation of the achieved data transfer rate r is given by

$$r = \frac{N \cdot b}{t} \quad (10)$$

where N is the number of transferred samples and b is the resolution in bit.

Table I shows the data throughput for the USB 2.0 Interface in comparison to standard measurement interfaces like GPIB and Ethernet.

	GPIB	Ethernet	USB 2.0
samples N	200000	200000	200000
resolution b	8 Bit	8 Bit	16 Bit
time t	0,37 s	0,11 s	0,047 s
transfer rate r	0,5 Mbyte/s	1,8 Mbyte/s	8,5 Mbyte/s

TABLE I
OVERVIEW OVER DATA RATES

The results show, USB 2.0 reaches a data transfer rate of about 8.5 Mbyte/s which is an improvement of a factor of 5 in comparison to Ethernet and 17 in comparison to GPIB.

VI. DIGITAL SIGNAL PROCESSING

The input signal is processed in real-time by several components that were realized in the FPGA. In Fig. 4 the block

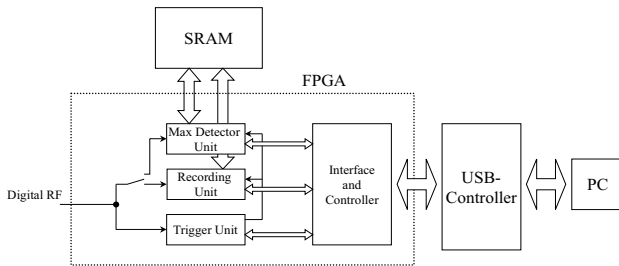


Fig. 4. Signal processing blocks

diagram of the different signal processing blocks are depicted. The recording unit supports the recording of individual samples and is controlled by the trigger unit. Triggered data acquisition [6] is used to trigger on single transients. In state of the art oscilloscopes triggering is done by a separate analogue trigger unit. In the following a trigger unit is described that is fully implemented digitally on the FPGA.

In the past a trigger mode called Fast-Frame [7] was used to characterize transient signal for a longer duration of time. Several measurements at different amplitude resolutions have to be performed to obtain the transient behavior for the full amplitude scale. The drawback was that the original pulse train could not be reconstructed.

The implemented FPGA-integrated maximum detector unit separates the input signal into several samples. Of each sample the maximum value is calculated and stored. Only a single measurement is necessary to obtain the transient behavior for the complete amplitude scale over the complete dwell time.

A. Recording Unit

By the Recording Unit the signal is digitized with 12 Bit and 200 MS/s. The ADC is connected via LVDS to the FPGA

to minimize any spurious emissions from the signal lines to the analog signal. The signal is demultiplexed by the FPGA and transferred to the SRAM. This unit is used to perform single shot measurements with the length n .

B. Trigger Unit

The signal is provided simultaneously to the internal trigger unit. The digital trigger unit processes the input signal in real-time. If the signal crosses a certain selectable threshold a trigger event is generated. This threshold corresponds to the trigger level of an analogue trigger unit. Post- and pre-triggering is implemented by an internal counter that generates from the trigger event an output signal for the ADC unit with a certain delay in time.

C. Maximum detector unit

During the maximum detection mode the signal is passed directly to the maximum detector unit. The signal is separated into different samples of the length n . The signal $d[k]$ describing the transient behavior of the input signal is calculated according to (11) where N is the total number of samples.

$$d[k] = \max_{i=kn}^{n(k+1)}(s[i]) \quad \forall \quad k = \{0.. \frac{N}{n} - 1\} \quad (11)$$

The signal is stored into the SRAM. The input signal with a data rate of 400 Mbyte/s is processed in realtime for several seconds. Afterwards it is transferred via USB to the PC for post-processing.

VII. RECONSTRUCTION OF ORIGINAL SIGNAL

In this section an algorithm is described that reconstructs the original transient signal. During this reconstruction the recorded transients are assigned to certain points in time.

A. Analysis of transient behavior

First a measurement of the input signal is performed in the maximum detection mode. Typically the input signal is recorded for two seconds. The whole used amplitude scale is divided into several intervals. The output signal $d[k]$ is discretized according to the intervals. An example is shown in Fig. 5.

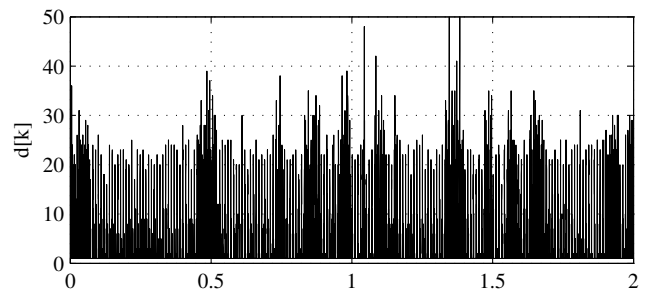


Fig. 5. Maximum detected signal

B. Single shot measurement

The measurement of individual samples is performed by the recording unit. During this recording the trigger unit is set up to trigger only on signals that have a maximum amplitude within a preselected amplitude interval. Several samples are recorded at each amplitude interval. All amplitude

intervals assigned by the signal $d[k]$ are selected during the measurement of individual samples.

At each amplitude interval the number of recorded samples is reduced. This is done by eliminating similar samples. Samples are similar if the maximum of the cross correlation function of the power spectra is higher than a preselected threshold. We obtain the relative frequency of each sample by counting the similar samples.

C. Distribution of samples on the timescale

The samples are distributed on the timescale according to the signal $d[k]$. Samples are placed on the timescale where they match to the amplitude interval given by $d[k]$. Within an amplitude interval the pulses are placed according to their relative frequency.

VIII. MEASUREMENT RESULTS

The total measurement time was evaluated. The measurement time is compared with a conventional EMI Receiver in the Quasi-Peak-Detector mode and a dwell time of 2 s.

	TDEMI	ESCS30
Measurement of time intervals	2 s	-
Recording of 50 signal samples	1:20 s	-
Measurement time	1:22 min	3:33 h
STFFT	1 min	-
Statistical Calculations	10 s	-
Peak-Detection	5 s min	-
Quasi-Peak-Detection	40 s min	-
Calculation time	1:55 min	-
Total measurement time:	3:17 min	3:33 h

TABLE II
MEASUREMENT TIME

The measurement of the EMI originating from a drill machine was with a LISN for conducted emission measurement. The measurement has been carried out in the 150 kHz - 30 MHz frequency range. In Fig. 6 result of the measurement in the Quasi-Peak-Detector mode is shown. The maximum difference between the result obtained with the EMI Receiver and the measurement result obtained with the FPGA based TDEMI measurement system is 2 dB.

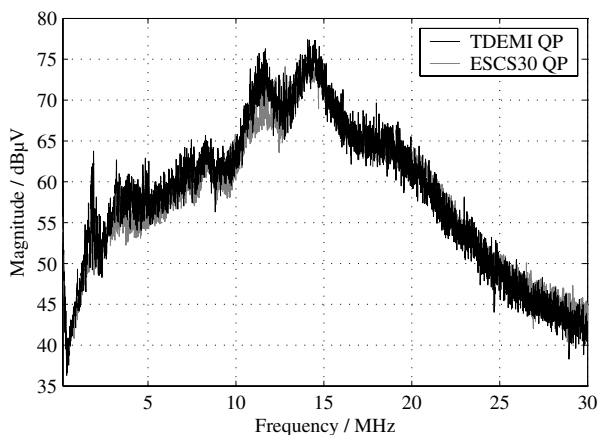


Fig. 6. Drill Machine

For disturbance analysis the signal at the IF-Frequency is fed to an external disturbance analyzer. In the following the demodulated IF-Signal of an EMI Receiver is compared

with the reconstructed IF-Signal of the TDEMI measurement system. During the measurement 50 amplitude intervals were selected. In Fig. 7 the result is shown. The time intervals

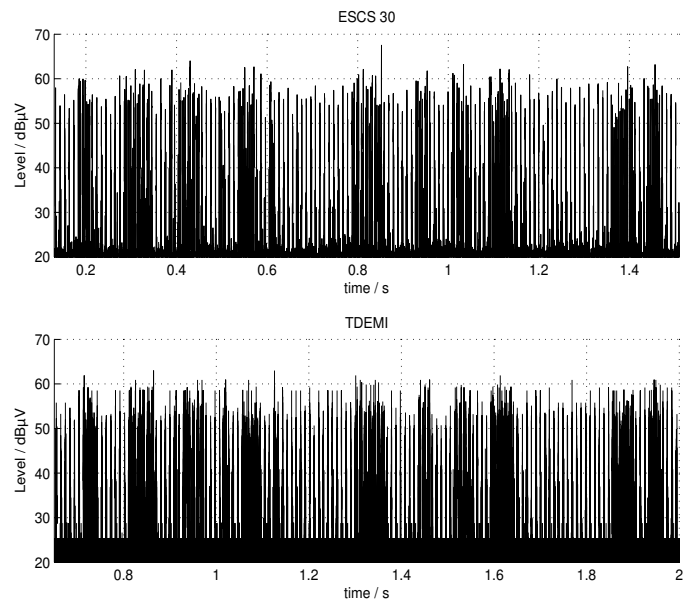


Fig. 7. IF-Signal

between pulses is within a accuracy of 40 μ s the same as measured with the EMI-Receiver. The amplitude of the IF-signal shows a maximum deviation of 8 dB. The average deviation is below 3 dB.

IX. CONCLUSION

A TDEMI measurement system that can perform a Quasi-Peak-Detection as well as a disturbance analysis has been presented. Measurement results show an average deviation of the IF-Signal about 3 dB. The reconstructed IF-Signal is provided by the TDEMI Measurement System at all scanned frequencies in parallel. Measurements performed in the Quasi-Peak-Detector mode show a maximum difference of 2 dB in comparison to the measurements obtained with an EMI-Receiver. The measurement time is reduced by a factor of 60.

ACKNOWLEDGMENT

The authors would like to thank Reinhard Schneider for the development of the USB-Interface.

REFERENCES

- [1] S. Braun, F. Krug, and P. Russer, "A novel automatic digital quasi-peak detector for a time domain measurement system," in *2004 IEEE International Symposium On Electromagnetic Compatibility Digest, August 9–14, Santa Clara, USA, 2004*.
- [2] CISPR16-1, *Specification for radio disturbance and immunity measuring apparatus and methods Part 1: Radio disturbance and immunity measuring apparatus*. International Electrotechnical Commission, 1999.
- [3] L. Cohen, "Time-Frequency Distributions - A Review," in *Proceeding of the IEEE*, vol. 77, no. 7, pp. 941–981, 1989.
- [4] A. V. Oppenheim and R. W. Schaffer, *Discrete-Time Signal Processing*. ISBN 0-13-214107-8, Prentice-Hall, 1999.
- [5] F. Krug, D. Mueller, and P. Russer, "Statistical Physical Noise Behavior Analysis of the Time Domain EMI Measurement System," in *2003 IEEE AP-S International Symposium on Antennas and Propagation, 22-27.06.2003, Columbus, USA*, vol. 3, pp. 212–215, 2003.
- [6] F. Krug and P. Russer, "Signal Processing Methods for Time Domain EMI Measurements," in *2003 IEEE International Symposium On Electromagnetic Compatibility Digest, May 11–16, Istanbul, Turkey*, pp. –, no. TH-P-R2.8, 2003.
- [7] Tektronix, *Digital Phosphor Oscilloscopes - TDS7000 Series*. Data sheet, 2001.

Device for exposure of inner ear hair cells to RF signals

A. El Ouardi ¹, T. Reinhardt ¹, J. Streckert ¹, A. Bitz ¹, V. Hansen ¹, J. Engel ², S. Münkner ²

¹University of Wuppertal, Chair of Electromagnetic Theory, Rainer-Gruenter-Straße 21, 42119 Wuppertal, Germany, +49 202 439 1666, elouardi@uni-wuppertal.de

²University Hospital Tübingen, Institute of Physiology II and Tuebingen Hearing Research Centre THRC, Tübingen, Germany

Abstract — A device for the 900 MHz, 1.8 GHz (GSM) and 2 GHz (UMTS) exposure of inner ear hair cells in vitro based on a fin-line is presented and analyzed. The vessel containing the cells is filled with extracellular solution (artificial cerebrospinal fluid) and placed upon the fins. The field strength in the slot between the fins amounts to 7000 V/m per 1 W input power, whereby fields of up to 700 V/m are achieved within the vessel with a good homogeneity of the distribution over the volume where the cells are located. With powers fairly below 1 W specific absorption rates (SAR) of up to 20 W/kg can be produced which is proven by numerical computations.

I. INTRODUCTION

The launch of the wideband UMTS in Europe combined with a necessary enhancement of the number of base station antennas has fuelled the ongoing public discussion about hypothetical health risks of weak electromagnetic fields. As a consequence a substantial amount of research funds has been provided by industrial and official organisations, at least in Germany, in order to intensify the scientific knowledge in this relevant field. The present project sponsored in this context by the Bundesamt für Strahlenschutz (BFS) within the frame of the "Deutsches Mobilfunk Forschungsprogramm" is designed to investigate possible influences on the auditory system on the basis of hair cells being exposed in vitro to rf electromagnetic fields which are modulated by GSM900, GSM1800 and UMTS-typical signals. The physiological design of the experiments implies the measurement of Ca currents through the cell membrane by application of the patch clamp technique. This contribution deals with the rf technical aspects of the project and reports about a newly developed exposure set-up on the basis of a fin-line.

II. BIOLOGICAL BACKGROUND

The underlying biological hypothesis for the experiments is an effect of modulated electromagnetic fields on the inner ear hair cells within the so-called organ of Corti of the cochlea which produce the acoustically stimulated signals transmitted from the ear to the brain. As an indicator for the performance of the inner ear hair cell system the Ca^{2+} -ion flux through the cell membrane is measured with help of the patch clamp technique. Therefore, organs of Corti from mice are prepared and kept in vitro in a dish with extracellular solution. Then a thin glass electrode filled with electrolyte is brought in contact with a single inner ear hair cell and the current due to Ca influx from the extracellular medium to the cell interior is measured (Fig. 1). A photograph of the central part of the physiological set-up used so far without rf exposure is given in Fig. 2. The dish with solution containing the organ of Corti, the patch

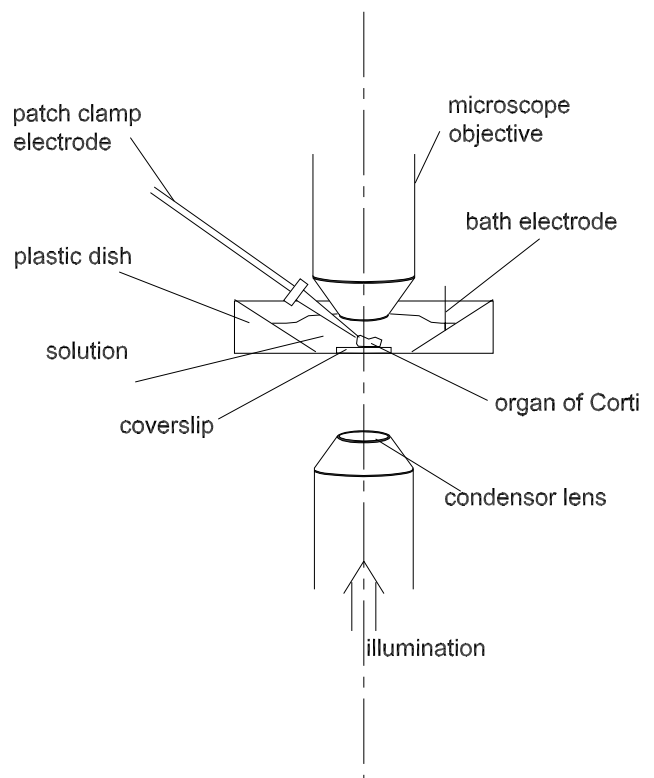


Fig. 1. Sketch of physiological set-up.



Fig. 2. Central part of the physiological set-up.

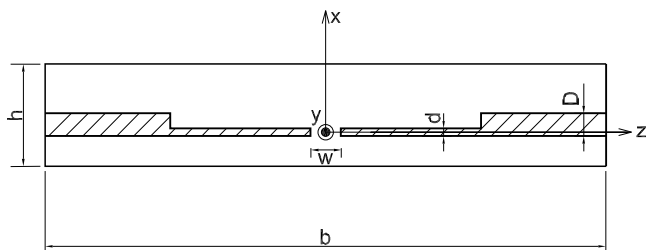


Fig. 3. Cross section of the fin-line at the position of the dish.

clamp-electrode for contacting a cell, a microscope objective for visual control of the contact, and two metal tubes for perfusion of the extracellular solution are clearly visible. Due to the location of the cells near the surface of the organ of Corti, which is placed on a glass slide at the bottom of the dish, an upright water immersion microscope must be used. Further this implies the positioning of the patch clamp electrode at a flat angle. Moreover, a light source below the bottom of the dish is needed.

III. RF EXPOSURE SYSTEM

A. Requirements

The development of a suitable exposure equipment is a challenging task because some strongly contrary requirements have to be fulfilled: The distance between the microscope objective for the observation of the cells and of the patch clamp electrode and the condensing lens for illumination is only 11 mm. Therefore, a field with a vertical extension in this range or even smaller is required. On the other hand a homogeneous field distribution over a sufficiently large area is necessary. Further on the structure must be open for the patch clamp electrode and two tubes for perfusion, for the microscope objective from above and for the condensing lens from underneath; for all these components rather large openings must be provided. However, no radiation and no uncontrolled coupling to the metallic objects of the physiological equipment close to the exposure area shall occur. Altogether, the exposure field must be well-defined, stable and determinable with and without the biological target and it must be possible to perform a reliable calibration.

B. Concept

The rf exposure of the cells shall be performed during the measurement of the membrane currents, thus the above mentioned physiological boundary conditions must be considered. In succeeding stages of the experiments mobile communication signals according to the GSM900, GSM1800 and UMTS standards as well as different specific absorption rates of up to 20W/kg shall be applied. In order to keep the accustomed handling of the patch clamp technique for the physiologist it was decided to integrate the set-up used so far (Fig. 2) within an rf waveguide and to couple a defined part of the transmitted power into the biological sample. Our first attempt for the development of the exposure set-up started with a flat rectangular waveguide which already had successfully been applied for earlier patch clamp experiments [1]. However, in that case much more space was available since an inverse microscope and a vertical patch clamp electrode could be used. Now, we change to a fin-line which is in principle a rectangular

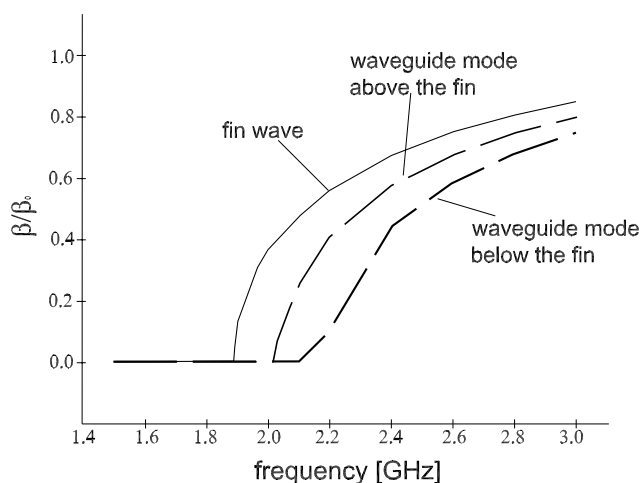


Fig. 4. Propagation constants vs. frequency of fin-wave and unwanted waveguide-modes.

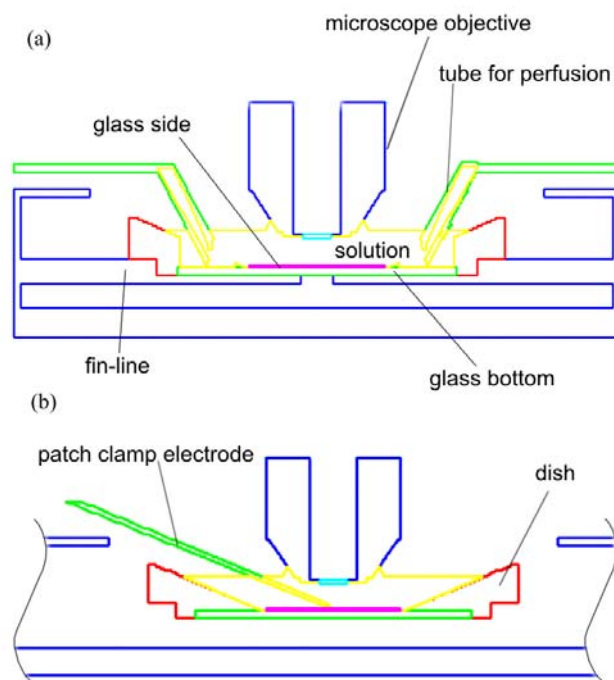


Fig. 5. Computer model of the fin-line with inserted plastic dish and objective. (a) in the cross section (b) in the length section

waveguide (and by this a closed structure) with two metal fins attached to the side walls [2].

In a properly designed fin-line a wave propagates which can approximately be regarded as a shielded slot line wave with a field concentrated to the area close to the slot. Numerical experiments yielded that a flat fin-line with a vertical asymmetry (Fig. 3) is a very promising structure for the above discussed requirements.

The cross-sectional dimensions are such that the cutoff frequencies of the two waveguide modes lie fairly above the onset of the fin wave (Fig. 4). This is also the reason why three separate waveguides must be constructed for the experiments at 900, 1800 and 2000 MHz. In a sufficient distance from the input and from the end of the waveguide the dish with the biological cells is inserted through a hole in the top and

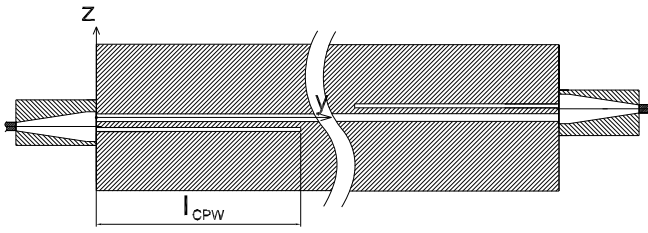


Fig. 6. Coaxial to fin-line transition via CPW for the excitation of the fin-wave.



Fig. 7. Picture of the fin-line for the *UMTS*-frequency-range: The vessel is placed in the center of the waveguide onto the gap between both fins through the opening in the upper wall.

placed straight above the slot between the fins (Fig. 5).

C. Excitation of the fin-line

In order to excite the fin wave by the TEM wave of the feeding coaxial cable a transformation via a coplanar waveguide (CPW) structure is used. Fig. 6 shows this transition. The length of the coplanar waveguide is optimized by numerical computations in order to achieve good match of coaxial- and fin-line. The conical transition of the coaxial waveguide is introduced to additionally decrease the reflection factor. Because of the conductivity $\kappa = 2.2 S/m$ of the medium which surrounds the hair cell, the field strength in direction of wave propagation is damped strongly inside the vessel. Thus, at the location of the cell which is in the center of the waveguide $\pm 2 mm$ a high field variation was observed. In order to minimize this field variation the fin-line is excited at both ports, whereas a phase-shift of 180° has to be considered, due to the asymmetric arrangement of the coplanar waveguides.

IV. RESULTS

In the following, results will be shown for the fin-line at a frequency of $2 GHz$. The input power in a transversal cut through the empty fin-line is $1 W$. The illumination of the cell is realized by use of a metallic coated glass window in the waveguide wall below the dish (Fig. 7). Fig. 8 shows the numerically calculated [3] magnitude of the electrical field in the center of the fin-line. The field is mainly concentrated between the fins with a maximum of the electrical field of about $|E|_{max} = 7000 V/m$, because of the small distance

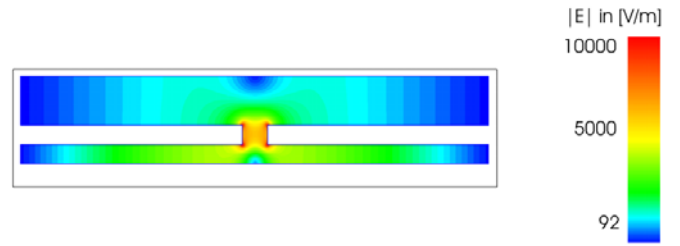


Fig. 8. Magnitude of the electrical field in the cross section of the fin-line for $1 W$ and $2 GHz$.

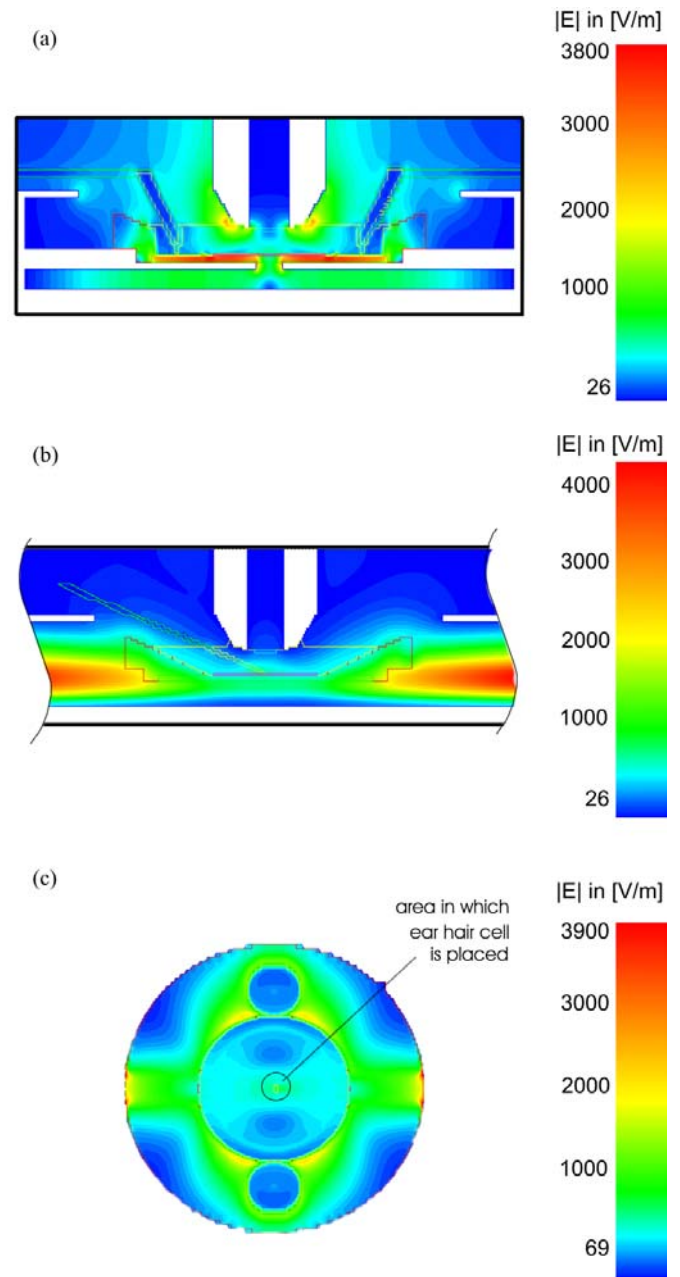


Fig. 9. Magnitude of the electrical field for $1 W$ and $2 GHz$ for the complete model. (a) cross section of the fin-line (b) length section (c) cut at the bottom of the vessel.

between waveguide walls and fins the field distribution in the remaining part of the waveguide isn't negligible compared to the field in the gap between the fins.

Fig. 9 gives the numerically calculated electric field distribution for the complete set-up (cf. Fig. 5) with dish, solution, glass slide, patch clamp electrode, tubes for perfusion and microscope objective.

The field distribution in the area where the cell can be located is given in Fig. 9c. The variation of the field at the cell due to the variation of the cell position and by this variation the position of the patch clamp electrode in the above-mentioned area is $E_{max}/E_{min} = 1.05$.

The SAR of the cell can be estimated by use of the electric field strength

$$SAR = \frac{1}{2\rho}\kappa|E|^2 \quad (1)$$

with $\rho = 1000 \text{ kg/m}^3$ and $\kappa = 2.2 \text{ S/m}$. Thus, for a SAR of 20 W/kg an input power of approx. 50 mW must be supplied. The resulting ratio of SAR_{max}/SAR_{min} is 1.1.

V. CONCLUSION

An in vitro exposure device for inner ear hair cells based on a fin-line was presented. The complete physiological set-up consisting of the dish, solution, glass slide, patch clamp electrode, tubes for perfusion and microscope objective is an integral part of the exposure device. The fin-line is excited at both ports to achieve low field variation in the region of the cell. For a SAR of 20 W/kg an input power of approx. 50 mW must be supplied. The ratio of SAR_{max}/SAR_{min} is 1.1.

REFERENCES

- [1] Linz, K. W., von Westphalen, C., Streckert, J., Hansen, V., Meyer, R.: "Membrane potential and currents of isolated heart muscle cells exposed to pulsed radio frequency fields." *Bioelectromagnetics* Vol. 20, no. 8, 497-511, 1999.
- [2] J. R. Knorr, "Millimeter- Wave Fin- Line Characteristics," *IEEE Transactions on Microwave and Techniques*, vol. MIT-28, no. 7, pp. 737-743, Jul. 1980.
- [3] CST GmbH: The MAFIA Collaboration. User's guide Mafia Version 3.20, Darmstadt, 1994.

Session 8a

Active Circuits

A GaAs Distributed Amplifier with more than 7 V_{pp} Output for 40 GBit/s Modulators

M. Häfele¹, K. Beilenhoff², and H. Schumacher¹

¹ Dept. of Electron Devices and Circuits, University of Ulm, D-89069 Ulm, Germany
Phone: + 49 731 5031589, Fax: +49 731 5026155, e-mail: mhaefe@ebs.e-technik.uni-ulm.de

²United Monolithic Semiconductors (UMS), S.A.S., Orsay, 91401 France

Abstract — In this paper, we report about a **Distributed Amplifier (DA)** with high output voltage swing sufficient to drive 40 GBit/s LiNbO₃ based Mach-Zehnder modulators. The amplifier was fabricated in a commercially available 150 nm GaAs power pHEMT technology. Measurements show a gain of 16 dB with an associated bandwidth of 40 GHz. For the 20 GHz fundamental, output power at the -1 dB gain compression point equals 21.7 dBm or 7.7V_{pp}.

I. INTRODUCTION

The increase of data communication in recent years demands for increasing bandwidth of the transmission systems. The driving motivation for an increasing bit rate is a reduced cost per bit. At lower bit-rates upgrading to four times the speed typically resulted in only 2.5 times the cost [1]. In fiber communication systems, speed per channel increased from 2.5 Gbit/s (OC-48) to 10 Gbit/s (OC-192) and future 40 Gbit/s (OC-768) are examined. With very advanced transistor technologies, also first results are published for 80 Gbit/s [2] and even 100 Gbit/s [3].

In case of 40 Gbit/s systems, the modulator driver is very challenging, because it simultaneously has to achieve a high output voltage swing of typically 5 to 7 V_{pp} [4] and a bandwidth exceeding 30 GHz. The increasing speed of silicon based technologies like SiGe, BiCMOS, or CMOS fulfill the bandwidth requirements for high bit-rate optical communication at low cost. For example SiGe HBTs with an f_t of 350 GHz [5] and SOI CMOS with up to 243 f_t [6] have been reported. However, increasing transistor speed is mainly achieved by strong lateral scaling which degrades breakdown voltage.

While InP based HBTs are the ideal candidate for high power applications at high frequencies [4], GaAs based circuits offer slightly degraded performance but with an advantage in terms of cost-effective production.

For the circuit concept, a distributed amplifier topology is chosen. The concept of distributed amplification has been around for over a half century [7] and is one of the most used concepts in optical communication due to its excellent bandwidth performance. The idea of a DA is to split one large device into several small ones and to compensate for parasitic capacitances by high characteristic impedance transmission lines. The resulting small signal structure at the input and output of the DA is designed to behave like a 50 Ω artificial transmission line and therefore shows both, small input and output reflections as well as flat gain over a large bandwidth. This makes a DA concept very attractive for 40 GBit/s circuits. Especially, the superposition of the signals on the drain line is ideally suitable to achieve high output power and therefore meet the requirements for driving a LiNbO₃ modulator.

II. CIRCUIT DESIGN

The amplifier is realized in the commercially available PPH15 process of United Monolithic Semiconductors (UMS). This is a high power 150 nm pseudomorphic GaAs HEMT process with an f_t of 75 GHz. The devices have an optimum transconductance of $g_{m,max} = 550 \text{ mS/mm}$ at $V_{GS} = -0.4 \text{ V}$, a breakdown voltage of $V_{bds} > 8 \text{ V}$, and a power density of $P_{-1 \text{ dB}} = 0.6 \text{ W/mm}$.

A DA with 6 stages was designed and the basic topology is shown in Fig. 1.

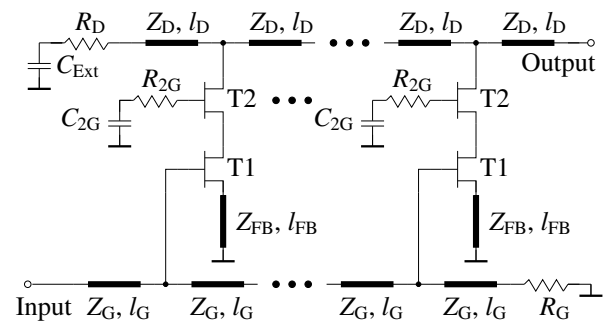


Fig. 1. The amplifier consists of 6 cascode stages. A resistor at the second gate together with source degeneration are used to enable stability of the amplifier.

Within the stages, cascode cells are used. Compared to a transistor in common source configuration a cascode provides several advantages:

- Unilateralization
- Possibility for gain variation
- Reduced Miller-effect
- Improved output resistance

A reduced Miller-effect decreases the input capacitance and thereby enhances the cut-off frequency of the artificial gate line. In case of DA design, the output conductance of the active device is essential, because it determines the attenuation and thereby the cut-off frequency. At frequencies close to DC parasitic output capacitance of a FET can be neglected, yielding an output resistance of the cascode equal to:

$$\Re\{Z_{22}\} \approx 2 \cdot r_{ds} + g_{m2} \cdot r_{ds}^2 \quad (1)$$

For high frequencies the cascode shows a negative resistance at its output terminal. Neglecting output conductance of the transistors ($g_{ds1} = g_{ds2} = 0$), the real part of the output impedance is:

$$\Re\{Z_{22}\} \approx \frac{-g_{m2}}{\omega^2(C_{ds1} + C_{gs2}) \cdot C_{ds2}} \quad (2)$$

where g_{m2} , C_{gs2} , and C_{ds2} are the transconductance, input capacitance, and output capacitance of the common gate transistor, C_{ds1} is the output capacitance of the common source transistor.

The negative resistance is used to compensate for losses on the artificial drain line and thereby, enhances cut-off frequency. However, a negative output resistance also gives rise to instabilities and is partly compensated by the resistor R_{2G} and inductive source degeneration, Z_{FB} . Other possibilities for stabilization of the DA are shown for example in [8], [9]. In order to have high voltage amplification, one can either use a large gate width for each stage or a large number of stages. While the first decreases cut-off frequency, the latter makes the amplifier more sensitive to process variations and typically decreases gain flatness. In this case the circuit is rather optimized for good gain flatness than cut-off frequency. Therefore the gate width is chosen relatively large ($100\ \mu\text{m}$), enabling high gain within 6 stages. Even with this large device size simulated cut-off frequency of 42 GHz showed sufficient margin to fulfill the frequency requirements after process variations.

The corresponding layout of the circuit is shown in Fig. 2.

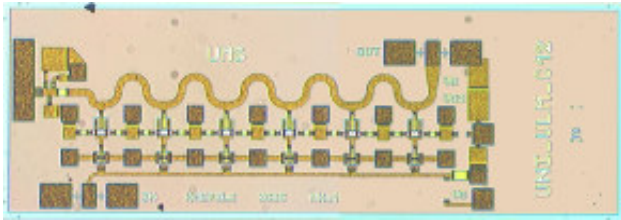


Fig. 2. Layout of the distributed amplifier (chip size: $2.38 \times 0.83\ \text{mm}^2$)

The large pad on the left hand side is used for external bias decoupling. For the measurements, a $100\ \text{nF}$ SMD capacitor is glued on that pad to enable bias decoupling down to very low frequencies. Because parasitics of this capacitor would degrade high frequency performance of the amplifier, down to frequencies of approximately 5 GHz bias decoupling is made on-chip. A detailed schematic for this circuitry is shown in Fig. 3.

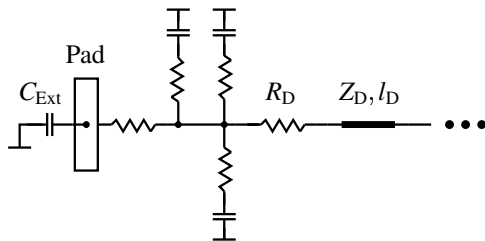


Fig. 3. Termination for the reverse traveling wave. Bias-decoupling of frequencies higher 5 GHz is done on-chip. A pad is provided to directly attach a SMD capacitor on top of the chip.

Parasitics due to physical connections to the capacitors, together with the capacitances itself result in resonances. This is attenuated by resistors. Additionally, the values for these resistors are chosen to compensate for gain ripples. Fig. 4 shows a micrograph of an external capacitor mounted on top of the amplifier.

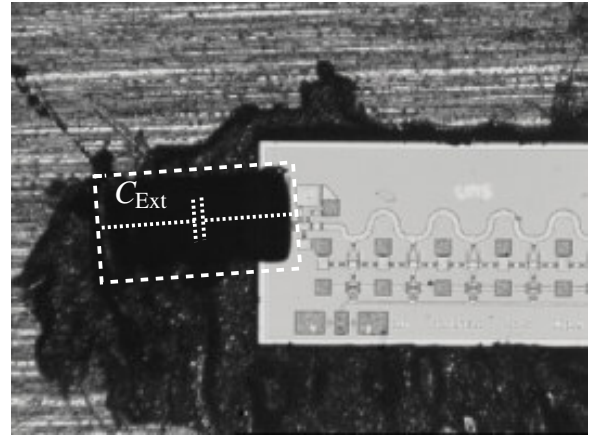


Fig. 4. Micrograph of an external SMD capacitor mounted on top of the GaAs-MMIC.

III. MEASUREMENT RESULTS

All measurements were performed with a drain biasing of 8.0 V, a second gate voltage of 3.7 V and a gate source voltage of $-0.3\ \text{V}$. This bias point gives a good compromise between small signal and power performance. The total DC-power consumption equals 1.6 W. On-wafer small signal measurements of this amplifier are shown in Fig. 5.

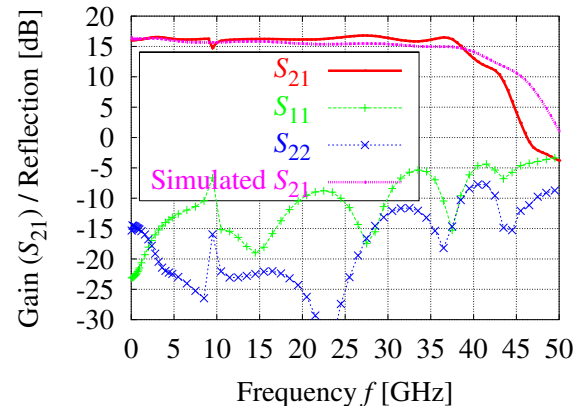


Fig. 5. Measured small signal parameters of the amplifier. Gain equals 16 dB at DC with a corresponding bandwidth of 40 GHz.

The gain equals to 16.0 dB with a corresponding cut-off frequency of 40 GHz. Up to 37 GHz the frequency response is very flat with gain-ripples of less than $\pm 0.5\ \text{dB}$. However, a resonance at approximately 10 GHz degrades gain by nearly 2 dB. The resonance is due to the cascode cell itself, which is verified by measurements on a test structure. While this resonance degrades small signal performances, it does not degrade overall stability of the amplifier. Input matching is better than $-8\ \text{dB}$ up to 30 GHz, except for the frequency band between 9 and 10 GHz. Output matching is lower $-10\ \text{dB}$ up to 37 GHz.

The output power performance versus frequency at the 1 dB gain compression point is shown in Fig. 6.

The output power equals to approximately 22 dBm at 0.5 GHz and is in very good agreement with simulations up to 10 GHz. However, at the 20 GHz fundamental measured output power equals 21.7 dBm which is more than 2 dB less

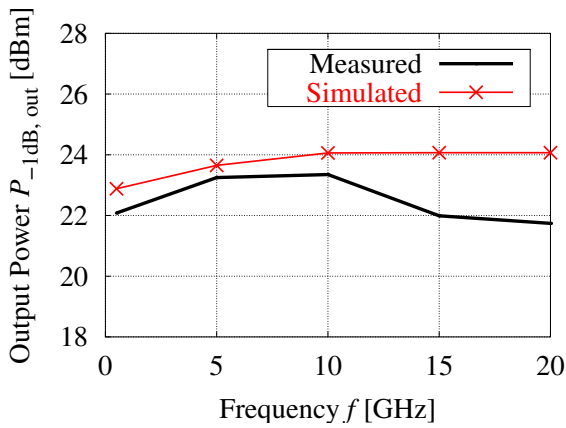


Fig. 6. Output power at -1dB gain compression. The measured output power at 20 GHz equals 21.7 dBm.

than simulated.

Group delay time performance which is important for low time jitter is shown in Fig. 7.

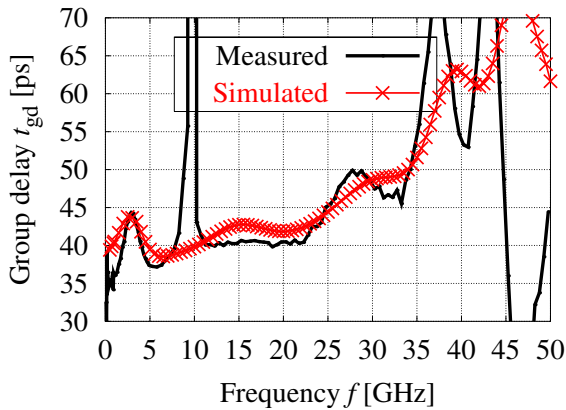


Fig. 7. The measured group delay equals ± 13 ps up to 33 GHz. At approximately 10 GHz the group delay is strongly degraded due to a resonance.

Neglecting the resonance at 10 GHz, measured group delay equals ± 13 ps up to 33 GHz and fits very well the simulation.

IV. SUMMARY

In this paper, we presented a distributed amplifier with a gain of 16.0 dB and a cut-off frequency of 40 GHz. Gain ripples are within ± 0.5 dB up to 37 GHz. Output power at the 20 GHz fundamental equals 21.7 dBm. This makes the amplifier capable for driving 40 Gbit/s LiNbO₃ modulators which require voltage swings up to $7V_{pp}$.

ACKNOWLEDGMENTS

The authors like to thank A. Trasser and P. Abele for fruitful discussions and U. Spitzberg for performing parts of the measurements. Special thanks go to UMS for fabrication of the circuits.

REFERENCES

- [1] R. DeSalvo, A. Wilson, J. Rollman, D. Schneider, L. Lunardi, S. Lumish, N. Agrawal, A. Steinbach, W. Baun, T. Wall, R. Ben-Michael, M. Itzler, A. Fejzuli, R. Chipman, G. Kiehne, and K. Kissa, "Advanced Components and Sub-System Solutions for 40 Gb/s Transmission," *IEEE Journal of Lightwave Technology*, vol. 20, no. 12, pp. 2154–2181, December 2002.
- [2] O. Wohlgemuth, P. Paschke, and Y. Baeyens, "SiGe broadband amplifiers with up to 80 GHz bandwidth for optical applications at 43 Gbit/s and beyond," *Digest of European Microwave Conference*, pp. 1087–1090, October 2003.
- [3] S. Masuda, T. Hirose, T. Takahashi, M. Nishi, S. Yokokawa, S. Iijima, K. Ono, N. Hara, and K. Joshin, "An Over 110-GHz InP HEMT Flip-chip Distributed Baseband Amplifier with Inverted Microstrip Line Structure for Optical Transmission Systems," *GaAs Digest*, pp. 99–102, 2002.
- [4] Y. Baeyens, N. Weimann, P. Roux, A. Leven, V. Houtsma, R. Kopf, Y. Yang, J. Frackowiak, A. Tate, J. Weiner, P. Paschke, and Y. Chen, "High Gain-Bandwidth Differential Distributed InP D-HBT Driver Amplifiers With Large ($11.3V_{pp}$) Output Swing at 40 Gb/s," *IEEE Solid-State Circuits*, vol. 39, no. 10, pp. 1697–1705, October 2004.
- [5] J. Rieh, B. Jagannathan, H. Chen, K. Schonenberg, S. Jeng, M. Khater, D. Ahlgren, G. Freeman, and S. Subbanna, "Performance and design considerations for high speed SiGe HBT's of $f_t/f_{max} = 375$ GHz/210 GHz," *Proc. IEEE Conf. Indium Phosphide and Related Materials*, pp. 374–377, May 2003.
- [6] N. Zamdmer, J. Kim, R. Trzcinski, J. Plochard, S. Narasimha, M. Khare, L. Wagner, and S. Chaloux, "A 243-GHz f_t and 208-GHz f_{max} , 90-nm SOI CMOS SoC technology with low-power millimeter-wave digital and RF circuit capability," *IEEE Symposium VLSI Technology*, 2004.
- [7] B. M. Ballweber, R. Gupta, and D.J. Allstot, "A Fully Integrated 0.5-5.5-GHz CMOS Distributed Amplifier," *IEEE Solid-State Circuits*, vol. 35, no. 2, pp. 231–239, October 2000.
- [8] M. Heins, C. Campbell, M. Kao, M. Muir, and J. Carroll, "A GaAs MHEMT Distributed Amplifier with 300-GHz Gain-Bandwidth Product for 40-Gb/s Optical Applications," *IEEE MTT-S Digest*, pp. 1061–1064, 2002.
- [9] M. Häfele, K. Beilenhoff, and H. Schumacher, "A GaAs PHEMT Distributed Amplifier with Low Group Delay Time Variation for 40 Gbit/s Optical Systems," *Digest of European Microwave Conference*, pp. 1091–1094, October 2003.

A New Digital Predistortion Method For Power Amplifiers Linearization

Ovidiu Leulescu¹, Teodor Petrescu²

¹PhD Student, ²Professor, Faculty of Electronics, Telecommunications and Information Technology, University POLITEHNICA of Bucharest, Romania, B-dul Iuliu Maniu 1-3, Cod: 061071, Sect. 6

E-mail: ¹ovidiu@munde.pub.ro, ²teodor.petrescu@munde.pub.ro

Tel: +40-21-4024618, Fax: +40-21-4024899

Abstract — RF predistorters are suitable for linearizing amplifier nonlinearity in high speed wireless applications. One method for modeling the nonlinear effects of the power amplifiers is to use the Volterra theory; therefore, the designing of a predistortion linearizer is realized by a circuit that creates an inverse of the model obtained from this theory (for example Wiener model) so that the power amplifier is linearized. The paper presents a new digital predistortion approach for the power amplifier linearization when we use a Wiener model for dynamic nonlinear modeling of the power amplifier. The advantage of the method is that the predistorter minimizes the total distortion power instead of reducing one specific intermodulation product by linearizing the bandpass response of the amplifier.

I. INTRODUCTION

The power amplifier (PA) is a major source of nonlinearity in a communication system. To increase efficiency, PAs are often driven into their nonlinear region, thus causing spectral regrowth as well as in-band distortion. Therefore modeling, simulation and linearization of the high PA nonlinearities, and in particular the impact these nonlinearities has in a modern digital communications system, is a current topic of intensive research worldwide.

Generally speaking, the system identification deals with the problem of how to estimate a model of a dynamical system from the measurements of the input and output signals. A lot of research studies have been done on modelling nonlinearities of a system [1]–[5].

Nonlinear systems presenting a dynamic nonlinearity have been modeled by Volterra series [5], [6] or in a distinct manner by Wiener models [4] (when the static nonlinearity follows the memory), Hammerstein models [2], [4] (when the static nonlinearity precedes the memory) or Wiener-Hammerstein models (when both the nonlinear blocks are present).

Nonlinearities are responsible for phenomena that degrade the system's performance and must be minimized. One solution to this problem is the linearization. Among all linearization techniques, digital baseband predistortion is one of the most cost effective. A predistorter, which (ideally) has the inverse characteristic of the PA, is used to compensate for the nonlinearity in the PA. Predistortion can be done by an adaptive method [7] but, for a fast signal, a direct predistortion method is more indicated.

In this paper we advance a new digital predistortion approach for the power amplifier linearization when we use a Wiener model for dynamic nonlinear modeling of the PA. The advantage of the method is that the predistorter minimizes the total distortion power instead of reducing one specific intermodulation product. Our analysis and computer simulation

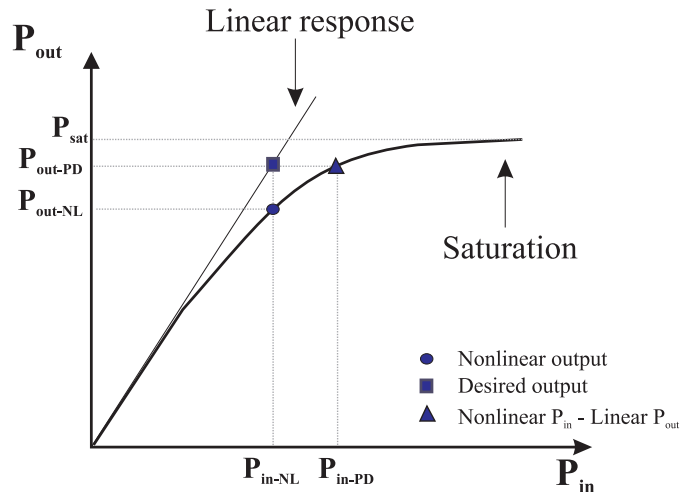


Fig. 1. Power amplifier P_{out} versus P_{in}

indicate that the method determines rapidly a very good first estimate of the static predistorter system. After that, the static predistorter is used in a dynamic predistortion of a PA. The minimization of the total intermodulation power is made by linearizing the bandpass response of the amplifier.

The outline of the paper is as follows. The static nonlinear predistorter model is presented in section II, while section III presents the theory verification by simulations. Finally, in section IV we draw the conclusions.

II. PREDISTORTION OF STATIC NONLINEARITY

Fig. 1 illustrates the typical relationship between the input power (P_{in}) and the output power (P_{out}) of a PA. Through the introduction of a PA predistorter, the P_{out} versus P_{in} curve can be forced to have a linear response over an useful range of input power levels. The slope of the Linear Output curve is the desired linear gain of the PA.

A sketch of the general system (nonlinear predistorter - PA model) is shown in Fig. 2. The nonlinear compartment of the PA is obtained with a memoryless Wiener model. We are interested to linearized the in-band compartment, therefore to eliminate the co-channel power interference and to reduce the adjacent channel power interference. In practice, predistorter not only generate the order of the nonlinearity for which they were designed but also generate residual nonlinearities of different orders. For that reason, it is important to design predistorters that reduce, as much as possible, the generation of unwanted nonlinearities. In this respect we will considered

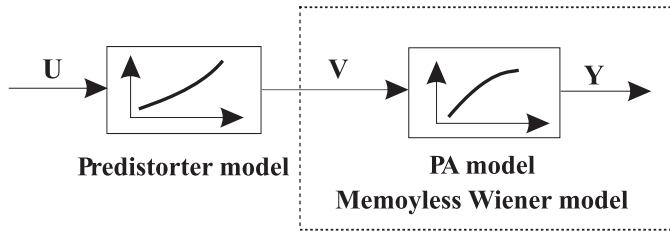


Fig. 2. Predistorter and model system for PA linearization

that, the predistorter and the PA model use a polynomial development of odd order, with the same order of nonlinearity. This assumption does not entail any loss of generality. Therefore, the static system input-output relation is:

$$y_k = \sum_{i=0}^N \alpha_{2i+1} \left(\sum_{r=0}^N \beta_{2r+1} u_k^{2r+1} \right)^{2i+1} \quad (1)$$

where u_k, y_k are the signals at the predistorter input respectively PA model output, β_{2r+1} and α_{2i+1} are the predistorter respectively the PA model nonlinear coefficients, N is the order of nonlinearity.

Taking into account the combinatory theory presented in Appendix I, the static system input-output relation (1) and the linearization condition, $y_k = Gu_k$, where G is the PA gain, we obtain the general equation for a system that allows the identification of the $N + 1$ static nonlinear predistorter coefficients (NPC):

$$\sum_{i=0}^N \alpha_{2i+1} \sum_{\xi_0, \xi_1, \dots, \xi_N=0}^{2i+1} \left[\binom{2i+1}{\xi_0, \xi_1, \dots, \xi_N} \beta_1^{\xi_0} \beta_3^{\xi_1} \dots \beta_{2N+1}^{\xi_N} \cdot u_k^{j=0}^{(2j+1)\xi_j} \right] = Gu_k \quad (2)$$

with the condition:

$$\sum_{r=0}^N \xi_r = 2i + 1 \quad (3)$$

First, it is necessary to state that the equation (2) always remains valid for all signals. Second, in order to obtain a unique system (more exactly, in order to deduce $N + 1$ relations from the equation (2)), we have to limit the general development to the $2N + 1$ order. This imposes the second condition for our evaluation system:

$$\sum_{r=0}^N (2r + 1)\xi_r \leq 2N + 1 \quad (4)$$

Finally, the system will result by u_k coefficients identification procedure applied in equation (2) and following the conditions (3) and (4):

$$\begin{cases} \alpha_1 \beta_1 = G \\ \alpha_1 \beta_3 + \alpha_3 \beta_1^3 = 0 \\ \dots \\ \alpha_1 \beta_{2N+1} + \dots + \alpha_{2N+1} \beta_1^{2N+1} = 0 \end{cases} \quad (5)$$

We introduce for the NPC determination a family of functions, F . This family has the properties that his elements can

be divided in N groups of functions, each group corresponding to a NPC evaluation. For example:

$$F_{2r+1} = \{f_{1,2r+1}(\beta_1), \dots, f_{r,2r+1}(\beta_1, \dots, \beta_{2r-1})\} \quad (6)$$

is the family's r group and it contains all the necessary functions to evaluate the coefficients β_{2r+1} .

One group contains functions that depend on the NPC formerly evaluated. A function represents all the possible combinations between the terms his depends on.

If $\beta_1, \beta_3, \dots, \beta_{2j-1}$ are the j permutable elements of a ring we will define the j functions of the r group as:

$$f_{j,2r+1}(\beta_1, \dots, \beta_{2j-1}) = \left(\sum_{p=1}^j \beta_{2p-1} \right)^\gamma \quad (7)$$

where $\gamma = f(j, r)$ has to be a natural odd number to satisfy the system (5) conditions. From the Theorem B in Appendix I will result:

$$\begin{aligned} f_{j,2r+1}(\beta_1, \dots, \beta_{2j-1}) &= \\ &= \sum_{\xi_1=0}^{\gamma} \dots \sum_{\xi_j=0}^{\gamma} \binom{\gamma}{\xi_1, \dots, \xi_j} \beta_1^{\xi_1} \dots \beta_{2j-1}^{\xi_j} \end{aligned} \quad (8)$$

with the condition:

$$\sum_{p=1}^j \xi_p = \gamma \quad (9)$$

In order to be in concordance with the limitations conditions expressed for (2), it is also necessary to limit our functions development. From (4), the limitation condition in the $f_{j,2r+1}$ case will result:

$$\sum_{p=1}^j (2p - 1)\xi_p = 2r + 1, r = \overline{1 : N} \quad (10)$$

With the F family previously defined, the system (5) can be rewritten as:

$$\begin{cases} \alpha_1 \beta_1 = G \\ \alpha_1 \beta_3 + \alpha_3 f_{1,3}(\beta_1) = 0 \\ \dots \\ \alpha_1 \beta_{2N+1} + \alpha_3 f_{N,2N+1}(\beta_1, \dots, \beta_{2N-1}) + \dots + \alpha_{2N+1} f_{1,2N+1}(\beta_1) = 0 \end{cases} \quad (11)$$

The complete transformation of the NPC systems from (5) to (11) will result if the relation $\gamma = f(j, r)$ will be established by following NPC system development. It is easy to observe in (5) that γ depends on the $2r + 1$ order, $r = \overline{1 : N}$. More exactly, because of the limitation condition (4):

$$\gamma \leq 2r + 1, r = \overline{1 : N} \quad (12)$$

Each function $f_{j,2r+1}$ depends on the $j - 1$ NPC formerly calculated. Following a system logic that will also imply the fact that for each NPC function the value of γ has to be smaller to fulfill the necessities for the condition (10), we obtain that γ depends on $2j - 1$.

Correlating the relation (3), which indicates that the β power summation for a certain term has to be an odd number, with the previous two observations it will be concluded that γ can be express in one of the two followings forms $\gamma_{1,2} = 2r + 1 - (2j - 1) \pm 1$, $r = \overline{1 : N}$ and $j = \overline{1 : r}$. By a simple application of this two solutions in the second equation of the system (11)

the only solution that remains to express γ , in function of the order of nonlinearities and of the NPC formerly calculated, will be:

$$\gamma = 2r + 1 - (2j - 1) + 1 = 2(r - j) + 3 \quad (13)$$

By this system transformation we obtain an iterative process that can be concluded in the form:

$$\beta_{2r+1} = \begin{cases} \frac{G}{\alpha_1}, & r = 0 \\ -\sum_{j=1}^r \frac{\alpha_{2(r-j)+3}}{\alpha_1} f_{j,2r+1}(\beta_1, \dots, \beta_{2j-1}), & r = \overline{1:N} \end{cases} \quad (14)$$

where $f_{j,2r+1} \in F_{2r+1} \subset F$:

$$\begin{aligned} f_{j,2r+1}(\beta_1, \dots, \beta_{2j-1}) &= \\ &= \sum_{\xi_1=0}^{2(r-j)+3} \dots \sum_{\xi_j=0}^{2(r-j)+3} \binom{2(r-j)+3}{\xi_1, \dots, \xi_j} \beta_1^{\xi_1} \dots \beta_{2j-1}^{\xi_j} \end{aligned} \quad (15)$$

when $r = \overline{1:N}$, $j = \overline{1:r}$ and with the conditions:

$$\begin{cases} \sum_{p=1}^j (2p-1)\xi_p = 2r+1 \\ \sum_{p=1}^j \xi_p = 2(r-j)+3 \end{cases} \quad (16)$$

III. APPLICATION AND ANALYSIS OF DIGITAL PREDISTORTION METHOD

For the computer simulation we have realized a program based on the theory developed in [1] and [8]. At each level of nonlinearity we have evaluated, for each frequency, the contribution of all terms generated, owing to the nonlinearity, by frequency in discussion and also the contributions of all other frequencies that can appear by different combination between different order terms. In this simulation we take into account the even order terms which also contribute, by frequency summation, at the odd order terms. We have assumed that the terms we are dealing with are symmetric functions of their arguments; any permutation of the arguments does not change the function values. It is not the purpose of this paper to present the method of memoryless Wiener model coefficients evaluation [9], therefore we will consider the coefficients, α_{2i+1} , $i = 0 : \overline{N}$, of the PA model already know.

From a practical point of view, an important observation is that the region of the P_{out} versus P_{in} curve (see Fig.1) that can be linearized using predistortion is limited by a number of variables: the number of coefficients available over the full input power range (for example a higher density of coefficients at the larger input power levels where the PA is most nonlinear), the transistor breakdown voltage, and the dynamic range of the digital-to-analog converters. All this can be avoided by reducing the PA gain. Fig. 3 presents the predistorter input-output characteristics for different gain values. It is obvious that some of the values on certain characteristics (for example on the G_{max} characteristic) can not be applied at the power amplifiers input. This affirmation is validated by the characteristics on Fig. 4, where the PA linear response for the maximum gain is presented. It can be seen that not all the points on the nonlinear PA response can

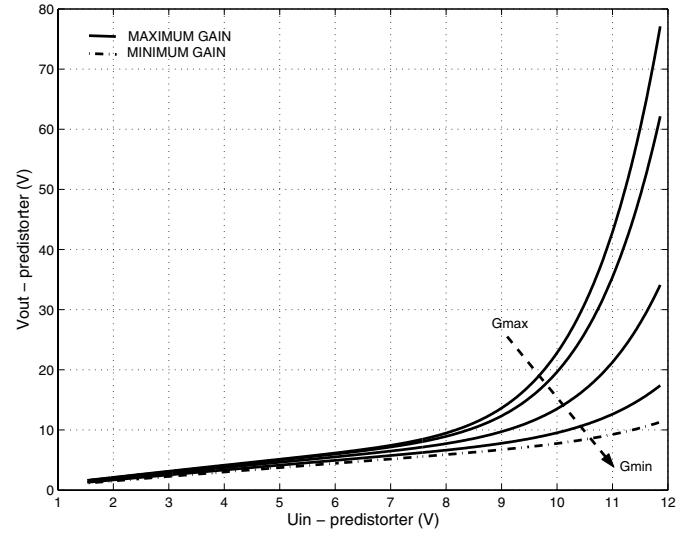


Fig. 3. Predistorter AM/AM characteristic for different desired gain values

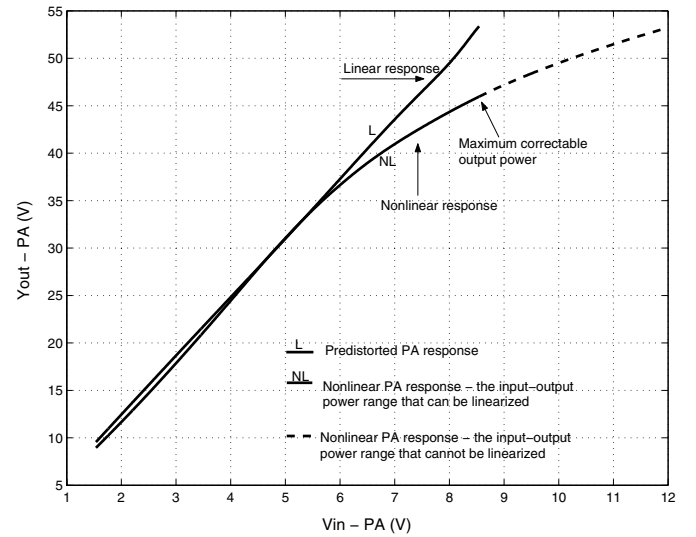


Fig. 4. AM/AM characteristics for PA (class AB) with and without predistorter evaluated at the G_{max}

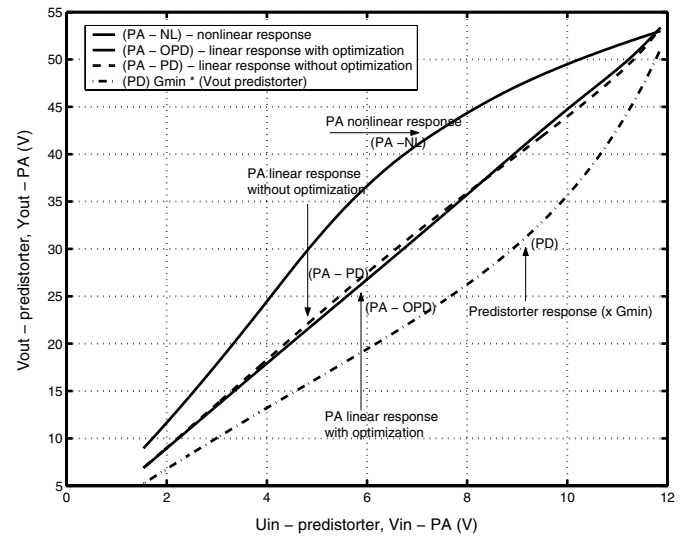


Fig. 5. AM/AM characteristics for PA (class AB) with and without predistorter evaluated at the G_{min}

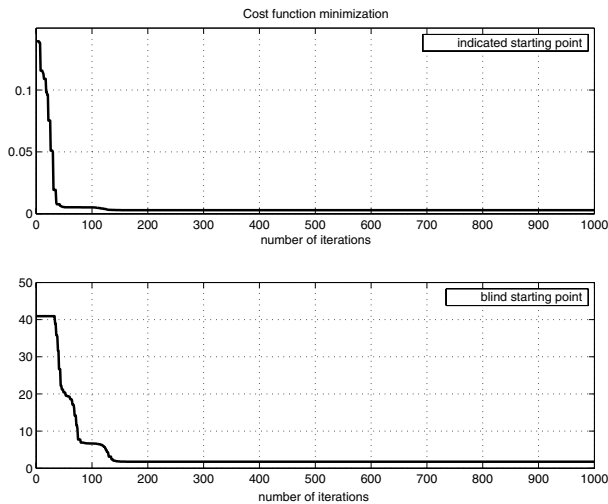


Fig. 6. Algorithm convergence: the upper figure indicates the convergence with the indicated starting point; the lower one indicates the convergence with a blind starting point

be linearized. In contrast, Fig. 5 presents the same PA output but for minimum gain value and therefore with a larger input power range levels. Obviously, from the theoretical point of view, the G_{max} case is more indicate (it offers the same output power with a smaller input power) but, from a practical point of view it will be necessary a bigger attention and certain limitation circuits to assure the good working of the system.

On the other hand, the theory advanced in this paper is a direct method for NPC evaluation. The method indicates at the first step an optimum point near the global one. In some cases where the level of nonlinearity is not very high, the global minimum can be obtained directly. However, this idea can not be generalized for any kind of nonlinearity because our method ignores in equation (2) all the terms which have an order bigger than $2N + 1$. In consequence, for a high level of nonlinearity where we have to take N at a sufficiently bigger value, we loose an important number of terms by simplification. Therefore the NPC can be obtained by means of an iterative method, starting at the nonlinear point indicated by our theory and following the minimization of a cost function.

This is presented in Fig. 5 where we can see that the minimum offered by a direct application of our theory is a good one and therefore the co-channel power interference will be drastically reduced. If necessary, we can obtain a better one by means of an optimization method. The iterative process will converge rapidly and efficiently. To prove our affirmation we compare in Fig. 6, from the point of view of the convergence and time convergence, the method presented in this paper with one that use an optimization algorithm which starts at a blind value [9].

IV. CONCLUSION

It has been proved that our approach can determine an optimum predistortion set of coefficients for a large level of nonlinearity. However, the limitation terms necessary for calculation in this method imply that a very high PA nonlinearity can not be totally linearized without an optimization algorithm. In this case we can obtain by our technique only an optimum starting point which assures a fast and efficient convergence to a global optimum set of coefficients. It has also been proved

that by choosing the right power level gain for the PA we can realize the desired predistortion procedure. We have to make a compromise between the PA gain and the accuracy of the predistortion. It is obvious that the minimization of both co-channel power interference and adjacent channel interference is made by linearizing the bandpass response of the amplifier.

APPENDIX I

We use this section to remember some theorems and definitions of the combinatory theory which will be necessary to prove our predistortion approach.

Theorem A If (a_1, a_2, \dots, a_m) is a set of $m \geq 1$ integers such as:

$$a_1 + a_2 + \dots + a_m = n, \quad m \geq 1, n \geq 0 \quad (17)$$

the number of possible combinations $M = (A_1, A_2, \dots, A_m)$ of N , where N is the number of possible combinations of n ($|N| = n$), such as $|A_i| = a_i, i = 1 : m$, will be equal to:

$$\frac{n!}{a_1! a_2! \dots a_m!} = \binom{n}{a_1, a_2, \dots, a_m} \quad (18)$$

Theorem B If x_1, x_2, \dots, x_m are the m permutable elements of a ring ($\Leftrightarrow x_i x_j = x_j x_i, 1 \leq i \leq j \leq m$) they can be written for all $n \geq 0$:

$$\left(\sum_{i=1}^m x_i \right)^n = \sum \binom{n}{a_1, a_2, \dots, a_m} x_1^{a_1} x_2^{a_2} \dots x_m^{a_m} \quad (19)$$

the last summation takes place after all m combination of integers (a_1, a_2, \dots, a_m) , $a_i \geq 0$ such as relation (17) are always satisfied.

REFERENCES

- [1] S. A. Mass, "Nonlinear Microwave Circuits", *IEEE Press*, New York, 1997.
- [2] A. Garulli, L. Giarrè and G. Zappa, "Identification of Approximated Hammerstein Model in a Worst-Case Setting", *IEEE Transactions on Automatic Control*, Vol.47, No.12, December 2002.
- [3] J. Schoukens, T. Dobrowiecki and R. Pintelon, "Identification of Linear Systems in the Presence of Nonlinear Distortions. A Frequency Domain Approach. Part I: Non-Parametric Identification. Part II: Parametric Identification.", *IEEE Proceedings of the 34th Conference on Decision & Control*, New Orleans, LA, December 1995.
- [4] P. Crama, J. Schoukens, "First estimates of Wiener and Hammerstein Systems Using Multisine Excitation", *IEEE Instrumentation and Measurement Technology Conference, Budapest, Hungary*, May 2001.
- [5] S. Benedetto, E. Biglieri and R. Daffara, "Modeling and Performance Evaluation of Nonlinear Satellite Links - A Volterra Series Approach", *IEEE Transaction on Aerospace and Electronics Systems*, Vol. AES-15, No.4, July 1979.
- [6] E. Ngoya et al., "Accurate RF and Microwave System Level Modeling of Wide Band Nonlinear Circuits", *IEEE MTT-S Digest*, 2000
- [7] A. A. M. Saleh and J. Salz, "Adaptive linearization of power amplifiers in digital radio systems", *Bell Syst. Tech.*, Vol.62, No.4, April 1983, pp. 1019-1033.
- [8] J. Carlos Pedro and N. Borges Carvalho, "Intermodulation Distortion in Microwave and wireless circuits", *Artech House*, London, 2003.
- [9] O. Leulescu, "A First Approximation Procedure of the Static Nonlinear Predistorter in the case of Power Amplifiers", *IEEE MTT-S Topical Workshop on Power Amplifiers for Wireless Communications*, San Diego, CA, September 2004

Design of a Monolithic 79 GHz Rectenna with MOTT Diodes

Michael Morschbach, Simon Diemer, Michael Oehme, Erich Kasper

University of Stuttgart, Institute of Semiconductor Engineering, 70569 Stuttgart, Germany,
+497116858011, morschbach@iht.uni-stuttgart.de

Abstract — In this paper a concept and first simulation results for a monolithic integrated rectenna on high resistivity silicon with Schottky diodes operating at MOTT operation is presented. Due to the expected low output voltage of the rectenna, a pre-amplification of the output voltage of the rectenna is done using a commercially available gain block.

As high resistivity silicon substrate, a common FZ (float zone) substrate was used. The layout of the vertical and lateral design is discussed. The simulation data according to the realized layout are shown. Additionally the mounting of the rectenna and a preamplifier into a DIP package is presented.

The monolithic integrated rectenna can be used as a field probe. By building an array out of single rectenna chips, also a detection of the angle can be done.

I. INTRODUCTION

According to the still increasing traffic volume, safety aspects are gaining more and more in importance. A basic approach is to monitor the surrounding of the vehicle with a radar signal, [1].

A straight forward concept for detection of mm-wave signals is a rectifying antenna (short: rectenna) which consists of a planar antenna and a rectifying detector. The rectifying detector can be realized with Schottky-diodes.

The aim of this work is a monolithic integrated, single chip, rectenna. With an integrated solution on high resistivity silicon a reliable and cost effective chip is achieved. A possible application area for the discussed rectenna can be found in the automotive sector. Possible tasks for the rectenna can be the determination of frequency, direction, intensity or polarization of a radar signal. According to the small dimensions of the rectenna, observation of the previous named parameters can be done during the operation of the radar system. By the usage of the rectenna, a self-monitoring radar system can be realized. Therewith a constant performance of the radar system will be achievable over the whole life cycle.

II. EPITAXIAL GROWTH AND FABRICATION

A. Epitaxy

The layers of the Schottky diode have been grown by molecular beam epitaxy (MBE). A high resistivity (HR) float zone (FZ) silicon substrate was used to reduce attenuation losses, [3]. The used FZ wafers have a resistivity of $\rho \geq 1000 \Omega\text{cm}$. According to the detection of signals up to 100 GHz, the cut-off frequency of the diodes has to be in the THz range. Cut-off frequencies of some THz can be achieved by the MOTT operation, [4]. To realize MOTT operation for the diodes, a special and very accurate doping profile is needed, [4] - [7]. Deposition of layers by MBE enables a very sharp transition, of several orders of magnitude, of the doping. Additionally, the doping concentration can be adjusted accurately in a wide range, from intrinsic (limited by the background doping of the system) to approximately 10^{20} cm^{-3} (depending on the dopant).

To guarantee a defect free and homogeneous surface, which is needed for a good crystal quality of the deposited layers, a 150 nm thick intrinsic buffer is grown. This buffer is used to overgrow possible surface defects of the substrate. This assures that the following layers can be grown defect free. For the ground contact of the diode a epitaxial Buried Layer (BL) is grown after the buffer. The BL is a 500 nm thick layer with a Sb doping concentration of 10^{20} cm^{-3} . According to the high doping concentration of the BL, a small layer resistance R_{SH} and therefore a small series resistance will be achieved. As final layer the so-called Schottky Layer (SL) is deposited. The SL is a 10^{15} cm^{-3} doped and 150 nm thick layer. The whole layer structure is shown in Fig. 1.

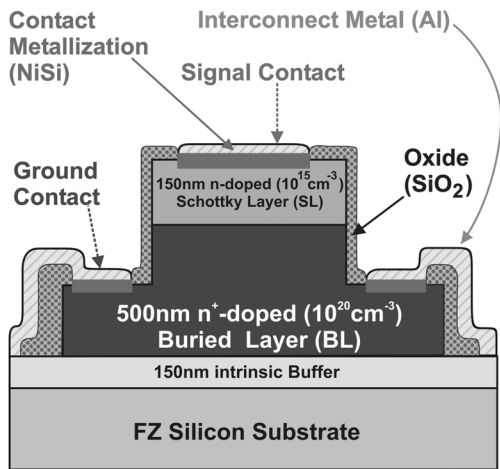


Fig. 1: Cross section of the realized Schottky diode, after etching the mesa, passivation of the surface and contacting with NiSi. Aluminum was used for the interconnect. Also the used layer stack is shown in the picture.

As a consequence of the used nickel-silicide contact of the diode, the layer thickness of the SL is reduced. The reduction of the low doped SL has to be taken into account during the layer design. If the reduction is not added to the aimed thickness, a higher capacitance of the diode is the consequence. The higher capacitance will lead to an reduced cut-off frequency of the diode and reduce the frequency band in which the diode can be used. The advantage of the NiSi contact is a reduced Schottky barrier height, [8]. This increases the current to voltage ratio and enables therefore even the detection of low power signals.

B. Fabrication

The diodes are realized within a Front End of Line (FEOL) process of Schottky-MEMS integration process. The integration process is described in detail in [9].

First the upper mesa area is defined in a dry etch process. With the definition of the upper mesa, the SL is etched down to the BL. In a second step the BL is etched down to the substrate and therefore the cathodes of the diodes are separated against each other. The etch edges are passivated with SiO₂. In the passivation oxide, contact holes are etched. The area of the contact holes on the upper mesa (SL) defines the electrical effective area for the Schottky contact. For the contact metallization nickel is deposited on the surface. Within an annealing step at 450°C, the nickel in the contact holes reacts with the silicon of the underlying layer to nickel silicide (NiSi). The nickel which lays on the passivation oxide can be removed after the silicidation process. Finally, for the interconnect aluminum is deposited and structured.

III. FUNCTIONALITY OF THE RECTENNA

The antenna functions as a band pass and therefore only the resonant frequency of the antenna is received. Based on the polarity of the diodes, one half-wave of the received signal is shortened to the mass using a radial stub. The remaining half-wave is smoothed by a low pass, consisting of a three-stage LC-filter. The gained signal can be treated as a DC current.

The whole rectenna is designed in microstrip topology. To suppress resonances within the substrate and to keep attenuation low, the substrate has to be thinned to a thickness of 200 μm. The circuit scheme is shown in Fig. 2.

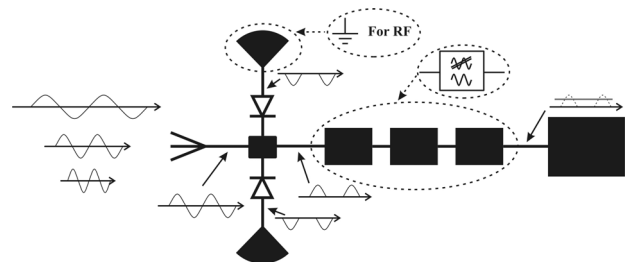


Fig. 2: Circuit schematic of the realized rectenna

IV. LAYOUT AND SIMULATION RESULTS

In this chapter the used layout of the rectenna is presented. Further the simulated results for the antenna part, receiving at 79 GHz, are shown.

A. Layout

The layout of the rectenna, as shown in Fig. 3, consists of the antenna unit, the rectifying unit and the smoothing unit. In the following the antenna unit will be discussed in more detail.

The antenna unit consists of half-wavelength stubs. These stubs stick alternately on the left and on the right hand side of a microstrip line. The distance between two half-wavelength stubs is also the half wavelength. The sensitivity as well as the selectivity of the antenna unit can be increased by using longer antenna branches. In our case a antenna branch consists of 8 alternate $\lambda/2$ -stubs with a open $\lambda/2$ -waveguide. The antenna unit is made up of two identical antenna branches.

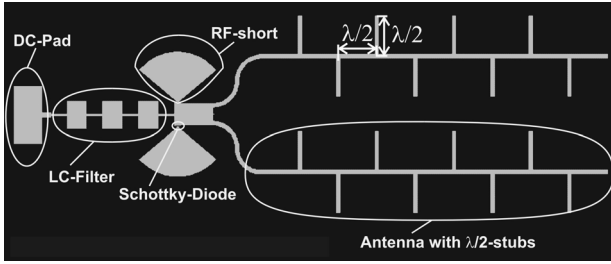


Fig. 3: Layout of the realized rectenna with labeled function blocks.

The receiving wavelength λ can be calculated as follows:

$$\lambda = \frac{c}{f_{\text{rec}} \cdot \sqrt{\epsilon_r}} \quad (1)$$

After equation (1) the receiving wavelength depends on the receiving frequency f_{rec} , the light velocity c and the square root of the permittivity of the substrate. The receiving wavelength is smaller compared to the wavelength in space as a consequence of the microstrip technology.

Based on equation (1) the parameters for the realized rectenna are summarized in Table 1. For the used silicon substrate a wavelength of approx. 1.1 mm is needed to receive a 79 GHz signal. Therefore the $\lambda/2$ -stubs are approx. 552 μm long. The microstrip line was designed for a characteristic impedance Z_0 of 50 Ω . The realized thickness of the substrate and the width of the signal line are calculated using the LineCalc tool provided by the used simulation tool ADS from Agilent Technologies. The following simulation results are calculated using Momentum included in ADS.

Table 1: Design parameters of the rectenna:

Parameter	Value
Receiving frequency	79 GHz
Permittivity of silicon ϵ_r	11.8
Velocity of light	$299.79 \cdot 10^6$ m/s
Wavelength λ	1.1047 mm
Half-wavelength $\lambda/2$	552 μm
Characteristic Impedance Z_0	50 Ω
Width of the microstrip line w_{line}	60 μm
Thickness of the substrate d_{sub}	200 μm

B. Simulation

Fig. 4 shows the simulated S_{11} -parameter of the antenna. The antenna is simulated as a radiating antenna. According to the principle of a reciprocal antenna, the same behavior for a receiving antenna is expected.

At the minimum, indicated by marker m2, the input reflection is lowest. According to the minimal reflected power at this point the maximum power can be radiated by the antenna. Therefore the receiving frequency for the realized antenna is expected to be 79.2 GHz. As can be seen, the simulated resonance frequency is only approx. 0.2 % larger than the targeted frequency. This low shift shows, that the wavelength calculated by using equation (1), is a very good estimation to design the antenna for a certain frequency.

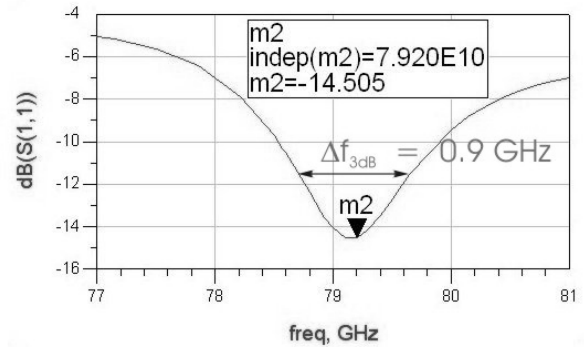


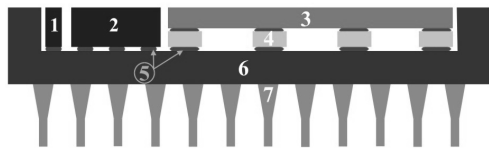
Fig. 4: Simulated S_{11} -parameter in dB for one antenna branch over the frequency.

According to the simulation shown in Fig. 4, a 3 dB-bandwidth of 0.9 GHz is expected for the antenna.

V. SIGNAL AMPLIFICATION BY MULTICHIP MODULE

To demonstrate the functionality of the monolithic rectenna-chip, a multichip module (MCM) will be fabricated. The MCM consists of the monolithic rectenna-chip, a preamplifier-chip and a resistor-chip for setting the gain. The MCM will be mounted into a 24 lead DIP ceramic package. Due to the low output signal of the rectenna chip the signal is amplified by a gain block in chip-form (AMP02GBC) which is also mounted in the DIP package. The amplification of the gain block is adjusted with a bare die resistor (TA22 1K 1%). The amplified signal will be displayed by an analog instrument.

Fig. 5 shows the schematic cross section through the packaged multichip module. The rectenna chip is approx. only half as thick as the amplifier. To get the same height for the chips, so that the bond bumps are on the same level, the rectenna chip has to be lifted up using spacers.



1: Resistor (commercial bare die) 5: Glue-Bumps
 2: Preamplifier (commercial bare die) 6: DIP
 3: Rectenna-Chip (SIMMWIC on FZ) 7: Pins
 4: Si-Spacer

Fig. 5: Cross section through the multi chip module housed in a 24 lead DIP ceramic package.

Fig. 6 shows the positions of the bond wires and the position of the rectenna, amplifier and resistor.

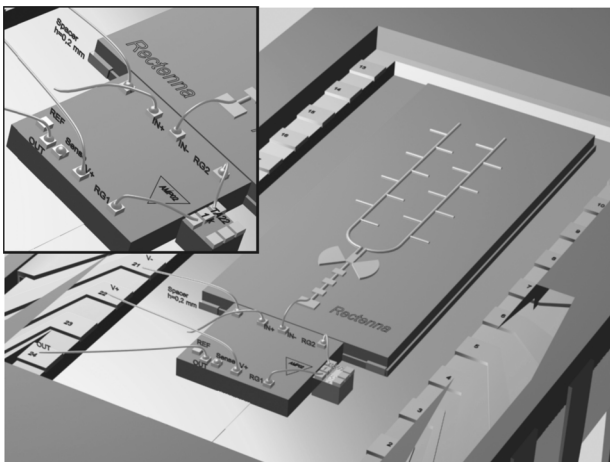


Fig. 6: 3D schematic of the multi chip module. The rectenna consists of two antenna branches. The wire bonds and the positions of the single chips are shown.

VI. CONCLUSION

The target for this research was to show that a monolithic integrated rectenna can be fabricated on high resistivity silicon. In the antenna part a microstrip waveguide with several $\lambda/2$ -stubs was used. This group antenna may further be optimized by geometrical variations.

With additional signal processing on the single chip solution and an improved antenna design, a small and cost effective chip for testing various radar applications in the automotive sector is possible. Due to the simple interrelation between the receiving frequency and the length of the $\lambda/2$ -stubs of the antenna, the rectenna can easily be scaled to receive other frequencies. Therefore the whole frequency range for automotive radar applications, from 75 up to 81 GHz, can be covered.

ACKNOWLEDGEMENT

The authors wish to acknowledge Mr. Matthies for the fabrication and Mr. Stefani for helpful discussions concerning the mounting of the rectenna. Also Mr. Schöllhorn is acknowledged for his assistance with the laser writer and helpful discussions.

REFERENCES

- [1] M. Ulm, Mikromechanische kapazitive Schalter für den Mikro- und Millimeterwellenbereich, Thesis, Chapter 1, pp. 1-8, Stuttgart, University of Stuttgart, 2003
- [2] M. Herrmann, D. Beck E. Kasper, J.-F. Luy, K. Strohm, J. Buechler, "Hybrid 90 GHz rectenna chip with CMOS preamplifier", *Proc. of the 26th Solid State Device Research Conference*, Bologna, Italy, Sept. 1996, pp. 527-530
- [3] C. Schöllhorn W. Zhao, M. Morschbach and E. Kasper, "Attenuation Mechanisms of Aluminum Millimeter-Wave Coplanar Waveguides on Silicon", *IEEE Electron Devices*, vol. 50, no.3, March 2003, pp. 740-746, USA
- [4] M. Morschbach, C. Schöllhorn, M. Oehme, E. Kasper, A. Müller, T. Buck, "Integrated Schottky Mixer Diodes with Cut-off Frequencies above 1 THz", *Proc. of the 34th European Microwave Conf.*, Amsterdam, Netherlands, October 2004, pp. 1133-1136
- [5] S. M. Sze, *Physics of Semiconductor Devices*, New York, John Wiley & Sons, 1969, Chapter 8, Section 7, p. 414
- [6] N.F. Mott, "Note on the Contact between a Metal and an Insulator or Semiconductor", *Proc. of the Cambridge Philosophical Society*, vol.34, pp.568-572, October, 1938
- [7] M. Mc. Coll and M. F. Millea, "Advantages of Mott barrier mixer diodes", *Proc. IEEE*, 61, pp. 499-504, 1973
- [8] M. Morschbach, C. Schöllhorn, M. Oehme, E. Kasper, "RF-Schottky diodes with Ni silicide for mixer applications", *Topical Meeting on Silicon Monolithic Integrated Circuits in RF Systems, Digest of Papers 2003*, vol. 1, pp. 122-125, 9-11 April 2003, Germany
- [9] C. Schöllhorn, M. Morschbach, S. Haak, J. Seidel and E. Kasper, "Systemintegration von Mikrowellen Schottky-Mischern und MEMS-HF-Schaltern", *Frequenz*, vol. 57, no. 3-4, pp. 45-50, March, 2003

EVM- und BER-optimierter differentieller Einseitenbandmodulator

Holger Erkens¹ und Holger Heuermann²,

Lehrstuhl für Hochfrequenztechnik, Fachhochschule Aachen

¹holger.erkens@rwth-aachen.de, +49 (0)241-60092107, ²heuermann@fh-aachen.de, +49 (0)241-60092108

Abstract— Various circuit concepts are known for modulation of a baseband signal on an RF carrier. IQ modulators are the devices of choice for SSB modulation in virtually any modern cellular phone system. Still, this concept suffers from the fact that the bit error rate (BER) increases rapidly with a badly matched modulator output.

This paper presents a new SSB modulator concept with an increased BER for poorly matched outputs. It features a coupler consisting of only two concentrated elements (inductivity and capacitor) as the key device. Therefore, the part count is also improved. The increased BER will be shown in comparison with a common IQ modulator on the basis of an ADS EDGE simulation.

I. EINLEITUNG

Bei der Umsetzung niederfrequenter Basisbandsignale erzeugen selbst Mischer mit günstigen Ausgangsspektren (z.B. Ring-Modulatoren) im Idealfall mindestens zwei hochfrequente Seitenbänder. Da beide Seitenbänder die gleiche Information enthalten, wird zur Einsparung von Übertragungsbandbreite nur ein Seitenband übertragen. Diese Einsparung kann mit Einseitenbandmodulatoren erzielt werden, wobei unterschiedliche Konzepte bekannt sind.

Einseitenbandmodulatoren¹ nach der Phasenmethode² ([8]) sind dabei die Alternative zu konventionellen Mixern mit nachgeschalteten steilflankigen Filtern. Der ESB-Modulator nach der Phasenmethode ist dabei das System der Wahl in allen preisgünstigen Transceiver-Schaltungen, da nur ein Synthesegenerator notwendig ist, auf aufwändige Filterschaltungen verzichtet werden kann und Mehrkanal-Betrieb ermöglicht wird. Ein entscheidender Nachteil ist jedoch, dass bei diesem System schon bei geringer Fehlanpassung am Ausgang eine starke BER³-Erhöhung zu beobachten ist.

Im Anschluss an die Beschreibung des herkömmlichen IQ-Modulators wird eine verbesserte Realisierungsform vorgestellt. Dieser neue IQ-Modulator soll durch Änderung der Mischer-Ansteuerung sowie den Austausch einer Komponente zwei Vorteile gegenüber dem konventionellen Konzept bieten. Erstes Ziel ist eine wesentliche Verbesserung des Ausgangsverhaltens bei Fehlanpassung zur allgemeinen Reduzierung der BER. Dies wird durch einen sehr einfach aufgebauten Koppler aus zwei konzentrierten Bauelementen erreicht, so dass sich als weiterer Vorteil die Anzahl der Bauelemente in der Komponente verringert. Gesamtziel ist also ein System,

¹kurz: ESB-Modulatoren.

²auch: IQ-Modulatoren.

³BER: Bit Error Rate.

das mit weitaus geringerem Platz- und Bauteilbedarf eine bessere Funktionalität als das bekannte System erbringt. Nach der Präsentation von Simulationsergebnissen, mit denen die Eignung des neuen Systems nachgewiesen wird, endet der Artikel mit dem Ausblick auf eine weitere Verbesserung des bekannten Modulatorkonzepts.

II. BEKANNTER EINSEITENBANDMODULATOR NACH DER PHASENMETHODE

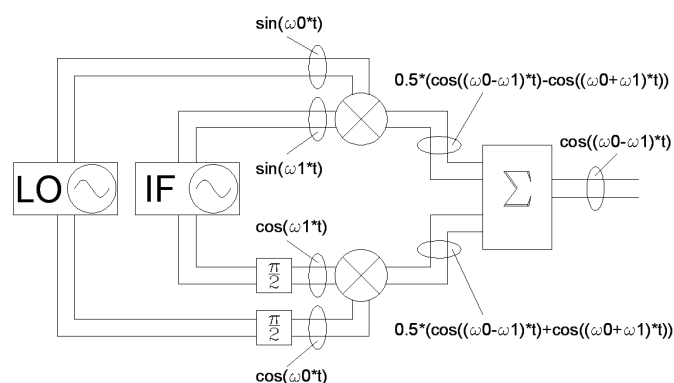


Fig. 1. Prinzipschaltbild des Einseitenbandmodulators nach der Phasenmethode. Substitutionen: $\omega_{LO} = \omega_0$, $\omega_{IF} = \omega_1$.

Fig. 1 stellt das Prinzipschaltbild eines herkömmlichen Einseitenbandmodulators dar. Das System besteht aus zwei Mixern, in denen das Basisband-Signal (IF-Signal) mit einem hochfrequenten Trägersignal (LO-Signal) in das Übertragungsband hochgemischt (im Zeitbereich multipliziert) wird. Dabei werden IF- und LO-Signal einerseits direkt (In-Phase-Anteil) und andererseits mit 90° Phasenverschiebung (Quadratur-Anteil) eingespeist.

Reduziert man das zu übertragende Signal auf eine monofrequente Sinus-Schwingung, so liegen an den Mixern einerseits die In-Phase-Signale $\sin(\omega_{LO} t)$ und $\sin(\omega_{IF} t)$ und andererseits aufgrund der Phasenverschiebung die Quadratur-Signale $\cos(\omega_{LO} t)$ und $\cos(\omega_{IF} t)$ an.

Nach Multiplikation in den Mixern und Überlagerung im Summierer ergibt sich folgendes Ausgangssignal:

$$S_{out} = \frac{\cos((\omega_{LO} - \omega_{IF})t)}{2} + \frac{\cos((\omega_{LO} + \omega_{IF})t)}{2}$$

$$+ \underbrace{\frac{\cos((\omega_{LO} + \omega_{IF})t)}{2} - \frac{\cos((\omega_{LO} - \omega_{IF})t)}{2}}_{=0}$$

$$S_{out} = \cos((\omega_{LO} - \omega_{IF})t). \quad (1)$$

Es wird also nur das untere Seitenband zur Übertragung bereitgestellt, da sich die Signale des oberen Seitenbands im Summierer vollständig destruktiv überlagern. Die Energie des oberen Seitenbands wird in einem Widerstand des Summierers absorbiert.

III. THEORIE DES NEUARTIGEN MODULATORS

Eine wichtige Rolle im neuen Modulordesign spielt der so genannte LC-Koppler. Er soll im Weiteren näher vorgestellt werden. Im Anschluss wird die Integration des LC-Kopplers in den neuartigen Modulator sowie das Funktionsprinzip des Gesamtsystems beschrieben.

A. Funktionsprinzip des LC-Kopplers

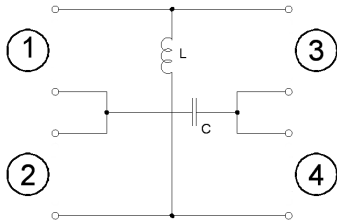


Fig. 2. Schaltung des differentiellen LC-90°-Kopplers.

Fig. 2 stellt den verwendeten LC-Koppler dar. Dieser Koppler funktioniert tadellos in rein differentiellen Systemen und nach Modifikationen in unsymmetrischen Systemen ([7]). Bei Einspeisung am differentiellen Tor 1 ist das differentielle Tor 4 vollständig entkoppelt. Dieses Tor ist bei Anwendung im ESB-Modulator mit der differentiellen Systemimpedanz abzuschließen. Das einlaufende Signal wird zu gleichen Teilen zu den differentiellen Toren 2 und 3 übertragen. Dabei ergibt sich als Phasendifferenz zwischen den übertragenen Signalen ein Wert von 90°. Abgesehen von der Torentkopplung dient die Komponente also zusätzlich als Phasenschieber. Beide Eigenschaften sind für die Funktion des vorgestellten Systems notwendig. Die beiden Elemente des Kopplers lassen sich dabei unter Berücksichtigung der Arbeitsfrequenz f_0 und der differentiellen Systemimpedanz Z_{odd} folgendermaßen auslegen:

$$C = \frac{1}{2\pi f_0 Z_{odd}} \quad \text{und} \quad L = \frac{Z_{odd}}{2\pi f_0}. \quad (2)$$

Der Koppler wurde für $f_0 = 1$ GHz und $Z_{odd} = 100 \Omega$ simuliert. Für diese Parameter ergaben sich die Bauelementwerte $C = 1.59$ pF und $L = 15.92$ nH. Reflexion und Transmissionen für das differentielle Tor 1 wurden in Fig. 3 dargestellt. Jenes Tor ist bestens angepasst und vom differentiellen Tor 4 entkoppelt ($S_{d11} = S_{d41}$). Die Übertragungsparameter S_{d21} und S_{d31} haben wie erwartet bei f_0 den gleichen Betrag (gleichmäßige Leistungsteilung). Signale zum differentiellen

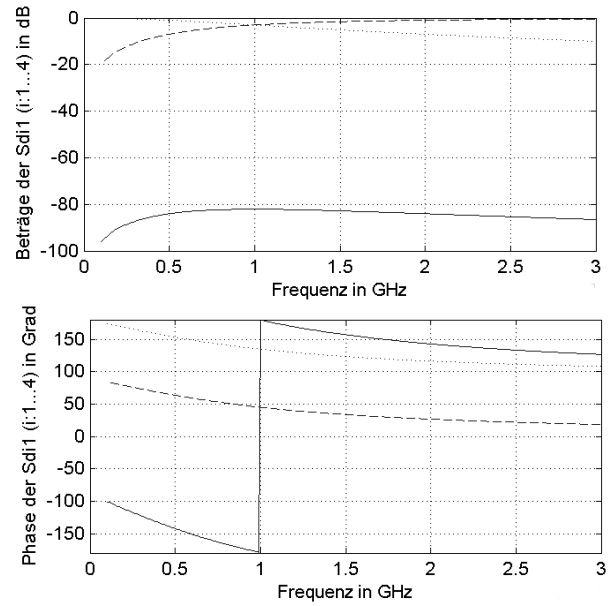


Fig. 3. Beträge und Phasen des differentiellen LC-Kopplers. Liniert: S_{d11} und S_{d41} , punktiert: S_{d21} , gestrichelt: S_{d31} .

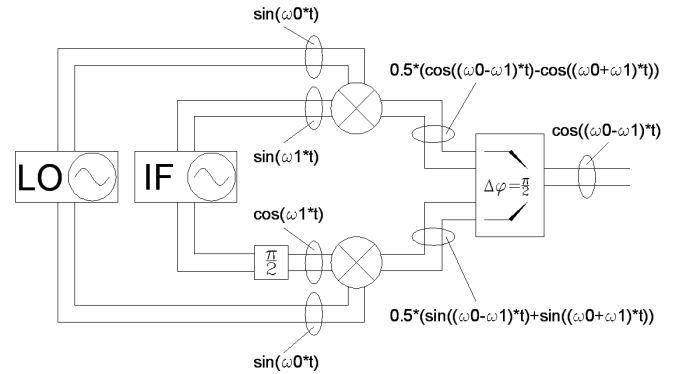


Fig. 4. Prinzipschaltbild des Einseitenbandmodulators mit LC-Koppler. Substitutionen: $\omega_{LO} = \omega_0$, $\omega_{IF} = \omega_1$.

Tor 2 eilen denen zum differentiellen Tor 3 um 90° vor. Durch entsprechende Wahl der Tore kann also das Vorzeichen der Phasendrehung gewählt werden.

B. Neuartiger Einseitenbandmodulator mit LC-Koppler

Die neue Variante des ESB-Modulators wird in Fig. 4 beschrieben. Da das LO-Signal diesmal bei beiden Mixern ohne Phasendrehung anliegt, ergeben sich zur Überlagerung mittels LC-Koppler andere Mischprodukte gegenüber dem zuvor beschriebenen IQ-Modulator.

Für den In-Phase-Mischer gilt nach wie vor:

$$S_{in-phase} = \sin(\omega_{LO} t) * \sin(\omega_{IF} t)$$

$$= \frac{\cos((\omega_{LO} - \omega_{IF})t)}{2} - \frac{\cos((\omega_{LO} + \omega_{IF})t)}{2}.$$

Der Quadratur-Mischer erzeugt nun aber folgendes Signal:

$$S_{quadrature} = \sin(\omega_{LO} t) * \cos(\omega_{IF} t)$$

$$= \frac{\sin((\omega_{LO} - \omega_{IF})t)}{2} + \frac{\sin((\omega_{LO} + \omega_{IF})t)}{2}.$$

Beide Signale werden im LC-Koppler überlagert. Dabei wird eines der Eingangssignale um den Betrag von 90° gegenüber dem anderen phasenverschoben. Für den ESB-Modulator soll nun das Quadratur-Signal um $+90^\circ$ verschoben werden. Dann ergibt sich als Ergebnis der Überlagerung nach einigen Umformungen:

$$S_{in-phase} + S_{quadrature} \cdot e^{j90^\circ} = \cos((\omega_{LO} - \omega_{IF})t). \quad (3)$$

Dieses Ergebnis zeigt, dass ein ESB-Modulator auch mit einem LC-Koppler realisierbar ist. Die Energie des oberen Seitenbands wird in einem an den LC-Koppler angeschlossenen Widerstand absorbiert.

Dem neuartigen ESB-Modulator liegt das Funktionsprinzip des balancierten Verstärkers ([1]) zugrunde. Dort werden zu verstärkende Signale zunächst mit einem Branchline-Koppler aufgeteilt und anschließend identischen Verstärkerstufen zugeführt. Zuletzt werden die verstärkten Signale in einem weiteren Branchline-Koppler zum endgültigen Ausgangssignal überlagert. Hier wird die Eigenschaft des Branchline-Kopplers ausgenutzt, dass ein Tor bei identischem Abschluss der beiden nicht von ihm entkoppelten Tore unempfindlich gegenüber Fehlanpassungen ist. Dies geschieht, da sich eventuell an den Verstärkern reflektierte Signalanteile am Ein- bzw. Ausgang des Kopplers destruktiv überlagern und im angeschlossenen Widerstand absorbiert werden.

Da ein LC-Koppler dem Branchline-Koppler bezüglich Leistungsteilung und Phasendrehung gleicht, kann man ihn ersatzweise verwenden. Dabei hat ein LC-Koppler viele Vorteile gegenüber dem Branchline-Koppler. Er ist aufgrund von nur zwei Bauelementen vor allem preiswerter und verlustärmer. Gegenüber dem meist in Leitungstechnik aufgebauten Branchlinekoppler ist er gerade im unteren Gigahertz-Bereich sehr kompakt.

IV. SIMULATION

A. Grundlegendes zur Testmethode

Der neue ESB-Modulator ist besonders interessant für modernste lineare Mobilfunkapplikationen, da sich eine Fehlanpassung des Mixers hier direkt in einer höheren Bitfehlerrate für die Datenübertragung niederschlägt. Daher wurde der Mobilfunkstandard EDGE (Enhanced Data rates for GSM Evolution) für die Simulation ausgewählt. EDGE stellt eine Weiterentwicklung von GSM dar und ist als Zwischen- bzw. Zusatzlösung zum kommenden UMTS-Standard geplant. Während bei dem bei GSM verwendeten GMSK in einem Zeittakt nur ein Bit durch Phasendrehung in 90° -Schritten übermittelt wird, ist bei 8PSK des EDGE-Standards die Übermittlung von drei Bits pro Zeittakt möglich. 8PSK ist jedoch fehleranfälliger als GMSK, da die verschiedenen Symbole in der IQ-Ebene näher beieinander liegen und tolerierbare Abweichungen aufgrund von Fehlern daher kleiner sein müssen.

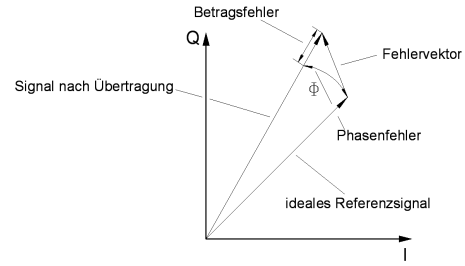


Fig. 5. Definition des Fehlervektors in der IQ-Ebene zur Erläuterung des EVM.

Ein Maß für die Größe der Abweichung ist der Fehlervektor, welcher in Fig. 5 erläutert wird. Aufgrund der komplexen Natur der IQ-Ebene teilt sich der Fehlervektor in Betrag und Phase auf. Da die Größe des Fehlervektors in einem direkten Verhältnis zur Bitfehlerrate steht, kann der Fehlervektor als Qualitätsmerkmal des ESB-Modulators herangezogen werden.

Es wird der Error Vector Magnitude⁴ betrachtet, der wie folgt definiert ist:

$$EVM = \frac{100\%}{S_{max}^2} * \sqrt{\frac{1}{N} \sum_{j=1}^N [(\delta I_j)^2 + (\delta Q_j)^2]}. \quad (4)$$

N : Anzahl der zur Auswertung verarbeiteten Symbole.

S_{max} : Betrag des vom IQ-Nullpunkt entferntesten Symbols.

δI_j : Realteil des Symbolfehlers.

δQ_j : Imaginärteil des Symbolfehlers.

B. Simulationsaufbau

Zur Prüfung der Leistungsfähigkeit des neuen ESB-Modulators wurde der System- und Schaltungssimulator ADS der Firma Agilent verwendet. Die aufgebaute Simulation basiert weitgehend auf der Beispielsimulation „EDGE Traffic Channel Measurement in RF“. Die Simulation besteht in erster Linie aus einem EDGE-Transmitter für 8PSK-modulierte Symbole sowie aus dem Modulator im Sub-Circuit und einem EVM-Test zur Auswertung der Übertragungsqualität.

Der Sub-Circuit besteht neben einigen Komponenten zur Signalbearbeitung vor allem aus den beiden Mixern sowie dem Koppler des neuen ESB-Modulators. Da das vorgestellte System für differentielle Leitungssysteme konzipiert wurde, findet vor den Mixern eine Konversion des unsymmetrischen Eingangssignals in ein Gegentaktsignal statt. Als Mixer wurden Gilbert-Zellen ausgewählt, da diese in zahlreichen Halbleiterschaltungen zu finden sind und damit einen realistischen Referenz-Mischer darstellen. Zur Nachbildung von direkt hinter dem Modulatorausgang geschalteten Übertragungsstrecken befindet sich dort eine elektrisch lange Leitung.

C. Simulationsergebnisse

Der bekannte ESB-Modulator nach Fig. 1 wurde mit dem neuartigen ESB-Modulator nach Fig. 4 in der ADS-Simulation verglichen. Die Ausgangsanpassung wurde dabei durch die Variation des Abschlusswiderstands verändert.

⁴kurz: EVM.

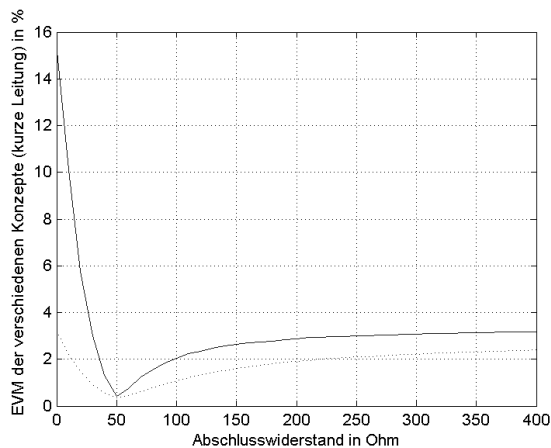


Fig. 6. Resultate für das herkömmliche und das neue Konzept. Die Ergebnisse für den neuen IQ-Modulator wurden punktiert dargestellt.

Die Ergebnisse für die EVM-Messung wurden in Fig. 6 dargestellt. Wie zu sehen ist, fällt der Fehlervektor wesentlich niedriger aus als bei dem herkömmlichen ESB-Modulator. Bei Anpassung verhalten sich beide Systeme ähnlich gut, der verbleibende Fehler beruht hier auf Nichtlinearitäten in den Verstärkerstufen. Das neue Konzept erzielt im Falle der Fehlanpassung deutlich bessere Ergebnisse.

V. FAZIT UND AUSBLICK

Wie die Simulationsergebnisse zeigen, ist der neuartige ESB-Modulator eine Komponente, welche merkliche Vorteile gegenüber der bislang bekannten Variante bietet. Dabei ist neben der wesentlich verbesserten Ausgangsanpassung vor allem der kostengünstigere und platzsparendere Aufbau zu nennen, da ein Phasenschieber und ein 0° -Koppler durch eine Komponente aus drei konzentrierten Bauelementen ersetzt werden können.

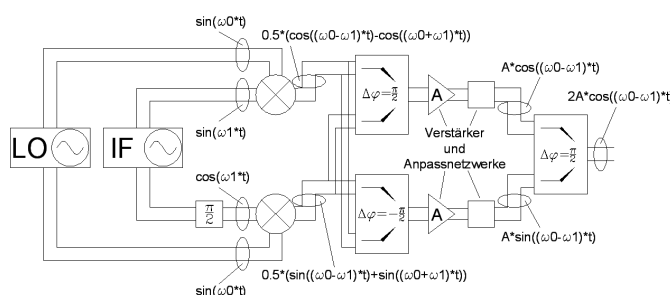


Fig. 7. Prinzipschaltbild eines Einseitenbandmodulators mit integrierter Verstärkerstufe. Substitutionen: $\omega_{LO} = \omega_0$, $\omega_{IF} = \omega_1$.

Leistungsverstärker in modernen Transmittern weisen zahlreiche Nachteile auf. Zur Darstellung soll eine Aufteilung in unsymmetrische und symmetrische Verstärker erfolgen.

Die meisten Verstärker sind noch in unsymmetrischer Leitungstechnik realisiert. Diese benötigen in der Halbleitertechnologie sehr aufwändige Durchkontaktierungen zur Herstel-

lung von Masseverbindungen. Weiterhin ist eine sehr hohe elektrische Durchbruchspannung gefordert, was in der Praxis bedeutet, dass die Leistungsverstärker gegenüber der restlichen Schaltung in einer eigenen Technologie gefertigt werden müssen. Deshalb ist die Herstellung von Leistungsverstärkern deutlich teurer als vergleichbar große Komponenten, die z.B. in günstiger Standard-CMOS-Technologie gefertigt werden können. In der Anwendung haben diese Verstärker den Nachteil, dass sie sehr niederohmige Ausgänge haben. Zur Anpassung dieser niederohmigen Ausgänge an die Systemimpedanz (i.d.R. 50Ω) werden sehr hochwertige und somit teure passive Komponenten benötigt, damit auf der Seite der hohen Ausgangsleistung zu große Verluste vermieden werden. Weiterhin lassen sich diese niederohmigen Ausgänge nur sehr schmalbandig anpassen. So wird in der Praxis für fast jedes Kommunikationsband ein eigener, individuell optimierter Leistungsverstärker eingesetzt. Ein weiterer Nachteil der unsymmetrischen Verstärker ist die je nach Betriebsart mehr oder weniger stark ausgeprägte Generation von Oberwellen. In der Praxis ist die erste Oberwelle das größte Störsignal, für welches am meisten Filteraufwand betrieben werden muss, damit das Ausgangssignal den Anforderungen des Kommunikationssystems gerecht wird.

Bei Verstärkern, deren innere Architekturen in symmetrischer Leitungstechnik realisiert sind, treten die meisten der genannten Nachteile der unsymmetrischen Verstärker nur in verringertem Ausmaß auf. Durchkontaktierungen werden nicht benötigt, die Ausgangsimpedanzen haben den doppelten Wert und die geradzahigen Oberwellen werden aufgrund der Architektur unterdrückt.

Die Verbindung der Vorteile des neuen IQ-Modulators und einer balancierten Push-Pull-Stufe ist in Fig. 7 dargestellt. In dieser Realisierungsform bietet die Schaltung neben den Vorteilen der guten Ausgangsanpassung und der geringen benötigten Chipfläche außerdem die oben beschriebenen Vorzüge eines balancierten Push-Pull-Verstärkers. Durch die Schaltung des Verstärkers nach dem Modulator wird außerdem nur das Seitenband verstärkt, welches im Anschluss auch tatsächlich gesendet wird. Daher eignet sich das System vor allem für batteriebetriebene Handsets, bei denen es auf Akkulaufzeit ankommt. Der Wirkungsgrad dieses Systems hängt in der Praxis in erster Linie von den Wirkungsgraden der Verstärker ab.

REFERENCES

- [1] CRIPPS, S. C.: *RF Power Amplifiers for Wireless Communications*, Artech House, Boston, 1. Auflage, 1999
- [2] ELLERBRUCH, D. A.: *UHF and microwave phase-shift measurements*, Proc. IEEE, vol. 55, Juni 1967, pp. 960-969
- [3] HEUERMANN, H.: *Grundlagen der Hoch- und Höchstfrequenztechnik*, Vorlesungsskript an der Fachhochschule Aachen, 2. Auflage, 2003
- [4] HEUERMANN, H.: *Grundlagen der Netzwerkanalyse*, Praktikumsunterlagen an der Fachhochschule Aachen, 1. Version, 2002
- [5] JAFFE, J. S. UND MACKAY, M. C.: *Microwave frequency translator*, IEEE Trans. Microwave Theory Tech., vol. MTT-13, Mai 1965, pp. 371-378
- [6] MÖLLER, M.: *Entwurf und Optimierung monolithisch integrierter Breitbandverstärker in Si-Bipolartechnologie für optische Übertragungssysteme*, Dissertation, Bochum, 1999
- [7] SCHIEK, B.: *Grundlagen der Hochfrequenzmesstechnik*, Springer-Verlag, Berlin, 1. Auflage, 1999
- [8] STADLER, E.: *Modulationsverfahren*, Vogel-Verlag, Würzburg, 5. Auflage, 1988

Low Phase Noise X-Band Clapp Push-Push Oscillator

M. Schott (schott@fbh-berlin.de), F. Lenk, and W. Heinrich
 Ferdinand-Braun-Institut für Höchstfrequenztechnik (FBH),
 Gustav-Kirchhoff-Str. 4, D-12489 Berlin, Germany.

Abstract— A MMIC colpitts oscillator in push-push configuration is presented using InGaP/GaAs HBTs. The output at the second harmonic enhances the frequency range while preserving the well-known advantages of the Colpitts concept. Moreover, additional features like enhanced load-pull immunity and inherent frequency divider functionality are included. The MMIC VCO reaches state-of-the-art phase-noise performance in X-band.

Keywords—Colpitts oscillator, Push-Push

I. INTRODUCTION

The Colpitts oscillator is known for its excellent frequency stability resulting in very low phase noise, high output power and the potential of high tuning bandwidth. However, looking at the literature one finds the Colpitts concept mostly applied in the lower microwave region. The reason is that the superior phase noise behavior is mainly caused by the feedback structure, consisting of two feedback capacitors between base-emitter and collector-emitter, respectively, which effectively short-circuit the intrinsic noise sources and the low-quality intrinsic transistor reactances. Beyond this, the collector-current conduction-angle is narrow and can also be adjusted by choosing the ratio of the feedback capacitors properly. According to the LTV-theory [8] the current into the resonator should flow in narrow pulses at the maximum of the tank voltage, which is the case in Colpitts-type oscillators. However, with increasing frequency the magnitude of the generated negative resistance decreases which is needed to compensate for the resonator losses. As a consequence, the advantages of the Colpitts concept decrease more and more with increasing frequency. In Section II it will be shown, that the application of Colpitts-oscillators in a push-push-configuration overcomes this bottleneck while contributing further valuable features as discussed in Section III.

II. THE NEGATIVE RESISTANCE APPROACH

Fig. 1 shows the reflection-oscillator approach of the classical Clapp-oscillator in grounded collector configuration. For simplicity, the HBT is reduced to the transconductance g_m . In a first step, the load resistance R_L is assumed to be infinite, which is the case in the differential push-push oscillator presented, where the output is located at the virtual ground plane (see fig. 2) Thus, the load resistance is not directly visible for the fundamental signal. The general case with $R_L > 0$ holds for fundamental single-ended oscillators. These two cases are treated in detail in the following:

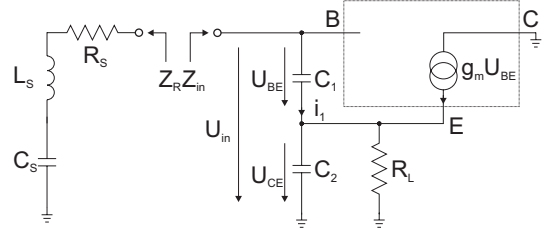


Fig. 1. Single ended Clapp-Oscillator with the transistor reduced to transconductance g_m

A. $R_L = \infty$

The base-collector voltage is

$$U_{in} = \frac{i_1}{j\omega C_1} + \frac{i_1 + g_m U_{BE}}{j\omega C_2} \quad (1)$$

and with $U_{BE} = i_1/(j\omega C_1)$ and $i_2 = i_1 + g_m U_{BE}$ one has

$$U_{in} = \frac{i_1}{j\omega C_1} + \frac{i_1}{j\omega C_2} - \frac{g_m i_1}{\omega^2 C_1 C_2} \quad (2)$$

The real part input impedance becomes

$$Re\{Z_{in,1}\} = -\frac{g_m}{\omega^2 C_1 C_2} \quad (3)$$

and the imaginary part is

$$Im\{Z_{in,1}\} = \frac{1}{j\omega C_1} + \frac{1}{j\omega C_2} \quad (4)$$

Thus we have a frequency depending input impedance with negative real part depending on g_m and the feedback capacitors. As frequency increases C_1, C_2 need to be decreased in order to maintain a constant negative real part. In fact, g_m itself decreases with frequency, which further reduces the appropriate capacitance values. The oscillation condition requires the negative real part to over-compensate the resonator losses, which are described by R_S :

$$R_S - \frac{g_m}{\omega_r^2 C_1 C_2} < 0 \quad (5)$$

The capacitive imaginary part is compensated to zero by a lumped inductor (Colpitts-configuration) or a series resonance circuit operating above its first resonant frequency (Clapp-configuration).

$$L_S = \frac{C_1 + C_2}{\omega_r^2 C_1 C_2} \quad (6)$$

As well known, a high loaded quality factor Q_L is of primary importance in minimizing phase noise. According to the Leeson-formula [1] one achieves a 6dB improvement in phase noise by doubling oscillator Q_L . A simple approximation for the loaded quality factor Q_L of the Clapp-configuration is given by [2]:

$$Q_L = \frac{1}{R_S} \sqrt{\frac{L_S}{C_S}} \quad (7)$$

Therefore, the ratio L_S/C_S must be maximized for highest Q_L but, since the losses R_S are mainly incorporated in the inductor, R_S follows L_S such that Q_L is limited by the inductor quality factor. Anyway, as frequency increases, $Re\{Z_{in,1}\}$ increases and is the true bottleneck for the maximum value of R_S thus limiting the maximum ratio L_S/C_S .

B. $R_L > 0$

Now we will consider the case of finite load resistance. The input impedance becomes

$$Z_{in} = \frac{1}{j\omega C_1} + \frac{R_L \frac{1}{j\omega C_2}}{R_L + \frac{1}{j\omega C_2}} + \frac{g_m R_L \frac{1}{j\omega C_2}}{j\omega C_1 \left(R_L + \frac{1}{j\omega C_2} \right)} \quad (8)$$

with the real part

$$Re\{Z_{in,2}\} = \frac{R_L (C_1 - C_2 g_m R_L)}{C_1 + C_1 C_2^2 \omega^2 R_L^2} \quad (9)$$

and the imaginary part

$$Im\{Z_{in,2}\} = \frac{1 + g_m R_L + C_1 C_2 \omega^2 R_L^2 + C_2^2 \omega^2 R_L^2}{-C_1 \omega - C_1 C_2^2 \omega^3 R_L^2} \quad (10)$$

By comparison we find $Re\{Z_{in,2}\} > Re\{Z_{in,1}\}$, i.e., the circuit with $R_L > 0$ provides less negative resistance than the one with $R_L = \infty$. This allows to choose a much higher L_S/C_S -ratio in push-push oscillator configurations than in their fundamental counterparts.

III. APPLICATION OF THE PUSH-PUSH CONCEPT

Looking into the literature, the majority of published push-push oscillators were designed with a feedback network according to T-rather than Π -configuration. One explanation is that since the feedback capacitors must bypass the transistor, modifications of the transistor layout cell are mostly inevitable resulting in uncertainties of the transistor model and thus reduced accuracy of the circuit simulation. The application of the push-push concept offers several advantages over single-ended designs:

- Since each transistor runs at half the desired output frequency, the usable frequency range of the devices can be extended, [7]

- Simultaneous generation of both the fundamental and second harmonic frequency is feasible, which relaxes the effort for PLL circuitry [6],[3]

- Phase noise reduction due to synchronization effects [4],[5]

- High immunity against load-pull. Because the second harmonic output is located at the virtual ground plane changes of the load affect the fundamental signal only indirectly (Section VI).

Beyond this, the Colpitts oscillator in push-push configuration additionally offers:

- High quality factor for frequencies below X-Band
- High output power at second harmonic: The amount of harmonic content can be adjusted by C_1/C_2
- Excellent phase noise properties due to short-circuited transistor noise sources and low-Q elements.

IV. CIRCUIT DESIGN

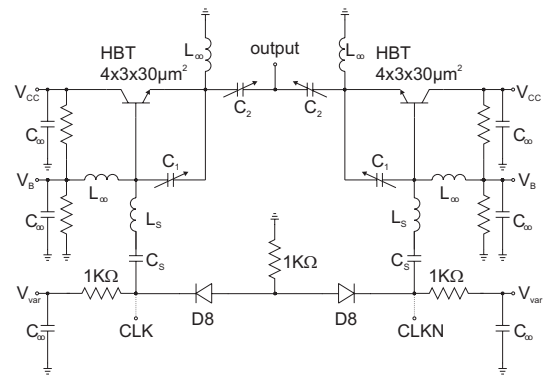


Fig. 2. Schematics of the X-band push-push Clapp oscillator. The second harmonic output is taken from the virtual ground plane.

The circuits are fabricated using the FBH 4" GaAs HBT MMIC process. The active elements are GaInP/GaAs HBTs. The transit frequencies are $f_t = 45$ GHz and $f_{max} = 170$ GHz. The epitaxial layers are grown with Metalorganic Vapor-Phase Epitaxy (MOVPE). Ledge technology is used to reduce $1/f$ noise. For further details see [10].

Fig. 2 shows the schematics of the X-band push-push oscillator realized. Inductors L_∞ and capacitors C_∞ are for biasing purposes only and do not affect the rf-behavior significantly. The circuit applies the known Clapp-oscillator with the second harmonic output port placed at the common node of the feedback capacitors C_2 . Circuit elements were chosen to obtain first-harmonic oscillation around $f_0 = 5GHz$. The fundamental signal (CLK and CLKN in Fig. 2) can be used to drive a frequency divider. To investigate phase noise and output power as a function of the feedback capacitors several versions of the MMIC were realized on the same wafer varying C_1 and C_2 . The feedback capacitors are placed close to the HBT as can be seen from the chip foto (Fig. 3). To

accomplish this the original transistor cell layout had to be modified. DC can be applied from one or both sides since the pads for V_{CC} and V_{Var} are interconnected on chip. V_{BE} is derived from V_{CC} using resistive dividers.

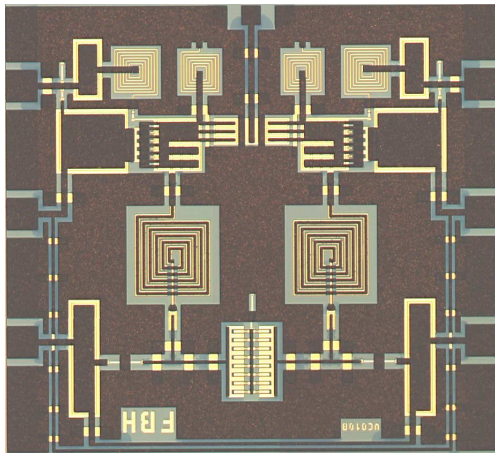


Fig. 3. Chipfoto of the X-band VCO. size: $1.4 \times 1.5 \text{ mm}^2$.

V. MEASUREMENT RESULTS

Fig. 6 shows typical tuning characteristics of the VCO. As for Clapp-VCOs the tuning range only depends on the series resonator between base and collector, it is not affected by the variations of C_1 or C_2 . The measured tuning range with app. 9% is very high. Unfortunately, because of the high rf-swing across the varactor the rf becomes rectified. The rectified voltage is around 2V, which results in a dc-current up to 1mA flowing from the circuit into the bias supply for applied tuning voltages below 2V. As a consequence the phase noise degrades within this range (Fig. 7) and the tuning curve contains an unwanted turning point. This problem can be eliminated by using anti-series varactors in each half structure such that a total of 4 varactors must have to be used. When DC is applied from one side only, the spectrum contains even and odd harmonics as well but the odd harmonics are suppressed by at least 20dB. Applying DC from both sides the odd harmonics are no longer detectable. The reason for this is, since V_{BE} is derived from V_{CC} small voltage drops across the interconnecting lines lead to larger unsymmetrie in the collector current. With next redesign both V_{BE} -pads will also be interconnected together on chip. In total, there were 3 variations for C_2 , and 7 variations for C_1 . As expected, output power increases with an increase of C_2 as V_{BE} becomes larger (Table I). The opposite occurs when increasing C_1 (Table II) but since the variation (in percent) is much lower than that of C_2 the dependence is not that strong. Fig. 4 presents measured phase noise over a large range of offset frequencies. As can be seen, phase noise decreases with increasing C_2 only at large offset frequencies.

C_2 [pF]	$L_{SSB}@100\text{kHz}$ [dBc/Hz]	$L_{SSB}@1\text{MHz}$ [dBc/Hz]	P_{out} [dBm]
0.72	-98.00	-117.00	-2.0
1.44	-99.35	-120.19	6.6
2.16	-101.84	-123.21	10.5

TABLE I
PHASE NOISE AS A FUNCTION OF C_2 ; $V_{CC} = 3\text{V}$, $V_{Var} = 10\text{V}$,
 $C_1 = 7.616\text{pF}$

C_1 [pF]	$L_{SSB}@100\text{kHz}$ [dBc/Hz]	$L_{SSB}@1\text{MHz}$ [dBc/Hz]	P_{out} [dBm]
6.68	-100.92	-122.26	11.4
7.148	-100.71	-121.82	11.5
7.616	-102.63	-123.78	11.2
8.084	-101.93	-123.14	10.7
8.552	-102.08	-123.08	10.5
9.02	-102.22	-123.01	10.0
9.488	-102.19	-122.83	9.9

TABLE II
PHASE NOISE AS FUNCTION OF C_1 ; $V_{CC} = 3\text{V}$, $V_{Var} = 10\text{V}$,
 $C_2 = 2.16\text{pF}$.

Obviously, only in this range phase noise is caused by additive white noise and the improvement is due to the increased output power. For lower frequencies upconverted 1/f-noise dominates, which is less sensitive to C_2 .

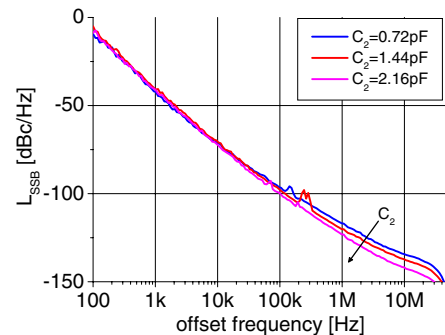


Fig. 4. Phase noise as function of C_2 ; $U_{CC} = 3\text{V}$, $V_{Var} = 10\text{V}$,
 $C_1 = 7.616\text{pF}$

VI. ENHANCED LOAD-PULL IMMUNITY

In [9] it is demonstrated how load-pull phenomena can affect both frequency tuning and phase-noise behavior. This parasitic effect can be discovered best by carefully evaluating the oscillator tuning characteristics for frequency hops

or steps. To avoid load-pulling usually buffer stages must be introduced. To demonstrate robustness of the circuit concept

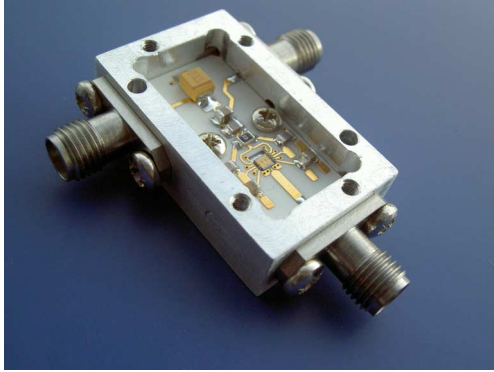


Fig. 5. Assembled X-band push-push Clapp-oscillator in test fixture to investigate the load-pull immunity. Bond wires are used as interconnects. $C_1 = 9.488pF$, $C_2 = 1.44pF$

against mismatch at the output the MMIC was mounted on a 20mil thick Rogers Duroid 4003 substrate with $\epsilon_r = 3.38$ and assembled into an aluminum housing (Fig. 5). Wire bonds were used as interconnects between pads and substrate. There was no compensating circuit on the substrate to

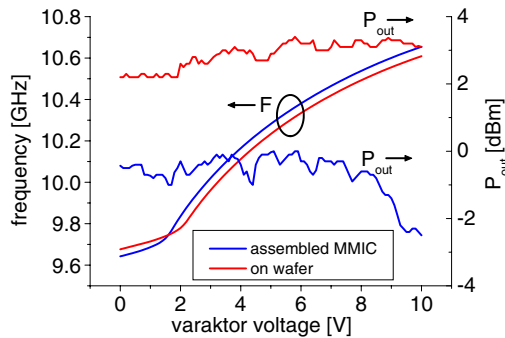


Fig. 6. Output power and frequency as function of tuning voltage, before and after assembly, $C_1 = 9.488pF$, $C_2 = 1.44pF$, $V_{CC} = 2.8V$; measurement is performed using a 10dB attenuator in the output path.

minimize the reflection coefficient in the output path. Fig. 6 compares output power and tuning characteristics before and after assembly. The frequency characteristics shows only a very small detuning effect and the insertion loss is around 3dB up to 8GHz. The increased loss beyond 8GHz is potentially caused by package resonances.

VII. CONCLUSIONS

In this paper the application of a Clapp-oscillator in push-push operation is presented. Since the load resistor is not visible for the fundamental frequency, the negative resistance generated by the regenerated transistor is larger in magnitude

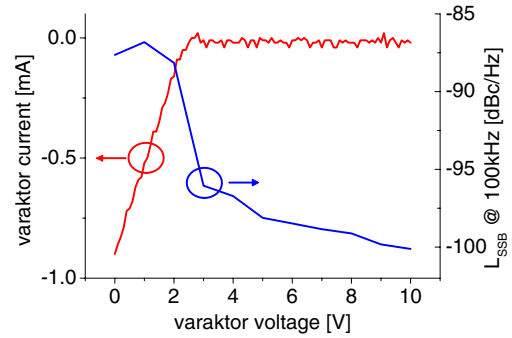


Fig. 7. Phase-noise degradation due to rf-rectification of the varactor; $C_1 = 9.488pF$, $C_2 = 1.44pF$, $V_{CC} = 2.8V$.

than for the conventional fundamental Colpitts type. This yields a higher Q_L since the resonator can be coupled more loosely and a higher operational frequency, respectively. The push-push oscillator with output at the virtual ground node offers high robustness against output mismatch and load pull and operates well without additional buffer stages.

The oscillator shows exceptionally low phase noise down to -100dBc/Hz @ 100kHz offset, together with high output power and a large tuning range at $2f_0$. In a next step, it will be investigated whether the noise can further be reduced by raising C_2 and there are additional versions planned, which contain the integrated frequency divider and eliminate the turning point of the tuning characteristic.

REFERENCES

- [1] D. B. Leeson, A Simple Model of Feedback Oscillator Noise Spectrum," *Proc. of IEEE*, vol. 54, pp. 329 – 330, 1966.
- [2] A. Blum, Praktikum Elektronik- Oszillatoren für harmonische Spannungen," *Universität des Saarlandes*, 2001.
- [3] M. Schott, H. Kuhnert, J. Hilsenbeck, J. Würfl, W. Heinrich, 38GHz Push-Push GaAs-HBT MMIC Oscillator," *IEEE MTT-S Int. Microwave Symp. Dig.*, vol. 2, pp. 839 – 841, 2001.
- [4] K. Kurokawa, Noise in Synchronized Oscillators," *IEEE Trans. Microwave Theory Tech.*, vol. 4, pp. 234 – 240, 1968.
- [5] H. C. Chang, X. Cao, U. K. Mishra, R. A. York, Phase noise in Coupled Oscillator: Theory and Experiment," *IEEE Trans. Microwave Theory Tech.*, vol. 45, pp. 604 – 615, 1997.
- [6] F. X. Sinnesbichler, B. Hautz, G. R. Olbrich, Low Phase Noise 58 Ghz SiGe Hbt Push-Push Oscillator with Simultaneous 29 Ghz Output," *IEEE MTT-S Int. Microwave Symp. Dig.*, vol. 1, pp. 35 – 38, 2000.
- [7] F. X. Sinnesbichler, H. Geltinger, G. R. Olbrich, A 38-GHz Push-Push Oscillator Based on 25-GHz f_T BJTs," *IEEE Microwave And Guided Wave Letters*, vol. 9, pp. 151 – 153, 1999.
- [8] T. H. Lee, A. Hajimiri, Oscillator Phase Noise: A Tutorial," *IEEE Journal of Solid-State Circuits*, vol. 35, pp. 326 – 336, 2000.
- [9] M. Schott, F. Lenk, P. Heymann, On the Load-Pull Effect in MMIC Oscillator Measurements," *33rd European Microwave Conference*, pp. 367 – 370, 2003.
- [10] J. Hilsenbeck, F. Lenk, W. Heinrich, J. Würfl, Low phase noise MMIC VCOs for Ka-band applications with improved GaInP/GaAs-HBT technology," *IEEE GaAs IC Symp. Dig.*, pp. 223 – 226, 2003.

Session 8b

Radar, Sensors, Imaging

A Forward Impulse Radiating Antenna for Subsurface Radars

A. Teggatz, A. Jöstingmeier, T. Meyer, and A. S. Omar

Institute of Electronics, Signal Processing and Communications, FEIT, University of Magdeburg
P.O. Box 4120, Universitätsplatz 2, 39106 Magdeburg, Germany, ateggatz@iesk.et.uni-magdeburg.de

Abstract — We will present a novel forward impulse radiating antenna (IRA) that has been optimized for subsurface radar applications using a 3d field simulator. Though this antenna possesses an inferior return loss compared to antennas developed for free space applications it yields images of subsurface objects with outstanding resolution when an appropriate calibration technique is applied. This technique locates the reference plane inside the ground and allows for removing the air-ground reflection as well as the antenna mismatch and losses. A prototype of the new antenna has already been built and will be presented.

I. INTRODUCTION

The detection of buried objects such as landmines or unexploded ordnance by means of ground penetrating radar (GPR) is an intensely investigated field of research. The antenna is the crucial hardware part of a GPR system because the imaging quality is strongly depending on the radiation characteristics of the antenna. The antenna parameters that have to be optimized according to the applied data processing algorithms include bandwidth, radiation pattern, phase center location, gain and radiation efficiency. Usually antennas are designed for free space applications. However, in a GPR the antenna has to meet completely different requirements since it is often located very close to the ground in order to receive a strong target signal. Therefore GPR antennas cannot be optimized without taking the environment into account.

In [1] it has already been demonstrated how the electromagnetic field simulator Microwave Studio (MWS) can be used to optimize the design of GPR antennas. The quality of an antenna is assessed by a series of B-scans for typical targets. Since a single B-scan already requires a large number of simulation runs it is necessary to automate the process of the antenna movement above the ground. This task is accomplished by controlling the field simulation tool from the main GPR simulation application by means of ActiveX.

The GPR simulator has been used to investigate a variety of antennas such as standard gain horns, TEM horns, conical spirals, log-periodic antennas and other types some of which have already been investigated in [2]. All of these antennas suffer from the disadvantage that the reflection at the air-soil interface is much stronger than the target reflection itself. Therefore we have suggested a novel forward radiating IRA which is named Orion-type due to its shape that resembles the Orion star ship. Simulations show that this antenna gives superior results concerning the detection of buried

objects when it is used together with the calibration technique that will also be presented within this contribution. Figs. 1 and 2 show the MWS model of the proposed Orion-type IRA.

II. ORION ANTENNA

The Orion-type antenna is mainly a forward radiating IRA with two metal arms, embedded in a dielectric material. The permittivity of this dielectric cone has been chosen close to the permittivity of the soil. Thus the overall mismatch due to the soil-air and the air-antenna interface can be decreased as the antenna is installed very close to the ground surface. In the investigated setup the distance between the IRA and the ground is only 10 mm. The cone is made of AK4 low loss dielectric material [3]. The relative permittivity of this material is almost frequency independent 3.85 which has been determined by a precision broadband measuring method [4].

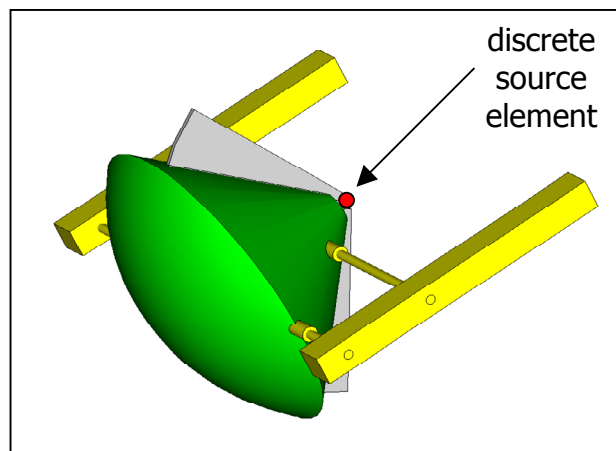


Fig. 1. Microwave Studio model of the Orion-type IRA.

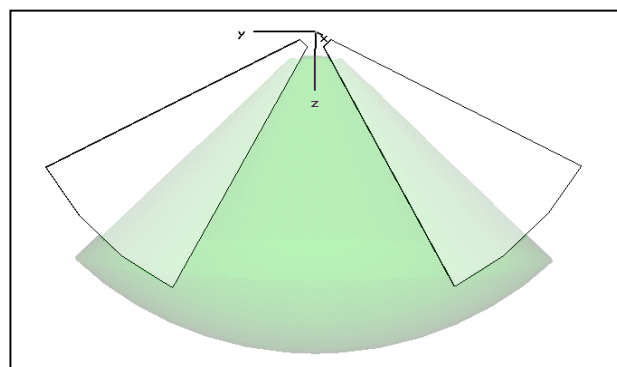


Fig. 2. Position of the metal arms inside the dielectric cone.

For feeding the antenna it is necessary to use a balun with a step up ratio of 4:1 in order to match the 50 Ohm feeding line impedance to the radiation impedance of the antenna that is about 200 Ohm. Furthermore the balun connects the unsymmetrical coaxial line with the symmetrical antenna structure and eliminates its common mode excitation. The free space performance of the Orion-type IRA strongly depends on the operating frequency. Fig. 4 indicates a poor directivity of the antenna at 1 GHz while Fig. 5 shows a pencil beam like

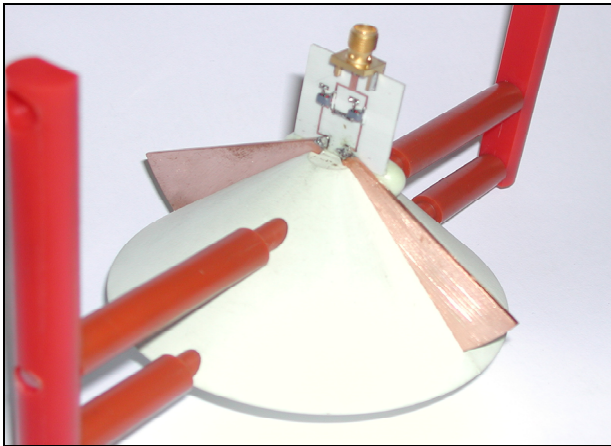


Fig. 3. Prototype of the Orion-type antenna.

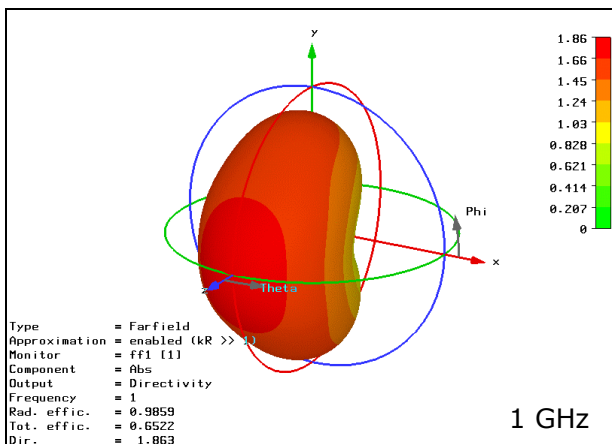


Fig. 4. Radiation pattern of the IRA at 1 GHz.

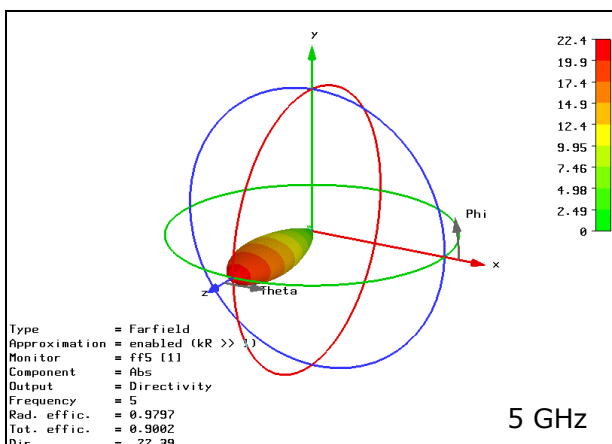


Fig. 5. Radiation pattern of the IRA at 5 GHz.

radiation pattern that has been observed at 5 GHz. Moreover the return loss of the Orion-type IRA which is presented in Fig. 6 is quite large compared to that of other antennas which have been optimized for free space operation. For example in Fig. 7 the measured and the simulated return loss of a double ridged TEM horn are given. Such horns have also been used in subsurface detection applications. Comparing the results presented in Figs. 6 and 7, it is obvious that the free space performance of the Orion-type impulse radiating antenna is inferior to that of the TEM horn.

However, it has been found from the simulations of the entire GPR environment that the Orion-type IRA basically illuminates the small area directly below the cone, and that the wave propagation in this region is in a good agreement to that of a wave traveling along a 1d transmission line. This is important because in order to apply a one-port calibration technique a 1d transmission line model must be valid for the field propagating inside the ground. Figs. 8 and 9 show the simulated radiation of the Orion-type IRA at 2 GHz in the presence of homogeneous soil with a permittivity of $\epsilon_r=3$. On the other hand, the TEM horn has an aperture which is much larger than the transverse dimensions of the Orion-type IRA leading to a wave propagation inside the ground which cannot be described by a 1d transmission model.

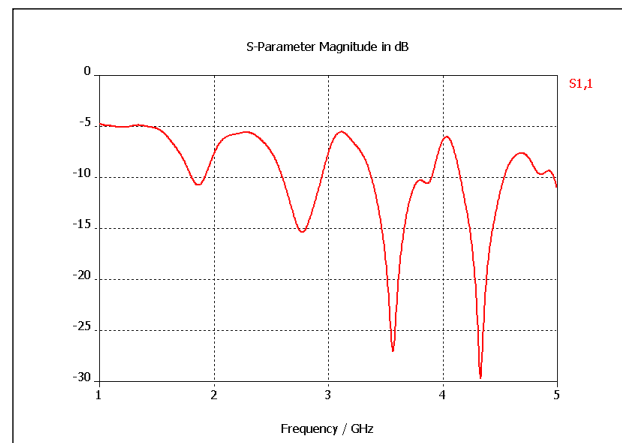


Fig. 6. Return loss of the Orion-type IRA for 1 GHz-5 GHz.

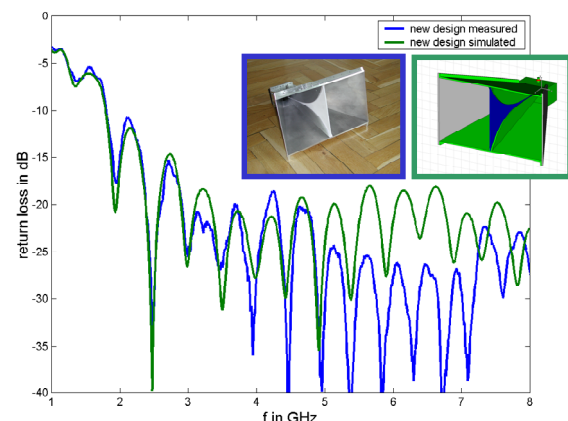


Fig. 7. Return loss of a TEM horn for 1 GHz-8 GHz.

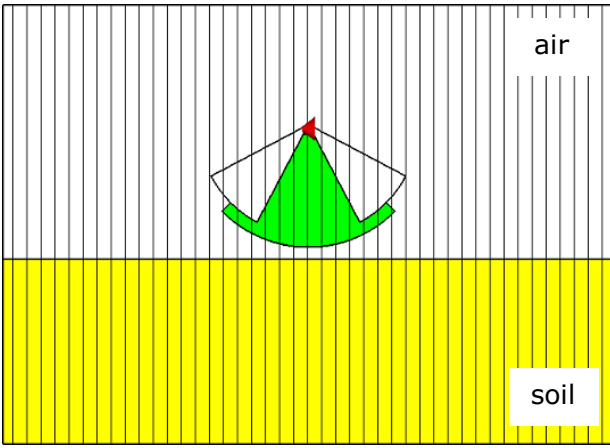


Fig. 8. MWS setup for the simulation of the radiation.

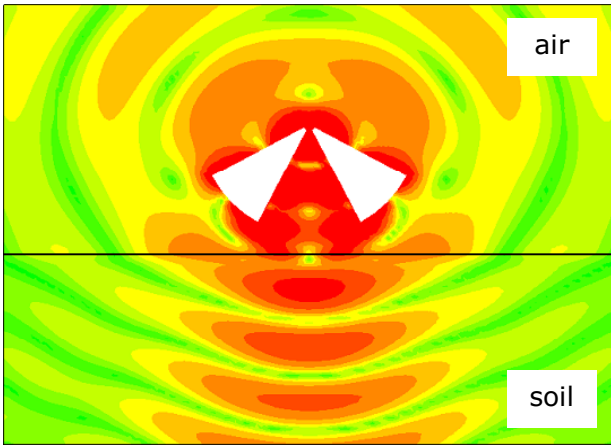


Fig. 9. Simulated radiation in the presence of soil at 2 GHz.

III. CALIBRATION PROCEDURE

A. Calibration Standards

Following the well-known standard one-port calibration procedure one has to take three different calibration standards into account, which are usually a match, a short and an offset short. Adapting this procedure to subsurface detection match means that the antenna radiates above the homogeneous ground for which we assume the relative permittivity of dry sand, namely, $\epsilon_r=3$.

The second standard, which is the short, defines the position of the reference plane. This standard is just a large metal plate located inside the ground at the depth of the reference plane. Since we are interested in the detection of targets that are buried within the first 200 mm underneath the surface, we put the reference plane at the center of this region, located at a depth of 100 mm. Finally we have to apply one or more offset shorts. The number of these offset short standards depends on the considered frequency range for the measurement. In our case the GPR utilizes the frequency range from 1 GHz to 5 GHz which is supposed to be a common frequency range for GPR. Accordingly, two offset shorts with offsets of 22 mm and 8 mm, respectively, have been chosen. This guarantees that the

additional line length which is introduced by the two offsets leads to a phase shift within an interval of $90^\circ \pm 25^\circ$ at any frequency in the considered range. Hence the equations for the error terms are sufficiently independent.

B. Error Coefficients

The time domain signals reveal that the antenna mismatch and the air-surface reflection have even a stronger effect than the reflections corresponding to the short and the offset short standards. The parameters of the error model [5] E_R , E_D and E_S are calculated from the corresponding frequency domain data. These error coefficients are a function of the frequency. Fig. 10 shows that they are continuous as expected at the transition frequency at which the calibration procedure switches from the first offset short to the second one.

$$S_{corr} = \frac{S_{meas} - E_D}{E_R + E_S(S_{meas} - E_D)} \quad (1)$$

The measured reflection coefficient is corrected by applying equation (1). The measured and the corrected reflection coefficient are denoted by S_{meas} and S_{corr} , respectively. Keeping in mind that E_D is just the measured reflection when the match standard is applied, the calibration procedure can be substituted by a simple so called background subtraction. In this case the term $E_S(S_{meas}-E_D)$ is considered to be small compared to the value of E_R . However the exclusive application of a background subtraction does neither yield the exact depth nor the accurate reflectivity of the buried object.

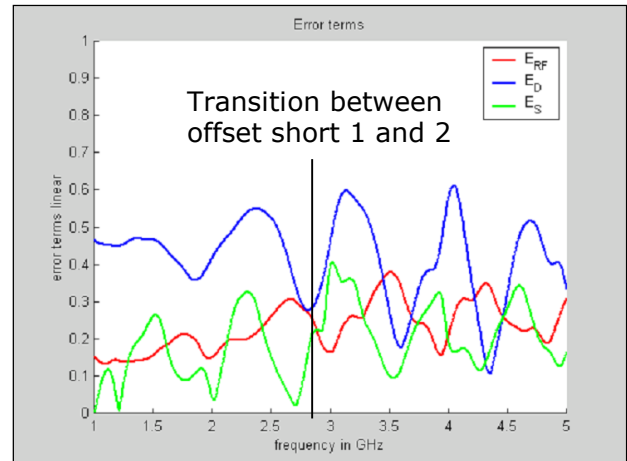


Fig. 10. Transition between the error coefficients.

IV. EXPERIMENTAL RESULTS

Fig. 12 shows what happens when the above-discussed correction is applied to an air layer located exactly at the position of the reference plane, that has been placed 100 mm underneath the surface of the ground. The antenna mismatch and the surface reflection, that appear in the Fig. 13, are completely eliminated after the application of the calibration procedure.

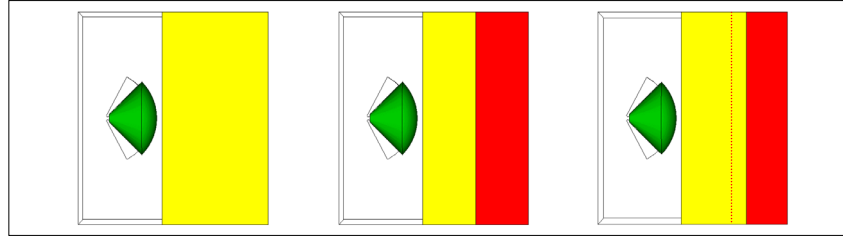


Fig. 11. Calibration standards - match, short and several different offset short.

At the same time the target signal, that appears to be weaker than the other reflections in the data without calibration, is obtained according to (2).

$$\Gamma = \left(\sqrt{\varepsilon_{rB}} - \sqrt{\varepsilon_{rO}} \right) / \left(\sqrt{\varepsilon_{rB}} + \sqrt{\varepsilon_{rO}} \right) \quad (2)$$

The value of the corrected reflection coefficient is exactly the theoretical value given by (2), where ε_{rB} and ε_{rO} are the permittivity of the background and the permittivity of the object, respectively. Furthermore the depth of the target is well-defined with respect to the reference plane in a depth of 100 mm. The performance of an ordinary background subtraction (results in Fig. 14) is inferior compared to the calibration procedure.

V. CONCLUSION

A novel forward radiating IRA concept has been introduced. The proposed antenna is suitable for subsurface radar applications. A GPR system using this antenna can be calibrated with respect to a reference plane inside the ground. The ability of the method to increase the accuracy and the performance of the GPR detection of buried objects has been demonstrated. The antenna mismatch and the air-surface reflection can be removed from the original data if the discussed error model will be applied. Hence the antenna gives superior results concerning the achievable resolution when it is used together with the suggested calibration technique.

REFERENCES

- [1] A. Teggatz, A. Jöstingmeier, T. Meyer and A. S. Omar, Simulation of a Ground Penetrating Radar Environment by Means of FDTD Methods Using an Automatic Control Approach, IEEE AP-S / URSI Int. Symp. Digest, vol. 2, pp. 2095-2098, Monterey, USA, June 2004.
- [2] R. V. de Jongh, A. G. Yarovoy, L. P. Ligthart, I. V. Kaploun A. D. Schukin, Design and Analysis of new GPR antenna concepts, in Proc. 7th Int. Conference On Ground-Penetrating Radar (GPR'98), vol. 1, pp. 81-89, Kansas, USA, May 1998
- [3] Cuming microwave corporation, C-Stock AK4 Datasheet http://www.cumingmw.com/micro_dielectric.html.
- [4] A. Jöstingmeier, T. Meyer and A. S. Omar, Material Measurements of Absorbers with Magnetic Losses, IEEE AP-S / URSI Int. Symp. Digest, vol. 4, pp. 66, Columbus, USA, June 2003.
- [5] M. Thumm, W. Wiesbeck und S. Kern, Hochfrequenzmesstechnik, BG Teubner, Stuttgart, Germany, 1998.

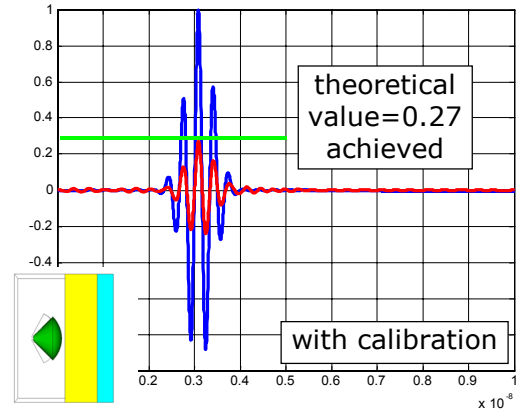


Fig. 12. Air layer object in the ground with calibration.

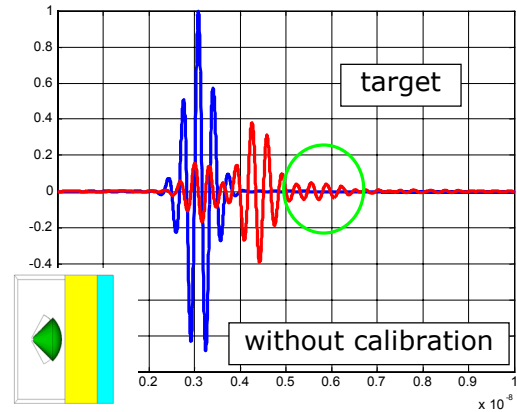


Fig. 13. Air layer object in the ground without calibration.

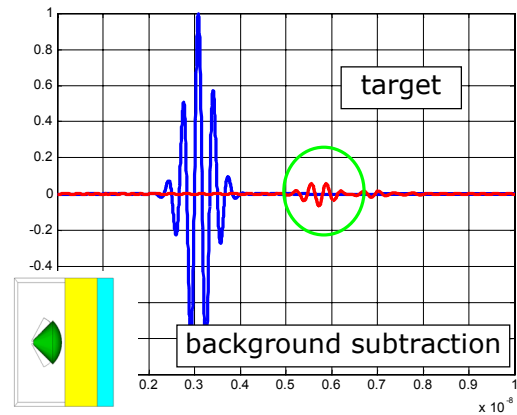


Fig. 14. Air layer object with background subtraction only.

Short Distance Related Security Millimeter-Wave Imaging Systems

A. Dallinger, S. Schelkshorn, J. Detlefsen
Technische Universität München
Lehrstuhl für Hochfrequenztechnik
Fachgebiet Hochfrequente Felder und Schaltungen
D-80333 München, Germany

Abstract — Homeland security as a current issue brought up many questions about nowadays state of the art security relevant technologies both for civilian and military applications. Our motivation is related to security applications for airport environments especially in terms of people screening and object detection beneath the clothing. When developing a system for this environment one has not only to take into account good image quality but also issues like available space and financial resources of the airport's operator. In this paper we report about general solutions to this task and about our approach in the millimeter-wave region specifically.

I. INTRODUCTION

Due to the very need for better security monitoring, e. g. in airport environments a major task is to enhance today's state of the art body scanners, which are mainly metal detectors, in order to find other potential hazards also. This increasing demand for screening personnel for concealed objects leads to additional research efforts related to suitable imaging systems and their industrial realization. Our goal is the development of a full body scanner which allows for people screening in security crucial environments in near real time.

The system must be able to detect dangerous objects beneath cloth either by an operator or automatically with an acceptable error rate. Furthermore the system must satisfy the requirements of high throughput checkpoints and likewise be reliable in automatic detection of concealed objects like metallic knives/guns, ceramic knives/guns and explosives.

II. GENERAL SYSTEM APPROACHES

The system to be developed is meant for short range (distance from sensor to person < 1 m) full body screening. In order to be able to resolve small objects ($< (1\text{ cm})^2$) placed on the humans body the required amount of pixels for a 2D image is in the order of 100×200 . If a real 3D image is needed one ends up with roughly $100 \times 100 \times 200$ pixels. This enormous amount of pixels has to be processed in near real time which is a very challenging task even with today's computers. A frame rate of better than 0.1 frames/sec would be appropriate.

There are several other issues to be considered. Some of them are addressed in the following.

A. Image Focusing

Independent of the type of sensor used the image has to be focused either by a physical aperture or by computational means (synthetic aperture).

a) Physical Apertures: focus by means of a lens or by an extended aperture. In terms of computational efficiency these systems are optimal due to their capability to focus an image with the speed of light and hence have a low computational load. The beamwidth of an aperture antenna is related to its size and the frequency which usually leads to huge apertures. To get an image the aperture has to be scanned which requires precise mechanics. A drawback is the field of view which is only big enough to fit onto a person several meters away from the sensor and only in the farfield a sharp beam is generated. Rotational folded optics [1], [2] can overcome some of the above mentioned problems. Lens antennas or focal plane systems can be small but have to be scanned [3] or ordered in big arrays to scan a full person in the time demanded [4].

b) Synthetic Aperture: techniques focus an image by computational means. One or several distributed sensors measure the holographic data along a certain path (the synthetic aperture). 2D images only need 1D apertures but additionally ultrawideband sensors. If 3D images are needed at least a 2D aperture is necessary which leads to a high hardware effort [5], [6].

In order to reduce the computational load approximations to the correlation kernel have to be made, e.g. by means of Born's approximation Maxwell's equations can be linearized. Because of the short range application one has to consider the phase curvature of the electromagnetic field. Approaches which can be found in the literature are mostly based on Fourier inversion [7], [8], [9] and plane wave decomposition [10] in order to be able to finally use FFTs. The focusing is completely done in the spatial frequency domain. Therefore interpolation kernels have to be applied and thus the image quality depends heavily on this implementation. In order to stay in time massive parallel computing is necessary [11].

B. Frequency Spectrum

Since it is not accepted by the general public to the time this paper has been written to perform personnel screening by applying low power X-ray backscattering techniques, which is already available [12] and gives very good results other techniques have to be discussed.

Due to the skin effect the electromagnetic waves of the MMW range and even more pronounced at terahertz frequencies do not penetrate deeply into the human body, which consists of tissue of some conductivity. The penetration depth is in the order of magnitude of millimeters or less. This is supported by measurements [13] of the complex permittivity ϵ_r of human skin. From calculating the respective Fresnel reflection coefficients in case of perpendicular incident waves

it is expected that skin behaves like a fairly good reflector, i.e. -3 dB to -4 dB reflectivity, see figure 1. Additionally the reflectivity is highly dependent on the body's geometry, especially on the curvature of its surface and determined by specular points.

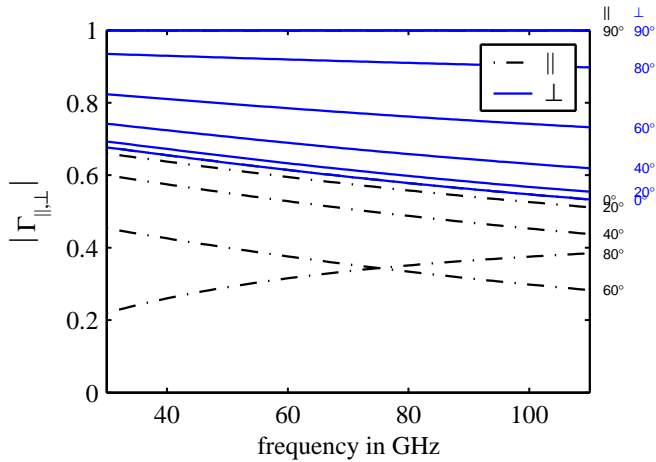


Fig. 1. Fresnel reflection coefficient $\Gamma_{||,\perp}$ of dry human skin

Since one sensor on its own will not fulfill the whole requirements in terms of acceptable false alarm rate a multisensor imaging system is needed which should be discussed on one hand in terms of spacial displacement, e.g. scanned apparatuses, several distributed sensors and on the other hand also taking into account data from physically different sensors, e.g. data fusion from thermal sensors and MMW sensors, [14].

C. Coherent vs. non-coherent illumination

Security checkpoints in airports are an indoor application and require an illuminating source even though using passive detectors [15]. Active illumination increases the SNR both for coherent and non-coherent systems and hence reduces interference effects from other equipment. An overview of some of the state of the art systems can be found in [16].

c) Non-coherent systems: are passive sensors which means that the spectral distribution of natural radiation which is emitted or reflected from a body at environmental temperatures is properly captured and displayed (radiometry). In contrast to outdoor applications the temperature contrast between the walls of the room, the hidden objects and the carrier of these objects is much lower for indoor environments resulting in images with reduced dynamic range.

d) Coherent systems: apply active sources. They preserve the phase information and hence allow for image reconstruction techniques necessary for synthetic aperture radars. Active illumination has the disadvantage of glint effects in the image due to the illumination geometry [3], [17].

III. EXPERIMENTAL MMW SYSTEM

To obtain preliminary image information we set up an experimental MMW measurement system. This measurement facility provides several mechanical, computer controlled and scan able positioning axes. One can use a common antenna positioner to rotate the object in a spherical manner. Also an alternative linear scanner which gives the opportunity to move the receiver system on a rectangular grid of approx. 1 m^2

with a minimum spacing of below $20 \mu\text{m}$ has been included additionally. All measurements have been accomplished in an anechoic antenna measurement chamber (to reduce unwanted clutter effects) at Technische Universität München. Common computer controlled network analysis equipment (HP 8510) with additionally MMW extensions is used for data acquisition.

A. MMW lens focused imaging

Our preliminary studies were carried out by a wide bandwidth active MMW lens focused (see figure 2) reflectometer system in order to obtain first characteristic images. In order



Fig. 2. lens antenna optimized for 94 GHz, focus at about 10 cm distance, beamwidth of approx. 7 mm, by placing the DUT at the beamwaist and by scanning the lens in front of the DUT a wideband, coherent reflectivity pixel image can be obtained with a resolution of approx. 7 mm.

to have a preliminary and uncomplicated setup a monostatic measurement setup was chosen, see figure 3. A subsequent system will apply a quasi-monostatic setup to enhance the system's dynamic range. This configuration is placed on a linear positioner and can be scanned in front of the Device Under Test (DUT). An advantage of this preliminary setup is its variability and very high frequency bandwidth of 35 GHz. But due to a non-continuous mechanical movement and a PLL stepped frequency operation of the system it is rather slow and hence not applicable for near real time usage. Figure 4



Fig. 3. measurement setup

shows an example of an imaged PVC dummy at the frequency range from 89 GHz–99 GHz, i.e. 10 GHz bandwidth, with a frequency increment of 100 MHz. These values yield an unambiguous range of 1.5 m and a range resolution of 1.5 cm.



Fig. 4. left: optical image (shown without clothing), right: processed MMW image in time domain, scanned area 35 cm \times 40 cm, dynamic range of intensity image -40 dB \dots 0 dB

The system's frequency sweep time is around 15 s which is the current limiting factor. The MMW image recovers the objects beneath the sweater very well. The image also shows a major disadvantage of perpendicular illumination. Parts of the body, which are directed perpendicular with respect to the incident field lead to spots of high reflectivity which overlay the received signal from the objects and clutter the image. The specular reflections are highly dependent on the TX-DUT-RX geometry and change rapidly as this geometry varies. To overcome that problem it is advisable to sense the DUT from many viewing angles.

IV. CONCLUSION

Systems intended for personnel security screening purposes are still not fully developed and remain a task for future research programs. MMW systems can provide an acceptable image quality and frame rate but cannot detect certain materials unambiguously due to the fact that materials do not show any specific signatures below approx. 500 GHz. Nevertheless anomalies on the human body can be resolved very good. Our follow-up system will apply computational focusing approaches in order to reduce cost for millimeter-wave hardware (sources and detectors) and data acquisition time.

REFERENCES

- [1] G.N. Sinclair, R.N. Anderton, and R. Appleby. Outdoor passive millimetre wave security screening. *IEEE 35th International Carnahan Conference on Security Technology*, pages 172–179, 16–19 October 2001.
- [2] R. Doyle, B. Lyons, J. Walshe, P. Curtin, A. H. Lettington, T. McEnroe, and J. McNaboe. Low cost millimetre wave camera imaging up to 140 GHz. In *34th European Microwave Conference - Amsterdam*, page 2004.
- [3] P.F. Goldsmith, C.-T. Hsieh, G.R. Huguenin, J. Kapitzky, and E.L. Moore. Focal plane imaging systems for millimeter wavelengths. *IEEE Transactions on Microwave Theory and Techniques*, 41(10):1664–1675, October 1993.
- [4] S. Clark, C. Martin, V. Kolinko, J. Lovberg, and P.J. Costianes. A real-time wide field of view passive millimeter-wave imaging camera. In *Proceedings. 32nd Applied Imagery Pattern Recognition Workshop*, pages 250 – 254, 15 - 17 Oct. 2003.
- [5] D.M. Sheen, D. L. McMakin, H. D. Collins, Hall. T. E., and R. H. Severtsen. Concealed explosive detection on personnel using a wideband holographic millimeter-wave imaging system. *SPIE*, 1996.
- [6] D.M. Sheen, D.L. McMakin, and T.E. Hall. Three-dimensional millimeter-wave imaging for concealed weapon detection. *IEEE Transactions on Microwave Theory and Techniques*, 49(9):1581–1592, September 2001.
- [7] D. L. Mensa. *High Resolution Cross-Section Imaging*. Artech House, Inc., 1991.
- [8] M. Soumekh. *Fourier Array Imaging*. Prentice Hall, Inc., 1994.
- [9] W. G. Carrara, R. S. Goodman, and R. M. Majewski. *Spotlight Synthetic Aperture Radar, Signal Processing Algorithms*. Artech House, Inc., 1995.
- [10] R. K. Dudley. *Mathematical Foundations of Electromagnetic Theory*. The IEEE/OUP Series on Electromagnetic Wave Theory, IEEE Press, 1994.
- [11] D. L. McMakin, D. M. Sheen, T. E. Hall, and R. H. Severtsen. Cylindrical holographic radar camera. In *SPIE Conference on Enforcement and Security Technologies, Boston Massachusetts*, volume 3575, pages 79 – 88, Nov. 1998.
- [12] www.rapiscan.com/.
- [13] S. Gabriel, R.W. Rau, and C. Gabriel. The dielectric properties of biological tissues: III. parametric models for the dielectric spectrum of tissues. *Phys. Med. Biol.*, 41:2271–2293, April 1996.
- [14] P.K. Varshney, Hua-Mei Chen, L.C. Ramac, M. Uner, D. Ferris, and M.; Alford. Registration and fusion of infrared and millimeter wave images for concealed weapon detection. In *Proceedings. International Conference on Image Processing, 1999. ICIP 99*, volume 3, pages 532 – 536, 24 - 28 Oct. 1999.
- [15] P. Coward and R. Appleby. Development of an illumination chamber for indoor millimetre-wave imaging. In *Passive Millimeter-Wave Imaging Technology VI and Radar Sensor Technology VII*, volume 5077, pages 54 – 61, 2003.
- [16] J. Detlefsen, A. Dallinger, and S. Schelkshorn. Approaches to millimeter-wave imaging of humans. In *Conference Digest of EURAD2004*, Oct. 14–15 2004.
- [17] A. Dallinger, S. Schelkshorn, and J. Detlefsen. Millimeter-wave imaging of humans – basic experiments. In *Conference digest IR-MMW2004/THz2004*, Sep. 27 - Oct. 1st 2004.

Non-contacting Localisation of Dielectric Objects with UWB-Pulses

A. Gülck, T. Lehmann, O. Schimmer, R. Knöchel

Microwave Group, Faculty of Engineering, University of Kiel, Kaiserstr. 2, 24143 Kiel, Germany, + 49 431 880-6151

Abstract — This paper deals with the localisation of dielectric objects using ultra-wideband pulses with a width of approximately 400 ps. Dielectric obstacles are irradiated with antennas using sub-nanosecond pulses and transmission techniques. In the receiver, the signals are sampled after interfering with the object under test (OUT) and processed with a PC using artificial neural networks. The accuracy of the spatial resolution is examined for various measurement examples. The obtained non-contacting localisation accuracy is much less than the involved wavelengths anticipate, and is independent of the permittivity of the material and adaptable to different shapes.

I. INTRODUCTION

Microwaves are frequently used for determining the position of objects for example in industrial processes. For this purpose FMCW- and carrier frequency pulse-radars are widely used. Compared to mechanical, optical or ultrasonic methods the microwave radars have the advantage of being largely independent of environmental influences and of having a greater penetration depth. Unfortunately, the microwaves are susceptible for interference caused by resonances and multiple reflections because of limitations due to narrow bandwidths.

This paper attempts to solve this problem by using baseband pulses as the interrogating signal. The corresponding spectrum of sub-nanosecond UWB pulses covers a frequency bandwidth of several GHz and is thus much more resistant against unwanted interferences. Pulses with a width of 400 ps are radiated by antennas. They then interact with scattering objects which may be located for example on a conveyor belt. Finally they are received by a small line array of antennas. In the cases under consideration, the longitudinal position of the OUT is known. The transversal position, however (dimension b in Fig. 1), is to be determined. After reception the signal has a duration of 800 ps due to the differentiating characteristics of the antennas. It is subsequently sampled and processed. The signal processing extracts the changes in amplitude and the pulse widening. Only the alterations relative to a reference measurement are taken into account in order to allow for changes in the environment. An artificial neural network is trained with a number of reference measurements and -objects and then estimates the position of the OUT.

The feasibility of the new approach is demonstrated by locating cubes of different dielectric materials with

varying permittivities. Being based on dielectric contrasts, the proposed method can be applied in practise, for example, for the detection of foreign bodies which may contaminate otherwise homogeneous materials.

II. EXPERIMENTAL SETUP

The experimental setup (Fig. 1) consists of three sub-sections. In the first sub-section a very short pulse is generated using the technology of [1]. The emitted pulse interrogates the OUT, which is located between the transmitting and receiving antennas in the second sub-section. Finally the received pulse is sampled and analog-to-digital converted in the third sub-section.

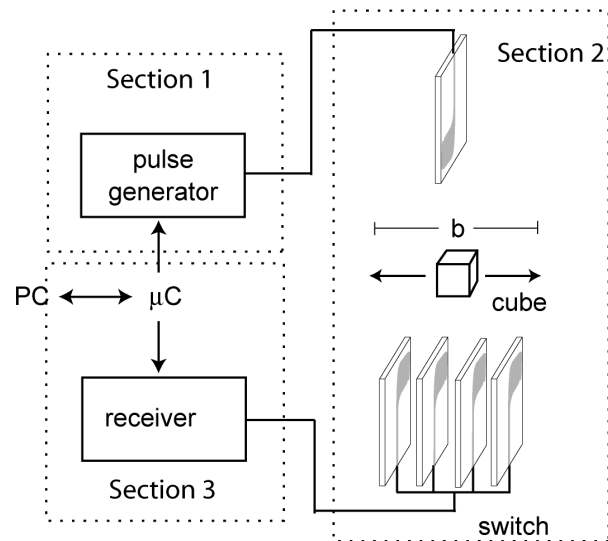


Fig. 1. Block circuit of the experimental setup including transversal length b .

The measurement pulse generated in the first sub-section is a quasi gaussian monocycle having a width of 400 ps. It is derived from a 20 MHz square wave linked to a differentiator. In order to remove the DC and low frequency content of a single pulse which can not be radiated by the antennas, a second inverted and delayed pulse, is subtracted from the first. Fig. 2 shows the amplified monocycle, which is fed into the antenna. Because of the very small pulse width the need for broadband antennas with a compact size and good reproducibility is obvious. Various types of antennas like logarithmic periodic dipole antennas, bow-tie and double-ridged horn antennas may fulfil these requirements in a more or less satisfactorily manner.

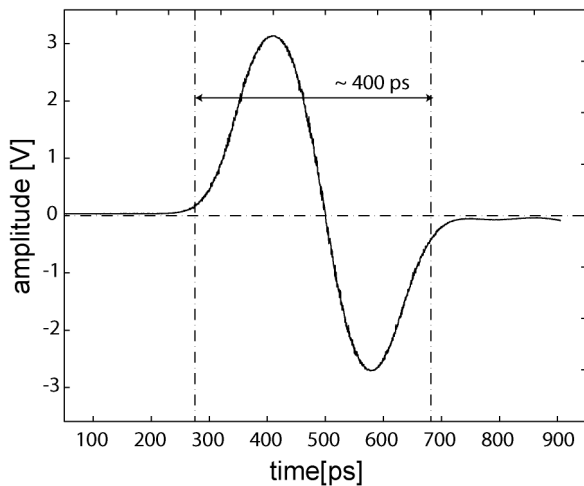


Fig. 2. Transmitted pulse consisting of a gaussian monocycle.

In order to obtain a high spatial resolution, the present receiver applies a line antenna array. In order to enable a small geometrical shape, antipodal Vivaldi antennas [2,3] are used. The antennas are manufactured from RO 5880 RF-substrate with a permittivity of $\epsilon_r=2.2$ and a thickness of $d=1.575$ mm using etching technology. The return loss is less than -10 dB for frequencies above 1 GHz. The antennas have a size of 80×100 mm. While propagating across the known distance between the antennas the transmitted pulse interrogates the scattering objects, which are located in an unknown position transversal to the direction of propagation (Section 2). As mentioned before the receiver consists of an array of 4 antennas lined up with a spacing of 50 mm. The array is positioned approximately 50 mm below the plane of the dielectric obstacles. A switch allows the connection of the receiver electronics to the individual antennas and to record 4 measurement signals successively.

The third sub-section comprises the circuitry for sampling the received pulse and applying further processing as shown in Fig. 3. Because of the hardware properties the compliance with the Nyquist criterion is not possible in real time. Therefore the sequential sampling technique is used, which allows for the reconstruction of a periodic signal under special circumstances even if it is sub sampled [e.g. 4]. Using a miniaturised sampling bridge composed of 4 diodes in beam-lead technology and a holding capacitor, the instantaneous pulse amplitude is stored and then digitised in a fast analog to digital converter. The sampling bridge is operated with short sampling pulses of 70 ps duration. The frequency response of the gate is shown in Fig. 4. To prevent the sampling diodes from being switched by the measurement signal unintentionally, an additional reverse voltage is applied. The charging time of the capacitor is below $1 \mu\text{s}$, corresponding to ~ 20 samples, using a frequency of 20 MHz.

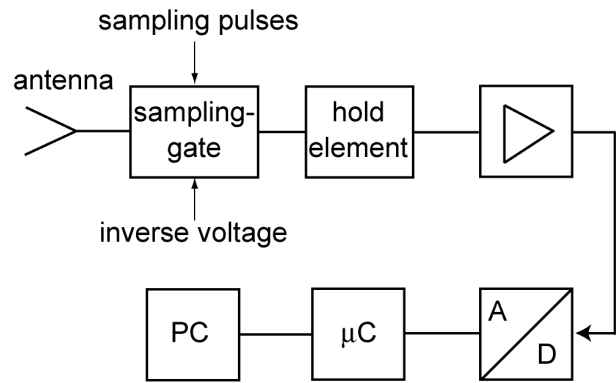


Fig. 3. Block diagram of the receiver.

III. MEASUREMENTS

During first measurements, various materials were investigated with the experimental setup. The objects under test were for example cubes with an edge length of 1 inch. The homogeneous materials consisted of ceramics and plastics with permittivities of $\epsilon_r = 4, 6, 9, 10, 12$ and 16. The cubes were measured separately at different positions between transmitting and receiving antennas.

Their position was varied continuously along the direction of the array transversal to the direction of pulse propagation. Due to the fact that the received pulses are compared with reference pulses, which were applied to the undisturbed space between the antennas, the influence of a surrounding material, in the present case air, cancels. It has no influence on the result, except it is very lossy or obscures the OUT by having a similar permittivity.

IV. DATA-PROCESSING AND ANALYSIS

In order to determine the position of the OUT, the signals of the 4 antennas were recorded successively and 80 values (amplitude) were transmitted to the controller. As many calculations as possible were made on the microcontroller, because of the slow transfer rate between the controller and PC, which limits the measurement speed. A more elaborate version of the measurement set-up could be increased very much in the data transmission rate. The signal carries information like attenuation, dispersion and multipath scattering. It is advantageous to find the position of the obstacle in two steps. At first the decision is made which pair of antennas carries most of the information content. These two antennas yield the best results for determining the position of the obstacle. Subsequently a non-linear data-processing, especially an artificial neural network performs the detailed analysis. Each pair of antennas has its own trained net for the corresponding positions. The nets used for this decision are RBF-nets (radial basis function nets). They provide continuous output values

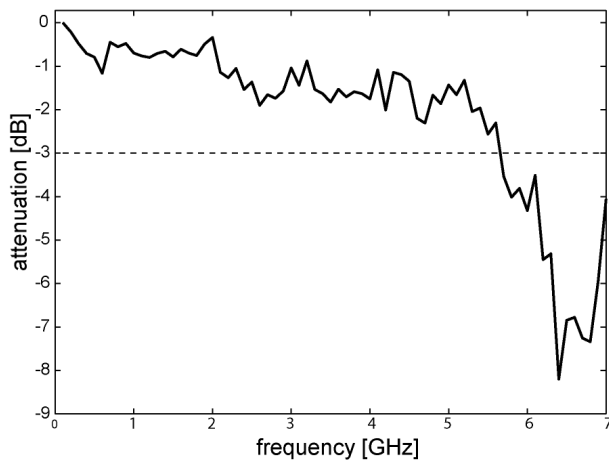


Fig. 4. Frequency response of the developed sampling gate.

and are deterministic. Therefore the same network is obtained after each training under identical conditions.

The location of b for the OUT in front of the four antennas varies over 250 mm. To check the data-processing (net), there are different datasets for training and validation [5,6]. The accuracy of determination of the location is independent of the permittivity of the object. The root mean square error for trained values ($RMSE_{train}$) is approximately 4 mm. For untrained position the $RMSE_{val}$ is smaller than 7 mm. The predicted and the true positions are plotted versus each other in Fig. 5.

The obtained spatial resolution is much higher than the directional characteristic of Vivaldi antennas anticipates.

V. CONCLUSION

A new method of localisation of objects independent of the dielectric properties has been presented. Ultra-wideband pulses illuminate the object in a transmission measurement. By expanding the receiver array with more antennas a larger geometrical width can be obtained. The flexible analysis using artificial neural networks makes a

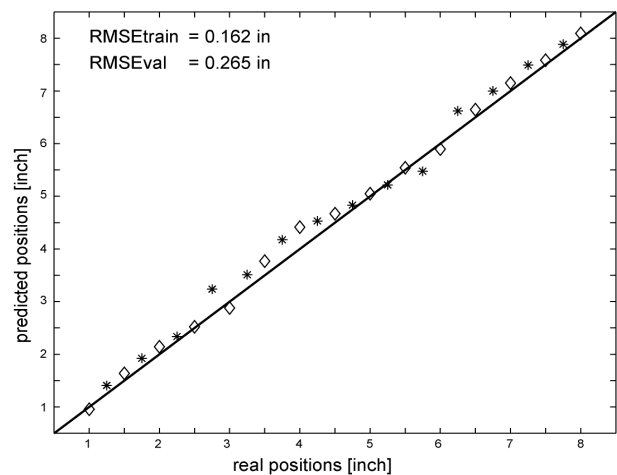


Fig. 5. Predicted position of homogeneous cubes independent from dielectric constant. Trained positions (diamond) and validated positions(asterisk).

quick and easy adaptation of the setup to different materials possible. Measurements show a root mean square error of validation of less than 7 mm over an observation range of 250 mm. Beside of localisation a distinction between different objects seems also to be possible

REFERENCES

- [1] O. Schimmer, A. Gülck, F. Daschner, J. Piotrowski, R. Knöchel "Non-contacting Determination of Moisture Content in Bulk Materials Using Sub-Nanosecond UWB-Pulses", *EuMW Proceedings*, No. 1789, Amsterdam, 2004.
- [2] J.D.S. Langley, P.S. Hall, P. Newham, "Novel ultrawide-bandwidth Vivaldi antenna with low crosspolarisation," in *Electronic Letters*, vol. 29, No. 23, 1993.
- [3] E. Gazit, "Improved design of the Vivaldi antenna", *IEE proceedings*, vol. 135, London, April 1988.
- [4] B. Schiek, "Meßsysteme der Hochfrequenztechnik", *Hüthig*, Heidelberg, 1984.
- [5] F. Daschner, "Multivariate Messdatenverarbeitung für die dielektrische Spektroskopie mit Mikrowellen zur Bestimmung der Zusammensetzung von Lebensmitteln", *Shaker*, Aachen, 2002.
- [6] S.V. Kartalopoulos, "Understanding Neural Networks and Fuzzy Logic", *IEEE Press*, New York, 1996.

Digital Beamforming for High Resolution Wide Swath SAR Imaging

Nicolas Gebert¹, Gerhard Krieger², Alberto Moreira³

German Aerospace Center (DLR), Microwaves and Radar Institute, P.O. Box 1116, 82234 Wessling, Germany

¹Phone: +49 8153/28-3331, Email: nico.gebert@dlr.de, ²Phone: +49 8153/28-3054, Email: gerhard.krieger@dlr.de

³Phone: +49 8153/28-2305, Email: alberto.moreira@dlr.de

Abstract — Synthetic Aperture Radar (SAR) is a well-proved instrument for remote sensing. Multi-aperture SAR-systems allow for digital beamforming on receive that will enable a wide swath SAR with high azimuth resolution. In classic multi-aperture systems, stringent requirements are imposed on sensor velocity and PRF to ensure uniform sampling of the synthetic aperture. This paper shows that an unambiguous reconstruction of the SAR signal is also possible in case of such a non-optimum PRF. For this, an innovative reconstruction algorithm is derived, which enables a recovery of the unambiguous Doppler spectrum also in case of a non-uniform sampling of the synthetic aperture. Further, the influence of perturbations on the reconstruction is presented and general system aspects are discussed.

I. INTRODUCTION

A. Synthetic Aperture Radar

Synthetic Aperture Radar (SAR) is an established remote sensing technique for high resolution imaging of the Earth surface. It consists of an air- or spaceborne side looking radar on a moving platform which takes advantage of the fact that a target contributes to the received signal as long as it is illuminated by the antenna footprint moving over it (cf. Fig. 1). Hence, a synthetic aperture of length L_{sa} is built by all the pulses which are backscattered and received coherently during the illumination time.

The characteristic of the SAR configuration is the time varying distance between sensor and target $r(t)$ while the platform moves over the synthetic aperture. For a linear flight track with constant velocity v in x -direction (so-called ‘azimuth’) this leads to the following expression for $r(t)$ in dependency of time t respectively the sensor position $x(t) = v \cdot t$ and the minimum slant range distance R_0 [1].

$$r(t) = \sqrt{R_0^2 + v^2 \cdot t^2} = \sqrt{R_0^2 + x(t)^2} \quad (1)$$

Considering the received signal $s_r(t)$, this leads to a delay caused by the 2-way propagation and an azimuth-modulation of the transmitted baseband signal $s_t(t)$ dependent on $r(t)$:

$$s_r(t) = s_t\left(t - \frac{2 \cdot r(t)}{c}\right) \cdot \exp\left(j \cdot \frac{4\pi}{\lambda} \cdot r(t)\right) \quad (2)$$

Where c is the speed of light and λ the carrier wavelength. The phase term can be expressed using quadratic approximation as follows:

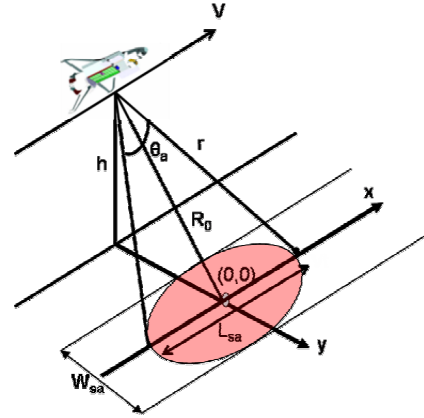


Fig. 1: SAR Geometry.

$$\varphi(t) \approx \frac{4\pi}{\lambda} \cdot \left(R_0 + \frac{(v \cdot t)^2}{2 \cdot R_0} \right) =: \varphi_0 + \omega_{az} \cdot t^2 \quad (3)$$

yielding the well-known chirp of the azimuth signal:

$$s_r(t) \approx s_t(t - t_0) \cdot \exp\left(j \cdot (\varphi_0 + \omega_{az} \cdot t^2)\right) \quad (4)$$

The bandwidth B_{az} of this azimuth modulation is determined by the geometry defining the maximum reception time t_{max} , the sensors’ velocity v and antenna length L_a :

$$B_{az} = \frac{\omega_{az}}{\pi} \cdot t_{max}^2 = \frac{\omega_{az}}{\pi} \cdot \left(\frac{L_{sa}}{v} \right)^2 = \frac{2 \cdot v}{L_a} \quad (5)$$

Processing of the received chirp signal is done by autocorrelation with an expected impulse response. Thus the shorter the antenna is, the longer L_{sa} is and the more pulses are correlated and hence the better the resolution is.

B. High Resolution Wide-Swath Imaging

In conventional SAR the unambiguous swath width and the achievable azimuth resolution pose contradicting requirements on system design. As mentioned above a good azimuth resolution requires a short antenna for a long synthetic aperture which leads to a high azimuth- or Doppler-bandwidth B_{az} . Hence, a high pulse repetition frequency (PRF) is needed to sample the Doppler-spectrum without aliasing. If a large unambiguous swath is to be imaged, a low PRF and a long antenna in elevation are favourable. This limitation can be expressed by the well-known minimum antenna area constraint determining the lower bound for a full resolution SAR:

$$Aa = Wa \cdot La > \frac{4 \cdot \lambda \cdot R_m \cdot \tan \eta \cdot v}{c} \quad (6)$$

Where R_m is the medium slant range, η the incidence angle and W_a the antenna height [2].

To overcome this fundamental limitation inherent to spaceborne strip-map SAR, several innovative techniques have been suggested which are based on a splitting of the receiving antenna into multiple sub-apertures (Fig. 2, middle, [3]-[8]). This enables the simultaneous reception of the backscattered signal with individual receiver channels. As shown in Fig. 2 on the left, the signal is mixed, digitized and stored by each receiver. Then, a posteriori, digital beamforming on receive is carried out by an appropriate combination of the sub-aperture signals. It is then possible to form multiple independent beams and to gather additional information about the direction of the scattered radar echoes.

The transmitter may be either on the same or on a different platform. A further extension of this concept is the distribution of the receiver apertures on multiple platforms (Fig. 2, right, [9]-[11]) leading to a multistatic SAR where the size of each individual receiver is reduced. The operation of such a multi-aperture system can be regarded as collecting additional azimuth samples while forming the synthetic aperture. These additional samples will then allow for a reduction of the PRF without an increase of azimuth ambiguities, thereby enabling the mapping of a wide image swath. In a classic DPC system, the PRF has to be chosen such that the SAR platform moves just one half of its antenna length between subsequent radar pulses. This imposes a stringent requirement on the relation between PRF, v and the antenna length, and any deviation from this relation will result in a non-uniform sampling of the synthetic aperture which leads to additional ambiguities in the signal.

II. RECONSTRUCTION ALGORITHM

A. Theory

In the following it will be shown that an unambiguous reconstruction of the SAR signal is also possible in case of such a non-optimum PRF. For this, an innovative reconstruction algorithm is presented, which enables a

recovery of the unambiguous Doppler spectrum also in case of a non-uniform sampling of the synthetic aperture.

The reconstruction is based on a generalization of the sampling theorem according to which a band-limited signal $u(t)$ is uniquely determined in terms of the samples $h_i(nT)$ of the responses $h_i(t)$ of n linear systems with input $u(t)$, sampled at $1/n$ of the Nyquist frequency [12]. This is independent from the $h_i(nT)$ as long as the samples do not coincide.

In our case, the functions h_i correspond to the bistatic ‘channel’ between the transmitter and each receiver i and consist of the bistatic phase and the joint antenna pattern [14]. The received signals are sampled with PRF and hence the signal bandwidth can be up to $N \cdot PRF$. Basically, the $h_i(t)$ provide the geometrical information of the configuration. A characterization of the whole system is given by the matrix H . It contains the frequency domain representations $H_i(f)$ of all the reference functions $h_i(t)$ shifted by multiples of the PRF.

Then, as shown in [13], the inversion of H yields in its columns a bandpass decomposition of the reconstruction filters P_i (cf. Fig. 3):

$$\mathbf{H}(\mathbf{f}) = \begin{bmatrix} H_1(f) & \dots & H_n(f) \\ H_1(f + PRF) & \dots & H_n(f + PRF) \\ \vdots & \ddots & \vdots \\ H_1(f + (n-1) \cdot PRF) & \dots & H_n(f + (n-1) \cdot PRF) \end{bmatrix} \quad (7)$$

$$\mathbf{H}^{-1}(\mathbf{f}) = \begin{bmatrix} P_{11}(f) & P_{12}(f + PRF) & \dots & P_{1n}(f + (n-1)PRF) \\ P_{21}(f) & P_{22}(f + PRF) & \dots & P_{2n}(f + (n-1)PRF) \\ \vdots & \vdots & \ddots & \vdots \\ P_{n1}(f) & P_{n2}(f + PRF) & \dots & P_{nm}(f + (n-1)PRF) \end{bmatrix} \quad (8)$$

The suppression of ambiguities is achieved by filtering each channel with its appropriate filter P_i and subsequent coherent combination of all receiver channels. Fig. 3 shows the linear system model for the signal reconstruction from a multi-aperture system with $N=3$ receivers.

The derived algorithm has a great potential for any multi-aperture system, be it a distributed SAR with multiple satellites or a single platform system relying on the displaced phase centre (DPC) technique, like the high resolution wide swath (HRWS) SAR [4] or the dual receive antenna approach with TerraSAR-X [8].

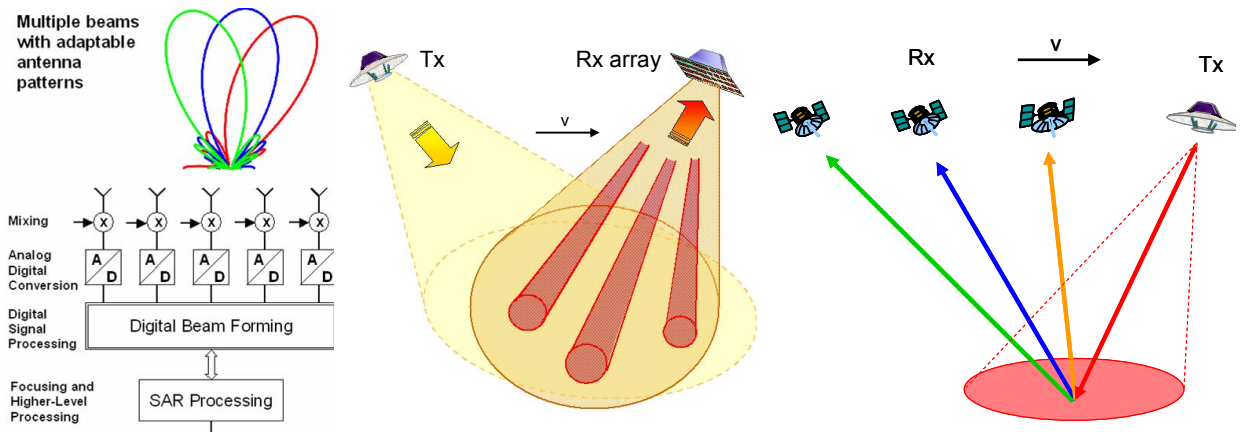


Fig. 2: Digital beamforming on receive principle (left). DPCA configuration (middle). Sparse satellite array (right).

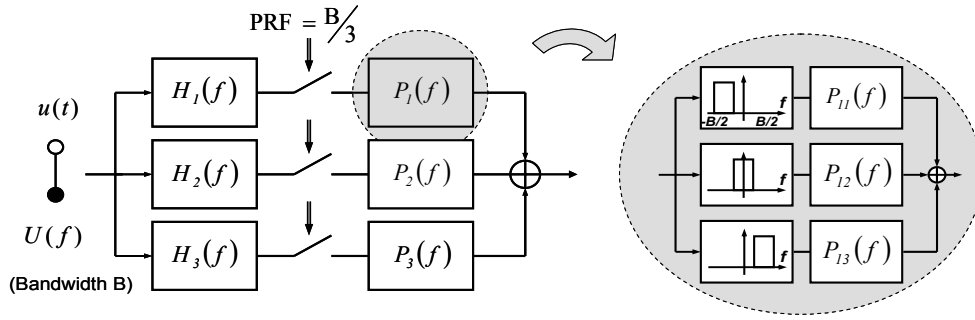


Fig. 3: Left: Reconstruction for multi-channel subsampling in case of three channels. Right: Each reconstruction filter P_i consists of N bandpass filters P_{ij} .

B. Quadratic Approximation

In principle, it is possible to use the multi-channel SAR signal model for a complete reconstruction of the scene reflectivity. However, in order to concentrate on the essential steps, we will only consider the azimuth modulation in the following derivation. The azimuth signal of a point target at azimuth time $t = 0$ and slant range R_0 for each individual receiver channel at position Δx_i relative to the transmitter may be described as

$$h_i(t, \Delta x_i) = \exp\left(-j \frac{2\pi}{\lambda} \left(\sqrt{R_0^2 + (vt)^2} + \sqrt{R_0^2 + (vt - \Delta x_i)^2} \right)\right) \quad (9)$$

when neglecting the envelope of the azimuth signal. The phase of the azimuth signal is proportional to the sum of the transmit and receive paths which are here approximated by the two square roots assuming a straight flight path with velocity v . A further simplification arises if we expand (9) in a Taylor series up to the second order which will lead to the quadratic approximation:

$$h_i(t, \Delta x_i) \cong \exp\left(-j \frac{4\pi}{\lambda} R_0\right) \cdot \exp\left(-j \frac{\pi \Delta x_i^2}{2\lambda \cdot R_0}\right) \cdot \exp\left(-j \frac{2\pi v^2}{\lambda} \frac{(t - (\Delta x_i/2v))^2}{R_0}\right) \quad (10)$$

Here, the first exponential describes a constant phase offset for a given slant range R_0 which is equal for all receivers while the second exponential accounts for an additional constant phase offset which is due to the different along-track displacements between each individual receiver and the transmitter. The time-varying azimuth modulation of the bistatic SAR is then given by the third exponential. By comparing (10) with the point target response of a monostatic SAR:

$$h_i(t, \Delta x_i) \cong \exp\left(-j \frac{4\pi}{\lambda} R_0\right) \cdot \exp\left(-j \frac{2\pi v^2 t^2}{\lambda \cdot R_0}\right) \quad (11)$$

it becomes clear that the bistatic azimuth response evolves from its monostatic counterpart by a time delay $\Delta t = \Delta x_i/2v$ and a phase shift $\Delta\varphi = -\pi \Delta x_i^2/2\lambda R_0$. Therefore, the multiple aperture system can be regarded as a monostatic SAR which is followed by additional time and phase shifts for each receiver channel.

C. Simulation Results

As demonstrated in more detail in [14] the algorithm has been tested with real SAR data acquired by the DLR E-SAR system and lead to accurate reconstruction results. For this, E-SAR data was low-pass filtered to obtain data over-sampled by a factor of 10. Then, two ambiguous ‘channels’ were generated, by taking every 20-th sample of the data. The offset between the data taken for two channels was only one sample and hence the resulting overall sampling was non-uniform. Fig.4 shows on the left the ambiguous image if only one sub-sampled channel is used. Fig.4 on the right presents the result after combining the two channels to the unambiguous image. Further, simulations for a TerraSAR X similar scenario were carried out and lead to promising results [15].

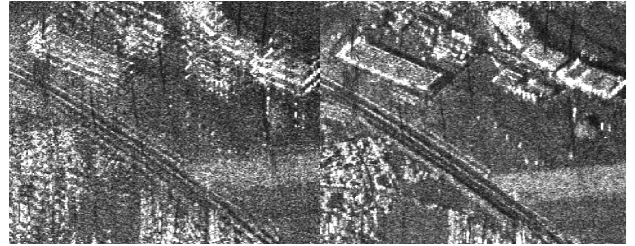


Fig. 4: Ambiguous image for one channel (left) and reconstruction after non-uniform DPC sampling (right).

III. SENSITIVITY AGAINST PERTURBATIONS

As mentioned before, the reconstruction in an ideal system is independent from the configuration as long as there are no identical samples. In a real scenario, where perturbations like noise and jitter are taken into account, the configuration which determines the effective sample positions has to be considered. In general, one can say that the sensitivity will increase the higher the actual sampling deviates from the case of uniform sampling.

For the simple case, where only white Gaussian noise is added to the signal in every receiver channel, the suppression of the ambiguities is not affected, but the noise floor after the coherent combination rises, the higher the non-uniformity of the samples is. In a first approximation, the noise generated by the amplifiers of the receive modules can be approximated as such white noise. The resulting linear SNR at the output can then be expressed as a function of the N filters P_i and the respective SNR_i at the input of the respective filter as follows:

$$SNR_{out} = \left(\sum_{i=1}^N \frac{E[|P_i|^2]}{N \cdot SNR_{in,i}} \right)^{-1}, \quad (12)$$

The subsequent plot gives an example for $N=2$ receivers. It shows the dependency of the SNR_{out} on the relative position of receiver 2 measured in percent of uniform distance. 100% of uniform distance correspond to a uniform sampling while 0% represent identical receiver positions. The values are normalized to the optimum SNR_{out} achieved for uniform sampling.

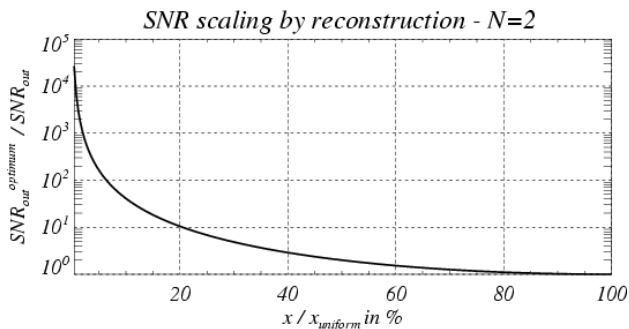


Fig. 5: Relative degradation of SNR_{out} for reconstruction in the presence of noise dependent on sample position.

The impact of jitter that can be caused by synchronization errors between the receivers, oscillator phase noise or errors when estimating the reference functions $h_i(nT)$, is different. First investigations of the effect when $h_i(nT)$ are subject to estimation errors were carried out and showed that the resulting error affects the correct reconstruction and additional azimuth ambiguities occur. The height of these ambiguities rises with increasing non-uniformity.

IV. SYSTEM ASPECTS AND HARDWARE REQUIREMENTS

In the case of the DPCA approach using a single platform, the receiver hardware becomes different from a conventional SAR system as digital beamforming on receive requires a completely independent operation of all elements in the receiver chain consisting of the antenna aperture elements, the low-noise amplifier, the demodulation and the final A/D conversion. Note that the suggested DPCA configurations support a complete separation between the transmit and receive chains. This offers the possibility to optimise the transmit and receive antennas separately and enables the use of innovative technologies like an integration of highly sensitive receive-only modules directly into the antenna elements. Another challenge is the large amount of data that rises with the number of receiver channels. This will require either broadband data links or the development of effective quantization and compression techniques to reduce the data volume without a significant loss of information. In a sparse array configuration, there is the need for multiple small satellites which have to fly in a close formation. Major challenges in such a configuration are precise orbit control, accurate baseline determination, and oscillator synchronisation.

V. SUMMARY & POTENTIALS

We have shown the benefit of multi-aperture SAR systems for high-resolution wide swath imaging. An innovative reconstruction algorithm was presented that allows for an unambiguous recovery of the azimuth spectrum even in the case of non-uniformly sampled data. The influence of noise on the reconstruction was demonstrated and an expression was given, how the noise floor rises when the algorithm is applied in the presence of white Gaussian noise. Finally, general system aspects were discussed.

Besides, such systems offer a wide variety of additional opportunities if compared to conventional monostatic SAR systems. One example is the presence of one or even more baselines allowing for interferometry, be it along-track to detect ground moving targets or be it cross-track to measure terrain heights. If more than one baseline is available, multi-baseline techniques can be used to increase the unambiguous range of the measured data. A challenge for the future is the combination of all these linear and nonlinear imaging techniques in a highly reconfigurable remote sensing instrument for a broad range of powerful applications.

REFERENCES

- [1] H. Klausing, W. Holpp, *Radar mit realer und synthetischer Apertur*, Oldenburg Verlag, 2000
- [2] J. Curlander, R. McDonough, *Synthetic Aperture Radar - Systems And Signal Processing*, J. Wiley & Sons, 1991
- [3] A. Currie and M.A. Brown, *Wide-Swath SAR*, IEE Proceedings - Radar Sonar and Navigation 139 (2), pp 122-135, 1992
- [4] G.D. Callaghan and I.D. Longstaff, *Wide Swath Spaceborne SAR Using a Quad Element Array*, IEE Radar Sonar and Navigation 146(3), pp 159-165, 1999
- [5] M. Suess, B. Grafmüller, R. Zahn, *A Novel High Resolution, Wide Swath SAR System*, IGARSS 2001
- [6] M. Younis, C. Fischer, W. Wiesbeck, *Digital Beamforming in SAR systems*, IEEE Trans. Geosci. Remote Sensing 41 (7), pp. 1735-1739, 2003
- [7] L. Brule, H. Baeggli, *Radarsat-2 Program Update*, IGARSS 2002.
- [8] J. Mittermayer, H. Runge, *Conceptual Studies for Exploiting the TerraSAR-X Dual Receiving Antenna*, IGARSS 2003.
- [9] N.A. Goodman, S.C. Lin, D. Rajakrishna, J.M. Stiles, *Processing of Multiple-Receiver Spaceborne Arrays for Wide Area SAR*, IEEE Trans. Geosci. Remote Sensing 40 (4), pp 841-852, 2002
- [10] G. Krieger and A. Moreira, *Potentials of Digital Beamforming in Bi- and Multistatic SAR*, IGARSS 2003
- [11] J.P. Aguttes, *The SAR Train Concept: Required Antenna Area Distributed over N Smaller Satellites, Increase of performance by N*, IGARSS 2003.
- [12] Papoulis, *Generalized Sampling Expansion*, IEEE Transactions on Circuits and Systems 24 (11), pp.652-654, 1977.
- [13] Brown, *Multi-Channel Sampling of Low-Pass Signals*, IEEE Transactions on Circuits and Systems 28 (2), pp.101-106, 1981
- [14] G. Krieger, N. Gebert, A. Moreira, *Unambiguous SAR Signal Reconstruction from Non-Uniform Displaced Phase Centre Sampling*, IEEE Geoscience and Remote Sensing Letters, Vol. 1, No. 4, October 2004
- [15] G. Krieger, N. Gebert, A. Moreira, *Unambiguous SAR Signal Reconstruction from Non-Uniform Displaced Phase Center Sampling*, IGARSS 2004

Highly Integrated X-band microwave modules for the TerraSAR-X calibrator

Rainer Lenz, Karin Schuler, Werner Wiesbeck

Universität Karlsruhe (TH),
Institut für Höchstfrequenztechnik und Elektronik,
Kaiserstrasse 12,
76131 Karlsruhe, Germany,
0049 (0) 721 608 6252

Abstract — In April 2006, the TerraSAR-X satellite will be launched. This paper describes the development of a novel and highly integrated, digitally controlled active X-band SAR system calibrator (DARC). It consists of both an active transponder path for absolute radiometric calibration and a calibrated receiver chain for antenna pattern evaluation of the satellite antenna. A total of 16 active transponder and receiver systems and 17 receiver only systems will be fabricated for a calibration campaign.

I. INTRODUCTION

Within the first half of 2006 the TerraSAR-X satellite will be launched in a private public partnership between the German Aerospace Center (DLR) and EADS Astrium GmbH. The SAR instrument is highly versatile by implementing multiple operation modes adapted to various applications. The calibration of the SAR instrument is crucial in order to guarantee and verify the data quality. This includes both internal and external calibration. The former is related to the instrument and control circuit design and is not subject of this paper. The external calibration includes measuring the response of known targets. By comparing the ideal response with the measured signals, a correction scheme is derived.

For extended targets, speckle noise adds to the common system noise. This causes variations in the intensity of the later SAR image. The standard variation is called radiometric resolution and is mainly responsible for the image quality. Speckle noise can be reduced by several measurements of the same scenery (multi-look-processing). Traditionally the external calibration uses passive man-made and natural targets. However active transponders are utilized for high accuracy applications requiring absolute radiometric calibration [1].

Additionally, this novel calibrator provides a calibrated input receiver path for satellite antenna pattern evaluation. The paper presents a novel system concept and hardware realization of a Digitally controlled Active ground Calibration system, which will be used during the operation and validation phase the of TerraSAR-X mission.

II. SYSTEM ARCHITECTURE

The calibrator system consists of a set of two antennas, a transmitter chain for the signal to be retransmitted to the satellite (transponder operation) and a detector

(receiver path) as shown in Figure 1. The LO signal for the downconversion unit is provided by a coaxial resonance oscillator. The signal is loop controlled by a PLL to guarantee high signal stability and low phase noise. Signal detection is performed by a dedicated logarithmic amplifier with a large dynamic range. Thus the system provides an active reference target for the SAR and simultaneously allows both analyzing the pulse signals transmitted by the satellite and monitoring the performance of the transponder itself by comparing the input to the retransmitted output signal.

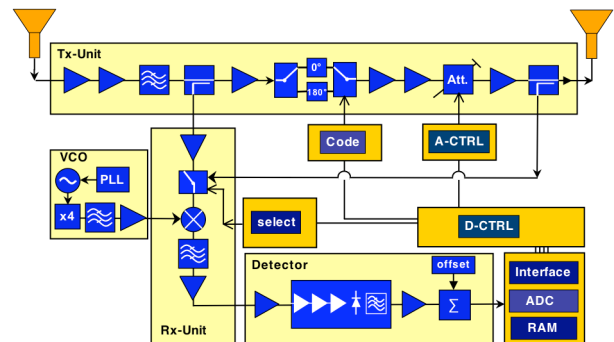


Figure 1: Block Diagram of Transponder Hardware

The RCS value is dependent on the amplification. The amplification can be adjusted digitally within a range of 20 dB. The attenuator setting is commanded by the digital unit. In order to tag each single transponder, two single pole double through switches are introduced. One path delays the signal by 180 degrees compared to the other path. The delay is controlled digitally. The switches change the path within the pulse breaks. As the PRF is within a range of several kHz, the switching speed is not critical. Leakage from the digital control command of the switches to the RF path is very low and will not deteriorate the signal quality. An electrical isolation of the digital unit from the analog RF unit is guaranteed by dedicated optocouplers.

The system has a nominal bandwidth of 150 MHz and an experimental bandwidth of 300 MHz. The center frequency is at 9.65 GHz. In order to suppress noise and leakage from TV-satellites which work at higher

frequencies in X-band (11.7 GHz to 12.75 GHz), a dedicated filter has to be introduced. The LO is set to 10.3 GHz. The image can be found between 10.8 GHz and 11.1 GHz, which is outside the satellite-TV frequency band. The IF-frequency is set between 500 MHz and 800 MHz.

III. SYSTEM PERFORMANCE

The calibrators will be distributed in southern Germany at certain longitudes and latitudes for the TerraSAR-X calibration campaign. The satellite transmit power is 63.03 dBm. The gain of the satellite antenna is 46.5 dBi and the minimum distance from the satellite to the transponder is 530 km. The calibrator has a set of two horn antennas with a gain of 21 dBi each. The dynamic range of the calibrator system is 45 dB. The maximum power density is -16 dBm/sm and the maximum input power after the antenna is -36 dBm. As the receive and transmit antennas are arranged so that they can receive both horizontal and vertical polarization an additional drop of 3 dB occurs reducing the maximum input power to -39 dBm. The maximum RCS required is 50 dBsm.

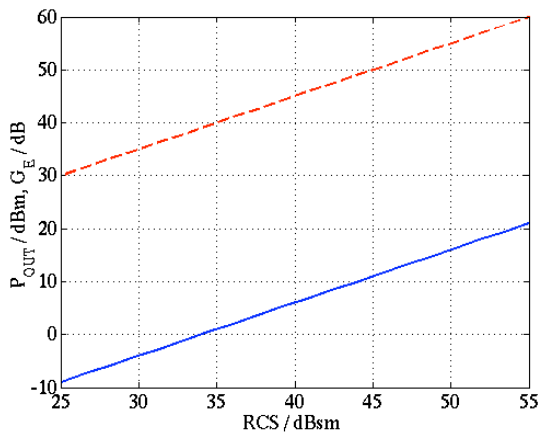


Figure 2: Electronic amplification (--) and corresponding output power (—)

The electronic amplification and output power of the transponder for the specified RCS-range (20 dBsm to 50 dBsm) can be read from Figure 2. In order to achieve the performance, a dedicated system architecture (see Figure 1) has been chosen. The input power is amplified by a low noise amplifier (LNA), whose noise figure is approximately 2.5 dB. In order to guarantee a low system noise figure, a second amplifier has to be inserted before a filter limits the noise power and a coupler feeds part of the signal to the detection unit. Within the passband of the filter the ripple must be below 0.3 dB in order to fulfill the overall specifications. Before the transmit signal is fed to the switches another amplifier has to cancel the insertion loss of the filter and coupler which is for both at approximately 9 dB. The switches introduce a phase modulation when switched between two pulses. Thus, a PN code can be applied to the transmit signal and

the transponder can be recognized unambiguously in the later SAR image. Next, two amplifiers are placed right before the digitally controllable attenuator which allows to choose a RCS value with steps of 0.5 dB within a range of 20 dB. Both amplifiers have to be placed here as the system noise figure would suffer at maximum attenuation if placed elsewhere. After the attenuator, the high power amplifier is placed. The 1-dB compression point of the system is at +25 dBm. For verification of the amplification and the RCS, a dedicated coupler at the output allows to feed a test signal to the detection unit. Figure 3 shows the system amplification and the system noise level as described above. The thru line is for maximum amplification and the dotted line for minimum amplification (maximum attenuation, minimum RCS).

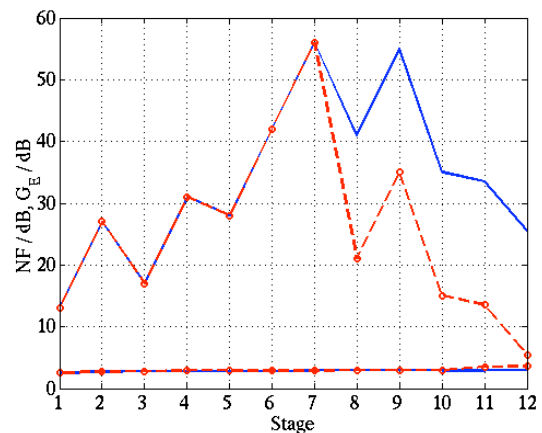


Figure 3: Simulation of gain and noise figure distribution for transponder operation

The first stage corresponds to the amplification after the LNA, the losses of filter and coupler are seen at stage three and the attenuator is at stage eight and the high power amplifier is at stage nine. Stage ten through nine (coupler at output, switch, mixer) characterize the signal which is fed to the detection unit for evaluation of the amplification. The system noise figure for transponder operation is at full attenuation below 3 dB, for the coupled signal path is at full attenuation at 3.6 dB (worst case). For fine tuning of the amplification, the amplifiers allow gain adjustment by applying an extra bias signal at the gates. Additionally, strong attention was given to the ripple suppression. Therefore, an alternating alignment of amplifier and lossy stages was chosen. As the amplifiers' input return loss is not equal zero, standing waves could occur between the amplifiers, yet a lossy stage in between attenuates reflected power waves traveling between two reflection points and suppress signal distortion.

For the input receiver path, the same simulation was run in order to find the right system architecture. Figure 4 shows the simulation results. The system noise figure for the input receiver path is always around 2.8 dB. The amplification can be read from the plot. Stage one corresponds the amplification after the LNA, amplifier,

filter, coupler, amplifier, switch and the mixer respectively.

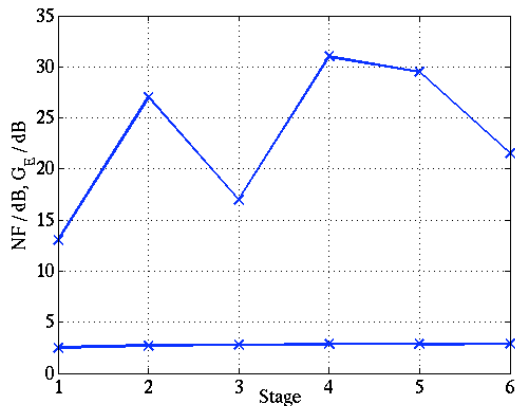


Figure 4: Simulation of gain and noise figure distribution of input receiver path.

The switch allows either to choose to detect the input signal or the output signal. As the same detection hardware is used for detection, the signal power levels have to be within the same power range. This is guaranteed with the system architecture as shown in Figure 1. For maximum input power, the IF signal power for the input receiver path is at -16.5 dBm and for the output receiver path at -12.5 dBm. An IF-amplifier decouples the mixer output from the detector input. It is not necessary to have exactly the same values. Two individual calibration signals will be introduced to characterize input and output receiver path. The correction coefficients are stored in a look-up table. The calibration routine will be run for each single calibrator and delivered with the system. The data correction has to be done after the data-take from the satellite in an offline signal processing routine.

The system architecture allows a later upgrade of the detection unit so that IQ detection becomes possible. IQ detection would allow to evaluate the satellite's complex chirp signal and draw further conclusions of the satellite's performance

IV. SIGNAL DETECTION

For detecting power levels, logarithmic detectors are a qualified and well-known principle. They offer a high dynamic range and are highly integrated. They assign power to a certain output voltage. The output of the detector is digitized using a 8 Bit AD-converter. There is a direct relationship between the dynamic range of a signal and the number of bits necessary for an AD-converter. In this system, the dynamic range of the signal is 45 dB. Therefore, a 8-Bit AD-converter was chosen. Here, the dynamic range is defined as the difference of the maximum signal power level and the noise floor. According to the transmitted power of the satellite, the system SNR varies, whereas the noise floor remains

constant. A 8-bit ADC can cover a maximum dynamic range of 48 dB. The maximum accuracy can only be expected at the maximum SNR. For lower SNR levels, the accuracy will be lower. In this system, the dynamic range of 45dB will be mapped into a voltage swing at the output of the logarithmic detector of 2 V. Thus, a value of $2 \text{ V}/256 = 8 \text{ mV}$ for the lowest significant bit is found. The detection slope of the detector is set to 40 mV/dB so that a variation of 0.3 dB in signal amplitude causes a variation of 12 mV which can be detected by the ADC at maximum SNR. Thus, for lower SNR levels, an effective number of bits can be defined which corresponds to the valid actual resolution. The difference between the effective number of bits and the nominal accuracy of the ADC converter are called noisy bits. In this system, the system noise figure as shown above is at approximately 3 dB. The maximum dynamic range is therefore 42 dB. The minimum input signal is -84 dBm and the noise floor is at -89 dBm. With the system noise figure, the effective SNR is 2 dB for the lowest input power. Thus the accuracy will not be very high in this case. The sampling rate of the AD-converter is set to 10 MSa/sec. The pulse duration varies between $2 \mu\text{s}$ and $60 \mu\text{s}$. For the signal processing, only the mean value of the pulse will be taken for antenna pattern evaluation. Thus, a processing for the gain for the SNR of $10 \cdot \log(\sqrt{N})$ can be achieved. N denotes the number of samples used for averaging. Thus, it is essential to use averaging in order to obtain accurate values for low signal levels. Low signal levels are associated with nulls in the antenna patterns.

V. MEASUREMENT OF FIRST PROTOTYPE

The noise figure for the input receiver path was measured with a dedicated noise figure meter which was run in a mixer measurement mode. In Figure 5, the noise figure measurement versus the system bandwidth is shown. The measurement agrees very well with the prediction from the simulation.

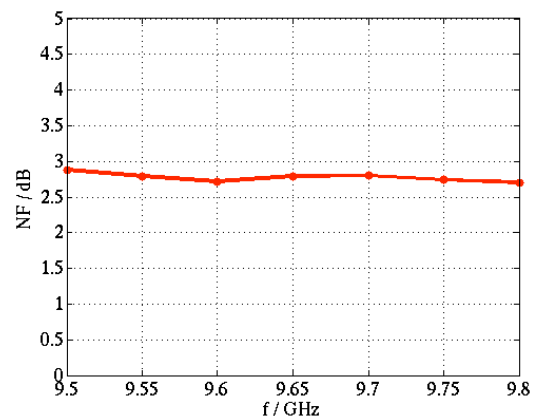


Figure 5: Noise Figure within system bandwidth

For the dynamic range measurement, the input power was swept from -84 dBm to -25 dBm. A pulsed source at 9.65 GHz was applied to the system input with a pulse

length of 10 ms. Thus averaging yields good results and allows to characterize the detection unit (Figure 6).

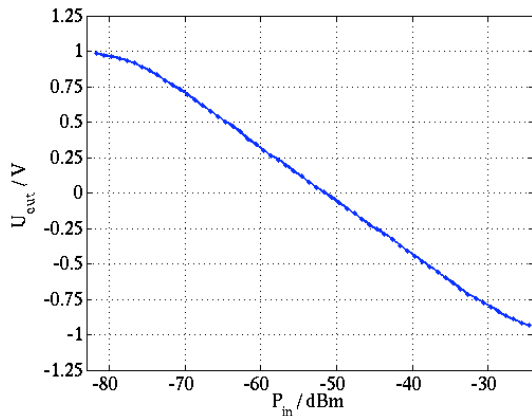


Figure 6: Dynamic range of input receiver path

The non-linearities at minimum and maximum input power agree well with the data-sheet. They will be compensated for by a calibration routine and a look-up table which allows to associate the AD-converted voltage level to the correct RF-power level. At minimum input power, the SNR becomes very low and the pulse amplitude will most probably be hidden in noise except high averaging is used.

In order to characterize the frequency dependence of the downconversion unit, the standard deviation of the AD-converted signal was calculated.

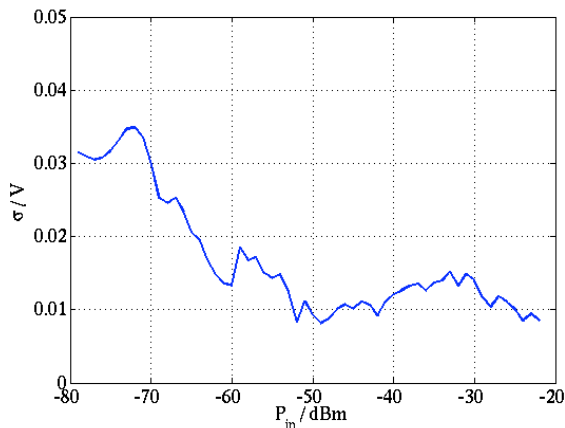


Figure 7: Standard deviation over system bandwidth

In Figure 7, the standard deviation versus frequency is shown dependant on the input power. The input power was increased by 1 dB steps. The pulse length was chosen to 10 ms in order to get good averaging results. In worst case at low SNR values, the uncorrected signal variation at low input power levels is around 0.75 dB. A

look-up table will provide correction coefficients in order to compensate for the frequency behavior. The picture of the receiver unit prototype is shown in Figure 8.

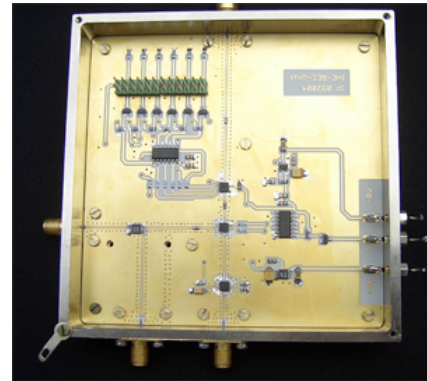


Figure 8: Picture of receiver unit prototype

VI. CONCLUSION

In this paper the design of highly integrated microwave modules for an active SAR system calibrator is presented. The calibrator consists both of an active transponder path for absolute radiometric calibration and a calibrated receiver chain for antenna pattern evaluation of satellites. The calibration device has to comply with very strict specifications in order to guarantee high accuracy [2]. Currently the modules are being fabricated. First performance results of the calibrator are expected after the launch of the TerraSAR-X satellite during the calibration campaign in southern Germany in April 2006.

ACKNOWLEDGEMENT

We would like to thank the German Aerospace Center (DLR) for the mandate to develop and produce the active radar calibrators. Furthermore, we would like to thank HBH Microwave GmbH Stutensee/Germany for technical support and fabrication.

REFERENCES

- [1] D. Hounam and K.-H. Wägel, "A Technique for the Identification and Localization of SAR targets Using Encoding Transponders", *IEEE Transactions on Geoscience and Remote Sensing*, vol. 39, no.1, January 2001
- [2] Bräutigam, B., Schwerdt, M., Bauer, R.: "TerraSAR-X CALIBRATION GROUND EQUIPMENT DESIGN DOCUMENT." *DLR, Technical Note, TX-IOCS-DD-4321 1.1_Draft*,(2004)

Cramér-Rao-Bound for Coherent Dual-Band Radar Range Estimation

Siart, U.; Tejero, S.; Detlefsen, J.

Technische Universität München, Institute for High-Frequency Engineering, 80290 München, Munich, Germany

Abstract—This paper investigates accuracy bounds on frequency estimation from dual-band observations as they may be obtained from multi-sensor platforms with several radar sensors operating in different frequency ranges. The Cramér-Rao lower bound is derived and the resulting minimum achievable resolution is given as a function of the frequency lag between the observation bands. It is seen that the theoretical resolution bound decreases as the frequency lag increases.

An iterative nonlinear least-squares estimation algorithm is used to coherently process dual-band radar information. Monte-Carlo simulations show that this estimator achieves smaller variance with dual-band observations as compared to equal bandwidth single-band observations.

I. INTRODUCTION

With increasing tendency, platforms with a variety of different radar sensors operating in different frequency regimes become available. Very often, a part of these sensors offer information about the same target scenery. It is a fundamental fact in estimation theory that any additional sensor improves the maximum reachable estimation accuracy. Provided sufficient sensor properties and processing algorithms, the signal energy as well as the bandwidth delivered from the individual sensors may be combined, making the totally covered bandwidth and the sum of the signal energies available. Classical radar signal theory predicts the gain resulting from proper use of bandwidth and signal energy.

The question remains whether there is also benefit if sensors provide frequency-domain information about the same scenery but at significantly distinct carrier frequencies. Can we expect better accuracy and resolution from the fact that there is a certain frequency difference between distinct measurement bands?

It is well known that radar range information can be represented in time domain and equivalently in frequency domain. Conversion between the impulse response (the actual range profile) and the frequency response of the complex reflectivity is generally possible by means of the Fourier transform. A point target with round trip time τ corresponds to a complex sinusoid in the frequency response. Detecting and locating radar point targets in frequency domain is thus equivalent to detecting exponentials in noisy measurements and estimating their parameters, the frequencies in particular. Therefore, the problem is at first reduced to estimating the frequencies of sinusoids in noise from multiple observation vectors. The resulting effect of a considerable distance between the observation windows along the sample axis on theoretical estimation accuracy bounds is of particular interest. It is shown that an important prerequisite is mutual coherency between the used measurement data. If mutual phase information can be employed, then improved frequency estimation accuracy is possible through a lag between the data windows.

II. DUAL-BAND RADAR DATA

In the following we assume that the time-domain radar response consists of P discrete echos, each with its round trip time τ_p and magnitude A_p . The idealized impulse response is then

$$h_0(t) = \sum_{p=1}^P A_p \delta_0(t - \tau_p) \quad (1)$$

where $\delta_0(t)$ is the Dirac delta pulse. With regard to the equivalence of information in time-domain and in frequency-domain we continue our considerations in frequency-domain. The corresponding frequency-domain complex reflectivity of an ideal multipath radar scenery is given by

$$r(f) = \sum_{p=1}^P A_p e^{-j\omega\tau_p}. \quad (2)$$

Let us further assume that this complex reflectivity is sampled at L_n discrete and equidistant frequencies within a frequency band \mathcal{B}_n with start frequency ω_{0n} and bandwidth B_n . With $\omega = \omega_{0n} + k\Delta\omega$ the resulting series of discrete reflectivity values is then

$$r_n[k] = \sum_{p=1}^P a_{pn} z_p^k \quad ; \quad k = 0, 1, 2, \dots, L_n - 1. \quad (3)$$

In this expression it is $z_p = e^{-j\Omega_p}$ with $\Omega_p = \Delta\omega\tau_p$ and

$$a_{pn} = A_p e^{-j\phi_{0pn}} \quad (4a)$$

with

$$\phi_{0pn} = \omega_{0n}\tau_p = \frac{\omega_{0n}}{\Delta\omega}\Omega_p = k_{0n}\Omega_p. \quad (4b)$$

For the series $r_n[k]$ and $r_m[k]$ in two subbands \mathcal{B}_n and \mathcal{B}_m the relation

$$\frac{a_{pn}}{a_{pm}} = e^{-j\Omega_p(k_{0n} - k_{0m})} \quad (5)$$

follows. Equation (5) states the phase relation between subbands \mathcal{B}_n and \mathcal{B}_m and it is thus termed the *coherency relation*. Provided the same point targets are active in frequency regimes \mathcal{B}_n and \mathcal{B}_m , (5) can be used during the process of estimating the values Ω_p from multiband radar reflectivity measurements.

Let us now restrict to the case of two subbands. The parameters of the assumed input data are illustrated in fig. 1. Two radar sensors with signal bandwidths $B_{1,2}$ provide information about the complex reflectivity of the radar scene. The variable k denotes the index of discrete frequency measurement points and $k_{01,02}$ correspond to the start frequencies of both measurement bands, respectively. In general, the available frequency bands do not adjoin each other and therefore, the distance between the bands is specified by the number D of unavailable samples in between.

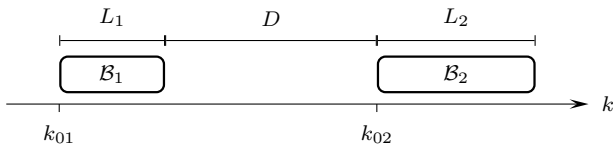


Fig. 1. Illustration of two frequency bands $\mathcal{B}_{1,2}$ with bandwidths $B_{1,2} = L_{1,2}\Delta\omega$ and the band distance D ($L_{1,2}$ and D are given in samples).

In the following, the process of estimating the frequencies of sinusoids in dual-band reflectivity measurements is under investigation. It is assumed that the sinusoid frequencies and magnitudes are identical in both subbands and thus, the same scattering centers are observed by the two radar sensors. Since the sinusoid frequencies directly correspond to the target ranges, the maximum achievable frequency estimation accuracy for the dual-band case is of particular interest in this contribution.

III. CRAMÉR-RAO LOWER BOUND FOR DUAL-BAND FREQUENCY ESTIMATION

Let us introduce a noisy measurement

$$x[k] = s[k; \boldsymbol{\theta}] + w[k], \quad k = 0, 1, \dots, L-1 \quad (6)$$

where s is the noiseless signal that depends on the vector parameter $\boldsymbol{\theta}$ and w is white Gaussian noise. Following [1], the Fisher information matrix is given by

$$[\mathbf{I}(\boldsymbol{\theta})]_{ij} = \frac{1}{\sigma^2} \sum_{k=0}^{L-1} \frac{\partial s[k; \boldsymbol{\theta}]}{\partial \theta_i} \frac{\partial s[k; \boldsymbol{\theta}]}{\partial \theta_j} \quad (7)$$

and the Cramér-Rao lower bound (CRLB) for estimation of the i -th parameter is

$$\text{var}\{\theta_i\} \geq [\mathbf{I}^{-1}(\boldsymbol{\theta})]_{ii}. \quad (8)$$

Now the maximum achievable range accuracy and range resolution using dual-band measurements are of question. It is of particular interest whether there is a possible processing gain due to the fact that two measurement frequency ranges are not adjacent but D samples apart from each other. This gain would then lie beyond the classically predictable gain that results from the sum of the bandwidths and, in the coherent case, from the sum of the signal energies.

A. Single frequency estimation

First we consider the signal

$$s[k; \boldsymbol{\theta}] = \cos(2\pi f_0 k + \phi) \quad (9)$$

observed in two windows where

$$\begin{aligned} k &= k_{01}, \dots, k_{01} + L_1 - 1 && \text{in } \mathcal{B}_1 \\ k &= k_{02}, \dots, k_{02} + L_2 - 1 && \text{in } \mathcal{B}_2 \end{aligned}$$

respectively. The parameter vector is $\boldsymbol{\theta} = [f_0 \ \phi]^T$ and f_0 is to be estimated. The CRLB for this case is shown in fig. 2 for increasing values of D . The length of the data windows are $L_1 = L_2 = 5$ and the signal-to-noise ratio is SNR = 0 dB. This plot does not take into account the phase relation between \mathcal{B}_1 and \mathcal{B}_2 , because the phase ϕ in \mathcal{B}_2 is assumed to be independent of f_0 and ϕ in \mathcal{B}_1 . Hence, this is termed the *non-coherent* case. The CRLB tends to infinity as f_1 approaches DC or the Nyquist limit. This is because at those frequencies

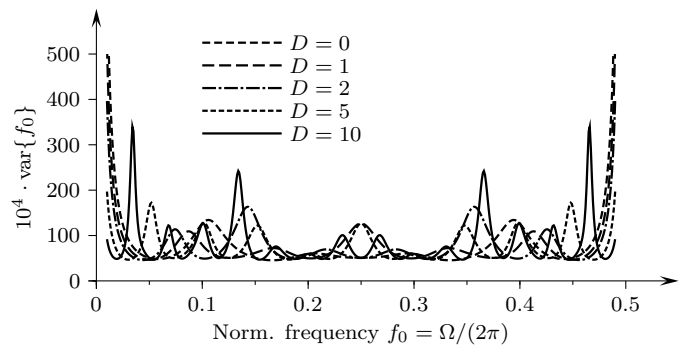


Fig. 2. Cramér-Rao-Bound for estimation of the frequency of a real sinusoid in noise using non-coherent dual-band data.

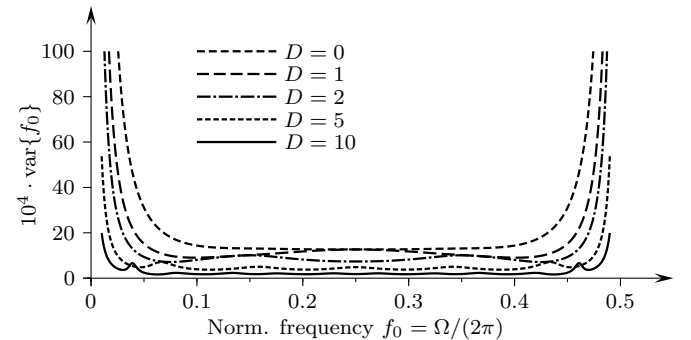


Fig. 3. Cramér-Rao-Bound for estimation of the frequency of a real sinusoid in noise using coherent dual-band data.

a slight change in f_1 does not alter the observation (10a) very much. It can be seen that the local maxima of the CRLB vary, dependent on which part of a period is observed in the two windows. However there's no significant decrease of the CRLB with increasing gap D .

We now write the two observations in the form

$$s_1[k] = \cos(2\pi f_0 k + \phi_1), \quad k = 0, 1, \dots, L_1 - 1 \quad (10a)$$

$$s_2[k] = \cos(2\pi f_0 k + \phi_2), \quad k = 0, 1, \dots, L_2 - 1 \quad (10b)$$

and take into account that $\phi_2 = \phi_1 - 2\pi f_0(L_1 + D)$. The parameter vector is now $\boldsymbol{\theta} = [f_0 \ \phi_1]^T$ and again, f_0 is to be estimated given the two observations (10). The resulting CRLB is shown in fig. 3. As this result now uses the phase relation between the data in two distinct windows, this is termed the *coherent case*. Because $|d\phi_2/df_0|$ increases with D , the CRLB now becomes smaller as the distance D becomes larger. Note, that the total number of used samples $L_1 + L_2$ remains constant in figs. 2 and 3.

B. Dual frequency estimation

In order to investigate the maximum achievable resolution, we start with the observations

$$s_1[k; \boldsymbol{\theta}] = \cos(2\pi f_1 k + \phi_1) + \cos(2\pi f_2 k + \phi_2) \quad (11a)$$

$$s_2[k; \boldsymbol{\theta}] = \cos(2\pi f_1 k + \phi_{12}) + \cos(2\pi f_2 k + \phi_{22}) \quad (11b)$$

of a signal containing two sinusoids with unknown normalized frequencies f_1 and f_2 . The phases $\phi_{1,2}$ are also considered unknown and so the parameter vector is given by $\boldsymbol{\theta} = [f_1 \ f_2 \ \phi_1 \ \phi_2]^T$. Since (11a,b) are observations of the same

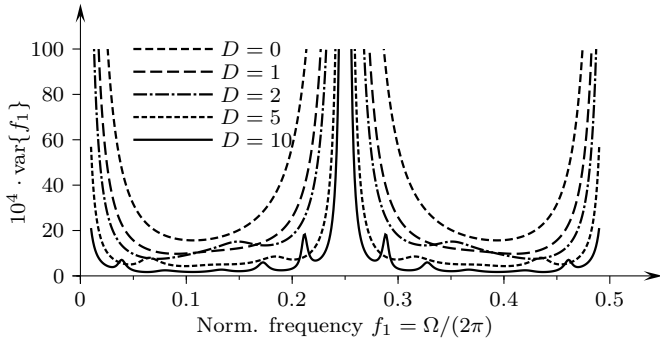


Fig. 4. Cramér-Rao-Bound for dual-band estimation of the frequency of a real sinusoid in noise when a second sinusoid with frequency $f = 0.25$ is present. The two subbands have equal length $L_1 = L_2 = 5$ in this plot.

signal, it follows that

$$\phi_{12} = \phi_1 - 2\pi f_1(L_1 + D) \quad (12a)$$

$$\phi_{22} = \phi_2 - 2\pi f_2(L_1 + D) \quad (12b)$$

with L_1 and D as illustrated in fig. 1. Extending (7) to two bands yields

$$[\mathbf{I}(\boldsymbol{\theta})]_{ij} = \frac{1}{\sigma^2} \left(\sum_{\mathcal{B}_1} \frac{\partial s_1[k; \boldsymbol{\theta}]}{\partial \theta_i} \cdot \frac{\partial s_1[k; \boldsymbol{\theta}]}{\partial \theta_j} + \sum_{\mathcal{B}_2} \frac{\partial s_2[k; \boldsymbol{\theta}]}{\partial \theta_i} \cdot \frac{\partial s_2[k; \boldsymbol{\theta}]}{\partial \theta_j} \right) \quad (13)$$

where the partial derivatives in \mathcal{B}_2 take into account the coherency property (12). From (13) the CRLB for estimating frequencies f_1 and f_2 are

$$\text{var}\{f_1\} \geq [\mathbf{I}^{-1}(\boldsymbol{\theta})]_{11} \quad (14a)$$

$$\text{var}\{f_2\} \geq [\mathbf{I}^{-1}(\boldsymbol{\theta})]_{22} \quad (14b)$$

respectively. A plot of (14a) for $f_2 = 0.25$ is shown in fig. 4. In this figure, both subbands have equal length $L_1 = L_2 = 5$ and signal-to-noise is SNR = 0 dB. As a parameter, the interband gap D varies. In the case $D = 0$ a single band with length $L = 10$ is used. In addition to the singularities at DC and its image, the minimum achievable variance for f_1 increases when f_1 comes close to f_2 . It can be seen, however, that the CRLB globally decreases as the interband gap D increases. At the same time the corridor around f_2 becomes narrower, indicating a better resolution. Since $\mathbf{I}^{-1}(\boldsymbol{\theta})_{11}$ depends on both f_1 and f_2 , this plot includes prior knowledge on the value of f_2 . It shows the CRLB for the estimation of f_1 beside a second signal at frequency $f_2 = 0.25$.

Let us now define the minimum achievable resolution as the frequency distance $\delta f = |f_2 - f_1|$ where $\text{var}\{f_1\}$ equals δf . In this way we assume, that a second frequency f_1 can be well discriminated from f_2 , as long as the estimator's variance is smaller than the actual difference between f_1 and f_2 . This value of δf can be derived from fig. 4 and the result is shown in fig. 5 versus the interband gap D . It can be seen that the achievable resolution improves with increasing D even when the total available bandwidth $B_1 + B_2$ remains constant, as it is the case in fig. 5. In this plot $L_1 + L_2 = 20$ so the classical Rayleigh resolution bound is $0.5/20 = 250 \cdot 10^{-4}$.

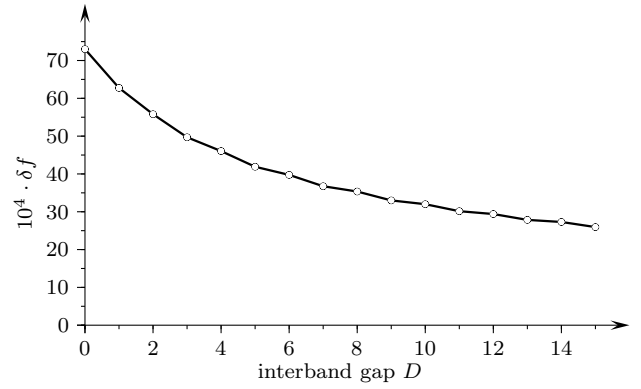


Fig. 5. Frequency resolution versus band distance D (derived from fig. 4)

IV. LEAST-SQUARES PARAMETRIC MODEL FITTING

Spectral estimation techniques based on autocorrelation sequence (ACS) estimation can generally process multi-band data because ACS estimation results are not altered by an arbitrary number of zeros padded to the data. In this way, autoregressive parametric models (AR, ARMA) as well as eigenanalysis based methods (MUSIC) are sufficient multi-band frequency estimators. They have to be considered incoherent techniques, however, since they do not depend on the actual frequency lag between the contributing sensors. As a consequence, ACS based methods do not employ phase information that would be available, if the contributing sensors were coherent and if they were illuminating the same radar scenery.

Fitting the exponential model described in (2)–(5) with a common parameter set to both measurement subband data takes into account phase and frequency relationships that are to be expected between the subband data, if they are different measurements of the same scenery. The algorithm used for dual-band frequency estimation uses the root-MUSIC algorithm to estimate initial pole angles. They serve as start values in a global exponential model which derives the complex sinusoid amplitudes through a least-squares fit to the dual-band measurement data. A nonlinear iterative minimization procedure then tunes the pole angles as well as their complex amplitudes to minimize the total squared deviation between the global signal model and the measured subband data. During each minimization cycle, the sinusoid amplitudes are adapted in due consideration of the modified pole angles. As a result we get pole angle estimates that fit better to the observed data than the initial values do. See [2] for a detailed description of the estimation procedure.

Figure 6 shows the variance and the mean of the resulting pole angle estimates versus signal-to-noise (SNR) for the single-band ($D = 0$) and for the dual-band ($D = 128$) case. The true pole angles are indicated by horizontal dashed lines. Their angular distance corresponds to the classical resolution limit $\Delta f = 360^\circ / (L_1 + L_2)$. It can be recognized that the variance of the pole angle estimates in the range $4 \text{ dB} \leq \text{SNR} \leq 20 \text{ dB}$ is significantly smaller for the dual-band case (fig. 6b). For low SNR and for $\text{SNR} > 30 \text{ dB}$ the quality of the estimates is equivalent to the single-band case.

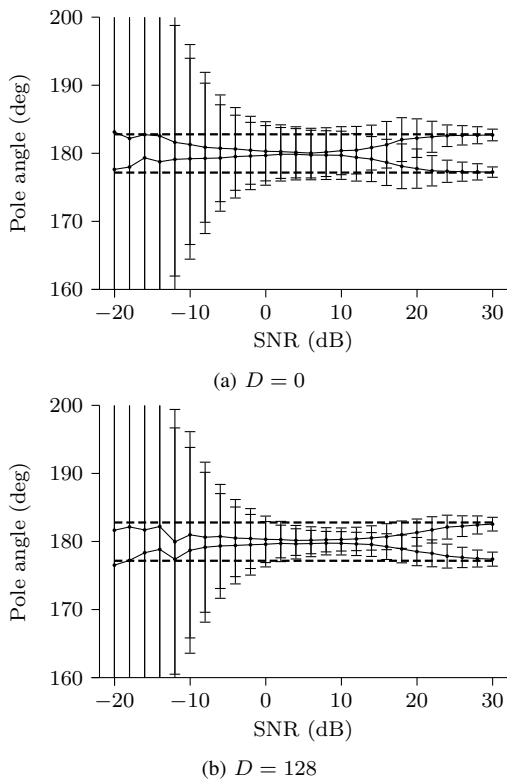


Fig. 6. Mean and variance of dual-band pole-angle estimation results using two subbands with equal length $L_1 = L_2 = 32$ and a model order of $P = 4$.

V. CONCLUSION

The Cramér-Rao lower bound (CRLB) for frequency estimation indicates the possibility to improve accuracy using subwindows with a considerable lag in between them. A meas-

ure for the resolution has been derived from the CRLB and it shows that lower estimation variance potentially yields higher resolution. Hence there is a gain in resolution without the need for additional bandwidth when using multi-frequency observations of the same radar scenery. The improved estimation quality is based on taking into account phase information between the used radar subbands. This can generally be done, when the same scatterers are active in all measured frequency ranges. Simulations using a global all-pole model fit to noisy dual-band data show that this procedure can reduce the frequency estimation variance by a factor of 1.5–1.8 in the range of $4 \text{ dB} \leq \text{SNR} \leq 20 \text{ dB}$.

REFERENCES

- [1] S. M. Kay, *Estimation Theory*, ser. Fundamentals of Statistical Signal Processing. Upper Saddle River: Prentice Hall, 1993, vol. 1.
- [2] U. Siart, S. Tejero, and J. Detlefsen, "Exponential modelling for mutual-cohering of subband radar data," in *Review of Radio Science*. Miltenberg, Germany: U.R.S.I., 2005, scheduled to be published.
- [3] Y. Bresler and A. Macovski, "Exact maximum likelihood parameter estimation of superimposed exponential signals in noise," *IEEE Trans. Acoust., Speech, Signal Processing*, vol. ASSP-34, no. 5, pp. 1081–1089, October 1986.
- [4] Y. T. Chan, J. M. M. Lavoie, and J. B. Plant, "A parameter estimation approach to estimation of frequencies of sinusoids," *IEEE Trans. Acoust., Speech, Signal Processing*, vol. ASSP-29, pp. 214–219, April 1981.
- [5] P. Stoica, R. L. Moses, B. Friedlander, and T. Sørderstrøm, "Maximum likelihood estimation of the parameters of multiple sinusoids from noisy measurements," *IEEE Trans. Acoust., Speech, Signal Processing*, vol. ASSP-37, pp. 378–392, March 1989.
- [6] R. Bamler, "Doppler frequency estimation and the cramer-rao bound," *IEEE Trans. Geosci. Remote Sensing*, vol. GRS-29, no. 3, pp. 385–390, May 1991.
- [7] P. Stoica and A. Nehorai, "MUSIC, maximum likelihood and cramer-rao bound," *IEEE Trans. Acoust., Speech, Signal Processing*, vol. ASSP-37, pp. 720–741, May 1989.
- [8] B. Friedlander, "On the computation of the cramer rao bound for ARMA parameter estimation," in *Proc. IEEE Int. Conf. on Acoustics, Speech and Signal Processing. ICASSP 84*, vol. 1, New York, 1984.